Institut für Geowissenschaften
Mathematisch-Naturwissenschaftliche Fakultät
Universität Potsdam

Kumulative Dissertationsschrift

Hercynian to Eocimmerian Evolution of the North Pamir in Central Asia

zur Erlangung des akademischen Grades

doctor rerum naturalium

»Dr. rer. nat.«

Eingereicht durch

Johannes Rembe, MSc

im Fachbereich Geowissenschaften

Eingereicht an der
Mathematisch-Naturwissenschaftlichen Fakultät
der Universität Potsdam

Potsdam, im Dezember 2022

Advisors

Prof. Edward R. Sobel, PhD University of Potsdam, Germany
Prof. Dr. Jonas Kley Georg-August University of Göttingen, Germany

Reviewers

Prof. Edward R. Sobel, PhD University of Potsdam, Germany
Prof. Alexander C. Robinson, PhD; Univeristy of Houston
Prof. Dr. Guido Meinhold; Technische Universität Bergakademie Freiberg

Published online on the
Publication Server of the University of Potsdam:
https://doi.org/10.25932/publishup-59751
https://nbn-resolving.org/urn:nbn:de:kobv:517-opus4-597510

Eidesstattliche Erklärung

Hiermit erkläre ich, dass ich die kumulative Dissertation ”Hercynian to Eocimmerian Evolution of the North Pamir in Central Asia” selbstständig verfasst und keine anderen, als die von mir angegebenen Quellen und Hilfsmittel genutzt habe. Die Stellen der Dissertation, die anderen Quellen entnommen wurden, sind durch Angaben der Herkunft kenntlich gemacht.
Bereits in einer Fachzeitschrift publizierte Teile der Dissertation sind als solche kenntlich gemacht. Ich erkläre weiterhin, dass die Dissertation bisher nicht in dieser oder anderer Form in einem anderen Prüfungsverfahren vorgelegt wurde.

Declaration of Authenticy

I herewith declare that I wrote this thesis on my own and did not use any unnamed sources or aid. Thus, to the best of my knowledge and belief, this thesis contains no material previously published or written by another person except where due reference is made by correct citation. This includes any thoughts taken over directly or indirectly from printed books and articles as well as all kinds of online material. It also includes my own translations from sources in a different language. I agree that the thesis may be tested for plagiarized content with the help of plagiarism software. I am aware that failure to comply with the rules of good scientific practice has grave consequences and may result in expulsion from the programme.

Potsdam, den…… ……..

Johannes Rembe, MSc

List of Abbreviations

σ	Sigma, standard deviation
σ(prop)	standard deviation with propagated systematic uncertainties
CA	Chemical abrasion
CL	Cathodoluminescence
d	Discordance
DI	Diiodomethane
EDX	Energy-dispersive x-ray spectroscopy
GFZ	German Research Centre for Geosciences
ICP-AES	Inductively coupled plasma atomic emission spectroscopy
ICP-MS	Inductively coupled plasma mass spectrometry
ID	Isotope dilution
IUGS	International Union of Geological Sciences
KDE	Kernel density estimation
KI	Kübler Index
LA	Laser ablation
LIP	Large igneous province
Ma	Million years before present
MDS	Multi dimensional scaling
MSWD	Mean squared weighted distances
Myr	Million years (time span)
NIST 614	Glass standard of the National Institute of Standards and Technology, USA
SEM	Scanning electron microscope
SHRIMP	Sensitive high resolution ion microprobe
SIMS	Secondary ion mass spectrometry
SPT	Sodium polytungstate
TIMS	Thermal ionization mass spectrometry
UP	University of Potsdam
UQ	The University of Queensland
UV	Ultraviolet
XRD	X-ray diffraction
XRF	X-ray fluorescence

Table of Contents

List of Figures

List of Tables

Abstract

The North Pamir, part of the India-Asia collision zone, essentially formed during the late Paleozoic to late Triassic–early Jurassic. Coeval to the subduction of the Turkestan ocean—during the Carboniferous Hercynian orogeny in the Tien Shan—a portion of the Paleo-Tethys ocean subducted northward and lead to the formation and obduction of a volcanic arc. This Carboniferous North Pamir arc is of Andean style in the western Darvaz segment and trends towards an intraoceanic arc in the eastern, Oytag segment. A suite of arc-volcanic rocks and intercalated, marine sediments together with intruded voluminous plagiogranites (trondhjemite and tonalite) and granodiorites was uplifted and eroded during the Permian, as demonstrated by widespread sedimentary unconformities. Today it constitutes a major portion of the North Pamir.

In this work, the first comprehensive Uranium-Lead (U-Pb) laser-ablation inductively-coupled-plasma mass-spectrometry (LA-ICP-MS) radiometric age data are presented along with geochemical data from the volcanic and plutonic rocks of the North Pamir volcanic arc. Zircon U-Pb data indicate a major intrusive phase between 340 and 320 Ma. The magmatic rocks show an arc-signature, with more primitive signatures in the Oytag segment compared to the Darvaz segment. Volcanic rocks in the Chinese North Pamir were indirectly dated by determining the age of ocean floor alteration. We investigate calcite filled vesicles and show that oxidative sea water and the basaltic host rock are major trace element sources. The age of ocean floor alteration, within a range of 25 Ma, constrains the extrusion age of the volcanic rocks. In the Chinese Pamir, arc-volcanic basalts have been dated to the Visean-Serpukhovian boundary. This relates the North Pamir volcanic arc to coeval units in the Tien Shan. Our findings further question the idea of a continuous Tarim-Tajik continent in the Paleozoic.

From the Permian (Guadalupian) on, a progressive sea-retreat led to continental conditions in the northeastern Pamir. Large parts of Central Asia were affected by transcurrent tectonics, while subduction of the Paleo-Tethys went on south of the accreted North Pamir arc, likely forming an accretionary wedge, representing an early stage of the later Karakul-Mazar tectonic unit. Graben systems dissected the Permian carbonate platforms, that formed on top of the uplifted Carboniferous arc in the central and western North Pamir. A continental graben formed in the eastern North Pamir. Zircon U-Pb dating suggest initiation of volcanic activity at ~260 Ma. Extensional tectonics prevailed throughout the Triassic, forming the Hindukush-North Pamir rift system. New geochemistry and zircon U-Pb data tie volcanic rocks, found in the Chinese Pamir, to coeval arc-related plutonic rocks found within the Karakul-Mazar arc-accretionary complex. The sedimentary environment in the continental North Pamir rift evolved from an alluvial plain, lake dominated environment in the Guadalupian to a coarser-clastic, alluvial, braided river dominated in the Triassic. Volcanic activity terminated in the early Jurassic. We conducted Potassium-Argon (K-Ar) fine-fraction dating on the Shala Tala thrust fault, a major structure

juxtaposing Paleozoic marine units of lower greenschist to amphibolite facies conditions against continental Permian deposits. Fault slip under epizonal conditions is dated to 204.8 ± 3.7 Ma (2σ), implying Rhaetian nappe emplacement. This pinpoints the Central–North Pamir collision, since the Shala Tala thrust was a back-thrust at that time.

Zusammenfassung

Der Nordpamir, ein Teil der Kollisionszone zwischen Indien und Asien, bildete sich im Wesentlichen zwischen dem oberen Paläozoikum und der Trias–Jura Grenze. Zeitgleich mit der Subduktion des Turkestan-Ozeans—während der herzynischen Orogenese im heutigen Tien-Shan-Gebirge—subduzierte ein Teil der Paläotethys. Dies führte im Verlauf des Karbons zur Bildung und im Perm zur Obduktion eines Vulkan- bzw. Inselbogens. Dieser karbonische Vulkanbogen des Nordpamirs kann in einen westlichen Teil mit andinem Aufbau (Darvaz-Segment) und einen intraozeanischen östlichen Teil (Oytag-Segment) eingeteilt werden. Eine Abfolge aus Vulkaniten und zwischengeschalteten, marinen Sedimenten, zusammen mit in diese Folge intrudierten Plagiograniten (Trondhjemit und Tonalit) sowie Granodioriten, wurde während des Perms gehoben und erodiert. Dies wird durch weit verbreitete Sedimentationslücken im Nord Pamir belegt.

In dieser Arbeit werden erstmals umfassende Uran-Blei Isotopen (U-Pb) Altersdaten (basierend auf Laserablation mit induktiv gekoppeltem Plasma-Massenspektroskopie) und geochemische Daten der Vulkanite und Plutonite des karbonischen Vulkanbogens des Nordpamirs präsentiert. Die U-Pb Zirkonalter zeigen für die Plutonite eine Hauptintrusionsphase zwischen 340 Ma und 320 Ma. Sowohl die untersuchten Vulkanite als auch die Plutonite zeigen eine Inselbogensignatur. Dabei weisen die Magmatite des östlichen Oytag-Segmentes primitivere geochemische Eigenschaften als gleichalte Gesteine des Darvaz-Segmentes auf. Um das Alter der kaum datierten mafischen Vulkanite des Inselbogens genauer eingrenzen zu können, wurden während der Ozeanbodenmetamorphose gebildete Kalzite untersucht. Ausgehend von der Annahme, dass die in Hohlräumen der Basalte ausgebildeten Sekundärminerale in einem Zeitraum von etwa 25 Ma nach dem Austreten der Vulkanite entstehen, weisen diese auf ein viséisches bis serpukhovisches Alter hin. Oxidatives Meerwasser und das basaltische Umgebungsgestein sind dabei Quellen der in den Kalziten eingebauten Spurenelemente. Die Untersuchungsergebnisse stellen eine geodynamische Beziehung des Vulkanbogens des Nordpamirs mit gleichalten Inselbogenkomplexen des Tien-Shan her. Des Weiteren stellen sie die Kontinuität kontinentaler Kruste zwischen Tarim und Karakum-Kraton im Paläozoikum in Frage.

Ab dem Perm setzte ein fortschreitender Rückzug des Meeres in der Region ein. Dies führte zu Erosion und kontinentalen Ablagerungsbedingungen im nordöstlichen Pamir spätestens ab dem Guadalupium (oberes Mittelperm). Das tektonische Regime Zentralasiens wurde im Perm durch Transversalverschiebungen und damit einhergehender Transpressions- und Transtensionstektonik bestimmt. Gleichzeitig dauerte die Subduktion der Paleotethys in Richtung Norden an. Dabei bildete sich schon im Perm ein Akkretionskeil—ein frühes Stadium des kimmerisch geprägten Karakul-Mazar Komplexes. Während des Perms zerschnitten Grabenstrukturen Teile der Karbonatplattform im zentralen und westlichen Nordpamir und formten ein kontinentales Grabensystem im nordöstlichen Pamir. Neue U-Pb Altersuntersuchungen an Zirkonen zeigen ein

Einsetzen vulkanischer Aktivität vor etwa 260 Ma. Dehnungstektonik war auch während der Trias vorherrschend. Infolgedessen entwickelte sich das Hindukusch-Nordpamir-Rift-System. Zirkon U-Pb Altersdaten und Gesamtgesteinsgeochemie der triassischen Vulkanite der Riftbeckenablagerungen im Chinesischen Nordpamir stellen einen engen Zusammenhang zu zeitgleich intrudierenden, triassischen Plutoniten des Karakul-Mazar Akkretionskeils her. Das Ablagerungsmilieu des untersuchten Abschnitts des kontinentalen Beckens war im Guadalupium durch Schwemmebenen und Seen bestimmt. Es entwickelte sich zu einem von gröber-klastischen Schwemmfächern dominierten Ablagerungsraum während der Trias. Die vulkanische Aktivität endete während des Trias-Jura Übergangs.

Kalium-Argon (K-Ar) Altersdatierungen an Ton-Feinfraktionen einer großen Deckenüberschiebung (Shala-Tala-Überschiebung) belegen eine teilweise Schließung des nordöstlichen Hindukusch-Nordpamir-Riftbeckens in der ausgehenden Trias. Entlang der Shala-Tala-Überschiebung werden Paleozoische, marine Sedimentgesteine der unteren Grünschiefer- bis Amphibolitfazies gegen anchizonale, kontinentale Ablagerungen des Perms versetzt. Überschiebungsbewegungen unter epizonalen Bedingungen werden auf 204.8 ± 3.7 Ma (2σ) datiert. Dies gibt einen genauen Zeitmarker für die Kollision von Zentral und Nord Pamir, da sich ab diesem Zeitpunkt große Rücküberschiebungen bilden konnten.

Allgemeinverständliche Zusammenfassung

Das Pamirgebirge in Zentralasien bildet mit dem Hochland von Tibet das größte Gebirgsplateau der Erde. Seine Entstehungsgeschichte wirft noch immer viele Fragen auf. Am Nordrand des Pamirgebirges befindet sich der Nordpamir. In diesem Gebiet schieben sich noch heute Gesteine des Erdaltertums und Erdmittelalters über Gesteine der Erdneuzeit und bilden dabei Gebirgsketten von mehr als 7000 Metern höhe. Diese Gebirgsbildung wird durch die, seit der mittleren Erdneuzeit, vor etwa 50 Millionen Jahren, andauernde Nordwärtsbewegung der indischen Kontinentalplatte verursacht. Um ein besseres Verständnis der bis heute andauernden Vorgänge in der Erdkruste des Pamirs zu erreichen, ist eine genaue Kenntnis des Aufbaus der beteiligten Erdkrustenblöcke notwendig. In dieser Arbeit untersuche ich die Entstehungsgeschichte des Nord Pamirs.

Die dafür unternommenen Untersuchungen konzentrierten sich auf die genaue Erfassung der Alter und der chemischen Zusammensetzung von magmatischen Gesteinen. Die chemischen Signaturen der magmatischen Gesteine lassen sich auf gut untersuchte Prozesse im Erdinneren zurückführen und erlauben eine recht genaue Einordnung zu einer plattentektonischen Situation. Diese wird dann mit dem Alter der Gesteinsprobe verbunden und lässt so eine Abfolge von erdgeschichtlichen Prozessen erkennen.

Die Untersuchungen des Nord Pamirs ergaben eine devonisch/ karbonische bis triassische Entstehungsgeschichte, welche den Zeitraum von vor 360 bis vor etwa 200 Millionen Jahren umfasst. Zunächst bildete sich durch das Abtauchen ozeanische Kruste im Paleotethys Ozean ab dem späten Devon ein vulkanischer Inselbogen, vergleichbar mit Inselbögen im heutigen Westpazifik. Vor etwa 340 bis 320 Millionen Jahren kristallisierten aufsteigende magmatische Schmelzen als Granite in der Kruste des Inselbogens. Im späten Karbon stieß der Inselbogen mit dem asiatischen Kontinent zusammen und wurde im Perm teilweise über die Wasseroberfläche gehoben und erodiert. Damit war die Basis für den heutigen Nordpamir gelegt. Kalkbildende Organismen produzierten auf dem von flachem Meer bedeckten, vulkanisch inaktiven Nordpamir-Inselbogen mächtige Kalksteinschichten. Die ozenanische Krustenplatte wurde nun weiter südlich unter den asiatischen Kontinent gedrückt. Damit verbundene Dehnungsbewegungen führten bereits im mittleren Perm, vor etwa 260 Millionen Jahren, zum zerbrechen der Karbonatplattformen und zur Bildung von Grabenbrüchen. Diese Grabenbildung ist mit dem Aufstieg von Magma verbunden, welches an der Oberfläche Vulkangestein bildete.

Der Magmatismus hielt bis in die Trias an. Im östlichen Nordpamir bildeten sich zu dieser Zeit verzweigte Flußsysteme, wärend im westlichen Nordpamir ein flaches Meer existierte. Vor etwa 205 Millionen Jahren schloß sich das Grabensystem teilweise, die Phase des aktiven Vulkanismus endete, und metamorphe Gesteine wurden aus 20 bis 30 Kilometern Tiefe an die Oberfläche gedrückt. Zu dieser Zeit stieß der Kontinentalblock des Zentralpamirs mit dem Nordpamir zusammen. Es bildete sich das Cimmerische Gebirge.

Preface

Long before I started to study the Geology of Central Asia, I was fascinated by the thousands of years old history of this cultural melting pot. Along the Silk Road(s), which crossed the region, people and goods once moved from east to west and vice versa. This led to an incredibly rich cultural heritage, today still visible in ancient buildings, in the local traditions, in food and clothing.

During my research I got more interested in this region and followed events happening in the past years. With great concern, I read about the developments in Afghanistan, that lead to a big distress among the people there. It is nearly impossible for me to envision the grief of generations that hoped for a prosperous future.

Likewise, the news from the Xinjiang Uygur Autonomous Region left me in anger and disbelief. How can an entire ethnic group be put under general suspicion? Here, a large group of people is being denied basic human rights. Systematic cultural reeducation and destruction of cultural and religious heritage sites cannot be right.

I have the sincere hope that one day people will be able to accept cultural differences, and that all oppressed ethnic groups of the region will be able to live in freedom and prosperity.

I dedicate this work to the people of Central Asia.

Publications and Author Contributions

This thesis is composed of four studies, published, or intended to be published in peer-reviewed journals. Chapters 2–4 are comprised of peer-reviewed and published studies; Chapter 5 is prepared as a manuscript. Chapter 1 forms the introduction; Chapter 6 synthesizes the results of Chapters 2–5 into a geodynamic history of the North Pamir. Throughout the thesis I will refer to the below listed Chapters instead of the publications.

Chapter 2. The Carboniferous Arc of the North Pamir

Johannes Rembe, Edward R. Sobel, Jonas Kley, Renjie Zhou, Rasmus Thiede, and Jie Chen

All authors contributed to the conceptualization of the study. Johannes Rembe, Edward R. Sobel, Jonas Kley, Rasmus Thiede and Jie Chen did fieldwork and sampling during several field campaigns. Renjie Zhou and Johannes Rembe planned and carried out analytical work. Drafting of the manuscript was done by Johannes Rembe. The text was refined by contributions from all authors. The manuscript was published in the peer-reviewed journal Lithosphere:
Rembe, J., Sobel, E.R., Kley, J., Zhou, R., Thiede, R., and Chen, J., 2021, The Carboniferous Arc of the North Pamir: Lithosphere, v. 2021, no. 1, doi: 10.2113/2021/6697858.

Chapter 3 Calcite U-Pb dating of altered ancient oceanic crust in the North Pamir

Johannes Rembe, Renjie Zhou, Edward R. Sobel, Jonas Kley, Jie Chen, Jian-Xin Zhao, Yuexing Feng, and Daryl L. Howard

Johannes Rembe, Renjie Zhou and Edward R. Sobel conceptualized the study. Johannes Rembe, Edward R. Sobel, Jonas Kley, and Jie Chen conducted fieldwork and sampling. Renjie Zhou, Johannes Rembe, Jian-Xin Zhao, Yuexing Feng, and Daryl L. Howard planned and carried out analytical work. Drafting of the manuscript was done by Johannes Rembe. The text was refined by contributions from Renjie Zhou, Edward R. Sobel and Jonas Kley. The manuscript was published in the peer-reviewed journal Geochronology:
Rembe, J., Zhou, R., Sobel, E.R., Kley, J., Chen, J., Zhao, J., Feng, Y., and Howard, D.L., 2022, Calcite U–Pb dating of altered ancient oceanic crust in the North Pamir, Central Asia: Geochronology, v. 4, no. 1, p. 227–250, doi: 10.5194/gchron-4-227-2022.

Chapter 4 Geochronology, Geochemistry, and Geodynamic implications of Permo-Triassic back-arc basin successions in the North Pamir, Central Asia

Johannes Rembe, Edward R. Sobel, Jonas Kley, Baiansuluu Terbishalieva, Antje Musiol, Jie Chen, and Renjie Zhou

Johannes Rembe, Edward R. Sobel and Jonas Kley conceptualized the study. Johannes Rembe, Edward R. Sobel, Jonas Kley, and Jie Chen conducted fieldwork and sampling. Renjie Zhou, Johannes Rembe, Baiansuluu Terbishalieva and Antje Musiol planned and carried out analytical work. Drafting of the manuscript was done by Johannes Rembe. The text was refined by contributions from Renjie Zhou, Edward R. Sobel, Baiansuluu Terbishalieva and Jonas Kley. The manuscript was published in the peer-reviewed journal Lithosphere:

Rembe, J., Sobel, E.R., Kley, J., Terbishalieva, B., Musiol, A., Chen, J., and Zhou, R., 2022, Geochronology, Geochemistry, and Geodynamic Implications of Permo-Triassic Back-Arc Basin Successions in the North Pamir, Central Asia: Lithosphere, v. 2022, no. 1, doi: 10.2113/2022/7514691.

Chapter 5. Evolution of the Pre-Cimmerian Paleo-Asian margin deduced from detrital zircon U-Pb data from the Qimgan volcano-sedimentary section (NE Pamir) and constraints for Late Triassic closure of a Cimmerian back-arc basin

Johannes Rembe, Edward Sobel, Jonas Kley, Renjie Zhou, Klaus Wemmer, Jie Chen

The study was conceptualized by Johannes Rembe, Edward R. Sobel and Jonas Kley. Johannes Rembe, Edward R. Sobel, Jonas Kley, and Jie Chen conducted fieldwork and sampling. Renjie Zhou, Klaus Wemmer and Johannes Rembe planned and carried out analytical work. Drafting of the manuscript was done by Johannes Rembe. The text was refined by contributions from all authors. The manuscript is ready to be submitted to a peer-reviewed journal.

Potsdam, …… …….

Date Signature principal advisor/ Unterschrift Hauptbetreuer

Acknowledgements

First, I want to express my gratitude to my supervisors Edward R. Sobel and Jonas Kley. They fully supported my research during the past years. I am thankful for our motivating discussions, that broadened my view each time and made me think in different directions. They, and all the other co-authors taught me a lot about scientific writing, they improved my English and showed me how to design a research study.

I explicitly want to thank my colleagues Martin Timmermann, Rasmus Thiede, and Konstanze Stübner for scientific discussions; I learned a lot from you.

A special thanks goes to Renjie Zhou, who gave me the opportunity to step into the field of Uranium-Lead dating. You made me feel welcome during my stay at The University of Queensland, Brisbane (UQ), and supported me so much during the analysis and evaluation of the LA-ICP-MS data. I likewise thank the team of the Radiogenic Isotope Facility Lab at UQ for their work and assistance.

For help in the field, I want to thank Langtao Liu, Jie Chen and Lu Chi, who made fieldwork possible. During the laboratory work I got a lot of support by Antje Musiol, Christina Günther and Baiansuluu Terbishalieva. I want to thank you, too, for your commitment!

Of course, I would not have managed to do this PhD without the motivating people I met during the past 14 years, since I started my career as a geologist. Being aware that I cannot list all of them here, I want to express my gratitude to my teachers Olaf Elicki, Christoph Breitkreutz, Lothar Ratschbacher, and Uwe Kroner from TU Bergakademie Freiberg, Andrea Di Giulio, and Pier Luigi Vercesi from Uni Pavia, and Milan Nowák from MU Brno for their support and motivation during my student career. Probably without knowing, you brought me back on track when I was about to lose my fascination for geology.

The people who supported me most during this long journey have been and are my friends and my beloved family. Your sympathy means a lot to me! Thank you all!

Chapter 1. Introduction

1.1 Overview

The initial goal of my work in the North Pamir was to do thermochronology and structural field mapping, construct balanced cross-sections through the Chinese North Pamir, and to connect them with thermochronological data to set time constraints and establish a detailed cooling—hence an uplift history. I was able to do a first field season in 2017, where I focussed on the poorly studied Palaeozoic to Mesozoic strata. Further field work was hindered by the restricted access to the Xinjiang Uyghur Autonomous Region from early 2018 onwards. So, I had to rephrase the research question and focussed more on the pre-Cenozoic evolution. My own set of samples were complemented by samples, provided to me by Edward Sobel and Rasmus Thiede, which they had collected on individual field seasons to the Chinese, Kyrgyz and Tadjik North Pamir in previous years. Those samples were collected predominantly for thermochronology, but field documentation, and sample size was sufficient to do geochemistry and mineral separates for U-Pb dating were available. A DAAD grant allowed me to start a collaboration with The University of Queensland, where I had the great opportunity to perform Laser-Ablation U-Pb dating under the supervision of Renjie Zhou. Further, I had the opportunity to do extensive geochemical work, including sample processing and preparation at the University of Potsdam under the supervision of Antje Musiol and Christina Günther. I also had the chance to do Potassium-Argon (K-Ar) dating at the Georg-August University of Göttingen under the supervision of Klaus Wemmer. We dated five samples, which were initially intended to be part of a much larger data set. All the aforementioned work resulted in three published manuscripts, presented in Chapter 2 to Chapter 4 and two unpublished manuscripts, of which one is presented in Chapter 5.

1.2 Central Asia—A Geopuzzle

The major geographic features of Central Asia are the extensive mountain belts, which form some of the highest peaks and the widest orogenic plateaus on earth. This region is inhabited by millions of people and—because of their active tectonic nature—are susceptible for geohazards but yield at the same time a high potential for resources. The modern topography is the result of the Cenozoic India-Asia collision, which affects a wide belt, spanning thousands of kilometres from the Himalayan mountain front to the Baikal rift in Siberia. The continental crust of Central Asia is very heterogenous, resulting from terrane and volcanic arc accretion to Proterozoic cratons, ongoing since the late Precambrian (e.g., Sengör *et al.,* 2018). Fault zones, tectonically active during the past, formed along weak zones in the crust, and were exploited by Cenozoic deformation. Studying the structure and evolution of this Geopuzzle of relatively inert blocks and intervening, repeatedly reactivated tectonic zones expands our knowledge about past and present

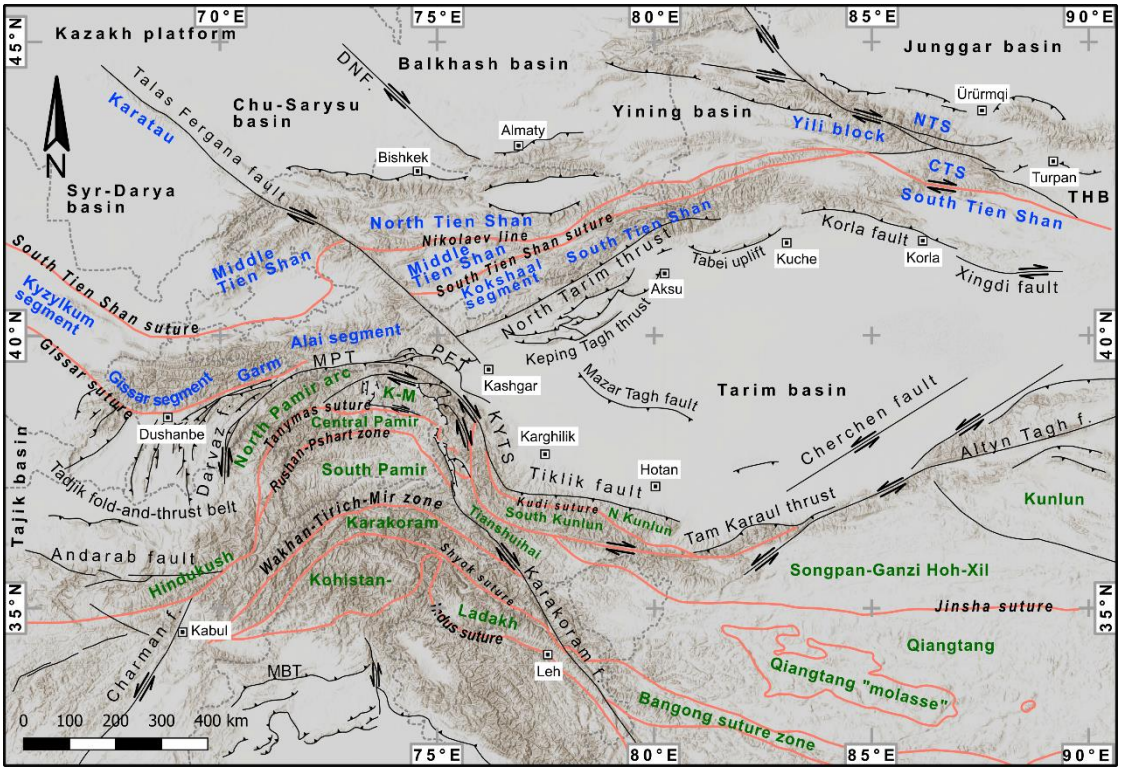

Figure 1: Geotectonic units of the Himalaya-Tibetan orogenic system and the Tien Shan. Units of the Tien Shan are in blue, units of the Pamir are labelled in green. Intervening sutures are marked in red, principle faults are marked in black; symbology of fault kinematic follows the conventional labeling. Structures are compiled from literature (Amidon & Hynek, 2010; Wang et al., 2011; Pelsmaeker et al., 2018; Kapp & DeCelles, 2019; Wu et al., 2019; Li et al., 2020). For a review of circum-Tarim Cenozoic faults see Laborde et al. (2019). Abbreviations—MPT–Main-Pamir-Thrust, PFT–Pamir-Frontal-Thrust, KYTS–Kashgar-Yesheng-Transfer-System, MBT–Main-Boundary-Thrust, K-M–Karakul-Mazar, CTS–Central Tien Shan, NTS–North Tien Shan, DNF–Dzhalair–Naiman fault.

geodynamics and provides a basis for the exploration of resources and the prediction of geohazards. From a first glance, the topography and structures of Central Asia (Figure 1) appear to be built up by several blocks, covered by wide sedimentary basins, with intervening orogenic belts and plateaus. The Tibetan orogenic plateau is rimmed by vast mountain belts, such as the Himalaya and Kunlun mountains. From geophysical data the exceptionally thick continental crust under the plateau, compared to the adjacent mountain chains, is visible (Figure 2). The present-day western end of the Tibetan Plateau is formed by the Pamir salient. Its evolution has to be seen in a broad context with the surrounding geotectonic units. To the east it is bordered by the cratonic Tarim block, to the north the Pamir interacts with the Tien Shan and the enigmatic Alai block. To the west, the Tajik basin and its fold-and-thrust belt form the foreland of the Pamir salient. The Pamir is historically subdivided into three principle units: (1) The North Pamir, consisting of anchizonal Carboniferous volcanic and plutonic rocks, Permo-Mesozoic sediments, and the higher metamorphic-grade Karakul-Mazar arc-accretionary complex, build up of meta-sediments and Mesozoic plutons.

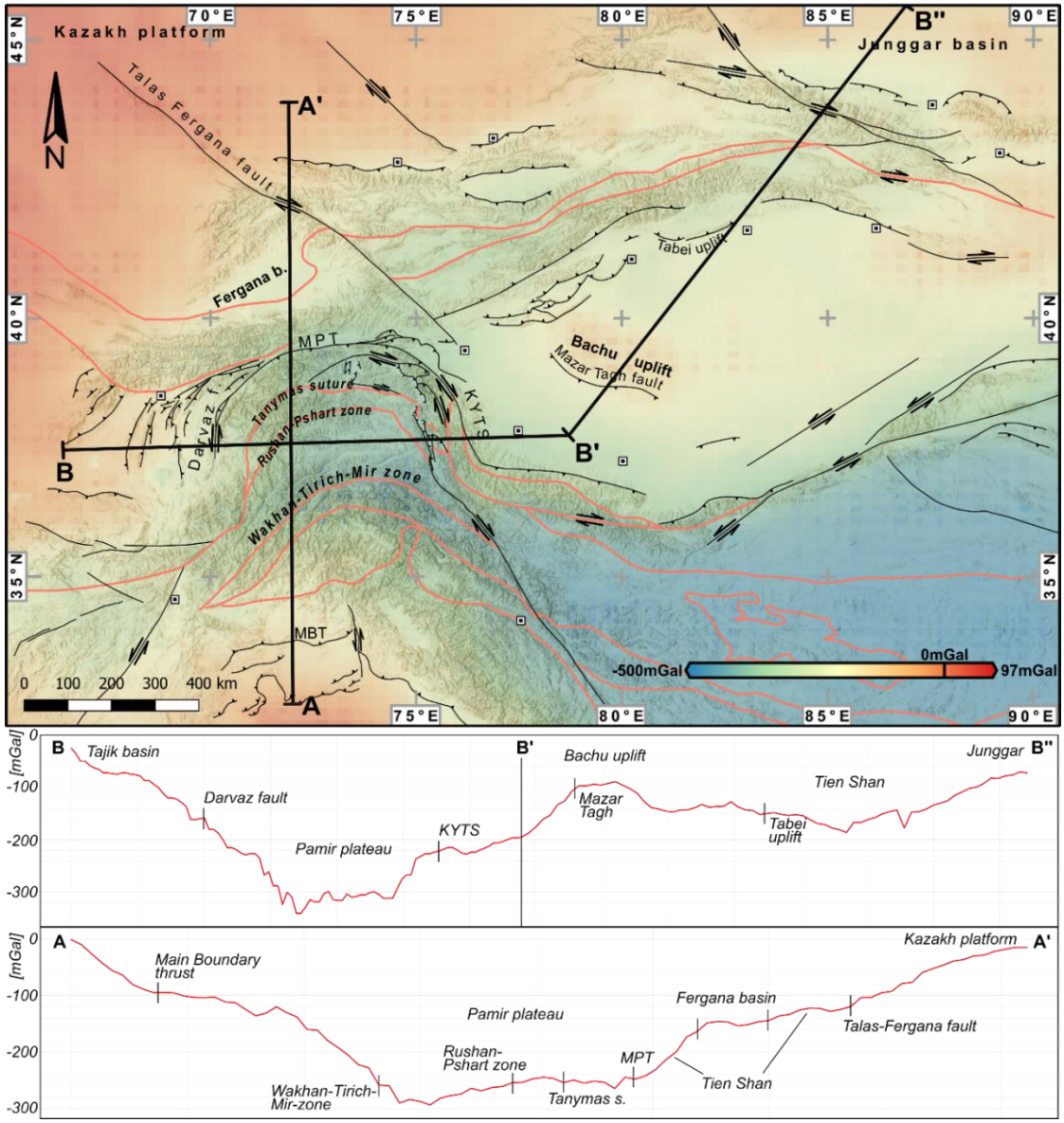

Figure 2: Bouguer anomaly map with superimposed shaded relief. It shows high values of up to 97 mGal (red) over the sedimentary basins of the Kazakh platform and values as low as -500mGal (blue) over the orogenic plateaus. High values (red) are the result of relatively thin continental crust and a shallow Moho, compared with the low values (blue) in Tibet and the Pamir that show the presence of a thickened orogenic root depressing the crust-mantle transition. The thickest continental crust on earth is found beneath the Andean and Pamir-Tibetan plateaus. Values in the Tien Shan are not much different from those in the Tarim basin. The Bouguer anomaly map is extracted from the World Gravity Map (WGM2012, Bonvalot et al., 2012), interpolated in QGis 3.2.1 (QGis Developer Team, 2018). Abbreviations—MPT–Main-Pamir-Thrust, KYTS–Kashgar-Yesheng-Transfer-System, MBT–Main-Boundary-Thrust.

(2) The Central Pamir, dominated by gneiss domes exhumed in the Cenozoic and overlying (meta-) sediments. (3) The South Pamir, like the Central Pamir, is dominated by Cenozoic gneiss domes and covering (meta-) sediments. The Central and South Pamir separated from the Gondwanan continent and drifted towards Paleo-Asia starting in the Permian (Schwab *et al.*, 2004; Angiolini *et al.*, 2013; Rutte *et al.*, 2017). Attempts to gain an understanding of the geological evolution of the Pamir date back to the beginning of the 20th Century (e.g., Rickmers, 1913; Finsterwalder *et al.*, 1932; Prynada, 1934; Nikolaev, 1936; Moskvin, 1937). Large advances, in

knowledge of the structural composition of the region, were first made by large scale geophysical surveys, focusing on gravimetric measurements and seismic tomography (e.g., Aliev *et al.*, 1976; Yusupkhodzhayev & Khasanov, 1978; Beloussov *et al.*, 1980; Zlavdinov, 1982; Desio & Poretti, 1991). An exceptionally low Bouguer gravity anomaly beneath the Pamir-Tibetan plateau (Figure 2) suggests a depression of the crust-mantle transition. These low gravity anomalies under the plateaus are confined by large-scale, Cenozoic fault zones. Early surveys revealed a crustal thickness of 55-65 km in the Pamir (as summarized in Aliev *et al.*, 1976). This and the complex structure of its slab(s) (e.g., Sippl *et al.*, 2013; Kufner *et al.*, 2016; Schneider *et al.*, 2019) made the Pamir an area of high research interest. Early on, the great similarity of geological features found in the Pamir and the Tibetan plateau have been noted (Molnar & Tapponnier, 1975; Bazhenov & Burtman, 1982; Sengör & Hsü, 1984; Burtman & Samygin, 2001). However, its remoteness and crosscutting political boundaries have complicated along-strike geological work.

The northern portion of the Pamir has been correlated with the West Kunlun (e.g., Burtman & Molnar, 1993; Matte *et al.*, 1996; Mattern *et al.*, 1996; Xiao *et al.*, 2003). The Gondwana-derived Central Pamir has been correlated with the Songpan-Ganzi unit (Yin & Harrison, 2000; Robinson *et al.*, 2004) or with the Qiangtang block (Schwab *et al.*, 2004). The South Pamir has been correlated with the Qiangtang block (Yin & Harrison, 2000; Robinson *et al.*, 2004) or was interpreted as an individual block without a correlative unit in Tibet (Schwab *et al.*, 2004). In more recent works, a correlation of the Karakul-Mazar unit, which is part of the traditional North Pamir, with the Songpan-Ganzi Hoh-Xil unit has been suggested (Robinson, 2009; Robinson *et al.*, 2012; Li *et al.*, 2020). Both regions comprise wide accretionary systems located to the north of the Cimmerian Tanymas-Jinsha suture zone. The geotectonic units to the south of this suture zone represent fragments of the Gondwanan continental margin, which drifted towards Paleo-Asia from the Permian on. Their collision with the Paleo-Asian margin in the late Triassic–early Jurassic marks the closure of the Paleo-Tethys ocean during the Cimmerian orogeny.

Based on the seemingly continuous Paleozoic-Mesozoic facies belts and suture zones, and led by the arcuate shape of the Pamir, about 300 km northward indentation of the Pamir salient with respect to the Tibetan plateau was postulated (Burtman & Molnar, 1993; Burtman, 2000). This indentation was interpreted to be caused by the northward advance of the Indian plate and successive intracontinental subduction since the India-Asia collision at 55 ± 10 Ma (Molnar & Tapponnier, 1975; Roecker, 1981; Hu *et al.*, 2016; Kufner *et al.*, 2016; Zheng & Wu, 2018; Li *et al.*, 2022). This theory has been challenged by recent findings which propose a pre-existent embayment in the Paleo-Asian southern margin (Chen *et al.*, 2018; Li *et al.*, 2020), and by the work presented in the following chapters. The doubts on the existence of a more or less straight southern Paleo-Asian margin prior to the India-Asia collision in the region of the present day Pamir, made up of a “cratonic Asia” Tajik-Tarim block, is further challenged by the documented magnitude of Cenozoic shortening along the supposedly 300km northward-thrusted Pamir salient.

Gągała *et al.* (2020) determined much smaller shortening amounts for the Tajik basin. They state that upper crustal shortening of ~ 170 km in the Tajik basin does not explain the slab length of ~300 km presented by Kufner *et al.* (2016). Shortening estimates of the Alai basin (~20 km, Coutand *et al.*, 2002) and the External Pamir in China (~40 km, Li *et al.*, 2019) likewise contradict the theory of hundreds of kilometers of Pamir indentation. Moreover, Kley *et al.* (2021) show that the geometry of the Main Pamir Thrust, exhuming the North Pamir, does not readily connect with the Pamir slab. Gągała *et al.* (2020) postulate a large amount of tectonic accretion of Tajik-Tarim continental crust into the North Pamir to explain the missing upper-crustal shortening on the seemingly down-going plate.

This brings up the question of the composition of the North Pamir, which we will address in Chapters 2–5.

1.3 The Carboniferous North Pamir Volcanic Arc

One facies girdle, postulated to be continuous from Northern Tibet into the North Pamir, is the Kunlun belt, which forms the northern margin of the Tibetan plateau. It is divided into the West Kunlun and the East Kunlun by the Altyn Tagh fault (Figure 1). This structure originated in the Mesozoic as a sinistral strike-slip fault with pulses of activity at 250–230 Ma, 165–160 Ma, and 100–89 Ma (40Ar/39Ar dating by Wang *et al.* (2005) and Arnaud *et al.* (2003)) and has been active from the Oligocene-earliest Miocene until the present (Yue *et al.*, 2001; Mériaux *et al.*, 2004; Zhang *et al.*, 2007; Elliott *et al.*, 2015). The West Kunlun formed during the early Paleozoic closure of the Proto-Tethys ocean, forming the Kudi-Qimanyute suture, which separates the North Kunlun terrane (a reworked portion of Tarim crust) from the South Kunlun metasedimentary sequence and the Tianshuihai block (e.g., Zhang *et al.*, 2018; Wang *et al.*, 2021; Zhu *et al.*, 2021). The Kudi ophiolite formed in a back-arc position during the Cambrian (e.g., Wang *et al.*, 2021) and the suture closed in the Silurian (e.g., Zhang *et al.*, 2018). The presence of Paleozoic intraoceanic pillow basalts and indicators of subduction processes in a volcanic arc, were invoked to explain lateral correlations with similar units of the North Pamir since an absolute age control on the North Pamir volcanic arc related rocks was sparse. It has been postulated that the Kudi suture zone, well described from the Kudi valley, south of the town of Karghilik, continues into the North Pamir, forming the “Paleozoic suture” or “Oytag-Kudi” suture (Burtman *et al.*, 1963; Burtman & Molnar, 1993; Pan, 1994; Xiao *et al.*, 2003).

In Chapter 2 and Chapter 3 we present and discuss geochronological and geochemical evidence for dissimilarity of the Paleozoic North Pamir compared to the West Kunlun. We emphasize the merits of generations of scientists working in the Tajik, Kyrgyz, and Chinese portions of the North Pamir and in the Western Kunlun; by compiling their findings we can set our results within a context with the complex geologic framework.

1.4 The Hindukush-North Pamir Rift System

A largely understudied component of the North Pamir are the volcano-sedimentary units of the Permo-Triassic. These units were deposited during a period between two large orogenic events affecting the North Pamir—the Hercynian accretion of the Carboniferous volcanic arc (see Chapter 2 and Chapter 3), and the Cimmerian orogeny in the late Triassic–early Jurassic (e.g., He *et al.*, 2019; Imrecke *et al.*, 2019). During the Carboniferous period marine conditions prevailed in large parts of Central Asia. Following the closure of the Turkestan ocean and the accretion of the Carboniferous North Pamir volcanic arc, continental sedimentary systems developed in the Tarim basin, while large parts of the North Pamir and the Hindukush remained under marine conditions (Burmakin *et al.*, 1961; Lyoskind *et al.*, 1963; Marushkin & Lyashkevich, 1969; Kafarsky & Pyjanov, 1970; Wolfart & Wittekindt, 1980; Leven *et al.*, 1992; Luchnikov, 2001; Zhao *et al.*, 2005; Leven, 2012; Zhu *et al.*, 2016). The North Pamir formed the southern margin of Asia at that time. Widespread volcanism demonstrates the active nature of this margin (Chapter 4 and Leven *et al.*, 1992; Liu & Wang, 2014; Salikhov & Sakiev, 2014). During this time an early Karakul-Mazar arc-accretionary wedge may have formed. However, the nature of the Permian volcanic activity in the North Pamir remains unclear.

During the Triassic, a more than 1000 km long region of back-arc basin extension and volcanism developed north of the Paleo-Tethys subduction zone, reaching from present day northeastern Iran (Aghdarband, e.g., Zanchetta *et al.*, 2013; Zanchi *et al.*, 2016; Balini *et al.*, 2019), through the Paropamisus and Afghan Hindukush (e.g., Hinze, 1964; Montenat, 2009; Siehl, 2017) into the North Pamir (Myntekin formation, Kyrgyz Altyn Darya valley, e.g., Luchnikov, 2001). In Chapter 4, we focus on the Permo-Triassic evolution of the North Pamir volcanic sequence. Geochemical data indicates a close relationship between the Triassic volcanism within the Karakul-Mazar arc-accretionary complex and the subduction of the Paleo-Tethys. Coeval, Permian post-Hercynian wrenching tectonics in the Tien Shan make a transtensional component of the back-arc opening likely. The Permo-Triassic continental sediments in the northeastern Pamir shows similarities with coeval Tarim sedimentary facies, as discussed in Chapter 5. In the Permo-Triassic sedimentary record of the North Pamir and the Hindukush, a continuous east to west sea-retreat is visible, with marine strata in the most parts of the North Pamir during the Permian, while erosion or non-deposition took place in the northeastern Pamir in the early Permian. In the late Guadalupian, following a lower Permian hiatus, the onset of continental-alluvial to lacustrine sedimentation in the northeastern Pamir, associated with intense mafic to intermediate volcanic activity may mark the initiation of rift basin formation. It has its equivalents in the western portions of the North Pamir, where marine strata is intercalated by volcaniclastic material during the mid-Permian (Leven *et al.*, 1992), and troughs start to dissect the Permian carbonate platforms (Hinze, 1964). During the Triassic, continental facies belts migrate further to the west, causing deposition of the continental Myntekin formation in Kyrgyzstan and the shallow marine to continental Doab

formation in Afghanistan. Phases of non-deposition or erosion during the Permian and Triassic (late Permian missing in NE Afghanistan (Wolfart & Wittekindt, 1980), and initiation of Triassic continental sedimentation during the Rhaetian in the Kyrgyz Myntekin formation (Luchnikov, 2001)) may be traced back to phases of subduction and roll-back, causing extension in the upper plate, and phases of subduction zone coupling or underplating, causing uplift and erosion in the upper plate. However, the discontinuous sedimentary record hinders a simple, lithostratigraphic correlation of along-strike units of the back-arc basin.

1.5 Aims and Scope

This work aims to give a holistic overview over the evolution of the North Pamir during the mid-Carboniferous to late Triassic. During this phase, two major orogenic events—the Hercynian and the Cimmerian orogeny—affected Central Asia. They essentially reshaped Asia`s southern margin and co-determined the geometry of the Cenozoic Alpine-Tibetan-Himalayan orogeny. The 4 following chapters focus on the Carboniferous (Chapter 2 and Chapter 3) and Permo-Triassic (Chapter 4 and Chapter 5) evolution of the present day North Pamir. New data is discussed in the light of pre-existing studies, which are laterally and temporally correlative. This results in a better understanding of the pre-Cenozoic (pre-India-Asia collision) constellation of the Asian crust in the Pamir. The definition of regional geotectonic entities and their correlation may facilitate a global understanding of the Alpine-Tibetan-Himalayan mountain belt and the role pre-existing features played during the India-Asia collision.

Chapter 2. The Carboniferous Arc of the North Pamir

2.1 Abstract

In this study we investigate the age and geochemical variability of volcanic arc rocks found in the Chinese, Kyrgyz, and Tajik North Pamir in Central Asia. New geochemical and geochronological data together with compiled data from the literature give a holistic view of an early to mid-Carboniferous intraoceanic arc preserved in the northeastern Pamir. This North Pamir volcanic arc complex involves continental slivers in its western reaches and transforms into a Cordilleran style collision zone with arc-magmatic rocks. These are hosted in part by Devonian to Carboniferous oceanic crust and the metamorphic Kurguvad basement block of Ediacaran age (maximum deposition age) in Tajikistan. We discuss whether a sliver of Carboniferous subduction related basalts and intruded tonalites close to the Chinese town of Mazar was part of the same arc. LA-ICP-MS U-Pb dating of zircons, together with whole rock geochemistry derived from tonalitic to granodioritic intrusions, reveal a major Visean to Bashkirian intrusive phase between 340 and 320 Ma ago. This clearly postdates Paleozoic arc-magmatic activity in the West Kunlun by ~100 Ma. This observation, along with geochemical evidence for a more pronounced mantle component in the Carboniferous arc-magmatic rocks of the North Pamir, disagrees with the common model of a continuous Kunlun belt from the West Kunlun into the North Pamir. Moreover, Paleozoic oceanic units younger than and west of Tarim cratonic crust challenge the idea of a continuous cratonic Tarim-Tajik continent beneath the Pamir.

2.2 Introduction

A common model for plate tectonic reconstructions of northern Tibet and the Pamir has been the assumption of a continuous magmatic belt extending from the West Kunlun into the northern Pamir (Burtman & Molnar, 1993; Pan, 1996). However, comparisons between the Paleozoic- early Mesozoic evolution of the poorly studied North Pamir and the adjacent, well-documented West Kunlun belt in northern Tibet reveal significant differences; these likely explain the different Cenozoic deformation styles of the adjacent regions. The Pamir orogen is the westward extension of the Tibetan Plateau. A common hypothesis is that the Pamir indented into the Tajik-Tarim basin in a late phase of the India-Asia collision, pushing the Pamir several hundred kilometers toward the north with respect to Tibet (e.g., Burtman and Molnar (Burtman & Molnar, 1993), Schwab et al. (Schwab *et al.*, 2004)). The Pamir and Tibet formed during the Phanerozoic as a result of successive accretions of Gondwana-derived crustal blocks. Today the Pamir and Tibet are part of the India-Asia collision zone — the largest active continental collision. At the longitude of the Pamir, the highest modern strain rates are found far to the north, along the Main Pamir Thrust (MPT) (Zubovich *et al.*, 2010; Perry *et al.*, 2019). In contrast, to the east, N–S shortening rates within northern Tibet are much smaller (Zhang *et al.*, 2004; Li *et al.*, 2016).

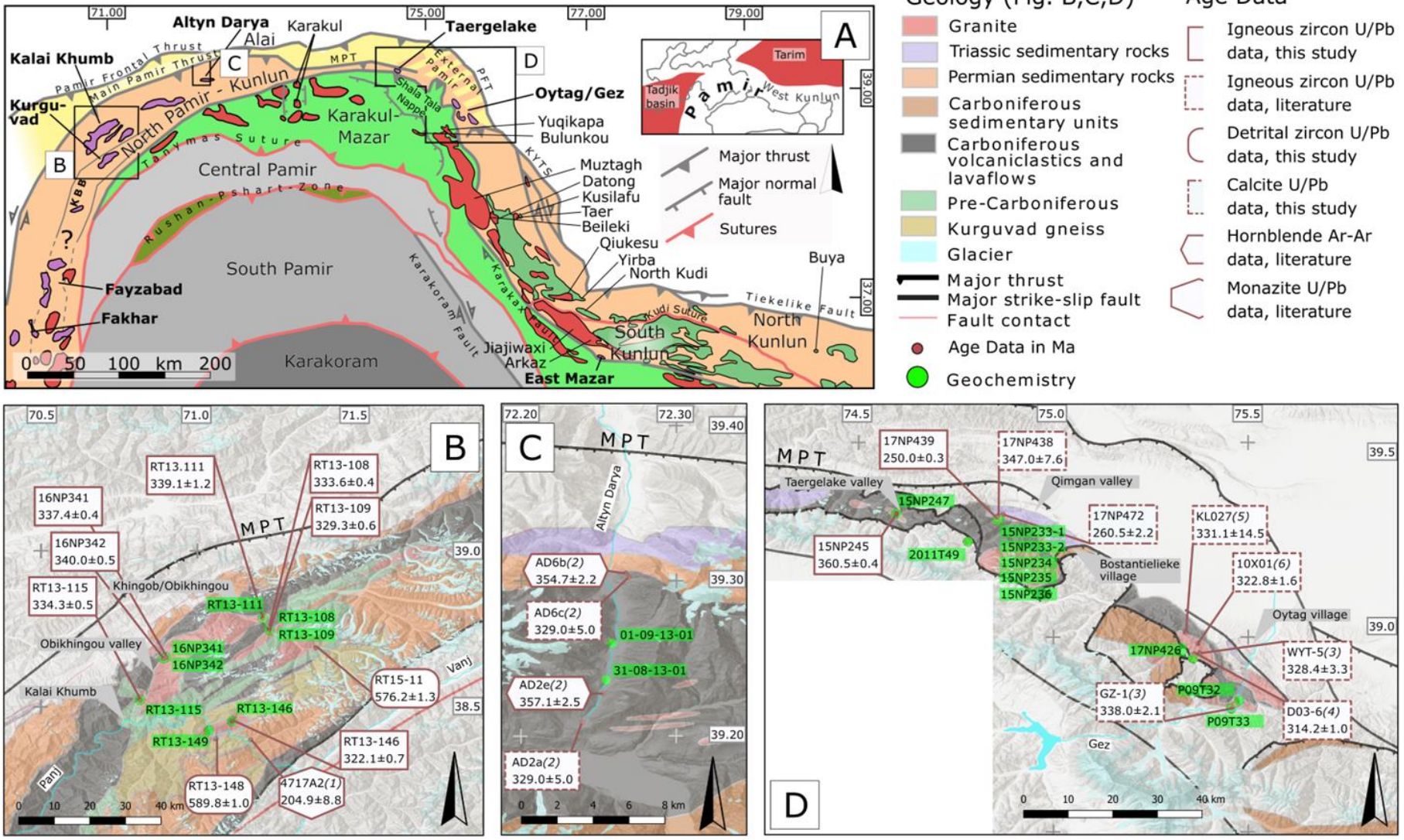
Altyn Darya
Alai
Karakul
Taergelake
Kalai Khumb
Kurgu-vad
Oytag/Gez
Yuqikapa
Bulunkou
Karakul-Mazar
North Pamir - Kunlun
Central Pamir
South Pamir
Muztagh
Datong
Kusilafu
Taer
Beileki
Qiukesu
Yirba
North Kudi
Buya
Fayzabad
Fakhar
Karakoram
Jiajiwaxi
Arkaz
East Mazar
South Kunlun
North Kunlun
Tarim
Tadjik basin
Pamir
West Kunlun
Major thrust
Major normal fault
Sutures
Geology (Fig. B,C,D)
Granite
Triassic sedimentary rocks
Permian sedimentary rocks
Carboniferous sedimentary units
Carboniferous volcaniclastics and lavaflows
Pre-Carboniferous
Kurguvad gneiss
Glacier
Major thrust
Major strike-slip fault
Fault contact
Age Data in Ma
Geochemistry
Age Data
Igneous zircon U/Pb data, this study
Igneous zircon U/Pb data, literature
Detrital zircon U/Pb data, this study
Calcite U/Pb data, this study
Hornblende Ar-Ar data, literature
Monazite U/Pb data, literature
MPT
Khingob/Obikhingou
Obikhingou valley
Kalai Khumb
Panj
Vanj
RT13.111 339.1±1.2
RT13-108 333.6±0.4
RT13-109 329.3±0.6
16NP341 337.4±0.4
16NP342 340.0±0.5
RT13-115 334.3±0.5
RT13-111
RT13-108
RT13-109
16NP341
16NP342
RT15-11 576.2±1.3
RT13-115
RT13-146
RT13-149
RT13-146 322.1±0.7
RT13-148 589.8±1.0
4717A2(1) 204.9±8.8
AD6b(2) 354.7±2.2
AD6c(2) 329.0±5.0
AD2e(2) 357.1±2.5
AD2a(2) 329.0±5.0
01-09-13-01
31-08-13-01
Altyn Darya
Taergelake valley
Qimgan valley
17NP439 250.0±0.3
17NP438 347.0±7.6
15NP247
15NP245 360.5±0.4
2011T49
15NP233-1
15NP233-2
15NP234
15NP235
15NP236
17NP472 260.5±2.2
KL027(5) 331.1±14.5
Bostantielieke village
10X01(6) 322.8±1.6
Oytag village
17NP426
WYT-5(3) 328.4±3.3
GZ-1(3) 338.0±2.1
P09T32
P09T33
D03-6(4) 314.2±1.0
Gez

Figure 3: Simplified map of the major tectonic units in the Pamir. Map (A) shows positions of outcrop areas in the Tajik (after Robinson (2015)) (B), Kyrgyz (C) and Chinese (D) North Pamir. Outcrop areas of Carboniferous granitoids (bold label, purple polygon) and early Paleozoic (green polygon) and Triassic (red polygon) granitoids mapped from literature are labelled. Sampling points for whole rock geochemistry samples processed for this study are marked with green boxes. Boxes with age data contain original and literature data. LA-ICP-MS Zircon U-Pb data is according to Table 2, column 5 in Ma ± 1σ. Further, Literature according to italic numbers in brackets: (1) Schmidt et al. (2011), (2) Schwab et al. (2004), (3) Jiang et al. (2008), (4) Ji et al. (2018), (5) Zhang et al. (2006), (6) Kang et al. (2015). (B) Map of the Tajik North Pamir between Panj and Obikhingou river valleys after Lyoskind et al. (1963); Vlasov et al. (1984); Burmakin et al. (1961); Kafarsky et al. Kafarsky & Pyjanov (1970). (C) Map of the Kyrgyz Alai Valley after Vlasov et al. Vlasov et al. (1984). (D) Map of the Chinese North Pamir between Gez and Taergelake river valleys by own mapping and Lu et al. Lu et al. (2013); Wang et al. Wang & Peng (2013); HIGS Henan Institute of Geological Survey (HIGS) (2014). Glacier polygons from GLIMS database (Raup et al., 2007). PFT—Pamir Frontal Thrust, MPT—Main Pamir Thrust, KBB—Kurguvad basement block, KYTS—Kashgar–Yesheng-Transfer-System.

The bulk of the convergence is accommodated, along the southern margin of Tibet, within the Himalaya. To understand the Cenozoic MPT and hence the difference between Pamir and Tibetan deformation styles, it is crucial to understand the pre-Cenozoic geologic evolution. The Pamir has traditionally been subdivided into the North, Central, and South Pamir terranes (Figure 3A). The North Pamir terrane was subdivided into the North Pamir Kunlun, which includes middle Paleozoic basalt, gabbro, and felsic plutons, and the North Pamir Karakul-Mazar terrane, which represents a late Paleozoic–early Mesozoic accretionary wedge intruded by felsic plutons (Schwab *et al.*, 2004; Robinson *et al.*, 2012). Despite strong deformation and fault dissection, the Chinese Gez valley is today the best-studied locality in the North Pamir. The Karakul-Mazar terrane was correlated with the Songpan-Ganzi Hoh-Xil complex of northern Tibet (Imrecke *et al.*, 2019), while the North Pamir Kunlun was correlated with the South Kunlun terrane of the West Kunlun in Tibet (e.g., (Matte *et al.*, 1996; Mattern *et al.*, 1996)). The West Kunlun is subdivided into the North and South Kunlun terranes, divided by the early Paleozoic Kudi suture. The North Kunlun corresponds to the margin of the Proterozoic Tarim block (Zhang *et al.*, 2013; Zhang *et al.*, 2018). This was described from the Kudi section, the best-studied section crossing the North and South Kunlun south of the town of Kargilik (Mattern *et al.*, 1996; Yuan *et al.*, 2002; Xiao *et al.*, 2003). However, there is little similarity between the North Pamir Kunlun and the South Kunlun terrane of the West Kunlun.

There is an ongoing debate about how and which units of the Tibetan Plateau/West Kunlun are the along-strike equivalent of units within the Pamir plateau. Two of those seemingly laterally contiguous structures — the Kudi-Oytag ophiolites and ophiolites along the Tanymas-Jinsha structure — were interpreted as the remnants of former suture zones related to the closure of the Proto- and Paleo-Tethys (Burtman & Molnar, 1993; Matte *et al.*, 1996; Mattern *et al.*, 1996; Pan, 1996; Mattern & Schneider, 2000; Schwab *et al.*, 2004). Based on this interpreted lateral continuity, estimates of the amount of largely Cenozoic northward indentation of the Pamir orogen, with respect to the Tibetan Plateau, were made (e.g. more than 300 km by Burtman and Molnar (Burtman & Molnar, 1993), 300–400 km by Burtman (Burtman, 2000)). Well-documented early Paleozoic magmatism, of either syn- or post-collisional nature, is thought to be related to the closure of the Proto Tethys along the Kudi suture zone (Wang *et al.*, 2002; Xiao *et al.*, 2005; Yuan *et al.*, 2005), which finally closed between 440 Ma (monazite U-Pb age of biotite schist from the Saitula group (Zhang *et al.*, 2018)) and 405 Ma (zircon U-Pb age of the A-type North Kudi Pluton (Yuan *et al.*, 2002)). This was followed by a Late Permian to Triassic intense magmatic phase related to the subduction of the Paleo Tethys and the collision of the Central Pamir-Qiangtang block with Asia (Yuan *et al.*, 2002; Xiao *et al.*, 2005; Huang *et al.*, 2013; Jiang *et al.*, 2013; Robinson, 2015), culminating in the formation of the Tanymas-Jinsha suture zone (Figure 3) between 243 Ma (zircon U-Pb age of anatectic Yuqikapa pluton (Jiang *et al.*, 2013)) and 190 Ma (metamorphic zircon U-Pb age population in amphibolite facies metasediments from Karakul-

Mazar accretionary complex (Robinson *et al.*, 2012)).A phase of volcanic quiescence has been proposed between the Silurian and Triassic in the NE Pamir and the West Kunlun (Xiao *et al.*, 2005; Zhang *et al.*, 2018).

In the North Pamir Kunlun, however, oceanic mafic to intermediate volcanic rocks and marine cherts of Upper Devonian to Bashkirian age (Pan, 1996; Schwab *et al.*, 2004; Lu *et al.*, 2013; Wang & Peng, 2013; Henan Institute of Geological Survey (HIGS), 2014) can be found. This narrow, ca. 400 km long zone (Figure 3A) spans from the Chinese Gez and Oytag (also called Wuyitake or Aoyitake) valleys (Zhang *et al.*, 2006; Jiang *et al.*, 2008; Kang *et al.*, 2015; Ji *et al.*, 2018) along the strike of the frontal Pamir mountain chain to the Tajik town of Kalai Khumb and continues into the northern reaches of the Hindu Kush/ Badakhchan region in Afghanistan (Burmakin *et al.*, 1961; Lyoskind *et al.*, 1963; Wolfart & Wittekindt, 1980; Bazhenov & Burtman, 1982). Oceanic rocks were assigned to the Kalai Khumb-Oytag basin (KOB), a marginal basin of the Paleo-Asian ocean (Burtman, 2010); this has also been named the Kunlun Arc (Schwab *et al.*, 2004) or the Pamir arc (Bazhenov & Burtman, 1982; Bazhenov & Burtman, 1986). Leucocratic granitoids, including tonalites and trondhjemites, are found as large intrusions within mafic volcanic rocks and are dated as Visean to Bashkirian (338–314 Ma (Zhang *et al.*, 2006; Jiang *et al.*, 2008; Kang *et al.*, 2015; Ji *et al.*, 2018)). These units are inferred to represent the remnants of an intraoceanic arc that marks a phase of intraoceanic subduction and the initial closure of an ocean basin (Jiang *et al.*, 2008). Granitoids in NW Afghanistan also intrude lower Carboniferous marine strata and yield K-Ar ages between 335 and 360 Ma (Mirzod *et al.* (1968) cited in Wolfart & Wittekindt (1980)).Whether the small occurrence of mafic volcaniclastic rocks and associated leucogranites of similar age, found in the Mazar tectonic mélange zone (Li *et al.*, 2006) east of the town of Mazar (Figure 3A, "East Mazar"), is part of the KOB must be discussed; this would increase the eastward extend of the basin.

In this paper, our new geochemical and geochronological data combined with our literature compilation demonstrates that the term North Pamir Kunlun is misleading. There is no evidence for a lateral continuation of the North Pamir Devonian to Carboniferous arc-magmatic sequence into the South Kunlun. Therefore, herein we use the term North Pamir arc as previously used by Bazhenov and Burtman Bazhenov & Burtman (1982), rather than the North Pamir Kunlun.

Rock units of the North Pamir arc experienced variable degrees of greenschist to lower amphibolite facies metamorphic overprint; higher metamorphic units potentially associated with Pennsylvanian to Permian subduction processes might have been identified by Li et al. (Li *et al.*, 2020) in the Tajik North Pamir arc (see discussion). Moreover, a non-metamorphic sedimentary succession of upper Permian to Eocene ages overlies Carboniferous rocks in the Chinese Qimgan valley (Figure 4) and shows no sign of a major post-Carboniferous collisional event affecting the NE Pamir. Therefore, the Permo-Triassic Qimgan basin (Sobel *et al.*, 2020) formed on a fragment of

Carboniferous oceanic crust, that is now situated in the External Pamir and was affected by thin-skinned deformation in Cenozoic time.

Following the initial observation that the North Pamir arc of the NE Pamir has many similarities with units further west (Konopelko *et al.*, 2019), and little in common with the West Kunlun to the east, the aim of this study is to better constrain the age and tectonic affinity of the Carboniferous arc-related rocks. Within this contribution, we present new and compiled geochemical and geochronological data from locations in the Tajik, Kyrgyz, and Chinese North Pamir and document that they have a common temporal evolution. We compare this data with the well-known tectonothermal events recorded in the West Kunlun. Thereby, we can test existing models of the northernmost suture zone in the Pamir and its relation to units in the West Kunlun to the east and the Hindu Kush/ Badakhshan to the west.

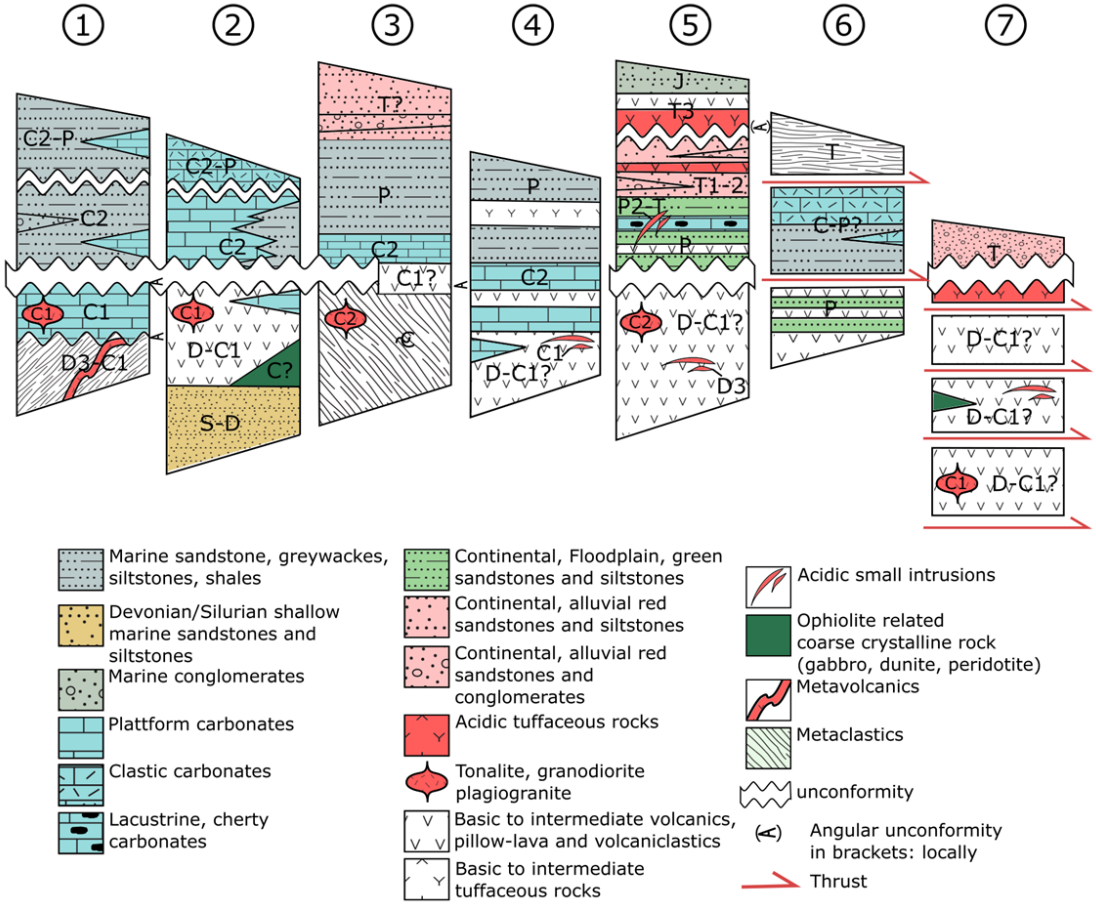

Figure 4: Schematic stratigraphic columns of the Kalai Khumb-Oytag basin. From west to east: (1) Synthesis of sections from Fakhar and Surkhab river valley after Wolfart and Wittekindt Wolfart & Wittekindt (1980), (2) Kalai Khumb after Leven Leven (2012), (3) Kurguvad after Schwab et al. Schwab et al. (2004), (4) Altyn Darya after Schwab et al. Schwab et al. (2004); Leven Leven (2013), (5) synthesis of sections in Qimgan/Akqi and Gez valleys, (6) synthesis of sections near Bostantielieke and Kawuke villages, (6) East Mazar after Li et al. Li et al. (2006). Thickness of stratigraphic units is not to scale. Abbreviations of geological periods: Є—Cambrian, O—Ordovician, S—Silurian, D—Devonian, D3—Upper Devonian, C—Carboniferous, C1—Mississippian, C2—Pennsylvanian, P—Permian, T—Triassic, T3—Upper Triassic, J—Jurassic.

2.3 Geology

2.3.1 Overview

Within this study we compare outcrops, literature data, and new field observations from the following sites (maps in Figure 3A and profiles in Figure 4): (1) the Badakhshan region in Afghanistan, (2) the Khalai Khumb and Obikhingou area in Tajikistan (Figure 3B), (3) the Kyrgyz Atyn Darya valley (Figure 3C), (4) the Chinese NE Pamir (Taergelake valley to Oytag valley, Figure 3D) and (5) the East Mazar area. Our study area is focused on locations (2)–(4). However, from excellent, detailed field descriptions, geological observations, and maps made during the last century (Wirtz *et al.*, 1964; Wolfart & Wittekindt, 1980; Bazhenov & Burtman, 1982; Boulin, 1988), significant similarities between the Carboniferous units exposed in Badakhshan and the Tajik Pamir can be inferred. This was proposed and discussed by previous studies (Bazhenov & Burtman, 1986; Boulin, 1988; Sengör *et al.*, 1993; Natal'in & Sengör, 2005).

2.3.2 Badakhshan

From northwestern Afghanistan, the Badakhshan and the southeastern Takhar regions, Lower Mississippian calc-alkaline lavas, volcaniclastics (Wirtz *et al.*, 1964; Wolfart & Wittekindt, 1980), and coral bearing limestones (Boulin, 1988) are known (Figure 4). In the Surkhab (aka Kunduz river) valley, Lower Mississippian units are composed of low-grade metamorphosed amygdaloid-basalts, andesites, and tuffs (Bazhenov & Burtman, 1982). Above an angular unconformity are non-metamorphic Visean limestones (Wolfart & Wittekindt, 1980). These are separated by a second angular unconformity from upper Pennsylvanian to Permian units dominated by littoral to sublittoral clastics and regional marls and platform limestones (Figure 4, Wolfart & Wittekindt, 1980; Boulin, 1988). The age of the dioritic intrusive rocks in the Badakhshan region is inferred from relative geologic relationship with disconformably overlying Permian sedimentary rocks (Hinze, 1964) and from K-Ar ages of 335–360 Ma from diorite and granodiorite found in the Surkhab river valley (Mirzod *et al.* (1968) cited in Wolfart & Wittekindt (1980)). Diorites, granodiorites, and granites intruded the sequence in the Fakhar area in the Khanabad river valley during the Mississippian (Doebrich *et al.*, 2006).

2.3.3 Kalai Khumb and Obikhingou

A Silurian to Permian succession was described along the Panj and Khingob/Obikhingou river valleys and tributaries located in the northwest Tajik Pamir (Figure 4, Vlasov *et al.*, 1984). Silurian to Devonian sediments are the oldest exposed low-grade metamorphic units in the region (Burmakin *et al.*, 1961; Lyoskind *et al.*, 1963; Vlasov *et al.*, 1984). A low-grade metamorphosed ophiolitic sequence described as Carboniferous (Ruzhentsev *et al.*, 1977) is part of a nappe sheet

overlying the metamorphosed Kurguvad basement block. The Kurguvad basement block was mapped as Proterozoic in age (Kafarsky & Pyjanov, 1970). Peak metamorphic conditions of the Kurguvad metamorphic suite were 540–650 °C and 5.5–7.6 kbar; concordant monazite $^{206}Pb/^{238}U$ and $^{208}Pb/^{232}Th$ ages are between 210 and 195 Ma (Schmidt *et al.*, 2011). All of the pre-Carboniferous units are covered by andesitic and basaltic pillow lavas, volcaniclastics and marly interbeds dated as upper Serpukhovian (Leven, 2012). Gabbros and leucogranites intruded this sequence. The Carboniferous gabbros and plagiogranites were grouped into the Obikhumbou complex (Mamadjanov *et al.*, 2017). This lower succession was previously interpreted as an oceanic island arc (Burtman, 2010). Above an erosional unconformity, an amagmatic Bashkirian carbonate sequence covers the top of the volcanic sequence (Leven, 2012). Our observations (below) show that the section has been metamorphosed to greenschist or lower amphibolite facies. A granitic intrusion covering more than 50 km² is also known from the Kurguvad basement block.

2.3.4 Altyn Darya

In the Altyn Darya valley of the Trans-Alai range, basic to acidic volcanic rocks were described (Figure 4, Schwab *et al.*, 2004). $^{40}Ar/^{39}Ar$ hornblende dating of two andesite samples yielded ages of ~ 356 Ma; zircons from two rhyolite samples yielded a Serpukhovian U-Pb ID-TIMS age of 329 Ma (Schwab *et al.*, 2004). This volcanic section is overlain by an upper Pennsylvanian to Permian sedimentary sequence consisting of carbonates with intercalated tuff and shales, as previously described from the Sauksai and Beleuli river sections. No unconformity between the lower and upper Carboniferous is reported (Leven, 2013). Our petrographic observations show that the section reached greenschist facies metamorphic conditions.

2.3.5 Chinese NE Pamir: Taergelake, Qimgan/Akqi, Gez and Oytag

Large volumes of Devonian to Mississippian volcaniclastic rocks are mapped in the Chinese Taergelake, Qimgan/Akqi, Gez and Oytag valleys (Figure 4, Henan Institute of Geological Survey (HIGS), 2014). Large leucogranite intrusions are mapped in these locations. In Gez and Oytag, these provided ages between 338 and 314 Ma by zircon U-Pb dating (Zhang *et al.*, 2006; Jiang *et al.*, 2008; Kang *et al.*, 2015; Ji *et al.*, 2018) and are interpreted as island arc derived (Jiang *et al.*, 2008). The Qimgan/Akqi section exposes a rather complete, unmetamorphosed sequence. We found upper Permian greenish-grey fine clastics and rare conglomerates and cross-bedded sandstones disconformably overlying the Carboniferous volcaniclastics (see Figure 4 and ages in Figure 3). The occurrence of mafic to intermediate volcaniclastic rocks and lava flows in the Permian succession decreases up section. We interpret the lower, fine-grained part of the sequence as floodplain deposits. Dark, silicified carbonates with monotonous ostracod fauna and remnants of charophytes are interpreted to represent a lacustrine environment. Plant detritus is abundant in siltstones. They are overlain by red, often cross-bedded coarse-grained clastic rocks, interpreted as

alluvial deposits of a terrestrial environment. Apparently, parts of the Pennsylvanian and the lower Permian sequence is missing in this section or is extremely condensed compared to the Altyn Darya section.

New field observations from the Bostantielieke valley, between Qimgan/Akqi and Gez show that the Permian sequence there was overthrusted by a sedimentary sequence containing thick greywackes, shales, phyllites, and prominent layer of dark marls, containing unidentified goniatites, crinoid fragments, brachiopods, and mollusks. We interpret these deposits as fully marine sediments. They are in turn overthrusted by greenschists, amphibolites, and marbles of the Karalkul-Mazar derived Shala Tala nappe (Chapter 5 and Rembe *et al.*, 2018; Rembe *et al.*, 2020). Foliation in the greenschist pervasively continues into the underlying dark marls. Therefore, we interpret both nappes to have been emplaced in the same episode. Lineation and microstructures indicate nappe transport to the NNE to NW under ductile conditions (Appendix A.6).

2.3.6 East Mazar

A tectonic horse, to the north east of the town of Mazar, was described as a Mississippian mafic to intermediate volcanic sequence (Figure 4, Li *et al.*, 2006). The section comprises altered basaltic to andesitic lava flows, intermediate to acidic tuffs, and volcanic breccias which were intruded by granitoids. The outcrop is crosscut by multiple faults. It is disconformably overlain by a thick Triassic conglomerate layer.

2.4 Methodology

2.4.1 Fieldwork and sample preparation

Data from 27 rock samples collected from the Tajik, Kyrgyz and Chinese North Pamir (Table 1) are presented in this study. We analyzed 12 granitoid samples and 8 mafic and intermediate volcanic rocks for petrology, geochemistry, and geochronology. The samples are from Carboniferous units in the Chinese and Tajik North Pamir as well as two Carboniferous volcanic samples from the Kyrgyz Altyn Darya valley. One sample is from a large granodiorite intruded into the Tajik Kurguvad block. To constrain the paleogeographic affinity of this poorly described basement block, two garnet bearing paragneiss samples were analyzed. Petrographic thin sections were made from all samples. Zircons were separated from 8 granitoid samples, two paragneiss samples and one aplitic dike sample using jaw crusher, disc grinder, water table, magnetic separation, and heavy liquids (SPT, DI). The zircons were poured onto a glass plate and arranged in lines on double sided sticky tape under a binocular microscope. In-line mounting in epoxy helps for better single-grain recognition. Mounted grains were polished to expose an internal surface and imaged with cathodoluminescence (CL) using the electron microprobe facility at the University of Potsdam (UP), Germany.

Two carbonate samples, collected from the Chinese Qimgan basin were cleaned, cut, and polished. Both zircon and calcite were dated with U-Pb geochronology using a laser ablation inductively coupled plasma mass spectrometer (LA-ICP-MS) at the School of Earth and Environmental Sciences, The University of Queensland.

A portion of the granitoid samples and all volcanic samples from the Chinese and Kyrgyz Pamir were also processed for whole-rock geochemistry (Table 2). They were cleaned, crushed, and milled in an agate mill to a particle size < 62 µm. Melt tablets for X-ray fluorescence spectroscopy (XRF) analysis to measure major and trace elements were prepared at UP using fluxing agent FX-X65-2 (lithium tetraborate: lithium metaborate, 66:34). Samples for rare earth elements (REE) and yttrium and scandium measurements were sintered with sodium peroxide at 480 °C and dissolved in hydrochloric acid. REE plus scandium and yttrium were then separated in ion exchange columns. Powder tablets were prepared from seven granite sample to determine the mineral composition by X-ray powder diffraction (see Table 1).

Table 1: Location and characteristics of all samples used for Chapter 2.

Sample	Location	Rock	Purpose	Mineralogy in TS	Mineralogy	Lat. (N)	Long. (E)
			Chinese North Pamir				
P09T32	Gez	Granitoid	GC, TS	qz-plg-ser-ep-chl		38.81628	75.45713
P09T33	Gez	Granitoid	GC, TS, XRD	qz-plg-ser-ep-chl	qz-ab-ep-chl	38.83728	75.47825
17NP426	Oytag	Granite gneiss	GC, TS	qz-plg-ser-ep		38.94553	75.35925
17NP439	Qimgan	Aplitic dike	ZrU/Pb, TS	gm-qz-chl		39.30928	74.86459
15NP233-1	Qimgan	Basalt	GC, TS	plg-gm-chl-vesc		39.30451	74.86297
15NP233-2	Qimgan	Basalt	GC, TS	plg-gm-chl-vesc		39.30451	74.86297
15NP235	Qimgan	Basalt	GC, TS	plg-ol-chl-gm-amp		39.30113	74.85742
15NP234	Qimgan	Basalt	GC, TS	plg-gm		39.30451	74.86297
2011T49	Qimgan	Basalt	GC, TS	plg-gm-chl-ep		39.2881	74.8889
17NP438	Qimgan	Carbonate pebble	CalU/Pb, TS	cal		39.30856	74.85677
17NP472	Qimgan	Lacustrine carbonate	CalU/Pb, TS	cal		39.31515	74.87224
15NP236	Qimgan	Pillow basalt	GC, TS	plg-gm		39.30488	74.8583
15NP245	Taergelake	Granitoid	ZrU/Pb	cf. 15NP247		39.31775	74.59724
15NP247	Taergelake	Granitoid	GC, TS, XRD	qz-plg-ser-ep-chl	qz-ab-chl-mc-ms	39.31775	74.59724
			Kyrgyz North Pamir				
01-09-13-01	Altyn Darya	Meta-basalt	GC, TS	plg-gm-amp-chl		39.25958	72.25892
31-08-13-01	Altyn Darya	Meta-basalt	GC, TS	plg-qz-amp-ep-chl-opk-gm		39.23586	72.255
			Tajik North Pamir				
16NP341	Obikhingou	Granitoid	ZrU/Pb, GC, TS, XRD	qz-plg-bt-ser-ep-chl-amp	qz-ab-chl-ms-cal	38.66072	70.90212
16NP342	Obikhingou	Cumulate	ZrU/Pb, GC, TS, XRD	chl-zo-qz-plg-opk	chl-zo-czo-ab-qz-bt	38.65702	70.89395
RT13-108	Khingob	Granitoid	ZrU/Pb, GC, TS	qz-plg-stp-amp-ep-chl-ser		38.75177	71.23224
RT13-109	Khingob	Granitoid	ZrU/Pb, GC, TS	qz-plg-bt-chl-ep		38.74758	71.23323
RT13-111	Khingob	Granitoid	ZrU/Pb, GC, TS, XRD	qz-ser-chl-plg-amp-ep	qz-ms-chl-ab-act-ep	38.78572	71.21192
RT13-115	Kalai Khumb	Granitoid	ZrU/Pb, GC, TS	qz-plg-ser-chl-ep-stp		38.52496	70.81857
RT13-146	Kurguvad	Granitoid	ZrU/Pb, GC, TS, XRD	qz-bt-ms-plg-kfsp-ep	qz-bt-ab-mc-ep	38.45605	71.11402
RT13-148	Kurguvad	Paragneiss	ZrU/Pb, TS	qz-bt-plg-grt-kfsp		38.3997	71.06168
RT13-149	Kurguvad	Granitoid	GC, TS, XRD	qz-bt-ep-kfsp-plg-ms	qz-bt-ep-ab-mc-chl	38.42699	71.04066
RT13-185	Kurguvad	Paragneiss	TS	qz-bt-grt-chl		38.4074	71.05962
RT15-11	Khingob	Paragneiss	ZrU/Pb	cf. RT13-148 and -185		38.69131	71.38139

TS—thin section, GC—geochemistry, ZrU/Pb—zircon U-Pb age measurement, CalU/Pb—calcite U-Pb age measurement, XRD—X-ray diffraction, gm—groundmass, mineral abbreviations according to IUGS (Siivola & Schmid, 2007).

Table 2: Age data of all samples used for Chapter 2.

Sample	Outcrop Area	Age[1] of youngest concordant single-grain [Ma] ± 1σ	Age[1] of youngest coherent group of concordant grains (TuffZirc, Ludwig, 2003) [Ma] ± 2σ	Age[2] of youngest coherent group of concordant grains (peakfit, Vermeesch, 2018) [Ma] ± 1σ	Number of grains
			Granitoids		
15NP245	Taergelake valley	334.7 ± 1.95*	361.80 +1.90 / -3.50	360.52±0.35	38
RT13-109	Khingob valley	219.0 ± 1.55*	329.00 +5.20 / -2.80	329.34±0.59	25
RT13-108	Khingob valley	318.0 ± 3.3	328.80 +4.30 / -1.30	333.55±0.44	33
RT13-111	Khingob valley	325.6 ± 2.25	334.10 +2.00 / -2.50	339.11±1.23	34
RT13-115	Panj valley	326.4 ± 2.4	329.75 +5.35 / -0.55	334.29±0.52	29
16NP342	Kalai Khumb	337.9 ± 1.2	340.10 +1.70 / -1.70	339.96±0.46	30
16NP341	Kalai Khumb	324.6 ± 1.2	338.90 +1.20 / -1.10	337.43±0.38	46
RT13-146	Kurguvad	297.2 ± 2.7*	326.95 +5.05 / -2.65	322.14±0.66	25
KL027 (Z06)	Oytag valley	323.6 ± 9.7	--	331.07±14.47	16
GZ-1 (J08)	Gez valley	248.1 ± 4.62*	--	338.03±2.09	13
WYT-5 (J08)	Oytag valley	449.4 ± 8.7	--	328.43±3.26	16
10X01 (K15)	Oytag valley	321.8 ± 2.3	--	322.76±1.57	19
D03-6 (J18)	Oytag valley	293 ± 1.85*	--	314.19±1.04	20
2RZ (L06)	East Mazar	--	--	338.52±8.31	13
AD2a (S04)	Altyn Darya	--	329 ± 5 ID-TIMS age	329 ± 5 ID-TIMS age	
AD6c (S04)	Altyn Darya	--	329 ± 5 ID-TIMS age	329 ± 5 ID-TIMS age	
			Kurguvad paragneiss		
RT15-11	Khingob valley	200.8 ± 1.8*	--	576.19±1.34	25
RT13-148	Panj valley	557.6 ± 5.5	--	589.75±1.01	82
Aplitic dike					
17NP439	Qimgan	242.3 ± 1.0	250.70 +0.90 / -2.30	250.04±0.28	31
Carbonate					
17NP472	Qimgan	260.49 ± 2.20	Discordia lower intercept age [Ma] ± 1s		34**
17NP438	Qimgan	347.02 ± 7.56			56**

*Data compiled from Zhang et al. (2006)(Z06); Jiang et al. (2008)(J08); Kang et al. (2015)(K15); Ji et al. (2018)(J18); Li et al. (2006)(L06); Schwab et al. (2004)(S04).[1] Discordance cut off for igneous zircons -10≤d[%]≤10; for detrital -10≤d[%]≤30; d=1-(206/238)/(207/206);[2] Discordance cut off for igneous and detrital zircons -10≤d[%]≤10; if Age <1000Ma d=1-(206/238)/(207/235), if Age >1000 d=1-(206/238)/(207/206); * lead loss presumed; **calcite ablation spots.*

2.4.2 LA-ICP-MS zircon U-Pb geochronology

262 zircon grains from 8 granitoid samples were dated (Appendix A.1 and Appendix A.7). Additionally, we dated 109 zircons from two paragneiss samples RT15-11-and RT13-148 and 56 zircons from an aplitic dike (17NP439). Paragneiss sample RT15-11 was mislabeled during processing as a granite, therefore only 51 zircons were mounted. Zircon 91500, with a $^{206}Pb/^{238}U$ age of 1062.4 ± 0.4 Ma and $^{206}Pb/^{207}Pb$ age of 1065.4 ± 0.3 Ma (Wiedenbeck *et al.*, 1995) was used as a primary reference material. Temora 2 zircons, with a $^{206}Pb/^{238}U$ age of 416.78 ± 0.33 Ma (Black *et al.*, 2004), was used as secondary reference material. Laser ablation was carried out with an ASI RESOlution 193 nm ArF excimer laser system in the Radiogenic Isotope Laboratory (RIF) at the University of Queensland. After air evacuation, He carrier gas was introduced into the laser

chamber at a flow rate of 0.35 l/min. A flow of 0.005 l/min N_2 gas was also introduced into the laser chamber to enhance the sensitivity of the measurements. The gas mixture was then transferred into the plasma torch of a Thermo iCAP RQ quadruple ICP-MS with 0.85 l/min Ar nebulizer gas. No reaction gas was employed. The laser spot size was 30 µm in diameter. Laser frequency was set to 10 Hz, with a measured instrument laser fluence of 2.9 J/cm^2. For each ablation spot, 3 s of blank was collected, followed by 20 s of ablation and 5 s of wash out. Before starting data acquisition, the ICP-MS signals were optimized by signal tuning. The zircons were measured during two analytical sessions, in October 2018 and in October 2019. Typically, we achieved over 300 cps for ^{238}U counts, ~1 for ^{238}U/^{232}Th, 0.22–0.25 for ^{206}Pb/^{238}U when measuring NIST612 glass using a line scan of 3 µm/s, 10 Hz, 50 µm round laser pit and 3 J/sm^2. Laser spot locations on the sample zircons were carefully chosen using CL images. Fractures and zones with strongly differing Th/U values were avoided.

The following isotopes were counted (dwell time in brackets): ^{88}Sr (0.005 s), ^{91}Zr (0.001 s), ^{200}Hg (0.01 s), ^{204}Pb (0.01 s), ^{206}Pb (0.045 s), ^{207}Pb (0.055 s), ^{208}Pb (0.01 s), ^{232}Th (0.01 s), ^{238}U (0.01 s). As a single cycle takes 0.155 s, during a 20 s ablation, approximately 120 measurements are taken for each mass. Reduction of the raw data was done in the program Iolite v2.5, which runs within the Igor Pro environment (Hellstrom *et al.*, 2008; Paton *et al.*, 2011) using the Vizual Age (Petrus & Kamber, 2012) data reduction scheme. The primary standard zircon 91500 was used to bracket each five unknown analysis to correct for machine drift. 91500 data were not corrected for common lead. Temora 2 zircons were treated as unknowns. The age of the primary standard was reproduced as a ^{206}Pb/^{238}U age of 1062.7 ± 0.2 Ma and Temora 2 gave a ^{206}Pb/^{238}U age of 420.70 ± 0.21 Ma and 417.80 ± 0.69 Ma in the 2018 and 2019 measurement sessions respectively. All unknowns were filtered for concordance and strontium content. LA-ICP-MS U-Pb dating and data processing were similar to Zhou *et al.* (2020).

2.4.3 LA-ICP-MS calcite U-Pb geochronology

Two limestone samples were chosen for calcite U-Pb age determination (Appendix A.8). Suitable ablation spots were identified by thin section examination of the samples. *In situ* calcite U-Pb analysis was also performed using the RIF LA-ICP-MS system. An ASI Resolution 193 nm excimer UV ArF laser ablation system equipped with a dual-volume Laurin Technic ablation cell was employed with an on-sample fluence of ~3 J/cm^2 and a spot size of 100 µm. All samples were measured using a Thermo iCAP RQ quadruple ICP-MS. Analyses consisted of 250 pulses at a repetition rate of 10 Hz. Each analysis consists of 20 s background acquisition followed by 30 s of sample ablation and 7 s washout. We used NIST 614 to correct for ^{207}Pb/^{206}Pb fractionation and for instrument drift in the ^{206}Pb/^{238}U ratio (Woodhead & Hergt, 2001). Data reduction and production of carbonate U-Pb isotopic ratios were undertaken with the software Iolite v2.5 (Hellstrom *et al.*, 2008; Paton *et al.*, 2011). An in-house carbonate reference material (CT10) of

known age (209.80 ± 0.48 Ma, Nguyen et al., 2019; Feng *et al.*, 2020) is used for normalization of $^{206}Pb/^{238}U$ ratios. Corrected data were regressed on Tera-Wasserburg plots using IsoplotR (Vermeesch, 2018) software to calculate the lower intercept ages. Our protocol is similar to recent carbonate *in situ* U-Pb LA-MC-ICP-MS dating reported elsewhere (Coogan *et al.*, 2016; Parrish *et al.*, 2018; Nuriel *et al.*, 2019), with the exception of using a different calcite reference material for the $^{206}Pb/^{238}U$ mass-bias correction.

2.4.4 XRF and ICP-AES whole rock geochemistry

XRF analysis (X-ray fluorescence spectroscopy) was done at the GeoForschungsZentrum Potsdam (GFZ) on a PANalytical AXIOS Advances XRF system. Calibrations were validated by analysis of international reference materials. ‘‘Monitor’’ samples and 130 certified reference materials were used for the correction procedures. The detection limit of the XRF system is generally 10 ppm. The rare earth elements plus yttrium and scandium were measured by Inductively coupled plasma atomic emission spectroscopy (ICP-AES) at UP on an Agilent ICP5100 machine following the procedure of Zuleger & Erzinger (1988). Long term precision for ICP-AES at UP is generally < 5%. High field strength elements were measured at the GFZ using standard ICP-MS procedures (Pretorius *et al.*, 2006; Romer & Hahne, 2010). The detection limit is generally ± 5% (Dulski, 2001). Concentrations of H_2O and CO_2 were determined from 20 mg of sample powder, weighed in tin foil. A Euro EA 3000 Elemental Analyser at UP was used for analysis.

2.4.5 XRD mineral phase analysis from powder samples and EDX mineral phase analysis from thin sections

Mineral analysis of 7 granitoid samples were obtained at UP using a PANalytical Empyrean powder X-ray diffractometer (XRD) with a Bragg-Brentano geometry. The XRD is equipped with a PIXcel1D detector using Cu K_α radiation (λ= 1.5419 Å) operating at 40 kV and 40 mA. θ/θ scans were run in a 2θ range of 4–70° with step size of 0.0131° and a sample rotation time of 1 s. It was equipped with a programmable divergence and anti-scatter slit and a large Ni-beta filter. The detector was set to continuous mode with an active length of 3.0061°. The total detection time was 21 min.

Double-polished thin sections of garnet bearing paragneiss from the Kurguvad basement block were analyzed with the scanning electron microscope (SEM: JEOL JSM-6510 SEM) at UP. Samples were carbon coated prior to analysis. The SEM is equipped with an Inca-Xact Energy Dispersive X-Ray detector (EDX) from Oxford Instruments. INCA analysis software (Oxford Instruments Analytical, 2006) was used to distinguish the element distribution in the minerals. Analyses were performed with a measurement time of 60 s using a tungsten cathode at 20 kV.

2.5 Results

2.5.1 New and previous findings from field geology and petrology

Field investigations show that the North Pamir arc experienced three phases of volcanism and related igneous intrusions. The first phase featured the emplacement of basaltic to andesitic lava flows, containing pillow lavas, mafic to intermediate tuff layers and cherts (Schwab *et al.*, 2004; Ji *et al.*, 2018). These voluminous volcanic deposits can be found along strike from Oytag in China into North Afghanistan (Bazhenov & Burtman, 1982). As previously described, the first period of volcanism was followed by the intrusion of voluminous plagiogranites (Zhang *et al.*, 2006). In a third phase, the plagiogranites were crosscut by mafic to intermediate dikes (Jiang *et al.*, 2008). Those dikes can be found in the Oytag plagiogranites as well as in the granitic intrusion in the Taergelake valley. Our field data and U-Pb data from the Chinese Qimgan basin, northwest of Oytag, shows that the basaltic to andesitic Carboniferous lava flows are overlain by an upper Permian to Triassic continental sequence (Figure 4, Sobel *et al.*, 2020). The lower part of the sequence is characterized by fine-grained greenish clastics, subordinate cross-bedded, red alluvial sandstones, and up to two meters thick lacustrine carbonate layers. The entire lower part of the Permo-Triassic continental basin hosts a large number of mafic to intermediate lava flows. We have obtained a new maximum age constraint for the continental basin by dating upper Permian sedimentary carbonate and an aplitic dike in the lower part of the section.

Granitoids

Several large leucocratic granitoid bodies are mapped along the length of the North Pamir arc (Figure 3). They are all dominated by quartz and plagioclase; some show minor amounts of K-feldspar. Twelve granitoid samples from different intrusions in the North Pamir arc were analyzed in this study (thin section photographs Figure 5 and Appendix A.3, modal mineral content Appendix A.11). They are medium to coarse grained and of light grey to pale green color (Figure 5). They are generally composed of 25–45 vol% of quartz and 35–55 vol% of plagioclase. Sample 17NP426 from the Oytag plagiogranite with a gneissic fabric yields higher amounts of quartz (60 vol%), while the plagioclase cumulate sample 16NP342 (Appendix A.3 G, H) from an outcrop close to the Tajik town of Kalai Khumb shows almost no quartz. Sample RT13-146 of a granite gneiss, found in the Kurguvad block in Tajikistan, is composed of 50 vol% quartz and just 10 vol% plagioclase. Plagioclases show common polysynthetic twinning and saussuritization up to complete replacement of the primary crystals (Figure 5D). In several samples, plagioclase starts to be replaced by epidote from its center (Figure 5E). Gez plagiogranites have strongly zoned plagioclase (Figure 5F). Orthoclase is largely absent and was only found in larger amounts (≤10 vol%) in samples 15NP247, RT13-146 and RT13-149. Tajik plagiogranites have a significant amount of primary biotite. The biotite grains show green to brown colors under plane light. Coarse,

greenish grains are interpreted as magmatic biotite that is in part replaced by brown, metamorphic biotite. In the Chinese samples, biotite and other mafic minerals are rare. Samples from the Tajik Pamir (RT13-108, RT13-115) host euhedral, unoriented aggregates of metamorphic stilpnomelane (Appendix A.3F). In three Tajik plagiogranite samples (RT13-108, RT13-115 and 16NP341), we found minor amounts (≤10 vol%) of altered amphiboles (Appendix A.3A, B).

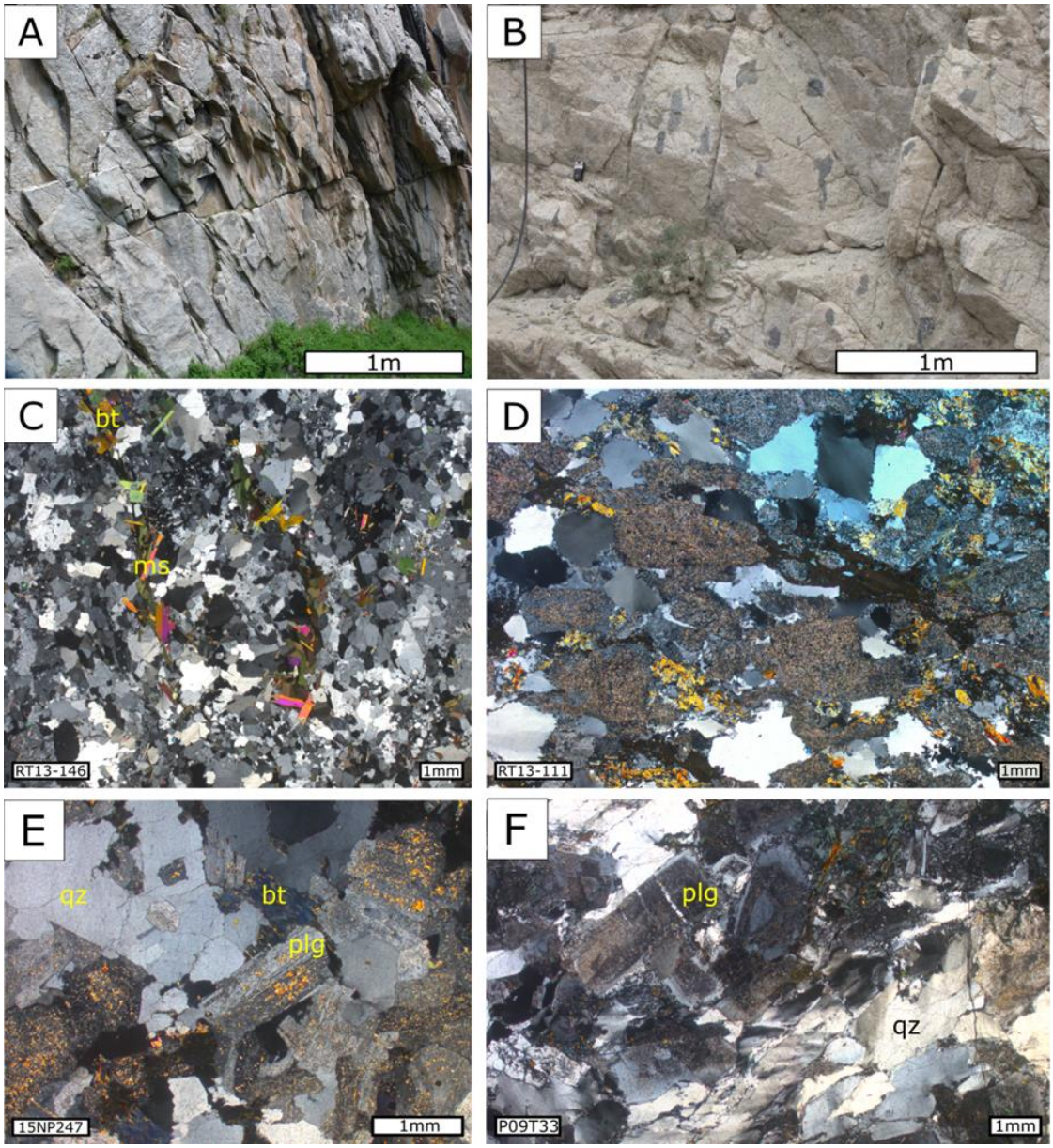

Figure 5: Granite Petrology. (A) Field photograph of Kurguvad granite. (B) Field photograph of leucocratic granite in Gez. Well-visible are mafic enclaves. (C) Microphotograph of Kurguvad granodiorite with quartz, muscovite (bright purple and orange interference colors) and biotite (mute brown and green interference colors). Feldspars are very fine-grained (Appendix A.3C). (D) Microphotograph of a tonalite from Tajik Khingob valley shows intense alteration of feldspar and ductile straining of quartz. Secondary minerals are epidote, chlorite, and sericite. (E) Microphotograph of a granite sample from Chinese Taergelake valley showing epidote growth in the centers of feldspars and pale blue chlorite that replaced biotite. (F) Microphotograph of a trondhjemite sample from Chinese Gez valley with ductile quartz straining and brittle fracturing of plagioclase crystals. Note the zonation in plagioclase crystals. (C–F) All Microphotographs are taken under cross polarized light.

Amphiboles have light brown pleochroic colors and are often replaced by epidote. Samples RT13-146 and -149 have a two-mica mineralogy with brown biotite and light grey to colorless muscovite (Figure 5C). All samples contain minor amounts of primary and secondary opaque minerals. Sample RT13-109 contains secondary calcite. Samples RT13-146 and 17NP426 plot in the quartz-rich granitoid field of the Streckeisen diagram (Streckeisen, 1976). The Kurguvad granitoid samples RT13-146 and -149 and the Taergelake sample 15NP247 are classified as granodiorites; all other samples are classified as tonalites when plotted in the Streckeisen diagram. All samples show evidence for ductile straining, as quartz grains show undulous extinction accompanied by various degrees of subgrain rotation recrystallization. Feldspars show idiomorphic habit and only gentle fracturing in the strained samples. Exceptions are the samples RT13-146 and -149 from the Kurguvad intrusion. Their feldspars are fine-grained and show recrystallisation patterns (Appendix A.3C). In the mylonitic sample 17NP426, feldspar formed an augen gneiss fabric and started to recrystallize to epidote and chlorite in the pressure shadows. From deformation patterns, we estimate a maximum temperature of clearly above 300 °C and below 500 °C for most samples and maximum temperatures above 500 °C for RT13-146 and -149 from the Kurguvad granite. Due to the abundant epidote and chlorite, we presume a greenschist facies metamorphic overprint of all granitoids of the North Pamir arc. Peak metamorphic conditions of the Kurguvad samples are estimated as lower amphibolite facies.

Volcanic rocks

The North Pamir arc hosts a wide variety of volcanic and volcaniclastic rocks (thin section photographs Appendix A.2). We examined 8 samples from basaltic to andesitic lava flows from Altyn Darya and the Qimgan valley. The lava flows are fine-grained, dark brown to green. Abundant vesicles are filled with secondary minerals, such as calcite. The greenish color and the abundance of calcite in all samples suggests metasomatism and spilitization. The samples from Altyn Darya show a clear greenschist facies metamorphic overprint and ductile straining. The lava flow samples show similar microscopic features: plagioclase, as phenocrysts or microliths, is abundant, with hornblende and rare olivine as phenocrysts. The samples show hyalopilitic textures, sometimes trachytic textures.

Paragneiss

We made thin sections from two Kurguvad paragneiss samples, RT13-148 and RT13-185 from the Panj valley. Quartz and biotite are the dominant mineral phases (thin section photographs in Appendix A.4), accompanied by garnet and minor amounts of feldspar and muscovite. Quartz and feldspar show dynamic recrystallisation structures. The ~150 µm garnets in sample RT13-148 have an inclusion-rich core and a clear rim. Garnets in sample RT13-185 are remnants of larger garnets (up to 500 µm) that were replaced partially by chlorite and biotite (Appendix A.4A, B). The remaining garnet fragments have a dark core, packed with small inclusions and a clear rim. The

complex structure of the garnets in RT13-185 hints at a multistage metamorphic history of the Kurguvad paragneiss.

Qimgan aplitic dike and carbonates

Carboniferous pillow basalts are disconformably overlain by a predominantly clastic sequence in the Chinese Qimgan valley. A light grey, aplitic dike was sampled in the stratigraphically lower part of the Qimgan basin (Figure 4). It crosscuts upper Permian fine-grained clastic strata. The primary mineral phases have been substantially replaced by secondary minerals. A primary porphyritic texture can be inferred from matrix replaced by fine-grained, dirty secondary minerals and phenocrysts replaced by brownish-colored secondary minerals.

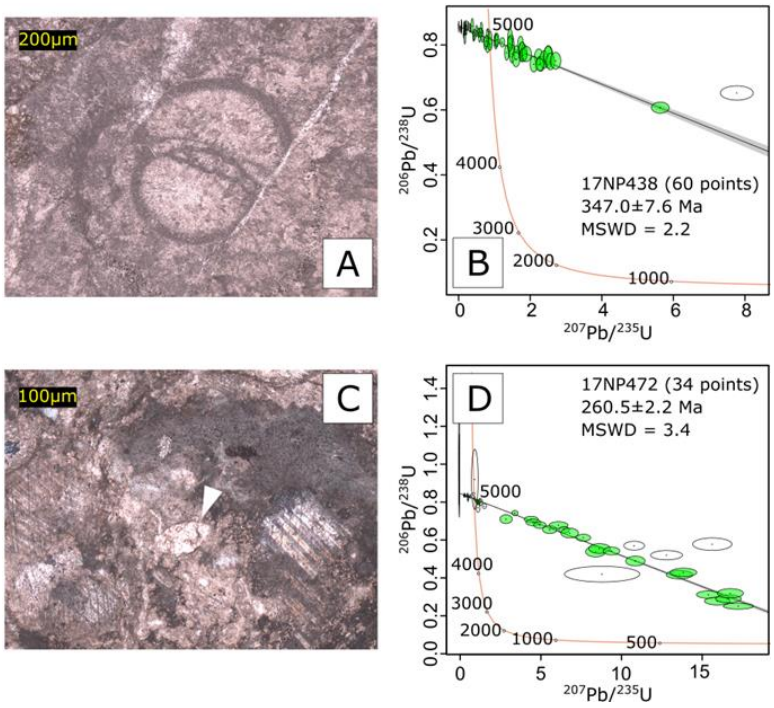

Figure 6: U-Pb Tera-Wasserburg plot of calcite age data. Microscopic images of carbonate sample 17NP438 (A, B: carbonate pebble from a red conglomerate) and sample 17NP472 (C, D: lacustrine carbonate) both from the lower part of the Qimgan basin, Chinese North Pamir. (A) Foraminifera in plane polarized light. (B) U-Pb Tera-Wasserburg concordia plot of calcite age data from sample 17NP438; 1σ-age-error is used. (C) Charophyte oogonium (white arrow) in a micritic carbonate overgrown by spary calcite. (D) U-Pb Tera-Wasserburg concordia plot of calcite age data from sample 17NP472; 1σ-age-error is used. Datapoints not used for regression are in white.

In the lower part of the Qimgan basin, we collected two carbonate samples for *in situ* U-Pb dating (Figure 6). Sample 17NP438 is a spary, light grey carbonate pebble from a red, conglomeratic, clay-rich debris flow deposit. The conglomerate contained clasts of serpentinites and sparry carbonates. The sampled carbonate clast contains planktonic foraminifera (Figure 6A) and unidentified shell fragments. Therefore, we interpret the carbonate pebbles to be derived from marine carbonate deposits. The primary fabric of carbonate sample 17NP472 is overprinted by sparry calcite. However, ostracod shells and remnants of lacustrine algae can be discerned (charophytes, Figure 6C). The carbonate strata, interpreted as lacustrine based on their fossil

content, are interbedded by fine-grained greenish siltstones and mudstones and occasional cross-bedded sandstones. Most carbonate layers show silicification and chert nodules.

2.5.2 New and published radiometric age data

An overview of the LA-ICP-MS U-Pb age data from all thirteen samples measured for this study as well as a compilation of literature data is provided in Table 2 (Figure 7). Detailed single-grain information from our own data is available in Appendix A.1A and Appendix A.7.

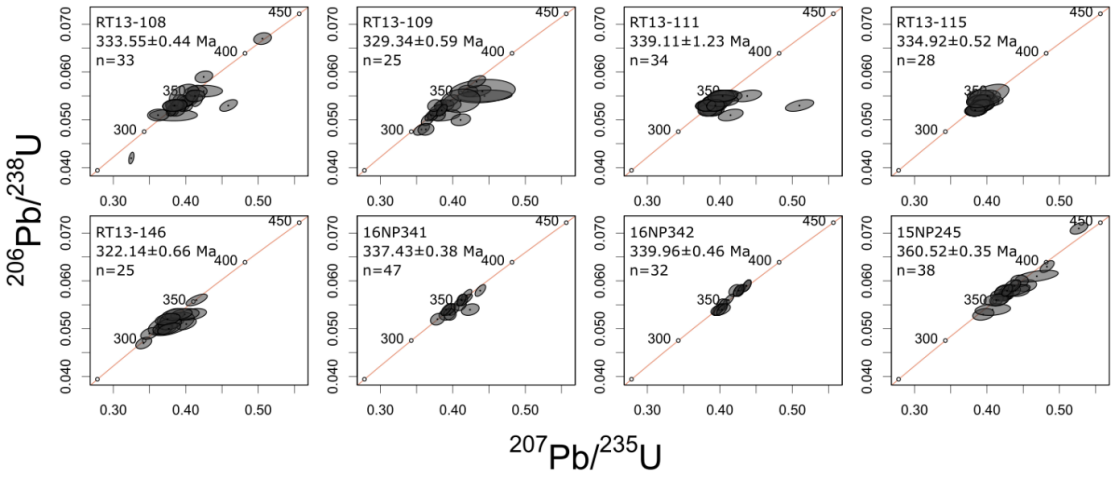

Figure 7: U-Pb Wetherill concordia plots of zircon U-Pb data from granitoid samples. All data points were plotted; however, for age calculation only those with -10%<disc(6_38/7_6)<10% were used. Displayed ages are calculated using the peakfit algorithm (Vermeesch, 2018). Error ellipses are shown semitransparent, overlapping error ellipses cause darker colors

We report three ages for the igneous samples: (1) the age of the youngest grain, (2) the median age of the largest age cluster calculated using the TuffZirc function of Ludwig (2008) and (3) the peakfit function of Vermeesch (2018). (2) and (3) give largely similar results for our data sets. For (1) and (2) we used the more conservative discordance criteria d=1-(206/238)/(207/206); this is recommended as both isotope ratios are measured directly in LA-ICP-MS dating and the lead isotope ratio is more sensitive to lead loss. Method (3) uses an age-dependent discordance criterion, i.e. for grains <1000Ma d=1-(206/238)/(207/235), for grains >1000 d=1-(206/238)/(207/206). For the detrital zircon samples, we report ages (1) and (3). The two carbonate samples gave lower intercept ages in the Tera-Wasserburg diagram. Generally, peakfit ages were preferred for interpretations. Thereby, we take into account that single young discordant grains may have experienced lead loss but still are mathematically concordant due to their large age error (Spencer *et al.*, 2016) or due to the very narrow space between concordia and the discordia line for young metamorphic events. Zircons from the granites and the aplitic dike show clear magmatic zoning in CL imaging. The zircons of paragneiss samples RT13-148 and RT15-11 are in part metamict. They do not show metamorphic overgrowths.

Granitoids

We compiled zircon U-Pb ages from the Chinese (Li *et al.*, 2006; Zhang *et al.*, 2006; Jiang *et al.*, 2008; Kang *et al.*, 2015; Ji *et al.*, 2018) and Kyrgyz North Pamir (Schwab *et al.*, 2004) and re-interpreted these ages based on the criteria described above (see Table 1). The Chinese studies focus on the tonalite outcrops in the Gez and Oytag (Aoyitake) valleys 80 km SW of Kashgar. Of the published age data from the Oytag and Gez plagiogranites in the Chinese Pamir, we extracted those ages which fall into a range of ± 10% of discordance. Those grains reveal two age populations: a younger one around 330 Ma and an inherited component of Ordovician to Silurian age (Jiang *et al.*, 2008). The younger age population is often left skewed, suggesting lead loss (Spencer *et al.*, 2016). Therefore, we do not use the youngest concordant zircon age for our interpretation. Previously published data of samples from the Oytag tonalite gave ages between 314 Ma and 331 Ma, the published data from samples in the Gez valley yielded an age of 338 Ma. Our zircon U-Pb analyses of samples from the Tadjik plagiogranites gave ages between 322 Ma and 340 Ma (Figure 7). Samples from the westernmost, most extensive intrusion (~370 km²), spanning from Darvaz in the south to the Khingob valley in the north, gave ages between 334 Ma to 339 Ma. The samples taken from intrusions further to the east — two from an intrusion cropping out in the Khingob valley and one from the Kurguvad granite — gave slightly younger ages between 322 Ma and 334 Ma. Contrasting to those large intrusions, sample 15NP245 from a seemingly smaller intrusion in the Chinese Taergelake valley, 120 km southwest of Kashgar, gave an age population of about 360 Ma. Zircons younger than 360 Ma from that sample do not form a coherent age group and are interpreted to be affected by lead loss.

Volcanic rocks

There is almost no geochronologic data available in the literature concerning the volcanic sequence of the North Pamir arc. Two andesites from the Kyrgyz Altyn Darya valley yielded lower Mississippian ages of 355 Ma and 357 Ma (hornblende $^{40}Ar/^{39}Ar$). Rhyolites dated in the same study with ID-TIMS on zircon gave a U-Pb age of 329 Ma (Schwab *et al.*, 2004).

Paragneiss

Two samples were taken from the metamorphic Kurguvad basement complex in Tajikistan. RT15-11 is from a unit mapped as granite. It was identified as a meta-sediment from the hand specimen; zircon ages show a similar distribution as detrital grains from paragneiss sample RT13-148 (Figure 8A). Both samples, RT15-11 and RT13-148 have age peaks at around 580 Ma, 722 Ma, 943 Ma and two minor age peaks at 2.0 Ga and 2.6 Ga (Figure 8, Appendix A.1B and C). Age peaks were calculated for both samples together, using the discrete mixture modelling algorithm (Galbraith & Laslett, 1993) implemented in the peakfit function of IsoplotR (Vermeesch, 2018).

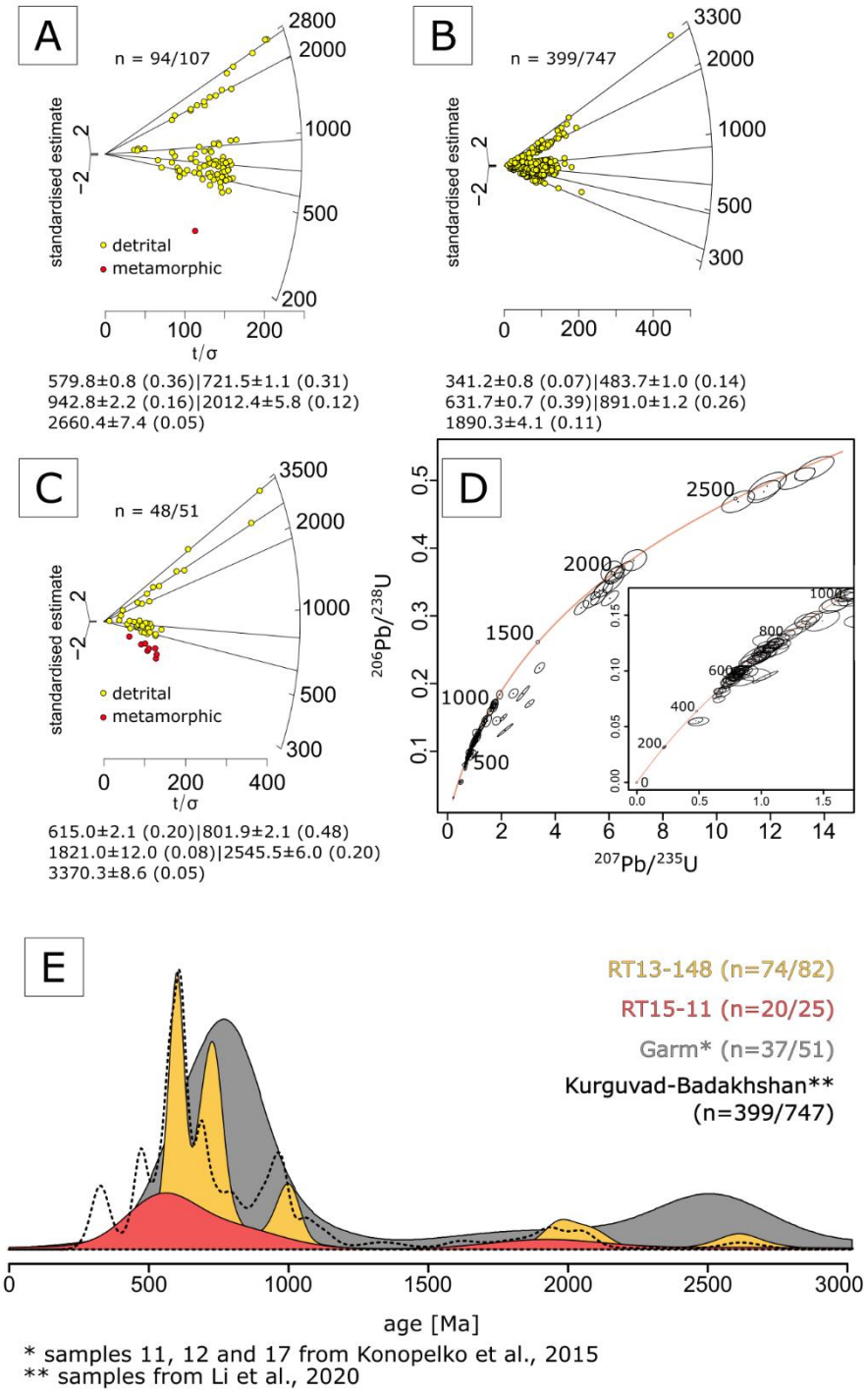

Figure 8: Detrital zircon U-Pb age data. (A) Radial plot (Galbraith, 1990) shows U-Pb age distribution of samples RT13-148 and RT15-11. Age peaks are listed below, including 1σ-error and probability in brackets. (B) Radial plot of all concordant U-Pb ages from the samples presented in Li et al. Li et al. (2020) for metamorphic rocks collected in the Kurguvad-Badakhshan complex. Age peaks are listed below, including 1σ-error and probability in brackets. (C) Radial plot of all concordant U-Pb ages from the samples that were used in (E) from Konopelko et al. (2015). Age peaks are listed below, including 1σ error and probability in brackets. (D) Wetherill concordia plot of samples RT13-148 and RT15-11. They indicate an Ediacaran maximum depositional age for the protolith of the Kurguvad paragneiss. (E) KDE plot of detrital U-Pb ages of samples RT13-148 and RT15-11 and detrital data from Konopelko et al. (2015) from gneisses found in the Garm basement block of the South Tien Shan. Samples from the Kurguvad-Badakhshan complex presented by Li et al. (2020) are plotted as dashed line. (A,C) Note that both samples show a metamorphic component, which was not used to plot the KDE (E).

We show, that the Kurguvad complex was intruded by a tonalite (RT13-146) at around 322 Ma. Therefore, a concordant grain in RT15-11 which yielded an age of 200.8 ± 1.8 Ma was classified as metamorphic and not included in the age peak calculation. The limited number of measured detrital zircon grains (RT15-11: 51 mounted, 25 measured; RT13-148: 120 mounted, 82 measured) allows for identification of major age peaks.

Qimgan aplitic dike and carbonates

To constrain the minimum age limit of the activity of the North Pamir arc, we dated two carbonates and a cross-cutting aplitic dike from the lower part of the Qimgan basin, 50 km to the northwest of the Oytag valley. The aplitic dike (sample 17NP439) yields two zircon age populations: 250 Ma and 417 Ma (Appendix A.1D and E). It crosscuts the lower part of the Qimgan basin. The inherited, older age peak is younger than inherited grains reported from the Gez plagiogranite (448 Ma and 468 Ma (Jiang *et al.*, 2008)). Carbonate samples were collected from a red conglomerate containing serpentinite and limestone pebbles (17NP438) and a dark lacustrine limestone (17NP472). Sample 17NP438 gave an age of roughly 347 Ma from 60 single ablation spots; sample 17NP472 yielded an age of 260 Ma from 34 single ablation spots (Figure 6B and D). These are lower intercept ages from the Tera-Wasserburg diagram. Outlier were carefully excluded in order to optimize the goodness of fit (weighted MSWD value).

2.5.3 New and published whole rock geochemistry

We compiled published whole rock geochemistry data for granitoids from the Oytag (Jiang *et al.*, 2008; Kang *et al.*, 2015; Ji *et al.*, 2018) and Gez sections (Jiang *et al.*, 2008) in the Chinese North Pamir and a tectonic sliver near Mazar (Li *et al.*, 2006) along the Karakax fault system in the Chinese West Kunlun. There is an extensive database of major element whole rock geochemical data from intrusive rocks from the North Pamir arc in Tajikistan by Mamadjanov et al. Mamadjanov *et al.* (2017) with which we compare our data and the data from the Chinese granitoids (Figure 9A and B). They interpret the occurrence of gabbro and tonalites/ plagiogranites as a continuous series of five major phases: emplacement of (1) gabbro, (2) quartz diorites, (3) tonalites, (4) plagiogranites and (5) leuco-plagiogranites. Mamadjanov *et al.* (2017) report trace elements as bulk analysis, those data were not used in our comparison. The granitoids intruded in most places into a thick pile of basic to intermediate volcanic and volcaniclastic rocks.

We also compiled whole rock geochemical data from volcanic rocks from the Oytag section (Ji *et al.*, 2018) in the Chinese North Pamir, East Mazar (Li *et al.*, 2006) in the Chinese West Kunlun and the Altyn Darya valley (Schwab *et al.*, 2004) in Kyrgyzstan (Figure 10). There is a large similarity amongst the volcanic rocks from the Chinese North Pamir and the Altyn Darya valley. Therefore, we present and plot our whole rock geochemical data from the volcanic rocks together with literature data from the Chinese volcanic rocks in Oytag and Gez and Altyn Darya, as they complement each other. The new geochemical data from this study are presented in Appendix A.9.

Granitoids

The granitoids of the North Pamir arc show SiO_2 contents between 63 and 78 wt%, MgO values between 0.3 wt% and 3.1 wt% and Al_2O_3 content between 12 and 16 wt%. They show relatively high Na_2O values between 4 and 6 wt% and low K_2O values between 0.1 and 4.2 wt%. They can be classified as peraluminous to metaluminous using the A/NK versus A/CNK plot of Shand (Figure 11, Shand (1943)). CIPW normed samples from Oytag/Gez plot in the trondhjemite field of the albite-anorthite-orthoclase diagram (Figure 9B (O'Connor, 1965)). Samples from the Tajik plagiogranites show a larger variability and higher normative anorthite (Ca) content (RT13-149, RT13-111) or higher normative orthoclase (K) content (RT13-108, RT13-115 and 15NP247).

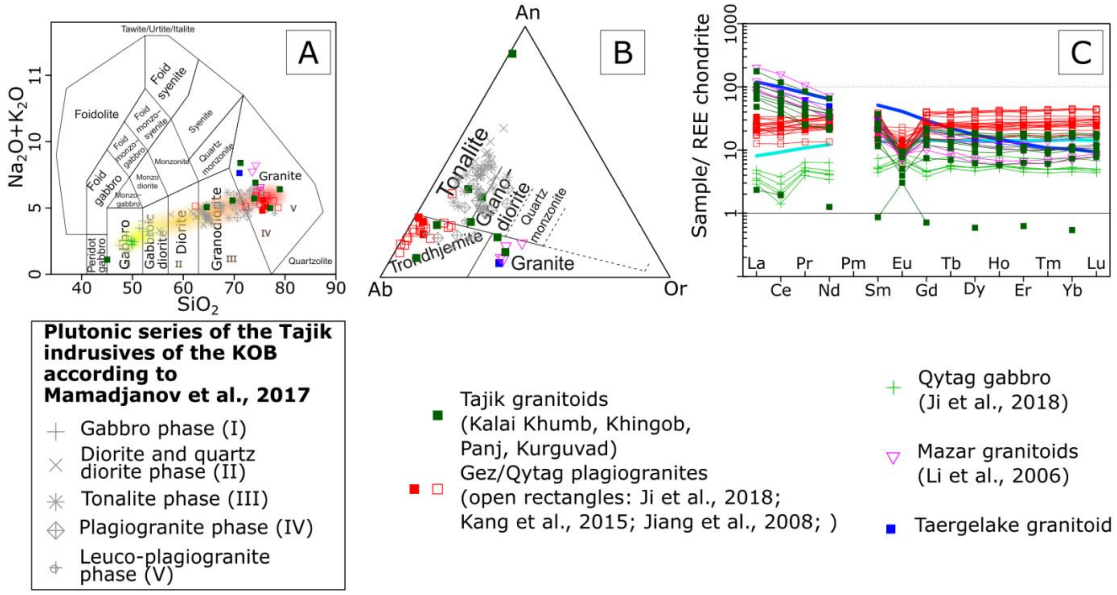

Figure 9: Geochemical characteristics of the North Pamir arc intrusive rocks. (A) General calc-alkaline trend of the North Pamir arc intrusive rocks. Our data supplements the extensive database of Mamadjanov et al. (2017) collected from the Carboniferous intrusive rocks in the Tajik part of the North Pamir arc. (B) Ab-An-Or diagram (O'Connor, 1965) for all granitoids of the North Pamir arc. (C) REE pattern for intrusive rocks cluster densely according to their outcrop region.

Samples RT13-146 and -149, which show orthoclase and plagioclase in thin section, plot along the tonalite-granodiorite border. The plagioclase cumulate sample 16NP342 from the Tajik Kalai Khumb intrusion is an exception, with a low SiO_2 content of 43 wt% and high Al_2O_3 (27 wt%), MgO (5 wt%) and CaO (15 wt%) contents. All samples can be classified as calc-alkaline (Figure 9A). Rare earth element (REE) data normalized to chondrite (Boynton, 1984) from the Oytag tonalites plot parallel to the N-MORB composition (Figure 9C) and show no to slightly negative Eu anomalies. The Tajik granitoids show enriched light REE compared to chondrite, more pronounced depleted Eu and lower amounts of heavy REE compared to the Oytag tonalites (Figure 9C). Plagioclase cumulate sample 16NP342 shows very low REE amounts and a strong positive Eu anomaly. C1 chondrite (McDonough & Sun, 1995) normalized La/Lu ratios fall between 0.6 and 1.6 in the Chinese tonalites and between 4 and 10.5 in the Tajik granitoids. The Taergelake

granite has a normalized La/Lu ratio of 10.8. The granite and two monzonite samples from East Mazar have the highest normalized La/Lu ratios of 11.8, 14.2 and 17.6 (Li *et al.*, 2006). Trace element data reveals Rb contents between 0.6 and 14 ppm in the Gez and Oytag tonalites (Jiang *et al.*, 2008; Kang *et al.*, 2015; Ji *et al.*, 2018) and between 26 (16NP341) and 131 ppm (RT13-115) in the Tajik granitoids. Ni contents generally range between 0.34 and 3.20 ppm with enrichment in RT13-111 (15.73 ppm) and 16NP342 (48.51 ppm). Th contents are between 1.03 ppm (17NP426) and 23.37 ppm (RT13-108). U concentrations are between 0.29 ppm (17NP426) and 4.67 ppm (RT13-108). Plagioclase cumulate sample 16NP342 shows a very primitive signature with Th content of 0.04 ppm and U content of 0.01 ppm. Plotting the granitoids in the Rb versus Y and Nb classification scheme (Pearce *et al.*, 1984), most samples fall in the field of volcanic arc granites (Figure 12). The granitoids show a typical arc signature; however, this signature is not homogenous along the strike of the North Pamir arc. The tonalites in Oytag are depleted and show a strong mantle influence, while the Tajik and East Mazar granites are more enriched.

Volcanic rocks

The SiO_2 content in volcanic rocks from the North Pamir arc range from 38 wt% in the Qimgan valley to 54 wt% in Altyn Darya (Figure 10A). These samples show Al_2O_3 contents between 13 and 17 wt% and MgO contents between 3.7 and 9.3 wt%. K_2O contents are relatively low (0.05 to 1.59 wt%) while Na_2O values are high (1.8 to 5.4 wt%). They can be classified as metaluminous using the A/NK versus A/CNK plot of Shand (Figure 11, Shand (1943)). As is evident from hand specimens and thin section observations, all volcanic samples were altered. Ocean floor metasomatism caused spillitization of the basaltic to andesitic lava flows. The volcanic rocks in the Altyn Darya valley have been strongly affected by greenschist facies metamorphism. General effects of low-T/low-P overprints on geochemistry are described elsewhere (Wood *et al.*, 1976; Floyd, 1977; Humphris & Thompson, 1978). In all samples, we presume that mobile elemental abundances have been disturbed. Therefore, classification schemes based on mobile components should be handled with care. All samples fall within a tholeiitic series based on the FeOt/MgO versus silica diagram (Figure 10A, Miyashiro (1975)).

However, samples from the Altyn Darya valley show higher FeOt/MgO ratios than the samples from the Gez and Oytag valleys but are similar to those from Qimgan. The K_2O versus silica plot does not show such a trend, as potassium, similar to sodium, rubidium, and strontium, are highly mobile even during low temperature alteration (Condie *et al.*, 1977; Cerling *et al.*, 1985). To get a robust geotectonic classification, we use the multiple major element classification scheme of Verma et al. Verma *et al.* (2006). The scheme is only applied to samples with SiO_2<52 wt%. Most samples plot in the island arc basalt field (Figure 13A). Likewise, in the Zr/Y versus Y plot (Pearce & Norry, 1979; Pearce, 1983), most samples plot in the island arc basalt field (Figure 13B).

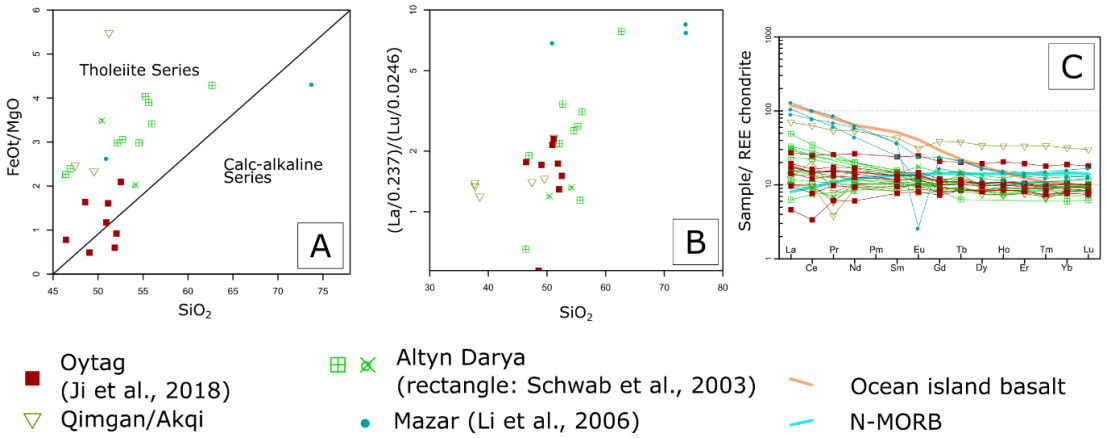

Figure 10: Geochemistry of volcanic rocks from the North Pamir arc. (A) They generally plot along a tholeiitic trend, after Miyashiro (1975). It is unclear whether the volcanic rocks from East Mazar also follow this trend. (B) C1 chondrite normalized La/Lu ratios are low for all basalt and andesite samples from the North Pamir arc. Samples from East Mazar show the highest values. (C) Volcanic rocks from Oytag and Qimgan show a flat REE pattern; those from Altyn Darya show a flat to slightly LREE enriched pattern. East Mazar rocks are most enriched in LREE.

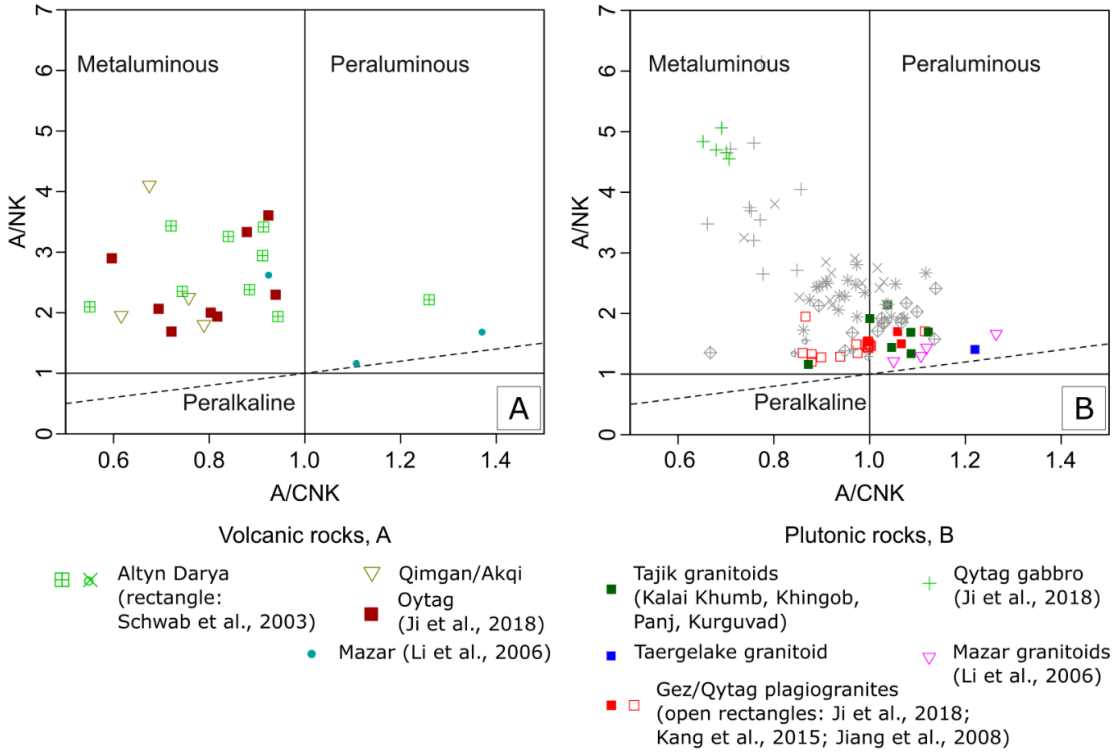

Figure 11: Geochemistry of plutonic rocks from the North Pamir. Classification plots after Shand (Shand, 1943) for volcanic (A) and plutonic (B) rocks of the North Pamir arc. Gray symbols in B are plutonic rock analysis presented by Mamadjanov et al. (Mamadjanov et al., 2017), explanation see Figure 9.

Rare earth element (REE) data normalized to chondrite (Boynton, 1984) shows variable patterns, varying from flat to slightly depleted light REE to moderately enriched light REE pattern (Figure 10C). C1 chondrite (McDonough & Sun, 1995) normalized La/Lu ratios fall between 1 and 2 for most samples (Figure 10B). A basalt from Oytag shows the lowest ratio of 0.5, similar to N-MORB (Sun & McDonough, 1989). Most andesites from Altyn Darya (e.g., AD1a, AD7c, AD6e; (Schwab

et al., 2004)) have values above 2; samples from East Mazar (D534/6, D1029/1-4, D1029/1-3; (Li *et al.*, 2006)) have the highest values between 6.9 and 8.5. Enrichment of light REE (Figure 10C) may be connected to contamination with continental material. Cr values range between 178 ppm (15NP233-1) and 431 ppm (15NP234); two samples yield Cr <10 ppm (2011T49 and 01-09-13-01).

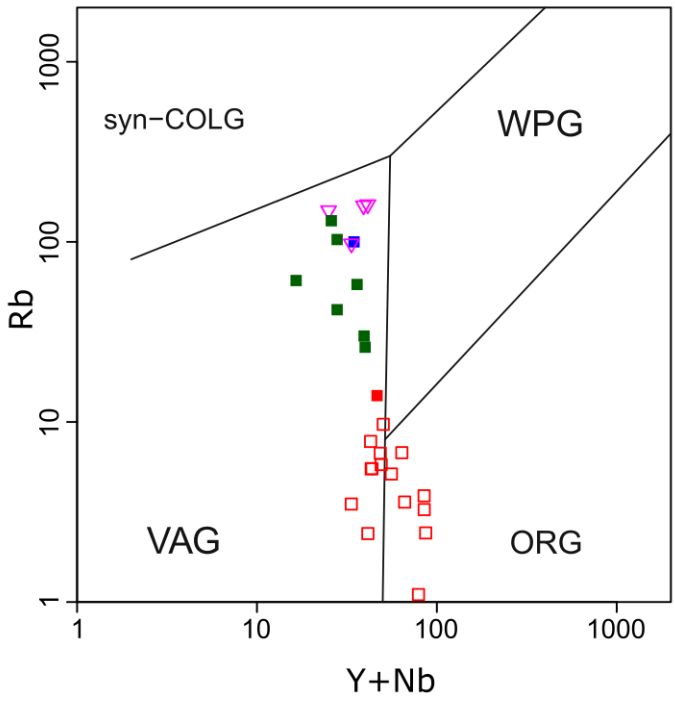

Figure 12: Y+Nb versus Rb classification (Pearce et al., 1984). For explanation of symbols, see Figure 11. syn-COLG—syn-collisional granites, WPG—within plate granites, VAG—volcanic arc granites, ORG—orogenic granites.

2.5.4 Results of XRD analysis of selected granite samples

Powder XRD analysis was performed on seven granitoid samples to determine the generally very fine -grained secondary and alteration mineral phases. When the abundance of mica in the sample is low, white and dark mica cannot be distinguished by their X-ray diffraction spectra. Therefore, data must be cross-checked with results from petrographic thin section examination. Results are summarized in Table 1. The XRD measurements confirm the presence of typical greenschist facies mineral assemblages. Chlorite and epidote are common. The spectra of sample 16NP342 shows evidence of clinozoisite and zoisite. The spectra of sample RT13-111 suggests the presence of actinolite. All plagioclases are identified as albite, in some samples as oligoclase. Potassium feldspars are of microclinic composition. XRD results agree well with whole rock CIPW normed feldspar classification (Figure 9B).

2.5.5 Results of EDX analysis of garnets from Kurguvad basement block

We used EDX to analyze polished thin sections of two biotite-garnet gneiss samples from the

Kurguvad basement block. They yielded two types of garnet. Semiquantitative EDX analysis on a scanning electron microscope reveals gentle zoning for the large, multi-stage garnets of sample RT13-185 and stronger zoning for the small, clearer garnets from sample RT13-146. Garnets show high almandine (XFe^{2+}) values around 80 mol% in sample RT13-185 and around 70 mol% in sample RT13-146. The pyrope (XMg) values are generally highest in the core and spessartine (XMn) values increase toward the rim (Appendix A.5).

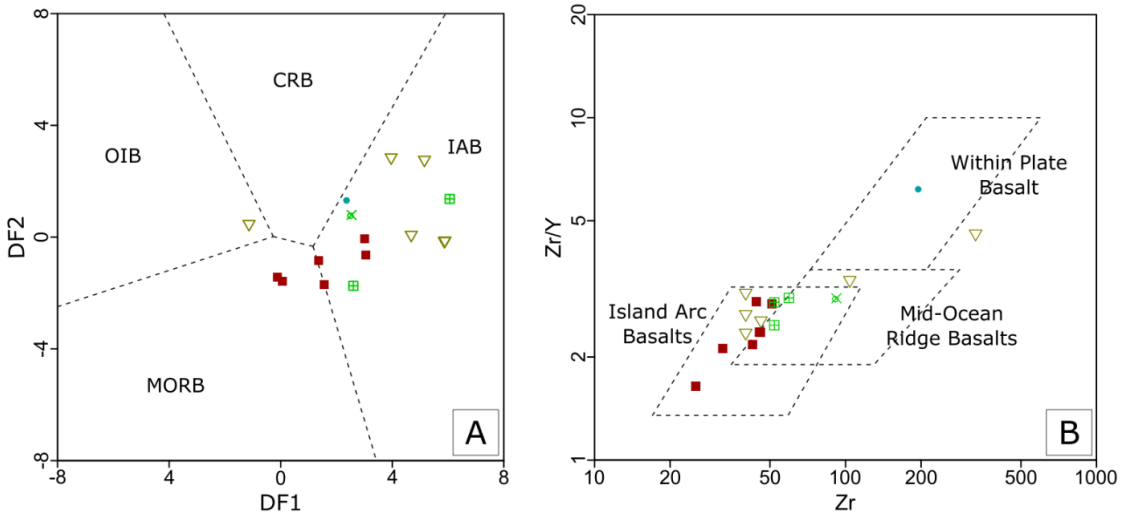

Figure 13: Geotectonic classification of basaltoid samples with SiO2 < 52 wt%. (A) Multi-element classification after Verma et al. (2006). OIB—ocean island basalt, MORB—mid ocean ridge basalt, CRB—continental rift basalt, IAB—island arc basalt. (B) Zr vs Zr/Y by Pearce & Norry (1979). For explanation of symbols, see Figure 11.

2.6 Discussion

2.6.1 Ages and tectonic setting

Our new geochemical results and compiled data confirm the existence of a volcanic North Pamir arc, which was active from the latest Devonian to Bashkirian — for at least 50 Ma (age compilation in Appendix A.10). Basaltic to andesitic rocks are characterized by typical arc tholeiitic compositions and low normalized La/Lu ratios. Granitoids with tonalitic to granodioritic composition intruded the volcanic sequence.

A minimum age for arc volcanism initiation in the North Pamir is given by the 360 Ma Taergelake granodiorite (sample 15NP245, Figure 7) and $^{40}Ar/^{39}Ar$ hbl ages of ~ 357 Ma from andesites in the Altyn Darya valley (Schwab *et al.*, 2004). The 360 Ma Taergelake intrusion has the oldest U-Pb age and the highest REE enrichment of all Chinese granites in this study. This is remarkable, as it represents a more evolved granitoid compared with the later-intruded Oytag tonalite, for example. So far, there is no good explanation for this. The younger age limit is presently defined by the youngest plutons in the Oytag valley, Chinese North Pamir (Ji *et al.*, 2018), by the onset of upper Permian continental deposition in the Chinese Qimgan basin (Figure 4), and by the overlying,

amagmatic, Bashkirian carbonate sedimentation in the Tajik North Pamir (Leven, 2012). The major preserved intrusive phase happened between 340 and 320 Ma, coevally in the Chinese and the Tajik North Pamir. Despite differences in geochemical composition, all granitoids from that time interval show similar petrographic properties and a relatively primitive composition. The granitoids of the Tajik North Pamir exhibit a generally more enriched REE pattern and a more pronounced negative Eu anomaly compared with those from the Oytag and Gez tonalites (Figure 9 and Appendix A.9; Jiang *et al.*, 2008; Kang *et al.*, 2015; Ji *et al.*, 2018). The more enriched nature of the Tajik granitoids might reflect a higher grade of continental contamination within the mantle wedge due to the presence of the Kurguvad continental basement block. The same can be stated for the East Mazar granites, which probably intruded in the vicinity of the Tianshuihai complex as a result of a Carboniferous reactivation of the Proto-Tethys subduction zone (Zhang *et al.*, 2018). However, interpretation of the East Mazar granites is hindered by their incorporation into the Karakax fault zone.

The vergence of the subduction zone cannot be constrained by our data. The southern margin of the North Pamir arc is largely overprinted by the late Triassic–early Jurassic Cimmerian orogeny. The northern margin is defined by the Cenozoic Main Pamir thrust, which has a larger offset in the western portion of the North Pamir arc. To the east of Taergelake, the position of the Main Pamir thrust is not well-constrained. Our field data from Qimgan valley (Figure 4; Sobel *et al.* (2020)) shows that the northern margin of the North Pamir Arc is covered by Permo-Triassic to Eocene sedimentary rocks.

2.6.2 The West Kunlun and the Kudi suture

The Kudi section, situated along the Xinjiang-Tibet highway south of Kargilik, is the type locality for the West Kunlun. The North and South Kunlun terranes are separated by the mid-Paleozoic Kudi suture (Pan, 1994; Matte *et al.*, 1996; Mattern *et al.*, 1996; Sobel & Arnaud, 1999; Wang *et al.*, 2002). The South Kunlun block is an accretionary complex formed between the colliding North Kunlun (the southern margin of Tarim) and Tianshuihai blocks (Zhang *et al.*, 2018; Zhang *et al.*, 2018). The South Kunlun terrane is characterized by an early Paleozoic accretionary sequence, pre-Cambrian sedimentary sequences, Cambrian ophiolites and Silurian to Ordovician arc volcanic rocks (Xiao *et al.*, 2005; Zhang *et al.*, 2007; Zhang *et al.*, 2018); none of these are found in the northeastern Pamir. Closure of the Kudi suture is dated as lower Silurian by a 440 Ma monazite age of the Saitula group of the South Kunlun (Zhang *et al.*, 2018), reflecting initiation of large scale obduction of metamorphic units due to collision of South and North Kunlun.

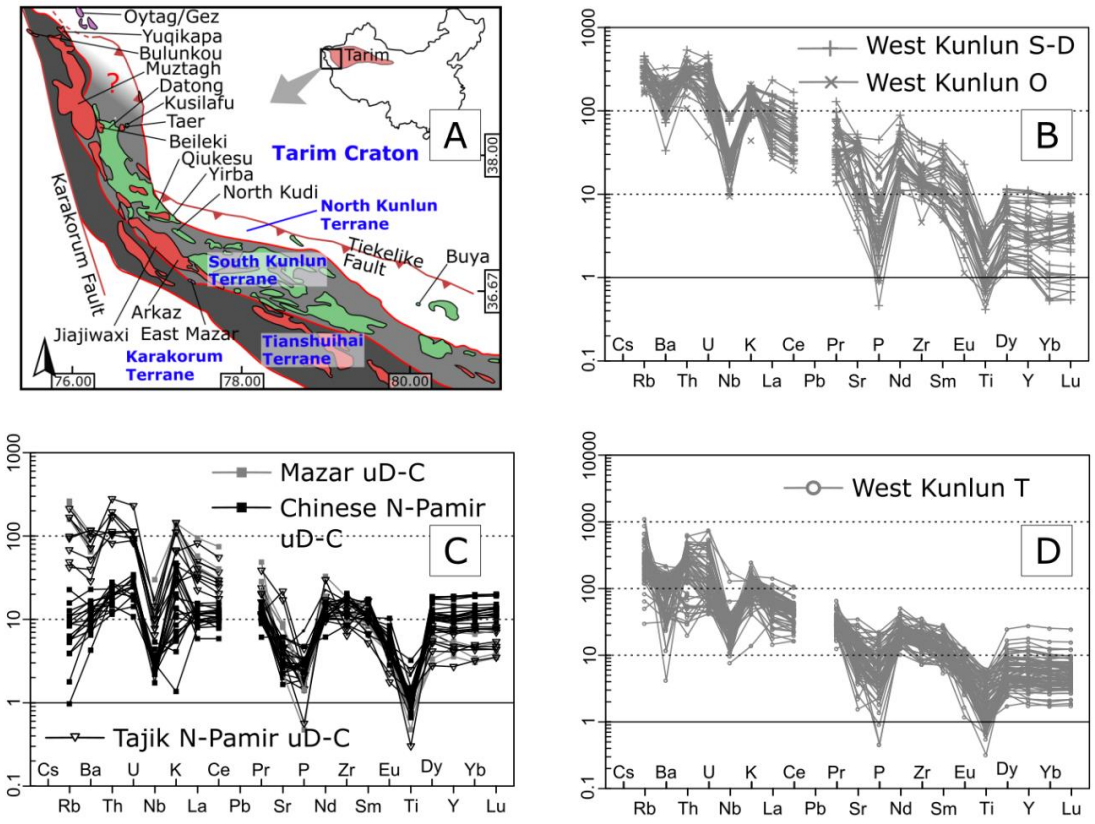

Figure 14: Comparison of granitoids from the North Pamir and the West Kunlun. (A) Map of the West Kunlun (polygon outlines after Zhang et al. Zhang et al. (2019) and own interpretations). Granitic intrusions which were used for this comparison are labelled; early Paleozoic intrusions are shown in green, late Paleozoic are shown in purple, Triassic intrusions are shown in red. Transition from South Kunlun terrane toward the North Pamir arc is unclear (red questionmark). (B–D) Spider diagram with element concentrations normalized against primitive mantle (Sun & McDonough, 1989). Comparison between early Paleozoic granitoids (O—Ordovician, S-D—Silurian to Devonian), late Paleozoic granitoids (uD–C—Upper Devonian (only Taergelake granite) to Carboniferous) and Mesozoic granitoids (T—Triassic). Data compiled from: (B) early Paleozoic plutons Datong (Li et al., 2019), Kusilafu (Li et al., 2019), Yirba (Yuan et al., 2002), Qiukesu (Jia et al., 2013), Buya (Ye et al., 2008), North Kudi (Yuan et al., 2002); (C) late Paleozoic plutons (see Fig. 1) Taergelake, Kalai Khumb, Obikhingou, Kurguvad, Panj (own data) and East Mazar (Li et al., 2006), Gez (Jiang et al., 2008), Oytag (Jiang et al., 2008; Kang et al., 2015; Ji et al., 2018); (D) Mesozoic plutons Yuqikapa (Jiang et al., 2013), Muztagh (Jiang et al., 2013), Bulunkou (Wang et al., 2016), Beileki/Taer (Huang et al., 2013), Taer (Jia et al., 2013), Karakul (not shown in (A), Schwab et al. (2004)), Arkaz (Yuan et al., 2002; Wang et al., 2016; Zhang et al., 2016), Jiajiwaxi (Wang et al., 2018).

The West Kunlun experienced two major intrusive phases: between 530 Ma and 400 Ma and between 240 Ma and 200 Ma (Figure 14). The older intrusive phase in the West Kunlun domain extends as far north as the shoshonitic Datong pluton (~450 Ma; Li *et al.* (2019), Yu *et al.* (2011)). The Yirba granodiorite (Figure 14A), cropping out in the Kudi section, intruded between 460 and 471 Ma during the mature phase of the Andean-type magmatic arc in the West Kunlun (Xiao *et al.*, 2005). The Datong pluton (Figure 14A), emplaced between 448 and 473 Ma (Liao *et al.*, 2010), likewise belongs to the mature phase. It marks the present, northwesternmost extent of the early Paleozoic plutons preserved in the West Kunlun. The Andean-type arc developed on top of a north (e.g., (Xiao *et al.*, 2005)) or south (e.g., (Zhang *et al.*, 2018; Zhang *et al.*, 2018)) dipping subduction zone with Proto-Tethyan oceanic crust being subducted between the North Kunlun, regarded as Tarim crust, and the Tianshuihai block. An accretionary complex — the South Kunlun terrane —

formed along the subduction zone. By that time, the South Kunlun accretionary complex experienced amphibolite facies metamorphism due to crustal thickening, subduction of the Proto-Tethys, and later collision of the continental block related to the Tianshuihai complex (Xiao *et al.*, 2005; Zhang *et al.*, 2018). Proto-Tethys subduction terminated in a late Silurian to early Devonian post-orogenic stage with emplacement of highly evolved A-type granites (Yuan *et al.*, 2002; Zhang *et al.*, 2019). Since at least the emplacement of the A-type North Kudi pluton at around 405 Ma (Yuan *et al.*, 2002), the post-orogenic extensional phase marks the termination of compressional, subduction related tectonics in the West Kunlun. Plutons associated with the younger, Permo-Triassic phase can be found in the West Kunlun as well as in the Tianshuihai and in the Karakul-Mazar accretionary complex, which forms the southern part of the North Pamir.

2.6.3 Comparison between the West Kunlun and the North Pamir

The North Pamir arc is clearly distinguishable from the two major volcanic arcs recorded in the West Kunlun, where volcanism occurred during the closure of the Proto-Tethys and collision of the Tianshuihai, South Kunlun and North Kunlun/ Tarim bocks in Silurian and Ordovician time (Jiang *et al.*, 2002; Yuan *et al.*, 2002; Xiao *et al.*, 2005; Yuan *et al.*, 2005; Li *et al.*, 2019), as well as during the closure of the Paleo-Tethys and accretion of the Cimmerian blocks (Huang *et al.*, 2013; Jiang *et al.*, 2013; Zhang *et al.*, 2018; Xin *et al.*, 2019). Volcanic rocks overlapping in age with the two major tectonothermal events of the West Kunlun have not been discovered in the North Pamir arc. Similarly, there are no arc volcanic rocks of Carboniferous age described from the West Kunlun. Instead, West Kunlun Carboniferous deposits represent amagmatic, shallow marine siliciclastic and platform carbonate successions (Jixiang, 1994). Although pillow-basalts, lava flows, and related clastic rocks from the Yixiekekhgou area, north of the town of Kudi, were previously interpreted as Carboniferous (Wang, 1996), a dacite from that section yielded a zircon U-Pb age of 492±9 Ma (Xiao *et al.*, 2005).

The Oytag (or Wuyitake) suture — namely a small outcrop of ultramafic rocks — is only found in the Gez valley (Jiang, 1992); no definitively correlative outcrops are known from the North Pamir arc to the west. A connection between Kudi and Oytag ultramafic rocks has long been proposed (Mattern *et al.*, 1996; Wang, 1996; Sobel & Dumitru, 1997; Xiao *et al.*, 2002; Schwab *et al.*, 2004). This led to the interpretation that the Kudi-Oytag suture zone, separating the North and South Kunlun terranes, stretches from the West Kunlun all around the North Pamir. This terminology has been applied despite mismatching geochemical and especially geochronological data from the granitoids in the Gez/Oytag section (Zhang *et al.*, 2006; Jiang *et al.*, 2008). The arc volcanic rocks of the Gez/Oytag section were related to an intraoceanic subduction zone (Xiao *et al.*, 2002; Jiang *et al.*, 2008) and have an island arc tholeiitic character. Volcanic rocks from the Kudi ophiolite show a wide range of geochemical characteristics; they are interpreted as N- and E-MORB ridge basalts (Xiao *et al.*, 2005), back-arc basin tholeiites, low-Ti island arc tholeiites, and island arc

tholeiites (Wang *et al.*, 2002; Yuan *et al.*, 2005). As geochronological information on the volcanic sequences is sparse, discrimination was difficult. However, amphibole and biotite $^{40}Ar/^{39}Ar$ ages from the Kudi ophiolite suggest a formation age prior to 460 Ma (Wang *et al.*, 2002). Hornblende $^{40}Ar/^{39}Ar$ ages from andesites of the Kyrgyz Altyn Darya valley yield ages of roughly 350 Ma (Schwab *et al.*, 2004), so 100 Ma younger than Kudi.

The difference between the North Pamir and the West Kunlun is even more obvious when comparing granitic intrusion history and metamorphism. Granites of the North Pamir arc show relatively uniform tonalitic to granodioritic composition and are not older than 360 Ma, with the main intrusive phase between 340 and 320 Ma. No post-collisional granitoids have been identified. In contrast, the granitoids of the West Kunlun are much older and show a higher compositional variability, including post-collisional A-type granitoids. Granitoids from all three volcanic phases (early Paleozoic, late Paleozoic, and Triassic) are related to subduction processes. Thus, they show similar trace element features. However, the Carboniferous granitoids are the least enriched ones (Figure 14), suggesting a higher mantle influence during that phase. Metamorphism in the North Pamir arc reached a maximum of lower amphibolite facies post 320 Ma, while the West Kunlun experienced amphibolite metamorphism between 440–430 Ma (Zhang *et al.*, 2018; Wang *et al.*, 2020).

If there is a continuation of the Oytag subduction zone toward the east, it should be situated south of the South Kunlun but not within the collision zone between the North Kunlun, the South Kunlun and the Tianshuihai complex. The East Mazar sliver might give a hint of a continuation of the subduction zone between the Tianshuihai complex and the South Kunlun in the westernmost part of the West Kunlun. Based on sedimentary facies and the lack of evidence for early Paleozoic orogenesis in the NE Pamir, it is also argued that a remnant of the Proto-Tethys remained open in the NE Pamir until the Cimmerian orogeny (Zhang *et al.*, 2018). Therefore, we speculate that collisional tectonics in the West Kunlun terminated westward, toward the North Pamir, during the early Paleozoic orogeny.

Geochemical data compiled from previous studies of the early Paleozoic and early Mesozoic intrusive rocks show certain similarities with the geochemical signature of intrusive rocks discussed in this study (Figure 14). All are related to subduction processes. The magmatic suites show negative Nb, P and Ti anomalies. The tonalites from the Oytag/Gez section show the least enrichment in large ion lithophile elements (LILE). Their enrichment is higher in the Tajik granitoids. Compared with the Triassic and early Paleozoic intrusive rocks, the Carboniferous magmatic suite is less enriched in LILE. The enrichment in LILE and depletion of high field strength elements (HFSE) such as Nb, P and Ti is typical for subduction related environments. Therefore, the Carboniferous granitoids show a stronger mantle component than the Triassic and early Paleozoic granitoids.

2.6.4 Relationship of the North Pamir arc with Carboniferous rocks in the Afghan Badakhchan

For the Carboniferous units of the Tajik North Pamir and their continuation into Afghanistan, a simple division into two zones was proposed by Bazhenov and Burtman (Bazhenov & Burtman, 1982). Zone 1 represents oceanic crust, characterized by early Paleozoic volcanics and intercalated open marine sediments. Carboniferous ultramafic units were also described from this zone (Lyoskind *et al.*, 1963; Ruzhentsev *et al.*, 1977). Zone 2 represents an active margin, characterized by arc volcanic rocks and accreted microcontinents (Kurguvad block, Fayzabad microcontinent). Middle Paleozoic rocks sharing characteristics with those zones can be found from the North Pamir into the Herat area and further west (Bazhenov & Burtman, 1982). We do not follow this bipartite division, as arc-tonalites and granodiorites appear to intrude both units. Instead, we interpret the arc to have formed on top of both pre- to early Carboniferous oceanic crust and continental slivers. It is likely that the Kurguvad microcontinental block separated from other Tarim-related crustal blocks of the region (e.g., Garm) in the early Paleozoic, leaving behind a patchwork of oceanic and continental crustal fragments — which later were accreted during subduction processes in the Carboniferous. Subduction zones may have formed along the flanks of microcontinental blocks during the middle-late Carboniferous compressive phase.

Another feature that can be followed into the Badakhshan area is the sedimentary hiatus between the Mississippian and Pennsylvanian (Figure 4). This hiatus has been recognized in many profiles, separating a magmatic phase in the Mississippian from an amagmatic and predominantly marine sedimentary phase in the Pennsylvanian. The duration of this hiatus seems to increase from west to east, when comparing the similar setting within the Chinese North Pamir. Sedimentary Pennsylvanian units are only found in the Chinese North Pamir as allochthonous units (Lu *et al.*, 2013). Hiati within sedimentary sections from Afghanistan, Tajikistan and Kyrgyzstan (Wolfart & Wittekindt, 1980; Bazhenov & Burtman, 1982; Schwab *et al.*, 2004; Leven, 2012; Leven, 2013) are temporally variable. They show a pattern of diachronous marine sedimentary environments changing from platform carbonate sedimentation to clastic shelf sedimentation and a more or less erosional, terrestrial phase in the upper Carboniferous to Permian (Boulin, 1988).

2.6.5 The Kurguvad block — detrital signal and metamorphism

The two Kurguvad paragneiss samples investigated using detrital zircon, RT13-148 and RT15-11 (Figure 8), have age peaks at 580 Ma, 722 Ma and 943 Ma. These are similar to newly published ages from metamorphic units of the Kurguvad-Badakhshan complex (Figure 8 and Li *et al.* (2020)). Two meta-sedimentary garnet-staurolite schists sampled by (Li *et al.*, 2020)(DV-7-27-15-1 and LY-7-18-17-2) gave a youngest age peak at around 310–360 Ma. This age peak likely reflects magmatic activity of the North Pamir arc. All other samples of that dataset together with our data

from samples RT13-148 and RT15-11 lack that peak. We show that a granodiorite intruded into the metamorphic Kurguvad basement in the Bashkirian. The new findings can be integrated to a sequence of processes affecting rock units of the NW Pamir. (1) The lower metamorphic grade of the Early Carboniferous Kurguvad granodiorite, compared to the surrounding metasediments (e.g., garnet-biotite schist, garnet-staurolite schist), strongly supports the existence of at least one pre-intrusion metamorphic phase in the Kurguvad basement. (2) The presence of Carboniferous zircon in metasedimentary rocks, presented by Li *et al.* (2020) just a few kilometers south-east of the Kurguvad intrusion, indicates late- to post-Carboniferous metamorphism. Metasediments yielding Carboniferous age peaks might reflect nappes of a Carboniferous accretionary wedge.

Peaks similar to the ones found in the Kurguvad block are known from gneisses of the Garm block in the Tajik Tien Shan (Konopelko *et al.*, 2015; Käßner *et al.*, 2017; Worthington *et al.*, 2017) and the Kyzylkum segment of the South Tien Shan (Mirkamalov *et al.* (2012) cited in Konopelko *et al.* (2015) and Konopelko *et al.* (2019)). These ages indicate an Ediacarian maximum depositional age (Figure 8) and suggest a linkage of the Kurguvad basement block to the Tien Shan basement at that time. A very pronounced 590 Ma age peak is also reported from NE Gondwana (Rojas-Agramonte *et al.*, 2011). The 943 Ma age peak may be related to igneous activity in Tarim, as suggested for a similar age peak between 1150 Ma and 800 Ma in the Garm gneisses (Konopelko *et al.*, 2015). The older age peaks at 2 Ga and 2.6 Ga are less pronounced in the Kurguvad gneiss. Similar peaks are reported from samples taken in the Quruqtagh, Central Tien Shan, that represents Precambrian Tarim basement (Shu *et al.*, 2011). Shu *et al.* (2011) link the late Archaen and early Paleo-Proterozoic age peaks to two poorly defined Proterozoic tectono-volcanic events between 1.8 and 2.0 Ga and 2.4 and 2.6 Ga that could be related to the early formation of the Tarim block.

Metamorphism of the Kurguvad basement block has not been thoroughly documentd. Peak amphibolite facies metamorphism was suggested by petrographic analysis and garnet-biotite (GARB) and garnet-biotite-muscovite-plagioclase (GBMP) thermobarometry of seven gneiss samples from the Kurguvad block (Schmidt *et al.*, 2011). These samples yielded temperatures and pressures of 540–650 °C and 5.5–7.6 kbar without staurolite and 600–650 °C and 6.5–8.2 kbar with staurolite, respectively. A monazite age of around 200 Ma reflects Cimmerian metamorphism. We obtained one zircon U-Pb age of 200.8 ± 1.8 Ma from sample RT15-11, which reflects the Cimmerian metamorphic imprint on the zircon fraction. The Kurguvad basement block must have also experienced pre-Carboniferous metamorphism, based on relative age relations. The complex garnets (APPENDIX 5) suggest a multi-phase metamorphic event. However, Konopelko *et al.* (2015) report concordant zircon U-Pb ages between 303 Ma and 406 Ma (Figure 8C) from the Garm basement block; these were interpreted to be metamorphic. This hints at a different metamorphic history in Garm compared to the Kurguvad basement block.

2.6.6 Metamorphism of the North Pamir arc

The metamorphic grade of the North Pamir arc has been estimated by petrological thin section analysis, supported by XRD mineral phase analysis. Excepting the Kurguvad block, no indication of metamorphic imprint higher than greenschist facies on the Carboniferous volcanic rocks and granitoids was found. The Kurguvad block experienced amphibolite facies metamorphism during the Cimmerian orogeny (Schmidt *et al.*, 2011). Our data cannot clarify whether the greenschist facies metamorphism of the North Pamir is related to the late Carboniferous to Permian arc obduction history or to a later, Cimmerian overprint.

2.7 Summary and implications

New and published geochemical and geochronological data provide a detailed view of the along-strike variations of the North Pamir Carboniferous granitoid intrusions and their host rocks. Geochemical data from the tholeiitic and mafic to intermediate rocks, cropping out in the Chinese Oytag and Qimgan valley and in the Kyrgyz Altyn Darya valley, document the formation of an island arc complex in the Upper Devonian to Bashkirian (Schwab *et al.*, 2004; Ji *et al.*, 2018). The North Pamir arc is chronologically and geochemically distinct from the volcanic arcs known from the West Kunlun.

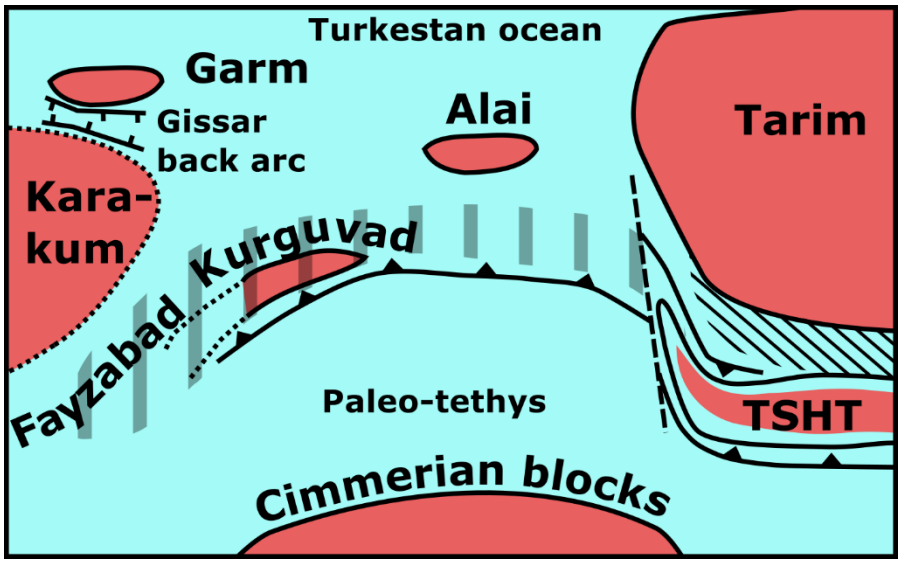

Figure 15: Paleogeographic constellation at the end of the Carboniferous. The North Pamir arc (bold hachures) is situated between the Tarim cratonic block and the Karakum block, whose existence has not yet been proven. South of Tarim, a branch of the Proto-Tethys remained open until the Carboniferous. The East Mazar arc volcanic rocks formed during its subduction. The Tianshuihai terrane (TSHT) together with the South Kunlun terrane, accreted in the Silurian to the southern margin of the Tarim croton (fine hachures). Cratonic blocs are shown in red, non-cratonic crust is shown in light blue, reconstruction after Zhang et al. (2018), and Konopelko et al. (2015).

Compiled literature data from the early Paleozoic and Triassic magmatic arc successions of the West Kunlun are compared with new and published data from the Carboniferous magmatic arc rocks of the North Pamir. The early Paleozoic succession in the West Kunlun records major

intrusive activity of a mature arc between 470 Ma and 450 Ma. The major Carboniferous intrusive activity in the North Pamir lasted from 340 Ma to 320 Ma. The Triassic arc-magmatic activity previously described from the West Kunlun and Karakul-Mazar lasted from 240 Ma to 200 Ma. As all three magmatic environments are subduction related, their granitoid rocks show similarities in geochemistry: enrichment in LILE and depletion of HFSE such as Nb, P and Ti (Figure 14). However, the North Pamir arc Carboniferous granites show less enrichment of LILE and a stronger mantle influence than the West Kunlun early Paleozoic and the Triassic granites. Collision and exhumation of metamorphic rocks of the West Kunlun started in the Silurian. A-type magmatism occurring in the lower Devonian marks a post-orogenic extensional phase (Yuan *et al.*, 2002). No magmatic rocks of that age have been recognized in the North Pamir.

Despite the loose stratigraphic control on the age of the volcanic sequence in the North Pamir, we show that all analyzed samples and complementary literature data share common geochemical characteristics. As the mafic and intermediate volcanic complexes show an arc signature, the name Kalai Khumb-Oytag basin (KOB, Burtman (2010)) might be used for the sub-basin of the Paleoasian ocean which hosted the arc. The arc itself should better be named the North Pamir arc, following Bazhenov & Burtman (1982). As we have shown, the term Kunlun arc (Schwab *et al.*, 2004) is inappropriate. The Kurguvad basement block with Ediacaran maximum depositional age and complex metamorphic history was part of the volcanic arc, at least for part of its history. This sliver of a continental basement block is quite similar to the Garm block in the Tien Shan, suggesting a joint Precambrian geologic evolution.

Starting with the emplacement of the Taergelake granite at around 360 Ma, large granitoids were emplaced within the arc until 314 Ma. Granitoids in the Chinese North Pamir have a more primitive composition and are classified as island arc granites within an intraoceanic subduction zone (Jiang *et al.*, 2008). The coeval tonalites and granodiorites that intruded volcanic sequences and the Kurguvad basement block in the Tajik North Pamir show more enriched REE patterns and are classified as continental volcanic arc granites. Our samples from the Tajik North Pamir arc fit well in stages 3–5 (tonalites to leuco-plagiogranites) established by Mamadjanov *et al.* (2017) for Late Paleozoic intrusives of that region. To date, there are no age constraints for the stage 1 and 2 intrusive rocks (i.e. gabbro and quartz diorites). We interpret the geochemical along-strike variance as the transition from intra-oceanic island arc subduction in the Chinese Pamir to Cordilleran type subduction in the Tajik North Pamir.

Granitoids in the East Mazar sliver of the Chinese West Kunlun show similar geochemical patterns as the Tajik granitoids, suggesting another Cordilleran type subduction zone to the east (Figure 15). However, there is also a connection to continental material in the Chinese Pamir, documented by an inherited zircon population with an age of 448 Ma from the Oytag granite (Jiang *et al.*, 2008) and the 417 Ma age population from the Triassic aplitic dike in Qimgan. Both age populations might be derived from the West Kunlun, where lower Devonian to Ordovician granitoids related

to the closure of the Proto-Tethys are common (Zhang *et al.*, 2019; Zhang *et al.*, 2019). We infer a Carboniferous sediment flux from the Proto-Tethys suture zone in the West Kunlun toward todays Chinese North Pamir and recycling of that detritus in the accretionary wedge.

The preserved length of the segment between Fakhar (Afghanistan) and Oytag (China) is around 500 km. However, it is likely that the geometry of the subduction system was modified by post-Carboniferous deformation. A partial obduction and erosion of the North Pamir arc in Pennsylvanian to Permian time can be inferred from disconformities and facies variations found in the Tajik and Chinese North Pamir. Facies distributions indicate a longer phase of crustal uplift and erosion in the Chinese North Pamir, where the Upper Devonian to Bashkirian arc volcanic units are followed by a continental Guadalupian to Triassic sequence. Whether the widespread presence of greenschist metamorphism in the North Pamir arc is related to this arc obduction event is not clear.

The existence of pre-Mesozoic oceanic crust to the north — in present day coordinates — of the advancing Cimmerian continents in the region of the todays North Pamir is in sharp contrast to the situation in the West Kunlun. New and existing data indicate the existence of a major oceanic domain in the North Pamir in late Paleozoic time and argues against a continuous Tarim-Tajik cratonic continent. This also challenges the hypothesis that the West Kunlun and North Pamir formed a continuous linear belt prior to the India-Asia collision; this removes a key paleogeographic constraint on the magnitude of Cenozoic indentation of the Pamir. A Carboniferous compressive phase partly closed the oceanic basin along an intra-oceanic subduction zone that laterally continued into a Cordilleran style subduction zone. In the east, closure and exhumation resulted in continental conditions, as shown by the Permo-Triassic volcano-sedimentary sequence found in the Qimgan valley. The lack of high-grade metamorphic units all along the North Pamir arc and ongoing marine sedimentation in the western parts of the basin, however, hint at a soft collision or slowdown of Carboniferous compressive tectonics. That left behind weaker crust to the west of Tarim compared to the well-amalgamated early Paleozoic terranes of the West Kunlun. The West Kunlun incorporated Tarim basement, in the North Kunlun domain (Zhang *et al.*, 2013). This E–W difference in rheology facilitated the advance of the Central Pamir further to the north compared to its eastward lateral equivalents, which may have caused a bending of the Cimmerian orogen.

Chapter 3. Calcite U-Pb dating of altered ancient oceanic crust in the North Pamir

3.1 Abstract

The North Pamir, part of the western syntax of the India-Asia collision zone, preserves remnants of a poorly understood Paleozoic intra-oceanic subduction zone. To constrain the age of this ancient ocean floor, we analyzed calcite phases in vesicular basalt and basaltic volcanic breccia with U-Pb geochronology using laser-ablation inductively-coupled-plasma mass-spectrometry (LA-ICP-MS). Dating of radial-fibrous to equant spary calcite yielded three meaningful Visean-Serpukhovian ages. REE + Y data reveal that the basaltic host rock of the calcite and oxidizing seawater are major sources of trace elements during calcite precipitation. U-Pb ages seem to be independent of REE + Y concentrations. Our results demonstrate the potential of calcite dating to constrain the age of ancient ocean floors. We challenge the hypothesis that a continuous early Paleozoic Kunlun Terrane extended from northern Tibet into the North Pamir.

3.2 Introduction

Constraining the timing of formation of ocean floor basalts is significant to develop models of various tectonic processes given the voluminous occurrence of ocean floor basalts in ophiolites, sections of ocean plate stratigraphy and exhumed subduction complexes, and remnants of island-arcs and oceanic plateaus in ancient convergent margins. However, mafic volcanic rocks, in which zircons are sparse, are challenging to date with radiometric methods. $^{40}Ar/^{39}Ar$ dating of separated phenocrysts or groundmass is frequently attempted (e.g., Waagstein *et al.*, 2002; Heath *et al.*, 2018). However, ocean floor alteration (OFA) often disturbs K-Ar isotopic compositions by secondary potassium gain (Staudigel *et al.*, 2013) or loss (Pringle, 1993), making $^{40}Ar/^{39}Ar$ dating more successful in providing high precision age data for fresh volcanic rocks but problematic if samples were affected by OFA.

Calcite veins and calcite-filled amygdules are commonly observed in submarine volcanic rocks. Studies show that calcite formation occurs during OFA by alkalinity-generating reactions shortly after the eruption of lavas (e.g. Spivack & Staudigel, 1994; Coogan *et al.*, 2016; Coogan & Gillis, 2018), driven by the infiltrating seawater and heat extraction from the oceanic crust. Such processes dominantly occur within ~25 Ma after rock consolidation (Coogan & Gillis, 2018). Therefore, dating the calcite phases in ocean floor volcanic rocks has the potential to constrain the timing of rock formation.

Calcite LA-ICP-MS U-Pb dating has been applied to a range of geological problems such as dating of deformation (e.g., Nuriel *et al.*, 2019), diagenesis, and sedimentation (e.g., Godeau *et al.*, 2018), especially since several international reference materials were established (Roberts *et al.*, 2017; Rasbury *et al.*, 2021). We present calcite LA-ICP-MS U-Pb dating of Paleozoic oceanic crust from Central Asia. Several types of calcite were dated from a volcanic sequence in the Carboniferous

North Pamir arc (Figure 16, e.g., Bazhenov & Burtman (1982)). Calcite U-Pb ages are consistent with regional geological data and existing radiometric ages from correlative volcanic units. With additional petrographic and geochemical data, our work sheds light on the potential of calcite U-Pb dating on ancient ocean floor volcanics and allows us to test tectonic models of the Pamir.

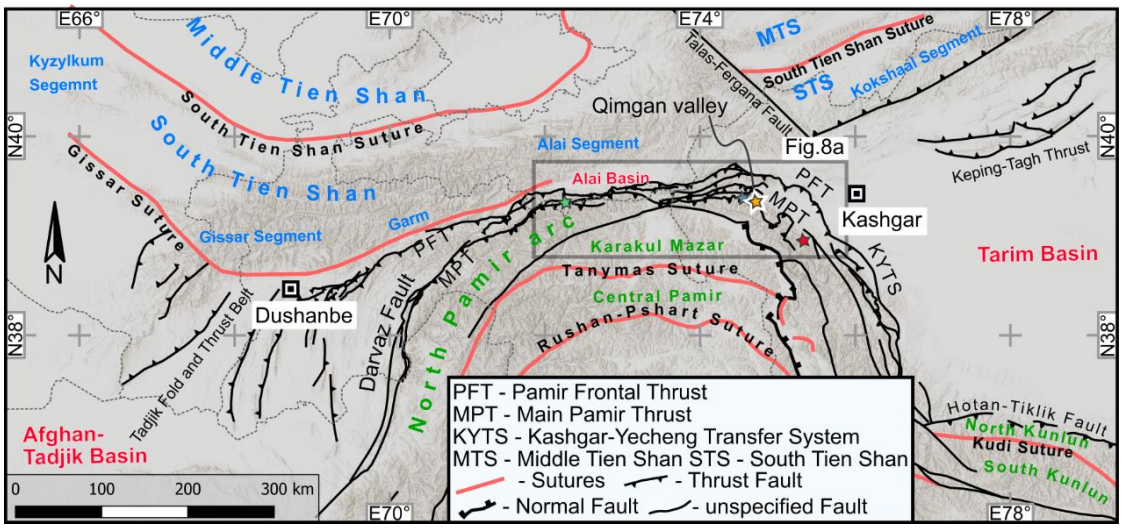

Figure 16: Map of the North Pamir and surroundings. The yellow star marks the position of the Qimgan valley, as noted. The meaning of the other star symbols is explained in Figure 23. Map drawn after Konopelko et al. (2019), Li et al. (2020), and Henan Institute of Geological Survey (HIGS) (2014).

3.3 Geological background and motivation

The North Pamir magmatic arc formed during subduction of the Paleo-Tethys oceanic lithosphere (e.g., Bazhenov & Burtman, 1982). The arc can be traced from the Chinese NE Pamir along strike into the Darvaz mountain range in the Gorno-Badakhshan province of Tadjikistan and further south into the Badakhshan province of Afghanistan (Figure 16). Outcrops in the Chinese Oytag and Gez valleys have been correlated with the South Kunlun Terrane in the north Tibetan West Kunlun by connecting ophiolitic sequences along the proposed Oytag–Kudi suture (e.g., Mattern *et al.*, 1996). However, existing age dating reveals dissimilarities of key rock units in this suture in the West Kunlun compared to the North Pamir. The West Kunlun Kudi suture closed in the Silurian, as interpreted from zircon and monazite LA-ICP-MS U-Pb dating of amphibolite-facies rock (Zhang *et al.*, 2018). In contrast, the North Pamir magmatic arc, to which the mafic volcanic rocks and associated plagiogranites in the Oytag and Gez valleys are assigned, seems to be much younger. It consists of poorly dated mafic and intermediate volcanics, associated volcaniclastic rocks, and subordinate cherts. A series of leucogranites and granodiorites that intruded the arc between 360 and 314 Ma has been dated recently (Chapter 2 and Zhang *et al.*, 2006; Jiang *et al.*, 2008; Kang *et al.*, 2015). The Oytag suture itself is represented by a small outcrop of altered ultramafic rocks in the Gez valley (Jiang, 1992). To date, no age data has been presented for those rocks. The green color of the North Pamir arc volcanic rocks implies thorough spilitization, making them unsuitable

for $^{40}Ar/^{39}Ar$ dating. We propose that abundant calcite associated with spilitic basalts are a product of OFA, and that calcite ages can serve as a constraint on the formation of ocean floor. Specifically, they provide the possibility of directly dating OFA as a proxy for the emplacement age of mafic volcanic rocks.

We conducted calcite dating based on detailed petrographic and geochemical observations in order to provide age constraints on the North Pamir arc volcanic rocks and test its correlation with the West Kunlun. For that purpose, we sampled 4 specimens at 3 different localities in the Chinese Qimgan valley (Figure 16). Samples 17NP436a and 17NP436b are from the same locality (sample location at N 39° 18′ 27″, E 74° 51′ 32″) and represent redeposited brecciated mafic volcanic rock with interstitial calcite cement that was formed during an early phase of brecciation (Figure 17a–c). Samples 15NP236 (sample location at N 39° 18′ 18″, E 74° 51′ 30″) and 15NP233 (sample location at N 39° 18′ 16″, E 74° 51′ 47″) are from two localities with amygdaloid-basalt, where 15NP236 was taken from a pillow basalt. We investigated amygdules filled exclusively with calcite (Figure 17e, f)

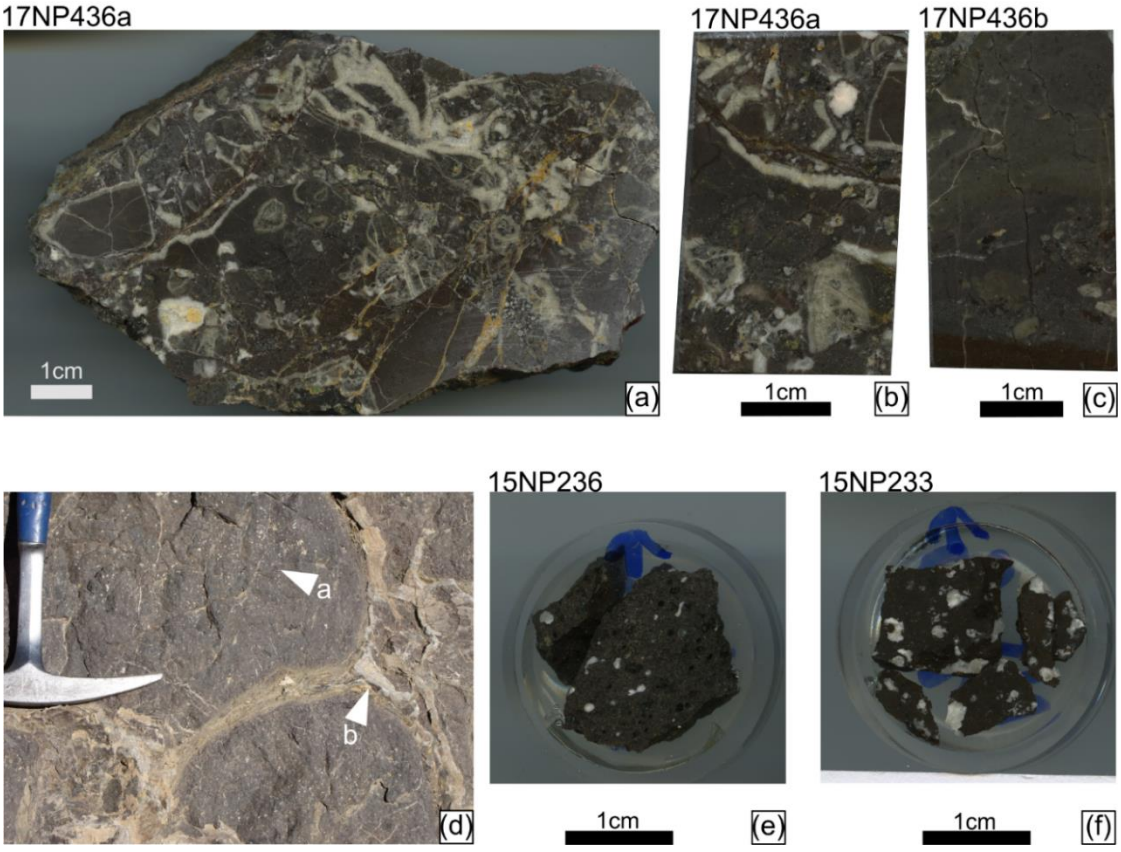

Figure 17: Sample photographs. Hand specimen of sample 17NP436a (a) and polished rock block used for LA-ICP-MS measurements of sample 17NP436a (b) and 17NP436b (c). Field photograph of well-preserved amygdaloidal pillow-basalts in Oytag valley near Qimgan valley (d), with white arrows pointing at calcite filled vesicles (arrow a) and massive interstitial calcite (arrow b). Polished rock specimen 15NP236 (e) and 15NP233 (f) of similar rock, were used for LA-ICP-MS.

3.4 Methods

3.4.1 Petrological microscopy, cathodoluminescence microscopy (CL) and X-ray fluorescence microscopy (XFM)

Petrographic thin sections of all samples were studied with conventional light microscopy and cathodoluminescence microscopy (CL). Polished thin sections of all samples were prepared. CL imaging was done using an Olympus BXFM-F microscope equipped with a Lumic hot-cathode electron source and a highly sensitive Olympus XC10 camera at the University of Potsdam. We recognized well preserved primary features (see Sect. 4.1), which were then identified on the rock chips prepared for laser ablation. Detailed sample petrography raises the chances of obtaining robust, meaningful ages, as emphasized recently by Roberts *et al.* (2021). High resolution reflected light images indicate the position of ablation spots in Appendix Figure A1 to Figure A4).

Additionally, we examined sample 17NP436a with scanning X-ray fluorescence microscopy (XFM). A polished slab cut parallel to the surface examined with LA-ICP-MS was prepared from the same rock chip. XFM maps were collected at the XFM beamline at the Australian Synchrotron (Howard *et al.*, 2020). The incident excitation energy was 18.5 keV. Pixel size and dwell time per pixel are indicated in Appendix Figures B1 to B4.

3.4.2 Laser-ablation inductively-coupled-plasma mass-spectrometry (LA-ICP-MS)

Rock samples were processed at the School of Earth and Environmental Sciences, The University of Queensland. Samples 15NP233 and 15NP236 were cut and mounted on one-inch diameter round mounts (Figure 17e, f); for samples 17NP436a and 17NP436b, we used polished rock chips (Figure 17b, c). Sample mounts were polished using standard polishing procedures and finished with a 0.25 micrometer diamond suspension.

LA-ICP-MS U-Pb dating and geochemical analysis was performed at the Radiogenic Isotope Facility of the Centre for Geoanalytical Mass Spectrometry, The University of Queensland following methods in Su *et al.* (2020) and Yang *et al.* (2021). Laser ablation was achieved using an ASI RESOlution 193 ArF nm excimer laser system. Following evacuation of air, He carrier gas was introduced into the laser cell at a flow rate of 0.35 l/min. 0.005 l/min of N_2 gas was also introduced to the laser cell to enhance the measurement sensitivity. The gas mixture was then introduced into the plasma torch of a Thermo iCAP RQ quadruple ICP-MS with 1.06 l/min Ar nebulizer gas. No reaction gas was employed. The laser was run with a 100 µm diameter round spot at 10 Hz, with a measured instrument laser-fluence (laser pulse energy per unit area) of 2.5 J/cm^2. For U-Pb dating, each spot had 8 s of background, 20 s of data acquisition, and 15 s of wash out. For trace elemental analysis, each spot had 6 s of background, 25 s of data acquisition, and 10 s of wash out. Prior to data acquisition, ICP-MS signals were optimized during tuning. For our

session, ~950 kcps of ^{238}U counts and ~ 0.22 of $^{206}Pb/^{238}U$ were achieved for measuring NIST612 glass using line scans of 3 µm/s, 10 Hz, 50 µm round laser pit, and 3 J/cm^2.

U-Pb isotopes for geochronology (^{206}Pb, ^{207}Pb, ^{208}Pb, ^{232}Th, and ^{238}U) were measured with the following dwell times, ^{206}Pb (0.025 s), ^{207}Pb (0.055 s), ^{208}Pb (0.005 s), ^{232}Th (0.005 s), and ^{238}U (0.02 s). Both glass standard NIST614 and matrix-matched calcite standards were measured, bracketing unknown spots. NIST614 glass was used for correction of $^{207}Pb/^{206}Pb$ fractionation and instrument drift in the $^{238}U/^{206}Pb$ ratio (Woodhead & Hergt, 2001). Raw data were processed using Iolite software v3.64 (Paton *et al.*, 2011). After the initial correction, a matrix-matched calcite reference material of known age was used for further correction of matrix-related mass bias impacting the measured $^{238}U/^{206}Pb$ ratios, following the approach described elsewhere, as summarized in Yang *et al.* (2021). We used cross-calibrated in-house calcite reference materials AHX-1D and PTKD-2 and an international reference material WC-1 (Roberts *et al.*, 2017) in our laser ablation session. The accuracy of unknown spots is checked by measuring WC-1 and PTKD-2 as monitoring standards. For WC-1 we obtained an age of 251 ± 1 Ma (2 σ), consistent with the recommended age of 254.4 ± 6.4 Ma (Roberts *et al.*, 2017). The in-house PTKD-2 standard gave an age of 154 ± 3 (2σ), consistent with our recommended age of 153.7 ± 1.7 Ma (2σ), calibrated by isotope dilution. Therefore, we note that the accuracy for our measurements can be calculated as 1.5 % for WC-1 and 0.3 % for PTKD-2. Uncertainty propagation was done according to the principles defined by Horstwood *et al.* (2016). We present two age uncertainties as ±α/β (2σ), where α is without propagated systematic uncertainties, and β is with propagated systematic uncertainties. We propagated our analytical errors (typically <5% (2σ) on $^{238}U/^{206}Pb$ ratios) by incorporating ^{238}U decay constant error, long-term variance of the reference materials $^{238}U/^{206}Pb$ ratios in the lab, and the analytical error of the monitor standard. This resulted in a total propagated systematic uncertainty of 4.6% (2σ) into the analytical error.

Trace elemental analysis was conducted in the same ablation areas as the U-Pb spots but without overlapping the U-Pb spots. Prior to data acquisition, ICP-MS signals were optimized during tuning while the oxide production rate was controlled to be as low as possible. The ThO/Th ratio during our session was <0.002 for NIST612 glass using line scans of 3 µm/s, 10 Hz, 50 µm round laser pit, and 3 J/cm^2. ^{43}Ca was measured as an internal standard. Data reduction was conducted using the Iolite software v3.64 (Paton *et al.*, 2011) with the Trace Element data reduction scheme. All reported concentrations were after international standardization using Ca (Ca = 40.1 %).

3.5 Results

3.5.1 Petrography and calcite occurrences

In the Chinese Qimgan valley, basaltic to andesitic volcanic rocks contain large amounts of calcite

in amygdules, in between single lava pillows, and volcanic breccia layers (Figure 17 and Appendix B.1 to Appendix B.4) Two samples, 15NP233 and 15NP236, are altered amygdaloid-basalts with published geochemistry (Appendix B.13, and Chapter 2). Samples 17NP436a and 17NP436b are from a volcanic breccia, rich in calcite cement fragments and calcite-overgrown, angular volcanic rock fragments. The samples were collected from 3 localities, whereas 17NP436a and 17NP436b are from the same locality.

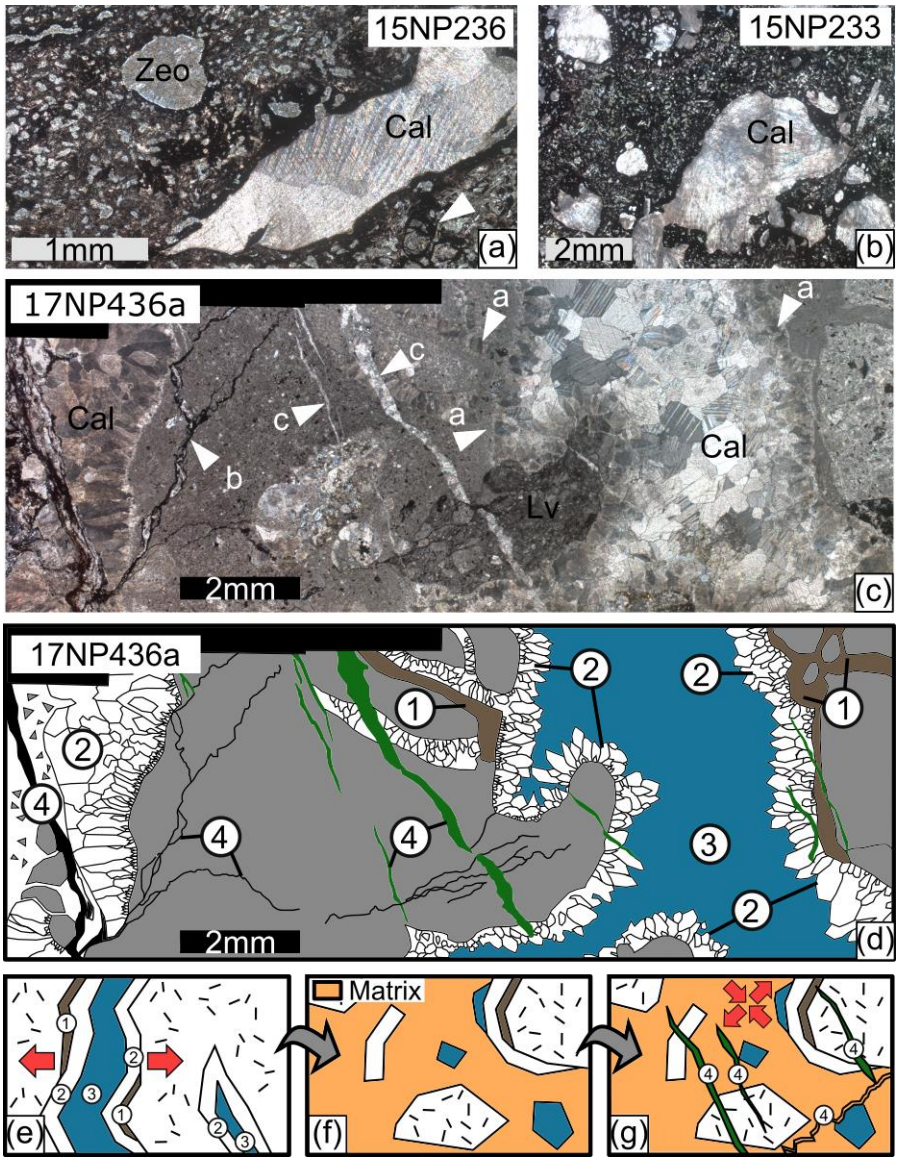

Figure 18: Calcite microstructures. Typical calcite-filled vesicles from sample 15NP236 (a), in this case with spary calcite and zeolite mineralization. The white arrow marks preserved perlitic structures. Botryoidal calcite was found in both amygdaloid-basalt samples, the example in (b) is from 15NP233. Panel (c) shows a thin section photograph of sample 17NP436a. White arrows indicate radial fibrous calcite (a), dark styloliths (b), calcite filled fissures (c). (a–c) Under crossed polarized light. Panel (d) shows a schematic sketch of microphotograph (c), delineating a sequence of 4 events: (1) formation of hydrothermal clay, (2) precipitation of fibrous-radial calcite along the walls of brecciated volcanic rock fragments, (3) late-stage equant calcite formation, (4) pressure solution and formation of styloliths (dark lines) and reprecipitation of dissolved calcite in fissures (green). Areas 2 and 3 are targets for laser ablation. In figures (e)-(f) a schematic sequence of events leading to the formation of the basaltic breccias is sketched. (e) Fracturing of the basaltic rock and formation of clay (1) and calcite cement phases (2) and (3). (f) disarticulation and sedimentation of debris containing isolated calcite cement fragments. (g) Late-stage pressure solution and fissure formation of phase (4). Red arrows schematically indicate stress regime.

Amygdules in samples 15NP233 and -236 show one generation of spary or botryoidal calcite with typical sweeping extinction under cross-polarized light (Figure 18a, b). Sample 15NP233 has vesicles up to 5 mm in diameter filled exclusively with calcite. Sample 15NP236 has much smaller vesicles, around 1 mm in diameter, filled with either calcite or zeolite. Both samples show high "Loss on Ignition" (LOI) values and anomalous major element values for whole rock geochemistry, accounting for high secondary, volatile rich mineral content (Appendix B.13).

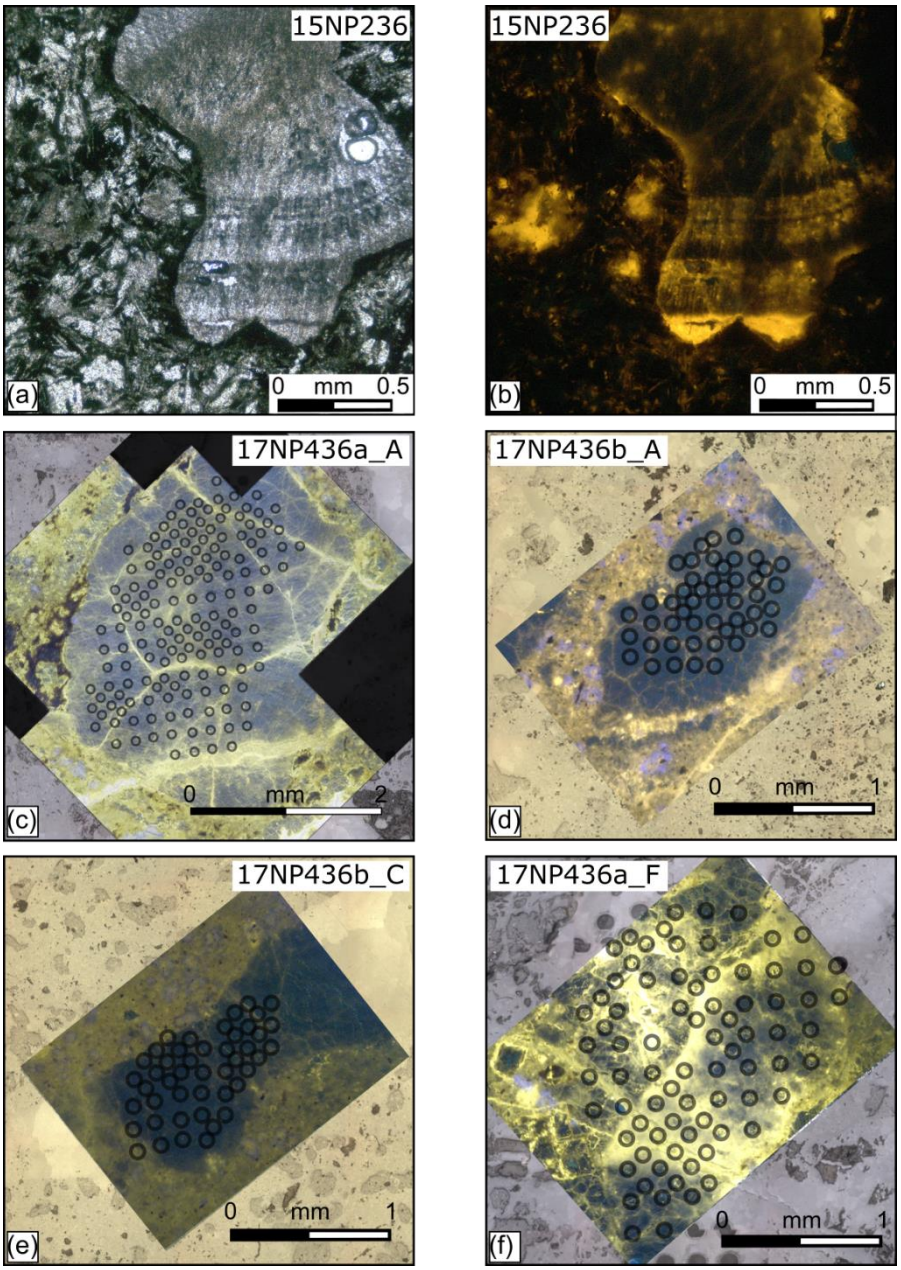

Figure 19: Cathodoluminescence images of exemplary calcite areas. Microphotographs under plain light (a) and cathodoluminescence (b) of an exemplary vesicle from sample 15NP236 show primary botryoidal structure of the calcite. Primary calcite seems non-luminescent to dull-luminescent. Cathodoluminescence images of ablation areas 17NP436a_A (c), 17NP436b_A (d) and 17NP436b_C (e) show relatively homogenous non-luminescent calcite cement fragments with a small portion of bright yellow veins. The calcite cement fragments are embedded in a dull-yellow luminescent volcaniclastic matrix. All three samples yielded high quality calcite U-Pb ages (MSWD < 2). Ablation area 17NP436a_F (f), which has a high portion of bright yellow calcite, yielded a less precise age (MSWD = 3.5). Ablation spots for geochemistry and U-Pb dating are marked with grey circles.

No fractures or veins cut across amygdules in these samples. In samples 17NP436a and b, fracture and pore space in basaltic rock fragments shows multiple calcite generations (Figure 18c, d). Most calcite formed prior to deposition of the breccia. Specifically, isolated cement fragments are fully embedded in a fine-grained matrix (e.g., in sample 17NP436b). They may have formed in fractures of a volcanic edifice and were redeposited after its collapse. In some cases, calcite cement is still attached to the basaltic clasts and a series of 4 consecutive mineralization phases can be recognized (numbered 1 to 4 in Figure 18d, schematically depicted in Figure 18e-g). Some of the volcanic rock fragments show an early, hydrothermal clay layer (Figure 18c and phase 1 in Figure 18d). The rock fragments—or if present, the clay coatings—are overgrown by a first generation of radial-fibrous calcite. Larger voids are filled with late, equant calcite (phase 2 and 3 in Figure 18d). The early, medium to coarse spary calcite cements (2 and 3 in Figure 18d) and the matrix are crosscut by fine-sparitic calcite filled fissures (4 in Figure 18d) The fissures are distinguishable from the spary calcite in transmitted and reflected light and were avoided during ablation.

Cathodoluminescence microscopy imaging reveals fibrous botryoidal textures of the vesicle-filling calcite of samples 15NP233 and 15NP236. They usually show no luminescence or a zonation of dull-yellowish and non-luminescent fringes (Figure 19a,b). Bright yellow luminescence irregularly occurs along the rims of the vesicles. Secondary fractures crosscutting the vesicular fabric were not observed. We prepared slides from the rock chips analyzed with LA-ICP-MS of samples 17NP436a and 17NP436b (Figure 19c-f). The basalt breccia samples 17NP436a and 17NP436b show non-luminescent to dull yellow luminescent spary calcite. Bright yellow luminescence was observed along hairline subzones, which are interpreted as grain boundaries. The largely non-luminescent spary calcite fragments stand out against the yellow luminescent altered volcaniclastic matrix. Matrix and spary calcite fragments are intersected by bright-yellow, late-stage calcite (phase 4 in Figure 18d) filled fractures (e.g., Figure 19c). They are clearly visible in transmitted and reflected light and were avoided during ablation.

In order to better understand calcite phases, we further study 17NP436a with high-resolution synchrotron X-ray fluorescence mapping (Howard *et al.*, 2020), following methods described in Vanghi *et al.* (2019). Sr maps show elevated concentration for the phase 2 and 3 calcite and much lower content in fissure filling calcite phase 4, suggesting different geochemical regimes (Appendix B.5 to Appendix B.8).

3.5.2 LA-ICP-MS U-Pb Dating

Four samples from three field sites were prepared for analysis. We obtained data from 839 single spots from 18 laser ablation areas (Appendix B.1 to Appendix B.4), 3–6 ablation areas per sample (Figure 20, Figure 21), data table in Appendix B.15. For age calculation, we used the IsoplotR program (Vermeesch, 2018) version 3.5 running in R version 3.6.0. Ages are calculated for individual ablation areas by linear regression in a Tera–Wasserburg plot. From the 839 single spot

ablation data only 16 had to be omitted due to U content below the detection limit.

17NP436a

Six ablation areas were targeted in basalt breccia sample 17NP436a (Figure 20a-f). They are placed on isolated coarse sparitic, equant calcite cement fragments (areas A, C, D, E) and coarse-sparitic radial-fibrous to equant calcite cement still connected to their basaltic substratum (areas B, F). Propagated errors are generally small (~5%) and MSWD values are low to moderate. Area A is an isolated fragment of coarse spary cement (Figure 19c) and yielded a lower intercept age of 331 ± 2/15 Ma (MSWD = 1.7) calculated from 119 single spot data points. Eighty-two ablation spots yielded a lower intercept age of 324 ± 4/16 Ma (MSWD = 2.3) for Area B. Sixty-four ablation spots gave a lower intercept age of 308 ± 7/16 Ma (MSWD = 2.5) for Area C. Area D gave a similar lower intercept age of 307 ± 6/15 Ma (MSWD = 4.2, n = 40). Area E gave a rather low age of 298 ± 10/17 Ma with an elevated MSWD of 4.7, defined by 37 ablation spots. Sixty-one ablation spots on area F (Figure 19f) defined a lower intercept age of 304 ± 7/16 Ma (MSWD = 3.5).

17NP436b

In basalt breccia sample 17NP436b, four ablation areas were targeted (Figure 20g-j). They are placed on isolated coarse sparitic, equant calcite cement fragments. Propagated errors are generally small (~5%) and MSWD values are low to moderate. Area A (Figure 19d) yielded a lower intercept age of 339 ± 6/17 Ma (MSWD = 1) defined by 38 ablation spots. Area B yielded a lower intercept age of 322 ± 3/15 Ma (MSWD = 4.8) defined by 47 ablation spots. Twenty-nine laser spots on area C (Figure 19e) yielded a lower intercept age of 328 ± 4/16 Ma (MSWD = 1.7). Twenty-three ablation spots gave a lower intercept age of 316 ± 9/17 Ma (MSWD = 2.4).

15NP236

Five ablation areas were targeted in vesicular basalt sample 15NP236 (Figure 21a-e). Each ablation area represents one calcite filled vesicle. Due to the small vesicles, only a few spots were placed per area. Propagated errors are moderate to large (6-36%) and MSWD values are low to moderate. Area A yielded a lower intercept age of 351 ± 29/33 Ma (MSWD = 2.2) defined by 14 single ablation spots. Fifteen ablation spots on area B gave a lower intercept age of 306 ± 64/65 Ma with a low MSWD of 1.4. Ten spots on area C gave an age of 350 ± 15/22 Ma (MSWD = 2.2). Area D yielded a very young age of 206 ± 73/73 Ma (MSWD = 0.84) defined by 10 ablation spots. A similarly young age of 272 ± 57/58 Ma (MSWD = 4.3) was defined by 18 laser spots for area E.

15NP233

Three ablation areas were placed on calcite in three filled vesicles in sample 15NP233 (Figure 21f-h). Propagated errors are small (~5%) and MSWD values are moderate. Area A gave an age of 324 ± 4/16 Ma (MSWD = 2.4) defined by 60 ablation spots. Ninty-nine ablation spots on area B yielded a similar age of 327 ± 5/16 Ma (MSWD = 2.5). Fifty-eight ablation spots on area C gave a slightly higher age of 337 ± 7/17 Ma (MSWD =9.8).

3.5.3 LA-ICP-MS Geochemistry

For each laser ablation area, we measured Ca, Mn, Sr, Zr, Ba and REE + Y geochemical data (a total of 380 single spot analyses) using LA-ICP-MS (data in Appendix B.14). Calcite REE patterns normalized to chondrite (Boynton, 1984) are mostly flat to slightly "U" shaped (Appendix B.9 to Appendix B.12). REE content of the vesicle-hosted calcite is higher (61 ppm mean total REE content in sample 15NP233, 59 ppm in sample 15NP236) compared to the breccia calcite cement (8 ppm in 17NP436a and 12 ppm in 17NP436b). LREE are enriched over MREE (La_n/Sm_n) and negatively correlate with enriched MREE over HREE values (Dy_n/Yb_n) in all samples. The vesicle-filling calcite shows both positive and negative Ce/Ce* values between 0.75 and 1.4; the breccia calcite cement shows negative values between 0.18 and 0.92. Negative Ce anomalies are usually associated with oxidizing conditions producing Ce^{4+} instead of Ce^{3+} (e.g., Alibo & Nozaki, 1999). We observe positive to slightly negative Gd anomalies ($Gd/Gd^* = Gd_n/sqrt(Eu_n \times Tb_n)$; Figure 22a). Positive Y_n/Ho_n anomalies are common (Figure 22b). Negative Ce/Ce* and Eu/Eu* anomalies together with higher Gd/Gd* and Y_n/Ho_n in the calcite cement of the volcanic breccia are interpreted to reflect a stronger influence of infiltrating seawater ($Ce/Ce^* = Ce_n/sqrt(La_n \times Pr_n)$; $Eu/Eu^* = Eu_n/sqrt(Sm_n \times Tb_n)$).

3.6 Discussion

3.6.1 Calcite age data and its significance

In newly formed submarine volcanic rocks, calcite formation marks the phase of alkalinity-generating reactions. Alkalinity describes the acid neutralizing capacity by formation of alkali and alkaline earth metal ion species during rock weathering (e.g., Spivack & Staudigel, 1994). This is crucial for interpreting OFA calcite U-Pb ages, implying that these ages should be no older than the "true" rock formation age. High temperature hydrothermal alteration is also a common phenomenon in submarine volcanic environments. This is, in contrast, restricted to discrete zones, such as veins, shear zones, and hydrothermal upflow zones (Honnorez, 2003; Harlov & Austrheim, 2013). It changes the mineral composition of the volcanic host rock completely, such that primary igneous textures are obliterated (e.g. epidosites, Honnorez, 2003). Such rock types must be avoided as they are unlikely to produce ages related to OFA. By dating isolated calcite, far from hydrothermal upflow zones, we determine the age range of OFA that occurred shortly after rock consolidation. This gives a minimum age estimate for ocean floor formation, if not the actual age of formation. This must not be mistaken for the radiometric ages of the volcanic rock itself (e.g., ages from zircon U-Pb dating).

We observed one botryoidal to spary calcite phase in the vesicular basalts (Figure 18a, Figure 19a and b). Four stages of mineralization were observed in the basaltic breccia: (1) hydrothermal clay, (2) radial-fibrous calcite, (3) coarse equant-spary calcite and (4) fissure filling calcite crosscutting

the entire fabric (Figure 18b-g). The presence of radial-fibrous and sparry, equant calcite crystals is typical of continuous calcite precipitation in a porous substratum (Gonzalez & Carpente, 1992). In a first phase, radial-fibrous calcite grows along the wall of the voids and successively reduces the porosity of the substratum, thereby hindering fluid flow. This reduces the calcite precipitation rate and the amount of nucleation, leading to larger, equant calcite crystals in the center of the voids. This model can be adopted for a first calcite phase (2 and 3 in Figure 18d). As the radial-fibrous and the equant calcite growth reflects one process, both calcite phases were chosen for ablation.

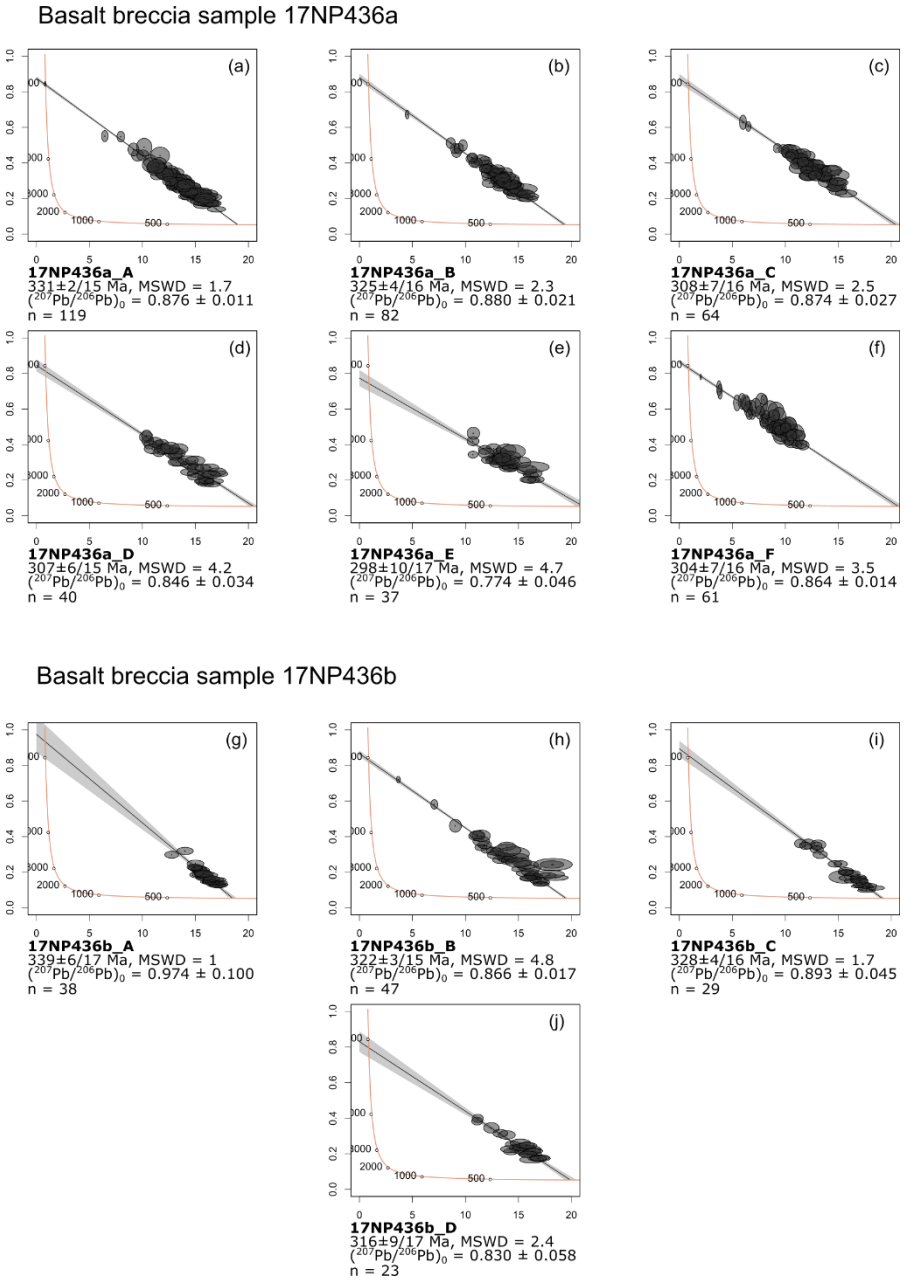

Figure 20: Tera-Wasserburg plots. Ablation area ages are from basalt breccia samples 17NP436a and 17NP436b. All errors are given as 2σ.

The phase 4 fine-sparitic filled fissures are interpreted to reflect a later tectonic event, expressed by differential stress, pressure solution and reprecipitation of calcite in open joints (Figure 18g). To explore the geologic significance of our age data, we first applied a very conservative filter, closely examining ages with MSWD < 2 and 2σ-error < 10%, as their isotope ratios are most likely measured from single homogenous domains (e.g., Lan *et al.* (2022)). Subsequently, we also discuss all ages for a full view of the age spectrum.

Our samples generally show a low variability in ablation area ages and initial Pb values (Figure 20 and Figure 21). 2σ-errors with propagated systematic uncertainties are typically around 5%. Only vesicular basalt sample 15NP236 shows high 2σ-errors. However, multi-stage calcite formation and possible subsequent alteration lead to MSWD values above two and elevated age errors. Primary calcite was eventually affected by alteration and crystallization of calcite with differing chemistry even within microscopically identified seemingly homogenous phases (e.g. phase 2 and 3 in Figure 18d).

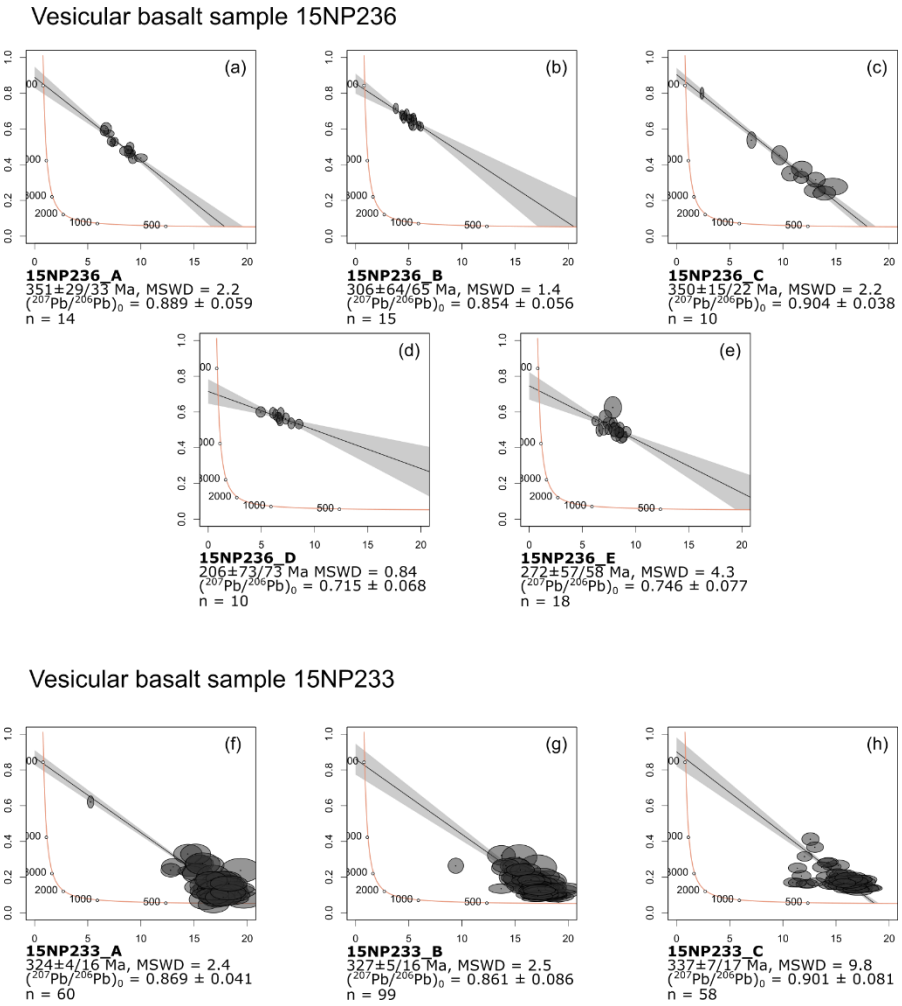

Figure 21: Tera-Wasserburg plots. Ablation area ages are from vesicular basalt samples 15NP236 and 15NP233. All errors are given as 2σ.

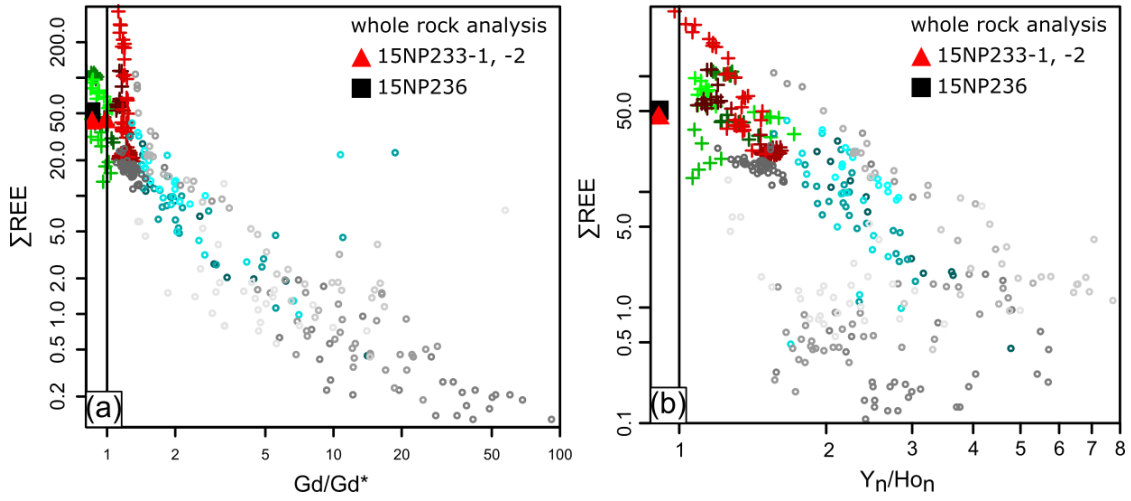

Figure 22: Rare-earth element plots. (a) Mixing trend between high total REE—negative Gd/Gd and low total REE—positive Gd/Gd* composition. (b) Higher Y_n/Ho_n values correlate with low total REE. Y and Ho normalized against chondrite values of Anders & Grevesse (1989). (e, f) + -15NP233, -236, **o** -17NP436A, -B; color-code see Appendix A.*

This is made visible by CL imaging of yellow-luminescent subzones penetrating non-luminescent phase 2 and 3 calcite zones in Figure 19f. However, ablation spots placed on ablation areas 17NP436a_A, 17NP436b_A and 17NP436b_C largely fall on what we interpret as phase 2 and 3, radial-fibrous to equant calcite, characterized by non-luminescence (Figure 19c-e). The lower intercept ages are 331 ± 2/15 Ma (17NP436a_A), 339 ± 6/17 Ma (17NP436b_A) and 328 ± 4/16 Ma (17NP436b_C), which consistently constraints the volcanic breccia to the Visean-Serpukhovian boundary. All ablation areas of basalt breccia samples 17NP436a and 17NP436b and vesicular basalt sample 15NP233 overlap within propagated 2σ-errors. Their scatter reflects either the mixed ages of multiple calcite formation events during the late Mississippian to Pennsylvanian which cannot be resolved, or minor isotope disturbance (by heating and/or fluid flow) during a much younger event. Vesicular basalt sample 15NP236 yielded less defined regressions, thus high age errors, caused by the small spread of the limited number of ablation spots. However, two ablation areas, 15NP236_B and 15NP236_D, gave MSWD values of 1.4 and 0.84 respectively, while yielding much different lower intercept ages. 15NP326_B gave an age of 306 ± 64/65 Ma, which overlaps with the ages of 15NP326_A (351 ± 29/33 Ma, MSWD = 2.2) and 15NP326_C (350 ± 15/22 Ma, MSWD = 2.2). 15NP236_D gave an age of 206 ± 73/73 Ma, which is apparently younger. This leads us to conclude that Carboniferous primary ages were affected by young events causing isotope disturbance and shift of the apparent, yet mixed ages towards younger values. This might be true to a limited degree for all samples with MSWD > 2.

Calcite ages are consistent with published radiometric ages of correlative rock units in the North Pamir arc, including two hornblende $^{40}Ar/^{39}Ar$ ages of ~350 Ma from a meta-andesite, zircon U-Pb ages of ~329 Ma from felsic to intermediate volcanics in Altyn Darya valley (Schwab *et al.*, 2004), and zircon U-Pb ages of ~360 to 314 Ma from island arc granites (Chapter 2 and Ji *et al.*,

2018) (Figure 23). All these ages are interpreted by the aforementioned authors to be primary magmatic ages and reflect the age of emplacement of those units.

3.6.2 Calcite REE + Y geochemistry

Whole rock geochemical data from altered basalt has a flat C1-normalized REE pattern (Boynton, 1984), implying an intra-oceanic arc origin (Chapter 2 and Jiang *et al.*, 2008). We suggest a possible control of the basalt geochemistry on calcite REE patterns; any process altering this signal would significantly change the calcite REE pattern (Debruyne *et al.*, 2016).

REE partition coefficients between aqueous solution and precipitating calcite have been experimentally studied (e.g., Voigt *et al.*, 2017; Perry & Gysi, 2018); results suggest that variable physicochemical conditions could lead to strongly differing integration of rare earth elements into the calcite lattice. We show that calcite cements of samples 17NP436a and b are distinguishable from vesicle fillings in samples 15NP233 and -236 (Figure 22a, b).

Calcite must be the major REE + Y sink as our samples do not show any intergrowing, co-precipitated mineral phase. The dominance of calcite hints at precipitation from CO_2-rich seawater derived hydrothermal fluids under low temperature conditions (Honnorez, 2003; Talbi & Honnorez, 2003). This happened in the upper few 100 meters of the oceanic crust. We assume a low mineralization temperature. Under this condition, Eu is trivalent and negative Eu/Eu* is directly inherited from the fluid reservoir (Debruyne *et al.*, 2016). Pronounced negative Ce/Ce* values are a typical inherited signal of oxidizing seawater (e.g., Alibo & Nozaki, 1999); in correlation with increasing Y_n/Ho_n values, they trace back to oxidative sorption by Fe-Mn O(OH) species (Debruyne *et al.*, 2016). Positive Gd/Gd* values may be interpreted as a seawater signal (e.g., Baar *et al.*, 1985). However, markedly positive Gd anomalies together with positive Y_n/Ho_n values are less commonly reported. Similar features were observed in high salinity waters from Jordan graben lakes (e.g., Möller *et al.*, 2007). Because ocean floor aquifer porosities are highly heterogenous (e.g., Fisher & Becker, 2000), the higher porosity of volcanic breccias 17NP436a and 17NP436b may have promoted seawater infiltration, leading to lower REE concentrations and more pronounced Ce/Ce*, Eu/Eu*, Gd/Gd* and Y_n/Ho_n anomalies compared to amygdaloidal basalt samples. We note that Gd anomalies strongly correlate with REE concentration. Although, LA-ICP-MS data acquisition was done according to international standards, we cannot completely exclude the possibility of polyatomic interference of the measured ^{157}Gd isotope with $^{141}Pr^{16}O^{+}$ (May & Wiedmeyer, 1998).

3.6.3 Implications on tectonic models of the Pamir

The results from petrological thin section examination, showing primary calcite fabrics, together with LA-ICP-MS trace element geochemistry, which reflect sea water infiltration, typical for OFA, are major arguments for preserved, primary U-Pb isotopic ratios. Our studies constrain the

emplacement age of arc volcanic rocks in the NE Pamir to Middle-Upper Mississippian (Visean-Serpukhovian) (Figure 23), significantly younger than correlative lithologies in the West Kunlun, which are dated to the Cambrian (e.g. Yixieke dacite, Xiao *et al.* (2005), Kudi ophiolite, Wang *et al.* (2021)). The results carry significant implications for the interpretation of the Mesozoic and Cenozoic geodynamic evolution of the Tibet-Pamir orogen. Since the pioneering works of Burtman *et al.* (1963), Burtman & Molnar (1993), Pan (1994), Mattern *et al.* (1996), Xiao *et al.* (2002) and references therein, the Kudi-Oytag suture, or the "Paleozoic suture", has been hypothesized to be a single, once continuous, E–W-striking feature that was bent towards the north by Cenozoic indentation of the Pamir into a postulated Tarim-Tajik block.

Recent publications outline an early Paleozoic history of the West Kunlun arc magmatism (Figure 24a). The southward subduction of the Proto-Tethys started in the Terreneuvian, dated by the 531 Ma Nanpingxueshan pluton in the Tianshuihai Group (Yin *et al.*, 2020). As a consequence of the development of the Yixieke volcanic arc (Xiao *et al.*, 2005) and the Yierba arc, the South Kunlun was intruded by the Yierba adakitic diorite at ca. 513 Ma (Yin *et al.*, 2020). In response to slab roll-back, the Kudi ophiolite formed in a back-arc position between 513–516 Ma (Wang *et al.*, 2021). The Proto-Tethys closed in the Silurian between 431–420 Ma (Wang *et al.*, 2020) with exhumation of metamorphic units starting from ca. 440 Ma, as dated by monazite U-Pb from the Saitula Group (Zhang *et al.*, 2018). Closure of the Proto-Tethys was followed by the intrusion of A-type post-orogenic granites, dated as 420–405 Ma by zircon U-Pb in the North Kudi granite (Yuan *et al.*, 2002; Liu *et al.*, 2014). However, corresponding early Paleozoic geologic events or rock records in the North Pamir have not been reported.

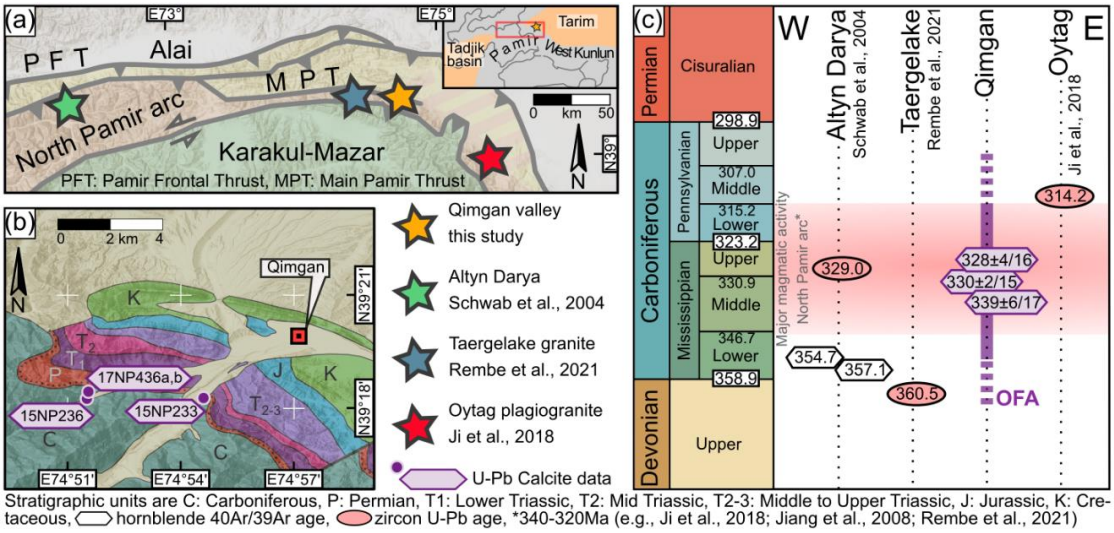

Figure 23: Results and regional age comparison. (a) Map of the northeastern Pamir with location of radiometric ages for the North Pamir arc volcanic rocks, shown in c. (b) Detailed field locations of samples in the Qimgan valley (map after Henan Institute of Geological Survey (HIGS) (2014)). There is a sedimentary hiatus between the Middle Pennsylvanian and the Guadalupian (Chapter 2). (c) Overview of selected literature data and newly obtained data for OFA of the North Pamir Carboniferous arc. Stratigraphic table and ages according to the International Chronostratigraphic Chart (Cohen et al., 2020).

Instead, previous works on mafic to intermediate volcanic rocks and granitoids of the North Pamir show major subduction related arc magmatic activity in the mid to late Carboniferous (Chapter 2 and Ruzhentsev *et al.*, 1977; Jiang *et al.*, 2008; Kang *et al.*, 2015; Ji *et al.*, 2018). Carboniferous arc magmatic rocks found in the Waqia (Tang *et al.*, 2020) and East Mazar (Li *et al.*, 2006) tectonic slivers reflect the closure of a remnant ocean basin, whereas major arc magmatic activity was focused on the North Pamir arc further to the west (Figure 24b). Stratigraphic relations and hiati point to a soft collision and obduction of that North Pamir arc in the early Permian (Chapter 2). No broad Paleozoic magmatic activity younger than Lower Devonian is known in the West Kunlun. The Carboniferous North Pamir arc granitoids intrude largely into poorly dated mafic volcanic rocks. Our calcite U-Pb ages agree with the only known ages of this volcanic unit from Schwab *et al.* (2004) (Figure 23). They corroborate the dissimilarity of the West Kunlun and North Pamir arc volcanic rocks, and therefore argue against the existence of a continuous Paleozoic suture extending from the Pamir to the West Kunlun.

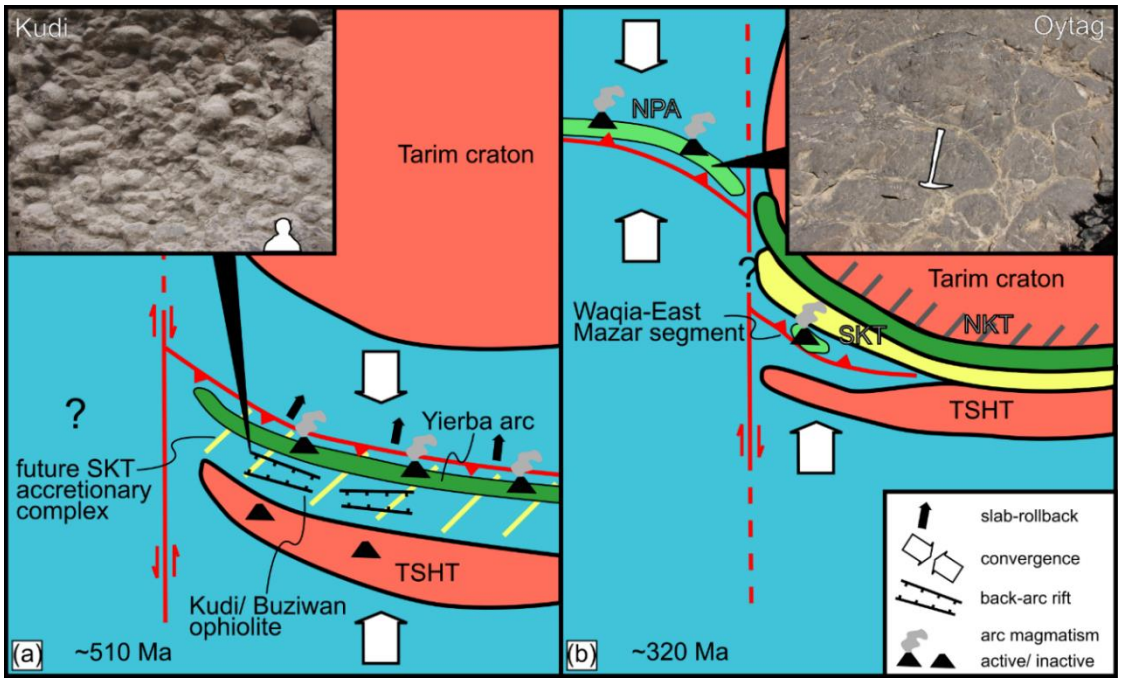

Figure 24: Paleogeographic reconstruction In the mid-Cambrian, the roll-back of the Proto-Tethys slab caused the formation of the Kudi ophiolite (a), exposed in the Buziwan valley (Wang et al., 2021). (b) Paleogeographic situation in the late Mississippian: The North Pamir arc formed along an intra-oceanic subduction zone (Jiang et al., 2008) forming the Oytag segment in its eastern branch. Subduction-related Waqia granite (Tang et al., 2020) and East Mazar granite (Li et al., 2006), both today part of tectonic slivers, suggest the presence of a remnant oceanic basin between Tianshuihai and the South Kunlun Terrane accretionary complex, as suggested by Zhang et al. (2018). Small photographs show pillow basalts in the Kudi section (in a) and Oytag near Qimgan (in b). SKT-South Kunlun Terrane, TSHT-Tianshuihai Terrane, NPA-North Pamir volcanic arc, NKT-North Kunlun Terrane.

Recent studies on the Gissar and Kyzylkum segment of the South Tien Shan (STS) of Uzbekistan (Figure 16), west of the North Pamir, document the presence of early Carboniferous metamorphism and constrain the volcanic age of meta-basalts from the northern Kyzylkum segment by zircon U-

Pb dating to 320–300 Ma (Konopelko *et al.*, 2019 and references therein). This is coeval with arc magmatic activity along the North Pamir arc. Konopelko *et al.* (2019) propose an archipelago model for the late Paleozoic suture zones in the STS, characterized by high-T metamorphism, rapid exhumation, and multiple subduction zones. This archipelago might have been connected to the Paleo-Tethys realm. We argue for a North Pamir arc continuing from the northeastern Pamir into the Tajik northwestern Pamir and the Gissar segment of the South Tien Shan.

3.7 Conclusion

Calcite phases in Paleozoic ocean floor volcanic rocks were studied with LA-ICP-MS. From four samples, we investigated a total of 18 laser ablation areas. Although systematic errors of lower intercept ages could be small (as low as <1 % at 2σ), we focus on propagated errors because they include the long-term variance of the reference materials, the analytical error of the monitor standard, and other important sources of errors. Three ablation areas yielded high quality lower intercept ages, 331 ± 15 Ma (17NP436a_A), 339 ± 17 Ma (17NP436b_A) and 328 ± 16 Ma (17NP436b_C), each with MSWD < 2 and propagated 2σ-error < 10%, which we interpret as representing the timing of individual geologic events. The majority of the remaining ablation area ages from volcanic breccia samples 17NP436a and 17NP436b as well as vesicular basalt sample 15NP233 overlap with this age within propagated 2σ-errors. They show slightly elevated MSWDs, implying that they are mixed ages. Sample 15NP236 has the most complex age results, possibly caused by more severe disturbance of the isotope ratios by younger events. Ages of samples 17NP436a, 17NP436b and 15NP233 agree with existing radiometric ages of correlative volcanic units in the North Pamir, demonstrating that calcite formed during ocean floor volcanism, due to coeval or subsequent ocean floor alteration, provides a valuable age constraint on the timing of volcanism. We note that these calcite ages do not directly date the formation of these volcanic rock but provide minimum age constraints within a timespan of about 25 Ma of ocean floor alteration.

Age data must be evaluated in the light of detailed petrographic analysis, including petrographic microscopy and cathodoluminescence microscopy, as well as geochemistry of the investigated calcite. Geochemical data supports our hypothesis of an ocean floor alteration-related origin of the investigated calcite. However, we underline that interpretation of REE content in calcite is not straight forward, since the trace element uptake by calcite is dependent on a multitude of factors.

The presence of Middle to Upper Mississippian ocean floor in the North Pamir argues against models invoking a continuous, early Paleozoic Kunlun belt, stretching from the West Kunlun far into the North Pamir. Instead, they support the presence of a mid to late Carboniferous volcanic arc system, tying the North Pamir more to comparative units in the Tien Shan.

Chapter 4. Geochronology, Geochemistry, and Geodynamic implications of Permo-Triassic back-arc basin successions in the North Pamir, Central Asia

4.1 Abstract

The Permo-Triassic period marks the time interval between Hercynian (Variscan) orogenic events in the Tien Shan and the North Pamir, and the Cimmerian accretion of the Gondwana-derived Central and South Pamir to the southern margin of the Paleo-Asian continent. A well preserved Permo-Triassic volcano-sedimentary sequence from the Chinese North Pamir yields important information on the geodynamic evolution of Asia`s pre-Cimmerian southern margin. The oldest volcanic rocks from that section are dated to the late Guadalupian epoch by a rhyolite and a dacitic dike that gave zircon U-Pb ages of ~260 Ma. Permian volcanism was largely pyroclastic and mafic to intermediate. Up section, a massive ignimbritic crystal tuff in the Chinese Qimgan valley was dated to 244.1 ± 1.1 Ma, a similar unit in the nearby Gez valley to 245 ± 11 Ma and an associated rhyolite to 233.4 ± 1.1 Ma. Deposition of the locally ~200 m thick crystal tuff unit follows an unconformity and marks the onset of intense, mainly mafic to intermediate, calc-alkaline magmatic activity. Triassic volcanic activity in the North Pamir was coeval with the major phase of Cimmerian intrusive activity in the Karakul-Mazar arc-accretionary complex to the south, caused by northward subduction of the Paleo-Tethys. It also coincided with the emplacement of basanitic and carbonatitic dikes and a thermal event in the South Tien Shan, to the north of our study area.
Evidence for arc-related magmatic activity in a back-arc position provides strong arguments for back-arc extension or transtension and basin formation. This puts the Qimgan succession in line with a more than 1000 km long realm of extensional Triassic back-arc basins known from the North Pamir in the Kyrgyz Altyn Darya valley (Myntekin formation), the North Pamir of Tajikistan and Afghanistan and the Afghan Hindukush (Doab formation), and further west from the Paropamisus and Kopet Dag (Aghdarband, NE Iran).

4.2 Introduction

A long history of subduction, collision, and terrane accretion shaped the Pamir salient in the Alpine-Zagros-Himalayan orogenic system (Figure 25) (e.g., Ruzhentsev *et al.*, 1977; Bazhenov & Burtman, 1982; Burtman & Molnar, 1993; Schwab *et al.*, 2004). The pre-Cenozoic portion of the Pamir orogen was significantly deformed by the Cenozoic collision of India and Asia. Pre-existing structures and anisotropies along Asia's southern margin played an important role during the collision (Li *et al.*, 2020). Therefore, a profound knowledge of pre-Cenozoic components in the Pamir orogen is crucial for a holistic view of deformation processes lasting until today. Northward subduction of Paleo-Tethyan lithosphere took place along the southern margin of Asia during the Permo-Triassic. This was the interval between two major orogenic events: 1) the late

Carboniferous to early Permian Hercynian Orogeny of Central Asia, which closed the Turkestan Ocean and parts of the Paleo-Tethys (Chapter 2 and e.g., Bazhenov & Burtman, 1986; Boulin, 1988; Biske *et al.*, 2013; Konopelko *et al.*, 2019) and 2) the late Triassic Cimmerian orogeny, caused by the accretion of Gondwana derived micro-continents to Asia's southern margin (e.g., Schwab *et al.*, 2004; Robinson *et al.*, 2012; He *et al.*, 2019; Imrecke *et al.*, 2019; Villarreal *et al.*, 2019).

Figure 25: Regional geography of the Pamir and surrounding areas. In color: outline of the Permian Tarim LIP (after Li et al., 2014; Xu et al., 2014, in orange) in the Tarim Basin (yellow). Segments of the South Tien Shan are in blue letters. A–Atbashy range, P–Pobeda massif

In this study, we aim to characterize the stratigraphic relationship, age, and magmatic genesis of the Permo-Triassic volcano-sedimentary sequence of the Chinese NE Pamir. Geochemical investigations, particularly on rocks of the bimodal Upper Triassic volcanic sequence, are used to test their genetic linkage and their connection to Triassic magmatic activity in the Karakul-Mazar volcanic arc and is regarded in context with other Permo-Triassic magmatic centers in the region. A comprehensive overview of Permian and Triassic magmatic activity in the Hindukush, the North Pamir, the Tarim basin and the Tien Shan is presented. We hypothesize that a ~1000 km long extensional back-arc domain was present, extending from the Chinese NE Pamir through the Hindukush and Paropamisus mountain ranges of Afghanistan into the Kopet Dag mountains of NE Iran.

4.3 Geological setting of the Pamir

The Pamir has been subdivided into 3 major tectonic units, the North, Central, and South Pamir (Bazhenov & Burtman, 1986; Matte *et al.*, 1996; Schwab *et al.*, 2004), separated by intervening

suture zones (Figure 26). The North Pamir is composed of rocks associated with a Carboniferous oceanic arc that accreted to the Paleo-Asian margin in the late Carboniferous to Permian due to closure of a part of the Paleo-Tethys (Chapter 3 and Ruzhentsev *et al.*, 1977; Bazhenov & Burtman, 1982; Rembe *et al.*, 2021; Rembe *et al.*, 2022). This process, along with the closure of the Turkestan Ocean, further north, is regarded as the Hercynian orogeny in Central Asia (Biske & Seltmann, 2010; Biske *et al.*, 2013). Major parts of the Tien Shan were consolidated during that period, with accretion of oceanic crust along multiple subduction zones (Alexeiev *et al.*, 2015; Loury *et al.*, 2016; Jourdon *et al.*, 2017; Konopelko *et al.*, 2017; Loury *et al.*, 2017; Worthington *et al.*, 2017; Loury *et al.*, 2018; Alexeiev *et al.*, 2019; Konopelko *et al.*, 2019). Ongoing convergence of the Paleo-Asian margin with the Karakum and Gissar blocks in the west and the Tarim craton in the east, resulted in a phase of high pressure metamorphism of oceanic and continental units. Eclogite facies peak metamorphic conditions were reached by 328–319 Ma and subsequent exhumation by 303–295 Ma (Atbashy range, South Tien Shan, e.g., Loury *et al.*, 2018; Satybaev *et al.*, 2018). Post-Hercynian, Permian tectonics in Central Asia were dominated by large scale strike slip faulting (e.g, Buslov *et al.*, 2004; Konopelko *et al.*, 2007; Rolland *et al.*, 2013; Loury *et al.*, 2018)

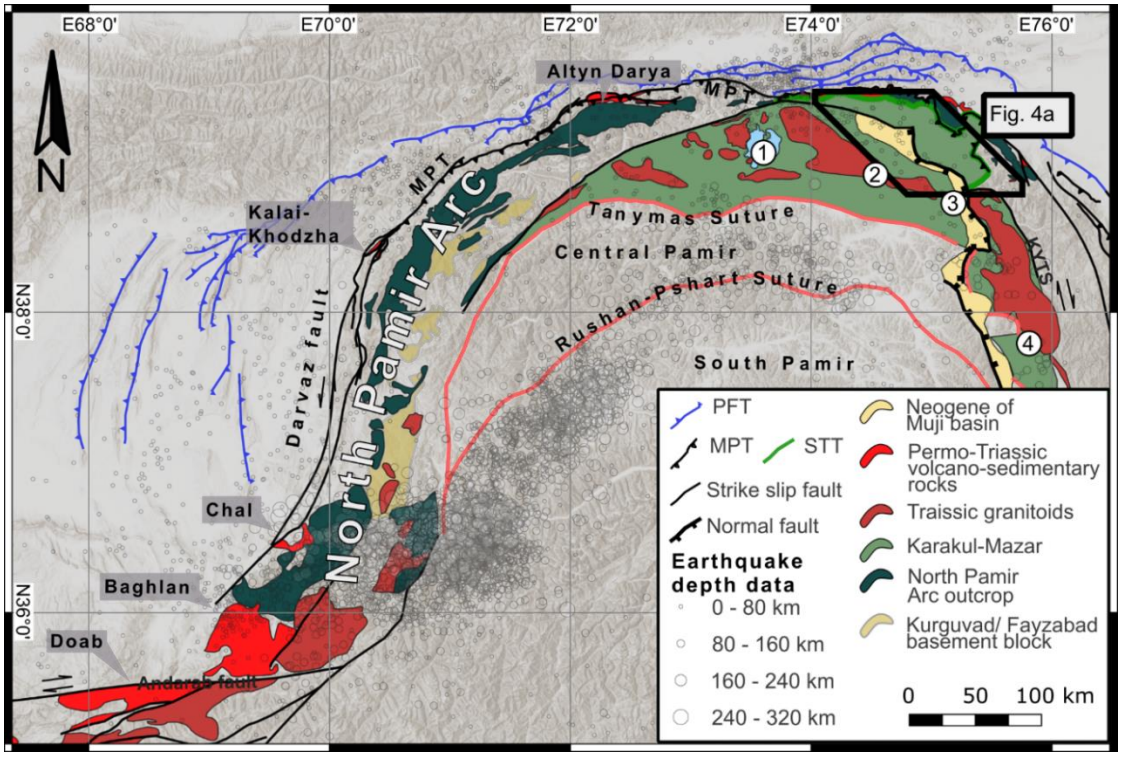

Figure 26: Distribution of Triassic volcano-sedimentary successions in the North Pamir and regional subdivision of the Pamir. Note that the Triassic basins are aligned along the Main Pamir Thrust (MPT) in the north. Major outcrop localities of Triassic volcano-sedimentary successions outside of our study area are named in grey boxes. Numbers indicate Triassic arc intrusions in the Karakul-Mazar and westernmost West Kunlun, from literature: 1) Karakul intrusion (Schwab et al., 2004), 2) Bulunkuo and Qiate intrusions (Jiang et al., 2013; Chen et al., 2021), 3) Yuqikapa intrusion (Jiang et al., 2013; Wang et al., 2016) ,4) Muztaga and Beileki/Taer intrusions (Huang et al., 2013; Jiang et al., 2013).

The Carboniferous volcanic arc of the North Pamir can be subdivided into the eastern Oytag segment, with more primitive island arc volcanic rocks and associated plagiogranites (tonalites and trondhjemites), and the western Darvaz segment, comprising Pre-Carboniferous meta-sedimentary rocks in the Kurguvad-Faizabad zone (also named the Kurguvad block) and Carboniferous basalts and associated granodioritic rocks of continental arc affinity (Chapter 2, Chapter 3 and Bazhenov & Burtman, 1982; Jiang *et al.*, 2008; Kang *et al.*, 2015; Rembe *et al.*, 2021; Rembe *et al.*, 2022). The Carboniferous volcanic arc system accreted in the late Carboniferous to early Permian. It is bordered to the south by the Permo-Triassic Karakul-Mazar block. This block formed as an accretionary system generated by Paleo-Tethys subduction during the northward advance of the Cimmerian terranes with Gondwanan provenance—the Central and South Pamir microcontinents (Robinson *et al.*, 2004; Robinson *et al.*, 2012; Angiolini *et al.*, 2013; Robinson, 2015; He *et al.*, 2019; Villarreal *et al.*, 2019). Triassic granitoids are well known from the Karakul-Mazar block, the adjacent West Kunlun to the east, and the Badakhshan region to the west. In the Karakul-Mazar and West Kunlun, they show high-K to shoshonitic composition and typical characteristics of continental arc, syn-collisional and post-collisional geotectonic settings (e.g., Chen *et al.*, 2021). The closure of the Paleo-Tethys formed the Tanymas suture zone between the Central Pamir and the Karakul-Mazar block.

Recent studies suggest that the Pamir salient formed due to deflection of Cimmerian terranes, which filled an embayment in the southern margin of the Paleo-Asian continent (Li *et al.*, 2020). Intrusive complexes, associated with the Paleo-Tethys subduction, found in the Chinese northeastern Pamir have been described in detail (Huang *et al.*, 2013; Jiang *et al.*, 2013; Zhang *et al.*, 2019; Chen *et al.*, 2021). However, volcanic rocks as part of a volcano-sedimentary sequence in the Chinese North Pamir have roughly similar ages, as shown in this contribution. In fact, Permo-Triassic volcano-sedimentary rocks are known to form a narrow strip along the northern edge of the North Pamir and seem to be aligned along the Main Pamir Thrust (MPT, Figure 26), which juxtaposes Paleozoic-early Mesozoic North Pamir units against sedimentary sequences of the External Pamir located in the Tarim, Alai and Tajik Basins. Similar Permo-Triassic rock units have been described from the Hindukush in northern Afghanistan (e.g., Hinze, 1964), the North Pamir of Tajikistan (e.g., Krestnikov, 1963; Leven *et al.*, 1992) and Kyrgyzstan (e.g., Budanov, 1993; Luchnikov, 2001).

4.4 Regional Permo-Triassic Volcanism

4.4.1 Hindukush of Afghanistan and the NW Pamir in Tajikistan and Kyrgyzstan

Permian successions of the Badakhshan area in North Afghanistan and the North Pamir of Kyrgyzstan and Tajikistan are characterized by fine-clastic and carbonate sediments (Figure 27). Several hundred-meter thick fusulina limestones were deposited in an open marine environment

on the southern shelf of the Paleo-Asian continent (Wolfart & Wittekindt, 1980; Leven, 2013). They unconformably overly remnants of the accreted Carboniferous arc and accreted pre-Carboniferous (meta-) sedimentary rocks (Chapter 2 and Lyoskind *et al.*, 1963; Wirtz *et al.*, 1964; Vlasov *et al.*, 1984; Leven, 2013). Permian volcanic rocks, mainly tuffites and epiclastic rocks are known from the upper Permian of Afghanistan (Hinze, 1964) and from the Darvaz range in Tadjikistan (Leven *et al.*, 1992). Leven *et al.* (1992) describes basaltic and andesitic tuffs and epiclastic rocks that make up large volumes of the Kungurian and Roadian strata (corresponds to the local Tethyan Bolorian and Kubergandian Stage). Permian volcanic rocks of the NW Pamir (Darvaz range and Badakhshan) are characterized as calc-alkaline and interpreted to have erupted in an ensilaic volcanic island arc (Salikhov & Sakiev, 2014). The Upper Permian is characterized by relative sea level changes causing repeated uplift and erosion, followed by marine deposition. Upper Permian strata is missing in North Afghanistan (Wolfart & Wittekindt, 1980).

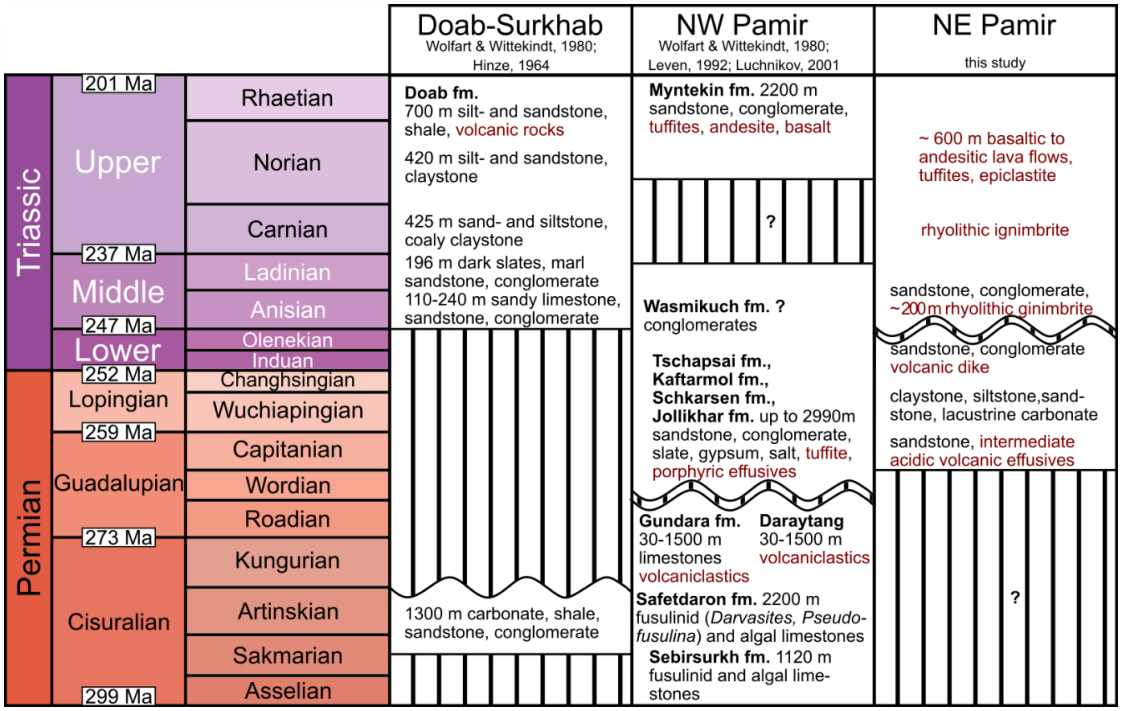

Figure 27: Simplified comparative stratigraphy of the Hindukush (Doab-Surkhab), NW Pamir and NE Pamir strata. Wavy line marks erosional unconformities, vertical stripes show presumed (question mark) or reported hiatus. Chronostratigraphic subdivision and rounded ages according to the International Chronostratigraphic Chart (Cohen et al., 2020).

The Triassic clastic sedimentation in North Afghanistan is marine and characterized by intense mafic to acidic volcanism. Weippert (1964) described the superbly exposed Triassic strata in the Doab area situated on the northern flank of the Hindukush (Figure 26 and Figure 27). The succession is subdivided into the lower (Anisian), middle (Ladinian), and upper (Carnian, Norian, Rhaetian) Doab formation. The lower Doab formation is characterized by sandstones and conglomerates, followed by shales and marls of the middle Doab formation. The upper Doab

formation comprises shales, siltstones, and sandstones. Lower and Middle Triassic strata in the Doab area lack volcanic rocks. However, intermediate to acidic Anisian to Ladinian volcanism is known from other localities along the northwestern flank of the Hindukush (Hinze, 1964; Wolfart & Wittekindt, 1980). In the Doab area, intense mafic to acidic Late Triassic volcanism produced an alternation of terrigenous sandstones and basaltic, andesitic, and rhyolitic rocks. The latter yielded Norian K-Ar ages (Blaise *et al.*, 1970).

In the more recent compilations of Montenat (2009) and Siehl (2017), data is summarized from the North Hindukush rift. This zone of Triassic extensional basins in a back-arc position of the Paleo-Tethys subduction zone, spanned from the West Hindukush into West Afghanistan (Paropamisus, e.g., Boulin, 1988) and most likely further into the Aghdarband basin of the Kopeh-Dag, NE Iran (Baud & Stämpfli, 1989; Balini *et al.*, 2019). The Doab Formation is of correct age, sedimentary style, and position to be viewed as part of this rift system. A direct lateral correlation is difficult, since detailed radiometric and bio-stratigraphic age data are sparse. Moreover, abrupt lateral facies changes hinder lithostratigraphic correlations.

Only Upper Triassic (Rhaetian) strata were described from the Altyn Darya Valley in the Kyrgyz North Pamir (Figure 27). Continental clastic deposits with pyroclastic acidic and effusive intermediate to mafic rocks are grouped into the Rhaetian ~2500 m thick Myntekin formation (Budanov, 1993; Luchnikov, 2001) and overlie Permian shallow marine strata (e.g., Leven *et al.*, 1992). The Triassic succession was deposited in graben structures and is laterally highly variable. Sedimentary rocks are immature with a high proportion of volcanic clasts (Luchnikov, 2001). Luchnikov (2001) compared the Myntekin Formation to similar continental Middle-to-Upper Triassic units in the area and interprets the laterally restricted, fault-bounded, volcano-sedimentary basin as a Triassic-Jurassic rift basin. Salikhov & Sakiev (2014) compiled major element geochemical data and found that calc-alkaline Triassic magmatism of the North Pamir shows more complex geochemical signatures than the Permian ensialic arc magmatism. They stress an ensimatic component, interpreted as a result of short-term rear-arc extension associated with increased mantle influence. In general, the Permian sedimentary coverage is much more widely distributed than the Triassic.

4.4.2 Northeast Pamir

In the northeastern, Chinese, Pamir, the Permo-Triassic volcano-sedimentary successions have been comparatively poorly studied. Our field work focused on the Triassic rocks in the Chinese Qimgan valley (Figure 26 and Figure 27). Our data show a coherent stratigraphic succession spanning at least the upper Guadalupian to the Cretaceous or the lower Paleogene. We also investigated a Permian deformed felsic sill in the Markansu valley, Permian andesitic to dacitic rocks in the upper Biertuokuoyi valley, and a variety of Middle to Upper Triassic volcanic rocks in the Oytag and Gez valleys (Figure 28). The Permian unconformably overlies Carboniferous

(Hercynian) island arc related rocks, identified as mainly basaltic to andesitic lava flows and tuffs and associated epiclastic rocks and intruded Carboniferous plagiogranites (see Chapter 2 and Chapter 3). In the Qimgan valley, two calcite U-Pb ages from the Permian strata and one zircon U-Pb age of a cross cutting aplitic dike give a temporal constraint for the deposition of Permian strata between 260 and 250 Ma (see Chapter 2). In Chapter 2 we described a foraminifera-bearing limestone clast, found in a polymictic conglomerate at the base of the Permian strata that yielded a lower Mississippian age (calcite U-Pb age 347 ± 8 Ma, MSWD = 2), indicating erosion of Carboniferous marine strata. An ostracod-rich lacustrine limestone from the Permian fine-grained clastic sequence gave an upper Guadalupian age (calcite U-Pb age 260 ± 2 Ma, MSWD = 3) and the crosscutting aplite yielded Lower Triassic, concordant Olenekian zircons (zircon U-Pb age 250.0 ± 0.3 Ma). Permian volcanic activity in the Qimgan succession is largely mafic to intermediate and pyroclastic, indicating high water supply in the parent magma. The abundance of volcanic rocks decreases from the base to a mid-Triassic angular unconformity which is overlain by a middle to late Triassic sequence of volcanic rocks. They contain a massive, several 100 m thick ignimbritic tuff layer that is covered by poorly sorted, mud-supported gravel layers. The top of the Triassic sequence is composed of a thick succession of andesitic and basaltic lava flows and tuffs.

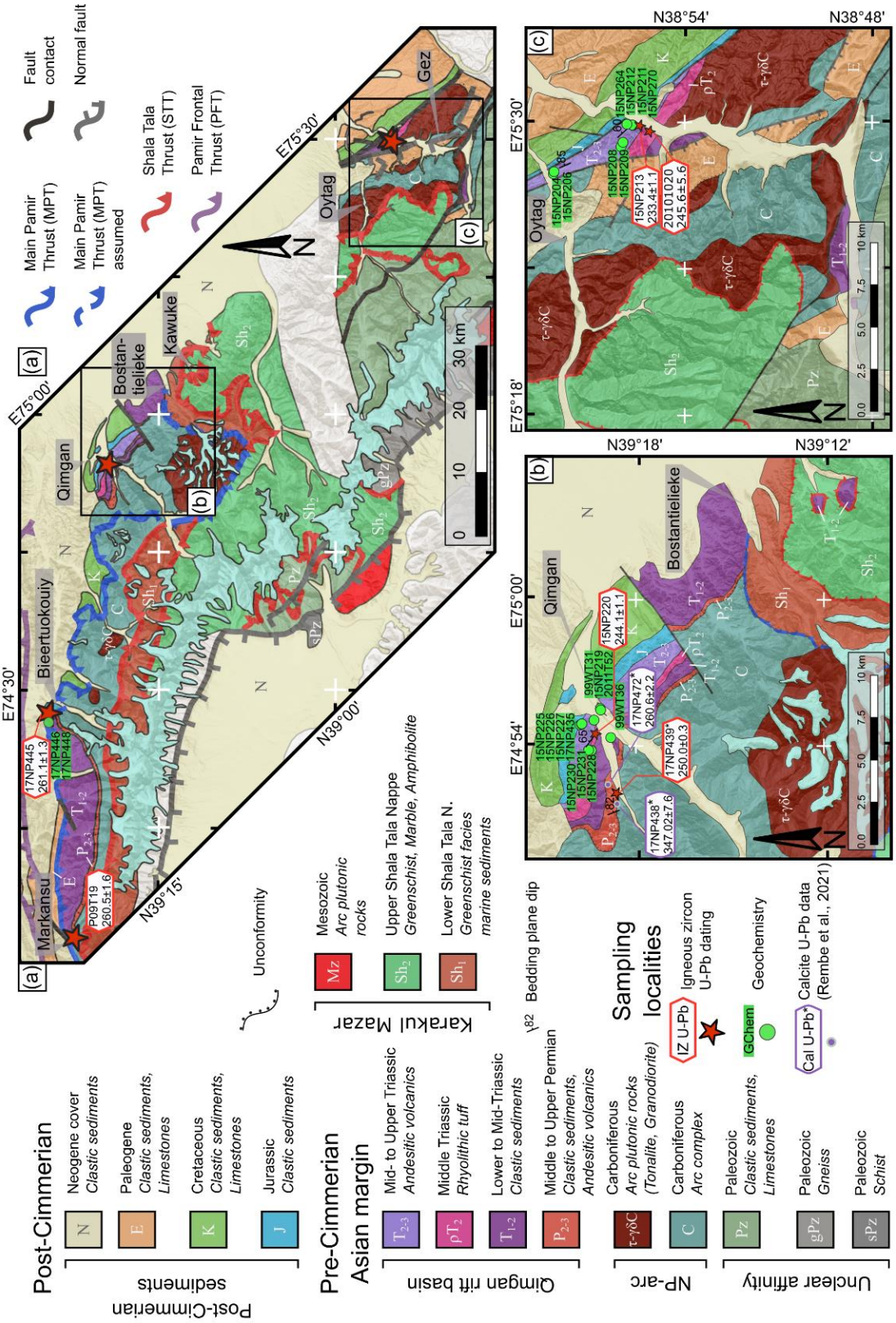

Figure 28:Geological map of the investigated area in the NE Pamir. Detailed maps show the distribution of geochemistry samples in the Qimgan (b) and Oytag/ Gez (c) valleys and extend of Permo-Triassic strata. Both regions exhibit coherent Permo-Triassic volcano-sedimentary successions that laterally are either truncated by steep, Cenozoic faults or unconformably covered by Cenozoic sediments. Age data marked with an asterisk (Cal U-Pb data and data from aplitic dike sample 17NP439 in Qimgan valley) are from Chapter 2.

4.5 Permo-Triassic magmatic activity in neighboring parts of Central Asia

4.5.1 The Permian Large Igneous Province in Tarim

The early Permian Large Igneous Province (LIP) in the western part of the Tarim basin is composed of large volumes of basaltic and rhyolitic rocks (e.g., Zhang *et al.*, 2010; Li *et al.*, 2014; Xu *et al.*, 2014; Liu *et al.*, 2019) that cover an area of about 250,000 km² (Figure 25). Igneous rocks of the LIP are: layered mafic-ultramafic intrusions, bi-modal dike swarms, granitic intrusions, kimberlites, flood basalts, rhyolites and associated pyroclastic rocks, that were emplaced in 3 major phases. Starting at ~300 Ma, diamond bearing kimberlites intruded which were followed by two bi-modal magmatic pulses at ~290 Ma and ~280 Ma (Xu *et al.*, 2014). The ~290 Ma pulse marks the most widespread phase of magmatic activity in Tarim and the adjacent Tien Shan. Recently, the age of the main flood basalt eruptions has been constrained as 289.8 ± 1.0 Ma and 284.3 ± 0.4 Ma by chemical-abrasion thermal-ionization mass-spectrometry (CA-TIMS) zircon U-Pb dating (Zhong *et al.*, 2022); these ages bracket a ~5.5 Ma long period of major mantle plume activity.

4.5.2 Magmatic activity in the Tien Shan

Following the Carboniferous arc related and subsequent collisional magmatism, shortening and subduction of the Turkestan ocean and the adjacent Paleo-Tethys, the Permian period was marked by post-collisional magmatic activity in the Tien Shan (e.g., Konopelko *et al.*, 2007; Biske *et al.*, 2013; Konopelko *et al.*, 2018; Loury *et al.*, 2018). This magmatic episode is closely linked to Permian strike-slip faulting and associated local transtension and transpression (Pirajno *et al.*, 2008; Wang *et al.*, 2008; Jong *et al.*, 2009; Biske & Seltmann, 2010; Wang *et al.*, 2010; Charvet *et al.*, 2011; de Boorder, 2012; Biske *et al.*, 2013; Rolland *et al.*, 2013; Jourdon *et al.*, 2017). In the eastern segment of the Tien Shan, post-collisional magmatism interfered with mantle plume magmatic activity of the Tarim LIP, which caused a mixed mantle-plume and post-collisional, arc-inherited, magmatism (Loury *et al.*, 2018; Han *et al.*, 2019). The peak of the Permian post-collisional magmatic activity in the Tien Shan was reached between 290–280 Ma (Seltmann *et al.*, 2011; Biske *et al.*, 2013; Konopelko *et al.*, 2018) and ceased by ~265 Ma dated from an anatectic granite from the Pobeda massif (South Tien Shan), associated with charnockite, emplaced in a strike slip setting (Loury *et al.*, 2018). High precision SHRIMP zircon data from Permian intrusions in the Kyzylkum segment of the South Tien Shan revealed Ladinian to Norian (240–220 Ma) overgrowths on the Permian zircons, interpreted to result from elevated thermal fluxes (Seltmann *et al.*, 2011). However, Triassic magmatic rocks are relatively rare in the Tien Shan. A porphyritic dike in the Kyzylkum segment (Figure 25) of the South Tien Shan dated as 236 Ma by U-Pb on zircon was reported by Hall (2007). Small volumes of basanite dikes and pipes were found

in the Gissar and Alai ranges and gave mica and hornblende $^{40}Ar/^{39}Ar$ age between 256–237 Ma (Käßner *et al.*, 2017). Younger, rare alkaline and carbonatitic rocks of the Alai segment in the South Tien Shan formed in a complex active continental margin extensional setting associated with mantle upwelling (Vrublevskii, 2017; Vrublevskii *et al.*, 2018). They gave apparent ages of between 200 and 220 Ma by $^{40}Ar/^{39}Ar$ dating of mica and amphibole, and phlogopite, apatite, amphibole, and whole rock Rb-Sr isochrone dating. However, high MSWD values for the Rb-Sr isochrone and forced plateau ages for the $^{40}Ar/^{39}Ar$ data require carful use of these ages.

4.5.3 The Triassic intrusions of the Karakul–Mazar arc-accretionary complex and the westernmost West Kunlun

Triassic intrusive rocks have been described from the Permo-Triassic Karakul-Mazar arc-accretionary complex and the western branch of the West Kunlun, such as the Karakul intrusion (Schwab *et al.*, 2004), the Yuqikapa intrusion (Robinson *et al.*, 2004; Bershaw *et al.*, 2012), the Muztaga, Yuqikapa, and Taer intrusions (Jiang *et al.*, 2013), Beileki/ Taer intrusion (Huang *et al.*, 2013), Bulunkuo intrusion (Wang *et al.*, 2016), and the Bulunkuo, Qiate, and Yuqikapa intrusions (Chen *et al.*, 2021) (Figure 26). Paleo-Tethys subduction might have commenced before the Permian (Chen *et al.*, 2021). Middle Triassic subduction and accretion lead to crustal melting and the emplacement of the Yuqikapa pluton between 245–243 Ma (Robinson *et al.*, 2004; Bershaw *et al.*, 2012; Jiang *et al.*, 2013) and the calc-alkaline Qiate leucogranite at 240 Ma (Chen *et al.*, 2021). The mechanism for the emplacement of the high-K calc-alkaline Taer and Muztaga intrusions (234–227 Ma) is a matter of discussion and has been interpreted as the result of either delamination of thickened lithosphere (Chen *et al.*, 2021) or slab break-off due to collision of the Karakul-Mazar block and the Central Pamir (Jiang *et al.*, 2013; Wang *et al.*, 2016). A biotite granite, found at the northern shore of Karakul Lake within the Karakul-Mazar block, gave a similar age of 227.0 ± 4.1 Ma (Schwab *et al.*, 2004) and might be associated with this phase. Norian to Rhaetian magmatism emplaced the high-K calc-alkaline Bulunkuo granodiorite (221–219 Ma) and related Arkaz (215–213 Ma) and Mazar plutons (~209 Ma) in the West Kunlun, due to continued northward subduction of the Paleo-Tethys (Chen *et al.*, 2021). Collision of the Central Pamir and the Karakul-Mazar block and formation of the Tanymas-Jinsha suture happened by the late Triassic (Villarreal *et al.*, 2019; Chen *et al.*, 2021). However, some authors suggest an earlier, Middle Triassic, closure, based on geochemical arguments (Jiang *et al.*, 2013; Wang *et al.*, 2016).

4.6 Methods

4.6.1 Field work and sample preparation

Sampling

Field work was undertaken in the northwest part of the North Pamir, ~100 km south-west of the town of Kashgar, China (Table 3, Figure 25 and Figure 26).

Table 3: Location and characteristics of all samples used for Chapter 4

Sample	Rock	Purpose	Mineralogy in TS	Mineralogy from XRD	Latitude (N)	Longitude (E)
			Markansu and Bieertuokouyi valley			
P09T19	Deformed felsic sill	IZ-UPb	-	-	39.3688	74.0494
17NP445	Rhyolite	IZ-UPb	cf. 17NP446	-	39.4053	74.4569
17NP446	Rhyolite	TS, GC	gm-kfsp-hem	-	39.4053	74.4569
17NP448	Intermediate tuff	TS, GC	fsp-cal-lv-gm	-	39.40642	74.448821
			Qimgan valley			
15NP219	Basaltic andesite	GC	-	-	39.31897	74.92573
15NP225	Basaltic andesite	TS, GC	plg-gm	plg-qz-hem-mnt-sa-cal	39.32964	74.91448
15NP226	Basaltic andesite	TS, GC	plg-gm-opk	-	39.32882	74.91501
15NP227	Basalt	TS, GC	plg-gm-cpx	ab-cal-qz-hem-clc-bt	39.3287	74.91522
15NP228	Dacitic dike	TS, GC	plg-gm-kfsp-cpx	qz-clc-hd-sa-ab-hem	39.32125	74.89802
15NP230	Rhyolithic tuff	TS, GC	gm-kfsp-plg-qz-mca-opk	qz-hem-ab-or-bt-clc	39.32508	74.89732
15NP231	Rhyolithic tuff	TS, GC	qz-plg-gm-kfsp-mca-opk	-	39.32508	74.89732
2011T52	Basalt	TS, GC	plg-gm-aug	an-qz-cal-mnt	39.3187134	74.9246562
99WT31	Basaltic andesite	TS, GC	plg-gm-opk	-	39.322222	74.917778
99WT36	Andesite	GC	-	-	39.313333	74.905833
15NP220	Rhyolithic tuff	IZ-UPb	cf. 15NP230	-	39.3215	74.9084
17NP475	Rhyolithic tuff	TS, IZ-UPb	gm-kfsp-plg-qz-mca-chl	-	39.32166	74.881959
17NP435	Intermediate ignimbrite	TS,GC	gm-pmc	-	39.322977	74.905659
			Oytag and Gez valley			
15NP264	Basaltic andesite	TS, GC	plg-opk-gm-aug	aug-an40-mnt-hem-ilm-qz	38.93077	75.49877
15NP204	Andesite	GC	-	qz-ab-or-kln-dol	38.97001	75.46497
15NP206	Basaltic andesite	GC	-	ab-clc-mag-dol-nsn	38.9696	75.4664
15NP208	Andesite	TS, GC	gm-plg	-	38.93393	75.48344
15NP209	Basalt	TS, GC	plg-gm	-	38.93287	75.4864
15NP211	Basalt	TS, GC	plg-gm-cpx-hbl	qz-cal-kln-hem-hd-ap	38.92758	75.49801
15NP212	Tuff	TS, GC	plg-gm-lth	qz-cal-sd-kln-hem-str	38.92799	75.49825
15NP270	Basaltic andesite	TS, GC	plg-gm-opk	-	38.93031	75.50143
20101020-3	Rhyolite	IZ-UPb	-	-	38.9188	75.4938
15NP213	Rhyolite	IZ-UPb	-	-	38.924	75.4978

TS—thin section, GC—geochemistry, IZ-UPb—igneous zircon U-Pb age measurement, XRD—X-ray diffraction, gm—groundmass, mineral abbreviations according to IUGS (Siivola & Schmid, 2007).

We collected samples in seven localities (Figure 28) and detailed field work focused on the

outcrops of the volcano-sedimentary Permo-Triassic sequence in the Qimgan and Gez valley areas (Figure 28b, c). The Qimgan valley exposes a largely undisturbed section of Carboniferous to Eocene strata. The Gez valley is tectonically more complex. Multiple, transecting subvertical faults hinder the correlation of Paleozoic to Paleogene strata in field.

Zircon U-Pb dating

To determine the crystallization age of igneous rocks, U-Pb isotopes were measured in zircons from five volcanic rock samples. Zircons were separated using jaw crusher, disc grinder, water table, magnetic separation, and heavy liquids (sodium polytungstate (SPT), diiodomethane (DI)). Zircons were poured onto a glass plate and arranged in lines on double-sided sticky tape under a binocular microscope. Zircons were sorted for clear appearance and size. Alignment of zircon grains in epoxy-resin helps for better single grain recognition. Mounted grains were polished to expose an internal surface and imaged with cathodoluminescence (CL) at the electron microprobe facility of the University of Potsdam.

Whole Rock Geochemistry and XRD

Twenty-one volcanic rock samples of fresh appearance were chosen for whole rock geochemistry. The samples were cleaned, crushed, and milled in an agate mill to a particle size < 62 µm. Melt tablets for X-ray fluorescence spectroscopy (XRF) analysis to measure major and trace elements were prepared at University of Potsdam using fluxing agent FX-X65-2 (lithium tetraborate : lithium metaborate, 66 : 34). Samples for rare earth elements (REE), yttrium, and scandium analysis were sintered with sodium peroxide at 480 °C and dissolved in hydrochloric acid. REE plus scandium and yttrium were then separated in ion exchange columns. Powder tablets were prepared from 10 samples to determine the mineral composition by X-ray powder diffraction (see Table 3).

4.6.2 Analytical work

Zircon LA-ICP-MS U-Pb dating

207 zircon grains from five volcanic rock samples (Table 3) were analyzed. Zircon U-Pb dating from all but one sample (20101020-3) was done according to the parameters described in section 2.4.2 and Zhou *et al.* (2020). Laser ablation of samples 17NP445, P09T19, 15NP220, 15NP213 was accomplished with an ASI RESOlution 193nm ArF excimer laser system at the Radiogenic Isotope Facility (RIF), The University of Queensland. Laser spot size was 30 µm. For each ablation spot, 3 s of blank was collected, followed by 20 s of ablation and 5 s of wash out. Zircons were carefully examined using CL images to place ablation spots. Fractures and zones with strongly differing Th/U values were identified and excluded. Using He carrier gas at a flow rate of 0.35 l/min and added N_2 gas for sensitivity enhancement, the gas mixture from the laser chamber was transferred to the plasma torch of a Thermo iCAP RQ quadrupole ICP-MS with 0.85 l/min Ar

nebulizer gas. The ICP-MS signals were optimized by signal tuning before starting data acquisition.

The following isotopes were counted (dwell time in brackets): ^{88}Sr (0.005 s), ^{91}Zr (0.001 s), ^{200}Hg (0.01 s), ^{204}Pb (0.01 s), ^{206}Pb (0.045 s), ^{207}Pb (0.055 s), ^{208}Pb (0.01 s), ^{232}Th (0.01 s), ^{238}U (0.01 s). Data reduction was done in the program Iolite v2.5, which runs within the Igor Pro environment (Hellstrom *et al.*, 2008; Paton *et al.*, 2011) using the Vizual Age (Petrus & Kamber, 2012) data reduction scheme. Each five unknowns were bracketed by the standard zircon 91500 with a ^{206}Pb/^{238}U age of 1062.4 ± 0.4 Ma (2σ) and ^{206}Pb/^{207}Pb age of 1065.4 ± 0.3 Ma (2σ) (Wiedenbeck *et al.*, 1995). Temora 2 zircons (^{206}Pb/^{238}U age of 416.78 ± 0.33 Ma (2σ) (Black *et al.*, 2004)) where treated as unknowns. The primary standard gave a ^{206}Pb/^{238}U age of 1062.7 ± 0.2 Ma (σ) and Temora 2 gave a ^{206}Pb/^{238}U age of 420.7 ± 0.2 (2σ) Ma in the measurement session. All unknowns were filtered for concordance and strontium content.

Sample 20101020-3 was measured at the University of Potsdam using a Thermo Scientific Element 2 ICP-MS coupled to a CETAC LSX 213 nm Nd:YAG laser. The laser spot size was set to 25 µm. Cathodoluminescence images were used to locate the laser spots on the zircon grains. All analyses were normalized to the GJ-1 zircon standard (Jackson *et al.*, 2004; Liu *et al.*, 2007; Schaltegger *et al.*, 2021) to correct for laser-induced elemental fractionation and mass discrimination by the instrument. Zircon GJ-1 yielded a ^{206}Pb/^{238}U age of 602.9 ± 6.6 Ma (2σ). The published weighted ID-TIMS ^{206}Pb/^{207}Pb age of GJ-1 is 608.53±0.37 Ma (2σ) with ^{206}Pb/^{238}U ages varying from 596.2 to 602.7 Ma (Jackson *et al.*, 2004); the ^{206}Pb/^{238}U age of this standard remains problematic, as discussed recently in Schaltegger *et al.* (2021). Schaltegger *et al.* (2021) present an ID-TIMS ^{206}Pb/^{238}U age of 600.28 ± 0.16 Ma (2σ). This is in agreement with our measurement. Data reduction was done in the program UranOS v. 2.02 (Dunkl *et al.*, 2014) similar to the procedure described in Bande *et al.* (2017).

Analytical 1σ-uncertainties of the samples measured at the Radiogenic Isotope Facility laboratory at The University of Queensland are mostly below 1%, the analysis performed at the University of Potsdam had a higher uncertainty of about 3%. We expanded the analytical uncertainty, as suggested by Horstwood *et al.* (2016) by propagating a total systematic uncertainty of 0.4% (2σ) into the population age, containing the long term variance of the ^{206}Pb/^{238}U signal measured on secondary zircon standard Temora 2, the accuracy of the measurement of primary zircon standard 91500 and the uncertainty of the ^{238}U decay constant. For sample 20101020-3 we propagated a total systematic uncertainty of 0.9% (2σ), containing the accuracy of the measurement of zircon standard GJ-1 and the uncertainty of the ^{238}U decay constant.

All results were handled in the statistics program R, version 3.6.0 (R. Development Core Team, 2019). We used the IsoplotR package version 3.6 (Vermeesch, 2018) to calculate and visualize age data. To derive meaningful sample ages, we applied the concordia distance filter (d_c) as presented

by Vermeesch (2020). We defined discordance threshold values for igneous zircon samples to -1<d_c<5.

XRF and ICP-AES whole rock geochemistry

Analyses by XRF (X-ray fluorescence spectroscopy) were done at the GeoForschungsZentrum Potsdam (GFZ) on a PANalytical AXIOS Advances XRF system. Analyses of international reference materials were used for calibrations. monitor samples and 130 certified reference materials were used for the correction procedures. The detection limit of the XRF system is generally 10 ppm. The rare earth elements plus yttrium and scandium were measured by inductively-coupled-plasma atomic-emission-spectroscopy (ICP-AES) at the University of Potsdam on an Agilent ICP5100 machine following the procedure of Zuleger & Erzinger (1988). Long term precision for ICP-AES at the University of Potsdam is generally < 5%. High field strength elements were measured at the GFZ using standard ICP-MS procedures (Pretorius *et al.*, 2006; Romer & Hahne, 2010). The detection limit is generally ± 5% (Dulski, 2001). Concentrations of H_2O and CO_2 were determined on 20 mg of sample powder, weighed in tin foil using a Euro EA 3000 Elemental Analyser at UP. Geochemical data was handled in R 3.6.0 (R. Development Core Team, 2019), using the GCDkit package version 6.0 (Janoušek *et al.*, 2006).

XRD analysis

Mineral analyses of 10 volcanic rock samples (Table 3) were obtained at UP using a PANalytical Empyrean powder X-ray diffractometer (XRD) with a Bragg-Brentano geometry. The XRD is provided with a PIXcel1D detector using Cu K_α radiation (λ= 1.5419 Å) operating at 40 kV and 40 mA. θ/θ scans were run in a 2θ range of 4–70° with step size of 0.0131° and a sample rotation time of 1 s. It was equipped with a programmable divergence and anti-scatter slit and a large Ni-beta filter. The detector was set to continuous mode with an active length of 3.0061°. The total detection time was 21 min.

4.7 Results

4.7.1 Fieldwork and Petrography

In the lower, Guadalupian to Lower Triassic strata of the succession, volcanic rocks are basaltic to andesitic, fine- to coarse-grained pyroclastic rocks, with locally occurring lava flows and dikes. They are interlayered with or intrude mainly fine-clastic, dark greenish grey volcanomictic sediments. In the well exposed Qimgan succession, the basal, fine-grained clastic sedimentary units trend into coarse-grained, red sandstones and conglomerates. Rare aphyric, greenish-grey dikes and sills penetrate the volcano-sedimentary strata. The effusive rocks appear dark grey to greenish grey in hand specimen and form up to 2 m thick, laterally traceable beds (Figure 29a). In the upper Biertuokuoyi valley, we sampled a pale red, up to 20 m thick rhyolite with feldspar

phenocrysts of almost 1 cm for geochemistry and zircon U-Pb dating. It was sampled close to the estimated basal contact with the underlying Carboniferous rocks (Figure 29b), which is covered by alluvial fans in this location.

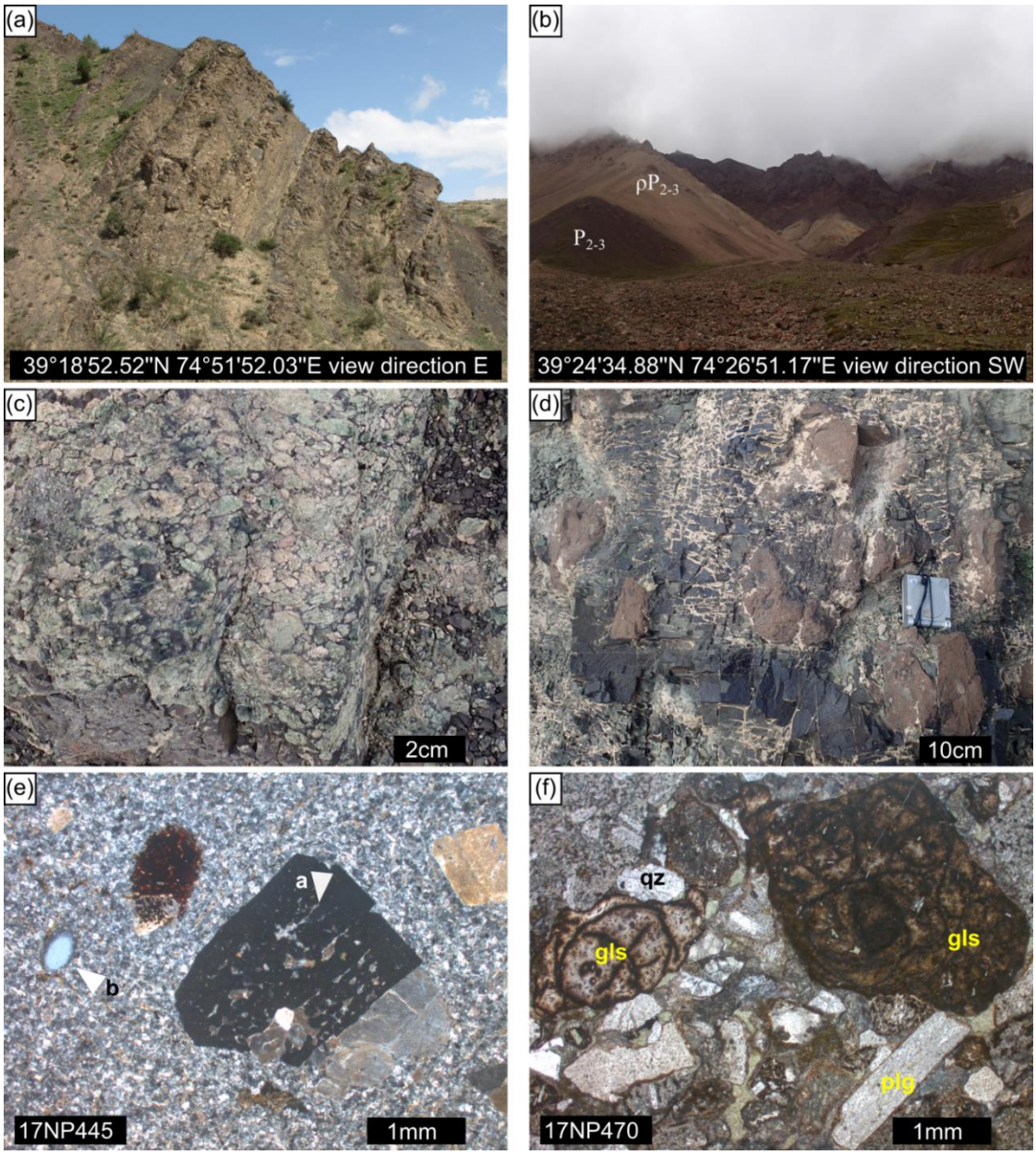

Figure 29: Field- and microphotographs of Permian volcanic rocks. Permian volcanic rocks crop out as fine- to coarse-grained volcaniclastic deposits and lava flows in the Qimgan valley (a, bed thickness ~1—2 m) and the upper Biertuokuoyi valley (b). The pale rose rhyolite (ρP_{2-3}) in b yielded an age of 261.1 ± 1.3 Ma. It is accompanied by volcaniclastic and epiclastic deposits (P_{2-3}). The contact with the underlying Carboniferous rocks is obscured by massive alluvial fans. Permian aphyric and less often phyric tuffs and lapilli-tuffs in the Qimgan valley (c). The presence of various tuffs and pepperite textures (d) indicate high water supply to the magmatic system and the interlayered sediments. The greenish mudstone in d was affected by contact metamorphism and turned into brittle hornfels, showing a different fracture behavior than the intruding brownish volcanic rock. In the thin section of rhyolite sample 17NP445 (e, cross-polarized light) from the upper Biertuokuoyi valley we found evidence for magma mingling, such as sieve textures in feldspar (white arrow a) and resorption of quartz (white arrow b). Thin sections of the fine-grained pyroclastic rocks, here from tuff sample 17NP470 (f, plane-polarized light), show fragmented quartz (qz) and plagioclase (plg) crystals and abundant perlitic glass fragments (gls).

In the Qimgan section study area, pyroclastic rocks (many aphyric) dominate over lava flows. In some volcanic rocks, small (<1 cm) plagioclase phenocrysts were observed. Distinctive lapilli-tuff layers are also present (Figure 29c). Aphyric lava flows in contact with mudstones formed pepperites (Figure 29d).

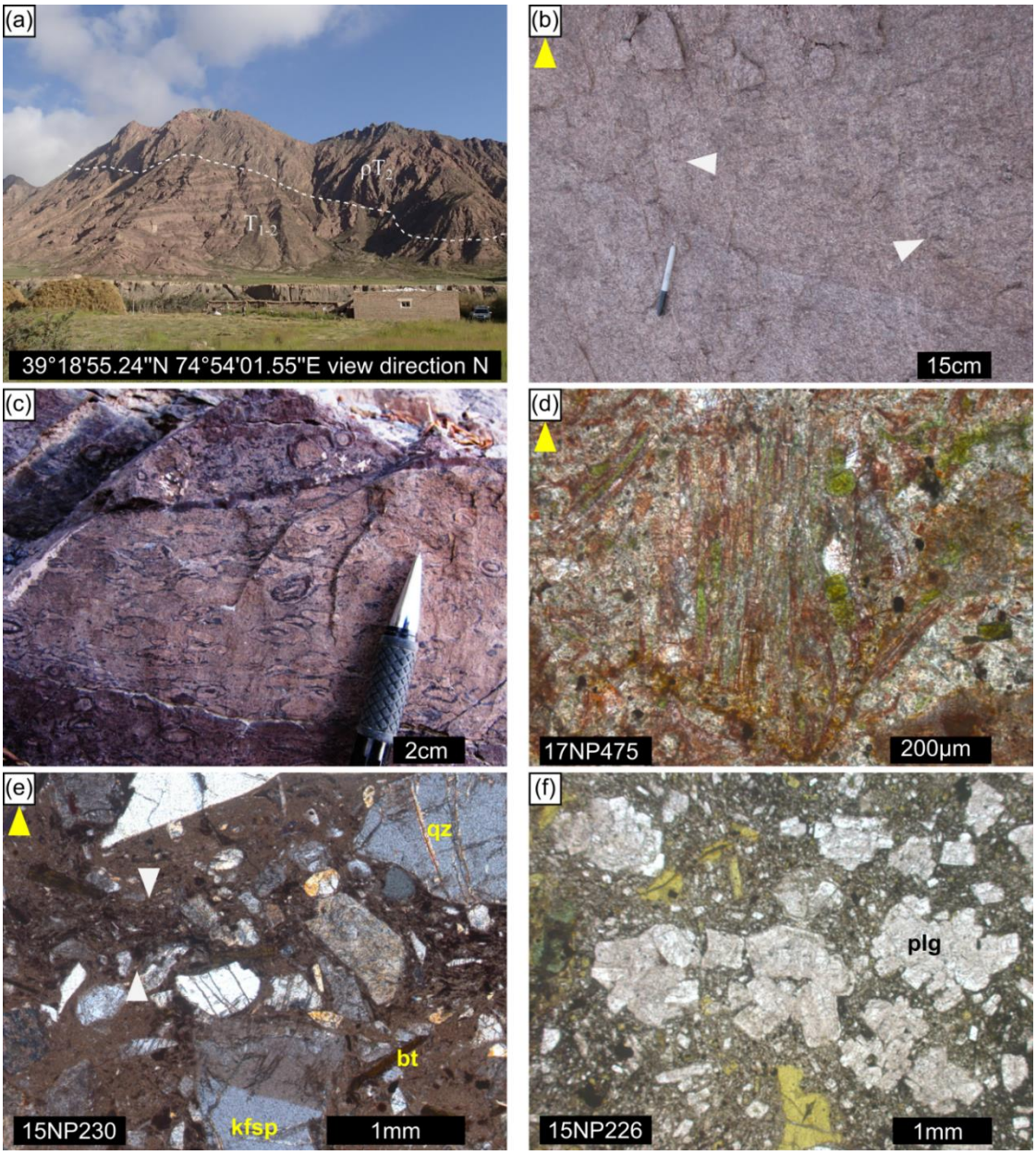

Figure 30: Field and microphotographs of Triassic volcanic rocks. Triassic volcanic rocks crop out in the Chinese Qimgan valley (a), the distinct angular unconformity (white dashed line) separates the Middle Triassic (ρT_2), red ignimbritic crystal tuff from the underlying (T_{1-2}), red sandstone and conglomerate beds. The medium-grained crystal-rich tuff (b) is characterized by homogenous crystal size and pale grey fiamme (white arrow). At the top of the ~200m thick ignimbrite, a layer of welded accretionary lapilli was found (c). Two distinct, brick-red, unwelded crystal tuff layers were found interbedded with the red clastic sediments below the unconformity. They show elongate pumice fragments (d, plane-polarized light) and lack zircons. Thin section photograph of the ignimbritic crystal tuff showing welded pumice (between white arrows) that forms fiamme textures (e, cross-polarized light). Phenocrysts are fragmented potassium feldspars (kfsp) and quartz (qz), the latter show frequent fracturing. Biotite (bt) appears as brownish green flakes. The basalts, basaltic andesites and andesites from the Middle to Upper Triassic are generally more phyric than the Permian mafic to intermediate rocks. Thin section (f, plan-polarized light) shows glomerophyric plagioclase. Yellow arrows in b, d, e indicate upward direction.

Microscopic textures typical of magma mingling, such as partially resorbed quartz crystals and sieve-textured feldspar were observed from the pale red rhyolite in the upper Biertuokuoyi valley (Figure 29e). The abundant tuff layers, found in the lower part of the Qimgan section, typically show small, fragmented plagioclase and quartz crystals, volcanic and sedimentary lithic fragments, and perlitic glass fragments (Figure 29f). The matrix in all sampled tuffs is altered and pseudomorphs of glass shards are rare.

In the upper, coarse-grained clastic unit of the Qimgan section, two brick-red crystal tuff layers were identified. Zircons, for U-Pb dating, were not present in collected tuff samples, thus the age estimates for the course clastic unit remain unclear. Since it is discordantly overlain by Mid-Triassic volcanic rocks (Figure 30a), it might be Lower to lower Middle Triassic. In the Lower to lower Middle Triassic units, sandstones and conglomerates form up to several meters thick, partly amalgamated beds that laterally persist over hundreds of meters. Besides the two crystal tuff layers, several aphyric, dark greenish dikes were found. A red, crystal rich, up to ~200 m thick ignimbrite (Figure 30b) forms the base of the Middle to Upper Triassic unit. Welded, accretionary lapilli tuff layers (Figure 30c) were observed along the top of the ignimbrite. After some tens of meters of coarse, matrix-supported conglomerates, an approximately 600 m thick package of poorly stratified basaltic to andesitic lava flows, associated tuffs and epiclastic breccias was found. This unit was the main target for geochemistry and is not only present in the Qimgan valley but also in the Gez and Oytag valleys (Figure 28b, c), where it is crosscut by multiple transpressive faults associated with the Kashgar-Yecheng-Transfer fault system (KYTS, Figure 27). Amongst the Upper Triassic mafic to intermediate volcanic rocks, lava flows with plagioclase, pyroxene and/or amphibole phenocrysts are common. Large hornblende-phyric andesites were observed not only in the Qimgan valley but also in Upper Triassic volcanic rocks from the Altyn Darya valley. Plagioclase forms as glomerocrysts in some basaltic andesites (e.g., Figure 30f). The mafic to intermediate Upper Triassic volcanic sequence is likely Carnian to Rhaetian in age; however, it was not dated radiometrically. The age estimate is based on the age of the underlying ~200 m thick Ignimbrite, presented in this study and the age of the overlying amagmatic, fine- to coarse-grained, lower Jurassic conglomeratic beds. Typical for the Jurassic in all outcrop areas are several coal seams; these are mined in the Gez valley.

4.7.2 Zircon U-Pb dating

Age determination

An age overview of the five samples dated for this study is given in Table 4, and Appendix C.1 lists the single grain U-Pb isotope data.

We report two ages for each sample: (1) the youngest concordant single grain age (± 2 σ propagated uncertainty) and (2) the age of the youngest coherent group of concordant grains (± 2 σ propagated

uncertainty), with a proportion value of greater than 0.2, calculated by the peak fit algorithm of IsoplotR (Vermeesch, 2018). For the calculation of both ages, we used a discordance cut-off range of $-1<d_c<5$. (relates to $-3<d_r=1-([^{206}Pb/^{238}U]/[^{207}Pb/^{206}Pb])<15$, Vermeesch, 2020), where d_c is the concordia distance as defined by Vermeesch (2020) and implemented in IsoplotR 3.6. The concordia distance is a modified version of the Aitchison distance discordance filter d_a and considers the correlated uncertainties of the U-Pb isotope pairs. Generally, we prefer peak fit ages (age (2)) as population ages for interpretation. This takes into account that single concordant grains may be mathematically seemingly concordant due to their large age error (Spencer *et al.*, 2016) or due to the minimal distance between concordia and discordia line for young isotope gain or loss. Since in our data set age (1) and age (2) differ partly by 10s of million years, what we interpret as result of lead loss (left-skewed age distribution curve, (Spencer *et al.*, 2016)), we decided to present both ages in Table 2 for a more complete view on the age distribution.

Table 4: LA-ICP-MS igneous zircon U-Pb age data of all samples investigated in Chapter 4.

Sample	Rock type	Location	Latitude	Longitude	Age[1] of youngest concordant single grain [Ma] ± 2σ(prop)	Age[1] of youngest coherent group of concordant grains (peakfit, Vermeesch, 2018) [Ma] ± 2σ(prop)	Number of grains
15NP213	Rhyolite	Gez valley	38.924	75.4978	228.6 ± 2.0	233.4 ± 1.1	44
15NP220	Welded chrystal tuff	Qimgan valley	39.3215	74.9084	219.4 ± 2.7	244.1 ± 1.1	89
17NP445	Rhyolite	Bieertuokouyi valley	39.4053	74.4569	244.1 ± 2.6	261.1 ± 1.3	23
20101020-3	Chrystal tuff	Gez valley	38.9188	75.4938	244 ± 16	246 ± 11	20
P09T19	Felsic sill	Markansu valley	39.3688	74.0494	236.9 ± 3.7	260.5 ± 1.6	31

[1] *Discordance filter is $-1<d_C<5$*

Ages of volcanic rocks

Starting in the western most outcrop area (Figure 28), dacitic sill sample P09T19 from the Markansu river valley and reddish rhyolite sample 17NP445 from upper Bieertuokuoyi gave similar peak fit ages of 260.5 ± 1.6 Ma and 261.1 ± 1.3, Ma respectively (Figure 31a, b). They are sampled close to the base of the Permo-Triassic basin. Further to the east we sampled an ignimbritic crystal-tuff cropping out in the Qimgan and the Gez valley. We dated 89 zircons from sample 15NP220 taken in the Qimgan valley and obtained a peak fit age of 244.1 ± 1.1 Ma for the youngest coherent group of concordant grains and an age of 219.4 ± 2.7 Ma for the youngest concordant single grain (Figure 31c, f). Sample 20101020-3 from the Gez valley yielded an age of 246 ± 11 Ma for the youngest coherent group of concordant grains and a similar age of 244 ± 16 Ma for the youngest concordant single grain (Figure 31d). The peak fit ages of both samples overlap within 2 σ age uncertainty. Sample 15NP213—a crystal-tuff, sampled close to the location of 20101020-3—gave a peak fit age of 233.4 ± 1.1 Ma (Figure 31e).

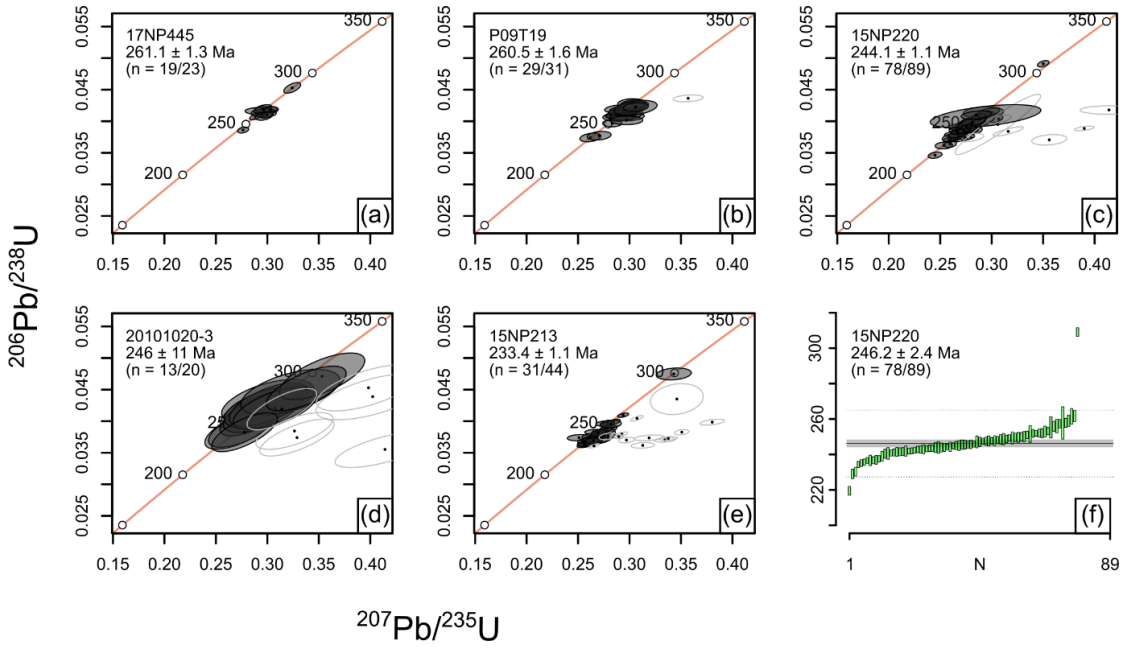

Figure 31: Wetherill plots of the zircon U-Pb age data for Permo-Triassic rocks. They are from the upper Biertuokuoyi valley (a), the Markansu valley (b), the Qimgan valley (c, f) and the Gez valley (d, e). Error ellipses are colored translucent grey, stacking of multiple ellipses will result in darker grey to black shades. Excluded, discordant error ellipses are plotted unfilled. The ages in a–e are peak fit ages ± 2σ (prop.), the age in f is a weighted mean age ± 2σ.

The new ages together with the age of an aplitic dike at the base of the Qimgan basin of 250.0 ± 0.3 Ma (cf. section 2.5.2) imply a volcanic phase that lasted from at least the Capitanian to the Carnian (~261–233 Ma).

4.7.3 Geochemistry

Whole rock geochemistry

We analyzed 21 volcanic rock samples for major and trace element concentrations mainly derived from Middle to Upper Triassic strata. Trace element values were normalized against primitive mantle (Sun & McDonough, 1989), REE were normalized against chondrite (Boynton, 1984). Samples 17NP446 and 17NP448 are from the Permian strata, sample 99WT36 is from the Upper Permian to Lower Triassic strata in the Qimgan valley (Figure 28). They are plotted and interpreted along with the Middle to Upper Triassic samples (Appendix C.2). Three analyses (of samples 17NP448, 15NP211 and 15NP212) yielded very high LOI values between 12.4 wt% and 25.5 wt% and very low SiO_2 values of 44.9 wt% and 25.6 %, respectively. They are regarded as substantially altered and were handled cautiously and excluded from discrimination plots. The remaining 18 samples are basic to acid rocks with SiO_2 concentrations between 48.4 and 74.6. MgO concentrations are low to moderate between 0.4 wt% and 6.8 wt%, K_2O values range between 0.2 wt% and 5.0 wt%, and Al_2O_3 values are high, between 13 and 21 wt%. TiO_2 concentrations are generally low, ranging from 1 wt% in the basic to intermediate rocks to 0.2 wt% in the rhyolitic samples. All samples have low Zr (44 to 286 ppm) and low Y (2.3 to 53 ppm) content.

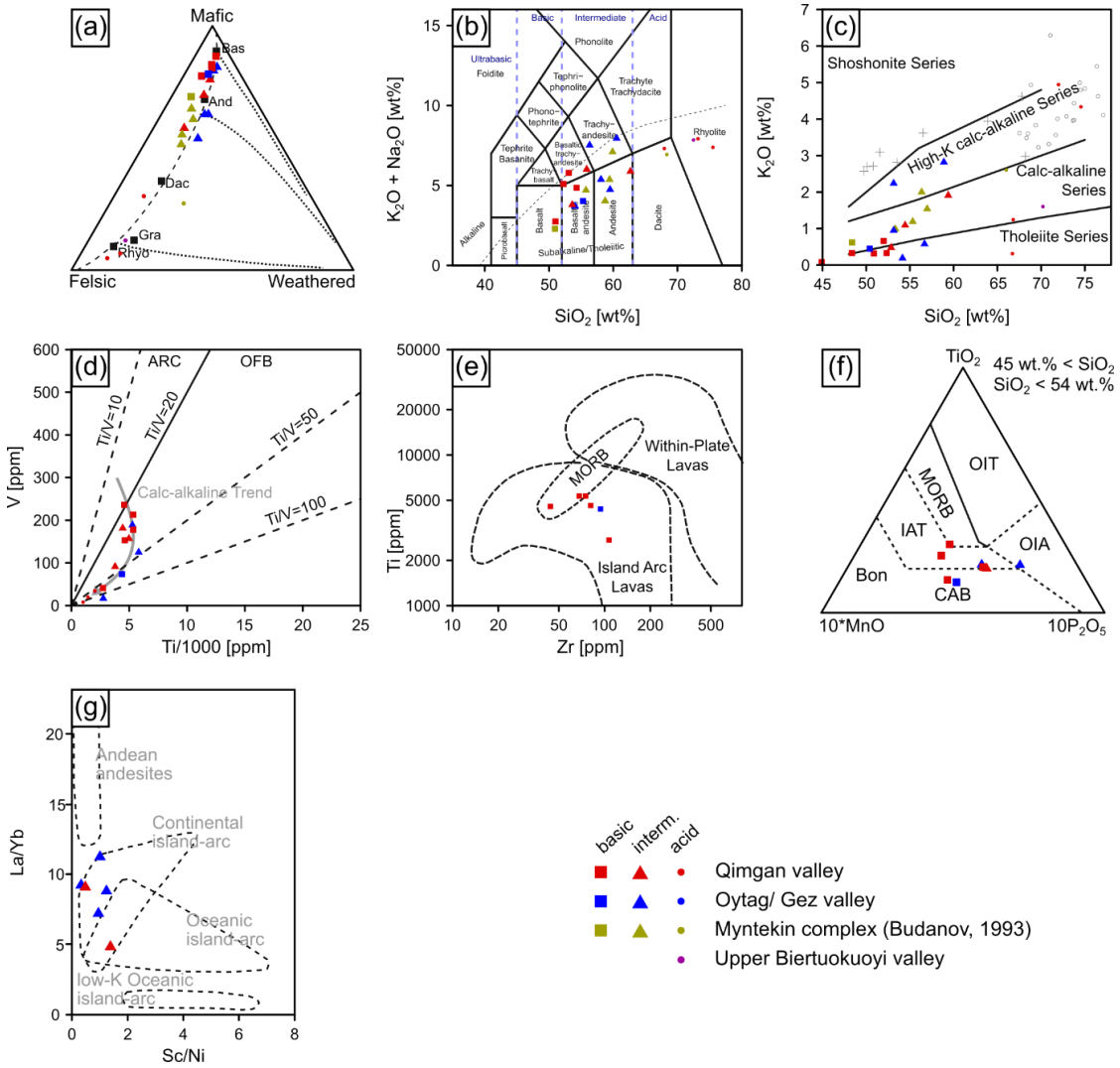

Figure 32: Geochemical characterization of Permo-Triassic volcanic rocks of the North Pamir. Note that literature data from the Myntekin formation (Budanov, 1993) is plotted along with newly presented samples in figures a, b, and c. (a) All sampled rocks plot close to the trajectory defined by fresh volcanic rocks in the Felsic-Mafic-Weathered ternary diagram developed by Ohta and Arai Ohta & Arai (2007). (b) According to the TAS diagram (Le Bas et al., 1986), the samples classify as basalts, basaltic andesites, andesites and their trachytic equivalents. Acidic rocks are classified as dacites and rhyolites that plot in the tholeiitic to high-K calc-alkaline series (c) according to the classification of Peccerillo and Taylor Peccerillo & Taylor (1976). Data from intrusive rocks ("o") and their mafic enclaves ("+") from the Karakul Mazar and West Kunlun are plotted for comparison (Schwab et al., 2004; Huang et al., 2013; Jiang et al., 2013; Wang et al., 2016). In the Ti/1000 against V diagram (d), the samples show a calc-alkaline trend, as defined by Shervais (1982). This matches well with a classification of the basic rocks as island arc lavas (e) according to the diagram of Pearce Pearce (1982) and as island-arc tholeiites and continental arc basalts (f) according to the classification of Mullen Mullen (1983). In the Sc/Ni vs. La/Yb plot of Bailey Bailey (1981), andesitic rocks are mainly identified as continental island arc andesites (g).

A pronounced positive Pb/Pb* anomaly with values between 1.4 and 4.6 ($Pb/Pb^* = Pb_N/sqrt(Ce_N*Pr_N)$) correlates with a negative Ti/Ti* anomaly with values between 0.2 and 1 ($Ti/Ti^* = Ti_N/sqrt(Eu_N*Dy_N)$).

All samples show petrographic and/ or geochemical (LOI) indications for alteration. However, plotted in the diagram of Ohta & Arai (2007) (Figure 32a), none of the 18 samples with moderate or low LOI diverges far from the unaltered rock trajectory. Sample 17NP435 (similar to high LOI samples 15NP211 and -212) has a Na_2O value below detection limit and for this reason was not

plotted in the diagram (Figure 32a), assuming that Na_2O was removed by secondary processes.

The investigated mafic to intermediate samples can be classified as basalt, basaltic andesite and andesite with some trachytic equivalents. Acid rocks are classified as dacites and rhyolites following Le Bas *et al.* (1986) (Figure 32b). Acid volcanic rocks are peraluminous whereas intermediate and mafic volcanic rocks are mainly metaluminous.

Some of the mafic to intermediate samples have low, tholeiitic K_2O values between 0.19 wt% and 0.58 wt%. Intermediate and acid samples show a higher scatter and can be classified as tholeiitic to even high-K calc-alkaline according to the scheme of Peccerillo & Taylor (1976)(Figure 32c). Plotted in the Na_2O+K_2O-CaO diagram of Frost *et al.* (2001)(not shown), two trends can be distinguished: a calcic and an alkali-calcic trend.

Since the concentration of alkaline elements and MgO or CaO may be changed during alteration (Staudigel *et al.*, 1981; Cerling *et al.*, 1985; Spivack & Staudigel, 1994), the use of more immobile elements for classification is helpful. Ti and V concentrations show a calc-alkaline trend (Figure 32d) as defined by Shervais (1982). This contradicts the classification of the mafic rocks as tholeiitic using the K_2O-SiO_2 diagram. Potassium mobility is a very common secondary effect in volcanic rocks (e.g., Staudigel *et al.*, 1981; Cerling *et al.*, 1985), therefor we regard the rocks as calc-alkaline.

Using the Zr-Ti diagram of Pearce (1982), mafic volcanic rock samples plot in the Island Arc Lavas field (Figure 32e) and in the MnO-TiO-P_2O_5 ternary diagram of Mullen (1983) mafic to intermediate rocks plot within the continental arc basalt (COB) and island arc tholeiite (IAT) fields (Figure 32f). We used the Sc/Ni vs La/Yb diagram presented by Bailey (1981) to classify orogenic andesitic rocks. The andesites have low Sc/Ni ratios and moderate La/Yb ratios and plot in the continental island arc field (Figure 32g). Total REE + Y concentrations are between 50 and 187 ppm. Light REE are enriched over heavy

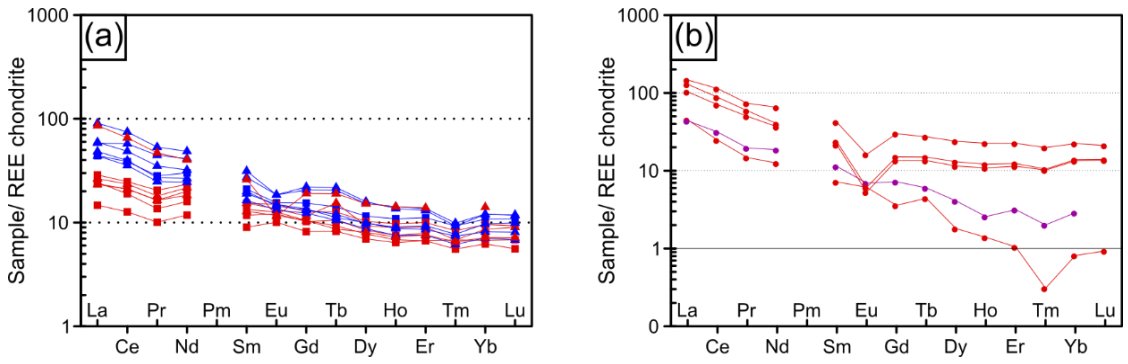

Figure 33: Rare earth elements (REE) normalized to C1-chondrite (Boynton, 1984) of the Permo-Triassic volcanic sequence. basic to intermediate rocks (a) show moderately enriched light REE and no to moderate Eu/Eu anomaly. Acid rocks (b) show more pronounced Eu/Eu* anomaly and more enriched light REE. Two samples (17NP446 and 15NP228) show anomalous REE pattern with less enriched light REE and low heavy REE concentration. Flat heavy REE element pattern of mafic rocks demonstrates shallow parental magma differentiation above the garnet stability field.*

REE with $(La/Lu)_N$ values ranging between 2 and 9 (Figure 33). Heavy REE show a flat chondrite-normalized pattern in mafic rock samples, suggesting a low-P spinel mantle source. The outliers are two rhyolitic samples (17NP446, 15NP228) with anomalously low heavy REE pattern. A progressively pronounced negative Eu anomaly develops from basalts to rhyolites, typical for plagioclase fractionation. Eu/Eu* values range between around 1 in the basic to intermediate samples and 0.3 for the Middle Triassic Qimgan rhyolitic ignimbrite.

XRD analysis

XRD analyses largely agree with petrography. Results show clinopyroxene as augite and hedenbergite. XRD analyses also classified common fine-grained groundmass and alteration minerals (Table 1). Calcite, hematite, and clay minerals (montmorillonite and kaolinite) are dominant secondary minerals.

4.8 Discussion

4.8.1 The Permo-Triassic North Pamir basin in the regional geodynamic setting

Ages of magmatic activity

The Permo-Triassic magmatic phase in the North Pamir spans at least ~28 Ma, from the Permian Capitanian stage into the Upper Triassic Carnian stage (~261–233 Ma). A thick pile of hitherto undated basic to intermediate rocks that overlies the rhyolitic crystal tuffs (~244–233 Ma) in Qimgan and Gez might extend this time span further into the Upper Triassic. The whole succession is conformably overlain by amagmatic, coal bearing Jurassic clastic sediments. A compilation of magmatic events during the Permo-Triassic in Central Asia explores a possible linkage based on the synchroneity and geodynamic settings, as follows:

In the *Tien Shan*, Permian magmatic activity close to the North Pamir is correlated with a Hercynian late- to post-collisional transcurrent geodynamic setting activating large NW-SE and ENE-WSW wrench faults (Jong *et al.*, 2009; Rolland *et al.*, 2013; Jourdon *et al.*, 2017; Loury *et al.*, 2018). The Permo-Triassic North Pamir volcanism postdates the major phase of magmatic activity in the Tien Shan (295–275 Ma, Biske *et al.* (2013)). However, extensional tectonics in the North Pamir, forming back-arc basins, partly overlaps with the late stages of Hercynian post-collisional transcurrent tectonics in the Tien Shan. It is behind the scope of this study to determine whether Permo-Triassic basin formation in the North Pamir was ruled by pure extensional or transtensional tectonics. Temporal coincidence with large scale transcurrent faulting in the nearby Tien Shan during the Permian makes an overall transcurrent geodynamic setting also in the North Pamir likely. It coincides with local magmatic activity connected to strike-slip faulting and ongoing exhumation in the North, Northeast and South Tien Shan north of Tarim (e.g. Narat range, 296–260 Ma, Biske *et al.* (2013); 267 Ma alkaline granite, Gissar segment (Konopelko *et al.*,

2017); 287–266 Ma anatectic granite, Pobeda massif, Kokshaal segment (Loury *et al.*, 2018)). The vast majority of Hercynian post-collisional magmatism in the Tien Shan ceased at that time (e.g., Seltmann *et al.*, 2011; Konopelko *et al.*, 2019), making a direct genetic linkage to the North Pamir volcanic rocks unlikely. Triassic volcanism in the North Pamir correlates with a high temperature event recorded in the Kyzylkum segment (240–220 Ma, Seltmann *et al.*, 2011), Late Permian to Triassic basanitic dikes from the Gissar and Alai segments (Käßner *et al.*, 2017), and Late Triassic alkaline and carbonatitic intrusions in the Alai segment of the South Tien Shan (Vrublevskii, 2017; Vrublevskii *et al.*, 2018). Geochemical data of the complex 220 Ma carbonatites and alkaline gabbro presented in Vrublevskii *et al.* (2018) indicate their intrusion in an extensional active continental margin setting. However, the Middle to Late Triassic was a phase of relative tectonic quiescence and widespread erosion in the Tien Shan (Morin *et al.*, 2021).

The *Tarim LIP* volcanism was partly coeval and interfered with Hercynian post-collisional igneous activity in the Tien Shan. Activity in the Tarim LIP terminated in the Cisuralian (e.g. Xu *et al.*, 2014). Recent, high precision ages of the major flood basalt units put a younger limit of about 284 Ma on the magmatism (Zhong *et al.*, 2022). Hence, the LIP clearly predates the volcanic rocks found in the Chinese North Pamir.

Evidence for Permian magmatism in the *Karakul-Mazar* arc-accretionary complex is scarce and restricted to the ~250 Ma Kayizi pluton of the West Kunlun (Liu *et al.*, 2010; Liu & Wang, 2014). This arc related magmatic activity, however, continues into the Triassic and is widespread in the nearby West Kunlun range. Middle to Upper Triassic calc-alkaline, arc related volcanism in the North Pamir coincides with major intrusive activity in the Karakul-Mazar domain and makes a correlation plausible.

It must be stated, however, that the situation of the North Pamir in the Permian remains relatively vague, as long as little is known about the geochemical compositions of the Permian volcanic rocks in the Hindukush and the North Pamir. We argue that a genetic-link to the north-vergent Paleo-Tethys subduction, which might have been active during that time (Chen *et al.*, 2021), is likely. Crustal extension in the North Pamir, forming the upper plate of the Paleo-Tethys subduction zone might be as well connected to slab retreat of the downgoing Paleo-Tethys slab. Trench migration towards the south could also explain the relatively wide Karakul-Mazar accretionary complex. However, steep subduction of a cold oceanic slab alone (not requiring rollback) is capable of causing back-arc extension (e.g., Lallemand *et al.*, 2005).

Petrogenesis of the Triassic volcanic rocks and implications for a Permo-Triassic Cimmerian extensional back-arc system

Middle to Late Triassic rocks show calc-alkaline trends typical for volcanic arcs (Figure 32). Andesites show features such as low Al_2O_3, TiO_2, Zr and Y content characteristic for collisional andesites as defined by Bailey (1981). They are classified as continental island arc andesites based on their La/Yb and Sc/Ni ratios (Figure 32g), which ties them to coeval arc volcanic rocks of the

Karakul-Mazar arc-accretionary complex to the south. Accordingly, trace elements of the volcanic rocks compared to the intrusive rocks of the Karakul-Mazar arc-accretionary complex show similar LILE enrichment with respect to HFSE, pronounced Pb positive anomaly and a Ti negative anomaly (Figure 33).

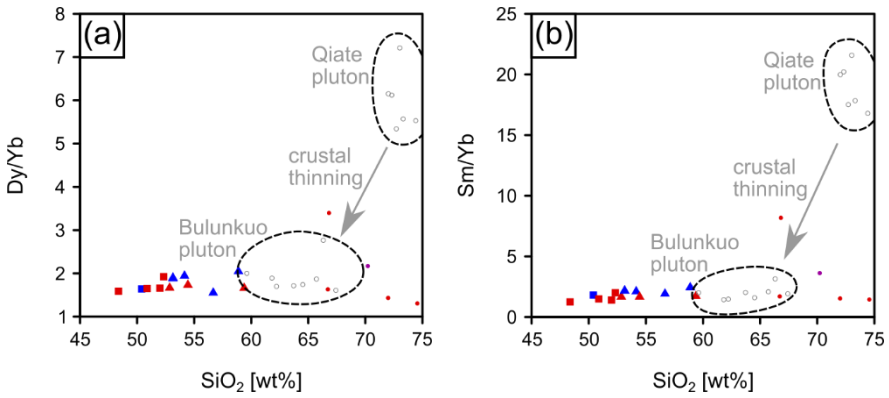

Figure 34: Comparison of element ratios of volcanic and intrusive arc-volcanic rocks. Volcanic rocks of the Qimgan and Gez suite show low Dy/Yb (a) and Sm/Yb (b) ratios similar to values derived from the Upper Triassic Bulunkuo intrusion (Qiate and Bulunkuo values taken from Chen et al. Chen et al. (2021)).

This is indicative of the influence of slab-derived volatiles during melt generation in a subduction zone. The flat heavy REE pattern of the mafic volcanic rocks indicate melt production in a shallow spinel-bearing mantle. We compared Sm/Yb and Dy/Yb from the Qiate (~240 Ma) and Bulunkuo (221–219 Ma) intrusions (Chen *et al.*, 2021) with the Qimgan and Gez Triassic volcanic suite (Figure 34). Low ratios, especially in mafic volcanic rocks, are indicative of melts that formed above the garnet stability field (Mamani *et al.*, 2010), in an area of normal, non-thickened continental crust. The Middle to Upper Triassic rocks of the Qimgan and Gez valley have ratios that resemble those of the Bulunkuo intrusion (Figure 34). Those findings challenge the idea of pre-Cimmerian (and pre-Cenozoic) cratonic Tarim-Tajik crust below the North Pamir (cratonic Asia), as it was implicated by previous studies (Kufner *et al.*, 2016; Rutte *et al.*, 2017).

The volcano-sedimentary Permo-Triassic sequence of Qimgan and Gez must be seen in context with the Karakul-Mazar arc-accretionary complex in the framework of the Paleo-Tethys subduction along the southern Asian continental margin prior and during the Cimmerian orogeny (Figure 35). Back-arc formation can be associated with the production of a variety of magma types (Taylor & Martinez, 2003; Martinez *et al.*, 2007; Bézos *et al.*, 2009), and arc-like volcanic rocks underline the genetic linkage of the back-arc basin volcanics and the Karakul-Mazar arc. The temporal and geochemical correlation with volcanic rocks of the volcano-sedimentary Myntekin complex (Budanov, 1993) and a continuation of the Permo-Triassic volcano-sedimentary suite from the northeastern North Pamir into the Afghan Badakhshan and Hindukush areas and further into the Paropamisus and Kopet Dag in NE Iran (e.g., Montenat, 2009; Zanchetta *et al.*, 2013; Zanchi *et al.*, 2016; Siehl, 2017; Balini *et al.*, 2019) traces a more than 1000 km long zone of

(Permo-)Triassic back-arc extension to the north of the Paleo-Tethys subduction zone. It connects the North Hindukush rift with the Myntekin Formation in the Altyn Darya valley and the Triassic Qimgan and Gez suite. Indicators of high thermal fluxes, alkaline and carbonatitic melt formation in the South Tien Shan, west of the Talas Fergana fault (Seltmann *et al.*, 2011; Käßner *et al.*, 2017; Vrublevskii, 2017; Vrublevskii *et al.*, 2018) and evidence for strike-slip activity (Rolland *et al.*, 2013) suggest a wide zone affected by extension and transtension in the Middle-Late Triassic (Figure 35).

From the Kungurian onwards, there is evidence for deposition of volcaniclastic material in a back-arc basin of the Paleo-Tethys subduction zone in the region (Hinze, 1964; Boulin, 1988; Leven *et al.*, 1992; Salikhov & Sakiev, 2014). Back-arc sedimentation and volcanism intensified in the Triassic, forming multiple, connected back-arc basins (e.g., Montenat, 2009; Siehl, 2017). However, a more precise geochemical classification of the Permian volcanic suites in the Hindukush and North Pamir is needed to show continuing volcanic arc and back-arc activity from the Permian into the Triassic. Regardless of the uncertainties arising from missing geochemical data, the newly described Permo-Triassic units from the northeast North Pamir must be seen in line with aforementioned areas, as they share the same age, island arc affinity and geodynamic position close to the Paleo-Tethys subduction zone.

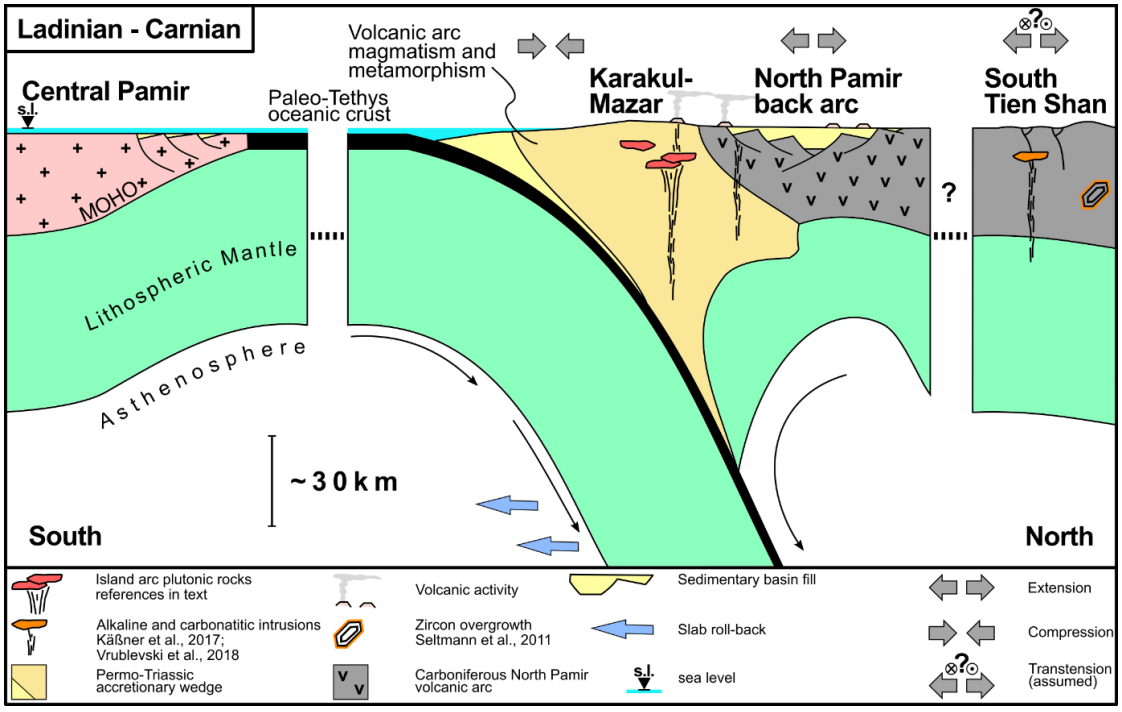

Figure 35: Paleogeographic reconstruction. The sketch shows the geodynamic situation along the South-Asian margin in the Ladinian to Carnian, during deposition of the Middle to Upper Triassic volcaniclastic unit. The Karakul-Mazar arc-accretionary complex forms along the subduction zone of the Paleo-Tethys ocean. In the back-arc, extension creates space for the sedimentation of Permian and Triassic volcano-sedimentary strata. During that time, potentially ongoing transtensional tectonics (Rolland et al., 2013) in the South Tien Shan may have provoked the emplacement of alkaline melts (Käßner et al., 2017; Vrublevskii et al., 2018) and zircon overgrowths (Seltmann et al., 2011). Large parts of Central Asia where under erosional or non-depositional conditions.

4.8.2 Implications for the modern Pamir

The shape of the present-day Pamir has frequently been discussed. The existence of linear facies belts along a paleo-Asian margin prior to the collision with India is one major argument for an indentation of Indian lithosphere and ~300 km northward displacement of the Pamir with respect to Tibet (Burtman & Molnar, 1993; Burtman, 2000). Recently a pre-existing embayment along the Paleo-Asian margin was postulated, significantly reducing the amount of shortening accommodated in the Pamir (Chapter 2 and Li *et al.*, 2020). The major constituents of the North Pamir are the Carboniferous North Pamir volcanic arc, the Permo-Triassic volcano-sedimentary back-arc basin, and the Karakul-Mazar derived Shala Tala nappe (e.g., Robinson, 2015). The Main Pamir Thrust (MPT), a likely Miocene thrust system (e.g., Sobel & Dumitru, 1997) forms the northern border of the North Pamir (Figure 26). It juxtaposes Paleozoic and Mesozoic units of the North Pamir against Mesozoic to Cenozoic units of the External Pamir. Shallow, active seismicity is documented from the northern margin of the North Pamir and the External Pamir fold and thrust belt (Figure 25, e.g.,Teshebaeva *et al.*, 2014; Qiao *et al.*, 2015; Li *et al.*, 2019; Patyniak *et al.*, 2021)). Remnants of the Permo-Triassic back-arc basin are found all along the fault trace of the MPT. They are mainly positioned in the hanging wall (e.g., Upper Biertuokuoyi, Altyn Darya) but also in the foot wall (Qimgan). We propose that crustal heterogeneities in the Hercynian crust (North Pamir volcanic arc), weakened by Triassic back-arc extension might have facilitated the nucleation of the MPT, thus codetermined Cenozoic deformation. The width of the basin, possibly decreased by the MPT, is crucial for a shortening estimation along that large scale fault structure. From the geochemical data collected from the Middle and Upper Triassic in Qimgan and Gez, we infer a relatively low magnitude of extension, since geochemistry of the volcanic rocks shows continental island-arc character. There is no evidence for ocean floor spreading and associated MORB magmatism.

4.9 Conclusion

The upper Biertuokuoyi, Qimgan and Gez volcano-sedimentary suite was deposited between ~ 260 Ma (Capitanian) and ~ 233 Ma (Carnian), possibly continuing into the late Upper Triassic. The Permo-Triassic basin formed on top of the Carboniferous North Pamir volcanic arc that accreted during the Hercynian orogeny to the southern margin of Asia. Volcanic rocks were emplaced throughout the Permo-Triassic in a back-arc position of the north verging Paleo-Tethys subduction zone over non-cratonic crust (spinel stability field) in close vicinity to the continental arc in the Karakul-Mazar and West Kunlun realms. The presented data in context with published findings from the NW Pamir, and the Badakhshan and Hindukush ranges allows us to connect the volcano-sedimentary sequences from the North Hindukush rift, the Myntekin formation and the Qimgan-Gez suite to form a ~ 1000 km long North Hindukush–North Pamir extensional or transtensional

back-arc zone. Middle-Late Triassic, extension related thermal imprint and volcanism in the South Tien Shan can be correlated. The presence of a Permo-Triassic extensional domain to the north of the Paleo-Tethys subduction zone might have facilitated northward thrusting in the North Pamir during the Cimmerian orogeny. However, we argue that reactivation of pre-existing structures and inhomogeneities related to that rift during the Cenozoic is likely, since all outcrops of the Permo-Triassic extensional basin are well aligned along the Miocene Main Pamir Thrust of the North Pamir.

Chapter 5. Evolution of the Pre-Cimmerian Paleo-Asian margin deduced from detrital zircon U-Pb data from the Qimgan volcano-sedimentary section (NE Pamir) and constraints for Late Triassic closure of a Cimmerian back-arc basin

5.1 Abstract

The Chinese Pamir exposes an anchizonal to greenschist facies, bimodal volcano-sedimentary succession of Permo-Triassic age. It disconformably overlies early- to mid-Carboniferous rocks of the North Pamir magmatic arc. The Permo-Triassic sedimentary succession is well exposed in the Chinese Qimgan valley and can be divided into three units. The lower unit is dominated by mafic to intermediate lava flows, volcaniclastic rocks and greenish volcanimictic silt- and sandstones. In the middle unit, the fine-grained sediments pass into reddish coarser-grained clastics with rare layers of rhyolitic tuffs. The top of the middle unit is truncated by an angular unconformity, which is overlain by a ~200 meters thick, Anisian, rhyolitic ignimbrite, followed by ~600 meters of intermediate and mafic lava flows. The sedimentary section shows (syn-) sedimentary extensional faulting. New detrital zircon U-Pb age spectra reveal mostly unimodal Triassic to Permo-Carboniferous age peaks. The Triassic zircons have elevated Th/U ratios compared to Permo-Carboniferous zircons, underlining their provenance in an extensional setting. The Permo-Triassic succession must be seen as part of a back-arc basin system that formed in the hinterland of the Cimmerian Permo-Triassic Karakul-Mazar arc-accretionary complex, associated with the closure of the Paleo-Tethys basin. These can be linked to similar successions in the Chinese North Pamir (Oytag, Gez, Bieertuokuoyi), which are all related to similar successions exposed in the Kyrgyz Altyn Darya valley (North Pamir) and the Afghan Hindukush.

Potassium-Argon data from the Shala-Tala thrust fault, which emplaces epizonal to amphibolite facies Karakul-Mazar derived units onto sedimentary units of the Permo-Triassic Qimgan back-arc succession, date the thrusting event to ~205 Ma. The partial closure of the Qimgan back-arc basin in the Rhaetian by a major back-thrust pinpoints the collision of the Central Pamir with the Karakul-Mazar arc-accretionary complex.

5.1.1 Introduction

The Pamir orogen in Central Asia is the western extension of the Tibetan Plateau, both of which result from a long-lasting, Phanerozoic sequence of subduction processes and terrane accretion along the southern margin of the Asian continent. The Pamir is traditionally subdivided into the North Pamir/ Karakul Mazar, Central Pamir, and South Pamir terranes (Figure 36). The Tanymas-Jinsha suture separates the Karakul Mazar unit from the Central Pamir; the Rushan-Pshart suture forms the boundary between the Central and South Pamir (Bazhenov & Burtman, 1982; Burtman & Molnar, 1993; Schwab *et al.*, 2004).

Major events that affected the Pamir were the formation of the North Pamir volcanic arc during the Carboniferous subduction of a portion of the Paleo-Asian ocean and accretion of the arc to Asia`s southern margin (see Chapter 2 and e.g., Bazhenov & Burtman, 1982), and the Permo-Triassic ongoing subduction of Paleo-Tethyan oceanic crust and formation of the Karakul-Mazar arc-accretionary complex—interpreted as a lateral equivalent of the Songpan-Ganzi Hoh-Xil complex of Tibet (Schwab *et al.*, 2004; Amidon & Hynek, 2010; Imrecke *et al.*, 2019). Subduction of the Paleo-Tethys culminated in the formation of the Tanymas-Jinsha suture zone between Karakul-Mazar and the Central Pamir in late Triassic to early Jurassic times (Dewey *et al.*, 1988; Leven, 1995; Robinson *et al.*, 2012; Robinson, 2015). It was later reworked by the Tanymas thrust fault, emplacing Karakul-Mazar derived rocks onto the Central Pamir (e.g., Burtman & Molnar, 1993; Rutte *et al.*, 2017). To the south of the Central Pamir, coeval closure of the Rushan ocean lead to the accretion of the South Pamir along the Rushan-Pshart suture zone (Villarreal *et al.*, 2019; Wang *et al.*, 2020). The accretion of the Karakoram block to the South Pamir along the Wakhan suture zone likely happened in early Jurassic time (Gaetani *et al.*, 1993; Angiolini *et al.*, 2013).

Figure 36: Geographic overview over the Pamir and its surroundings. In color: outline of the Permian Tarim Large Igneous Province (LIP) (after Li et al., 2014; Xu et al., 2014, in orange) and the Kuche depression (light orange) in the Tarim Basin (yellow). 1–Tanymas-Jinsha suture, 2–Rushan-Pshart suture, 3–Wakhan-Tirich Boundary Zone, 4–Shyok suture.

This short summary makes it obvious that the end-Triassic Cimmerian orogeny had a major influence reshaping the Asian southern continental margin. Triassic granitoid intrusive rocks found in the Karakul Mazar unit and especially in the West Kunlun have been studied extensively (e.g., Schwab *et al.*, 2004; Xin *et al.*, 2019; Zhang *et al.*, 2019; Chen *et al.*, 2021). These studies

described characteristics of Andean-style continental arc evolution and gave an insight into mid-crustal levels of the collision zone. However, due to the limited amount of surface outcrops, there is less knowledge about the Permo-Triassic volcano-sedimentary sequences in the North Pamir. They provide important information about surface processes in the vicinity of the Paleo-Tethys subduction zone.

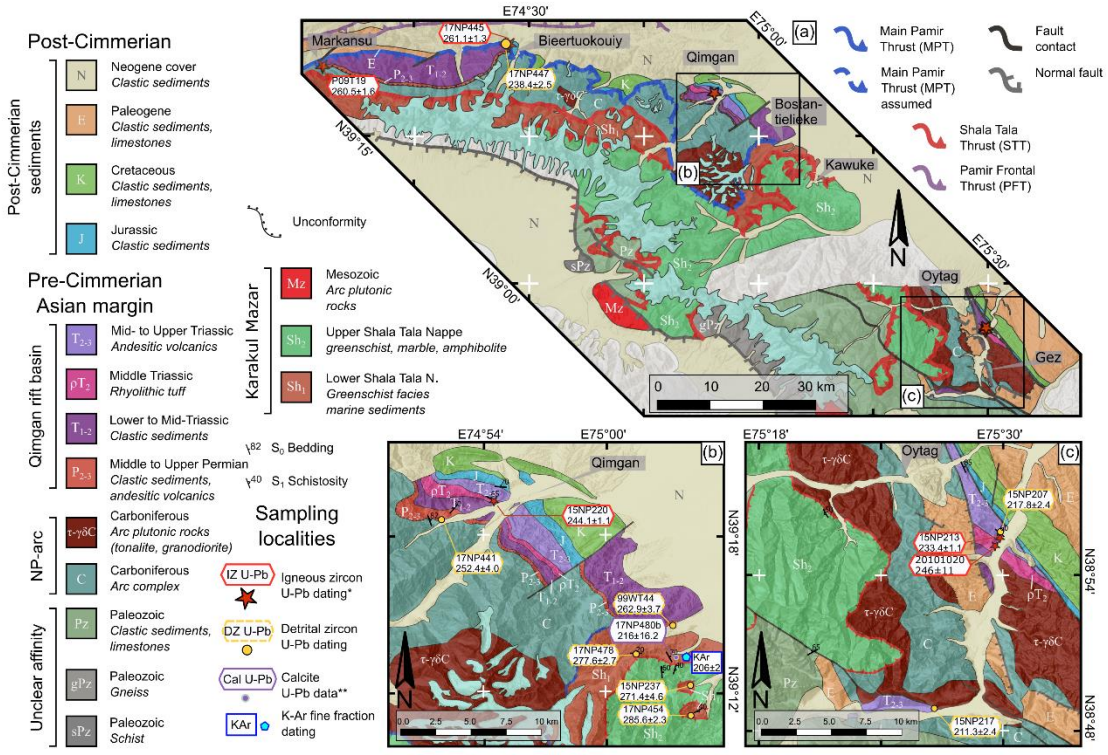

Figure 37: Detailed geological map of the study area (redrawn after own observations and (Henan Institute of Geological Survey (HIGS), 2014; Henan Institute of Geological Survey (HIGS), 2014). Map (a) gives locations of igneous (see Chapter 4) and detrital zircon U-Pb samples in the upper Bieertuokuoyi valley and the Markansu valley. Figures b and c show sample localities of samples in Qimgan and Gez valley, respectively. Ages are given as [Ma] ± 2σ propagated error (prop) for zircon U-Pb data.

Bazhenov & Burtman (1982) and Wolfart & Wittekindt (1980) compiled stratigraphic sections from the Hindukush/ Badakhshan (Bamyan, Doab-Surkhab, Bangui) area in Afghanistan and the Darvaz and Trans-Alai ranges in Tajikistan. The Permian and Triassic strata in all sections are usually marine. The Permian is characterized by fine clastic or carbonaceous sedimentation. This is followed in Afghanistan by a Middle to Upper Triassic clastic sequence with intercalated intermediate to acidic tuff layers and lava flows. In Tajikistan, the Permian-Lower Triassic sedimentary strata is overlain by a Middle to Upper Triassic andesite- and tuff-bearing unit, that is interlayered with carbonaceous shales and conglomerates (Luchnikov, 2001). This is followed by a Late Triassic unit composed of basalts, andesites, tuffs and associated volcaniclastic rocks, interlayered with sand- and siltstones. Permo-Triassic volcano-sedimentary units rim the Pamir salient and form the Hindukush-North Pamir rift basin, spanning from eastern Iran through central

Afghanistan into the North Pamir. It can be connected to the Qimgan basin in the northeastern North Pamir (Figure 37) (see Chapter 3 and Baud & Stämpfli, 1989; Montenat, 2009; Siehl, 2017). In this work we provide a holistic overview of the Permo-Triassic sedimentary rocks in the North Pamir and the adjacent areas. We present the first detrital zircon U-Pb geochronological study of the basin fill of the easternmost segment of the North Hindukush-North Pamir rift basin and discuss the new findings in the light of high-quality field geological studies published in the past. We also constrain the timing of late Triassic-early Jurassic thrusting along the Shala Tala fault zone and a potential closure of the back-arc basin by dating fine-fractions of deformed marine rock units using the K-Ar method. Uniform detrital zircon U-Pb age signals throughout this part of the basin as well as a common petrography tie the deformed units, exposed within the Shala Tala nappe to undeformed counterparts in the foot wall block of the Late Triassic-early Jurassic Shala Tala thrust. Our work helps understanding the Cimmerian orogeny and thrusting events in the North Pamir, contributing to a better understanding of crustal architecture that affects the present day regional deformation pattern.

5.1.2 Geological outline of the Permo-Triassic in West Tarim and the North Pamir

North Pamir

The Permian period follows a phase of island arc collision and ocean closure in the region, well documented from the Tien Shan (e.g., Konopelko *et al.*, 2007; Biske *et al.*, 2013) and the North Pamir (see Chapter 2 and e.g., Li *et al.*, 2022). During the Carboniferous—Permian transition, the South Tien Shan (e.g., Biske *et al.* (2019)) and the North Pamir Carboniferous volcanic arc (see Chapter 2) were accreted and consolidated. This was followed by large scale transpressive faulting in the South Tien Shan (Rolland *et al.*, 2013; Loury *et al.*, 2018). The Permian strata of the North Pamir is characterized by mostly marine sediments with laterally variable deep to shallow marine facies and common hiati (Leven *et al.*, 1992; Leven, 2013). In the Tajik Darvaz range, a part of the North Pamir, the marine Permian was subdivided into the distal, clastic Chelamchin formation, the medial, fusulinoid limestone bearing Safetdaron formation, and the proximal, clastic Kulyakhin formation, which are followed by the distal Gundarin and the proximal Daraytang formations. The clastic Kulyakhin and Daraytang formations comprise substantial amounts of resedimented volcaniclastic material and andesitic tuffs (Leven *et al.*, 1992). The Triassic (Rhaetian) Myntekin formation, characterized by continental clastic and volcanic rocks, overlies Permian strata following a basin wide hiatus (Luchnikov, 2001). The volume of volcanic material increased in the Triassic. The Triassic succession is dominated by pyroclastic rocks of intermediate to acidic composition and subordinate basaltic and andesitic lava flows and breccia. Budanov (1993) describes a 1200—2000 m thick, Triassic volcano-sedimentary sequence at the confluence of the Mynteke and Kashkasu rivers. Both are left tributaries of the Altyn Darya in Kyrgyzstan (Figure

38a, for location of the Alty Darya valley, see Figure 26). It is characterized by a lower unit of volcanimictic coarse-clastic rocks as well as rhyolitic to andesitic pyroclastic rocks and an upper unit of rhyolitic to basaltic lava flows and interlayered coal-bearing sandstones and conglomerates. The Myntekin formation at its type-locality in the Altyn Darya valley is similar to the Triassic of the Qimgan section (Figure 38b). Both are dominated by continental clastic sediments and intercalated mafic to acidic volcanic rocks. The Triassic volcano-sedimentary sequence found in the NE Pamir (see Chapter 4,) can be linked to back-arc basin successions further to the west

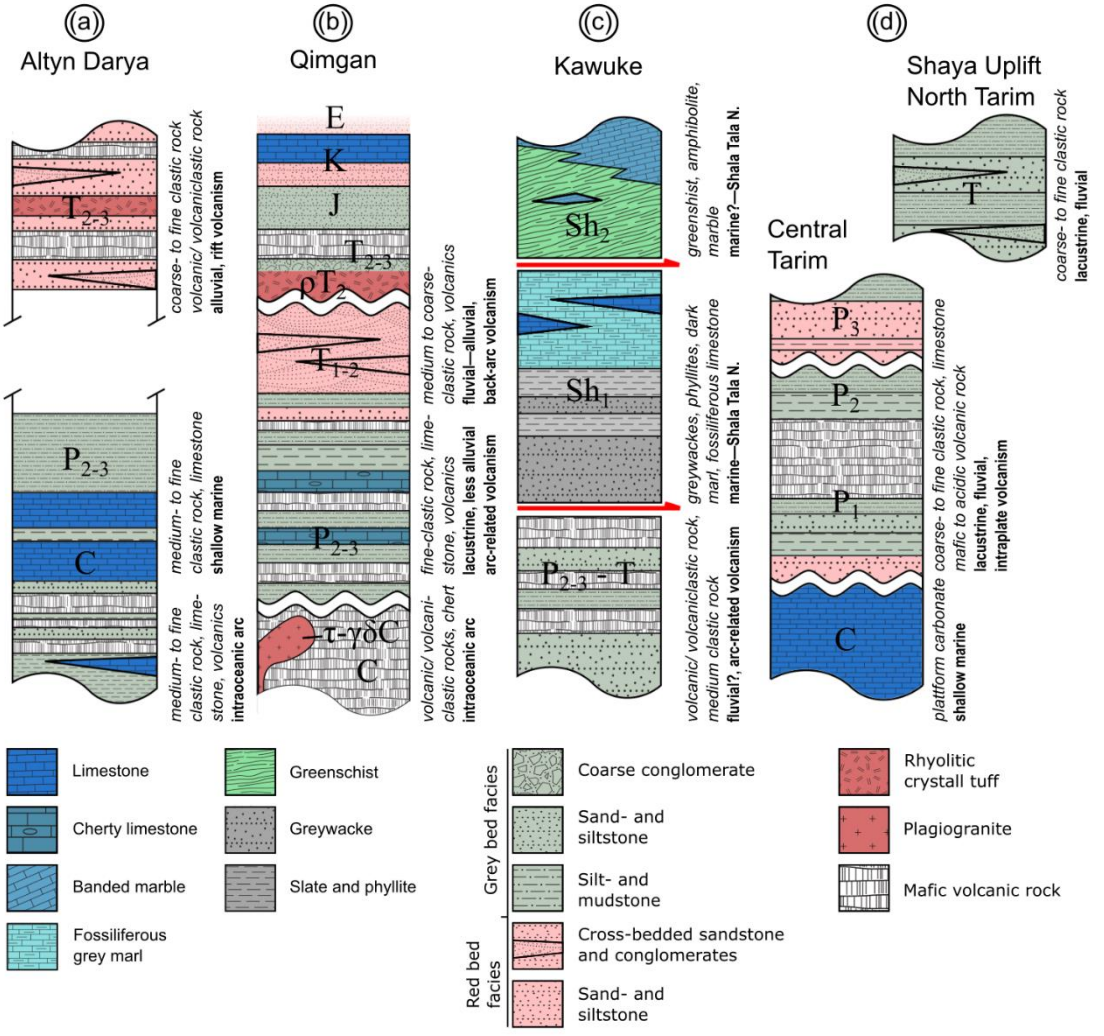

Figure 38: Sketch of stratigraphic profiles in the NE Pamir. The Altyn-Darya section (a) shows fine-grained Permian strata with marine carbonates followed by coarse- to fine-clastic, continental strata in the Triassic. Permian strata in Altyn Darya and further to the west is amagmatic, while the Triassic Myntekin complex contains basic to acidic volcanic rocks (Budanov, 1993). Note that a portion of the section was not observed. The Qimgan profile (b) exhibits an entirely volcano-sedimentary Permo-Triassic succession. In the Kawuke area (c), further east, this Permo-Triassic section is overthrust by the low-grade metamorphic marine lower Shala Tala nappe (Sh_1) (this study), of presumably early Permian age (deduced from unspecific Goniatites and a detrital zircon U-Pb MDA of ~277Ma). This in turn is overthrust by a greenschist to amphibolite facies metamorphic upper Shala Tala nappe (Sh_2) (Robinson, 2015). In the Tarim basin (sections in d), the Permian fine-grained continental strata contain basic to intermediate volcanic rocks derived from the Tarim Large Igneous Province (P_2, Tarim LIP). The Triassic was a time of erosion in large parts of the Tarim basin; only small basins along the Tien Shan front preserve an amagmatic coarse-clastic succession (e.g. in the Kuche depression, exposed in the Shaya uplift). Altyn Darya, Qimgan and Kawuke profiles are drawn after own field observations, stratigraphy of the western Tarim basin is based on descriptions in Liu et al. (2011) and from the Shaya uplift zone, NW Tarim after Liu et al. (2012a).

(Myntekin formation, Altyn Darya valley (Budanov, 1993; Luchnikov, 2001); Doab formation, Hindukush (Hinze, 1964; Weippert, 1964; Siehl, 2017), Aghdarband window, Kopet Dag (Baud & Stämpfli, 1989; Zanchetta *et al.*, 2013; Zanchi *et al.*, 2016; Balini *et al.*, 2019)).

The collision of the Central Pamir with Asia's southern margin in the late Triassic to early Jurassic led to the obduction of metamorphic units of the Karakul-Mazar accretionary wedge. Large parts of the eastern North Pamir are covered by the Karakul-Mazar derived Shala Tala nappe (Figure 37) (Robinson *et al.*, 2004; Robinson, 2015; Rembe *et al.*, 2020). It is composed of marine meta-sediments and meta-igneous rocks, namely, greywacke, phyllite, marl, marble, greenschist and amphibolite.

This nappe partly overthrust the Permo-Triassic Qimgan basin and the volcano-sedimentary basin fill was locally ductily strained during this process. In the Chinese Kawuke valley, structural relations between the Permian strata and greenschist to amphibolite facies Karakul-Mazar derived units can be studied (Figure 38c). We present new detrital zircon U-Pb data from tectonic windows exposing strata of the lower Shala Tala nappe, lithologically resembling undeformed, Permian units found in the Qimgan basin.

West Tarim

The Tarim Basin borders the Pamir to the east. Permian and Triassic strata are well documented by subsurface well log data. Following a basin wide unconformity (e.g., Li *et al.*, 2014), Carboniferous, marine platform carbonates and intertidal deposits are overlain by Permian fluvio-deltaic strata, which is rapidly followed by lacustrine fine clastic strata in the center of the basin (Figure 38d) (Liu *et al.*, 2011). The facies-shift from Carboniferous to Permian time marks the turnover from marine to continental deposition in Tarim. Early Permian sedimentation was accompanied by extensive, within-plate volcanism connected to the Permian Large Igneous Province (LIP, Figure 36) (Yang *et al.*, 2006; Li *et al.*, 2008; Yu *et al.*, 2011; Li *et al.*, 2012; Zhang *et al.*, 2012). Major volcanic phases peak around 280 Ma, 290 Ma and 300 Ma (Xu *et al.*, 2014), with two extensive flood basalt eruption phases at 289.8 ± 1.0 Ma and 284.3 ± 0.4 Ma, dated by chemical-abrasion thermal-ionization mass-spectrometry (CA-TIMS) of zircon (Zhong *et al.*, 2022). The volcanic sequence is in turn overlain by Permian fine clastic lacustrine sediments (Liu *et al.*, 2011). Lacustrine strata are followed by fluvial deposits of the upper Permian, which in turn were incised by widespread erosion during the Triassic. Subbasins along the northwestern margin of Tarim are the result of flexural foreland deformation caused by the advance of the South Tien Shan (Liu *et al.*, 2012). They accommodate Triassic fluvio-lacustrine sediments, that have been explored for hydrocarbon reservoirs in the Kuche depression (Figure 36 and Figure 38d) (e.g., Shi *et al.*, 2010; Chen *et al.*, 2011; Liu *et al.*, 2012; Liu *et al.*, 2012). The Triassic paleo-climate was semi-arid to sub-humid, according to pollen analysis from the Kuche depression (Liu *et al.*, 2012). Braided river, deltaic and lacustrine Triassic deposits are dominant in the central and northern Tarim basin. However, in large parts of the eastern, western, and southern Tarim basin, the Triassic

was a phase of erosion or non-deposition.

Afghan Badakhshan and Hindukush

The Permian strata in the Hindukush is dominated by marine clastic and carbonate sediments. They discordantly cover volcanic and metamorphic units affected by the late Carboniferous to early Permian Hercynian orogeny (e.g., Wirtz *et al.*, 1964; Wolfart & Wittekindt, 1980; Leven *et al.*, 1992). In the Surkhab and Bagui valleys of North Afghanistan, patchy outcrops of Cisuralian fusulinid (*Quasifusulina*, *Darvasites*, *Paraschwagerina*) bearing limestones overlie a basal conglomerate. They are in turn overlain by an alternating sequence of clay-, silt- and sandstone (Wolfart & Wittekindt, 1980). The upper Permian is largely missing. Permian marine sediments are discordantly overlain by the Upper Triassic siliciclastic sequence, best described from the Doab area. The mainly siliciclastic, marine suite is grouped into the Doab formation. It is characterized by a lower unit of sandstones and conglomerates, followed by shales and marls of the middle Doab formation, which in turn is overlain by shales, siltstones, and sandstones of the upper Doab formation. Volcanic and epiclastic rocks are found throughout the sequence.

5.2 Methods

5.2.1 Field work and sample preparation

Sampling

Field work was concentrated in the north-west portion of the North Pamir, ~100 km SW of the town of Kashgar, southern Xinjiang, China. We collected samples in 4 localities (upper Bieertuikouyi valley, Qimgan valley, Kawuke/ Bostantielieke, Gez valley; Figure 37a). We sampled a broad range of units. 17NP478 was collected from a thick-bedded greywacke of the lower Shala Tala nappe (Sh_1) in the Bostantielieke valley; 99WT44 was sampled from an outcrop mapped as Lower to Mid-Triassic (T_{1-2}) rocks nearby. 15NP237 and 17NP454 are from deformed red conglomerates (Sh_1), found in tectonic windows of the upper Shala Tala nappe in the Kawuke valley. Sample 17NP441 was collected from a Permian sandstone (P_{2-3}) in Qimgan valley and sample 17NP447 from a Triassic sandstone in the upper Bieertuokuoyi valley. The youngest samples from the Middle to Upper Triassic (T_{2-3}) were collected in the Gez valley. Detailed field work was focused on the outcrops of the volcano-sedimentary Permo-Triassic sequence in the Qimgan and Kawuke/ Bostantielieke areas (Figure 37b, location of profiles in Appendix D.1). The Qimgan valley exposes a largely undisturbed section of Carboniferous to Eocene strata. We used conventional field mapping techniques and examined five profiles in Permian to Jurassic strata at a scale of ~5 m or finer. We applied sedimentological facies analysis according to Miall (1985), where suitable (facies types are presented in Appendix D.2). For this study, we investigated 29 petrographic thin sections (Table 5).

Table 5: Overview of the samples used for Chapter 5.

Sample	Rock	Purpose	Map age*	Latitude (N)	Longitude (E)
		Upper Bieertuokouyi valley			
17NP447	Sandstone	TS, DZ	T_3	39.406064	74.456925
		Qimgan valley			
17NP441	Sandstone	TS, DZ	P_2	39.31	74.866
17NP444	Limestone	TS	P_2	39.310575	74.86525
17NP468	Sandstone	TS	P_2	39.309117	74.859263
17NP469	Cherty limestone	TS	P_2	39.310575	74.86525
17NP474	Sandstone	TS	P_2	39.314663	74.883134
		Bostan Tielieke/ Kawuke valley			
17NP454	Conglomerate	TS, DZ	C_2P_1	39.184725	75.069937
99WT44	Sandstone	TS, DZ	P_2	39.242222	75.055278
17MP478	Sandstone	TS, DZ	P_1	39.223968	75.025066
15NP237	Sandstone	TS, DZ	C_2P_1	39.20403	75.0696
17NP483	slate	TS, K-Ar	P_1	39.221432	75.057663
17NP484	phyllite	TS, K-Ar	P_1	39.219012	75.057162
17NP485	dark fossiliferous marl	TS, K-Ar	P_1	39.216371	75.056281
17NP486	dark fossiliferous marl	TS, K-Ar	P_1	39.21403	75.057299
17NP487	greenschist	TS, K-Ar	P_1	39.21403	75.057299
		Gez valley			
15NP217	Sandstone	TS, DZ	P_1	38.81429	75.44386
15NP207	Sandstone	TS, DZ	T_3	38.928	75.4983

TS—thin section; DZ—sample for detrital zircon U-Pb dating; K-Ar—sample for K-Ar dating
** based on map sheets Yingjisha J43C002003, Kuergan J43C001002, Kashgar J43C001003*

Zircon U-Pb dating

For the provenance study, we extracted zircons from 8 sandstone samples using jaw crusher, disc grinder, water table, magnetic separation, and heavy liquids (SPT, DI). The obtained zircons were poured onto a glass plate and arranged in lines on double sided sticky tape under a binocular microscope. No sorting or selection was done. Alignment of zircon grains in epoxy-resin helps for better single grain recognition. Mounted grains were polished to expose an internal surface and imaged with cathodoluminescence (CL) at the electron microprobe facility of the University of Potsdam (UP), Germany.

K-Ar fine fraction dating

From the Shala Tala Nappe outcrop at Bostantielieke valley, we selected five samples for K-Ar age determination, to constrain the age of thrusting along the Shala Tala thrust. They were cleaned of altered parts, gently crushed, and sieved. The fraction <63µm was used to extract fractions <2µm and 2-6µm by settling in Atterberg cylinders. A second <2µm fraction was separated in the same way and used to separate the fractions <0.2µm using an ultra-centrifuge. All these fine fractions were examined with XRD for mineralogical composition and determination of the illite crystallinity.

5.2.2 Analytical work

Zircon LA-ICP-MS U-Pb dating

974 zircons from 8 detrital rock samples were dated. Zircon U-Pb dating was done according to the parameters described in section 2.4.2 and Zhou *et al.* (2020). Laser ablation was done with an ASI RESOlution 193nm ArF excimer laser system at the Radiogenic Isotope Facility (RIF), The University of Queensland (UQ). Laser spotsize was 30 µm. For each ablation spot, 3 s of blank was collected, followed by 20 s of ablation and 5 s of wash out. Cathodoluminescence images of the sample zircons were used to place laser ablation spots. Thus, fractures and zones with strongly differing Th/U values were identified and excluded. Using He carrier gas at a flow rate of 0.35 l/min and added N_2 gas for sensitivity enhancement, the gas mixture from the laser chamber was transferred to the plasma torch of a Thermo iCAP RQ quadrupole ICP-MS with 0.85 l/min Ar nebulizer gas. The ICP-MS signals were optimized by signal tuning before starting data acquisition.

The following isotopes were counted (dwell time in brackets): ^{88}Sr (0.005 s), ^{91}Zr (0.001 s), ^{200}Hg (0.01 s), ^{204}Pb (0.01 s), ^{206}Pb (0.045 s), ^{207}Pb (0.055 s), ^{208}Pb (0.01 s), ^{232}Th (0.01 s), ^{238}U (0.01 s). Data reduction was done in the program Iolite v2.5, which runs within the Igor Pro environment (Hellstrom *et al.*, 2008; Paton *et al.*, 2011) using the Vizual Age (Petrus & Kamber, 2012) data reduction scheme. Each five unknowns where bracketed by the standard zircon 91500 with a ^{206}Pb/^{238}U age of 1062.4 ± 0.4 Ma and ^{206}Pb/^{207}Pb age of 1065.4 ± 0.3 Ma (Wiedenbeck *et al.*, 1995). Temora 2 zircons (^{206}Pb/^{238}U age of 416.78 ± 0.33 Ma (Black *et al.*, 2004)) were treated as unknowns. The primary standard gave a ^{206}Pb/^{238}U age of 1062.7 ± 0.2 Ma and Temora 2 gave a ^{206}Pb/^{238}U age of 420.7 ± 0.2 Ma. Long term variance of the secondary reference material, uncertainty of the ^{206}Pb/^{238}U decay constant and the accuracy of the primary reference material led to the propagation of a total systematic uncertainty (Horstwood *et al.*, 2016) of 0.4% (2σ). All unknowns were filtered for concordance and strontium content.

The results were handled in the statistic program R, version 3.6.0 (R. Development Core Team, 2019).

K-Ar dating and illite crystallinity

Potassium and argon isotopic composition measurements were done at the Georg-August University, Göttingen. Details of argon and potassium analytical methodologies for the laboratory in Göttingen are given in Wemmer (1991).The argon isotopic composition was measured in a stainless-steel extraction and purification line coupled to a Thermo Scientific ARGUS VI ™ noble gas mass spectrometer operating in static mode. The amount of radiogenic ^{40}Ar was determined by isotope dilution method using a highly enriched ^{38}Ar spike from Schumacher, Bern (Schumacher, 1975). The spike is calibrated against the biotite standard HD-B1 (Fuhrmann *et al.*, 1987).The age calculations are based on the constants recommended by the IUGS quoted in Steiger & Jäger

(1977). Potassium was determined in duplicate by flame photometry using a BWB-XP flame photometer™. The samples were dissolved in a mixture of HF and HNO_3 according to the technique of Heinrichs & Herrmann (2013). The analytical error for the K-Ar age calculations is given on a 95% confidence level (2σ).

Illite crystallinity determinations are a sensitive indicator for the degree of very low-grade metamorphism in clastic sediments. Since the beginning of the development of this method by Weaver (1960) and Kübler (1984), many publications have proven the utility of illite crystallinity in many applications. Reviews of the preparation techniques and the interpretation have been given for example by Kisch (1991) and Krumm (1992).

Illite crystallinity, the peak width at half height of the 10 Å peak, was determined using an in house program at the University of Göttingen. Digital measurement of illite crystallinity was carried out by step scan (301 points, 7-10° (2Θ), scan step 0.010° (2Θ), integration time 4 s, receiving slit 0.1mm, automatic divergence slit).

All samples have been investigated in duplicates (A and B). The measurements were carried out in the "air dry" and the "ethylene glycol saturated" state to detect expandable layers of smectite type minerals.

Illite crystallinity is expressed as Kübler Index in (KI, Δ°2Θ), the limits for diagenesis/ anchizone and anchizone/ epizone are 0.420 and 0.250°2Θ (Kübler, 1967; Kübler, 1968; Kübler, 1984), respectively. These limits were checked in the interlaboratory standardization program of Warr & Rice (1994). The given KI values are nearly identical to their crystallinity index standard (CIS). The following correlation to mineral facies is appropriate: diagenetic zone to the zeolite facies, anchizone to the prehnite-pumpellyite facies plus the pumpellyite-actinolite facies, and epizone to the greenschist facies.

5.3 Results

5.3.1 Fieldwork and Thin section examination

Sedimentary Rocks of the Qimgan succession

Strata exposed in the coherent Qimgan section provides a record of the evolution of the Permo-Triassic back-arc. The volcano-sedimentary section can be divided into a lower, fine-grained unit (corresponding to Profile 1 and 2, Appendix D.3 and Appendix D.4), an intermediate coarse-grained unit (corresponding to Profiles 4 and 3, Appendix D.5 and Appendix D.6) and an upper unit dominated by volcanic rocks (lower part of Profile 5, Appendix D.7).

The base of the Qimgan profile is composed of a 3–5 m thick, matrix supported conglomerate layer (Gms, Lithofacies classification after Miall (1987) in brackets, Profile 1, Appendix D.3), interpreted as a debris flow deposit, marking the initial rift phase.

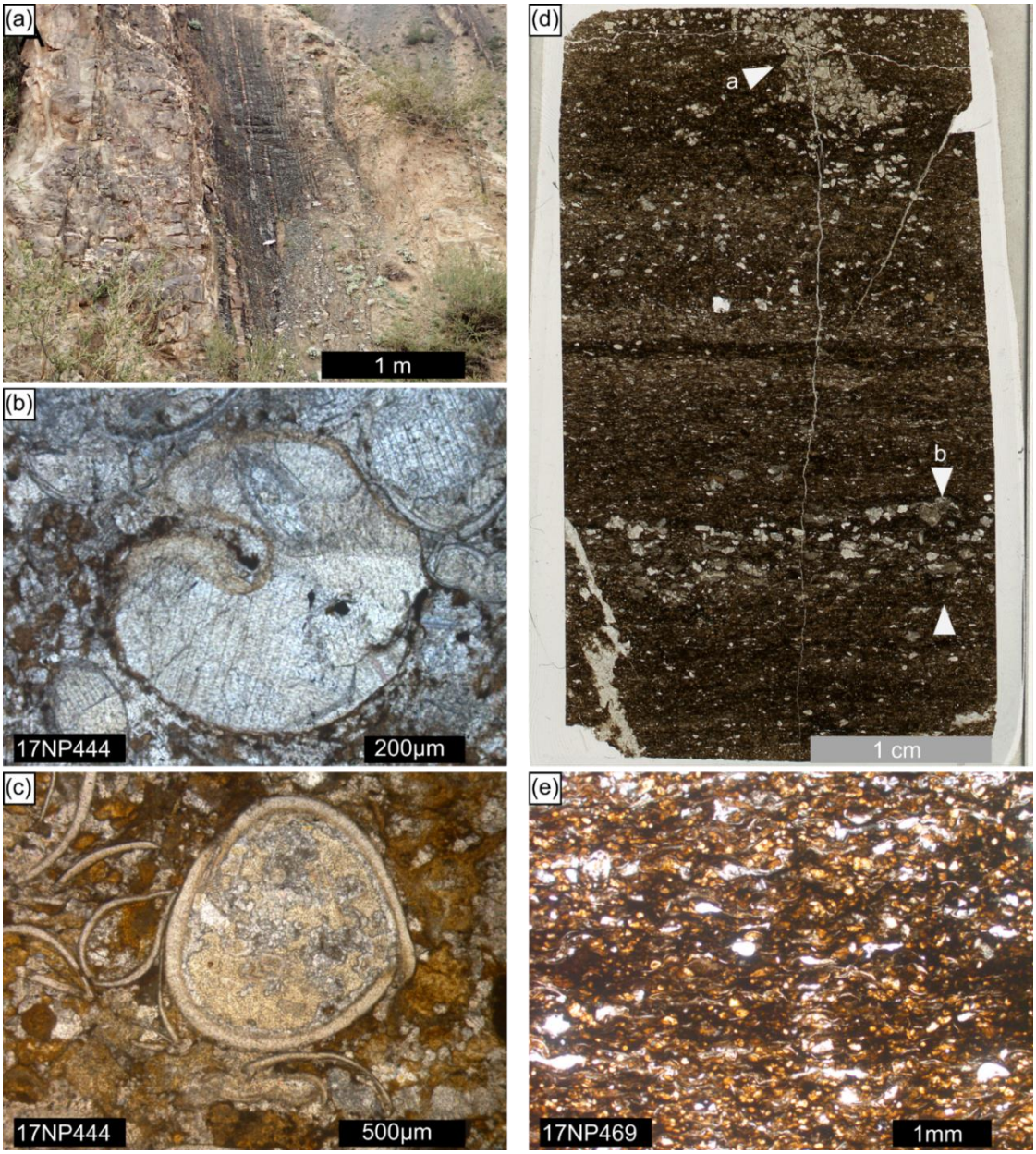

Figure 39: Field- and mircophotographs of the lacustrine Permian sedimentary rocks. In the lower part of the profile, partly silicified limestone layers were found. Light grey limestones form up to two-meter-thick bends and occasionally grade into thinly bedded, dark limestones (a). Thin beds of dark, silicified limestones show millimeter to centimeter scale lamination (b) build-up of ostracod-rich and -poor layers and layers of angular crystals (white arrows, b). Lamination is crosscut by a burrow (white arrow a, Fodinichnia) dragging clastic material into deeper levels. Fossil diversity is generally low, with ostracods and gastropods in the light grey limestones (c, d) and thin shelled ostracods in the dark, laminated limestones (e).

In the field, carbonate, basalt and serpentinite clasts were identified. The conglomerate overlies the mafic Carboniferous volcanic rock sequence of the North Pamir volcanic arc. U-Pb Calcite dating of a carbonate pebble found in the debris flow deposit gave an age of 347 ± 8 Ma (MSWD = 2.2) (Chapter 2), which reflects erosion of Mississippian carbonate platform rocks, such as are preserved in sections further west (e.g. Leven, 2013).

Reverse faults of unclear temporal assignment, which dissect the sequence in the lowest part, seem to have little offset. The conglomerate is overlain by a sequence of mafic to intermediate volcanic

and volcaniclastic rocks that are interlayered by greenish, fine-grained siliciclastic rocks. Throughout the entire lower unit, mafic to intermediate dykes crosscut the strata.

Large portions of the mud- and silt stones seem to lack sedimentary structures and can be described as massive silt and mudstone (Fsc). Partly silicified, laminated to thinly bedded carbonate layers (Pt, P1 and P1c, Figure 39a) were found within the fine-grained unit. They form up to several meter thick intervals. Calcite U-Pb dating of a lacustrine carbonate of the section gave a late Guadalupian age of 260.5 ± 2.2 Ma (MSWD = 3.4), interpreted as a depositional age (see Chapter 2).

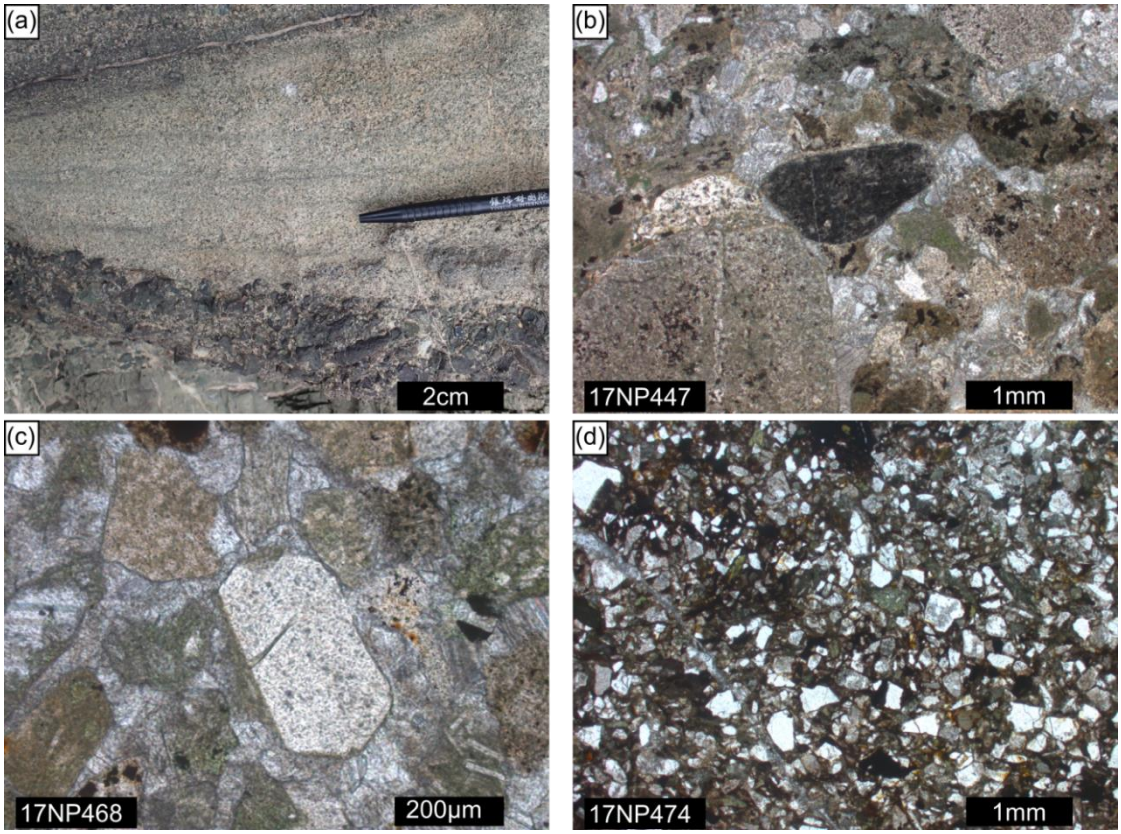

Figure 40: Field and microphotographs of Permian clastic sediments. (a) Mafic volcanic clasts from an incised lava flow are found at the base of a greenish sandstone of the lower, fine-clastic unit in profile 1. (b) Lithic arenite build up of altered volcanic lithic fragments. (c) Idiomorph feldspar crystal found in a lithic arenite indicating little transport of the sediment. The greenish volcanic clasts show small feldspar laths. (d) Lithic arenite with altered volcanic clasts (brown and green colors) and angular quartz and feldspar fragments. Thin section photographs (b, c, d) are under plane polarized light.

The dark limestones reveal a few millimeters to centimeters spaced lamination of ostracod-rich and - poor layers and intercalated layers with idiomorphic feldspar crystals (Figure 39d, e). Ostracod shells are mostly compacted in the laminated limestone. Sample 17NP444 of a lighter limestone shows uncompacted ostracod shells and gastropods (Figure 39b, c). Bioturbation was observed in the laminated limestone sample 17NP469 (Figure 39d). The fauna assemblage seems monotonous, which indicates a restricted environment with extreme conditions, e.g., a hypersaline lagoon or lake.

The light light-grey limestones show a larger size variety of ostracod carapaces and disarticulated valves, indicating little sorting effects due to transport, hence an autochthonous fossil assemblage. The dark, laminated limestones show more disarticulated ostracod valves and better sorting, indicating transportation of the material. They show evidence for turbiditic mass transportation and deposition of volcanimictic sediments, in particular angular feldspar crystals (Figure 39d) potentially derived from ash fall. Light-colored limestones might be interpreted as shallow-water facies, while dark, laminated limestones can be regarded as deep-water facies.

Beside the fine-clastic units, occasional massive or cross-bedded sandstones occur and show frequently erosive contacts with underlying volcanic rocks (Figure 40a).

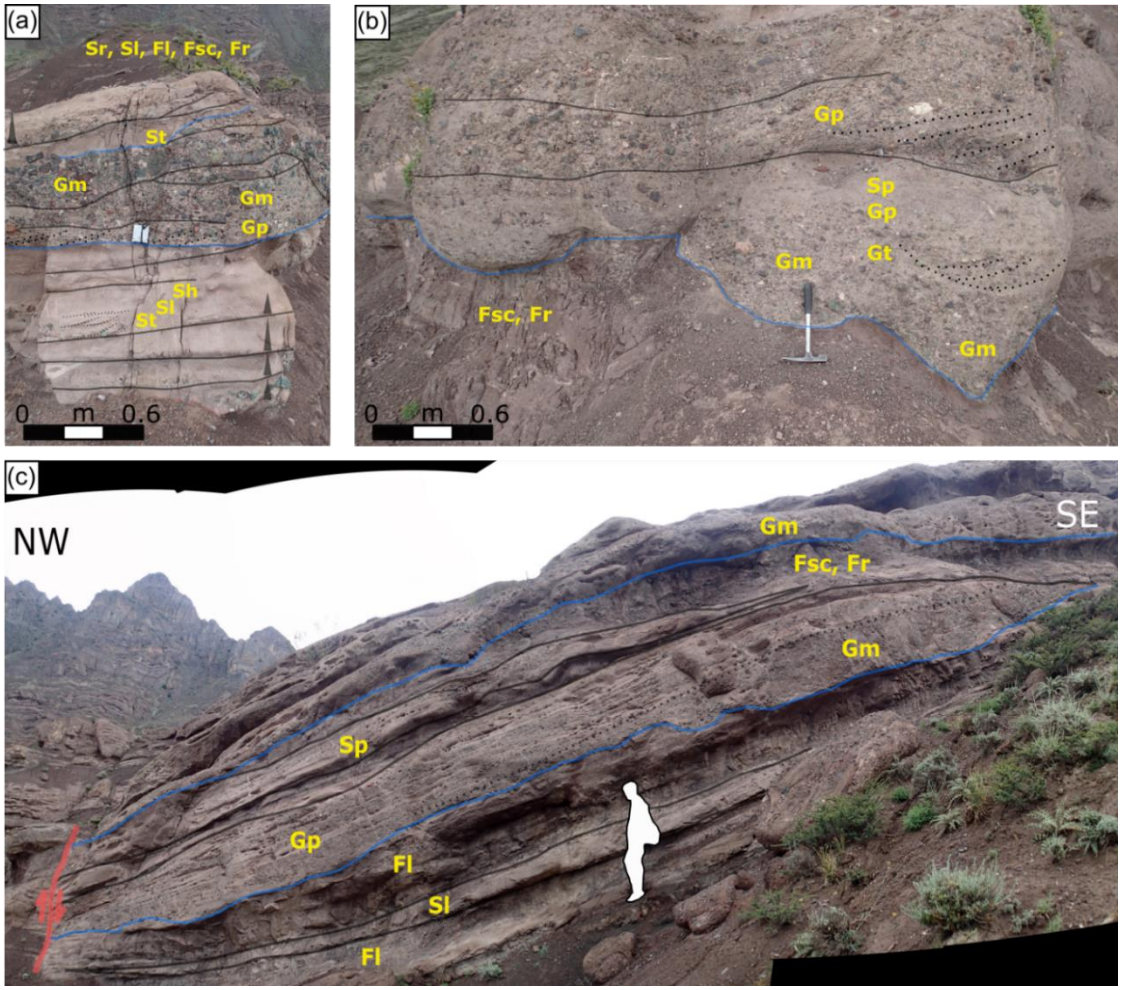

Figure 41: Field photographs of sedimentary deposits in the intermediate, coarse-clastic unit. (a) A coarse-clastic distributary channel cuts into a sandy bedform. Upsection, it was abandoned and is overlain by fine-clastic material (Sr, Sl, Fl). (b) A coarse-clastic distributary channel cuts into overbank fines with root traces (Fr). (c) An overbank deposit (Fl, Sl) is eroded by a distributary channel, hosting coarse gravel bars (Gm, Gp), later it was abandoned and filled with finer clastic material (Fsc). Eventually soil formation and rooting occurred (Fr) before another distributary channel crosscut the fine strata on the top of the outcrop. Person (1.6 m) for scale.

They are volcanimictic and immature (Figure 40b-d). Changes from lacustrine to fluvial facies are abrupt and indicate potentially tectonically driven changes in the depositional environment. The

intermediate unit (Profiles 4 and 3, Appendix D.5 and Appendix D.6) is dominated by red, alluvial sandstone, conglomeratic sandstone, and conglomerate (Figure 41). Sheet-like sand bodies and wide channels filled with conglomeratic sandstones are typical. Bed thickness and grain size increase towards the top of the unit. In turn, the abundance of siltstone and clay-stone layers decreases. The coarse-clastic beds fill channels with erosive bases (Figure 41b). Channel fill architecture shows common trough and planar cross bedding (Figure 41c; Gm, Gp, Gt, Sp, St). Pebbles from conglomerates were identified as mafic and intermediate volcanic rocks and subordinate sedimentary intraclasts. The sandstones show a low grade of maturity. They are dominated by lithic fragments, angular feldspar, and quartz in varying proportions. Coarse-clastic channel fill (gravel-bars followed by sandy bedforms) may grade into silt- to mudstones with frequent rooting (overbank fines), indicating abandonment of the channel by lateral channel migration or event like deposition (Figure 41a).

Where overbank fines are incised, they frequently show scouring along the erosive base (Figure 41b). Limestones are absent in the coarse-clastic, intermediate unit. The volume of volcanic rocks decreases in this unit.

The uppermost unit overlies an angular unconformity and is largely composed of a ~ 200 m thick rhyolitic, welded crystal tuff and associated volcaniclastic rocks. The tuff yielded a zircon U-Pb age of 244.1 ± 1.1 Ma (see Chapter 4), constraining the upper unit to the Anisian. That in turn is overlain by a ~ 600 m thick pile of intermediate lava-flows and associated volcaniclastic and epiclastic rocks. A ~ 10 m thick layer of coarse conglomerate was found between the acidic and intermediate volcanic rocks. The Mid- to Upper Triassic intermediate volcanic rocks are concordantly overlain by fluvial-alluvial Jurassic sediments (Profile 5 in Appendix D.7).

The Shala Tala nappe system in the Bostantielieke/ Kawuke section

Field observations revealed the bipartite nature of the Shala Tala nappe in the Bostantielieke/Kawuke sections. The nappe consists of a lower unit (Sh_1, Figure 37), that contains epizonal-grade, marine sedimentary strata. The upper Shala Tala nappe (Sh_2, Figure 37) is composed of greenschist (Figure 42a, b), amphibolite and marl. Since both units are clearly distinguishable by their metamorphic grade, they have to be seen as separate thrust sheets originating from different positions in the Karakul-Mazar arc-accretionary complex. Rock types of the lower unit are greywackes, phyllites and fossiliferous marl (Figure 42c, d). They show pervasive ductile deformation and form the base of the Shala Tala nappe stack in the NE Pamir. In the Bostantielieke valley they exhibit structures indicating en-block thrusting with the Sh_2 unit. To constrain the age of thrusting, we sampled a profile through unit Sh_1 and one sample from the overlying greenschist, which we interpret to be from Sh_2, for K-Ar fine fraction dating. Red, deformed conglomerates found in the Kawuke valley (Figure 42e, f) are macroscopically similar to undeformed conglomerates of the Qimgan succession.

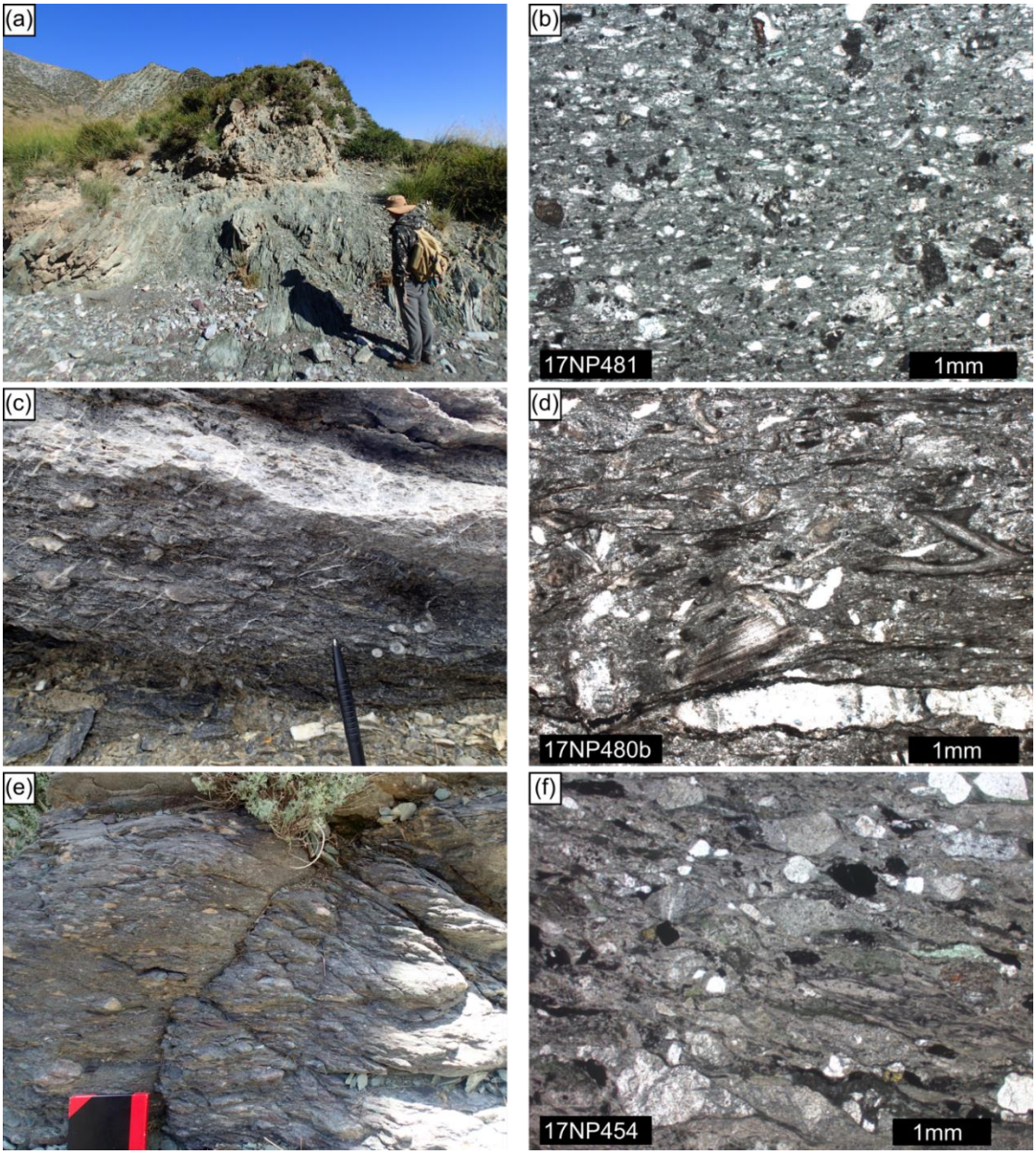

Figure 42: Field- and microphotographs of low-grade metamorphic rocks of the Shala Tala nappe system. (a) Greenschist outcrop in Kawuke valley (person 1.7 m). (b) Thin section of greenschist facies volcaniclastic rock from nearby Bostantielieke valley. These strata are regarded as part of the upper Shala Tala nappe (Sh_2). (c) Deformed fossil rich, dark marl with crinoid fragments and goniatites forming σ-clasts of the lower Shala Tala nappe (Sh_1), Kawuke valley. (d) Thin section from a deformed fossil rich, dark marl from Kawuke valley shows ductile deformation. (e) Deformed red conglomerate, exposed in a tectonic window in the Kawuke valley. (f) A thin section of a sample from that outcrop in (e) shows ductile deformation of the clayey matrix and fine-grained clasts. Thin sections (b, d, f) are under plane polarized light.

In the field, they were interpreted as $T_{1\text{-}2}$, which is not in accordance with the zircon U-Pb age distribution data, described below. This unit is now classified as Sh_1 but might represent a shallower marine, proximal facies compared to the open marine greywackes, slates and marls.

5.3.2 U-Pb dating

Age determination

To determine the maximum depositional age (MDA, e.g., Dickinson & Gehrels, 2009, review of methods in Coutts *et al.*, 2019 and Vermeesch, 2021) and to identify the peak and distribution of detrital zircon populations, we report three ages for each sample:

(1) the youngest concordant single grain age, (2) the age of the youngest coherent group of concordant grains with a proportion value greater than 0.2, calculated by the peak fit algorithm implemented in IsoplotR (Vermeesch, 2018), and (3) the maximum likelihood age (Galbraith & Laslett, 1993; Vermeesch, 2021). All three ages will be presented and discussed. For the calculation of age (1) we used a narrow discordance cut-off range of $-1<d_c<5$. For the calculation of age (2) and age (3) we used a more forgiving $-1.67<d_c<6.54$ (relates to $-5<d_r=1-(^{206}Pb/^{238}U/^{207}P/^{206P}b)<20$, Vermeesch, 2020), where d_c is the concordia distance as described by Vermeesch (2020) and implemented in IsoplotR 3.6 (Vermeesch, 2018).

Table 6: Age results from the detrital zircon samples presented in Chapter 5. All ages are with ± 2σ propagated error.

Sample	Location	Latitude	Longitude	Age[1] of youngest concordant single grain [Ma] ± 2s(prop	Age[2] of youngest coherant group of concordant grains (peakfit, Vermeesch, 2018) [Ma] ± 2s(prop)	Maximum Likelihood Age[2] (Vermeesch, 2021) [Ma] ± 2σ(prop)	Assigned map unit	Number of grains
15NP217	Gez valley	38.8143	75.4439	211.4 ± 2.2	242.8 ± 1.0	211.3 ± 2.4	T_{2-3}	140
15NP207	Gez valley	38.928	75.4983	217.8 ± 2.4	246.3 ± 1.0	217.8 ± 2.4	T_{2-3}	151
17NP447	Bieertuokouyi valley	39.4064	74.4488	238.4 ± 2.0	252.0 ± 1.1	238.4 ± 2.5	T_{1-2}	80
17NP441	Qimgan valley	39.31	74.866	252.2 ± 3.7	271.9 ± 1.1	252.4 ± 4.0	P_{2-3}	102
99WT44	Bostan Teleke	39.24222	75.055278	261.6 ± 3.4	304.4 ± 1.3	262.9 ± 3.7	P_{2-3}	88
15NP237	Kawuke valley	39.20403	75.0696	232.1 ± 2.2*	275.8 ± 1.2	271.4 ± 4.6	Sh_1	182
17NP478	Bostan Teleke	39.22397	75.025066	277.7 ± 2.5	307.7 ± 1.3	277.6 ± 2.7	Sh_1	131
17NP454	Kawuke valley	39.18473	75.069937	283.3 ± 2.5	296.7 ± 1.2	285.6 ± 2.3	Sh_1	103

*[1]Concordance is defined as $-1<d_c<5$, [2]Concordance is defined as $-1.67<d_c<6.54$, *single concordant grain, regarded as contamination and not considered for the calculation of age (2).*

The concordia distance is a modified version of the Aitchison distance discordance filter d_a and considers the correlated uncertainties of the U-Pb isotope pairs. Generally, peak fit ages (age (2)) may tend to overestimate the true depositional age, while single grain ages (age (1)) may give too young ages. This can be caused by geological issues, such as seemingly mathematically concordant grains due to their large age error (Spencer *et al.*, 2016) or due to the minimal distance between concordia and discordia line for young metamorphic events disturbing isotope ratios. Recently, the maximum likelihood age (Vermeesch, 2021) was presented to overcome statistical flaws of age (1) and age (2) and other methods frequently used to calculate MDA (Coutts *et al.*, 2019). All ages

are presented with propagated 2σ-error. We used the $^{206}Pb/^{238}U$ age for zircons younger than 1000 Ma, for older zircons the $^{206}Pb/^{207}Pb$ age was preferred. All LA-ICP-MS zircon U-Pb data can be found in Appendix D.8

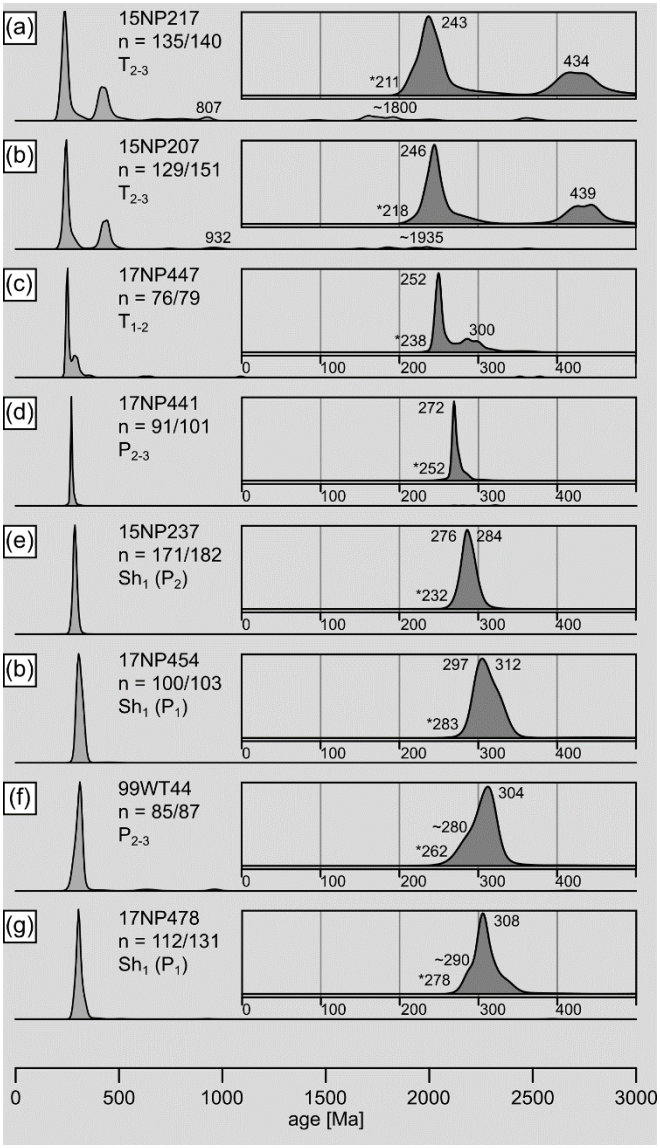

Figure 43: Detrital zircon U-Pb age spectra presented as kernel density esimates (KDE). The small inlets show age spectra in the interval from 0 to 500 Ma with age peaks (peak fit, age 2) in Ma calculated by the finite mixture algorithm of Galbraith & Laslett (1993). Ages marked with asterisk are the youngest concordant single grain ages (age 1). For sample location see Figure 37. Samples are sorted according to their major age-peak age.

Maximum depositional ages (MDA)

Deriving the MDA from a detrital age distribution is not a trivial task (Coutts *et al.*, 2019; Vermeesch, 2021). We presume that an adjacent volcanic arc has a strong influence on the age distributions. All Permian samples show unimodal distributions, supporting this hypothesis (Cawood *et al.*, 2012). Moreover, frequent arc-volcanic rocks are intercalated with the investigated sediments. The presence of a near-depositional age zircon population in the sedimentary record is

likely. Therefore, the maximum likelihood age approach (age (2)) was used to define the MDA of the investigated rock units and assign a map unit (Table 6).

Detrital age distribution data

The 8 detrital zircon samples show age peaks between 243 Ma and 1.8 Ga. Kernel density estimates (KDE, e.g., Sircombe & Hazelton, 2004; Vermeesch, 2012) are used to visualize age population distributions in Figure 43. KDE were calculated using IsoplotR (Vermeesch, 2018) with an adaptive kernel, as implemented in the "*kde"* function. Age peaks were determined using the *"radialplot"* function with k set to "auto" for the finite mixture modelling algorithm of Galbraith & Laslett (1993). Based on the Bayes Information Criterion, an optimal number of age peaks is selected, presented along with their proportion. In the following, the youngest concordant single zircon crystal ages are marked with an asterisk and given in brackets.

Permo-Carboniferous age peaks between 272 Ma and 308 Ma are reported from five samples (17NP441 in Qimgan, 99WT44 and 17NP478 in Bostan Tielieke, and 15NP237 and 17NP454 in Kawuke). All five samples are assigned to the Permian, based on their MDA. Samples 17NP454, 99WT44 and 17NP478 gave age peaks around the Carboniferous-Permian boundary, between 297 and 308 Ma. Samples 99WT44 and 17NP478 gave left skewed KDEs, with a shoulder at around 280–290 Ma. Samples 15NP237 and 17NP441 yielded lower Permian (late Cisuralian) age peaks of 275.8 ± 1.2 (*232.1 ± 2.2 Ma) and 271.9 ± 1.1 (*252.2 ± 3.7 Ma), respectively. The youngest concordant grain of sample 15NP237 is identified as an outlier and potentially results from contamination during processing.

The youngest age peaks, of Middle to Late Triassic age, were found in samples 15NP207 with 246.3 ± 1.0 Ma (*217.8 ± 2.4 Ma) and 15NP217 with 242.8 ± 1.0 Ma (*211.4 ± 2.2 Ma), both from the Gez valley section. A slightly older, Lopingian, age peak of 252.0 ± 1.1 Ma (*238.4 ± 2.0 Ma) was found for sample 17NP447 from the upper Bieertuokuoyi valley. All three samples 15NP207, 15NP217 and 17NP447 are assigned to the Triassic based on their MDA. They yield a second prominent age peak: Middle Triassic sample 17NP447 provided a Permo-Carboniferous age peak of 299.9 ± 1.3 Ma, which was not identified by the peak fit algorithm for sample 15NP207 and 15NP217 but is visible as a shoulder of their KDEs. A broad, lower Silurian age peak was found for samples 17NP207 and 17NP217, that seems to be unique to the Upper Triassic samples. Similarly, a Neoproterozoic and a Paleoproterozoic age peak with low proportion values, seem to be restricted to those samples.

5.3.3 K-Ar dating

We sampled 5 deformed, fine-grained sedimentary rocks at an outcrop along a tributary of the Bostantielieke valley (Table 5). The outcrop exposes greywacke, slate and phyllitic shale as well as dark, fossiliferous marl of the lower Shala Tala nappe unit (Sh_1) and greenschist of the upper

Shala Tala nappe (Sh_2) at the top of the section. We interpret the unit as allochthonous. The fossil content of crinoids, brachiopods and goniatids indicate open marine depositional conditions. The units underly higher-grade metamorphic rocks of the upper Shala Tala nappe, consisting of greenschist, banded marble, and amphibolite.

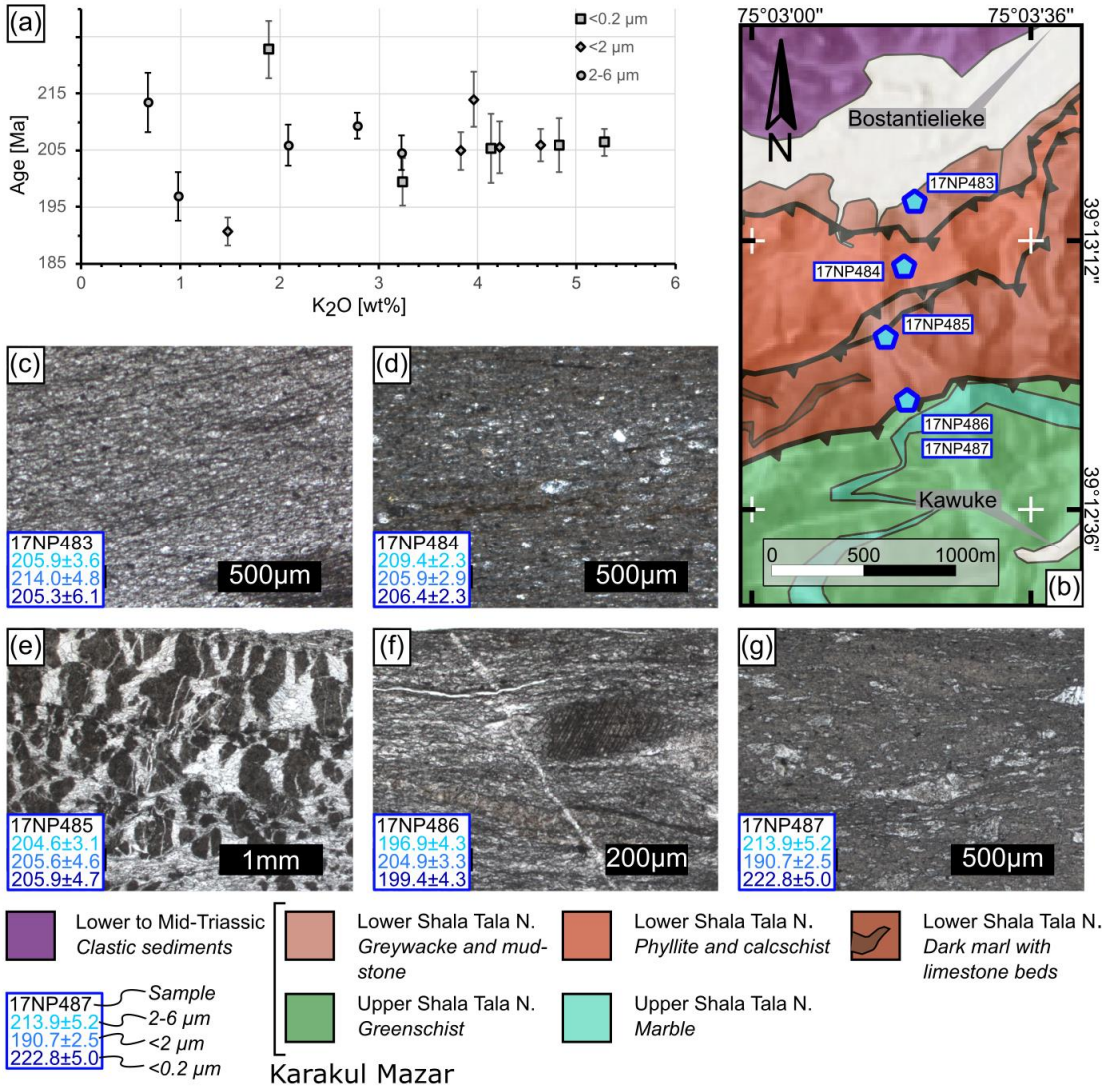

Figure 44: Results of K-Ar dating and sample microphotographs. Potassium-Argon age data scatters around ~205 Ma. Scatter increases with decreasing K content of the samples (a). Datapoints are shown with 2σ-age-error bars. The map inset in b shows the sample location along the Shala Tala thrust zone in the Bostantielieke valley. Microphotographs c–g show exemplary thin sections of the investigated samples with obtained ages given as [Ma] ± 2σ.

Both units overthrust parts of the Permo-Triassic Qimgan basin. Coarse conglomeratic sandstones, resembling those found in the Qimgan valley, crop out in tectonic windows in the Kawuke valley (Figure 37b, field and thin section photographs in Figure 42e, f). The nappe is interpreted as part of the Shala Tala Nappe system described in Robinson *et al.* (2004) and Robinson (2015). The fine fraction K-Ar dating revealed ages between 190 Ma and 222 Ma with weighted mean ages of 206.6 ± 1.4 Ma (2σ, 2-6 µm fraction), 201.2 ± 1.4 Ma (2σ, <2 µm fraction), and 205.0 ± 1.8 Ma (2σ, <0.2

µm fraction). Scatter of the measurements is larger for samples with lower K_2O values. The Kübler Index for all samples is smaller than 0.250°2Θ, indicating epizonal, greenschist facies conditions of deformation around 300 °C along the fault zone. The weighted mean age of all analysis is 204.8 ± 3.7 Ma (2σ). Since all measurements overlap within 2σ, the weighted mean age can be interpreted as age of last deformation along the thrust zone.

5.4 Discussion

5.4.1 Depositional environment

Kawuke/ Bostantielieke section (P_{2-3}, Sh_1, Sh_2)

The northern side of the Bostantielieke valley is composed of volcanimictic sandstones and mafic to intermediate volcanic rocks of upper Guadalupian age (MDA of 99WT44 is 262.9 ± 3.7 Ma, P_{2-3}). They are regarded as the footwall of the Shala Tala thrust. They were deposited in a tectonically active environment, potentially during an early phase of the Qimgan basin. On the southern side of the Bostantielieke valley, along the ridge towards the Kawuke valley, epizonal, marine sediments of the allochthonous Sh_1 unit are exposed. Greywackes, slates and dark, fossil-rich marls were deposited in an open marine environment in the late Cisuralian (MDA of greywacke sample 17NP478 is 277.6 ± 2.7 Ma). Alternations of dark slates and massive greywacke beds are interpreted as turbidity current deposits. The overlying dark marls show an open marine fauna (disarticulated Crinoids, Brachiopods, Goniatids) that was deposited in a lower shelf position by turbiditic mass transport. The entire Sh_1 succession shows ductile deformation and is faulted. Patches of Sh_1 strata occur as windows in the lower parts of the Kawuke valley. The Cisuralian to early Guadalupian red sandstones and conglomeratic sandstones preserve few sedimentary features. Their immature nature and poor to moderate sorting argue for sedimentation by mass flow and minor alluvial transport.

The greenschist to amphibolite facies meta-sedimentary and meta-igneous rocks of the Sh_2 unit consist of greenschist, amphibolite and banded marble. They might have been deposited in a marine environment and were eventually incorporated into the Karakul Mazar accretionary wedge, where they experienced regional metamorphism.

Qimgan section (P_{2-3}, T_{1-2}, ρT_2, T_{2-3})

Investigations of the well exposed, coherent Qimgan section (Figure 37b) reveals a change from Upper Permian greenish-grey fine clastic sediments with intercalated mafic to intermediate lava flows, volcaniclastic rocks and lacustrine carbonates to lower–middle (?) Triassic coarser clastic, red sandstones and conglomerates with rare volcanic rocks and no carbonates. The Permian strata was dated to the Guadalupian to Lopingian Epoch (P_{2-3}) by U-Pb data from a lacustrine carbonate (261 ± 2 Ma, Chapter 2) and the zircon U-Pb MDA of a nearby sampled sandstone (252.4 ± 4.0

Ma, see Table 6 and details in Appendix D.9). This is roughly coeval with the zircon U-Pb age of the Kayizi granodiorite (250.7 ± 4.7Ma, Liu *et al.*, 2010), the oldest documented pluton of the Permo-Triassic suite in the West Kunlun. The sediments were deposited in a tectonically active environment, which caused relative baselevel changes and rapidly shifting facies belts. Matrix supported, coarse conglomeratic mass flow layers at the base of the succession, close to the sedimentary contact with the Carboniferous volcanic deposits, are interpreted as a basal conglomerate marking the onset of Middle-Late Permian extension in the back-arc of the Paleo-Tethys subduction zone. Rapid facies shifts occured during the deposition of P_{2-3} strata, varying between alluvial-fluvial facies (cross-bedded strata with erosive base, e.g., Figure 40a), and shallow to deep lacustrine facies (Figure 39). Deposition of a monotonous fauna in the shallow to deep lacustrine strata and common ash-fall laminae, together with turbiditic flow deposits in the latter, demonstrate a tectonically and volcanically active, hence ecologically stressed environment. The section continues upward into Lower to Middle Triassic sandstone and conglomerate dominated red-beds, which are interpreted as alluvial plain deposits, dominated by braided rivers with sheet-like channel bodies and intercalated clay- and siltstone deposits forming overbank fines on a flood plain, associated with soil formation (root marks). The relative scarcity of volcanic deposits in these red-bed deposits suggests a period of relative volcanic quiescence. However, the presence of synsedimentary, normal faults demonstrates that extensional or transtensional tectonism was still active. Tilting and erosion of the P_{2-3} and T_{1-2} units was followed by the deposition of the thick ρT_2 ignimbritic crystal tuff. It marks the onset of intensified volcanic activity during the Anisian–Norian Epoch, which was likely continued until the Rhaetian. Sedimentary beds comprised a minor proportion of the sequence until the deposition of the fluvial-alluvial Jurassic sandstones and conglomerates. The amagmatic, Jurassic deposits conformably overly the T_{2-3} calc-alkaline volcanic and volcaniclastic rocks and postdate the Central Pamir–North Pamir collision, hence the end of the Cimmerian orogeny in the North Pamir.

5.4.2 Potential Source regions

We compared the Permian unimodal detrital zircon samples with volcanic rocks of the Tarim LIP, the Tien Shan and the Qimgan basin. The multimodal Triassic detrital zircon samples were compared with a compilation of detrital zircon U-Pb ages from Triassic strata found in the Central Pamir (He *et al.*, 2019), representing Karakul-Mazar derived detritus, and with detrital zircon data from Triassic strata of the West Songpan-Ganzi Hoh-Xil complex (Ding *et al.*, 2013), which is a lateral equivalent of the Karakul Mazar arc-accretionary complex. We also examined detrital zircon U-Pb data obtained from Triassic strata of the Kuche depression (Liu *et al.*, 2013) and the Turpan-Hami basin (Zhang *et al.*, 2019), which were sourced from the Tien Shan. If possible, literature ages were carefully re-evaluated according to the discordance criterion discussed above, to ensure comparability. Our own and literature data were plotted on adaptive kernel density

estimation diagrams (KDE) and non-metric multidimensional scaling (MDS), as implemented in the *"kde"* and *"mds"* function in IsoplotR (Vermeesch, 2013).

Permian strata

The detrital data from the Permo-Triassic samples document long-lasting magmatic activity in the North Pamir and adjacent regions. Mostly unimodal distributions of the Permian samples suggest a strong influence of an active magmatic source, e.g., a volcanic arc (Cawood *et al.*, 2012), without a significant contribution from pre-Hercynian basement rocks.

The oldest age-peaks are of late Pennsylvanian age and are accompanied by Cisuralian shoulders (17NP478, 99WT44) or show a Cisuralian peak and a Pennsylvanian shoulder (17NP454) (Figure 43). All three samples have comparable age distributions implying a common source. However, there is little evidence for Permian magmatic activity in the North Pamir prior to ~260 Ma (see Chapter 4). Magmatic activity in the Carboniferous North Pamir volcanic arc ceased in the late Serpukhovian to early Bashkirian (Chapter 2 and Ji *et al.*, 2018). The arc was accreted to the southern margin of Asia in the Pennsylvanian to Cisuralian period, interpreted from frequent sedimentary hiati in the Permo–Carboniferous record and the deposition of Permian carbonate platform successions on top of deeply eroded arc-volcanic sequences exposing Mississippian plutonic rocks (Burmakin *et al.*, 1961; Lyoskind *et al.*, 1963; Kafarsky & Pyjanov, 1970; Leven *et al.*, 1992; Leven, 2012; Leonov *et al.*, 2018). A pebble of sparitic marine limestone in the mid-late Permian debris flow deposits at the base of the Qimgan profile (Chapter 2, Appendix D.3) gave a Lower Mississippian age of 347 ± 8 Ma, supporting the hypothesis of uplift and erosion of early Carboniferous units possibly connected with the North Pamir arc (see discussion in section 2.6). Accretion of the North Pamir volcanic arc was roughly coeval with the closure of the Turkestan ocean in the Kyrgyz Tien Shan, which resulted in the collision of the Kazakh microcontinent and the Tarim craton (e.g., de Grave *et al.*, 2012). The oldest documented granite from Karakul-Mazar related arc-accretionary units is the ~250 Ma Kayizi pluton (Liu *et al.*, 2010; Liu & Wang, 2014) and the oldest documented volcanic rock of the Qimgan basin is of late Guadalupian age (261.1 ± 1.3 Ma, Chapter 4), postdating the Cisuralian age peaks by at least 20 Myrs.

Another prominent early Permian igneous source is the Tarim LIP, which was active between 300 and 280 Ma (Xu *et al.*, 2014). We compared our detrital data set with data from igneous zircon analyses from the Tarim LIP and with igneous zircon data from the Qimgan basin (see Chapter 4) itself. Data from the Tarim LIP is compiled from Liu et al. (2019) (CA-ID-TIMS and LA-ICP-MS data), Shangguan et al. (2016) (SIMS data), Yu et al. (2011) (SHRIMP data), and Zhang et al. (2010) (SHRIMP data). Neither nearby volcanic sources alone can explain the detrital age distributions. However, we argue that the voluminous early Permian LIP and the coeval post-collisional magmatism of the Tien Shan between 295 Ma and ~275 Ma (Konopelko *et al.*, 2007; Seltmann *et al.*, 2011; Biske *et al.*, 2013; Rolland *et al.*, 2013) and Permian volcanism in the Qimgan basin are likely to have contributed large volumes of detrital input into the sedimentary

basin. This might be reflected by age peaks of samples 15NP237 (276 Ma, MDA: 271.4 ± 4.6 Ma) and 17NP441 (272 Ma, MDA: 252.4 ± 4.0 Ma). Samples 17NP478, 17NP454 and 15NP237 from the allochthonous lower Shala Tala nappe unit (Sh1) have MDA at least 10 Ma older than the oldest autochthonous sample 99WT44 (MDA: 262.9 ± 3.7). Overlapping age distributions with the P_{2-3} samples and common sedimentology (17NP454 and 15NP237 red clastics), however, may indicate a connected sedimentary system, routing sediments from proximal facies belts to distal, marine (greywacke sample 17NP478) facies belts.

Triassic strata

The Triassic samples 17NP447, 15NP207 and 15NP217 show multimodal age distributions. Lower Triassic sample 17NP447 exhibits a major age peak at ~252 Ma and a minor age peak at ~300 Ma. The latter likely reflects uplift and erosion of Permian strata along the rift shoulders. Norian samples 17NP207 and 17NP217 overly the remarkable Anisian and Ladinian crystal tuffs exposed in the Qimgan and Gez valleys. To test a genetic linkage to the adjacent Karakul Mazar arc-accretionary complex, we compiled data from Triassic strata in the Central Pamir and the western Songpan-Ganzi Hoh-Xil complex of Tibet, which is regarded as a lateral equivalent of the Karakul Mazar unit (Figure 46) (Schwab *et al.*, 2004; Amidon & Hynek, 2010; Ding *et al.*, 2013; He *et al.*, 2019; Imrecke *et al.*, 2019). He et al. (2019) described Triassic clastic units from the Karakul-Mazar accretionary complex and the Central Pamir.

Samples from a Triassic marine synorogenic unit (named "flysch" unit by He *et al.* (2019)), deposited in a fore-arc position of the Central Pamir, show some remarkable similarities to the Norian samples. To further test their relationship to Triassic sedimentary strata sourced by the Tien Shan, we compiled detrital datasets from the Kuche depression (Liu *et al.*, 2013) and the nearby Turpan basin (Zhang *et al.*, 2019). We use a multi-dimensional scaling (MDS) diagram to visualize dissimilarities amongst the samples. The diagram (Figure 45a) presents the data in a 2-dimensional space, that can be read as a map, where similar samples are grouped together. The nearest neighbors are connected by solid lines. The Kuskal stress value (Figure 45b) is used to evaluate the quality of the modelled MDS (Vermeesch, 2013, and references therein). We note three major result: (1) Triassic samples from the Qimgan basin are nearest neighbors (T_{QB} cluster in Figure 45a), (2) Samples of the Triassic "flysch" unit (He *et al.*, 2019) form a cluster different from T_{QB}. (3) Samples from the Kuche and Turpan-Hami basins (Liu *et al.*, 2013; Zhang *et al.*, 2019) and samples from the Karakul-Mazar Songpan-Ganzi Hoh-Xil complex (Ding *et al.*, 2013; He *et al.*, 2019) share large similarities. The low Stress-value of 7.3% indicates a good to fair fit of the model (Figure 45b). In the cumulative probability plot (Figure 45c), the unimodal samples cluster tightly together.

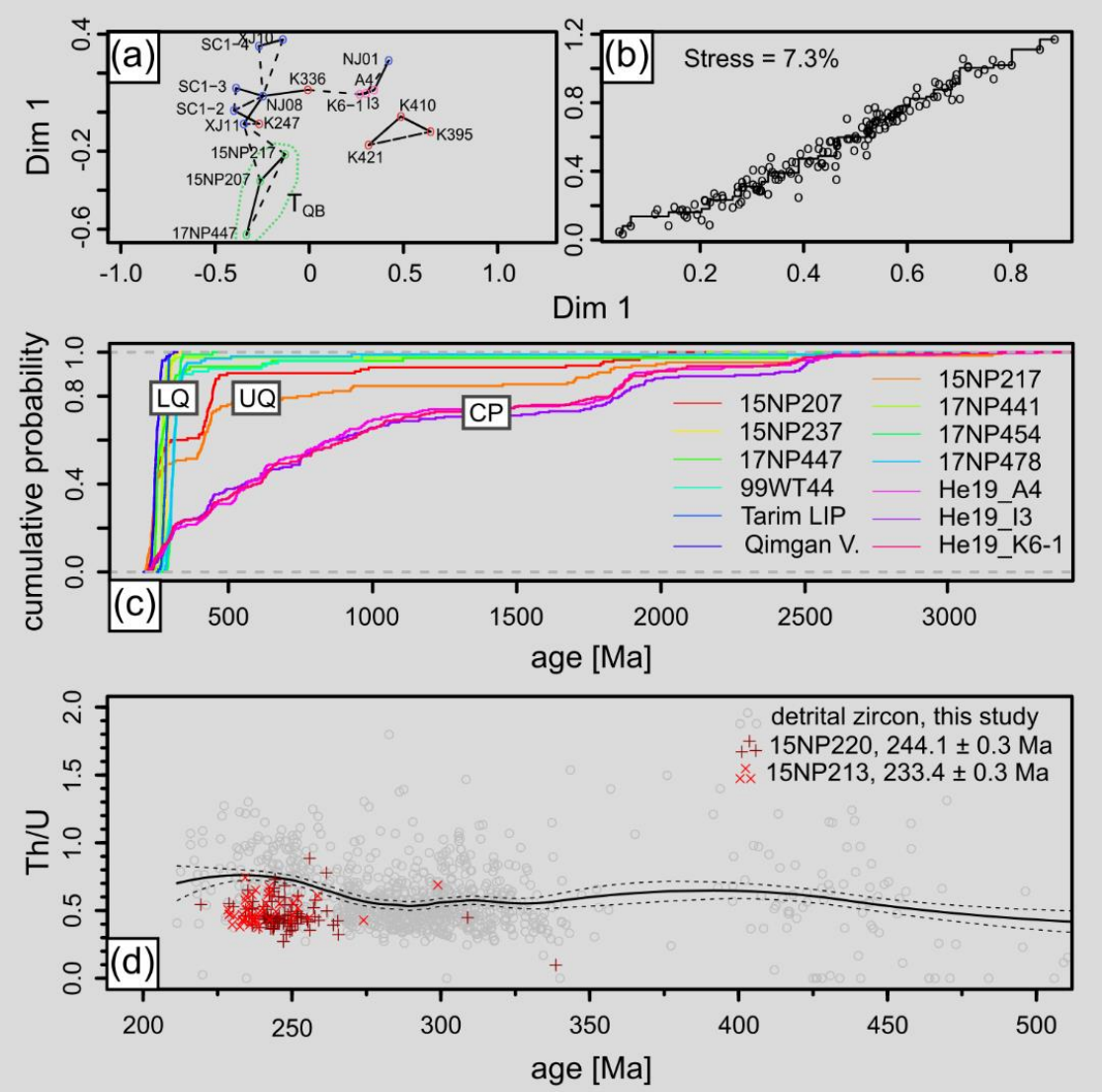

Figure 45: Analysis of detrital zircon U-Pb age data. (a) Multi-dimensional scaling, visualizes the relative similarity between samples from the Triassic Qimgan basin (green, marked T_{QB}), the Central Pamir (pink) (He et al., 2019), the Triassic Kuche and Turpan-Hami basins (blue) (Liu et al., 2013; Zhang et al., 2019) and the Songpan-Ganzi Hoh-Xil (red) (Ding et al., 2013). (b) Kuskal's Stress-1 value, with ~20% being poor, ~10% being fair, ~5% being good, ~2.5% being excellent and 0 being perfect, indicates a fair to good fit of the model in (a) (Vermeesch, 2013). (c) Cumulative probability plot, with samples from the lower Qimgan valley succession (LQ, mainly P_{2-3}) showing congruent, unimodal distributions. Samples 15NP207 and 15NP2017, representing the upper Qimgan valley succession (UQ, T_{2-3}) have a common bimodal distribution. All samples diverge from the detrital samples from the Central Pamir (CP, He et al., 2019). (d) The zircon Th/U diagram, plotted along with the rolling average of the detrital zircon Th/U values (black line). It demonstrates significantly higher mean Th/U values for Mid-Permian to Triassic detrital zircon grains compared to the Carboniferous to Early Permian record. However, igneous zircons from rhyolithic tuff samples (15NP220, 15NP213) presented in Chapter 5 plot below the rolling average line, suggesting a different source rock for the high Th/U zircons.

Dissimilarities among the Permian to Triassic samples are well resolved. We can distinguish clearly between two groups in the Qimgan basin: A unimodal group from the "lower Qimgan basin" (LQ) with peak fit ages of uppermost Carboniferous to uppermost Permian, and a bimodal group with a Triassic peak fit age and Norian MDA (upper Qimgan basin, UQ, namely 15NP207 and 15NP217). Samples from the Central Pamir (He *et al.*, 2019) show a much wider range of age peaks and can be classified as derived from a collisional source after Cawood *et al.* (2012).

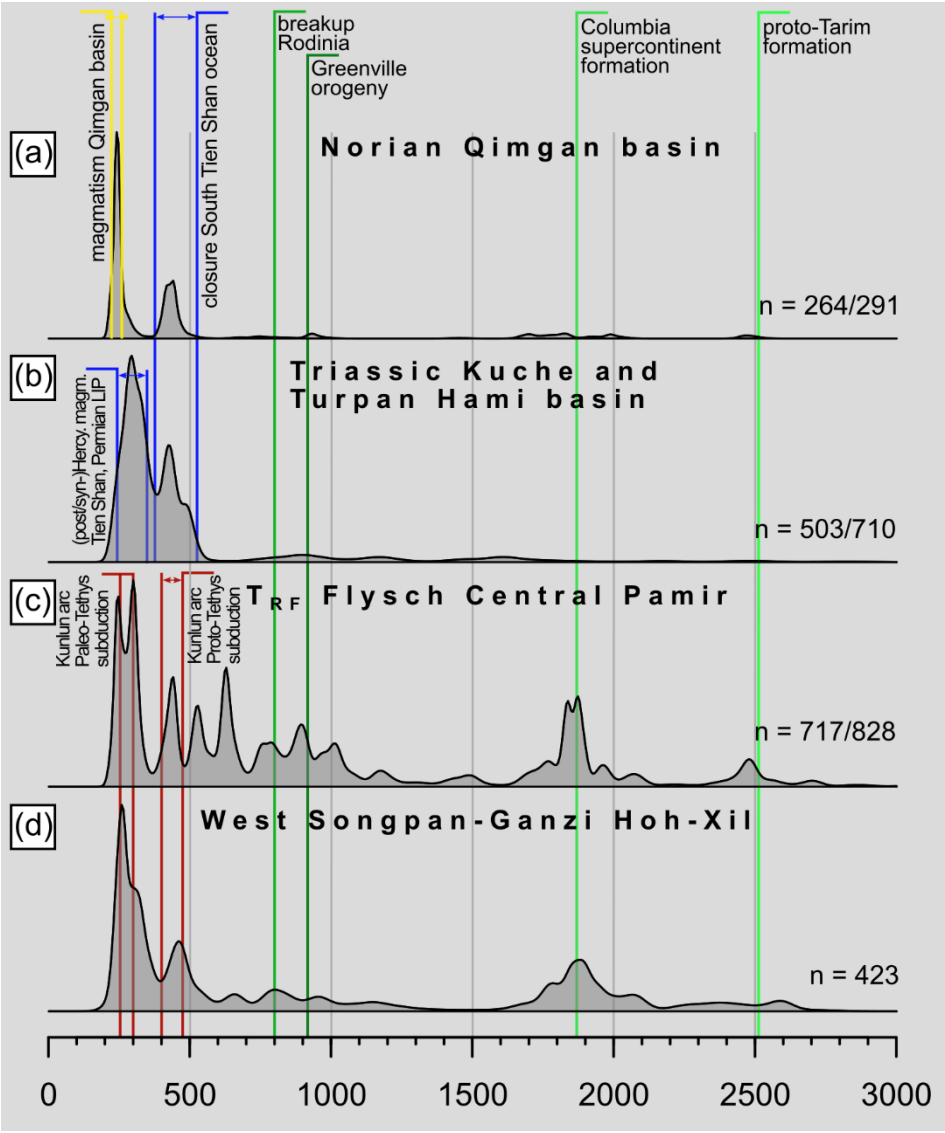

Figure 46: Kernel density estimation plots of detrital zircon samples. Diagrams (a) from the Norian sandstone samples 17NP407 and 17NP417, (b) from Triassic sandstones of the Kuche basin (NJ11-008, NJ11-001, XJ12-11, XJ12-10 (Liu et al., 2013)) and the Turpan Hami basin (SC1-2, SC1-3, SC1-4 (Zhang et al., 2019)), (c) from the Triassic "flysch" from the Central Pamir with Karakul-Mazar affinity (A4, K6-1, I3 (He et al., 2019)), and (d) from Triassic strata of the West Songpan-Ganzi Hoh-Xil complex (2007K421, 2007K420, 2007K410, 2007K395, 2007K336, 2007K247 (Ding et al., 2013)). Major geologic events of the region are marked with colored lines and labelled. Green lines mark events associated with the evolution of the Tarim cratonic crust, blue lines indicate events associated with the consolidation of the Tien Shan, red lines label events related to the evolution of the Kunlun arc during the subduction of the Proto- and Paleo-Tethys. The yellow lines mark the time interval of documented volcanic activity in the Qimgan basin (~260 – ~233Ma, cf. Chapter 4). n—number of ages used for KDE/total number of ages.

The comparison of the Norian Qimgan detrital zircon U-Pb age distribution with data from the Kuche and the Turpan-Hami basin, reveals remarkable similarities (Figure 46). Both show only minor contribution from Precambrian source rock. This distinguishes them from the Karakul-Mazar Songpan-Ganzi Hoh-Xil samples, which show a major peak at 1800–1900 Ma, correlative with the formation of the enigmatic Columbia supercontinent (Shu *et al.*, 2011; Ding *et al.*, 2013). The Triassic Karakul-Mazar Songpan-Ganzi Hoh-Xil units were predominantly sourced from rocks with Tarim (Tarim affinity: green marks in Figure 46) and Kunlun (red marks in Figure 46)

affinity. Triassic units deposited along the northern margin of Tarim and in the Qimgan basin, instead had their sources in the Tien Shan orogen. Why the Permo-Carboniferous age peak, dominant in the amagmatic Triassic strata from the Kuche and Turpan-Hami basin, is minor in the Norian Qimgan basin deposits, remains unclear.

5.4.3 Interpretation of the Th/U record

Th/U ratios may help to unravel provenance changes in the detrital zircon record, as it was demonstrated by e.g. Rubatto (2002) and Yakymchuk *et al.* (2018). The 974 detrital zircons show a mean and a median Th/U ratio of 0.6, a maximum at 3.6, and a minimum <<0.1. All detrital zircons in this study were examined with CL imaging and showed predominantly magmatic zoning. Most of the investigated zircons yield Th/U ratios above 0.1. The elevated median of 0.6 also speaks for zircon crystallization in magmatic systems with monazite absent. Hence, most of the detrital zircons from the Permo-Triassic Qimgan basin can be regarded as sourced from magmatic rocks. Th/U ratios may then be used as indicator of the geodynamic regime responsible for magmatism (McKay *et al.*, 2018). Based on the studies of e.g. Kirkland *et al.* (2015), McKay *et al.* (2018) empirically showed, that decreased Th/U ratios and low variability is connected to continental arc magmatism under long-term stable conditions. In contrast, increased Th/U ratios and high variability may be connected to relatively short-lived, continental rift processes. To examine the time dependent changes in Th/U ratios of the detrital zircon record in our data set, we used a local polynomial regression fitting (Cleveland *et al.*, 1992), implemented as the *"loess"* function in the stats package in R (Figure 45d). In the interval from 350 to 200 Ma, Th/U values increase significantly between 275 and 250 Ma. We plotted the Th/U values of Triassic rhyolitic crystal tuffs from Qimgan and Gez valley (15NP220, and -213, Chapter 4). Most of these datapoints plot below the regression, and hence, cannot explain higher Th/U values. However, all of the igneous rocks, analyzed for zircon U–Pb are acidic. Since Th/U values negatively correlate with silica content, coeval silica poor rocks, like the basalts and basaltic andesites from Qimgan, might be the source of zircons with elevated Th/U values at that time.

5.4.4 Formation of the Shala Tala back-thrust

The outcrops of Permo-Triassic strata are dispersed along the northern edge of the North Pamir, often in the vicinity of the Main Pamir Thrust, a major Cenozoic structure. However, in the Chinese Kawuke valley, we studied a section that exposes deformed Cisuralian marine sediments (Sh_1) which are overthrust by a greenschist to amphibolite facies nappe stack (Sh_2). The whole sequence is interpreted to belong to the Shala Tala thrust system. Five K-Ar ages from the Permian Sh_1 sediments reveal a uniform Rhaetian (~205 Ma, Figure 44) age and low KI values, indicating ductile deformation and illite crystallization under epizonal conditions. We argue that these ages reflect the last phase of activity of this strand of the Shala Tala nappe system, overthrusting Permo-

Triassic sediments of the Hindukush–North Pamir back-arc basin. Thrusting is interpreted as a far field effect of the closure of the Paleo-Tethys and marks a phase of back-arc compression due to the ongoing convergence of the Central and the North Pamir and the formation of the Shala Tala nappe as a back thrust sheet of the Karakul Mazar arc-accretionary complex. This is coeval with late Triassic–early Jurassic ages connected to the collisional phase of the Cimmerian orogeny in the Pamir (e.g., metamorphism in the Kurguvad block, monazite Th-Pb/U-Pb age of 195–210 Ma Schmidt *et al.*, 2011), and in the Tibetan Plateau (collision of the Gondwana derived Qiangtang block and Qaidam and South China block, Roger *et al.*, 2008). It is also the time of widespread sedimentary hiati and discordance in sediments of the Central and South Pamir, as result of collision/ deformation, uplift and erosion and the subsequent deposition of post-orogenic sediments (He *et al.*, 2019; Villarreal *et al.*, 2019).

5.5 Conclusion

The investigation of Permo-Triassic volcano-sedimentary successions in the NE Pamir reveals a close relationship to coeval units deposited on the northern margin of the Tarim craton. The Permo-Triassic suite in the NE Pamir belongs to the Qimgan basin, the far eastern end of the Hindukush-North Pamir back arc basin and was deposited starting from the latest Guadalupian on. We postulate a sedimentary system sourced in the Paleozoic Tien Shan draining southward into the Qimgan back arc basin. Sedimentary facies are similar to the continental deposits of the Permo-Triassic North Tarim basins. Correlative units further west, in Tajikistan and Afghanistan, show a turn-over from Permian open marine carbonate to marginal marine, clastic sedimentation, witnessing a westward sea regression that started in the late Carboniferous, when Tarim turned from marine to continental.

The detrital zircon U-Pb age distributions demonstrate a change of source lithologies from the Permian to the Triassic. Large portions of the Permian sediments were sourced from coeval volcanic activity. This is also true for the Triassic strata; however, a second age peak is interpreted as sourced from the Ordovician–Silurian Tien Shan pre-Hercynian basement rocks.

During the Rhaetian, the back-arc basin experienced shortening and was partly overthrust by the Shala Tala nappe. A K-Ar fine fraction mean age of 204.8 ± 3.7 Ma (2σ) from Permian Sh_1 strata pinpoints the time of Central Pamir-North Pamir collision by dating the propagation of shortening into a hinterland back-thrust that juxtaposes epizonal (Sh_1) and greenschist–amphibolite (Sh_2) facies units against anchizone units of the Qimgan basin (P_{2-3}).

Chapter 6. Synthesis, Conclusion and Scientific Perspectives

6.1 The Carboniferous

During the Palaeozoic, large parts of the Asian continent were amalgamated. Old cratonic basement blocks, the Siberian and Russian cratons, and magmatic arcs in between formed the Paleo-Asian continent. The two major cratons were amalgamated during the formation of the Central Asian Orogenic Belt (CAOB), also named the Altaids (e.g., Sengör & Natal'in, 1996; Sengör *et al.*, 2018). The role of Palaeozoic units in the North Pamir and the West Kunlun, farther to the (present) south, was long debated. For a long time, access for scientists was limited to a small number of mountain roads following major rivers, such as the Karakum Highway, following the Ghez valley in the Chinese Pamir, and the Kudi valley in the West Kunlun. This, and the limited amount of dated samples, lead to the assumption that the early Palaeozoic Kunlun belt, well known from the East Kunlun mountains and observed in the Kudi valley, continues into the North Pamir (Bazhenov & Burtman, 1982; Burtman & Molnar, 1993; Pan, 1994; Matte *et al.*, 1996; Mattern *et al.*, 1996; Mattern & Schneider, 2000; Xiao *et al.*, 2002). Our study and compiled literature show that plagiogranites related to the Carboniferous subduction of a portion of the Paleo-Tethys delineate a wide zone of volcanic arc formation, affecting units in the Afghan Hindukush and the North Pamir. Carboniferous magmatic activity, while well-known from the East Kunlun (e.g., Xiong *et al.*, 2012; Xu *et al.*, 2019; Jiao *et al.*, 2020), is absent in the West Kunlun. Granodioritic rocks located along major fault zones within isolated tectonic horses have to be seen independently from the early Paleozoic geology of the West Kunlun. They formed potentially in the Waqia (Tang *et al.*, 2020) and East Mazar (Li *et al.*, 2006) segments, of a subduction zone that closed a remnant of the Proto-Tethys during the Carboniferous, as suggested by Zhang *et al.* (2018). However, we suspect that the presence of large scale, orogen parallel strike-slip movement could as well be responsible for the shift of slivers from the North Pamir arc towards the west, given the overall transcurrent nature of Central Asian post-Hercynian tectonics, documented from the nearby Tien Shan (e.g., Buslov *et al.*, 2004; Konopelko *et al.*, 2007; Loury *et al.*, 2016; Jourdon *et al.*, 2017; Loury *et al.*, 2018).

Our newly provided data on the age and geochemistry of the mafic to intermediate arc-volcanic rocks and the intruded plagiogranites, complements previous studies (e.g., Schwab *et al.*, 2004; Jiang *et al.*, 2008; Kang *et al.*, 2015) and broadens the data-base for rocks of this hitherto understudied zone of the Pamir. The Carboniferous rocks of the North Pamir volcanic arc can be subdivided into an intraoceanic arc—the Oytag segment—present in the northeastern and central North Pamir, and the contemporaneous and most likely connected Andean style Darvaz segment in the northwestern North Pamir. The Darvaz segment contains the enigmatic Kurgovad-Vanch zone. Metasediments of the Faizabad-Kurgovad block (F-K block in Figure 47) were recently dated

to the early to mid-Paleozoic (see discussion in section 2.6.5 and Li *et al.*, 2022). Basement units of Neoproterozoic age, tie the Kurgovad unit to the Karakum continent (Li *et al.*, 2022). The Carboniferous volcanic arc units seem to relate directly to contemporaneous subduction zones, preserved in the present day Gissar and Garm segments of the South Tien Shan (Worthington *et al.*, 2017; Konopelko *et al.*, 2019). Explaining the absence of Hercynian metamorphic rocks in the North Pamir calls for an uplift process for the arc-volcanic rocks that does not require the arc to be subducted. Therefore, we propose a relatively complex zone of multiple north- and south dipping subduction zones resulting in a soft collision, uplift and partial erosion of the arc and the related arc granitoids in the Kurguvad-Faizabad basement block during the late Carboniferous to early Permian (Figure 47). The proposed south-dipping subduction zone, north of the Carboniferous arc, may have been blocked by the enigmatic Alai block and the Central Tianshan. Both units may have played an important role during the obduction of the Carboniferous North Pamir arc.

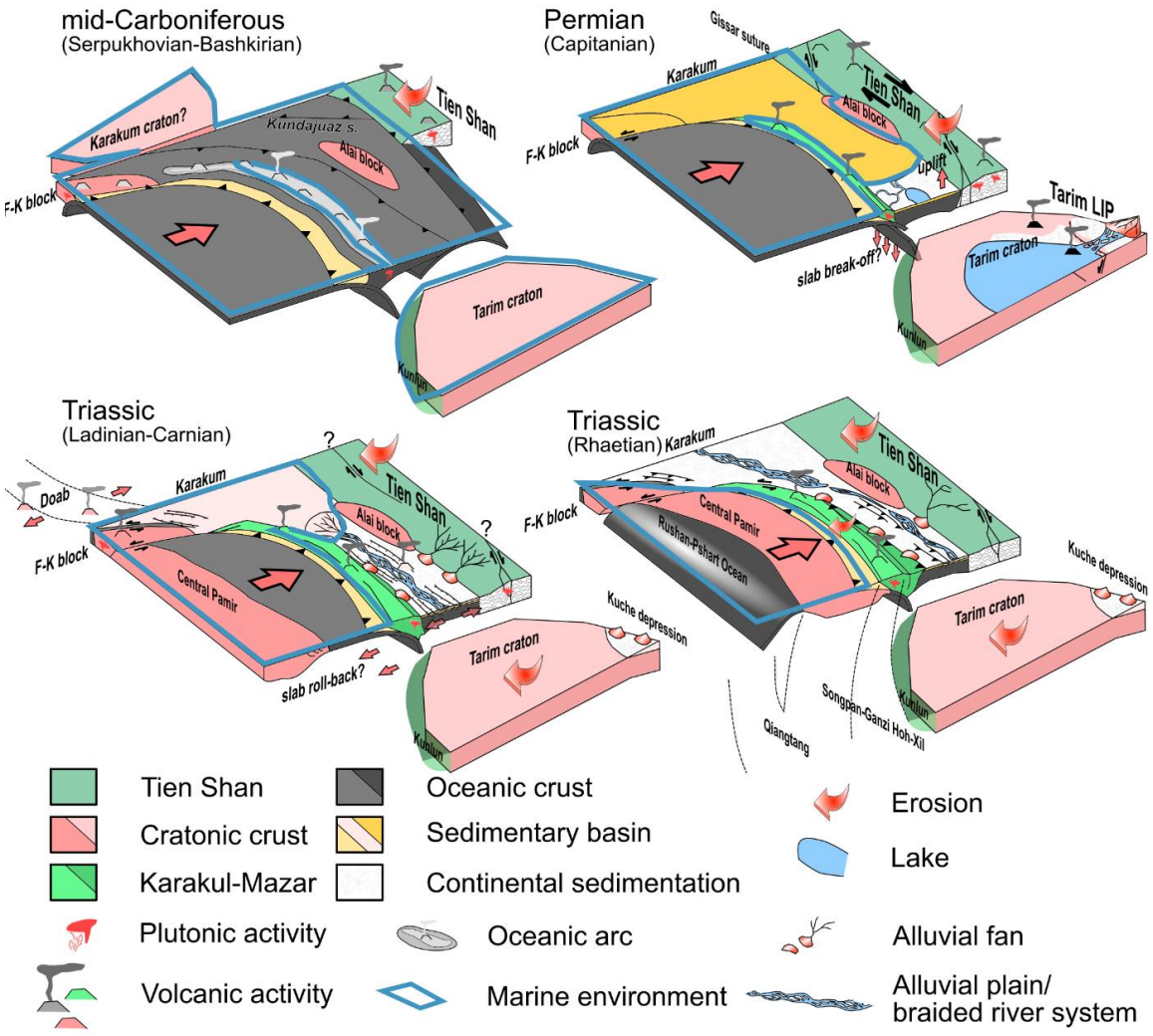

Figure 47: Conceptual sketches of the evolution of the North Pamir from the mid-Carboniferous to the late Triassic. Individual elements are not to scale. Interpretations are based on our own observations and literature data discussed in the previous chapters. F-K block—Fayzabad-Kurguvad block

6.2 The Permian

Large parts of the North Pamir and Hindukush expose diachronous hiati and the sedimentation of Permian marine rocks on top of deeply eroded Carboniferous crust (e.g., Kafarsky & Pyjanov, 1970; Wolfart & Wittekindt, 1980; Luchnikov, 2001). This suggests phases of uplift and erosion in the Carboniferous North Pamir. In the northeast, autochthonous early Permian strata is missing; in the Tajik Pamir, upper Carboniferous to Permian marine strata was deposited on top of metamorphic rocks of the Kurguvad-Faizabad block and the Carboniferous Kurguvad granodiorite (see Chapter 2 (Lyoskind *et al.*, 1963; Kafarsky & Pyjanov, 1970; Vlasov *et al.*, 1984; Li *et al.*, 2022)). A similar situation is described from the Afghan Hindukush (Weippert, 1964). Large parts of the region were under open marine conditions throughout the Permian, which is reflected by thick fusulinid-bearing limestones and fine-clastic sediments. Early Permian allochthonous marine-turbiditic siliciclastic and carbonaceous sediments found at the base of the Shala Tala nappe in the northeastern Pamir resemble that facies belt. However, the autochthonous mid-upper Permian units of the northeastern Pamir show sedimentary facies that can be related to similar continental facies realms deposited in the Tarim basin at that time. The Permian volcanic rocks remain enigmatic, since no clear relationship to a potentially active Karakul-Mazar arc-accretionary complex or the likewise magmatically active Tien Shan was found. We performed detrital U-Pb zircon analysis on 8 samples from the Permo-Triassic sedimentary record of the northeastern Pamir. In these analysis a high proportion of Permian zircons was found. They might be derived from the Tarim LIP, the Tien Shan or potentially from a not yet identified early phase of Karakul-Mazar arc-activity. To elucidate the relationship of Permian volcanism in the North Pamir with the surrounding magmatic centers, more systematic work on the Permian effusive and volcaniclastic rocks is needed. This could also shed light on the early evolutionary phases of the Triassic Hindukush-North Pamir rift system.

6.3 The early-mid Triassic (Induan to Carnian)

During the Triassic, graben formation in the back-arc of the Paleo-Tethys subduction zone created the Hindukush-North Pamir rift system (Figure 47). Lower to Middle Triassic basal conglomerates discordantly overly Permian carbonates in the Hindukush (Doab/ Surkhab) and the Paropamisus (Koh-e Dewandar) (e.g., Boulin, 1988; Luchnikov, 2001; Siehl, 2017). Whether normal faulting already commenced in the Permian is unclear. The deposition of a continuous sequence of continental sediments on top of Carboniferous arc-volcanic rocks in the northeastern Pamir, connected with erosion of rift shoulders (polymictic basal conglomerate in the Qimgan succession) from the upper Guadalupian on, suggests a phase of lower to mid-Permian erosion followed by upper Guadalupian basin formation in that part of the North Pamir. The early to mid-Triassic sediments in the northeastern Pamir reflect the development of an alluvial plain. Large parts of

Tarim, the North Pamir (e.g., present day Altyn Darya valley) and the Tien Shan were being actively eroded or had a hiatus from deposition at that time. Marine conditions prevailed to the west, as demonstrated by the clastic, marine lower and middle Doab formation in the Hindukush. A local angular unconformity is followed by the deposition of thick crystal tuffs in the northeastern Pamir. Two tuff layers are dated to the Anisian to Ladinian and precede a phase of intense mafic and intermediate volcanism in the Chinese North Pamir, resulting in a several hundred meter thick mafic to intermediate volcanic and volcaniclastic rock sequence of arc-magmatic affinity. This phase might have extended into the Rhaetian. The continental volcanic arc signature of the andesites demonstrates the close relation of those rocks to the nearby Karakul-Mazar arc-accretionary complex.

6.4 The late Triassic (Norian and Rhaetian)

Sedimentary conditions changed towards continental environments in the entire area (North Pamir, Hindukush), which can be interpreted as a slow-down of subsidence/ progressive basin filling (Figure 47). Detrital zircon distributions from Permo-Triassic sandstones show a shift of the principal age peak from ~300 Ma towards younger ages, and the first appearance of a secondary, Ordovician–Silurian age peak—interpreted as Tien Shan basement signal—in Norian samples. The volcano-sedimentary successions of the Norian–Rhaetian Myntekin and upper Doab formation and potentially the upper Qimgan basin, demonstrate ongoing volcanic activity and subduction. There is a wide consensus that the collision of the Central Pamir terrane with the North Pamir happened during the late Rhaetian to Hettangian (e.g., Angiolini *et al.*, 2013; He *et al.*, 2019; Kapp & DeCelles, 2019). Widespread hiati, both in the North Pamir/ Hindukush (Weippert, 1964; Wolfart & Wittekindt, 1980; Luchnikov, 2001; Montenat, 2009) and the Central Pamir sedimentary successions (He *et al.*, 2019), suggest a phase of uplift and erosion on both blocks, associated with their collision.

By dating the prominent Shala Tala thrust fault, which juxtaposes Paleozoic epizonal to amphibolite facies rocks on top of the Permo-Triassic Qimgan succession to the mid-Rhaetian, we provide a temporal constrain for a major back-thrusting event, partially closing the back-arc realm of the Hindukush-North Pamir back-arc basin. Detrital zircon U-Pb distributions of the mid-Permian rocks of the undeformed Qimgan succession in the foodwall, resemble those of the overthrusting, epizonal units of similar lithology, which show pervasive straining of quartz pebbles; this suggests uplift from below temperatures hotter than the 300°C isotherm. K-Ar data constrains this thrusting event along the Shala Tala fault to ~205 Ma (cf. Chapter 5). The Rhaetian continental sediments are succeeded by Jurassic post-orogenic sediments that show abundand coal-seams and are free of volcanic rocks.

6.5 Geodynamic Implications and Outlook

6.5.1 The Cimmerian Orogeny

There is widespread evidence for back-arc basin development along the Paleo-Tethyan subduction zone in Eurasia during the Permo-Triassic period. This zone of extensional back-arc formation, sedimentation and back-arc magmatism can be traced from the units of the Meliata-Maliac and Pindos ocean basins exposed in the European Alps, Carpathians, and Balkans (Stampfli & Kozur, 2006; Froitzheim *et al.*, 2008; Stampfli & Hochard, 2009; Putis *et al.*, 2019; Yuan *et al.*, 2020; Pál-Molnár *et al.*, 2021; Villaseñor *et al.*, 2021; Huang *et al.*, 2022; Villasenor *et al.*, 2022), into the Black-and Caspian sea area (Zonenshain & Pichon, 1986), the Caucasus (Kazmin & Tikhonova, 2006; Adamia *et al.*, 2011) and further into the Aghdarband basin of northern Iran (Baud & Stämpfli, 1989; Zanchi *et al.*, 2016; Balini *et al.*, 2019), the Paropamisus and Hindukush area of Afghanistan (Boulin, 1988; Boulin, 1990; Montenat, 2009; Siehl, 2017), through the North Pamir, the East Kunlun (Zhao *et al.*, 2019) and the Qinling (Li *et al.*, 2014). East of that, the Paleo-Tethyan ocean branches into multiple subbasins, which closed diachronously, starting with the middle Triassic collision of the South China and North China block, which formed the Mianlue suture. The Indo-China block further to the south exposes Permo-Triassic back-arc successions in Laos (Shi *et al.*, 2021) and Thailand (Phajuy & Singtuen, 2019; Hara *et al.*, 2021), that, however, are complicated to link to the West Qingling, as discussed elsewhere (Richards & Şengör, 2017; Wang *et al.*, 2020). This pulse of back-arc opening along the southern Eurasian continental margin between the early Permian and the late Triassic is known as the Eocimmerian phase (Stampfli & Kozur, 2006). The back-arc basins opened diachronously and were either closed by the Cimmerian orogeny in the late Triassic to early Jurassic (e.g., Küre basin, Hindukush rift) or remained open until the end of the Jurassic (Meliata-Maliac basin, Pindos basins)(e.g., Bonev & Stampfli, 2003). Remnants of the well-studied Meliata ocean, exposed in the European Eastern Alps and the Carpathians suggest a Guadalupian (~264 Ma) opening (Putis *et al.*, 2019; Villaseñor *et al.*, 2021). Further east, the Crimea-Küre (Tauric)-Svanetia basin opened in a similar back arc position of the Paleo-Tethys subduction zone in the late Permian to early Triassic (Scythian stage) (Tüysüz & Yiğitbaş, 1994; Kozur *et al.*, 2000; Kazmin & Tikhonova, 2006; Nikishin *et al.*, 2012). The Crimea-Küre-Svanetia basin of the Caucasus is kinematically linked to the Aghdarband basin of the Iranian Kopet Dag (Baud & Stämpfli, 1989). The latter opened during the early-middle Triassic (Baud & Stämpfli, 1989) parallel to the early to mid-Permian Fariman back-arc basin (Zanchetta *et al.*, 2013). The timing of initiation of back-arc basin extension in the Hindukush-North Pamir rift system remains uncertain. Deposition of ~260 Ma volcanic rocks on top of Carboniferous arc-volcanic rocks gives an approximate pinpoint for the change from erosion/ non-deposition to basin formation/ deposition in the northeastern Pamir (Chapter 4), associated with extensional tectonics.

To the east of the North Pamir, there seems to be a gap in the West Kunlun, south of the Tarim craton, where no Triassic basin successions are known. Further east, in the East Kunlun, back arc extension started in the mid- to late Permian between 266 and 255 Ma (Zhao *et al.*, 2019). The related back-arc basin in the West Qinling opened coevally in the late Permian (Li *et al.*, 2014). Stampfli & Kozur (2006) present an overview of paleogeographic domains, linking the Hercynian to Alpine tectonic events along the southern rim of the Paleo Eurasian continent in the western Paleo-Tethyan realm. The linkage of the comparatively well studied European and west Asian units seems straight forward. However, the linkage of this zone to Permo-Triassic extensional basins further east, in the East Kunlun, West Qinling and Laos/ Thailand, remains vague, as demonstrated by conflicting reconstructions for the eastern Paleo-Tethys (e.g., Richards & Şengör, 2017; Wang *et al.*, 2020; Wu *et al.*, 2020). The Permo-Triassic Hindukush-North Pamir back-arc basin represents an important link between the eastern and western Tethyan realms.

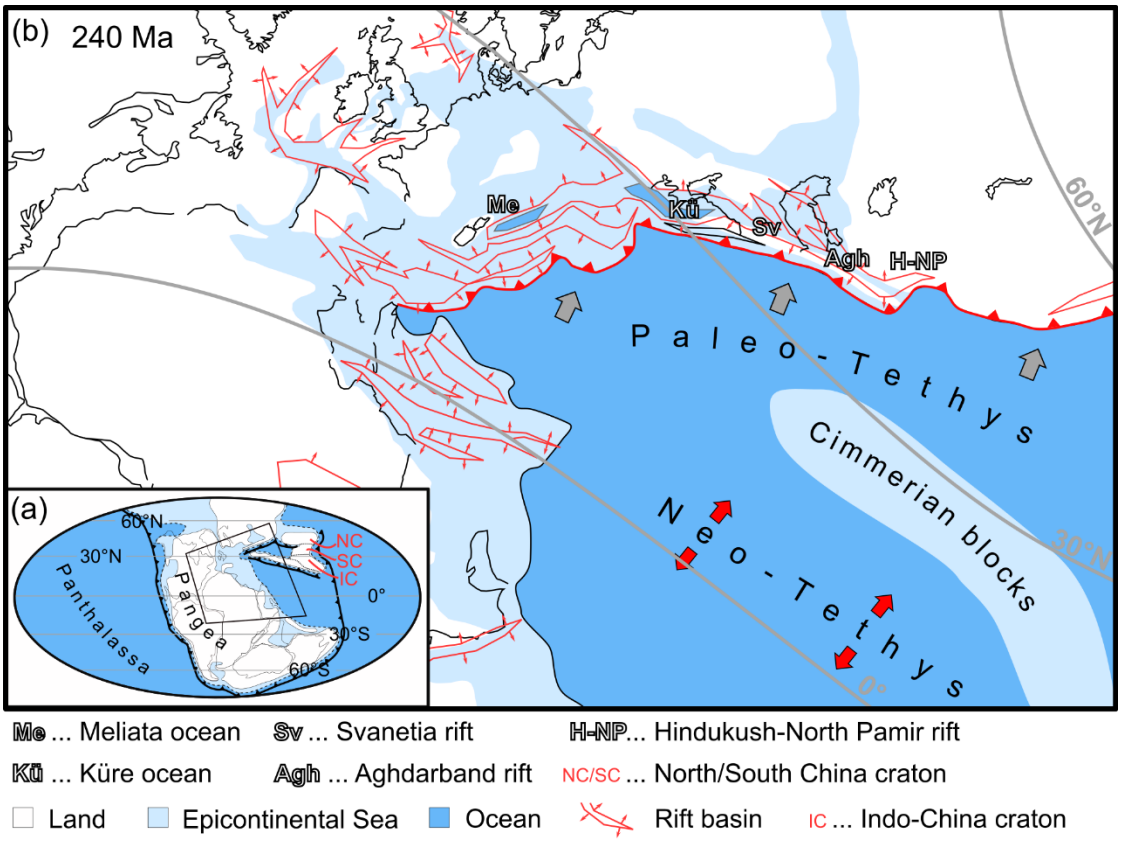

Figure 48: Paleogeography at the Anisian-Ladianian boundary. (a) Inlet map, showing the location of map (b) and the position of the North and South China craton, and the Indo-China craton in the eastern Tethyan realm. Map modified after Metcalfe (2011). (b) Map of the western Tethyan realm, depicting the position of back-arc rift basins to the north of the Paleo-Tethys subduction zone. Location of the riftbasins after Stampfli & Kozur (2006) and Barrier et al. (2018). Position of modern coastlines is shown for orientation.

The presence of a several thousand kilometers long belt of extensional basins along the southern Asian margin calls for a relative persistent mechanism affecting the Paleo-Tethyan subduction zone. However, the varying size of the basins and the presence of zones seemingly unaffected by

Permo-Triassic extension (e.g., East Kunlun), highlight regional inhomogeneities. A comprehensive explanation for the mechanisms of back-arc evolution in the Eocimmerian is still pending. Further work should be focused on an interregional spatio-temporal correlation of basin formation. This might shed light on the question whether a uniform mechanism, for instance slab roll-back along the entire Paleo-Tethys subduction zone caused by a uniform mantle convection system (e.g., Coltice *et al.*, 2017), is responsible for the formation of the extensional south Eurasian belt.

6.5.2 Cenozoic Deformation

This work provides a comprehensive overview of the pre-Cenozoic history of the North Pamir, which is crucial to understand the Cenozoic evolution. The significant influence of pre-existing crustal inhomogeneities on the geometry and timing of subsequent orogenic events is well known (Vauchez *et al.*, 1998; Robert *et al.*, 2014; Balázs *et al.*, 2017; Schliffke *et al.*, 2021). Reactivation of pre-Cenozoic, large scale fault zones during the India-Asia collision is documented in the Tien Shan (e.g., Jolivet *et al.*, 2010; Jourdon *et al.*, 2018; Nachtergaele *et al.*, 2018; Rolland *et al.*, 2020). In the Pamir, the Tanymas suture zone, separating the Central Pamir from the North Pamir, was reactivated during the Cenozoic, forming the Paleogene Central Pamir antiformal thrust-sheet stack (Rutte *et al.*, 2017). Cenozoic deformation is largely concentrated along the Main Pamir Thrust (MPT) and the Pamir Frontal Thrust (PFT). The MPT juxtaposed units of the North Pamir against Meso-Cenozoic sedimentary units of the External Pamir and was active from early-mid Miocene to Pliocene times (Sobel & Dumitru, 1997; Sobel *et al.*, 2013). The PFT became active in the mid-Miocene to Pliocene and remains active until today (Coutand *et al.*, 2002; Thompson *et al.*, 2015; Li *et al.*, 2019). We have shown that post-Variscan to Eocimmerian extensional or transtensional tectonics affected the present-day North Pamir. Outcrops of Permo-Triassic volcano-sedimentary rocks of the Hindukush-North Pamir rift are well aligned along the Main Pamir Thrust and can be found in both the hanging wall and the foot wall position. Further investigations are needed to test the hypothesis that the MPT originated along a reactivated, primarily Permo-Triassic extensional or transtensional structure. The presence of Cimmerian (see Chapter 4) and Eoalpine, mid-Cretaceous (Robinson *et al.*, 2004) thrust systems in the North Pamir document the longevity of compressional tectonics in the region. Cenozoic shortening estimates for the MPT are rather vague (Kley *et al.*, 2021). Recent shortening estimates for the Cenozoic suggest much less “indentation” of the Pamir with respect to the Tibetan Plateau (e.g., Coutand *et al.*, 2002; Li *et al.*, 2019). To explain the Cenozoic tectonic evolution of the Pamir, models are needed that reconcile upper crustal constraints and bring them together with geophysical findings. We suggest a model that considers an arcuate post-Cimmerian/ pre-Cenozoic geometry, weakened North Pamir crust, and low Cenozoic shortening amounts in the northern and northeastern Pamir.

6.6 Future Research

Our work has enhanced the understanding of the North Pamir. It has shown the temporal and geodynamic relationship of Carboniferous units, found in the North Pamir, with coeval units described from the Tien Shan. Likewise, Permo-Triassic units can be linked to the Eocimmerian evolution of the southern Eurasian margin. A better understanding of the pre-Cenozoic structure of the southern Paleo-Asian margin finally enables us to identify and investigate Cenozoic, tectonically active structures in a greater detail. From this work three major scientific questions arise. (1) How does the North Pamir Carboniferous arc fit into the mosaic of the Central Asian Orogenic Belt and how is it related to the closure of the Turkestan ocean? (2) Do Eocimmerian volcano-sedimentary back-arc basin successions of the southern Eurasian extensional zone provide an answer to the underlaying geodynamic processes along the Paleo-Tethys subduction zone, and do these geodynamic processes relate to the largest known mass-extinction at the Permo-Triassic boundary? (3) Can we test, to which extend pre-existing structures determined the behaviour of the North Pamir crust during the India-Asia collision?

A special aspect of this research should be the inclusion of archived material from previous expeditions to the Afghan part of the Pamir. Advanced techniques, requiring minor sample size, help a great deal to fill gaps in the scientific record.

References

Adamia, S., Alania, V., Chabukiani, A., Kutelia, Z., and Sadraze, N., 2011, Great Caucasus (Cavcasioni): A Long-lived North-Tethyan Back-Arc Basin: Turkish Journal of Earth Sciences, v. 20, no. 5, p. 611–628, doi: 10.3906/yer-1005-12.

Alexeiev, D.V., Biske, Y.S., Djenchuraeva, A.V., Kröner, A., and Getman, O.F., 2019, Late Carboniferous (Kasimovian) closure of the South Tianshan Ocean: No Triassic subduction: Journal of Asian Earth Sciences, v. 173, p. 54–60, doi: 10.1016/j.jseaes.2019.01.021.

Alexeiev, D.V., Biske, Y.S., Wang, B., Djenchuraeva, A.V., Getman, O.F., Aristov, V.A., Kröner, A., Liu, H., and Zhong, L., 2015, Tectono-Stratigraphic framework and Palaeozoic evolution of the Chinese South Tianshan: Geotectonics, v. 49, no. 2, p. 93–122, doi: 10.1134/S0016852115020028.

Alibo, D.S., and Nozaki, Y., 1999, Rare earth elements in seawater: particle association, shale-normalization, and Ce oxidation: Geochimica et Cosmochimica Acta, v. 63, 3-4, p. 363–372.

Aliev, S.A., Beliaevsky, N.A., Butovskaya, E.M., Volvovsky, B.S., Volvovsky, I.S., Krasnopevtseva, G.V., Pak, V.A., Polshkov, M.K., Rubailo, V.I., and Sollogub, V.B., 1976, The seismic experiment in the northern Pamirs, *in* Charles L. Drake, ed., Geodynamics: Progress and Prospects, Wiley Online Library, p. 128–136.

Amidon, W.H., and Hynek, S.A., 2010, Exhumational history of the north central Pamir: Tectonics, v. 29, no. 5, doi: 10.1029/2009TC002589.

Anders, E., and Grevesse, N., 1989, Abundances of the elements: Meteoritic and solar: Geochimica et Cosmochimica Acta, v. 53, no. 1, p. 197–214.

Angiolini, L., Zanchi, A., Zanchetta, S., Nicora, A., and Vezzoli, G., 2013, The Cimmerian geopuzzle: new data from South Pamir: Terra Nova, v. 25, no. 5, p. 352–360, doi: 10.1111/ter.12042.

Arnaud, N., Tapponnier, P., Roger, F., Brunel, M., Scharer, U., Wen, C., and Zhiqin, X., 2003, Evidence for Mesozoic shear along the western Kunlun and Altyn-Tagh fault, northern Tibet (China): Journal of Geophysical Research, v. 108, B1, doi: 10.1029/2001JB000904.

Baar, H.J. de, Brewer, P.G., and Bacon, M.P., 1985, Anomalies in rare earth distributions in seawater: Gd and Tb: Geochimica et Cosmochimica Acta, v. 49, no. 9, p. 1961–1969, doi: 10.1016/0016-7037(85)90090-0.

Bailey, J.C., 1981, Geochemical criteria for a refined tectonic discrimination of orogenic andesites: Chemical Geology, v. 32, 1-4, p. 139–154.

Balázs, A., Burov, E., Matenco, L., Vogt, K., Francois, T., and Cloetingh, S., 2017, Symmetry during the syn- and post-rift evolution of extensional back-arc basins: The role of inherited orogenic structures: Earth and Planetary Science Letters, v. 462, p. 86–98, doi: 10.1016/j.epsl.2017.01.015.

Balini, M., Nicora, A., Zanchetta, S., Zanchi, A., Marchesi, R., Vuolo, I., Hosseiniyoon, M., Norouzi, M., and Soleimani, S., 2019, Olenekian to Early Ladinian stratigraphy of the western part of the Aghdarband window (Kopeh-Dag, NE Iran): Riv. Ital. Paleontol. Stratigr, v. 125, no. 1, p. 283–315, doi: 10.13130/2039-4942/11446.

Bande, A., Sobel, E.R., Mikolaichuk, A., Schmidt, A., and Stockli, D.F., 2017, Exhumation history of the western Kyrgyz Tien Shan: Implications for intramontane basin formation: Tectonics, v. 36, no. 1, p. 163–180, doi: 10.1002/2016TC004284.

Barrier, E., Vrielynck, B., Brouillet, J.-F., and Brunet, M.-F., 2018, Paleotectonic Reconstruction of the Central Tethyan Realm. Tectonono-Sedimentary-Palinspastic Maps from Late Permian to Pliocene: Paris, Commission for the Geological Map of the World (CGMW/ CCGM).

Baud, A., and Stämpfli, G.M., 1989, Tectonogenesis & Evolution of a Segment of the Cimmerides: The Volcano-Sedimentary Triassic of Aghdarband (Kopet-Dagh, North-East Iran), *in* Tectonic Evolution of the Tethyan Region, Springer, Dordrecht, p. 265–275.

Bazhenov, M.L., and Burtman, V.S., 1982, The kinematics of the Pamir arc: Geotectonics, v. 16.

Bazhenov, M.L., and Burtman, V.S., 1986, Tectonics and paleomagnetism of structural arcs of the Pamir-Punjab syntaxis: Journal of geodynamics, v. 5, 3-4, p. 383–396.

Beloussov, V.V., Belyaevsky, N.A., Borisov, A.A., Volvovsky, B.S., Volkovsky, I.S., Resvoy, D.P., Tal-Virsky, B.B., Khamrabaev, I., Kaila, K.L., Narain, H., Marussi, A., and Finetti, J., 1980, Structure of the lithosphere along the deep seismic sounding profile: Tien Shan—Pamirs—Karakorum—Himalayas: Tectonophysics, v. 70, 3-4, p. 193–221, doi: 10.1016/0040-1951(80)90279-6.

Bershaw, J., Garzione, C.N., Schoenbohm, L., Gehrels, G., and Tao, L., 2012, Cenozoic evolution of the Pamir plateau based on stratigraphy, zircon provenance, and stable isotopes of foreland basin sediments at Oytag (Wuyitake) in the Tarim Basin (west China): Journal of Asian Earth Sciences, v. 44, p. 136–148, doi: 10.1016/j.jseaes.2011.04.020.

Bézos, A., Escrig, S., Langmuir, C.H., Michael, P.J., and Asimow, P.D., 2009, Origins of chemical diversity of back-arc basin basalts: A segment-scale study of the Eastern Lau Spreading Center: Journal of Geophysical Research, v. 114, B6, doi: 10.1029/2008JB005924,

Biske, Y., Alexeiev, D.V., Ershova, V.B., Priyatkina, N.S., DuFrane, S.A., and Khudoley, A.K., 2019, Detrital zircon U Pb geochronology of middle Paleozoic sandstones from the South Tianshan (Kyrgyzstan): Implications for provenance and tectonic evolution of the Turkestan Ocean: Gondwana Research, v. 75, p. 97–117, doi: 10.1016/j.gr.2019.04.010.

Biske, Y.S., Konopelko, D.L., and Seltmann, R., 2013, Geodynamics of late Paleozoic magmatism in the Tien Shan and its framework: Geotectonics, v. 47, no. 4, p. 291–309, doi: 10.1134/S001685211304002X.

Biske, Y.S., and Seltmann, R., 2010, Paleozoic Tian-Shan as a transitional region between the Rheic and Urals-Turkestan oceans: Gondwana Research, v. 17, 2-3, p. 602–613, doi:

10.1016/j.gr.2009.11.014.

Black, L.P., Kamo, S.L., Allen, C.M., Davis, D.W., Aleinikoff, J.N., Valley, J.W., Mundil, R., Campbell, I.H., Korsch, R.J., Williams, I.S., and Foudoulis, C., 2004, Improved 206Pb/238U microprobe geochronology by the monitoring of a trace-element-related matrix effect; SHRIMP, ID–TIMS, ELA–ICP–MS and oxygen isotope documentation for a series of zircon standards: Chemical Geology, v. 205, no. 1, p. 115–140, doi: 10.1016/j.chemgeo.2004.01.003.

Blaise, J., Bordet, P., Lang, J., af DeLapparent, Leutwein, F., and Sonet, J., 1970, Mesures géochronologiques de quelques roches cristallines d'Afghanistan central: CR Acad. Sci. Paris, v. 270, p. 2772–2775.

Bonev, N.G., and Stampfli, G.M., 2003, New structural and petrologic data on Mesozoic schists in the Rhodope (Bulgaria): geodynamic implications: Comptes Rendus Geoscience, v. 335, no. 8, p. 691–699, doi: 10.1016/S1631-0713(03)00122-6.

Bonvalot, S., Balmino, G., Briais, A., Kuhn, M., Peyrefitte, A., Vales, N., Biancale, R., Gabalda, G., Moreaux, G., and Reinquin, F., 2012, World Gravity Map: Paris, Bureau Gravimetrique International.

Boulin, J., 1988, Hercynian and Eocimmerian events in Afghanistan and adjoining regions: Tectonophysics, v. 148, no. 3, p. 253–278, doi: 10.1016/0040-1951(88)90134-5.

Boulin, J., 1990, Neocimmerian events in Central and Western Afghanistan: Tectonophysics, v. 175, no. 4, p. 285–315, doi: 10.1016/0040-1951(90)90177-A.

Boynton, W.V., 1984, Cosmochemistry of the rare earth elements: meteorite studies, *in* Developments in geochemistry, Elsevier, p. 63–114.

Budanov, V.I., 1993, Endogenous formations of the Pamirs: Dushanbe, Donish, 300 p.

Burmakin, A.V., Starshinin, D.A., and Likhachev, V.I., 1961, Geological map of the USSR of 1:200000 scales: Sheet J-42-XI: Nedra, Moscow, Russian Geological Research Institute.

Burtman, V.S., 2000, Cenozoic crustal shortening between the Pamir and Tien Shan and a reconstruction of the Pamir–Tien Shan transition zone for the Cretaceous and Palaeogene: Tectonophysics, v. 319, no. 2, p. 69–92, doi: 10.1016/S0040-1951(00)00022-6.

Burtman, V.S., 2010, Tien Shan, Pamir, and Tibet: History and geodynamics of Phanerozoic oceanic basins: Geotectonics, v. 44, no. 5, p. 388–404, doi: 10.1134/S001685211005002X.

Burtman, V.S., and Molnar, P.H., 1993, Geological and geophysical evidence for deep subduction of continental crust beneath the Pamir, Geological Society of America.

Burtman, V.S., Peive, A.V., and Ruzhentsev, S.V., 1963, The main lateral faults of the Tien Shan and Pamir: Faults and Horizontal Movements of the Earth's Crust, p. 152–172.

Burtman, V.S., and Samygin, S.G., 2001, Tectonic evolution of High Asia in the Paleozoic and Mesozoic: Geotektonika, v. 35, no. 4, 34-54.

Buslov, M.M., Fujiwara, Y., Iwata, K., and Semakov, N.N., 2004, Late paleozoic-early Mesozoic geodynamics of Central Asia: Gondwana Research, v. 7, no. 3, p. 791–808.

Cawood, P.A., Hawkesworth, C.J., and Dhuime, B., 2012, Detrital zircon record and tectonic setting: Geology, v. 40, no. 10, p. 875–878, doi: 10.1130/G32945.1.

Cerling, T.E., Brown, F.H., and Bowman, J.R., 1985, Low-temperature alteration of volcanic glass: Hydration, Na, K, 18O and Ar mobility: Chemical Geology: Isotope Geoscience section, v. 52, no. 3, p. 281–293, doi: 10.1016/0168-9622(85)90040-5.

Charvet, J., Shu, L., Laurent-Charvet, S., Wang, B., Faure, M., Cluzel, D., Chen, Y., and Jong, K. de, 2011, Palaeozoic tectonic evolution of the Tianshan belt, NW China: Science China Earth Sciences, v. 54, no. 2, p. 166–184, doi: 10.1007/s11430-010-4138-1.

Chen, S., Chen, H., Zhu, K., and Tao, Y., 2021, Petrogenesis of the Middle–Late Triassic S- and I-type granitoids in the eastern Pamir and implications for the Tanymas–Jinshajiang Paleo-Tethys Ocean: International Journal of Earth Sciences, v. 110, p. 1213–1232, doi: 10.1007/s00531-021-02013-z.

Chen, X., Chen, H., Lin, X., Cheng, X., Yang, R., Ding, W., Gong, J., Wu, L., Zhang, F., and Chen, S., 2018, Arcuate Pamir in the Paleogene? Insights from a review of stratigraphy and sedimentology of the basin fills in the foreland of NE Chinese Pamir, western Tarim Basin: Earth-Science Reviews, v. 180, p. 1–16, doi: 10.1016/j.earscirev.2018.03.003.

Chen, X., Dong, Y., Chen, H., and WANG, J., 2011, Identification and Application of Sequence Boundaries and System Tract Boundaries for the Triassic of Tarim Basin: Acta Sedimentologica Sinica, v. 29, no. 5, p. 917–925.

Cleveland, W.S., Grosse, E., and Shyu, W.M., 1992, Local Regression Models, *in* Chambers, J.M., Hastie, T.J., eds., Statistical Models in S, Routledge.

Cohen, K., Harper, D.A., and Gibbard, P., 2020, International Chronostratigraphic Chart (v 2020/03): International Commission on Stratigraphy.

Coltice, N., Gérault, M., and Ulvrová, M., 2017, A mantle convection perspective on global tectonics: Earth-Science Reviews, v. 165, p. 120–150, doi: 10.1016/j.earscirev.2016.11.006.

Condie, K.C., Viljoen, M.J., and Kable, E.J.D., 1977, Effects of alteration on element distributions in archean tholeiites from the Barberton greenstone belt, South Africa: Contributions to Mineralogy and Petrology, v. 64, no. 1, p. 75–89, doi: 10.1007/BF00375286.

Coogan, L.A., and Gillis, K.M., 2018, Low-Temperature Alteration of the Seafloor: Impacts on Ocean Chemistry: Annual Review of Earth and Planetary Sciences, v. 46, no. 1, p. 21–45, doi: 10.1146/annurev-earth-082517-010027.

Coogan, L.A., Parrish, R.R., and Roberts, N.M.W., 2016, Early hydrothermal carbon uptake by the upper oceanic crust: Insight from in situ U-Pb dating: Geology, v. 44, no. 2, p. 147–150, doi: 10.1130/G37212.1.

Coutand, I., Strecker, M.R., Arrowsmith, J.R., Hilley, G., Thiede, R.C., Korjenkov, A., and Omuraliev, M., 2002, Late Cenozoic tectonic development of the intramontane Alai Valley, (Pamir-Tien Shan region, central Asia): An example of intracontinental deformation due to the

Indo-Eurasia collision: Tectonics, v. 21, no. 6, 3-1-3-19, doi: 10.1029/2002TC001358.

Coutts, D.S., Matthews, W.A., and Hubbard, S.M., 2019, Assessment of widely used methods to derive depositional ages from detrital zircon populations: Geoscience Frontiers, v. 10, no. 4, p. 1421–1435, doi: 10.1016/j.gsf.2018.11.002.

de Boorder, H., 2012, Spatial and temporal distribution of the orogenic gold deposits in the Late Palaeozoic Variscides and Southern Tianshan: How orogenic are they?: Ore Geology Reviews, v. 46, p. 1–31, doi: 10.1016/j.oregeorev.2012.01.002.

de Grave, J., Glorie, S., Ryabinin, A., Zhimulev, F., Buslov, M.M., Izmer, A., Elburg, M., and Vanhaecke, F., 2012, Late Palaeozoic and Meso-Cenozoic tectonic evolution of the southern Kyrgyz Tien Shan: Constraints from multi-method thermochronology in the Trans-Alai, Turkestan-Alai segment and the southeastern Ferghana Basin: Journal of Asian Earth Sciences, v. 44, p. 149–168, doi: 10.1016/j.jseaes.2011.04.019.

Debruyne, D., Hulsbosch, N., and Muchez, P., 2016, Unraveling rare earth element signatures in hydrothermal carbonate minerals using a source–sink system: Ore Geology Reviews, v. 72, p. 232–252, doi: 10.1016/j.oregeorev.2015.07.022.

Desio, S.A., and Poretti, G., 1991, Gravity anomalies in North-Eastern Afghanistan and on the Pamirs syntaxis: Rendiconti Lincei, v. 2, no. 2, p. 131–144, doi: 10.1007/BF03001417.

Dewey, J.F., Shackleton, R.M., Chengfa, C., and Yiyin, S., 1988, The tectonic evolution of the Tibetan Plateau: Philosophical Transactions of the Royal Society of London. Series A, Mathematical and Physical Sciences, v. 327, no. 1594, p. 379–413, doi: 10.1098/rsta.1988.0135.

Dickinson, W.R., and Gehrels, G.E., 2009, Use of U–Pb ages of detrital zircons to infer maximum depositional ages of strata: A test against a Colorado Plateau Mesozoic database: Earth and Planetary Science Letters, v. 288, 1-2, p. 115–125, doi: 10.1016/j.epsl.2009.09.013.

Ding, L., Yang, D., Cai, F.L., Pullen, A., Kapp, P., Gehrels, G.E., Zhang, L.Y., Zhang, Q.H., Lai, Q.Z., Yue, Y.H., and Shi, R.D., 2013, Provenance analysis of the Mesozoic Hoh-Xil-Songpan-Ganzi turbidites in northern Tibet: Implications for the tectonic evolution of the eastern Paleo-Tethys Ocean: Tectonics, v. 32, no. 1, p. 34–48, doi: 10.1002/tect.20013.

Doebrich, J.L., Wahl, R.R., Chirico, P.G., Wandrey, C.J., Bohannon, R.G., Orris, G.J., Bliss, J.D., Wasy, A., and Younusi, M.O., 2006, Geologic and mineral resource map of Afghanistan, Geological Survey (US), 2006-1038.

Dulski, P., 2001, Reference materials for geochemical studies: New analytical data by ICP-MS and critical discussion of reference values: Geostandards Newsletter, v. 25, no. 1, p. 87–125, doi: 10.1111/j.1751-908X.2001.tb00790.x.

Dunkl, I., Mikes, T., Frei, D., Gerdes, A., Tolosana-Delgado, R., and Eynatten, H. von, 2014, UranOS: data reduction program for time-resolved U/Pb analyses: http://www.sediment.uni-goettingen.de/staff/dunkl/software/uranos.html.

Elliott, A.J., Oskin, M.E., Liu-Zeng, J., and Shao, Y., 2015, Rupture termination at restraining bends: The last great earthquake on the Altyn Tagh Fault: Geophysical Research Letters, v. 42, no. 7, p. 2164–2170, doi: 10.1002/2015GL063107.

Feng, Y., Liu, D., Zhao, J., Pan, W., and Cheng, T., 2020, In-situ LA-MC-ICPMS U-Pb dating method for low-uranium carbonate minerals: Chinese Science Bulletin, v. 65, 2-3, p. 150–154, doi: 10.1360/TB-2019-0355.

Finsterwalder, R., Nöth, L., Reinig, W.F., Ficker, H., and Rickmers, W.R., 1932, Wissenschaftliche Ergebnisse der Alai-Pamir Expedition 1928: Geodätische, topographische, und glaziologische Ergebnisse: Berlin, D. Reimer/E. Vohsen, Volume 1.

Fisher, A.T., and Becker, K., 2000, Channelized fluid flow in oceanic crust reconciles heat-flow and permeability data: Nature, v. 403, no. 6765, p. 71–74.

Floyd, P.A., 1977, Rare earth element mobility and geochemical characterisation of spilitic rocks: Nature, v. 269, no. 5624, p. 134–137, doi: 10.1038/269134b0.

Froitzheim, N., Plasienka, D., and Schuster, R., 2008, Alpine tectonics of the Alps and Western Carpathians, *in* McCann, T., ed., The Geology of Central Europe, Mesozoic and Cenozoic: London, Geological Society of London, Volume 2, p. 1141–1232.

Frost, B.R., Barnes, C.G., Collins, W.J., Arculus, R.J., Ellis, D.J., and Frost, C.D., 2001, A geochemical classification for granitic rocks: Journal of Petrology, v. 42, no. 11, p. 2033–2048, doi: 10.1093/petrology/42.11.2033.

Fuhrmann, U., Lippolt, H.J., and Hess, J.C., 1987, Examination of some proposed K-Ar standards: 40Ar39Ar analyses and conventional K-Ar data: Chemical Geology: Isotope Geoscience section, v. 66, 1-2, p. 41–51.

Gaetani, M., Jadoul, F., Erba, E., and Garzanti, E., 1993, Jurassic and Cretaceous orogenic events in the North Karakoram: age constraints from sedimentary rocks: Geological Society, London, Special Publications, v. 74, no. 1, p. 39–52, doi: 10.1144/GSL.SP.1993.074.01.04.

Gągała, Ł., Ratschbacher, L., Ringenbach, J.-C., Kufner, S.-K., Schurr, B., Dedow, R., Abdulhameed, S., Le Garzic, E., Gadoev, M., and Oimahmadov, I., 2020, Tajik Basin and Southwestern Tian Shan, Northwestern India-Asia Collision Zone: 1. Structure, Kinematics, and Salt-tectonics in the Tajik Fold-and-thrust Belt of the Western Foreland of the Pamir: Tectonics, v. 39, e2019TC005871, doi: 10.1029/2019TC005871.

Galbraith, R.F., 1990, The radial plot: Graphical assessment of spread in ages: International Journal of Radiation Applications and Instrumentation. Part D. Nuclear Tracks and Radiation Measurements, v. 17, no. 3, p. 207–214, doi: 10.1016/1359-0189(90)90036-W.

Galbraith, R.F., and Laslett, G.M., 1993, Statistical models for mixed fission track ages: Nuclear tracks and radiation measurements, v. 21, no. 4, p. 459–470.

Godeau, N., Deschamps, P., Guihou, A., Leonide, P., Tendil, A., Gerdes, A., Hamelin, B., and Girard, J.-P., 2018, U-Pb dating of calcite cement and diagenetic history in microporous

carbonate reservoirs: Case of the Urgonian Limestone, France: Geology, v. 46, no. 3, p. 247–250, doi: 10.1130/G39905.1.

Gonzalez, L.A., and Carpente, S.J., 1992, Inorganic Calcite Morphology: Roles of Fluid Chemistry and Fluid Flow: SEPM Journal of Sedimentary Research, v. 62, no. 3, p. 382–399, doi: 10.1306/D426790B-2B26-11D7-8648000102C1865D.

Hall, G., 2007, Muruntau Uzbekistan: revisited: West Australian Geologist, v. 465, no. 3.

Han, Y., Zhao, G., Cawood, P.A., Sun, M., Liu, Q., and Yao, J., 2019, Plume-modified collision orogeny: The Tarim–western Tianshan example in Central Asia: Geology, v. 47, no. 10, p. 1001–1005, doi: 10.1130/G46855.1.

Hara, H., Tokiwa, T., Kurihara, T., Charoentitirat, T., and Sardsud, A., 2021, Revisiting the tectonic evolution of the Triassic Palaeo-Tethys convergence zone in northern Thailand inferred from detrital zircon U–Pb ages: Geological Magazine, v. 158, no. 5, p. 905–929, doi: 10.1017/S0016756820001028.

Harlov, D.E., and Austrheim, H., editors, 2013, Metasomatism and the chemical transformation of rock: The role of fluids in terrestrial and extraterrestrial processes: Heidelberg, London, Springer, Lecture notes in earth system sciences, 2193-8571.

He, J., Kapp, P., Chapman, J.B., DeCelles, P.G., and Carrapa, B., 2019, Structural setting and detrital zircon U–Pb geochronology of Triassic–Cenozoic strata in the eastern Central Pamir, Tajikistan: Geological Society, London, Special Publications, v. 483, no. 1, p. 605–630, doi: 10.1144/SP483.11.

Heath, M., Phillips, D., and Matchan, E.L., 2018, An evidence-based approach to accurate interpretation of 40Ar/39Ar ages from basaltic rocks: Earth and Planetary Science Letters, v. 498, p. 65–76, doi: 10.1016/j.epsl.2018.06.024.

Heinrichs, H., and Herrmann, A.G., 2013, Praktikum der analytischen Geochemie: Berlin, Heidelberg, Springer-Verlag.

Hellstrom, J., Paton, C., Woodhead, J., and Hergt, J., 2008, Iolite: Software for spatially resolved LA-(quad and MC) ICPMS analysis, *in* Sylvester, P., ed., Laser ablation ICP-MS in the earth sciences: Current practices and outstanding issues: Vancouver, Mineralogical Association of Canada. Short course series, Volume 40.

Henan Institute of Geological Survey (HIGS), 2014, The 1:250000 Geological Map of the Peoples Republic of China (J43C001002, Kuergan), China Coal Xi' and Map Printing Co., Ltd.

Henan Institute of Geological Survey (HIGS), 2014, The 1:250000 Geological Map of the Peoples Republic of China (J43C002003, Yingjisha), China Coal Xi' and Map Printing Co., Ltd.

Hinze, C., 1964, Die geologische Entwicklung der östlichen Hindukush-Nordflanke (Nordost-Afghanistan), *in* Wirtz, D., Hinze, C., et al., eds., Zur Geologie von Nordost-und Zentral-Afghanistan. Geologisches Jahrbuch, p. 19–75.

Hinze, C., 1964, Die geologische Entwicklung der östlichen Hindukush-Nordflanke (Nordost-

Afghanistan), *in* Wirtz, D., Hinze, C., et al., eds., Zur Geologie von Nordost- und Zentral-Afghanistan: Hannover, Bundesanstalt für Bodenforschung, p. 19–75.

Honnorez, J., 2003, Hydrothermal alteration vs. ocean-floor metamorphism. A comparison between two case histories: the TAG hydrothermal mound (Mid-Atlantic Ridge) vs. DSDP/ODP Hole 504B (Equatorial East Pacific): Comptes Rendus Geoscience, v. 335, 10-11, p. 781–824, doi: 10.1016/j.crte.2003.08.009.

Horstwood, M.S.A., Košler, J., Gehrels, G., Jackson, S.E., McLean, N.M., Paton, C., Pearson, N.J., Sircombe, K., Sylvester, P., and Vermeesch, P., 2016, Community-derived standards for LA-ICP-MS U-(Th-) Pb geochronology–Uncertainty propagation, age interpretation and data reporting: Geostandards and Geoanalytical Research, v. 40, no. 3, p. 311–332, doi: 10.1111/j.1751-908X.2016.00379.x.

Howard, D.L., Jonge, M.D. de, Afshar, N., Ryan, C.G., Kirkham, R., Reinhardt, J., Kewish, C.M., McKinlay, J., Walsh, A., and Divitcos, J., 2020, The XFM beamline at the Australian Synchrotron: Journal of Synchrotron Radiation, v. 27, no. 5, p. 1447–1458, doi: 10.1107/S1600577520010152.

Hu, X., Garzanti, E., Wang, J., Huang, W., An, W., and Webb, A., 2016, The timing of India-Asia collision onset – Facts, theories, controversies: Earth-Science Reviews, v. 160, p. 264–299, doi: 10.1016/j.earscirev.2016.07.014.

Huang, J., Yang, R., YANG, J., and Chunlong, C.U., 2013, Geochemical Characteristics and Tectonic Significance of Triassic Granite from Taer Region, the Northern Margin of West Kunlun: Acta Geologica Sinica - English Edition, v. 87, no. 2, p. 346–357.

Huang, Q., Neubauer, F., Liu, Y., Genser, J., Guan, Q., Chang, R., Yuan, S., and Yu, S., 2022, Permian-Triassic granites of the Schladming complex (Austroalpine basement): Implications for subduction of the Paleo-Tethys Ocean in the Eastern Alps: Gondwana Research, v. 109, p. 205–224, doi: 10.1016/j.gr.2022.05.006.

Humphris, S.E., and Thompson, G., 1978, Trace element mobility during hydrothermal alteration of oceanic basalts: Geochimica et Cosmochimica Acta, v. 42, no. 1, p. 127–136, doi: 10.1016/0016-7037(78)90222-3.

Imrecke, D.B., Robinson, A.C., Owen, L.A., Chen, J., Schoenbohm, L.M., Hedrick, K.A., Lapen, T.J., Li, W., and Yuan, Z., 2019, Mesozoic evolution of the eastern Pamir: Lithosphere, doi: 10.1130/L1017.1.

Jackson, S.E., Pearson, N.J., Griffin, W.L., and Belousova, E.A., 2004, The application of laser ablation-inductively coupled plasma-mass spectrometry to in situ U–Pb zircon geochronology: Chemical Geology, v. 211, 1-2, p. 47–69, doi: 10.1016/j.chemgeo.2004.06.017.

Janoušek, V., Farrow, C.M., and Erban, V., 2006, Interpretation of whole-rock geochemical data in igneous geochemistry: introducing Geochemical Data Toolkit (GCDkit): Journal of Petrology, v. 47, no. 6, p. 1255–1259, doi: 10.1093/petrology/egl013.

Ji, W.H., Chen, S.J., Li, R.S., He, S.P., Zhao, Z.M., and Pan, X.P., 2018, The origin of Carboniferous-Permian magmatic rocks in Oytag area, West Kunlun: Back-arc basin?: Acta Petrologica Sinica, v. 34, no. 8, p. 2393–2409.

Jia, R.-Y., Jiang, Y.-H., Liu, Z., Zhao, P., and Zhou, Q., 2013, Petrogenesis and tectonic implications of early Silurian high-K calc-alkaline granites and their potassic microgranular enclaves, western Kunlun orogen, NW Tibetan Plateau: International Geology Review, v. 55, no. 8, p. 958–975.

Jiang, C.F., 1992, Opening-closing tectonics of Kunlun Mountains: Geol. Memoirs. MGMR, v. 12, p. 1–224.

Jiang, Y.-H., Jia, R.-Y., Liu, Z., Liao, S.-Y., Zhao, P., and Zhou, Q., 2013, Origin of Middle Triassic high-K calc-alkaline granitoids and their potassic microgranular enclaves from the western Kunlun orogen, northwest China: A record of the closure of Paleo-Tethys: Lithos, 156-159, p. 13–30.

Jiang, Y.-H., Jiang, S.-Y., Ling, H.-F., Zhou, X.-R., Rui, X.-J., and Yang, W.-Z., 2002, Petrology and geochemistry of shoshonitic plutons from the western Kunlun orogenic belt, Xinjiang, northwestern China: implications for granitoid geneses: Lithos, v. 63, 3-4, p. 165–187.

Jiang, Y.-H., Liao, S.-Y., Yang, W.-Z., and Shen, W.-Z., 2008, An island arc origin of plagiogranites at Oytag, western Kunlun orogen, northwest China: SHRIMP zircon U–Pb chronology, elemental and Sr–Nd–Hf isotopic geochemistry and Paleozoic tectonic implications: Lithos, v. 106, 3-4, p. 323–335, doi: 10.1016/j.lithos.2008.08.004.

Jiao, D., Liu, C., Liu, W., Su, H., He, J., Zhao, Z., Ye, B., and Xu, X., 2020, Petrogenesis and tectonic significance of the late Devonian-early Carboniferous Jianxiashan pluton in the western domain of the eastern Kunlun Orogen, northern Tibetan Plateau: Geological Journal, v. 55, no. 9, p. 6198–6215.

Jixiang, Y., 1994, Carboniferous Sedimentary Environment and Tectonic Setting in the Western Kunlun and Adjacent Regions, *in* Du, Z., Qingsong, Z., et al., eds., Proceedings of International Symposium on the Karakorum and Kunlun Mountains, Kashgar, China Meteorological Press.

Jolivet, M., Dominguez, S., Charreau, J., Chen, Y., Li, Y., and Wang, Q., 2010, Mesozoic and Cenozoic tectonic history of the central Chinese Tian Shan: Reactivated tectonic structures and active deformation: Tectonics, v. 29, no. 6, p. 1–30, doi: 10.1029/2010TC002712.

Jong, K. de, Wang, B., Faure, M., Shu, L., Cluzel, D., Charvet, J., Ruffet, G., and Chen, Y., 2009, New 40Ar/39Ar age constraints on the Late Palaeozoic tectonic evolution of the western Tianshan (Xinjiang, northwestern China), with emphasis on Permian fluid ingress: International Journal of Earth Sciences, v. 98, no. 6, p. 1239–1258, doi: 10.1007/s00531-008-0338-8.

Jourdon, A., Le Pourhiet, L., Petit, C., and Rolland, Y., 2018, The deep structure and reactivation of the Kyrgyz Tien Shan: Modelling the past to better constrain the present: Tectonophysics,

v. 746, p. 530–548.

Jourdon, A., Petit, C., Rolland, Y., Loury, C., Bellahsen, N., Guillot, S., Le Pourhiet, L., and Ganino, C., 2017, New structural data on Late Paleozoic tectonics in the Kyrgyz Tien Shan (Central Asian Orogenic Belt): Gondwana Research, v. 46, p. 57–78.

Kafarsky, and Pyjanov, 1970, Geological Map of the USSR of 1:200000 scales: Sheet J-42-XII: Nedra, Moscow, Russian Geological Research Institute.

Kang, L., Xiao, P.X., Gao, X.F., Wang, C., Yang, Z.C., and Xi, R.G., 2015, Geochemical characteristics, petrogenesis and tectonic setting of oceanic plagiogranites belt in the northwestern margin of western Kunlun: Acta Petrologica Sinica, v. 31, no. 9, p. 2566–2582.

Kapp, P., and DeCelles, P.G., 2019, Mesozoic–Cenozoic geological evolution of the Himalayan-Tibetan orogen and working tectonic hypotheses: American Journal of Science, v. 319, no. 3, p. 159–254, doi: 10.2475/03.2019.01.

Käßner, A., Ratschbacher, L., Pfänder, J.A., Hacker, B.R., Zack, G., Sonntag, B.-L., Khan, J., Stanek, K.P., Gadoev, M., and Oimahmadov, I., 2017, Proterozoic–Mesozoic history of the Central Asian orogenic belt in the Tajik and southwestern Kyrgyz Tian Shan: U-Pb, 40Ar/39Ar, and fission-track geochronology and geochemistry of granitoids: GSA Bulletin, v. 129, 3-4, p. 281–303, doi: 10.1130/B31466.1.

Kazmin, V.G., and Tikhonova, N.F., 2006, Evolution of Early Mesozoic back-arc basins in the Black Sea-Caucasus segment of a Tethyan active margin: Geological Society, London, Special Publications, v. 260, no. 1, p. 179–200.

Kirkland, C.L., Smithies, R.H., Taylor, R., Evans, N., and McDonald, B., 2015, Zircon Th/U ratios in magmatic environs: Lithos, 212-215, p. 397–414, doi: 10.1016/j.lithos.2014.11.021.

Kisch, H.J., 1991, Illite crystallinity: recommendations on sample preparation, X-ray diffraction settings, and interlaboratory samples: Journal of Metamorphic Geology, v. 9, no. 6, p. 665–670.

Kley, J., Voigt, T., Sobel, E.R., Rembe, J., and Jie, C., 2021, Transect across the External Pamir thrust belt and Main Pamir Thrust along the Altyn Darya valley, Kyrgyzstan: EGU General Assembly Conference Abstracts, EGU21-12484, doi: 10.5194/egusphere-egu21-12484.

Konopelko, D., Biske, G., Seltmann, R., Eklund, O., and Belyatsky, B., 2007, Hercynian post-collisional A-type granites of the Kokshaal Range, southern Tien Shan, Kyrgyzstan: Lithos, v. 97, 1-2, p. 140–160.

Konopelko, D., Biske, Y.S., Kullerud, K., Ganiev, I., Seltmann, R., Brownscombe, W., Mirkamalov, R., Wang, B., Safonova, I., and Kotler, P., 2019, Early Carboniferous metamorphism of the Neoproterozoic South Tien Shan-Karakum basement: New geochronological results from Baisun and Kyzylkum, Uzbekistan: Journal of Asian Earth Sciences, v. 177, p. 275–286.

Konopelko, D., Klemd, R., Mamadjanov, Y., Hegener, E., Knorsch, M., Fidaev, D., Kern, M., and

Sergeev, S.A., 2015, Permian age of orogenic thickening and crustal melting in the Garm Block, South Tien Shan, Tajikistan: Journal of Asian Earth Sciences, v. 113, p. 711–727.

Konopelko, D., Seltmann, R., Mamadjanov, Y., Romer, R.L., Rojas-Agramonte, Y., Jeffries, T., Fidaev, D., and Niyozov, A., 2017, A geotraverse across two paleo-subduction zones in Tien Shan, Tajikistan: Gondwana Research, v. 47, p. 110–130.

Konopelko, D., Wilde, S.A., Seltmann, R., Romer, R.L., and Biske, Y., 2018, Early Permian intrusions of the Alai range: Understanding tectonic settings of Hercynian post-collisional magmatism in the South Tien Shan, Kyrgyzstan: Lithos, 302-303, p. 405–420, doi: 10.1016/j.lithos.2018.01.024.

Kozur, H.W., Aydin, M., Demir, O., Yakar, H., Göncüoglu, M.C., and Kuru, F., 2000, New stratigraphic and palaeogeographic results from the Palaeozoic and early Mesozoic of the Middle Pontides (northern Turkey) in the Azdavay, Devrekani, Küre and Inebolu areas: implications for the Carboniferous-Early Cretaceous geodynamic evolution and some related remarks to the Karakaya oceanic rift basin: Geologia Croatica, v. 53, no. 2, p. 209–268.

Krestnikov, V.N., 1963, History of the geological development of the pamirs and adjacent regions of asia in the mesozoic-cenozoic (triassic-lower cretaceous): International Geology Review, v. 5, no. 1, p. 5–27.

Krumm, S., 1992, Illitkristallinität als Indikator schwacher Metamorphose: methodische Untersuchungen, regionale Anwendungen und Vergleiche mit anderen Parametern: Erlangen, Institut für Geologie der Universität Erlangen-Nürnberg, Erlanger Geologische Abhandlungen, Volume 120, 75 p.

Kübler, B., 1967, La cristallinité de l'illite et les zones tout à fait supérieures du métamorphisme: Etages tectoniques, p. 105–121.

Kübler, B., 1968, Evaluation quantitative du métamorphisme par la cristallinité de l'illite: Bulletin Centre de Researches de Pau-SNPA, v. 2, p. 385–397.

Kübler, B., 1984, Les indicateurs des transformations physiques et chimiques dans la diagenese temperature et calorimetrie: Thermométrie et barométrie géologiques, v. 2, p. 489–596.

Kufner, S.-K., Schurr, B., Sippl, C., Yuan, X., Ratschbacher, L., Ischuk, A., Murodkulov, S., Schneider, F., Mechie, J., and Tilmann, F., 2016, Deep India meets deep Asia: Lithospheric indentation, delamination and break-off under Pamir and Hindu Kush (Central Asia): Earth and Planetary Science Letters, v. 435, p. 171–184, doi: 10.1016/j.epsl.2015.11.046.

Laborde, A., Barrier, L., Simoes, M., Li, H., Coudroy, T., van der Woerd, J., and Tapponnier, P., 2019, Cenozoic deformation of the Tarim Basin and surrounding ranges (Xinjiang, China): A regional overview: Earth-Science Reviews, v. 197, p. 1–35, doi: 10.1016/j.earscirev.2019.102891.

Lallemand, S., Heuret, A., and Boutelier, D., 2005, On the relationships between slab dip, back-arc stress, upper plate absolute motion, and crustal nature in subduction zones: Geochemistry,

Geophysics, Geosystems, v. 6, no. 9, 1-18, doi: 10.1029/2005GC000917.

Lan, Z., Roberts, N.M.W., Zhou, Y., Zhang, S., Li, Z., and Zhao, T., 2022, Application of in situ U-Pb carbonate geochronology to Stenian-Tonian successions of North China: Precambrian Research, v. 370, p. 1–11.

Le Bas, M.J., Le Maitre, R.W., Streckeisen, A., Zanettin, B., and IUGS Subcommission on the Systematics of Igneous Rocks, 1986, A chemical classification of volcanic rocks based on the total alkali-silica diagram: Journal of Petrology, v. 27, no. 3, p. 745–750.

Leonov, M.G., Rybin, A.K., Batalev, V.Y., Matyukov, V.E., and Shchelochkov, G.G., 2018, Hissar–Alai and the Pamirs: Junction and Position in the System of Mobile Belts of Central Asia: Geotectonics, v. 52, no. 1, p. 73–87, doi: 10.1134/S0016852118010090.

Leven, E.J., 1995, Permian and Triassic of the Rushan-Pshart Zone (Pamir): Riv. Ital. Paleontol. Stratigr, v. 101, no. 1, p. 3–16.

Leven, E.J., 2012, The Bashkirian Stage of Southwestern Darvaz, the Pamir Mountains: Stratigraphy and paleotectonics: Stratigraphy and Geological Correlation, v. 20, no. 3, p. 240–260, doi: 10.1134/S0869593812020050.

Leven, E.J., 2013, Stratigraphy of the Carboniferous-Permian volcanosedimentary sequences of the Northern Pamir, Tajikistan: Stratigraphy and Geological Correlation, v. 21, no. 6, p. 601–608, doi: 10.1134/S0869593813060063.

Leven, E.J., Leonova, T.B., and Dmitriev, V.Y., 1992, Perm'Darvaz-Zaalaiskoi zony Pamira. Fuzulinidy, ammonoidei, stratigrafiya (The Permian System in the Darvaz-Transalai Zone of Pamir: Fusulines, Ammonoids, Stratigraphy), Barskov, IS, Ed: Tr. Paleontol Inst. Ross. Akad. Nauk, v. 253, p. 1–204.

Li, B., Yao, J., Ji, W.H., Zhang, J., Yin, Z., Chen, G., Lin, X., Zhang, Q., KONG, W., Wang, F., and LIU, X., 2006, Characteristics and zircon SHRIMP U-Pb ages of the arc magmatic rocks in Mazar, southern Yecheng, West Kunlun Mountains.: Geological Bulletin of China, Z1, 25(1-2), p. 124–132.

Li, D., Yang, S., Chen, H., Cheng, X., Li, K., Jin, X., Li, Z., Li, Y., and Zou, S., 2014, Late Carboniferous crustal uplift of the Tarim plate and its constraints on the evolution of the Early Permian Tarim Large Igneous Province: Lithos, v. 204, p. 36–46, doi: 10.1016/j.lithos.2014.05.023.

Li, L., Meng, Q., Pullen, A., Garzione, C.N., Wu, G., Wang, Y., Ma, S., and Duan, L., 2014, Late Permian–early Middle Triassic back-arc basin development in West Qinling, China: Journal of Asian Earth Sciences, v. 87, p. 116–129.

Li, T., Chen, J., Fang, L., Chen, Z., Thompson, J.A., and Jia, C., 2016, The 2015 Mw 6.4 Pishan Earthquake: Seismic Hazards of an Active Blind Wedge Thrust System at the Western Kunlun Range Front, Northwest Tibetan Plateau: Seismological Research Letters, v. 87, no. 3, p. 601–608, doi: 10.1785/0220150205.

Li, T., Chen, Z., Chen, J., Thompson Jobe, J.A., Burbank, D.W., Li, Z., He, X., Zheng, W., Zhang, P., and Zhang, B., 2019, Along-strike and downdip segmentation of the Pamir frontal thrust and its association with the 1985 Mw 6.9 Wuqia earthquake: Journal of Geophysical Research: Solid Earth, v. 124, no. 9, p. 9890–9919.

Li, W., Chen, Y., Yuan, X., Xiao, W., and Windley, B.F., 2022, Intracontinental deformation of the Tianshan Orogen in response to India-Asia collision: Nature Communications, v. 13, no. 1, p. 3738, doi: 10.1038/s41467-022-30795-6.

Li, Y., Robinson, A.C., Zucali, M., Gadoev, M., Oimuhammadzoda, I., Lapen, T.J., and Carrapa, B., 2022, Mesozoic Tectonic Evolution in the Kurgovat-Vanch Complex, NW Pamir: Tectonics, v. 41, no. 10, e2021TC007180, doi: 10.1029/2021TC007180.

Li, Y., Xiao, W., and Tian, Z., 2019, Early Palaeozoic accretionary tectonics of West Kunlun Orogen: Insights from Datong granitoids, mafic–ultramafic complexes, and Silurian–Devonian sandstones, Xinjiang, NW China: Geological Journal, v. 54, no. 3, p. 1505–1517.

Li, Y.-P., Robinson, A.C., Gadoev, M., and Oimuhammadzoda, I., 2020, Was the Pamir salient built along a Late Paleozoic embayment on the southern Asian margin?: Earth and Planetary Science Letters, v. 550, p. 116554.

Li, Y.-P., Robinson, A.C., Lapen, T.J., Righter, M., and Stevens, M.K., 2020, Muztaghata Dome Miocene Eclogite Facies Metamorphism: A Record of Lower Crustal Evolution of the NE Pamir: Tectonics, v. 39, no. 7.

Li, Z., Li, Y., Chen, H., Santosh, M., Yang, S., Xu, Y., Langmuir, C.H., Chen, Z., Yu, X., and Zou, S., 2012, Hf isotopic characteristics of the Tarim Permian large igneous province rocks of NW China: Implication for the magmatic source and evolution: Journal of Asian Earth Sciences, v. 49, p. 191–202.

Li, Z., Yang, S., Chen, H., Langmuir, C.H., Xing, Y., XiuBin, L., and YinQi, L., 2008, Chronology and geochemistry of Taxinan basalts from the Tarim basin: evidence for Permian plume magmatism: Acta Petrologica Sinica.

Liao, S.-Y., Jiang, Y.-H., Jiang, S.-Y., Yang, W.-Z., Zhou, Q., Jin, G.-D., and Zhao, P., 2010, Subducting sediment-derived arc granitoids: evidence from the Datong pluton and its quenched enclaves in the western Kunlun orogen, northwest China: Mineralogy and Petrology, v. 100, 1-2, p. 55–74.

Liu, C., Guo, J., and YIN, Q., 2011, Permian sequence stratigraphy of shallow water basin in Tarim Basin: Global Geology, v. 14, no. 4, p. 221–230.

Liu, C., Zhang, L., Guo, J., and Wang, M., 2012, Application of sequence stratigraphy to Triassic terrestrial strata in Tahe area of Tarim Basin: Journal of Central South University, v. 19, no. 5, p. 1388–1398, doi: 10.1007/s11771-012-1155-6.

Liu, D., Jolivet, M., Yang, W., Zhang, Z., Cheng, F., Zhu, B., and Guo, Z., 2013, Latest Paleozoic–Early Mesozoic basin–range interactions in South Tian Shan (northwest China) and their

tectonic significance: Constraints from detrital zircon U–Pb ages: Tectonophysics, v. 599, p. 197–213, doi: 10.1016/j.tecto.2013.04.018.

Liu, H.-Q., Xu, Y.-G., Zhong, Y.-T., Luo, Z.-Y., Mundil, R., Riley, T.R., Le Zhang, and Xie, W., 2019, Crustal melting above a mantle plume: Insights from the Permian Tarim Large Igneous Province, NW China: Lithos, v. 326, p. 370–383.

Liu, J., Wang, H., Shehong, L.I., LaiXi, T., and GuangLi, R., 2010, Geological and geochemical features and geochronology of the Kayizi porphyry molybdenum deposit in the northern belt of western Kunlun, NW China: Acta Petrologica Sinica, v. 26, no. 10, p. 3095–3105.

Liu, J.P., and Wang, H., 2014, Geology and Geochronology of the Kayizi Porphyry Mo Deposit in Western Kunlun, NW China: Advanced Materials Research, 962-965, p. 292–295.

Liu, X., Gao, S., Diwu, C., Yuan, H., and Hu, Z., 2007, Simultaneous in-situ determination of U-Pb age and trace elements in zircon by LA-ICP-MS in 20 μm spot size: Chinese Science Bulletin, v. 52, no. 9, p. 1257–1264.

Liu, Y., Hu, Xiufang, Wang, Daoxuan, Yan, Z., Qiang, Z., and Lei, W., 2012, Characteristics of Triassic lithofacies palaeogeography in Tarim Basin [J]: Fault-Block Oil & Gas Field, v. 19, no. 6, p. 696–700.

Liu, Z., Jiang, Y.-H., Jia, R.-Y., Zhao, P., Zhou, Q., Wang, G.-C., and Ni, C.-Y., 2014, Origin of Middle Cambrian and Late Silurian potassic granitoids from the western Kunlun orogen, northwest China: a magmatic response to the Proto-Tethys evolution: Mineralogy and Petrology, v. 108, no. 1, p. 91–110.

Loury, C., Rolland, Y., Cenki-Tok, B., Lanari, P., and Guillot, S., 2016, Late Paleozoic evolution of the South Tien Shan: Insights from P–T estimates and allanite geochronology on retrogressed eclogites (Chatkal range, Kyrgyzstan): Journal of geodynamics, v. 96, p. 62–80.

Loury, C., Rolland, Y., Guillot, S., Lanari, P., Ganino, C., Melis, R., Jourdon, A., Petit, C., Beyssac, O., Gallet, S., and Monié, P., 2018, Tectonometamorphic evolution of the Atbashi high- P units (Kyrgyz CAOB, Tien Shan): Implications for the closure of the Turkestan Ocean and continental subduction-exhumation of the South Kazakh continental margin: Journal of Metamorphic Geology, v. 36, no. 8, p. 959–985.

Loury, C., Rolland, Y., Guillot, S., Mikolaichuk, A.V., Lanari, P., Bruguier, O., and Bosch, D., 2017, Crustal-scale structure of South Tien Shan: implications for subduction polarity and Cenozoic reactivation: Geological Society, London, Special Publications, v. 427, no. 1, p. 197–229.

Loury, C., Rolland, Y., Lanari, P., Guillot, S., Bosch, D., Ganino, C., Jourdon, A., Petit, C., Gallet, S., Monié, P., and Riel, N., 2018, Permian charnockites in the Pobeda area: Implications for Tarim mantle plume activity and HT metamorphism in the South Tien Shan range: Lithos, 304-307, p. 135–154.

Lu, S., Du Fengjun, and Ren, J., 2013, Aitikaierdingsayi Map Sheet and Yinjisha County Map

Sheet (Scale 1:250000): Beijing, China University of Geosciences Press.

Luchnikov, V.S., 2001, Геология и минерально-сырьевые ресурсы Республики Таджикистан: Geology and mineral resources of the Republic of Tajikistan. Collection of scientific papers., 287 p.

Ludwig, K.R., 2008, User's manual for Isoplot/Ex Version 3.70 (2009). A geochronological toolkit for Microsoft Excel: Berkeley Geochronological Centre Special Publication, v. 4, p. 1–76.

Lyoskind, S.Y., Novikova, L.A., and Dolgonos, L.G., 1963, Geological map of the USSR of 1:200000 scales: Sheet J-42-XVII: Nedra, Moscow, Russian Geological Research Institute.

Lyoskind, S.Y., Novikova, L.A., and Yakusheva V. M., 1963, Geological map of the USSR of 1:200000: Sheet J-42-XV: Nedra, Moscow, Russian Geological Research Institute.

Mamadjanov, Y., Niyozov, A., Aminov, J., Melnichenko, A.K., Hodghiev, A.K., Varzieva, T.B., Oshurmamadov, A.K., Kadyrov, I., Shomuhimov, D., and Yagibekov, J., 2017, The study of petrological and geochemical features and geodynamic formation conditions of ore-bearing granitoids of the Pamir-Tien Shan.

Mamani, M., Wörner, G., and Sempere, T., 2010, Geochemical variations in igneous rocks of the Central Andean orocline (13 S to 18 S): Tracing crustal thickening and magma generation through time and space: Bulletin, v. 122, 1-2, p. 162–182.

Martinez, F., Okino, K., Ohara, Y., Reysenbach, A.-L., and Goffredi, S.K., 2007, Back-arc basins: Oceanography, v. 20, no. 1, p. 116–127.

Marushkin, and Lyashkevich, 1969, Geological Map of the USSR of 1:200000 scales: Sheet J-42-VI: Nedra, Moscow, Russian Geological Research Institute.

Matte, P., Tapponier, P., Arnaud, N., Bourjot, L., Avouac, J.P., Vidal, P., Liu, Q., Pan, Y., and Wang, Y., 1996, Tectonics of Western Tibet, between the Tarim and the Indus: Earth and Planetary Science Letters, v. 142, p. 311–330.

Mattern, F., and Schneider, W., 2000, Suturing of the Proto-and Paleo-Tethys oceans in the western Kunlun (Xinjiang, China): Journal of Asian Earth Sciences, v. 18, no. 6, p. 637–650.

Mattern, F., Schneider, W., Li, Y., and Li, X., 1996, A traverse through the western Kunlun (Xinjiang, China): Tentative geodynamic implications for the Paleozoic and Mesozoic: Geologische Rundschau, v. 85, no. 4, p. 705–722.

May, T.W., and Wiedmeyer, R.H., 1998, A table of polyatomic interferences in ICP-MS: Atomic spectroscopy, v. 19, p. 150–155, doi: 10.46770/AS.1998.05.002.

McDonough, W.F., and Sun, S.-S., 1995, The composition of the Earth: Chemical Geology, v. 120, 3-4, p. 223–253.

McKay, M.P., Jackson, W.T., and Hessler, A.M., 2018, Tectonic stress regime recorded by zircon Th/U: Gondwana Research, v. 57, p. 1–9, doi: 10.1016/j.gr.2018.01.004.

Mériaux, A.-S., Ryerson, F.J., Tapponnier, P., van der Woerd, J., Finkel, R.C., Xu, X., Xu, Z., and Caffee, M.W., 2004, Rapid slip along the central Altyn Tagh Fault: Morphochronologic

evidence from Cherchen He and Sulamu Tagh: Journal of Geophysical Research, v. 109, B6, p. 1–23, doi: 10.1029/2003JB002558.

Metcalfe, I., 2011, Palaeozoic–Mesozoic history of SE Asia: Geological Society, London, Special Publications, v. 355, no. 1, p. 7–35, doi: 10.1144/SP355.2.

Miall, A.D., 1985, Architectural-element analysis: a new method of facies analysis applied to fluvial deposits: Earth-Science Reviews, v. 22, no. 4, p. 261–308.

Miall, A.D., 1987, Recent developments in the study of fluvial facies models, *in* Ethridge, F.G., Flores, R.M., et al., eds., Recent developments in fluvial sedimentology: Contributions from the third International fluvial sedimentology conference: Tulsa, SEMP Society for Sedimentary Geology. Special publication, Volume 39.

Mirkamalov, R.H., Chirikin, V.V., Khan, R.S., Kharin, V.G., and Sergeev, S.A., 2012, Results of U–Pb (SHRIMP) dating of granitoid and metamorphic complexes of the Tien Shan fold belt (Uzbekistan): Vestnik SPbGU, v. 7, no. 1, p. 3–25.

Mirzod, S.H., Kolchanov, V.P., and Manucharyanc, O.A., 1968, Afghanistan. Brief information about the geological structure and mineral resources: Bjull. Moskovskogo Obchch. Isp. Pri., v. 43, p. 31–52.

Miyashiro, A., 1975, Classification, characteristics, and origin of ophiolites: The Journal of Geology, v. 83, no. 2, p. 249–281.

Möller, P., Rosenthal, E., Geyer, S., Guttman, J., Dulski, P., Rybakov, M., Zilberbrand, M., Jahnke, C., and Flexer, A., 2007, Hydrochemical processes in the lower Jordan valley and in the Dead Sea area: Chemical Geology, v. 239, 1-2, p. 27–49.

Molnar, P., and Tapponnier, P., 1975, Cenozoic Tectonics of Asia: Effects of a Continental Collision: Science, v. 189, no. 4201, p. 419–426.

Montenat, C., 2009, The Mesozoic of Afghanistan: GeoArabia, v. 14, no. 1, p. 147–210, doi: 10.2113/geoarabia1401147.

Morin, J., Jolivet, M., Shaw, D., Bourquin, S., and Bataleva, E., 2021, New sedimentological and palynological data from the Yarkand-Fergana Basin (Kyrgyz Tian Shan): Insights on its Mesozoic paleogeographic and tectonic evolution: Geoscience Frontiers, v. 12, no. 1, p. 183–202, doi: 10.1016/j.gsf.2020.04.010.

Moskvin, A.V., 1937, Geography and geology of East Karategin: Tajik-Pamir expedition of 1935, p. 682–739.

Mullen, E.D., 1983, MnO/TiO2/P2O5: a minor element discriminant for basaltic rocks of oceanic environments and its implications for petrogenesis: Earth and Planetary Science Letters, v. 62, no. 1, p. 53–62.

Nachtergaele, S., Pelsmaeker, E. de, Glorie, S., Zhimulev, F., Jolivet, M., Danišík, M., Buslov, M.M., and de Grave, J., 2018, Meso-Cenozoic tectonic evolution of the Talas-Fergana region of the Kyrgyz Tien Shan revealed by low-temperature basement and detrital

thermochronology: Geoscience Frontiers, v. 9, no. 5, p. 1495–1514.

Natal'in, B.A., and Sengör, A.M., 2005, Late Palaeozoic to Triassic evolution of the Turan and Scythian platforms: the pre-history of the Palaeo-Tethyan closure: Tectonophysics, v. 404, 3-4, p. 175–202.

Nguyen et al., 2019, LA-(MC)-ICPMS U-Pb geochronology – Potential calcite reference materials., Goldschmidt Barcelona.

Nikishin, A.M., Ziegler, P., Bolotov, S., and Fokin, P., 2012, Late Palaeozoic to Cenozoic Evolution of the Black Sea-Southern Eastern Europe Region: A View from the Russian Platform: Turkish Journal of Earth Sciences, v. 21, no. 5, p. 571–634, doi: 10.3906/yer-1005-22.

Nikolaev, V.A., 1936, Essay on magmatic geology of Pamir and Darvaz: Scientific Findings of the Tajik-Pamir Expedition of the USSR Academy of Sciences. M.-L.: Publishing House of the USSR Academy of Sciences, p. 329–387.

Nuriel, P., Craddock, J., Kylander-Clark, A.R.C., Uysal, I.T., Karabacak, V., Dirik, R.K., Hacker, B.R., and Weinberger, R., 2019, Reactivation history of the North Anatolian fault zone based on calcite age-strain analyses: Geology, v. 47, no. 5, p. 465–469.

O'Connor, J.T., 1965, A classification for quartz-rich igneous rocks: Geological Survey Professional Paper, v. 525, p. 79.

Ohta, T., and Arai, H., 2007, Statistical empirical index of chemical weathering in igneous rocks: A new tool for evaluating the degree of weathering: Chemical Geology, v. 240, 3-4, p. 280–297.

Oxford Instruments Analytical, 2006, INCA Energy Operator Manual: High Wycombe.

Pál-Molnár, E., Kiri, L., Lukács, R., Dunkl, I., Batki, A., Szemerédi, M., Almási, E.E., Sogrik, E., and Harangi, S., 2021, Timing of magmatism of the Ditrău Alkaline Massif, Romania – A review based on new U–Pb and K/Ar data: Central European Geology, v. 64, no. 1, p. 18–37, doi: 10.1556/24.2021.00001.

Pan, Y., 1994, Discovery and evidence of the fifth suture zone of Qinghai-xizang plateau: Chinese Journal of Geophysics, v. 2, no. 37, p. 184–192.

Pan, Y., editor, 1996, Geological evolution of the Karakorum and Kunlun Mountains: Beijing, Seismological Press.

Pan, Y., 1996, Geological Evolution of the Karakorum and Kunlun Mountains: Beijing, Seismological Press.

Parrish, R.R., Parrish, C.M., and Lasalle, S., 2018, Vein calcite dating reveals Pyrenean orogen as cause of Paleogene deformation in southern England: Journal of the Geological Society, v. 175, no. 3, p. 425–442.

Paton, C., Hellstrom, J., Paul, B., Woodhead, J., and Hergt, J., 2011, Iolite: Freeware for the visualisation and processing of mass spectrometric data: Journal of Analytical Atomic

Spectrometry, v. 26, no. 12, p. 2508–2518.

Patyniak, M., Landgraf, A., Dzhumabaeva, A., Baikulov, S., Williams, A.M., Weiss, J.R., Hilley, G.E., Preusser, F., Abdrakhmatov, K.E., Arrowsmith, R.J., and Strecker, M.R., 2021, The Pamir Frontal Thrust Fault: Holocene Full-Segment Ruptures and Implications for Complex Segment Interactions in a Continental Collision Zone: Journal of Geophysical Research: Solid Earth, v. 126, no. 12, e2021JB022405, doi: 10.1029/2021JB022405.

Pearce, J.A., 1982, Trace element characteristics of lavas from destructive plate boundaries, *in* Thorpe, R.S., ed., Andesites: Orogenic Andesites and Related Rocks: Chichester, John Wiley & Sons, p. 528–548.

Pearce, J.A., 1983, Role of the sub-continental lithosphere in magma genesis at active continental margins, *in* Hawkesworth, C., Norry, M.J., eds., Continental Basalts and Mantle Xenoliths: Chesire, Shiva Publishing. Shiva geology series.

Pearce, J.A., Harris, N.B.W., and Tindle, A.G., 1984, Trace Element Discrimination Diagrams for the Tectonic Interpretation of Granitic Rocks: Journal of Petrology, v. 25, no. 4, p. 956–983, doi: 10.1093/petrology/25.4.956.

Pearce, J.A., and Norry, M.J., 1979, Petrogenetic implications of Ti, Zr, Y, and Nb variations in volcanic rocks: Contributions to Mineralogy and Petrology, v. 69, no. 1, p. 33–47.

Peccerillo, A., and Taylor, S.R., 1976, Geochemistry of Eocene calc-alkaline volcanic rocks from the Kastamonu area, northern Turkey: Contributions to Mineralogy and Petrology, v. 58, no. 1, p. 63–81.

Pelsmaeker, E. de, Jolivet, M., Laborde, A., Poujol, M., Robin, C., Zhimulev, F.I., Nachtergaele, S., Glorie, S., Clercq, S. de, Batalev, V.Y., and de Grave, J., 2018, Source-to-sink dynamics in the Kyrgyz Tien Shan from the Jurassic to the Paleogene: Insights from sedimentological and detrital zircon U-Pb analyses: Gondwana Research, v. 54, p. 180–204, doi: 10.1016/j.gr.2017.09.004.

Perry, E.P., and Gysi, A.P., 2018, Rare Earth Elements in Mineral Deposits: Speciation in Hydrothermal Fluids and Partitioning in Calcite: Geofluids, v. 2018, p. 1–19, doi: 10.1155/2018/5382480.

Perry, M., Kakar, N., Ischuk, A., Metzger, S., Bendick, R., Molnar, P., and Mohadjer, S., 2019, Little Geodetic Evidence for Localized Indian Subduction in the Pamir-Hindu Kush of Central Asia: Geophysical Research Letters, v. 46, no. 1, p. 109–118.

Petrus, J.A., and Kamber, B.S., 2012, VizualAge: A Novel Approach to Laser Ablation ICP-MS U-Pb Geochronology Data Reduction: Geostandards and Geoanalytical Research, v. 36, no. 3, p. 247–270, doi: 10.1111/j.1751-908X.2012.00158.x.

Phajuy, B., and Singtuen, V., 2019, Petrochemical characteristics of Tak volcanic rocks, Thailand: Implication for tectonic significance: ScienceAsia, v. 45, no. 4, p. 350.

Pirajno, F., Mao, J., Zhang, Z., Zhang, Z., and Chai, F., 2008, The association of mafic–ultramafic

intrusions and A-type magmatism in the Tian Shan and Altay orogens, NW China: implications for geodynamic evolution and potential for the discovery of new ore deposits: Journal of Asian Earth Sciences, v. 32, 2-4, p. 165–183.

Pretorius, W., Weis, D., Williams, G., Hanano, D., Kieffer, B., and Scoates, J., 2006, Complete trace elemental characterisation of granitoid (USGS G-2, GSP-2) reference materials by high resolution inductively coupled plasma-mass spectrometry: Geostandards and Geoanalytical Research, v. 30, no. 1, p. 39–54.

Pringle, M.S., 1993, Age Progressive Volcanism in the Musicians Seamounts: A Test of the Hot Spot Hypothesis for the Late Cretaceous Pacific, *in* Pringle., S.M., ed., The Mesozoic Pacific: Geology, Tectonics and Volcanism: A Volume in Memory of Sy Schlanger, Geophysical Monography Series, Volume 77, p. 187–215.

Prynada, V.D., 1934, Ancient Mesozoic plants of Pamir. Tadzhik integrated expedition of 1932: Reports of the expedition. Geology of Pamir. Union Expeditional Committee GGGGU, Acad Sci USSR, Leningrad Department, v. 9, p. 1–100.

Putis, M., Ondrejka, M., Uher, P., Ruzicka, P., Nemec, O., Koller, F., Li, X.-H., Li, Q.-L., Larionov, A., Siman, P., and Nemeth, Z., 2019, Geochronology of Permian-Triassic tectono-magmatic events from the Inner Western Carpathian and Austroalpine units, *in* Broska, I., Kohut, M., et al., eds., Proceedings of the Geologica Carpathica. Geologica Carpathica 70, Slovakia: Smolenice, Slovak Academy of Science, p. 192.

QGis Developer Team, 2018, QGis: Bonn: QGis Developer Team.

Qiao, X., Wang, Q., Yang, S., Li, J., Zou, R., and Ding, K., 2015, The 2008 Nura Mw6.7 earthquake: A shallow rupture on the Main Pamir Thrust revealed by GPS and InSAR: Geodesy and Geodynamics, v. 6, no. 2, p. 91–100, doi: 10.1016/j.geog.2015.01.005.

R. Development Core Team, 2019, R: A language and environment for statistical computing. Vienna, Austria: R Foundation for Statistical Computing; 2011: URL: https://www. R-project. org.[Google Scholar].

Rasbury, E.T., Present, T.M., Northrup, P., Tappero, R.V., Lanzirotti, A., Cole, J.M., Wooton, K.M., and Hatton, K., 2021, Tools for uranium characterization in carbonate samples: case studies of natural U–Pb geochronology reference materials: Geochronology, v. 3, no. 1, p. 103–122, doi: 10.5194/gchron-3-103-2021.

Raup, B., Racoviteanu, A., Khalsa, S.J.S., Helm, C., Armstrong, R., and Arnaud, Y., 2007, The GLIMS geospatial glacier database: A new tool for studying glacier change: Global and Planetary Change, v. 56, 1-2, p. 101–110, doi: 10.1016/j.gloplacha.2006.07.018.

Rembe, J., Sobel, E., Kley, J., Zhou, R., Wemmer, K., Jie Chen, and Liu, L., 2020, Cimmerian timing of nappe emplacement in the North East Pamir: Utrecht/Online, GeoUtrecht 2020.

Rembe, J., Sobel, E.R., Kley, J., Zhou, R., Thiede, R., and Chen, J., 2021, The Carboniferous Arc of the North Pamir: Lithosphere, v. 2021, no. 1, p. 1–26, doi: 10.2113/2021/6697858.

Rembe, J., Sobel, E.R., Kley, J., Zhou, R., Wemmer, K., Chen, J., and Liu, L., 2018, The influence of Mesozoic structures on the Cenozoic Pamir: The most external occurence of the Karakul-Mazar nappe, Chinese Pamir: Jena, TSK 2018.

Rembe, J., Zhou, R., Sobel, E.R., Kley, J., Chen, J., Zhao, J., Feng, Y., and Howard, D.L., 2022, Calcite U–Pb dating of altered ancient oceanic crust in the North Pamir, Central Asia: Geochronology, v. 4, no. 1, p. 227–250, doi: 10.5194/gchron-4-227-2022.

Richards, J.P., and Şengör, A.C., 2017, Did Paleo-Tethyan anoxia kill arc magma fertility for porphyry copper formation?: Geology, v. 45, no. 7, p. 591–594, doi: 10.1130/G38954.1.

Rickmers, W.R., 1913, The Duab of Turkestan: A physiographic sketch and account of some travels, The University Press.

Robert, A.M.M., Letouzey, J., Kavoosi, M.A., Sherkati, S., Müller, C., Vergés, J., and Aghababaei, A., 2014, Structural evolution of the Kopeh Dagh fold-and-thrust belt (NE Iran) and interactions with the South Caspian Sea Basin and Amu Darya Basin: Marine and petroleum geology, v. 57, p. 68–87, doi: 10.1016/j.marpetgeo.2014.05.002.

Roberts, N.M.W., Rasbury, E.T., Parrish, R.R., Smith, C.J., Horstwood, M.S.A., and Condon, D.J., 2017, A calcite reference material for LA-ICP-MS U-Pb geochronology: Geochemistry, Geophysics, Geosystems, v. 18, no. 7, p. 2807–2814, doi: 10.1002/2016GC006784.

Roberts, N.M.W., Žák, J., Vacek, F., and Sláma, J., 2021, No more blind dates with calcite: Fluid-flow vs. fault-slip along the Očkov thrust, Prague Basin: Geoscience Frontiers, v. 12, no. 4, p. 101143.

Robinson, A.C., 2009, Geologic offsets across the northern Karakorum fault: Implications for its role and terrane correlations in the western Himalayan-Tibetan orogen: Earth and Planetary Science Letters, v. 279, 1-2, p. 123–130.

Robinson, A.C., 2015, Mesozoic tectonics of the Gondwanan terranes of the Pamir plateau: Journal of Asian Earth Sciences, v. 102, p. 170–179.

Robinson, A.C., Ducea, M., and Lapen, T.J., 2012, Detrital zircon and isotopic constraints on the crustal architecture and tectonic evolution of the northeastern Pamir: Tectonics, v. 31, no. 2.

Robinson, A.C., Yin, A., Manning, C.E., Harrison, T.M., Zhang, S.-H., and Wang, X.-F., 2004, Tectonic evolution of the northeastern Pamir: Constraints from the northern portion of the Cenozoic Kongur Shan extensional system, western China: Geological Society of America Bulletin, v. 116, 7-8, p. 953–973.

Roecker, S.W., 1981, Seismicity and tectonics of the Pamir-Hindu Kush region of central Asia: Cambridge, Massachusetts Institute of Technology.

Roger, F., Jolivet, M., and Malavieille, J., 2008, Tectonic evolution of the Triassic fold belts of Tibet: Comptes Rendus Geoscience, v. 340, 2-3, p. 180–189.

Rojas-Agramonte, Y., Kröner, A., Demoux, A., Xia, X., Wang, W., Donskaya, T., Liu, D., and Sun, M., 2011, Detrital and xenocrystic zircon ages from Neoproterozoic to Palaeozoic arc

terranes of Mongolia: significance for the origin of crustal fragments in the Central Asian Orogenic Belt: Gondwana Research, v. 19, no. 3, p. 751–763.

Rolland, Y., Alexeiev, D.V., Kröner, A., Corsini, M., Loury, C., and Monié, P., 2013, Late Palaeozoic to Mesozoic kinematic history of the Talas–Ferghana strike-slip fault (Kyrgyz West Tianshan) as revealed by 40Ar/39Ar dating of syn-kinematic white mica: Journal of Asian Earth Sciences, 67-68, p. 76–92.

Rolland, Y., Jourdon, A., Petit, C., Bellahsen, N., Loury, C., Sobel, E.R., and Glodny, J., 2020, Thermochronology of the highest central Asian massifs (Khan Tengri - Pobedi, SE Kyrgyztan): Evidence for Late Miocene (ca. 8 Ma) reactivation of Permian faults and insights into building the Tian Shan: Journal of Asian Earth Sciences, v. 200, p. 104466, doi: 10.1016/j.jseaes.2020.104466.

Romer, R.L., and Hahne, K., 2010, Life of the Rheic Ocean: scrolling through the shale record: Gondwana Research, v. 17, 2-3, p. 236–253.

Rubatto, D., 2002, Zircon trace element geochemistry: partitioning with garnet and the link between U–Pb ages and metamorphism: Chemical Geology, v. 184, 1-2, p. 123–138, doi: 10.1016/S0009-2541(01)00355-2.

Rutte, D., Ratschbacher, L., Khan, J., Stübner, K., Hacker, B.R., Stearns, M.A., Enkelmann, E., Jonckheere, R., Pf?nder, J.A., Sperner, B., and Tichomirowa, M., 2017, Building the Pamir-Tibetan Plateau-Crustal stacking, extensional collapse, and lateral extrusion in the Central Pamir: 2. Timing and rates: Tectonics, v. 36, no. 3, p. 385–419, doi: 10.1002/2016TC004294.

Rutte, D., Ratschbacher, L., Schneider, S., Stübner, K., Stearns, M.A., Gulzar, M.A., and Hacker, B.R., 2017, Building the Pamir-Tibetan Plateau—Crustal stacking, extensional collapse, and lateral extrusion in the Central Pamir: 1. Geometry and kinematics: Tectonics, v. 36, no. 3, p. 342–384.

Ruzhentsev, S., Pospelov, I., and Sukhanov, A.N., 1977, Tectonics of Khalaihumb-Sauksau zone of the North Pamir: Geotectonics, v. 4, p. 68–80.

Salikhov, F.S., and Sakiev, K.S., 2014, Stages of sedimentation in the Permian-Triassic North Pamirs: Bulletin of the Institute of the National Academy of Sciences of the Kyrgyz Republic, v. 4, no. 2.

Satybaev, M., Ding, L., Takasu, A., Bakirov, A., Sakiev, K., Cai, F., Orozbaev, R., Bakirov, A., and Baslakunov, J., 2018, Petrology of metamorphic rocks from the Atbashy complex, Southern Tien-Shan, Kyrgyzstan: Geoscience Frontiers, v. 9, no. 6, p. 1795–1807, doi: 10.1016/j.gsf.2017.11.005.

Schaltegger, U., Ovtcharova, M., Gaynor, S.P., Schoene, B., Wotzlaw, J.-F., Davies, J.F.H.L., Farina, F., Greber, N.D., Szymanowski, D., and Chelle-Michou, C., 2021, Long-term repeatability and interlaboratory reproducibility of high-precision ID-TIMS U-Pb geochronology: Journal of Analytical Atomic Spectrometry, v. 36, no. 7, p. 1466–1477, doi:

10.1039/D1JA00116G.

Schliffke, N., van Hunen, J., Gueydan, F., Magni, V., and Allen, M.B., 2021, Curved orogenic belts, back-arc basins, and obduction as consequences of collision at irregular continental margins: Geology, v. 49, no. 12, p. 1436–1440, doi: 10.1130/G48919.1.

Schmidt, J., Hacker, B.R., Ratschbacher, L., Stübner, K., Stearns, M., Kylander-Clark, A., Cottle, J.M., Alexander, A., Webb, G., Gehrels, G., and Minaev, V., 2011, Cenozoic deep crust in the Pamir: Earth and Planetary Science Letters, v. 312, 3-4, p. 411–421, doi: 10.1016/j.epsl.2011.10.034.

Schneider, F.M., Yuan, X., Schurr, B., Mechie, J., Sippl, C., Kufner, S.-K., Ratschbacher, L., Tilmann, F., Oimahmadov, I., Gadoev, M., Minaev, V., Abdybachaev, U., Orunbaev, S., Ischuk, A., and Murodkulov, S., 2019, The Crust in the Pamir: Insights From Receiver Functions: Journal of Geophysical Research: Solid Earth, v. 124, no. 8, p. 9313–9331, doi: 10.1029/2019JB017765.

Schumacher, E., 1975, Herstellung von 99, 9997% 38Ar für die 40K/40Ar Geochronologie: Geochronologia Chimia, v. 24, p. 441–442.

Schwab, M., Ratschbacher, L., Siebel, W., McWilliams, M., Minaev, V., Lutkov, V., Chen, F., Stanek, K., Nelson, B., Frisch, W., and Wooden, J.L., 2004, Assembly of the Pamirs: Age and origin of magmatic belts from the southern Tien Shan to the southern Pamirs and their relation to Tibet: Tectonics, v. 23, no. 4, 1-31.

Seltmann, R., Konopelko, D., Biske, G., Divaev, F., and Sergeev, S., 2011, Hercynian post-collisional magmatism in the context of Paleozoic magmatic evolution of the Tien Shan orogenic belt: Journal of Asian Earth Sciences, v. 42, no. 5, p. 821–838.

Sengör, A.M., Cin, A., Rowley, D.B., and Nie, S.Y., 1993, Space-time patterns of magmatism along the Tethysides: A preliminary study: The Journal of Geology, v. 101, no. 1, p. 51–84.

Sengör, A.M., and Hsü, K.J., 1984, The Cimmerides of eastern Asia: history of the eastern end of Paleo-Tethys: Mémoires de la Société géologique de France (1924), v. 147, p. 139–167.

Sengör, A.M., and Natal'in, B.A., 1996, Turkic-type orogeny and its role in the making of the continetal crust: Annual Review of Earth and Planetary Sciences, v. 24, no. 1, p. 263–337, doi: 10.1146/annurev.earth.24.1.263.

Sengör, A.M., Natal'in, B.A., Sunal, G., and van der Voo, R., 2018, The Tectonics of the Altaids: Crustal Growth During the Construction of the Continental Lithosphere of Central Asia Between ~750 and ~130 Ma Ago: Annual Review of Earth and Planetary Sciences, v. 46, no. 1, p. 439–494.

Shand, S.J., 1943, Eruptive rocks: their genesis, composition, and classification, with a chapter on meteorites: London, Thomas Murby & Co.

Shervais, J.W., 1982, Ti-V plots and the petrogenesis of modern and ophiolitic lavas: Earth and Planetary Science Letters, v. 59, no. 1, p. 101–118.

Shi, M., Xu, B., Wu, Z., Liu, S., Pieter Goosen, G., Peng, Z., Nie, F., and Liang, H., 2021, Geochronology and petrogeochemistry of Late Permian volcanic rocks in the B.Xiengnou area, Northwestern Laos: China Geology, v. 4, no. 1, p. 1–16, doi: 10.31035/cg2021005.

Shi, X., Wang, J., Jin, Z., Wang, Z., an Liu, Li, P., Guan, Q., and YANG, Y., 2010, The Sequence Characteristic of Triassic and Its Significance in Petroleum Exploration in Tabei Area, Tarim Basin: Xinjiang Petroleum Geology, v. 31, no. 5, p. 477.

Shu, L.S., Deng, X.L., Zhu, W.B., Ma, D.S., and Xiao, W.J., 2011, Precambrian tectonic evolution of the Tarim Block, NW China: new geochronological insights from the Quruqtagh domain: Journal of Asian Earth Sciences, v. 42, no. 5, p. 774–790.

Siehl, A., 2017, Structural setting and evolution of the Afghan orogenic segment – a review: Geological Society, London, Special Publications, v. 427, no. 1, p. 57–88, doi: 10.1144/SP427.8.

Siivola, J., and Schmid, R., 2007, List of mineral abbreviations, Cambridge University Press: New York.

Sippl, C., Schurr, B., Yuan, X., Mechie, J., Schneider, F.M., Gadoev, M., Orunbaev, S., Oimahmadov, I., Haberland, C., Abdybachaev, U., Minaev, V., Negmatullaev, S., and Radjabov, N., 2013, Geometry of the Pamir-Hindu Kush intermediate-depth earthquake zone from local seismic data: Journal of Geophysical Research: Solid Earth, v. 118, no. 4, p. 1438–1457, doi: 10.1002/jgrb.50128.

Sircombe, K.N., and Hazelton, M.L., 2004, Comparison of detrital zircon age distributions by kernel functional estimation: Sedimentary Geology, v. 171, 1-4, p. 91–111, doi: 10.1016/j.sedgeo.2004.05.012.

Sobel, E., Rembe, J., Kley, J., Zhou, R., Terbishalieva, B., and Chen, J., 2020, Control of pre-existing crustal architecture on Cenozoic formation of the Pamir: Vienna, EGU 2020.

Sobel, E.R., and Arnaud, N., 1999, A possible middle Paleozoic suture in the Altyn Tagh, NW China: Tectonics, v. 18, no. 1, p. 64–74.

Sobel, E.R., Chen, J., Schoenbohm, L.M., Thiede, R.C., Stockli, D.F., Sudo, M., and Strecker, M.R., 2013, Oceanic-style subduction controls late Cenozoic deformation of the Northern Pamir orogen: Earth and Planetary Science Letters, v. 363, p. 204–218.

Sobel, E.R., and Dumitru, T.A., 1997, Thrusting and exhumation around the margins of the western Tarim basin during the India-Asia collision: Journal of Geophysical Research: Earth Surface, v. 102, B3, p. 5043–5063.

Spencer, C.J., Kirkland, C.L., and Taylor, R.J.M., 2016, Strategies towards statistically robust interpretations of in situ U–Pb zircon geochronology: Geoscience Frontiers, v. 7, no. 4, p. 581–589.

Spivack, A.J., and Staudigel, H., 1994, Low-temperature alteration of the upper oceanic crust and the alkalinity budget of seawater: Chemical Geology, v. 115, 3-4, p. 239–247.

Stampfli, G.M., and Hochard, C., 2009, Plate tectonics of the Alpine realm: Geological Society, London, Special Publications, v. 327, no. 1, p. 89–111, doi: 10.1144/sp327.6.

Stampfli, G.M., and Kozur, H.W., 2006, Europe from the Variscan to the Alpine cycles, *in* D. G. Gee, R. A. Stephenson, eds., European Lithosphere Dynamics, Geological Society of London. Memoirs, Volume 32, p. 57–82.

Staudigel, H., Hart, S.R., and Richardson, S.H., 1981, Alteration of the oceanic crust: processes and timing: Reports of the Deep Sea Drilling Project, v. 9, p. 10–12.

Staudigel, H., Plank, T., White, B., and Schmincke, H.-U., 2013, Geochemical Fluxes During Seafloor Alteration of the Basaltic Upper Oceanic Crust: DSDP Sites 417 and 418, *in* Bebout, G.E., Scholl, D.W., et al., eds., Subduction top to bottom: Washington, American Geophysical Union. Geophysical Monograph Series, Volume 96, p. 19–38.

Steiger, R.H., and Jäger, E., 1977, Subcommission on geochronology: convention on the use of decay constants in geo-and cosmochronology: Earth and Planetary Science Letters, v. 36, no. 3, p. 359–362.

Streckeisen, A., 1976, To each plutonic rock its proper name: Earth-Science Reviews, v. 12, no. 1, p. 1–33.

Su, A., Chen, H., Feng, Y., Zhao, J., Nguyen, A.D., Wang, Z., and Long, X., 2020, Dating and characterizing primary gas accumulation in Precambrian dolomite reservoirs, Central Sichuan Basin, China: Insights from pyrobitumen Re-Os and dolomite U-Pb geochronology: Precambrian Research, v. 350, no. 105897, p. 1–14.

Sun, S.-S., and McDonough, W.F., 1989, Chemical and isotopic systematics of oceanic basalts: implications for mantle composition and processes: Geological Society, London, Special Publications, v. 42, no. 1, p. 313–345.

Talbi, E.H., and Honnorez, J., 2003, Low-temperature alteration of mesozoic oceanic crust, Ocean Drilling Program Leg 185: Geochemistry, Geophysics, Geosystems, v. 4, no. 5, p. 1–21.

Tang, W., Wang, S., Liu, Y., Yao, X., and Li, M., 2020, Origin of Carboniferous intra-oceanic arc granitoids from the eastern Pamir and implications for the Paleo-Tethyan ocean: Journal of Asian Earth Sciences, v. 204, no. 104558, p. 1–13.

Taylor, B., and Martinez, F., 2003, Back-arc basin basalt systematics: Earth and Planetary Science Letters, v. 210, 3-4, p. 481–497, doi: 10.1016/S0012-821X(03)00167-5.

Teshebaeva, K., Sudhaus, H., Echtler, H., Schurr, B., and Roessner, S., 2014, Strain partitioning at the eastern Pamir-Alai revealed through SAR data analysis of the 2008 Nura earthquake: Geophysical Journal International, v. 198, no. 2, p. 760–774, doi: 10.1093/gji/ggu158.

Thompson, J.A., Burbank, D.W., Li, T., Chen, J., and Bookhagen, B., 2015, Late Miocene northward propagation of the northeast Pamir thrust system, northwest China: Tectonics, v. 34, no. 3, p. 510–534.

Tüysüz, O., and Yiğitbaş, E., 1994, The Karakaya basin: a Palaeo-Tethyan marginal basin and its

age of opening: Acta Geologica Hungarica, v. 37, 3–4, p. 327–350.

Vanghi, V., Borsato, A., Frisia, S., Howard, D.L., Gloy, G., Hellstrom, J., and Bajo, P., 2019, High-resolution synchrotron X-ray fluorescence investigation of calcite coralloid speleothems: Elemental incorporation and their potential as environmental archives: Sedimentology, v. 66, no. 7, p. 2661–2685.

Vauchez, A., Tommasi, A., and Barruol, G., 1998, Rheological heterogeneity, mechanical anisotropy and deformation of the continental lithosphere: Tectonophysics, v. 296, 1-2, p. 61–86.

Verma, S.P., Guevara, M., and Agrawal, S., 2006, Discriminating four tectonic settings: Five new geochemical diagrams for basic and ultrabasic volcanic rocks based on log — ratio transformation of major-element data: Journal of Earth System Science, v. 115, no. 5, p. 485–528, doi: 10.1007/BF02702907.

Vermeesch, P., 2012, On the visualisation of detrital age distributions: Chemical Geology, v. 312, p. 190–194.

Vermeesch, P., 2013, Multi-sample comparison of detrital age distributions: Chemical Geology, v. 341, p. 140–146, doi: 10.1016/j.chemgeo.2013.01.010.

Vermeesch, P., 2018, IsoplotR: a free and open toolbox for geochronology: Geoscience Frontiers, v. 9, no. 5, p. 1479–1493.

Vermeesch, P., 2020, On the treatment of discordant detrital zircon U–Pb data: Geochronology Discussions, p. 1–19, doi: 10.5194/gchron-2020-38.

Vermeesch, P., 2020, Unifying the U–Pb and Th–Pb methods: joint isochron regression and common Pb correction: Geochronology, v. 2, no. 1, p. 119.

Vermeesch, P., 2021, Maximum depositional age estimation revisited: Geoscience Frontiers, v. 12, no. 2, p. 843–850, doi: 10.1016/j.gsf.2020.08.008.

Villarreal, D.P., Robinson, A.C., Carrapa, B., Worthington, J., Chapman, J.B., Oimahmadov, I., Gadoev, M., and MacDonald, B., 2019, Evidence for Late Triassic crustal suturing of the Central and Southern Pamir: Journal of Asian Earth Sciences: X, v. 3, no. 100024, p. 1–12.

Villasenor, G., Catlos, E., elliott, b., Kohut, M., Broska, I., Etzel, T., Kyle, J.R., and Stockli, D., 2022, Timing of rifting in the Central Western Carpathians post-Variscan orogeny and provenance of the Meliata Ocean: Authorea Preprints, doi: 10.1002/essoar.10503163.1.

Villaseñor, G., Catlos, E.J., Broska, I., Kohút, M., Hraško, Ľ., Aguilera, K., Etzel, T.M., Kyle, J.R., and Stockli, D.F., 2021, Evidence for widespread mid-Permian magmatic activity related to rifting following the Variscan orogeny (Western Carpathians): Lithos, 390-391, p. 106083.

Vlasov, B.G., Dyakov, J.A., and Cherev, E.S., 1984, Geological Map of the Tajik SSR and Adjacent Territories: Saint Petersburg, Vsesojuznoi Geological Institute Leningrad.

Voigt, M., Mavromatis, V., and Oelkers, E.H., 2017, The experimental determination of REE partition coefficients in the water-calcite system: Chemical Geology, v. 462, p. 30–43.

Vrublevskii, V.V., 2017, Origin of carbonatites of the Matcha alkaline pluton from Turkestan-Alai ridge, Kyrgyz Southern Tien Shan: IOP Conference Series: Earth and Environmental Science, v. 110, no. 1, p. 12023, doi: 10.1088/1755-1315/110/1/012023.

Vrublevskii, V.V., Morova, A.A., Bukharova, O.V., and Konovalenko, S.I., 2018, Mineralogy and geochemistry of triassic carbonatites in the Matcha alkaline intrusive complex (Turkestan-Alai Ridge, Kyrgyz Southern Tien Shan), SW Central Asian orogenic belt: Journal of Asian Earth Sciences, v. 153, p. 252–281.

Waagstein, R., Guise, P., and Rex, D., 2002, K/Ar and 39 Ar/ 40 Ar whole-rock dating of zeolite facies metamorphosed flood basalts: the upper Paleocene basalts of the Faroe Islands, NE Atlantic: Geological Society, London, Special Publications, v. 197, no. 1, p. 219–252, doi: 10.1144/GSL.SP.2002.197.01.09.

Wang, B., Faure, M., Shu, L., Cluzel, D., Charvet, J., Jong, K. de, and Chen, Y., 2008, Paleozoic tectonic evolution of the Yili Block, western Chinese Tianshan: Bulletin de la Société Géologique de France, v. 179, no. 5, p. 483–490.

Wang, B., Faure, M., Shu, L., Jong, K. de, Charvet, J., Cluzel, D., Jahn, B., Chen, Y., and Ruffet, G., 2010, Structural and geochronological study of high-pressure metamorphic rocks in the Kekesu section (Northwestern China): implications for the late Paleozoic tectonics of the southern Tianshan: The Journal of Geology, v. 118, no. 1, p. 59–77.

Wang, B., Shu, L., Faure, M., Jahn, B., Cluzel, D., Charvet, J., Chung, S.-L., and Meffre, S., 2011, Paleozoic tectonics of the southern Chinese Tianshan: insights from structural, chronological and geochemical studies of the Heiyingshan ophiolitic mélange (NW China): Tectonophysics, v. 497, 1-4, p. 85–104.

Wang, C., Liu, L., Korhonen, F., Yang, W.-Q., Cao, Y.-T., He, S.P., Zhu, X.-H., and Liang, W.-T., 2016, Origins of Early Mesozoic granitoids and their enclaves from West Kunlun, NW China: implications for evolving magmatism related to closure of the Paleo-Tethys ocean: International Journal of Earth Sciences, v. 105, no. 3, p. 941–964.

Wang, C., LIU, H., Deng, J., LIU, X., ZHAO, F., Wang, C., and TIAN, X., 2018, Isotope Geochronologic and Geochemical Constraints on the Magmatic Associations of the Collisional Orogenic Zone in the West Kunlun Orogen, China: Acta Geologica Sinica - English Edition, v. 92, no. 2, p. 482–498.

Wang, P., Zhao, G., Han, Y., Liu, Q., Yao, J., Yu, S., and Li, J., 2020, Timing of the final closure of the Proto-Tethys Ocean: Constraints from provenance of early Paleozoic sedimentary rocks in West Kunlun, NW China: Gondwana Research, v. 84, p. 1–12.

Wang, P., Zhao, G., Liu, Q., Han, Y., Zhang, Y., Yao, J., and Yu, S., 2021, Slab-controlled progressive evolution of the Kudi back-arc ophiolite in response to the rollback of the Proto-Tethys oceanic slab, in Western Kunlun, NW Tibetan Plateau: Lithos, 380-381, no. 105877, p. 1–16.

Wang, S., and Peng, S., 2013, Regional Geological Survey Report of the People's Republic of China: Scale 1:250000: Yecheng County Map Sheet: Beijing, China University of Geosciences Press.

Wang, S., Tang, W., Liu, Y., Liu, X., and Yao, X., 2020, Rushan-Pshart Paleo-Tethyan suture deduced from geochronological, geochemical, and Sr-Nd-Hf isotopic characteristics of granitoids in Pamir: Lithos, 364-365, no. 105549, p. 1–15.

Wang, T., 1996, Characteristics of Sedimentary Rocks and their Environmental Evolution, *in* Pan, Y., ed., Geological evolution of the Karakorum and Kunlun Mountains: Beijing, Seismological Press.

Wang, Y., Xue, S., Deng, J., Wang, Q., Li, C., and Ripley, E.M., 2020, Triassic arc mafic magmatism in North Qiangtang: Implications for tectonic reconstruction and mineral exploration: Gondwana Research, v. 82, p. 337–353.

Wang, Y., Zhang, X., Wang, E., Zhang, J., Li, Q., and Sun, G., 2005, 40Ar/39Ar thermochronological evidence for formation and Mesozoic evolution of the northern-central segment of the Altyn Tagh fault system in the northern Tibetan Plateau: Geological Society of America Bulletin, v. 117, 9-10, p. 1336–1346, doi: 10.1130/B25685.1.

Wang, Z., Sun, S., Li, J., and Hou, Q., 2002, Petrogenesis of tholeiite associations in Kudi ophiolite (western Kunlun Mountains, northwestern China): implications for the evolution of back-arc basins: Contributions to Mineralogy and Petrology, v. 143, no. 4, p. 471–483, doi: 10.1007/s00410-002-0358-5.

Warr, L.N., and Rice, A.H., 1994, Interlaboratory standardization and calibration of day mineral crystallinity and crystallite size data: Journal of Metamorphic Geology, v. 12, no. 2, p. 141–152.

Weaver, C.E., 1960, Possible uses of clay minerals in search for oil: AAPG Bulletin, v. 44, no. 9, p. 1505–1518.

Weippert, D., 1964, Zur Geologie des Gebietes Doab-Saughan-Hajar (Nordost-Afghanistan), *in* Wirtz, D., Hinze, C., et al., eds., Zur Geologie von Nordost-und Zentral-Afghanistan. Geologisches Jahrbuch, p. 153–183.

Wemmer, K., 1991, K/Ar-Altersdatierungsmöglichkeiten für retrograde Deformationsprozesse im spröden und duktilen Bereich--Beispiele aus der KTB-Vorbohrung (Oberpfalz) und dem Bereish der Insubrischen Linie (N-Italien): Göttingen, Im Selbstverlag der Geologischen Institute der Georg-August-Universität, Volume 51.

Wiedenbeck, M., Allé, P., Corfu, F., Griffin, W.L., Meier, M., Oberli, F., Quadt, A. von, Roddick, J.C., and Spiegel, W., 1995, Three Natural Zircon Standards for U-Th-Pb, Lu-Hf, Trace Element and REE Analyses: Geostandards and Geoanalytical Research, v. 19, no. 1, p. 1–23.

Wirtz, D., Hinze, C., Gabert, G., and Benda, L., editors, 1964, Zur Geologie von Nordost-und Zentral-Afghanistan, Geologisches Jahrbuch, 242 p.

Wirtz, D., Hinze, C., Gabert, G., Benda, L., Weippert, D., and Fesefeldt, K., editors, 1964, Zur Geologie von Nordost- und Zentral-Afghanistan: Hannover, Bundesanstalt für Bodenforschung.

Wolfart, R., and Wittekindt, H., 1980, Geologie von Afghanistan: Von Reinhard Wolfart u. Hanspeter Wittekindt. Mit 76 Abb., 41 Tab. u. 3 Übersichtskt. im Text u. auf 16 Beil: Berlin, Stuttgart, Borntraeger, Beiträge zur regionalen Geologie der Erde, Volume 14, 500 p.

Wood, D.A., Gibson, I.L., and Thompson, R.N., 1976, Elemental mobility during zeolite facies metamorphism of the Tertiary basalts of eastern Iceland: Contributions to Mineralogy and Petrology, v. 55, no. 3, p. 241–254, doi: 10.1007/BF00371335.

Woodhead, J.D., and Hergt, J.M., 2001, Strontium, neodymium and lead isotope analyses of NIST glass certified reference materials: SRM 610, 612, 614: Geostandards Newsletter, v. 25, 2-3, p. 261–266.

Worthington, J.R., Kapp, P., Minaev, V., Chapman, J.B., Mazdab, F.K., Ducea, M.N., Oimahmadov, I., and Gadoev, M., 2017, Birth, life, and demise of the Andean-syn-collisional Gissar arc: Late Paleozoic tectono-magmatic-metamorphic evolution of the southwestern Tian Shan, Tajikistan: Tectonics, v. 36, no. 10, p. 1861–1912.

Wu, C., Zheng, W., Zhang, P., Zhang, Z., Jia, Q., Yu, J., Zhang, H., Yao, Y., Liu, J., Han, G., and Chen, J., 2019, Oblique Thrust of the Maidan Fault and Late Quaternary Tectonic Deformation in the Southwestern Tian Shan, Northwestern China: Tectonics, v. 38, no. 8, p. 2625–2645, doi: 10.1029/2018TC005248.

Wu, F., Wan, B., Zhao, L., Xiao, W.J., and Zhu, R., 2020, Tethyan geodynamics: Acta Petrologica Sinica, v. 36, no. 6, p. 1627–1674, doi: 10.18654/1000-0569/2020.06.01.

Xiao, W., Han, F., Windley, B.F., Yuan, C., Zhou, H., and Li, J., 2003, Multiple Accretionary Orogenesis and Episodic Growth of Continents: Insights from the Western Kunlun Range, Central Asia: International Geology Review, v. 45, no. 4, p. 303–328.

Xiao, W., Windley, B.F., Hao, J.I.E., and Li, J., 2002, Arc-ophiolite obduction in the Western Kunlun Range (China): implications for the Palaeozoic evolution of central Asia: Journal of the Geological Society, v. 159, no. 5, p. 517–528.

Xiao, W.J., Windley, B.F., Chen, H.L., Zhang, G.C., and Li, J.L., 2002, Carboniferous-Triassic subduction and accretion in the western Kunlun, China: Implications for the collisional and accretionary tectonics of the northern Tibetan Plateau: Geology, v. 30, no. 4, p. 295–298.

Xiao, W.J., Windley, B.F., Liu, D.Y., Jian, P., Liu, C.Z., Yuan, C., and Sun, M., 2005, Accretionary tectonics of the Western Kunlun Orogen, China: A Paleozoic–Early Mesozoic, long-lived active continental margin with implications for the growth of Southern Eurasia: The Journal of Geology, v. 113, no. 6, p. 687–705.

Xin, W., Sun, F.-Y., Zhang, Y.-T., Fan, X.-Z., Wang, Y.-C., and Li, L., 2019, Mafic–intermediate igneous rocks in the East Kunlun Orogenic Belt, northwestern China: Petrogenesis and

implications for regional geodynamic evolution during the Triassic: Lithos, 346-347, no. 105159, p. 1–55.

Xiong, F.-H., Ma, C.-Q., Zhang, J.-Y., and Liu, B., 2012, The origin of mafic microgranular enclaves and their host granodiorites from East Kunlun, Northern Qinghai-Tibet Plateau: implications for magma mixing during subduction of Paleo-Tethyan lithosphere: Mineralogy and Petrology, v. 104, no. 3, p. 211–224.

Xu, X., Liu, C., Liu, W., Ye, B., Zhao, Z., and Ma, B., 2019, Geochronology and geochemistry of the Late Devonian–Early Carboniferous volcanic rocks in Aksu River area, western end of the East Kunlun Orogen: Geological Journal, v. 192, no. 1, p. 1–21.

Xu, Y.-G., Wei, X., Luo, Z.-Y., Liu, H.-Q., and Cao, J., 2014, The Early Permian Tarim Large Igneous Province: main characteristics and a plume incubation model: Lithos, v. 204, p. 20–35.

Yakymchuk, C., Kirkland, C.L., and Clark, C., 2018, Th/U ratios in metamorphic zircon: Journal of Metamorphic Geology, v. 36, no. 6, p. 715–737.

Yang, P., Wu, G., Nuriel, P., Nguyen, A.D., Chen, Y., Yang, S., Feng, Y., Ren, Z., and Zhao, J., 2021, In situ LA-ICPMS UPb dating and geochemical characterization of fault-zone calcite in the central Tarim Basin, northwest China: Implications for fluid circulation and fault reactivation: Chemical Geology, v. 568, no. 120125, p. 1–12.

Yang, S.-F., Li, Z., Chen, H.-L., Chen, W., and Yu, X., 2006, 40 Ar-39 Ar dating of basalts from Tarim Basin, NW China and its implication to a Permian thermal tectonic event: Journal of Zhejiang University-Science A, v. 7, no. 2, p. 320–324.

Ye, H.-M., Li, X.-H., Li, Z.-X., and Zhang, C.-L., 2008, Age and origin of high Ba–Sr appinite–granites at the northwestern margin of the Tibet Plateau: implications for early Paleozoic tectonic evolution of the Western Kunlun orogenic belt: Gondwana Research, v. 13, no. 1, p. 126–138.

Yin, A., and Harrison, T.M., 2000, Geologic evolution of the Himalayan-Tibetan orogen: Annual Review of Earth and Planetary Sciences, v. 28, no. 1, p. 211–280.

Yin, J., Xiao, W., Sun, M., Chen, W., Yuan, C., Zhang, Y., Wang, T., Du, Q., Wang, X., and Xia, X., 2020, Petrogenesis of Early Cambrian granitoids in the western Kunlun orogenic belt, Northwest Tibet: Insight into early stage subduction of the Proto-Tethys Ocean: Bulletin, v. 132, 9-10, p. 2221–2240.

Yu, X., Yang, S.-F., Chen, H.-L., Chen, Z.-Q., Li, Z., Batt, G.E., and Li, Y.-Q., 2011, Permian flood basalts from the Tarim Basin, Northwest China: SHRIMP zircon U–Pb dating and geochemical characteristics: Gondwana Research, v. 20, 2-3, p. 485–497.

Yu, X.F., Sun, F.Y., Li, B.L., Ding, Q.F., Chen, G.J., Ding, Z.J., Chen, J., and Huo, L., 2011, Caledonian diagenetic and metallogenic events in Datong district in the western Kunlun: Evidences from LA-ICP-MS zircon U-Pb dating and molybdenite Re-Os dating: Acta

Petrologica Sinica, v. 27, no. 6, p. 1770–1778.

Yuan, C., Sun, M., Zhou, M., Xiao, W., and Zhou, H., 2005, Geochemistry and petrogenesis of the Yishak Volcanic Sequence, Kudi ophiolite, West Kunlun (NW China): implications for the magmatic evolution in a subduction zone environment: Contributions to Mineralogy and Petrology, v. 150, no. 2, p. 195–211, doi: 10.1007/s00410-005-0012-0.

Yuan, C., Sun, M., Zhou, M., Zhou, H., Xiao, W., and Li, J., 2002, Tectonic Evolution of the West Kunlun: Geochronologic and Geochemical Constraints from Kudi Granitoids: International Geology Review, v. 44, no. 7, p. 653–669, doi: 10.2747/0020-6814.44.7.653.

Yuan, S., Neubauer, F., Liu, Y., Genser, J., Liu, B., Yu, S., Chang, R., and Guan, Q., 2020, Widespread Permian granite magmatism in Lower Austroalpine units: significance for Permian rifting in the Eastern Alps: Swiss Journal of Geosciences, v. 113, no. 1, p. 1–25, doi: 10.1186/s00015-020-00371-5.

Yue, Y., Ritts, B.D., and Graham, S.A., 2001, Initiation and long-term slip history of the Altyn Tagh fault: International Geology Review, v. 43, no. 12, p. 1087–1093.

Yusupkhodzhayev, K.I., and Khasanov, P.K., 1978, Study of the crust structure along the Arys'-Tashkent-Osh-Zorkul' profile from gravimetric date: International Geology Review, v. 20, no. 6, p. 677–682, doi: 10.1080/00206817809471437.

Zanchetta, S., Berra, F., Zanchi, A., Bergomi, M., Caridroit, M., Nicora, A., and Heidarzadeh, G., 2013, The record of the Late Palaeozoic active margin of the Palaeotethys in NE Iran: constraints on the Cimmerian orogeny: Gondwana Research, v. 24, 3-4, p. 1237–1266.

Zanchi, A., Zanchetta, S., Balini, M., and Ghassemi, M.R., 2016, Oblique convergence during the Cimmerian collision: evidence from the Triassic Aghdarband Basin, NE Iran: Gondwana Research, v. 38, p. 149–170.

Zhang, C., Lu, S., Yu, H., and Ye, H., 2007, Tectonic evolution of the Western Kunlun orogenic belt in northern Qinghai-Tibet Plateau: Evidence from zircon SHRIMP and LA-ICP-MS U-Pb geochronology: Science in China Series D: Earth Sciences, v. 50, no. 6, p. 825–835, doi: 10.1007/s11430-007-2051-z.

Zhang, C., Yu, H., Ye, H., Zhao, Y., and Zhang, D., 2006, Aoyitake plagiogranite in western Tarim Block, NW China: Age, geochemistry, petrogenesis and its tectonic implications: Science in China Series D: Earth Sciences, v. 49, no. 11, p. 1121–1134, doi: 10.1007/s11430-006-1121-y.

Zhang, C.-L., Li, Z.-X., Li, X.-H., Xu, Y.-G., Zhou, G., and Ye, H.-M., 2010, A Permian large igneous province in Tarim and Central Asian orogenic belt, NW China: Results of a ca. 275 Ma mantle plume?: GSA Bulletin, v. 122, 11-12, p. 2020–2040.

Zhang, C.-L., Zou, H.-B., Li, H.-K., and Wang, H.-Y., 2013, Tectonic framework and evolution of the Tarim Block in NW China: Gondwana Research, v. 23, no. 4, p. 1306–1315, doi: 10.1016/j.gr.2012.05.009.

Zhang, C.-L., Zou, H.-B., Ye, X.-T., and Chen, X.-Y., 2018, Tectonic evolution of the NE section of the Pamir Plateau: New evidence from field observations and zircon U-Pb geochronology: Tectonophysics, v. 723, p. 27–40.

Zhang, C.-L., Zou, H.-B., Ye, X.-T., and Chen, X.-Y., 2018, Tectonic evolution of the West Kunlun Orogenic Belt along the northern margin of the Tibetan Plateau: Implications for the assembly of the Tarim terrane to Gondwana: Geoscience Frontiers, v. 10, no. 3, p. 973–988.

Zhang, D., Zhou, T., Yuan, F., Jowitt, S.M., Fan, Y., and Liu, S., 2012, Source, evolution and emplacement of Permian Tarim Basalts: Evidence from U–Pb dating, Sr–Nd–Pb–Hf isotope systematics and whole rock geochemistry of basalts from the Keping area, Xinjiang Uygur Autonomous region, northwest China: Journal of Asian Earth Sciences, v. 49, p. 175–190, doi: 10.1016/j.jseaes.2011.10.018.

Zhang, P.-Z., Molnar, P., and Xu, X., 2007, Late Quaternary and present-day rates of slip along the Altyn Tagh Fault, northern margin of the Tibetan Plateau: Tectonics, v. 26, no. 5, p. 1–24, doi: 10.1029/2006TC002014.

Zhang, P.-Z., Shen, Z., Wang, M., Gan, W., Bürgmann, R., Molnar, P., Wang, Q., Niu, Z., Sun, J., Wu, J., Hanrong, S., and Xinzhao, Y., 2004, Continuous deformation of the Tibetan Plateau from global positioning system data: Geology, v. 32, no. 9, p. 809–812, doi: 10.1130/G20554.1.

Zhang, Q., Liu, Y., Wu, Z., Huang, H., Li, K., and Zhou, Q., 2019, Late Triassic granites from the northwestern margin of the Tibetan Plateau, the Dahongliutan example: petrogenesis and tectonic implications for the evolution of the Kangxiwa Palaeo-Tethys: International Geology Review, v. 61, no. 2, p. 175–194.

Zhang, Q., Wu, Z., Chen, X., Zhou, Q., and Shen, N., 2019, Proto-Tethys oceanic slab break-off: Insights from early Paleozoic magmatic diversity in the West Kunlun Orogen, NW Tibetan Plateau: Lithos, v. 346, no. 105147, p. 1–15.

Zhang, S., LIU, C., BAI, J., Wang, J., MA, M., GUAN, Y., and Peng, H., 2019, Provenance Variability of the Triassic Strata in the Turpan-Hami Basin: Detrital Zircon Record of Indosinian Tectonic Reactivation in the Eastern Tianshan: Acta Geologica Sinica - English Edition, v. 93, no. 6, p. 1850–1868.

Zhang, Y., Niu, Y., Hu, Y., Liu, J., Ye, L., Kong, J., and Duan, M., 2016, The syncollisional granitoid magmatism and continental crust growth in the West Kunlun Orogen, China – Evidence from geochronology and geochemistry of the Arkarz pluton: Lithos, v. 245, p. 191–204, doi: 10.1016/j.lithos.2015.05.007.

Zhao, W., Zhang, S., Wang, F., Cramer, B., Chen, J., Sun, Y., Zhang, B., and Zhao, M., 2005, Gas systems in the Kuche Depression of the Tarim Basin: Source rock distributions, generation kinetics and gas accumulation history: Organic Geochemistry, v. 36, no. 12, p. 1583–1601.

Zhao, X., Fu, L., Wei, J., Bagas, L., Santosh, M., Liu, Y., Zhang, D., and Zhou, H., 2019, Late

Permian back-arc extension of the eastern Paleo-Tethys Ocean: Evidence from the East Kunlun Orogen, Northern Tibetan Plateau: Lithos, 340-341, p. 34–48.

Zheng, Y., and Wu, F., 2018, The timing of continental collision between India and Asia: Science Bulletin, v. 63, no. 24, p. 1649–1654, doi: 10.1016/j.scib.2018.11.022.

Zhong, Y.-T., Luo, Z.-Y., Mundil, R., Wei, X., Liu, H.-Q., He, B., Huang, X.-L., Tian, W., and Xu, Y.-G., 2022, Constraining the duration of the Tarim flood basalts (northwestern China): CA-TIMS zircon U-Pb dating of tuffs: Geological Society of America Bulletin, v. 134, 1-2, p. 325–334.

Zhou, R., Aitchison, J.C., Lokho, K., Sobel, E.R., Feng, Y., and Zhao, J., 2020, Unroofing the Ladakh Batholith: constraints from autochthonous molasse of the Indus Basin, NW Himalaya: Journal of the Geological Society.

Zhou, R., Aitchison, J.C., Lokho, K., Sobel, E.R., Feng, Y., and Zhao, J., 2020, Unroofing the Ladakh Batholith: constraints from autochthonous molasse of the Indus Basin, NW Himalaya, v. 177, no. 4, p. 818–825.

Zhu, G., Liu, W., Wu, G., Ma, B., Nance, R.D., Wang, Z., Xiao, Y., and Chen, Z., 2021, Geochemistry and U-Pb-Hf detrital zircon geochronology of metamorphic rocks in terranes of the West Kunlun Orogen: Protracted subduction in the northernmost Proto-Tethys Ocean: Precambrian Research, v. 363, no. 106344, p. 1–18.

Zhu, W., Shenghe, W.U., Zhijun, Y.I., Tao, H.A., Yiming, W.U., Yong, L.I., Wenjie, F., Ya'nan, L.U., and Cao, C., 2016, Braided river delta outcrop architecture: A case study of Triassic Huangshanjie Formation in Kuche depression, Tarim Basin, NW China: Petroleum Exploration and Development, v. 43, no. 3, p. 528–536.

Zlavdinov, I.Z., 1982, Structure of the lithosphere along the Tien Shan—Pamir—Karakorum—Himalaya profile: International Geology Review, v. 24, no. 4, p. 419–421, doi: 10.1080/00206818209452424.

Zonenshain, L.P., and Pichon, X., 1986, Deep basins of the Black Sea and Caspian Sea as remnants of Mesozoic back-arc basins: Tectonophysics, v. 123, 1-4, p. 181–211.

Zubovich, A.V., Wang, X., Scherba, Y.G., Schelochkov, G.G., Reilinger, R., Reigber, C., Mosienko, O.I., Molnar, P., Michajljow, W., and Makarov, V.I., 2010, GPS velocity field for the Tien Shan and surrounding regions: Tectonics, v. 29, no. 6, p. 1–23.

Zuleger, E., and Erzinger, J., 1988, Determination of the REE and Y in silicate materials with ICP-AES: Fresenius' Zeitschrift für Analytische Chemie, v. 332, no. 2, p. 140–143.

Appendix

A. Supplementary Material for Chapter 2

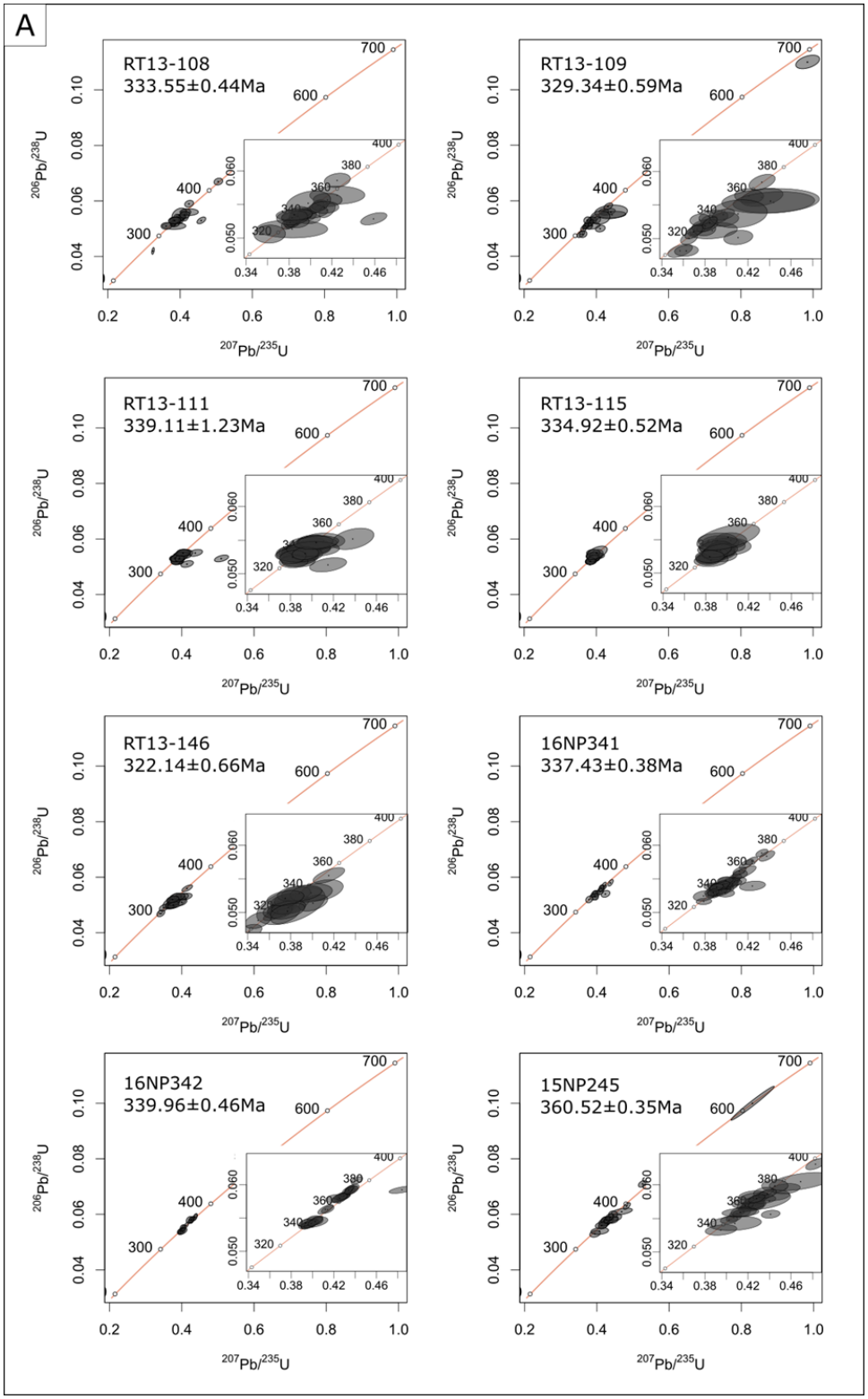

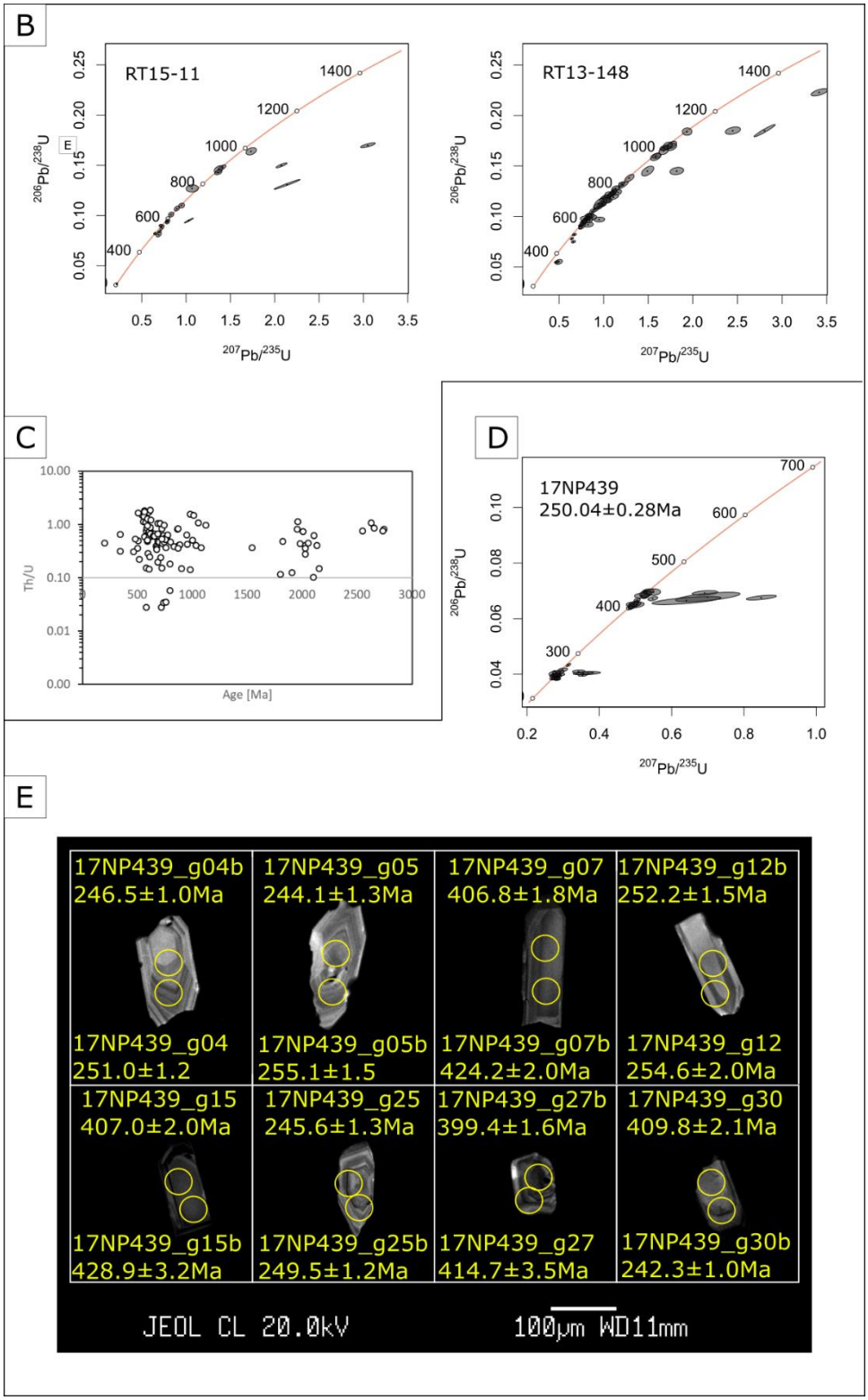

Appendix A.1: Igneous and detrital zircon age data plots. (A) U-Pb Wetherill Concordia plots of all granitoid samples dated in this study. Age range of large figures is 200–700 Ma, small insets show age range between 300 and 400 Ma. (B) U-Pb Wetherill concordia plots of the two detrital zircon samples from the Kurguvad paragneiss. (C) Th/U ratios are similar for all age groups and show typical magmatic zircon values. (D) U-Pb Wetherill concordia plot of the zircons extracted from an aplitic dyke in the lower Qimgan basin. Two zircon populations can be distinguished: an inherited upper Silurian to lower Devonian group and a younger group which is interpreted as the formation age of the dyke. (E) Typical CL images of zircons in sample 17NP439 with two single-spot ages per zircon grain. Overgrowth of younger zircon on an inherited core is rare (cf. 17NP439_g30).

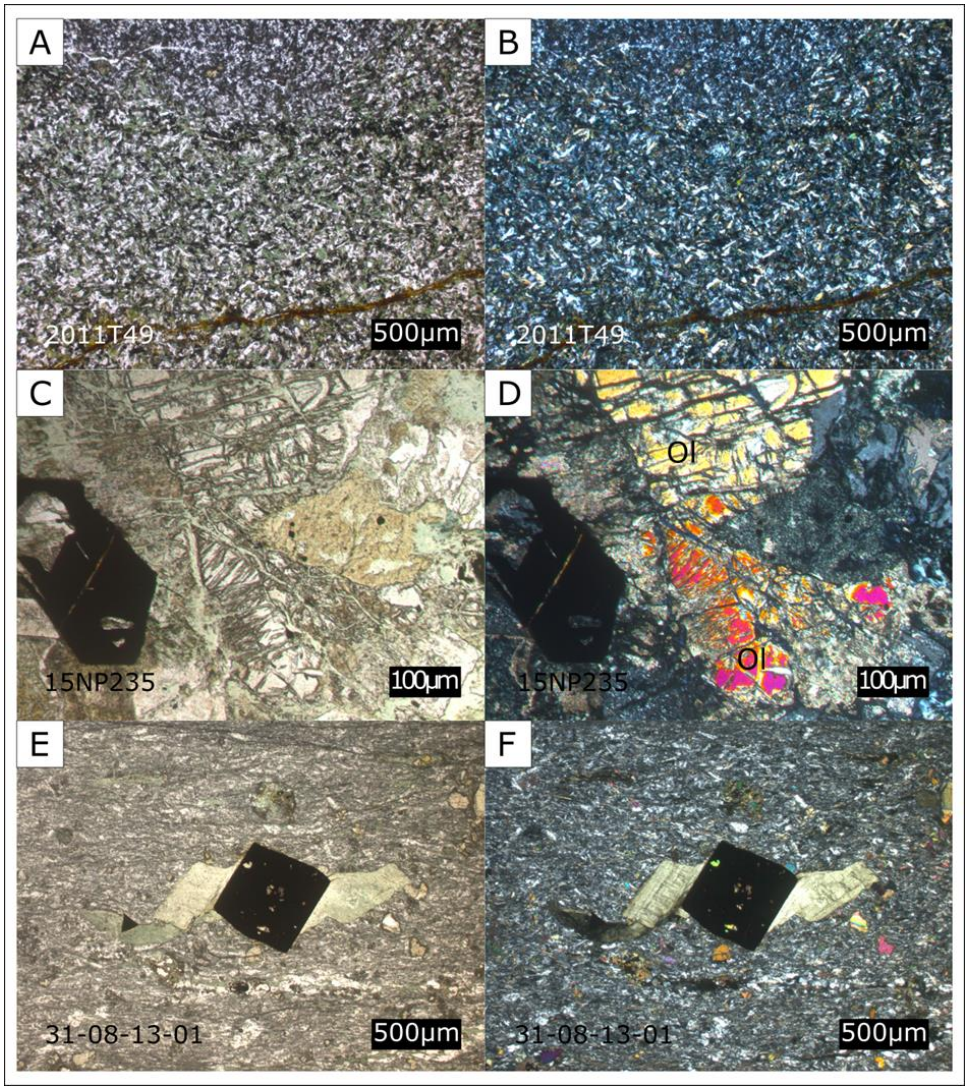

Appendix A.2: Microphotographs of volcanic rocks. (A,B) Dolerite from upper Qimgan valley with typical greenschist facies mineral association in plane (A) and cross (B) polarized light. (C,D) Olivine bearing basalt from lower Qimgan valley in plane (A) and cross (B) polarized light. (E,F) Sheared basaltic andesite from Altyn Darya, showing fragments of amphiboles in matrix and metamorphic chlorite and epidote in plane (A) and cross (B) polarized light.

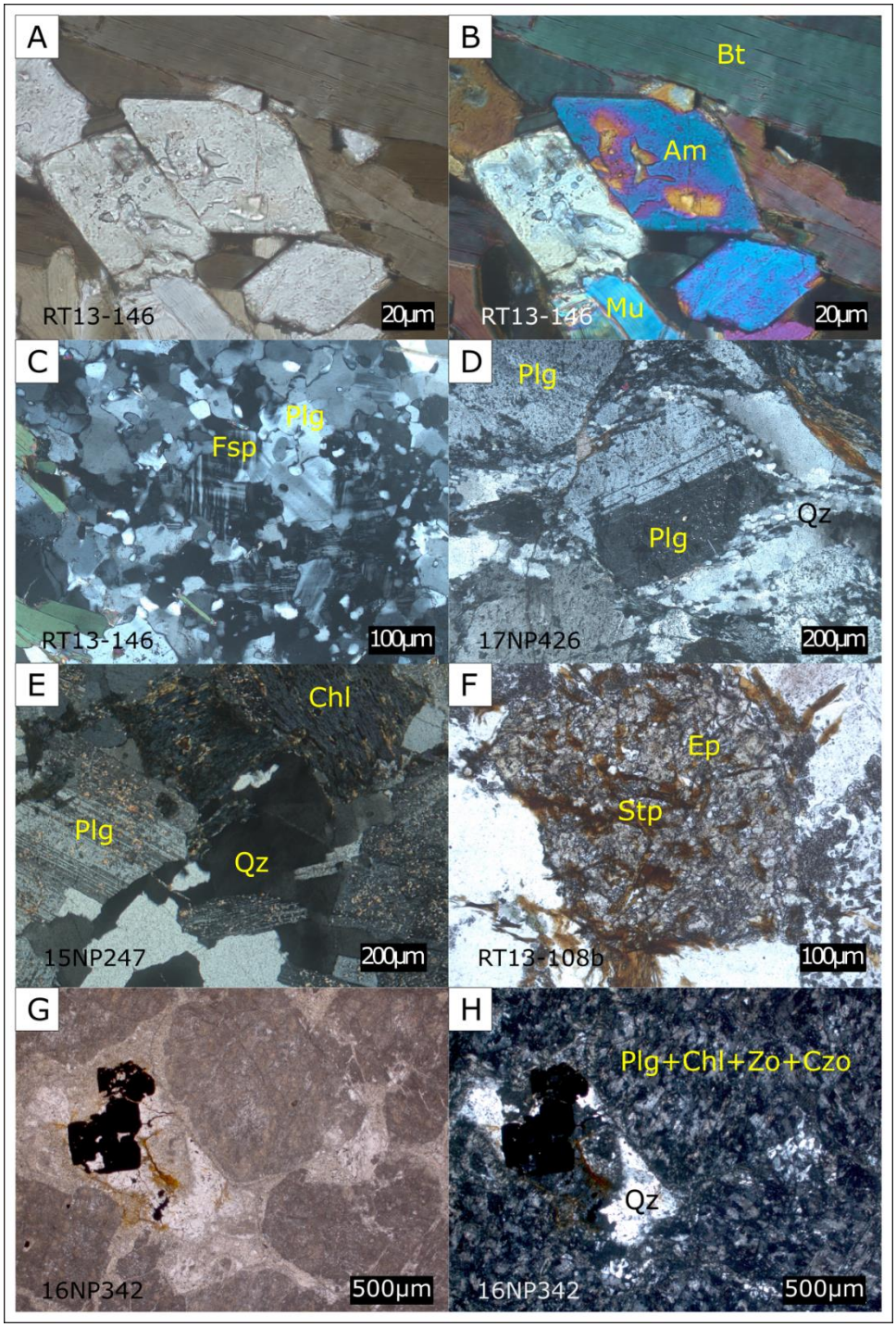

Appendix A.3: Microphotographs of plutonic rocks. Small, idiomorphic amphiboles together with large biotite and small muscovite crystals in granodiorite sample RT13-146 from the Kurguvad intrusion in plane (A) and cross (B) polarized light. (C) Microclinic feldspar and plagioclase in sample RT13-146 from the Kurguvad intrusion showing evidence of recrystallization in cross polarized light. (D) Plagioclase crystal showing intact magmatic shape and recrystallized quartz crystals in tonalite sample 17NP426 from the Gez intrusion. Plagioclases form porphyroclasts in a mylonitic shear zone between the Karakul-Mazar derived Shala Tala nappe and the Gez tonalite. (E) Magmatic fabric in sample 15NP247 from Taergelake granite with metamorphic chlorite. Plagioclase shows initial saussuritization. (F) Low-grade metamorphic mineral association in sample RT13-108 with epidote and stilpnomelane. (G,H) Plagioclase cumulate sample 16NP342 with preserved primary fabric. Plagioclase is almost completely replaced by greenschist-facies minerals chlorite and zoisite. Quartz and opaque minerals are present as interstitial phases. Microphotograph in plane (G) and cross (H) polarized light.

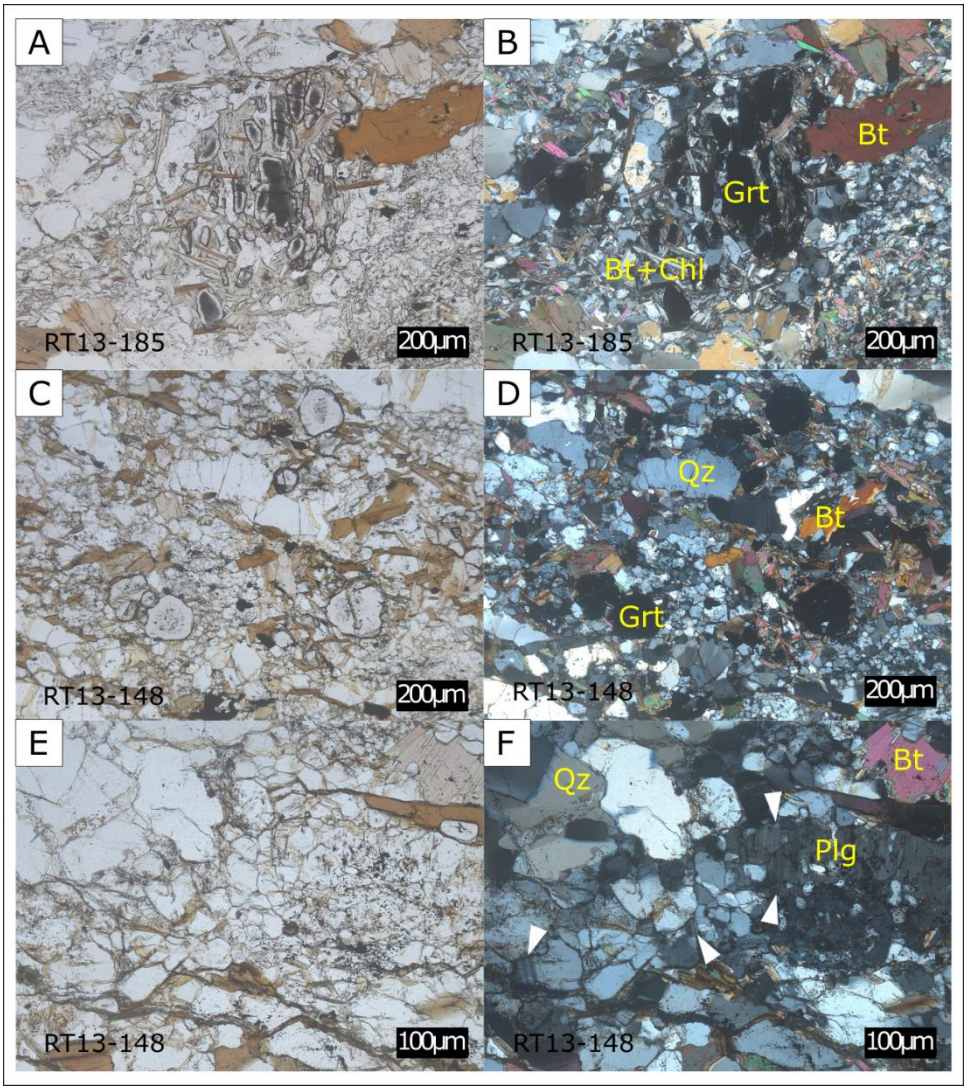

Appendix A.4: Microphotographs of paragneiss samples. Fabric of the paragneiss samples from the Kurguvad basement complex, which forms the host rock of the Kurguvad granodiorite and was part of the Carboniferous island arc. Garnets in sample RT13-185 show complex fabric (A plane, B cross polarized light). In a first phase, up to 500 µm large garnets grew. Those where replaced by fine-grained biotite, first along fractures in the garnet. This process stopped and small, inclusion rich remnants of the old garnet remained. A second, clear garnet generation grew around the old remnants. The fine-grained biotite that replaced the first-generation garnet was partly replaced by chlorite later. Sample RT13-148 (C plane, D cross polarized light) also shows two stages of garnet growth, with an older, inclusion-rich core and a younger, clear rim. However, no evidence of garnet break-down was found. Feldspar is not abundant in either samples. It can be found in small, fragmented grains (E plane, F cross polarized light) that show recrystallization (arrows).

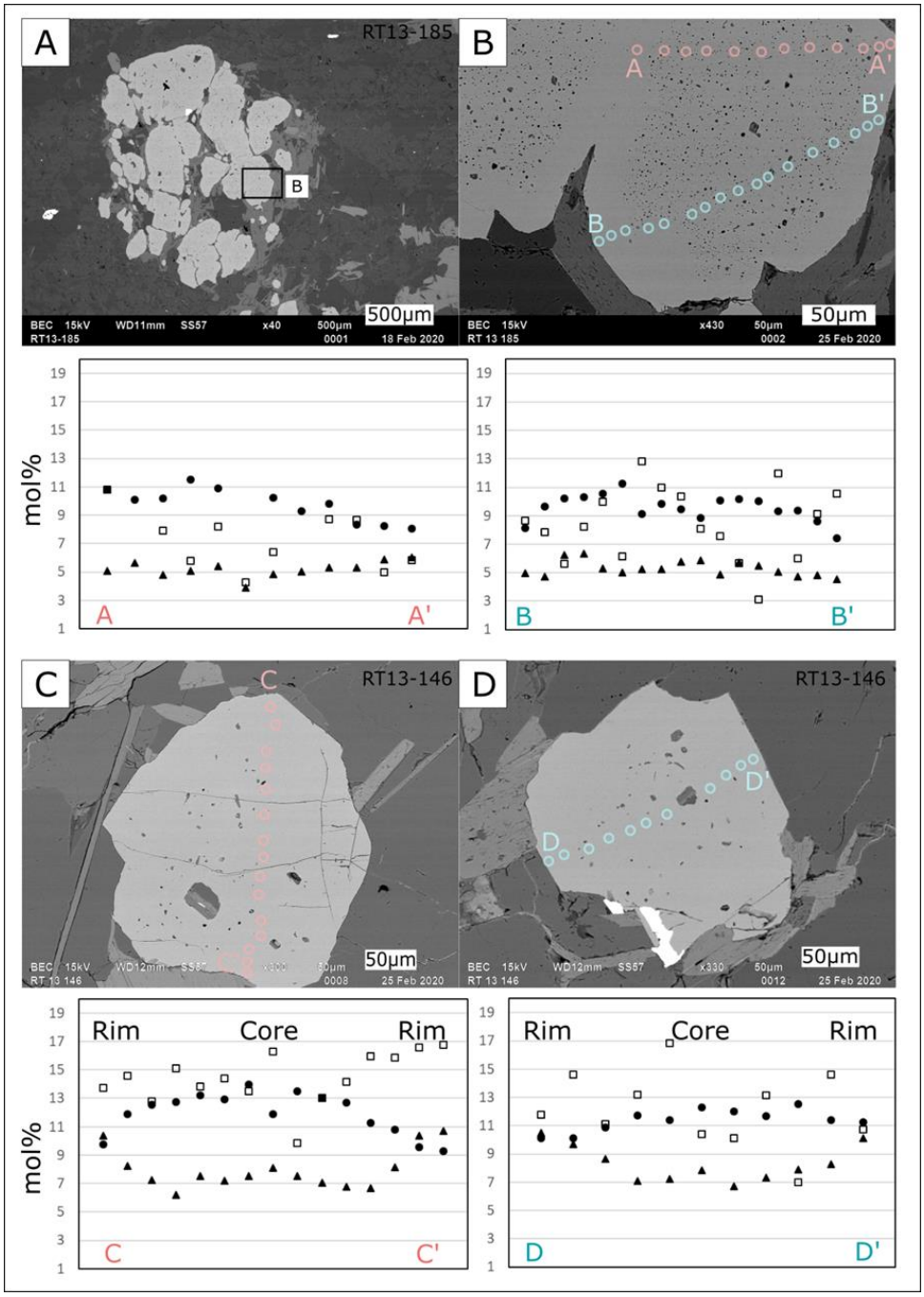

Appendix A.5: SEM microphotographs of garnet from Kurguvad paragneiss. Semi-quantitative profiles carried out on a scanning electron microscope using an Energy Dispersive X-ray detector (EDX). All garnets are identified as Almandine with XFe values between 70 and 84 mol%. They show weak core and rim differences in Pyrope (XMg, black dots) and Spessartine (XMn, triangles) content in sample RT13-185 (A, B). Clearer core-rim difference for these components is seen in sample RT13-146 (C, D). The Grossular (XCa, squares) component does not reflect that trend. Both samples are from the Kurguvad paragneiss sampled in the Panj valley.

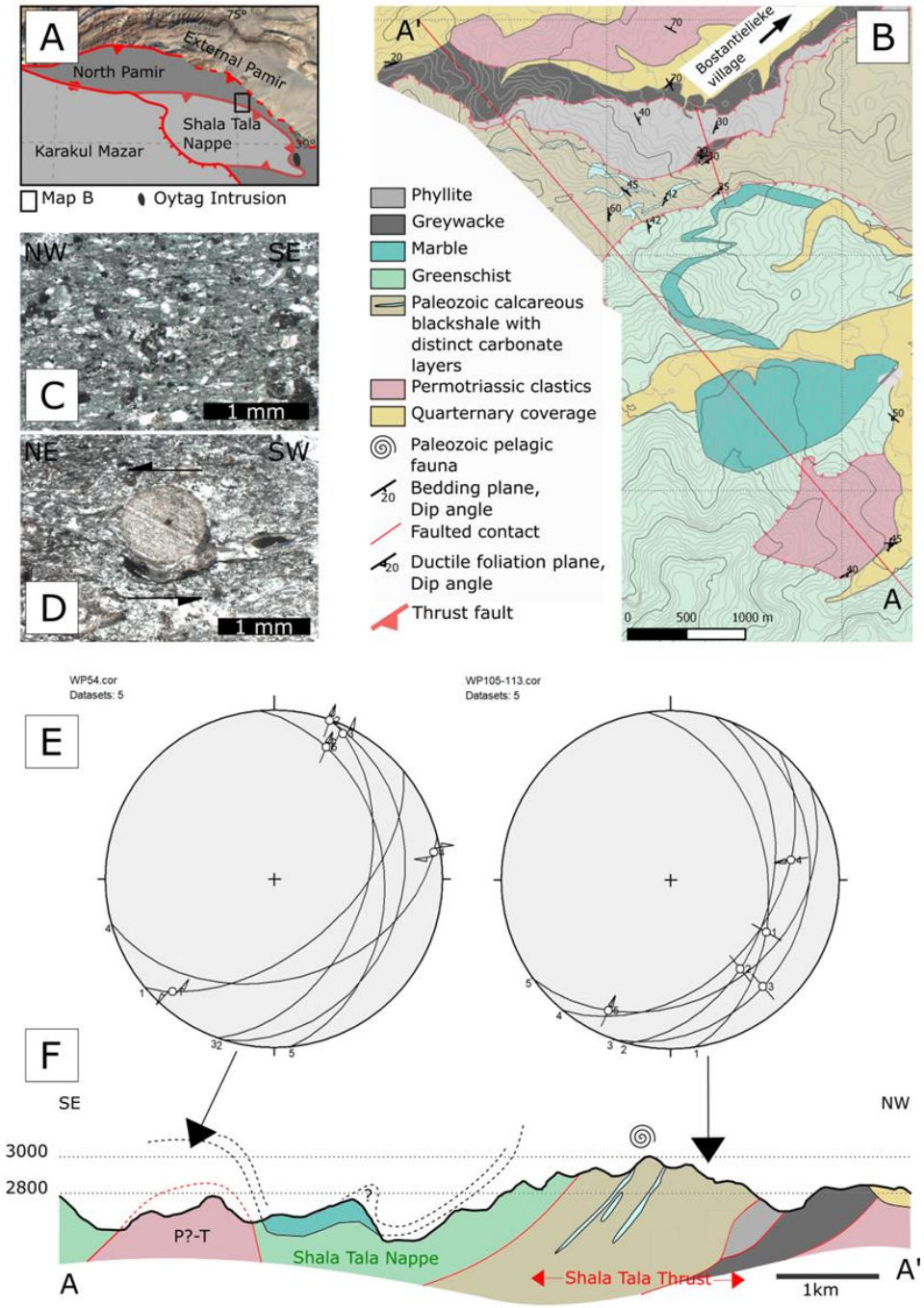

Appendix A.6: Map of the Shala Tala nappe, NE Pamir. (A, B) Overview map, showing the position of the Shala Tala Nappe (A after Robinson et al. [23]) and the location of map B. Microphotograph (C) shows a greenschist thin section, cut perpendicular to main transport direction, (D) marl sample with crinoid fragment, showing SW–NE transport direction. Schmidt net projections (E) show SE to E ward dipping foliation and NE to NW ward transport direction. Field data was collected along a transect A–A' (map B). The section crosses the Shala Tala thrust that places the greenschist to amphibolite facies Shala Tala Nappe on top of the lower greenschist facies North Pamir. Strongly sheared, marine, Paleozoic units are incorporated in the thrust zone. They comprise black shales, phyllitic shales, turbiditic greywackes and fossiliferous dark marls.

Appendix A.7: LA-ICP-MS zircon U-Pb data tables. Error correlation is calculated as the quotiend of the propagated relative errors. Discordance is calculated as [1 - (206/238 age)/(207/206 age)] x 100 and [1 - (206/238 age)/(207/235 age)] x 100 respectively. We used 206/238 vs. 207/206 Discordance as critical parameter.

Sample RT13-108	Sample Type: igneous					Latitude:	38.75177	Longitude:	71.23224											
	Conventional concordia								Ages						Discordance		~U[ppm]	Th/U		
Sample #	207Pb	±2σ	206Pb	±2σ	error corr.	207Pb	±2σ	206Pb	±2σ	207Pb	±2σ	Best Age	±1σ	206/238	206/238					
grain number	235U		238U		206/238 vs 207/235	235U		238U		206Pb				207/206	207/235					
RT13-108_g001	0.325	0.003	0.042	0.001	0.429	286.0	2.5	262.4	3.3	462.0	25.0	262.4	1.7	43%	8%	3260	0.48			
RT13-108_g002	0.383	0.027	0.051	0.001	-0.010	327.0	20.0	322.8	6.7	320.0	160.0	322.8	3.4	-1%	1%	85	0.73			
RT13-108_g003	0.379	0.005	0.052	0.001	0.355	326.4	3.9	327.5	4.1	328.0	30.0	327.5	2.1	0%	0%	917	0.33			
RT13-108_g004	0.397	0.007	0.053	0.001	0.262	339.2	5.1	334.8	3.9	365.0	42.0	334.8	2.0	8%	1%	670	0.41			
RT13-108_g005	0.397	0.010	0.053	0.001	-0.075	338.7	7.3	333.2	4.4	404.0	60.0	333.2	2.2	18%	2%	297	0.48			
RT13-108_g006	0.403	0.011	0.054	0.001	0.253	345.1	8.1	338.4	4.5	380.0	58.0	338.4	2.3	11%	2%	142	0.32			
RT13-108_g007	0.395	0.006	0.054	0.001	0.055	337.8	4.1	337.5	3.8	342.0	32.0	337.5	1.9	1%	0%	704	0.31			
RT13-108_g008	0.425	0.010	0.059	0.001	0.222	359.4	7.5	367.2	5.3	305.0	53.0	367.2	2.7	-20%	-2%	255	0.36			
RT13-108_g009	0.383	0.009	0.053	0.001	-0.083	329.1	6.2	333.2	3.9	287.0	53.0	333.2	2.0	-16%	-1%	262	0.54			
RT13-108_g010	0.384	0.006	0.052	0.001	0.585	330.8	4.5	328.8	4.6	348.0	29.0	328.8	2.3	6%	1%	1170	0.39			
RT13-108_g011	0.385	0.010	0.053	0.001	0.201	330.8	7.3	333.7	4.2	302.0	60.0	333.7	2.1	-10%	-1%	177	0.52			
RT13-108_g012	0.404	0.006	0.054	0.001	0.382	345.2	4.2	341.7	3.8	368.0	33.0	341.7	1.9	7%	1%	872	0.32			
RT13-108_g013	0.506	0.010	0.067	0.001	0.182	415.4	6.6	419.1	4.6	396.0	42.0	419.1	2.3	-6%	-1%	448	0.28			
RT13-108_g014	0.362	0.012	0.051	0.001	0.046	313.8	9.2	318.1	6.6	325.0	93.0	318.1	3.3	2%	-1%	506	0.51			
RT13-108_g015	0.425	0.021	0.056	0.001	0.020	363.0	14.0	353.6	6.6	430.0	120.0	353.6	3.3	18%	3%	465	0.25			
RT13-108_g016	0.385	0.005	0.052	0.001	0.324	330.6	3.6	328.8	3.5	320.0	30.0	328.8	1.8	-3%	1%	709	0.44			
RT13-108_g017	0.388	0.009	0.052	0.001	0.168	333.0	6.5	328.8	4.1	377.0	52.0	328.8	2.1	13%	1%	263	0.41			
RT13-108_g018	0.385	0.004	0.053	0.001	0.029	330.5	3.0	331.2	3.5	315.0	27.0	331.2	1.8	-5%	0%	1047	0.41			
RT13-108_g019	0.074	0.008	0.001	0.000	0.236	71.7	7.3	8.2	0.5	3890.0	160.0	8.2	0.3	100%	89%	212	1.00			
RT13-108_g020	0.409	0.006	0.055	0.001	0.141	348.2	4.4	344.4	4.2	346.0	40.0	344.4	2.1	0%	1%	607	0.49			
RT13-108_g021	4.934	0.049	0.318	0.004	0.620	1807.6	8.5	1777.0	18.0	1862.0	17.0	1862.0	8.5	5%	2%	292	0.99			
RT13-108_g022	0.391	0.007	0.054	0.001	-0.043	336.2	5.5	338.7	4.0	315.0	46.0	338.7	2.0	-8%	-1%	350	0.39			
RT13-108_g023	0.381	0.005	0.052	0.001	0.291	327.8	3.7	328.8	3.6	325.0	31.0	328.8	1.8	-1%	0%	1005	0.34			
RT13-108_g024	0.407	0.005	0.055	0.001	0.249	346.9	3.4	344.4	3.5	347.0	27.0	344.4	1.8	1%	1%	809	0.27			
RT13-108_g025	0.416	0.011	0.056	0.001	-0.003	352.9	8.0	349.4	5.0	376.0	65.0	349.4	2.5	7%	1%	716	0.31			
RT13-108_g026	0.416	0.006	0.054	0.001	0.461	352.7	4.5	339.9	5.5	409.0	34.0	339.9	2.8	17%	4%	1070	0.37			
RT13-108_g027	0.398	0.017	0.055	0.002	0.306	339.0	13.0	346.5	9.1	232.0	100.0	346.5	4.6	-49%	-2%	159	0.44			
RT13-108_g028	0.395	0.005	0.053	0.001	0.065	337.9	3.9	335.9	3.9	357.0	36.0	335.9	2.0	6%	1%	978	0.44			
RT13-108_g029	0.388	0.007	0.053	0.001	0.221	333.7	4.8	334.4	4.7	304.0	44.0	334.4	2.4	-10%	0%	851	0.41			
RT13-108_g030	0.459	0.010	0.053	0.001	0.514	383.8	7.1	332.1	4.6	698.0	40.0	332.1	2.3	52%	13%	742	0.39			
RT13-108_g031	0.413	0.011	0.055	0.001	0.063	350.6	8.2	342.5	4.5	447.0	72.0	342.5	2.3	23%	2%	334	0.50			
RT13-108_g032	0.383	0.012	0.053	0.001	0.117	328.4	9.0	333.1	5.4	310.0	76.0	333.1	2.7	-7%	-1%	229	0.41			
RT13-108_g033	0.385	0.014	0.053	0.001	0.165	330.0	11.0	336.2	4.4	258.0	81.0	336.2	2.2	-30%	-2%	105	0.27			

Sample RT13-109	Sample Type: igneous					Latitude:	38.74758	Longitude:	71.23323								
	Conventional concordia					Ages								Discordance		~U[ppm]	Th/U
Sample #	207Pb	±2σ	206Pb	±2σ	error corr.	207Pb	±2σ	206Pb	±2σ	207Pb	±2σ	Best Age	±1σ	206/238	206/238		
_grain number	235U		238U		206/238 vs 207/235	235U		238U		206Pb				207/206	207/235		
RT13-109_g001	0.357	0.0094	0.0482	0.00081	0.50437	310.1	7	303.5	5	343	54	303.5	2.5	0.1151603	0.0212835	276	0.6199628
RT13-109_g002	0.365	0.0065	0.05005	0.00078	0.40104	316	4.9	314.8	4.8	333	40	314.8	2.4	0.0546547	0.0037975	1129	0.5521811
RT13-109_g003	0.387	0.019	0.05119	0.001	0.20304	333	13	321.8	6.1	370	100	321.8	3.05	0.1302703	0.0336336	62.03	0.3225806
RT13-109_g004	0.411	0.011	0.05017	0.00087	0.19957	349.3	8.2	315.5	5.3	561	61	315.5	2.65	0.4376114	0.096765	292.3	0.5154639
RT13-109_g005	0.384	0.0063	0.05252	0.00077	0.2449	329.9	4.7	329.9	4.7	318	44	329.9	2.35	-0.0374214	0	493	0.4282655
RT13-109_g006	0.38	0.0084	0.05137	0.00077	0.10318	326.4	6.1	322.9	4.7	361	52	322.9	2.35	0.1055402	0.010723	255	0.3029385
RT13-109_g007	0.381	0.0068	0.05191	0.00076	0.5403	327.6	5	326.2	4.7	358	33	326.2	2.35	0.0888268	0.0042735	1196	0.3861004
RT13-109_g008	0.398	0.011	0.05287	0.00085	0.18499	339.6	7.7	332.1	5.2	382	60	332.1	2.6	0.1306283	0.0220848	385	0.5271481
RT13-109_g009	0.373	0.006	0.05136	0.00072	0.40543	321.7	4.5	322.9	4.4	260	35	322.9	2.2	-0.2419231	-0.0037302	1462	0.3570154
RT13-109_g010	0.388	0.011	0.05321	0.00084	0.18951	333.2	8	334.2	5.1	315	62	334.2	2.55	-0.0609524	-0.0030012	163.4	0.2354603
RT13-109_g011	0.433	0.016	0.05616	0.0011	0.3643	364	11	352.2	6.8	401	82	352.2	3.4	0.1216958	0.0324176	192	0.1683502
RT13-109_g012	0.421	0.011	0.05635	0.00089	-0.038036	358	7.9	353.4	5.4	417	68	353.4	2.7	0.152518	0.0128492	806	0.6410256
RT13-109_g013	0.244	0.0037	0.03468	0.00049	0.51113	221.7	3.1	219.8	3.1	240	33	219.8	1.55	0.0841667	0.0085701	1176	0.1114827
RT13-109_g014	0.397	0.0085	0.05358	0.0007	0.40955	340.4	6.2	336.4	4.3	342	42	336.4	2.15	0.0163743	0.0117509	392	0.5291005
RT13-109_g015	0.38	0.01	0.05194	0.00075	0.34286	326.9	7.2	326.4	4.6	324	56	326.4	2.3	-0.0074074	0.0015295	203.1	0.5107252
RT13-109_g016	0.37	0.0069	0.05103	0.00087	0.59989	319.2	5.1	320.8	5.4	299	36	320.8	2.7	-0.0729097	-0.0050125	644	0.4071661
RT13-109_g017	3.36	0.13	0.2231	0.004	0.56311	1498	29	1298	21	1765	59	1765	29.5	0.2645892	0.1335113	74.2	0.0895255
RT13-109_g018	0.375	0.0076	0.0528	0.00071	0.14565	324.2	5.8	331.7	4.4	284	50	331.7	2.2	-0.1679577	-0.0231339	567	0.3306878
RT13-109_g019	0.444	0.031	0.0554	0.0013	0.18576	370	22	347.6	8	470	140	347.6	4	0.2604255	0.0605405	21	0.3087373
RT13-109_g020	0.441	0.037	0.0556	0.0015	0.15833	367	26	348.5	9.2	460	180	348.5	4.6	0.2423913	0.0504087	30.57	0.3321156
RT13-109_g021	0.363	0.009	0.04819	0.00067	0.13574	313.8	6.7	303.4	4.1	365	58	303.4	2.05	0.1687671	0.0331421	238	0.3675119
RT13-109_g022	0.411	0.022	0.0537	0.0017	0.138	349	16	337.3	10	490	150	337.3	5	0.3116327	0.0335244	294.7	0.4083299
RT13-109_g023	0.385	0.0057	0.05236	0.00074	0.57067	330.2	4.2	329	4.5	316	30	329	2.25	-0.0411392	0.0036342	1284	0.4334634
RT13-109_g024	0.433	0.01	0.05841	0.00095	0.46033	364.8	7.4	365.9	5.8	366	46	365.9	2.9	0.0002732	-0.0030154	390	0.3047851
RT13-109_g025	0.985	0.027	0.1103	0.0018	0.43814	699	15	674.3	11	837	53	674.3	5.5	0.1943847	0.0353362	294	0.4215852

Sample RT13-146	Sample Type: igneous					Latitude:	38.45605	Longitude:	71.11402								
	Conventional concordia					Ages								Discordance		~U[ppm]	Th/U
Sample #	207Pb	±2σ	206Pb	±2σ	error corr.	207Pb	±2σ	206Pb	±2σ	207Pb	±2σ	Best Age	±1σ	206/238	206/238		
_grain number	235U		238U		206/238 vs 207/235	235U		238U		206Pb				207/206	207/235		
RT13-146_g001	0.409	0.016	0.0533	0.0013	0.37206	347.7	11	334.6	7.7	455	87	334.6	3.85	0.2646154	0.0376762	278.9	0.4403347
RT13-146_g002	0.342	0.0094	0.04719	0.00087	0.39831	298.2	7.1	297.2	5.4	307	60	297.2	2.7	0.0319218	0.0033535	401	0.2704896
RT13-146_g003	5.42	0.39	0.0687	0.0042	0.49836	1900	66	427	25	4560	110	427	12.5	0.9063596	0.7752632	2.76	0.0578035
RT13-146_g004	0.372	0.011	0.05062	0.00077	0.47729	320.9	8.2	318.3	4.7	342	65	318.3	2.35	0.0692982	0.0081022	431	0.3741115
RT13-146_g005	0.378	0.016	0.05105	0.0012	0.58868	325	12	321	7.1	392	71	321	3.55	0.1811224	0.0123077	669	0.5170631
RT13-146_g006	0.38	0.026	0.051	0.0023	0.49269	326	20	320	14	450	110	320	7	0.2888889	0.0184049	1404	0.5482456
RT13-146_g007	0.812	0.038	0.05939	0.0012	0.56457	606	21	371.9	7.4	1626	74	371.9	3.7	0.7712792	0.3863036	266	0.3892565
RT13-146_g008	0.401	0.011	0.05141	0.00099	0.45056	342.9	8.6	323.2	6	502	60	323.2	3	0.3561753	0.0574512	467.6	0.533049
RT13-146_g009	0.37	0.01	0.05042	0.00086	0.39183	319.4	7.7	317.1	5.3	349	61	317.1	2.65	0.091404	0.007201	429	0.4340278
RT13-146_g010	0.368	0.011	0.04997	0.00096	0.76105	317.8	8.2	314.3	5.9	347	56	314.3	2.95	0.0942363	0.0110132	521	0.4935834
RT13-146_g011	1.135	0.065	0.02643	0.00095	0.0045986	766	30	168.1	5.9	3603	100	168.1	2.95	0.9533444	0.7805483	16.01	1.618123
RT13-146_g012	10.78	0.3	0.4713	0.0093	0.48714	2501	26	2488	41	2521	44	2521	22	0.01309	0.0051979	19.96	2.7247956
RT13-146_g013	0.376	0.01	0.05165	0.00094	0.53152	323.7	7.5	324.6	5.8	341	58	324.6	2.9	0.0480938	-0.0027804	644	0.6761325
RT13-146_g014	0.35	0.01	0.04882	0.001	0.41411	304.2	7.5	307.2	6.2	288	64	307.2	3.1	-0.0666667	-0.0098619	367.7	0.4081633
RT13-146_g015	0.375	0.011	0.04968	0.0011	0.53024	323.9	8.3	312.5	6.5	413	60	312.5	3.25	0.2433414	0.035196	598	0.4970179
RT13-146_g016	0.373	0.01	0.05159	0.0009	0.3479	321.7	7.7	324.3	5.5	296	60	324.3	2.75	-0.0956081	-0.0080821	502	0.7440476
RT13-146_g017	0.415	0.012	0.05551	0.00096	0.65257	352.4	8.4	348.9	6.1	393	57	348.9	3.05	0.1122137	0.0099319	616	0.7457122
RT13-146_g018	0.378	0.011	0.05194	0.00081	0.34532	325.2	8.3	326.4	4.9	316	64	326.4	2.45	-0.0329114	-0.00369	302.9	0.4705882
RT13-146_g019	0.368	0.011	0.05019	0.00085	0.22818	317.5	8.3	315.7	5.2	342	67	315.7	2.6	0.0769006	0.0056693	213.3	0.3025719
RT13-146_g020	0.385	0.011	0.05281	0.00089	0.24643	330.3	7.8	331.7	5.4	335	61	331.7	2.7	0.0098507	-0.0042386	409.6	0.5624297
RT13-146_g021	0.399	0.016	0.05291	0.0011	0.26595	340.1	11	332.3	6.7	394	87	332.3	3.35	0.156599	0.0229344	181.6	0.3209243
RT13-146_g022	0.378	0.013	0.05075	0.00081	0.30911	324.7	9.5	319.1	5	360	74	319.1	2.5	0.1136111	0.0172467	246	0.3266906
RT13-146_g023	0.388	0.017	0.05285	0.00098	0.30945	332	13	332	6	339	92	332	3	0.020649	0	132.6	0.3685957
RT13-146_g024	0.375	0.014	0.05212	0.00092	0.32999	322.5	10	327.5	5.6	308	77	327.5	2.8	-0.0633117	-0.0155039	221.8	0.3237294
RT13-146_g025	0.377	0.013	0.05021	0.00097	0.46591	325.4	9.2	315.8	6	381	70	315.8	3	0.1711286	0.0295022	389	0.3780718

Sample RT13-111	Sample Type: igneous												Latitude:	38.78572	Longitude:	71.21192		
	Conventional concordia					Ages								Discordance			~U[ppm]	Th/U
Sample #	207Pb	±2σ	206Pb	±2σ	error corr.	207Pb	±2σ	206Pb	±2σ	207Pb	±2σ	Best Age	±1σ	206/238	206/238			
_grain number	235U		238U		206/238 vs 207/235	235U		238U		206Pb				207/206	207/235			
RT13-111_g001	0.3911	0.0092	0.05285	0.00075	0.15935	334.6	6.7	332	4.6	343	57	332	2.3	0.03207	0.0077705		186.5	0.385505
RT13-111_g002	0.396	0.016	0.05385	0.00087	0.050356	338.7	11	338.1	5.3	323	87	338.1	2.65	-0.0467492	0.0017715		184	0.4690432
RT13-111_g003	0.3912	0.012	0.05239	0.00078	0.13899	334.8	9	329.2	4.8	331	68	329.2	2.4	0.0054381	0.0167264		290	0.4533092
RT13-111_g004	0.384	0.014	0.0532	0.00087	0.15346	329	10	334.1	5.4	234	77	334.1	2.7	-0.4277778	-0.0155015		129.7	0.4291845
RT13-111_g005	0.4028	0.012	0.0537	0.00077	0.30064	343.4	8.6	337.2	4.7	346	64	337.2	2.35	0.0254335	0.0180547		375	0.5408329
RT13-111_g006	0.39	0.013	0.05332	0.00091	0.12246	334.1	9.5	334.9	5.6	324	74	334.9	2.8	-0.033642	-0.0023945		236.8	0.4456328
RT13-111_g007	0.388	0.013	0.05345	0.00078	0.090957	332.5	9.5	335.7	4.8	288	73	335.7	2.4	-0.165625	-0.0096241		179.1	0.4464286
RT13-111_g008	0.3939	0.012	0.05347	0.00081	0.049784	337.5	8.7	335.8	4.9	315	70	335.8	2.45	-0.0660317	0.005037		175.5	0.3974563
RT13-111_g009	0.3839	0.011	0.05278	0.00078	0.15998	329.7	7.8	331.6	4.8	305	63	331.6	2.4	-0.0872131	-0.0057628		418.2	0.6093845
RT13-111_g010	0.402	0.013	0.05476	0.00082	0.022027	342.5	9.6	343.7	5	338	74	343.7	2.5	-0.0168639	-0.0035036		273	0.4470273
RT13-111_g011	0.415	0.014	0.05134	0.00086	0.37751	352.1	9.9	322.7	5.3	526	70	322.7	2.65	0.3865019	0.083499		374	0.4518753
RT13-111_g012	0.397	0.015	0.05436	0.00087	0.019606	338.8	11	341.2	5.3	311	84	341.2	2.65	-0.0971061	-0.0070838		159	0.4206984
RT13-111_g013	0.3943	0.011	0.05268	0.00083	0.37309	337.3	7.9	331	5.1	380	63	331	2.55	0.1289474	0.0186777		365.2	0.4844961
RT13-111_g014	0.411	0.016	0.05489	0.00095	0.020897	349	11	345	5.9	369	89	345	2.95	0.0650407	0.0114613		142.1	0.399361
RT13-111_g015	0.4016	0.013	0.05364	0.00079	0.19933	343.2	8.9	336.8	4.8	383	66	336.8	2.4	0.1206266	0.018648		287	0.4378284
RT13-111_g016	0.388	0.013	0.05211	0.00084	0.34822	332.6	9.7	327.4	5.1	369	71	327.4	2.55	0.1127371	0.0156344		179.2	0.5099439
RT13-111_g017	0.385	0.013	0.05327	0.00084	0.055904	329.9	9.9	334.5	5.2	298	77	334.5	2.6	-0.1224832	-0.0139436		141.8	0.4071661
RT13-111_g018	0.387	0.013	0.05194	0.00074	-0.054927	331.4	9.5	326.4	4.6	327	74	326.4	2.3	0.0018349	0.0150875		265.6	0.4288165
RT13-111_g019	0.392	0.014	0.05347	0.00083	0.12983	335.3	10	335.8	5.1	326	77	335.8	2.55	-0.0300613	-0.0014912		183.9	0.4127115
RT13-111_g020	0.3853	0.011	0.05336	0.00079	0.30661	331.4	8.1	335.1	4.8	291	62	335.1	2.4	-0.1515464	-0.0111648		455	0.5534034
RT13-111_g021	0.384	0.014	0.05278	0.00079	0.0081377	329.3	10	331.6	4.8	314	81	331.6	2.4	-0.056051	-0.0069845		197.2	0.5777008
RT13-111_g022	0.401	0.013	0.05388	0.0008	0.039651	342.2	9.4	338.3	4.9	351	73	338.3	2.45	0.0361823	0.0113968		279	0.5219207
RT13-111_g023	0.3932	0.012	0.05352	0.00088	0.030659	336.2	9.1	336.1	5.4	328	74	336.1	2.7	-0.0246951	0.0002974		188.7	0.3782148
RT13-111_g024	0.3948	0.011	0.05306	0.0008	0.17809	337.5	8.3	333.3	4.9	367	62	333.3	2.45	0.0918256	0.0124444		269	0.5955926
RT13-111_g025	0.438	0.016	0.0552	0.0013	0.37681	368.7	11	346.2	8.1	534	95	346.2	4.05	0.3516854	0.0610252		268.7	0.4269855
RT13-111_g026	0.405	0.015	0.05464	0.00079	0.015324	344.8	10	343	4.8	346	78	343	2.4	0.0086705	0.0052204		286	0.3716091
RT13-111_g027	0.383	0.011	0.05181	0.00074	0.075749	329	7.8	325.6	4.5	351	63	325.6	2.25	0.0723647	0.0103343		382.4	0.5617978
RT13-111_g028	0.51	0.016	0.05305	0.00087	0.47633	417.8	11	333.2	5.3	911	61	333.2	2.65	0.6342481	0.2024892		389.1	0.6609385
RT13-111_g029	0.4037	0.013	0.05478	0.00079	0.046574	344.7	9	343.8	4.8	353	70	343.8	2.4	0.0260623	0.002611		286	0.4653327
RT13-111_g030	0.388	0.018	0.05286	0.00091	0.11035	333	13	332	5.6	340	100	332	2.8	0.0235294	0.003003		99.5	0.3249919
RT13-111_g031	0.401	0.02	0.05369	0.0009	0.082781	341	15	337.1	5.5	390	110	337.1	2.75	0.135641	0.011437		224.7	0.3760812
RT13-111_g032	0.3823	0.01	0.0525	0.00081	0.18644	328.5	7.7	329.8	5	326	60	329.8	2.5	-0.0116564	-0.0039574		479	0.3938558
RT13-111_g033	0.3939	0.01	0.05302	0.00076	0.14319	337.1	7.3	333.1	4.7	379	56	333.1	2.35	0.1211082	0.0118659		519	0.6594566
RT13-111_g034	0.404	0.017	0.05466	0.00081	0.24497	343	12	343.1	4.9	352	85	343.1	2.45	0.0252841	-0.0002915		226.7	0.5793743

Sample RT13-115	Sample Type: igneous					Latitude:	38.52496	Longitude:	70.81857								
	Conventional concordia					Ages								Discordance		~U[ppm]	Th/U
Sample #	207Pb	±2σ	206Pb	±2σ	error corr.	207Pb	±2σ	206Pb	±2σ	207Pb	±2σ	Best Age	±1σ	206/238	206/238		
_grain number	235U		238U		206/238 vs 207/235	235U		238U		206Pb				207/206	207/235		
RT13-115_g001	0.3938	0.012	0.05352	0.00073	0.14615	336.7	8.6	336.1	4.5	337	66	336.1	2.25	0.0026706	0.001782	415	0.2079002
RT13-115_g002	5.319	0.12	0.3322	0.0053	0.51717	1871.1	20	1851	25	1894	39	1894	19.5	0.0227033	0.0107423	86.3	0.8718396
RT13-115_g003	0.5748	0.013	0.07475	0.0012	0.6036	461	8.7	464.7	6.9	460	47	464.7	3.45	-0.0102174	-0.008026	1253	0.4329004
RT13-115_g004	0.383	0.0095	0.05214	0.00075	0.078478	329.2	7	327.7	4.6	332	57	327.7	2.3	0.0129518	0.0045565	1120	0.4464286
RT13-115_g005	0.3852	0.012	0.05239	0.00084	0.23427	330.6	8.8	329.2	5.2	331	70	329.2	2.6	0.0054381	0.0042347	687.3	0.1650165
RT13-115_g006	0.398	0.02	0.05396	0.0011	0.054263	339	14	338.8	6.7	390	120	338.8	3.35	0.1312821	0.00059	206.8	0.3274394
RT13-115_g007	0.3938	0.011	0.05287	0.00076	0.22385	337	7.7	332.1	4.6	386	58	332.1	2.3	0.1396373	0.0145401	637	0.2096436
RT13-115_g008	0.3871	0.012	0.05364	0.00079	0.19513	332.9	8.3	337.2	5	297	67	337.2	2.5	-0.1353535	-0.0129168	473	0.3803728
RT13-115_g009	0.3855	0.0098	0.05245	0.00075	0.2295	330.9	7.2	329.6	4.6	332	53	329.6	2.3	0.0072289	0.0039287	578	0.2066116
RT13-115_g010	0.3853	0.0098	0.05243	0.00074	0.19863	330.7	7.2	329.4	4.6	345	56	329.4	2.3	0.0452174	0.0039311	420	0.2265519
RT13-115_g011	0.4023	0.012	0.0542	0.00084	-0.10516	343.1	8.5	340.2	5.2	368	67	340.2	2.6	0.0755435	0.0084523	492	0.1908761
RT13-115_g012	0.394	0.014	0.0546	0.00083	-0.030532	337.5	10	342.7	5.1	303	78	342.7	2.55	-0.1310231	-0.0154074	227	0.2613013
RT13-115_g013	0.3947	0.01	0.05306	0.00072	0.16921	337.6	7.3	333.3	4.4	378	54	333.3	2.2	0.118254	0.012737	777	0.3468609
RT13-115_g014	0.3945	0.012	0.05262	0.00077	0.11669	338	8.5	330.6	4.7	374	65	330.6	2.35	0.1160428	0.0218935	347	0.2770083
RT13-115_g015	0.4037	0.012	0.05491	0.00093	-0.011251	344.9	8.8	344.6	5.7	369	71	344.6	2.85	0.0661247	0.0008698	387	0.3327787
RT13-115_g016	0.391	0.015	0.0549	0.0009	0.06788	335.7	11	344.5	5.5	267	85	344.5	2.75	-0.2902622	-0.0262139	115.4	0.1931994
RT13-115_g017	0.3858	0.011	0.05249	0.00073	0.22482	331	7.7	329.8	4.5	347	59	329.8	2.25	0.0495677	0.0036254	480.1	0.2300966
RT13-115_g019	0.3898	0.011	0.05336	0.00078	0.43387	334	7.9	335.1	4.8	341	56	335.1	2.4	0.0173021	-0.0032934	480	0.0442478
RT13-115_g020	0.3891	0.012	0.05384	0.00082	0.24115	333.2	9	338.4	4.9	308	65	338.4	2.45	-0.0987013	-0.0156062	342	0.215378
RT13-115_g021	0.3934	0.01	0.05372	0.00076	0.19081	336.6	7.6	337.3	4.7	340	57	337.3	2.35	0.0079412	-0.0020796	549	0.2332634
RT13-115_g022	0.395	0.01	0.05329	0.00078	0.16746	337.8	7.5	334.7	4.8	374	58	334.7	2.4	0.1050802	0.009177	423.1	0.3275467
RT13-115_g023	0.385	0.013	0.05193	0.00078	0.1652	330.8	9.8	326.4	4.8	362	78	326.4	2.4	0.0983425	0.0133011	647	0.3309067
RT13-115_g024	0.3886	0.01	0.05291	0.00075	0.074672	333.2	7.4	332.4	4.6	350	57	332.4	2.3	0.0502857	0.002401	597	0.2796421
RT13-115_g025	1.192	0.034	0.1278	0.0019	0.15757	797	16	775.1	11	834	60	775.1	5.5	0.0706235	0.027478	423	0.4987531
RT13-115_g026	0.394	0.013	0.05341	0.00082	0.22709	336.6	9.8	335.4	5	344	74	335.4	2.5	0.025	0.0035651	256	0.3623188
RT13-115_g027	0.3906	0.011	0.05332	0.00086	0.43796	334.5	8.1	334.9	5.2	342	58	334.9	2.6	0.0207602	-0.0011958	408	0.3065604
RT13-115_g028	0.3838	0.011	0.05247	0.00075	0.078175	329.5	7.9	329.7	4.6	354	59	329.7	2.3	0.0686441	-0.000607	401	0.1727116
RT13-115_g029	0.401	0.024	0.0554	0.0016	0.52345	342	17	347.7	9.8	393	75	347.7	4.9	0.1152672	-0.0166667	432	0.226706

Sample 16NP342	Sample Type: igneous					Latitude:	38.657017	Longitude:	70.89395								
	Conventional concordia					Ages								Discordance		~U[ppm]	Th/U
Sample #	207Pb	±2σ	206Pb	±2σ	error corr.	207Pb	±2σ	206Pb	±2σ	207Pb	±2σ	Best Age	±1σ	206/238	206/238		
_grain number	235U		238U		206/238 vs 207/235	235U		238U		206Pb				207/206	207/235		
16NP342_g01	0.3998	0.004	0.05408	0.00045	0.50809	341.4	2.9	339.5	2.7	358	20	339.5	1.35	0.051676	0.0055653	423	0.3813883
16NP342_g02	0.3929	0.0047	0.05387	0.00043	0.38725	336.7	3.4	338.2	2.6	333	23	338.2	1.3	-0.0156156	-0.004455	311.4	0.3345601
16NP342_g03	0.4261	0.0043	0.05794	0.00045	0.4885	360.6	3	363.1	2.8	340	17	363.1	1.4	-0.0679412	-0.0069329	573.4	0.6101281
16NP342_g04	0.4143	0.0049	0.05627	0.00048	0.53546	351.8	3.5	352.9	3	364	20	352.9	1.5	0.0304945	-0.0031268	382.9	0.4185852
16NP342_g05_a	0.401	0.011	0.05436	0.00067	0.40209	341.8	7.9	341.2	4.1	344	55	341.2	2.05	0.0081395	0.0017554	323.2	0.3577818
16NP342_g05_b	0.4268	0.0073	0.05806	0.00055	0.61176	360.8	5.2	363.8	3.4	336	28	363.8	1.7	-0.0827381	-0.0083149	595	0.6596306
16NP342_g06	0.3984	0.0051	0.05428	0.00045	0.55538	340.7	3.7	340.8	2.8	333	22	340.8	1.4	-0.0234234	-0.0002935	424	0.3938558
16NP342_g07	0.4289	0.0046	0.05829	0.00054	0.55911	362.5	3.2	365.2	3.3	358	18	365.2	1.65	-0.0201117	-0.0074483	599	0.5656109
16NP342_g08	0.484	0.01	0.05922	0.00044	0.59526	400	7.1	370.9	2.7	564	39	370.9	1.35	0.3423759	0.07275	3233	0.8176615
16NP342_g09_a	0.4207	0.0069	0.0579	0.0005	0.30663	357.2	5.1	362.9	3.1	328	34	362.9	1.55	-0.1064024	-0.0159574	626	0.447828
16NP342_g09_b	0.4025	0.0061	0.05463	0.00057	0.097908	343.4	4.4	342.9	3.5	346	39	342.9	1.75	0.0089595	0.001456	386.1	0.3806624
16NP342_g10	0.4355	0.004	0.05904	0.00046	0.57175	367	2.9	369.8	2.8	348	16	369.8	1.4	-0.0626437	-0.0076294	662	0.5913661
16NP342_g11	0.4301	0.0047	0.05822	0.00047	0.62732	363.1	3.3	364.8	2.9	341	18	364.8	1.45	-0.0697947	-0.0046819	2137	1.0245902
16NP342_g12	0.4417	0.0044	0.06062	0.00048	0.52283	371.4	3.1	379.4	2.9	327	18	379.4	1.45	-0.1602446	-0.0215401	1137	0.5402485
16NP342_g13	0.4368	0.004	0.0593	0.00044	0.48556	367.9	2.8	371.4	2.7	344	17	371.4	1.35	-0.0796512	-0.0095135	936	0.7150518
16NP342_g14	0.4274	0.0047	0.05826	0.00049	0.47108	361.3	3.3	365	3	345	20	365	1.5	-0.057971	-0.0102408	622	0.5506608
16NP342_g15	0.395	0.0044	0.0539	0.00039	0.49934	337.9	3.2	338.4	2.4	326	21	338.4	1.2	-0.0380368	-0.0014797	359	0.3883495
16NP342_g16	0.4293	0.0049	0.05828	0.00052	0.69821	362.5	3.5	365.1	3.1	347	17	365.1	1.55	-0.0521614	-0.0071724	569	0.5643341
16NP342_g17	0.432	0.0034	0.05909	0.00042	0.61984	364.6	2.4	370.1	2.5	338	12	370.1	1.25	-0.0949704	-0.015085	1765	0.7320644
16NP342_g18	0.4371	0.0054	0.05928	0.00065	0.54065	368.1	3.8	371.2	3.9	350	23	371.2	1.95	-0.0605714	-0.0084216	509	0.443459
16NP342_g19	0.3941	0.0041	0.05381	0.00039	0.38799	337.3	3	337.9	2.4	334	19	337.9	1.2	-0.0116766	-0.0017788	408.7	0.4083299
16NP342_g20	0.3968	0.0059	0.05405	0.0006	0.57026	339.1	4.3	339.3	3.6	326	27	339.3	1.8	-0.0407975	-0.0005898	349	0.4196391
16NP342_g21	0.4348	0.0037	0.05937	0.00045	0.59528	366.8	2.6	371.8	2.7	332	15	371.8	1.35	-0.1198795	-0.0136314	1285	0.7052186
16NP342_g22	0.4122	0.0059	0.05629	0.00059	0.71586	350.3	4.2	353	3.6	341	21	353	1.8	-0.0351906	-0.0077077	437.5	0.5232862
16NP342_g23	0.4333	0.0036	0.05893	0.00043	0.62328	365.4	2.6	369.1	2.6	347	12	369.1	1.3	-0.0636888	-0.0101259	1539	0.8409014
16NP342_g24	0.4041	0.0047	0.05469	0.00051	0.53441	344.8	3.3	343.2	3.1	329	20	343.2	1.55	-0.0431611	0.0046404	436.9	0.4547522
16NP342_g25	0.399	0.0057	0.05412	0.00052	0.6404	341.1	4.2	339.7	3.1	340	24	339.7	1.55	0.0008824	0.0041044	437	0.5488474
16NP342_g26	0.4369	0.0048	0.05918	0.00051	0.55494	367.9	3.4	370.6	3.1	351	19	370.6	1.55	-0.0558405	-0.007339	542	0.5672793
16NP342_g27	0.3937	0.0053	0.05425	0.00045	0.50667	336.9	3.8	340.5	2.8	314	24	340.5	1.4	-0.0843949	-0.0106857	333	0.3646973
16NP342_g28	0.4027	0.0055	0.05445	0.00056	0.64145	343.8	4	341.8	3.4	338	23	341.8	1.7	-0.0112426	0.0058173	484	0.4854369
16NP342_g29	0.4341	0.0035	0.05918	0.00045	0.61942	366	2.5	370.6	2.8	332	12	370.6	1.4	-0.1162651	-0.0125683	2614	0.7087172
16NP342_g30	0.4256	0.0055	0.05795	0.0006	0.44548	359.9	3.9	363.1	3.7	329	25	363.1	1.85	-0.1036474	-0.0088914	674	0.2762431

Sample 16NP341	Sample Type: igneous					Latitude:	38.660717	Longitude:	70.902117								
	Conventional concordia					Ages								Discordance		~U[ppm]	Th/U
Sample #	207Pb	±2σ	206Pb	±2σ	error corr.	207Pb	±2σ	206Pb	±2σ	207Pb	±2σ	Best Age	±1σ	206/238	206/238		
_grain number	235U		238U		206/238 vs 207/235	235U		238U		206Pb				207/206	207/235		
16NP341_g01	0.3915	0.0054	0.05326	0.00044	0.314	335.7	4	334.5	2.7	360	28	334.5	1.35	0.0708333	0.0035746	275.2	0.3202049
16NP341_g02	0.397	0.0068	0.05381	0.00044	0.09567	339.6	4.9	337.9	2.7	359	36	337.9	1.35	0.0587744	0.0050059	150.3	0.2982404
16NP341_g03	0.3914	0.0068	0.05381	0.00048	0.18672	336.1	5.1	337.8	3	307	40	337.8	1.5	-0.1003257	-0.005058	143.7	0.299222
16NP341_g04	0.4037	0.0065	0.05447	0.00043	0.27494	345	4.8	341.9	2.6	352	33	341.9	1.3	0.0286932	0.0089855	201.5	0.3350084
16NP341_g05	0.3997	0.0068	0.05418	0.0005	0.42598	341.1	5	340.1	3	336	34	340.1	1.5	-0.0122024	0.0029317	178.8	0.5521811
16NP341_g06	0.4375	0.006	0.0584	0.00063	0.60161	368.4	4.2	365.9	3.9	376	23	365.9	1.95	0.0268617	0.0067861	702	0.5640158
16NP341_g07	0.3924	0.0089	0.05326	0.00067	0.18259	335.9	6.5	334.5	4.1	370	49	334.5	2.05	0.0959459	0.0041679	323.5	0.3595829
16NP341_g08	0.3951	0.0074	0.0538	0.00056	0.47201	338	5.4	337.8	3.4	356	39	337.8	1.7	0.0511236	0.0005917	329.2	0.4106776
16NP341_g09	0.4037	0.0061	0.05419	0.00042	0.060673	344.5	4.5	340.2	2.6	377	33	340.2	1.3	0.0976127	0.0124819	230.5	0.3132832
16NP341_g10	0.4162	0.0093	0.05597	0.0008	0.72931	353.2	6.7	351.1	4.9	366	38	351.1	2.45	0.0407104	0.0059456	300	0.7256894
16NP341_g10	0.4242	0.0098	0.05396	0.00058	0.26026	358.8	7	338.8	3.6	496	45	338.8	1.8	0.3169355	0.0557414	545.9	0.5379236
16NP341_g11	0.4009	0.005	0.05344	0.00038	0.26994	342.1	3.6	335.6	2.3	385	25	335.6	1.15	0.1283117	0.0190003	309	0.3203075
16NP341_g12	0.3887	0.0052	0.05263	0.00041	0.46099	333.2	3.8	330.7	2.5	343	25	330.7	1.25	0.0358601	0.007503	327	0.4139073
16NP341_g13	0.4068	0.0047	0.05481	0.00044	0.22062	346.4	3.4	344	2.7	361	24	344	1.35	0.0470914	0.0069284	403	0.3846154
16NP341_g14	0.3941	0.0052	0.05333	0.00036	0.099871	337.2	3.8	334.9	2.2	348	29	334.9	1.1	0.0376437	0.0068209	296	0.3414135
16NP341_g15	0.3888	0.0079	0.05387	0.00044	0.078114	333.6	5.7	338.2	2.7	295	45	338.2	1.35	-0.1464407	-0.013789	92.1	0.3057169
16NP341_g16	0.3938	0.008	0.05398	0.00066	0.56654	337.9	6	338.9	4	314	37	338.9	2	-0.0792994	-0.0029595	471	0.522466
16NP341_g17	0.4045	0.0047	0.05397	0.00044	0.23648	345.1	3.3	338.8	2.7	387	25	338.8	1.35	0.1245478	0.0182556	300.5	0.5070994
16NP341_g18	0.391	0.005	0.05293	0.00044	0.46291	334.9	3.6	332.5	2.7	331	25	332.5	1.35	-0.0045317	0.0071663	429	0.618697
16NP341_g19	0.4185	0.0055	0.0572	0.00059	0.6608	354.8	3.9	358.5	3.6	336	21	358.5	1.8	-0.0669643	-0.0104284	533	0.635324
16NP341_g20	0.4001	0.0055	0.05403	0.0004	0.001	341.5	4	339.2	2.5	368	32	339.2	1.25	0.0782609	0.006735	196.3	0.3013864
16NP341_g21	0.4052	0.006	0.05475	0.0004	0.19655	345.2	4.4	343.6	2.5	350	32	343.6	1.25	0.0182857	0.004635	240.3	0.3769318
16NP341_g22	0.3928	0.0051	0.05341	0.00042	0.23195	336.3	3.7	335.4	2.6	352	25	335.4	1.3	0.0471591	0.0026762	336	0.3700962
16NP341_g23	0.4103	0.0067	0.05466	0.0005	0.21719	348.8	4.8	343	3.1	369	35	343	1.55	0.0704607	0.0166284	149	0.3824092
16NP341_g24	0.3791	0.0059	0.05165	0.00039	0.12373	326.1	4.3	324.6	2.4	326	31	324.6	1.2	0.0042945	0.0045998	272.6	0.5643341
16NP341_g25	0.4034	0.0089	0.05446	0.00044	0.13309	344.2	6.4	341.9	2.7	347	49	341.9	1.35	0.0146974	0.0066822	98.6	0.297885
16NP341_g26	0.3935	0.0058	0.05389	0.00041	0.059496	336.7	4.2	338.3	2.5	323	34	338.3	1.25	-0.0473684	-0.004752	214	0.2984184
16NP341_g27	0.3888	0.0074	0.05296	0.00046	0.10727	334.9	5.4	332.7	2.8	332	45	332.7	1.4	-0.0021084	0.0065691	248.3	0.5299417
16NP341_g28	0.3926	0.0057	0.05327	0.00043	0.26507	336	4.2	334.6	2.6	354	30	334.6	1.3	0.0548023	0.0041667	179.5	0.4814636
16NP341_g29	0.3957	0.0068	0.05345	0.0005	0.024007	338.9	4.8	335.6	3.1	368	36	335.6	1.55	0.0880435	0.0097374	136.6	0.3998401
16NP341_g30	0.3991	0.0053	0.05413	0.00044	0.22436	340.8	3.9	339.8	2.7	344	28	339.8	1.35	0.0122093	0.0029343	387	0.2910361

Sample 16NP341 continued

	Conventional concordia					Ages							Discordance		~U[ppm]	Th/U
Sample #	207Pb	±2σ	206Pb	±2σ	error corr.	207Pb	±2σ	206Pb	±2σ	207Pb	±2σ	Best Age	±1σ	206/238	206/238		
_grain number	235U		238U		206/238 vs 207/235	235U		238U		206Pb				207/206	207/235		
16NP341_g31	0.386	0.0046	0.0527	0.00041	0.22986	331.3	3.4	331.1	2.5	346	26	331.1	1.25	0.0430636	0.0006037	940	0.5254861
16NP341_g32	0.4238	0.0045	0.05768	0.00049	0.55817	358.7	3.2	361.5	3	336	19	361.5	1.5	-0.0758929	-0.007806	7040	0.7007708
16NP341_g33	0.3789	0.0079	0.05248	0.00062	0.23938	326	5.8	329.7	3.8	296	45	329.7	1.9	-0.1138514	-0.0113497	881	0.3052503
16NP341_g34	0.4084	0.0047	0.05521	0.00044	0.29485	348.3	3.5	346.4	2.7	365	22	346.4	1.35	0.0509589	0.0054551	491.6	0.3952569
16NP341_g35	0.3997	0.0068	0.05471	0.00049	0.12208	341.1	5	343.4	3	326	38	343.4	1.5	-0.0533742	-0.0067429	142.7	0.3294893
16NP341_g36	0.4126	0.0056	0.05568	0.00052	0.19484	350.6	4	349.6	3.1	347	31	349.6	1.55	-0.0074928	0.0028523	295.5	0.4152824
16NP341_g37	0.3994	0.0056	0.05478	0.0004	0.20063	341.4	4	343.8	2.4	327	30	343.8	1.2	-0.0513761	-0.0070299	229	0.3483107
16NP341_g38	0.4329	0.0046	0.05886	0.00046	0.52953	365.4	3.2	368.7	2.8	333	19	368.7	1.4	-0.1072072	-0.0090312	657	0.5617978
16NP341_g39	0.3955	0.0043	0.05322	0.00037	0.23497	338.2	3.1	334.2	2.3	355	23	334.2	1.15	0.0585915	0.0118273	406	0.3617945
16NP341_g40	0.395	0.0054	0.05389	0.00044	0.20377	337.8	3.9	338.3	2.7	341	28	338.3	1.35	0.0079179	-0.0014802	264	0.4317789
16NP341_g41	0.3909	0.0059	0.05377	0.00054	0.63635	335.2	4.3	337.6	3.3	314	25	337.6	1.65	-0.0751592	-0.0071599	427	0.4203447
16NP341_g42	0.3968	0.0051	0.05416	0.00039	0.29279	339.1	3.7	340	2.4	339	25	340	1.2	-0.0029499	-0.0026541	266	0.3425831
16NP341_g43	0.399	0.007	0.05289	0.00048	0.018139	340.8	5.1	332.3	2.9	414	43	332.3	1.45	0.197343	0.0249413	262.9	0.5546312
16NP341_g44	0.391	0.0051	0.05375	0.00042	0.29973	334.9	3.7	337.5	2.6	326	27	337.5	1.3	-0.0352761	-0.0077635	302.1	0.3314551
16NP341_g45	0.4121	0.005	0.05616	0.00051	0.5233	350.3	3.6	352.2	3.1	325	25	352.2	1.55	-0.0836923	-0.0054239	482	0.6389776
16NP341_g46	0.3879	0.0044	0.05299	0.00041	0.34552	333	3.2	332.9	2.5	326	22	332.9	1.25	-0.0211656	0.0003003	441.3	0.6150062

Sample RT13-148	Sample Type: detrital					Latitude:	38.3997	Longitude:	71.06168								
	Conventional concordia					Ages								Discordance		~U[ppm]	Th/U
Sample #	207Pb	±2σ	206Pb	±2σ	error corr.	207Pb	±2σ	206Pb	±2σ	207Pb	±2σ	Best Age	±1σ	206/238	206/238		
_grain number	235U		238U		206/238 vs 207/235	235U		238U		206Pb				207/206	207/235		
RT13-148_g001	5.612	0.12	0.3269	0.0045	0.63876	1917.5	19	1823.4	22	2030	34	2030	17	0.1017734	0.0490743	421	0.3568879
RT13-148_g002	1.09	0.031	0.1222	0.0018	0.34326	750	15	744	10	779	57	744	5	0.0449294	0.008	171.1	0.9803922
RT13-148_g003	0.745	0.021	0.0904	0.0019	0.65163	564.8	12	557.6	11	602	51	557.6	5.5	0.0737542	0.0127479	271	1.4224751
RT13-148_g004	11.756	0.25	0.4834	0.0067	0.60106	2584.9	20	2542	29	2628	32	2628	16	0.0327245	0.0165964	179.1	1.0636035
RT13-148_g005	0.86	0.028	0.1007	0.0016	0.07669	632	15	618.5	9.4	676	69	618.5	4.7	0.0850592	0.0213608	125	1.8382353
RT13-148_g006	3.419	0.076	0.2232	0.0032	0.62471	1508.2	18	1298.6	17	1825	37	1825	18.5	0.2884384	0.1389736	319	0.4828585
RT13-148_g007	0.988	0.023	0.11274	0.0016	0.25263	697.2	12	688.6	9.3	742	47	688.6	4.65	0.0719677	0.0123351	529	0.481232
RT13-148_g008	0.67	0.019	0.08221	0.0013	0.41026	520.2	12	509.3	7.8	574	57	509.3	3.9	0.1127178	0.0209535	266	1.6202203
RT13-148_g009	1.201	0.029	0.13211	0.0019	0.4922	800.5	13	799.9	11	806	46	799.9	5.5	0.0075682	0.0007495	425	0.4653327
RT13-148_g010	0.773	0.023	0.09513	0.0014	0.095667	580.8	13	585.8	8.5	563	65	585.8	4.25	-0.0404973	-0.0086088	157	0.8471705
RT13-148_g011	1.112	0.026	0.12504	0.0018	0.31391	759	13	759.4	10	768	48	759.4	5	0.0111979	-0.000527	482	0.3706449
RT13-148_g012	6.93	0.19	0.3822	0.0063	0.28313	2100	24	2086	30	2132	47	2132	23.5	0.021576	0.0066667	33.1	0.4
RT13-148_g013	0.496	0.034	0.0546	0.0015	0.30547	411	22	342.5	9.5	790	140	342.5	4.75	0.5664557	0.1666667	78.6	0.6468305
RT13-148_g014	1.058	0.036	0.1219	0.0019	0.11181	733	17	741.6	11	698	72	741.6	5.5	-0.0624642	-0.0117326	77.1	0.4708098
RT13-148_g015	0.871	0.042	0.0994	0.0023	0.20811	638	24	611	14	730	110	611	7	0.1630137	0.0423197	35.6	0.243309
RT13-148_g016	1.22	0.047	0.1313	0.0032	0.84707	811	22	797	18	872	52	797	9	0.0860092	0.0172626	154.2	0.1838235
RT13-148_g017	6.089	0.16	0.3662	0.006	0.30454	1987	23	2011	28	1959	45	1959	22.5	-0.0265442	-0.0120785	44.2	1.1248594
RT13-148_g018	1.289	0.043	0.1383	0.0026	0.57958	845	18	835	15	845	61	835	7.5	0.0118343	0.0118343	88.5	0.3800836
RT13-148_g019	0.76	0.034	0.0913	0.0027	0.57176	573	19	563	16	587	82	563	8	0.0408859	0.017452	61.5	0.5931198
RT13-148_g020	0.844	0.027	0.0963	0.0018	0.43189	620	15	592.3	11	757	68	592.3	5.5	0.2175694	0.0446774	211	0.9363296
RT13-148_g021	1.115	0.027	0.1243	0.0019	0.36477	761.1	13	755.3	11	782	46	755.3	5.5	0.0341432	0.0076205	452	0.5540166
RT13-148_g022	1.697	0.039	0.16779	0.0022	0.39991	1006.9	15	999.9	12	1031	43	999.9	6	0.0301649	0.006952	330.2	0.5037783
RT13-148_g023	1.017	0.024	0.11896	0.0017	0.46171	712.3	12	724.6	9.5	683	46	724.6	4.75	-0.0609078	-0.017268	532	0.1531394
RT13-148_g024	0.914	0.03	0.1072	0.0019	0.65324	658	16	656.3	11	678	64	656.3	5.5	0.0320059	0.0025836	123.8	0.5988024
RT13-148_g025	1.766	0.042	0.1712	0.0025	0.46133	1032.4	15	1018.9	14	1053	44	1053	22	0.0323837	0.0130763	292	1.0729614
RT13-148_g026	0.949	0.053	0.1109	0.0028	0.62909	676	27	678	16	660	87	678	8	-0.0272727	-0.0029586	246	0.3401361
RT13-148_g027	1.059	0.028	0.1163	0.0019	0.2618	732.4	14	710	11	812	54	710	5.5	0.1256158	0.0305844	198.9	0.2387205
RT13-148_g028	1.82	0.063	0.145	0.0025	0.22832	1054	23	872.7	14	1476	66	872.7	7	0.4087398	0.1720114	60.6	0.8298755
RT13-148_g029	1.027	0.034	0.1187	0.0019	0.19312	716	17	723.1	11	726	67	723.1	5.5	0.0039945	-0.0099162	78.5	0.8291874
RT13-148_g030	1.075	0.026	0.12147	0.0017	0.36737	742.4	13	739	9.8	737	48	739	4.9	-0.0027137	0.0045797	424.8	0.6112469
RT13-148_g031	1.067	0.024	0.11971	0.0016	0.41087	737.5	12	728.9	9.5	772	44	728.9	4.75	0.055829	0.011661	560.6	0.4389816

Sample RT13-148 continued

	Conventional concordia					Ages							Discordance		~U[ppm]	Th/U
Sample #	207Pb	±2σ	206Pb	±2σ	error corr.	207Pb	±2σ	206Pb	±2σ	207Pb	±2σ	Best Age	±1σ	206/238	206/238		
_grain number	235U		238U		206/238 vs 207/235	235U		238U		206Pb				207/206	207/235		
RT13-148_g032	5.656	0.14	0.3381	0.0057	0.83938	1925	21	1877	27	1979	36	1979	18	0.0515412	0.0249351	197	0.4334634
RT13-148_g033	0.8127	0.019	0.09708	0.0013	0.30673	603.7	10	597.3	7.9	620	45	597.3	3.95	0.0366129	0.0106013	856	0.2875216
RT13-148_g034	1.754	0.052	0.1693	0.0028	0.29053	1030	19	1008	16	1082	57	1082	28.5	0.0683919	0.0213592	67.8	0.3617945
RT13-148_g035	1.001	0.029	0.1141	0.0017	0.25871	703	15	696.3	10	744	57	696.3	5	0.0641129	0.0095306	157.9	0.4692633
RT13-148_g036	0.835	0.028	0.10114	0.0016	0.21939	617	16	621.1	9.2	632	70	621.1	4.6	0.0172468	-0.0066451	73.4	1.2115338
RT13-148_g037	0.8259	0.019	0.09774	0.0013	0.36064	611.2	10	601.1	7.9	647	46	601.1	3.95	0.0709428	0.0165249	791	0.7054674
RT13-148_g038	0.661	0.019	0.07462	0.0012	0.35437	514.7	11	463.9	6.9	750	57	463.9	3.45	0.3814667	0.0986983	208.3	0.3062787
RT13-148_g039	0.821	0.024	0.10084	0.0014	0.15877	609.1	13	619.3	8.3	582	64	619.3	4.15	-0.0640893	-0.016746	153.5	0.665336
RT13-148_g040	6.559	0.14	0.3679	0.0052	0.64991	2053.6	19	2019	25	2105.8	34	2105.8	17	0.0412195	0.0168485	364	0.6116208
RT13-148_g041	0.951	0.023	0.1101	0.0015	0.094055	678.4	12	673.3	8.4	701	47	673.3	4.2	0.039515	0.0075177	418	0.3675119
RT13-148_g042	0.985	0.031	0.1122	0.0019	0.36633	698	16	685.3	11	767	66	685.3	5.5	0.1065189	0.0181948	96.2	0.6644518
RT13-148_g043	0.6437	0.015	0.07782	0.0011	0.55561	504.4	9.2	483.1	6.8	611	43	483.1	3.4	0.209329	0.0422284	1081	0.532198
RT13-148_g044	1.493	0.056	0.1449	0.0037	0.5465	930	23	872	21	1058	69	872	10.5	0.1758034	0.0623656	129.6	0.3571429
RT13-148_g045	0.743	0.022	0.0913	0.0014	-0.20936	564.7	13	563.2	8.5	574	67	563.2	4.25	0.0188153	0.0026563	108.7	1.8027763
RT13-148_g046	4.976	0.11	0.3122	0.0043	0.65046	1814.9	19	1751	21	1906	37	1906	18.5	0.0813221	0.0352086	394.3	0.1261034
RT13-148_g047	5.355	0.13	0.3235	0.0048	0.54271	1877	20	1807	23	1957	38	1957	19	0.0766479	0.0372936	101.7	0.805153
RT13-148_g048	1.113	0.044	0.1186	0.0022	0.57199	759	21	722.7	12	855	67	722.7	6	0.1547368	0.0478261	94.2	0.5359057
RT13-148_g049	2.449	0.07	0.1854	0.0028	0.37856	1257	21	1096.3	15	1546	50	1546	25	0.2908797	0.1278441	71	0.3695492
RT13-148_g050	11.88	0.29	0.4916	0.0083	0.60772	2597	24	2577	36	2654	39	2654	19.5	0.0290128	0.0077012	301.8	0.8467401
RT13-148_g051	0.791	0.022	0.096	0.0017	0.083651	590.8	13	590.7	10	598	66	590.7	5	0.0122074	0.0001693	128.5	0.4803074
RT13-148_g052	0.87	0.022	0.10476	0.0015	0.30128	636.3	13	642.2	8.7	639	54	642.2	4.35	-0.0050078	-0.0092724	275	0.6079027
RT13-148_g053	0.827	0.046	0.0919	0.0021	0.13221	610	25	567	13	820	120	567	6.5	0.3085366	0.0704918	58.78	1.7241379
RT13-148_g054	0.824	0.02	0.0989	0.0016	0.6478	610.3	11	608.1	9.7	661	47	608.1	4.85	0.0800303	0.0036048	814	0.1449275
RT13-148_g055	1.166	0.029	0.12376	0.0017	0.3132	784.1	14	752.2	9.7	887	47	752.2	4.85	0.1519729	0.0406836	613	0.5202914
RT13-148_g056	0.995	0.029	0.1123	0.0016	0.46016	700	15	686.7	9.2	755	56	686.7	4.6	0.0904636	0.019	270	0.1964637
RT13-148_g057	1.117	0.027	0.12513	0.0017	0.37145	762.2	13	760	9.9	778	48	760	4.95	0.0231362	0.0028864	399	0.034904
RT13-148_g058	0.952	0.049	0.0965	0.0022	0.083673	684	27	594	13	1048	99	594	6.5	0.4332061	0.1315789	108.1	0.5076142
RT13-148_g059	0.475	0.023	0.0552	0.0011	0.45492	395	16	346.3	6.8	681	91	346.3	3.4	0.4914831	0.1232911	142.8	0.3125977
RT13-148_g060	6.16	0.16	0.3493	0.0062	0.72666	1998	23	1931	29	2057	39	2057	19.5	0.0612543	0.0335335	219.4	0.4458315
RT13-148_g061	2.805	0.097	0.1853	0.0047	0.95934	1357	26	1098	25	1804	38	1804	19	0.3913525	0.1908622	568	0.1153403
RT13-148_g062	1.936	0.045	0.1836	0.0026	0.020352	1094.5	15	1086.5	14	1124	43	1124	21.5	0.033363	0.0073093	389.3	0.9727626

Sample RT13-148 continued

	Conventional concordia					Ages								Discordance		~U[ppm]	Th/U
Sample #	207Pb	±2σ	206Pb	±2σ	error corr.	207Pb	±2σ	206Pb	±2σ	207Pb	±2σ	Best Age	±1σ	206/238	206/238		
_grain number	235U		238U		206/238 vs 207/235	235U		238U		206Pb				207/206	207/235		
RT13-148_g063	0.8144	0.019	0.09922	0.0013	0.28304	604.7	11	609.8	7.7	598	49	609.8	3.85	-0.0197324	-0.0084339	525	0.7355104
RT13-148_g064	0.84	0.023	0.10046	0.0015	0.34548	618.4	12	617.1	8.6	636	53	617.1	4.3	0.029717	0.0021022	305	0.877193
RT13-148_g065	1.718	0.043	0.1704	0.0025	0.29933	1015.8	16	1014.4	14	1015	48	1015	24	0.0005911	0.0013782	183.3	1.4947683
RT13-148_g066	1.673	0.044	0.1646	0.0025	0.29482	997	17	982.4	14	1032	50	982.4	7	0.048062	0.0146439	139.8	0.1402525
RT13-148_g067	0.793	0.019	0.09655	0.0013	0.25801	592.6	11	594.1	7.8	604	47	594.1	3.9	0.0163907	-0.0025312	418.9	1.2787724
RT13-148_g068	12.972	0.28	0.5028	0.0066	0.66157	2677.3	20	2625	28	2732.4	32	2732.4	16	0.0393061	0.0195346	376	0.7581501
RT13-148_g069	0.789	0.042	0.0981	0.002	0.069291	589	24	602.8	12	540	120	602.8	6	-0.1162963	-0.0234295	28.9	0.556483
RT13-148_g070	0.982	0.025	0.1177	0.0018	0.80211	694.8	13	717.3	11	644	44	717.3	5.5	-0.1138199	-0.0323834	903	0.0276243
RT13-148_g071	10.8	0.25	0.4687	0.0066	0.52846	2504.9	21	2477	29	2549	36	2549	18	0.0282464	0.0111382	94.4	0.748503
RT13-148_g072	1.079	0.024	0.12161	0.0017	0.46407	743.1	12	740.4	9.6	764	42	740.4	4.8	0.0308901	0.0036334	958	0.0336587
RT13-148_g073	0.8099	0.019	0.09838	0.0014	0.31565	602.1	11	605.4	8.3	628	47	605.4	4.15	0.0359873	-0.0054808	511	0.567215
RT13-148_g074	0.773	0.033	0.0937	0.0021	0.43231	581	19	578.5	12	631	84	578.5	6	0.0832013	0.0043029	77.5	0.7621951
RT13-148_g075	1.592	0.043	0.1596	0.0024	0.27601	966	17	954.2	13	1021	51	954.2	6.5	0.0654261	0.0122153	181.5	0.4239084
RT13-148_g076	1.679	0.039	0.1677	0.0023	0.3842	1001.8	15	1000.3	13	1035	42	1035	21	0.0335266	0.0014973	286.3	0.4060089
RT13-148_g077	0.947	0.045	0.1127	0.0036	0.60303	672	24	688	21	635	84	688	10.5	-0.0834646	-0.0238095	36.1	1.0559662
RT13-148_g078	0.821	0.021	0.09787	0.0014	0.13109	608.2	12	601.9	8.5	628	56	601.9	4.25	0.0415605	0.0103584	226.9	1.7006803
RT13-148_g079	1.136	0.037	0.1282	0.0021	0.366	770	17	777.7	12	783	62	777.7	6	0.0067688	-0.01	99.9	0.6337136
RT13-148_g080	1.039	0.03	0.1162	0.0018	0.083481	723	15	708.9	10	773	60	708.9	5	0.0829237	0.0195021	545.5	1.0449321
RT13-148_g081	0.773	0.019	0.09387	0.0013	0.008588	581.3	11	578.4	7.6	621	55	578.4	3.8	0.068599	0.0049888	339	1.0989011
RT13-148_g082	1.583	0.048	0.159	0.0029	0.45893	965	20	951	16	992	59	951	8	0.0413306	0.0145078	166.4	0.6313131

Sample RT15-11	Sample Type: detrital					Latitude:	38.69131 Longitude:	71.38139									
	Conventional concordia					Ages								Discordance		~U[ppm]	Th/U
Sample #	207Pb	±2σ	206Pb	±2σ	error corr.	207Pb	±2σ	206Pb	±2σ	207Pb	±2σ	Best Age	±1σ	206/238	206/238		
_grain number	235U		238U		206/238 vs 207/235	235U		238U		206Pb				207/206	207/235		
RT15-11_g001	1.408	0.034	0.1477	0.0024	0.56547	892.9	14	887.7	13	912	44	887.7	6.5	0.0266447	0.0058237	382	0.4116921
RT15-11_g002	1.735	0.048	0.1644	0.0026	0.35919	1020	18	982.4	15	1104	50	982.4	7.5	0.1101449	0.0368627	128.5	1.5523129
RT15-11_g003	0.693	0.024	0.0807	0.0018	0.43369	536	15	500.4	11	658	74	500.4	5.5	0.2395137	0.0664179	119.1	0.3557453
RT15-11_g004	1.369	0.042	0.1456	0.0025	0.41393	874	18	877.1	14	881	58	877.1	7	0.0044268	-0.0035469	135	0.4
RT15-11_g005	5.793	0.14	0.34	0.005	0.5009	1945	21	1886	24	2005	38	2005	19	0.0593516	0.0303342	128.7	0.7423905
RT15-11_g006	0.832	0.025	0.1006	0.0015	0.20502	613	14	617.9	8.9	591	65	617.9	4.45	-0.0455161	-0.0079935	124.1	0.761035
RT15-11_g007	6.036	0.13	0.3259	0.0045	0.70607	1980.6	19	1819	22	2157	34	2157	17	0.1566991	0.0815914	548	0.149925
RT15-11_g009	0.951	0.027	0.10979	0.0015	0.16598	677.6	14	671.5	8.8	686	59	671.5	4.4	0.021137	0.0090024	148	0.3965107
RT15-11_g010	13.63	0.3	0.5174	0.0074	0.65261	2725.1	22	2688	31	2746	33	2746	16.5	0.0211216	0.0136142	157.5	0.8084074
RT15-11_g011	1.364	0.033	0.1433	0.0023	0.4255	873.2	14	863.2	13	891	48	863.2	6.5	0.0312009	0.0114521	413	0.81103
RT15-11_g012	1.032	0.042	0.0945	0.0022	0.963	718	21	582	13	1152	51	582	6.5	0.4947917	0.189415	1032	0.1538462
RT15-11_g013	0.79	0.02	0.09447	0.0015	0.22957	591.8	12	581.9	8.6	626	54	581.9	4.3	0.0704473	0.0167286	233.9	1.0752688
RT15-11_g014	1.07	0.057	0.1266	0.0025	-0.054591	736	27	768	14	640	120	768	7	-0.2	-0.0434783	22.4	0.5945303
RT15-11_g015	6.191	0.14	0.3596	0.0052	0.49796	2004.4	19	1980	25	2028	37	2028	18.5	0.0236686	0.0121732	277.7	0.2747253
RT15-11_g016	0.73	0.019	0.08788	0.0015	0.6303	557.5	11	542.9	8.7	613	49	542.9	4.35	0.1143556	0.0261883	611	1.4992504
RT15-11_g018	0.2204	0.0056	0.03165	0.00057	0.61382	202.2	4.6	200.8	3.6	210	52	200.8	1.8	0.0438095	0.0069238	1305	0.4474273
RT15-11_g019	0.898	0.025	0.10674	0.0015	0.36491	652.1	13	653.7	8.8	647	53	653.7	4.4	-0.0103555	-0.0024536	215.5	0.6747638
RT15-11_g020	2.077	0.051	0.1498	0.0022	0.8676	1140.4	17	899.7	13	1626	38	899.7	6.5	0.446679	0.2110663	997	0.1506024
RT15-11_g021	2.14	0.12	0.1313	0.0039	0.98127	1148	39	795	22	1885	57	795	11	0.5782493	0.3074913	1410	0.0581395
RT15-11_g022	0.702	0.018	0.08362	0.0012	0.38605	539.6	11	517.7	7.3	644	51	517.7	3.65	0.196118	0.0405856	670	0.2245173
RT15-11_g023	3.051	0.068	0.1704	0.0024	0.78517	1420.8	17	1015.3	13	2102.8	34	2102.8	17	0.5171676	0.2854026	1880	0.1026483
RT15-11_g024	0.716	0.018	0.08991	0.0013	0.16297	548	11	555	7.8	530	56	555	3.9	-0.0471698	-0.0127737	323	1.1281588
RT15-11_g025	0.6539	0.015	0.08184	0.0011	0.12116	510.7	9.2	507.1	6.4	517	48	507.1	3.2	0.0191489	0.0070491	1022	0.4995005
RT15-11_g026	6.222	0.15	0.3617	0.0053	0.64499	2007	21	1990	25	2028	37	2028	18.5	0.0187377	0.0084704	319	0.4068348
RT15-11_g027	0.7871	0.017	0.09427	0.0013	0.48565	589.4	9.8	580.7	7.7	639	39	580.7	3.85	0.0912363	0.0147608	1836	0.0280112

Sample 17NP439	Sample Type: igneous					Latitude:	39.309282	Longitude:	74.864591								
	Conventional concordia					Ages								Discordance		~U[ppm]	Th/U
Sample #	207Pb	±2σ	206Pb	±2σ	error corr.	207Pb	±2σ	206Pb	±2σ	207Pb	±2σ	Best Age	±1σ	206/238	206/238		
_grain number	235U		238U		206/238 vs 207/235	235U		238U		206Pb				207/206	207/235		
17NP439_g01	0.2832	0.007	0.03839	0.0005	0.39212	253.5	5.6	242.8	3.1	337	50	242.8	1.55	0.2795252	0.0422091	212	0.5649718
17NP439_g01b	0.343	0.014	0.04097	0.00044	0.18324	299	11	258.9	2.7	593	83	258.9	1.35	0.5634064	0.1341137	124.7	0.6203474
17NP439_g02	0.4993	0.009	0.06564	0.00068	0.49378	411.5	6.1	409.8	4.1	410	35	409.8	2.05	0.0004878	0.0041312	345	1.4925373
17NP439_g02b	0.5046	0.0071	0.06666	0.00053	0.25691	414.6	4.8	416	3.2	401	29	416	1.6	-0.0374065	-0.0033767	219	1.2515645
17NP439_g03	0.502	0.018	0.06494	0.00084	0.32961	413	12	405.6	5.1	444	76	405.6	2.55	0.0864865	0.0179177	98.3	0.8071025
17NP439_g03b	0.535	0.013	0.06983	0.0007	0.22261	435.1	8.7	435.1	4.2	442	51	435.1	2.1	0.0156109	0	55.04	0.7173601
17NP439_g04	0.2758	0.0067	0.0397	0.00036	0.043245	248.1	5.3	251	2.3	197	53	251	1.15	-0.2741117	-0.0116888	130.3	0.4621072
17NP439_g04b	0.2773	0.0062	0.03895	0.00033	0.25937	248.2	4.9	246.5	2	260	48	246.5	1	0.0519231	0.0068493	127.55	0.5356186
17NP439_g05	0.2828	0.0075	0.03859	0.0004	0.16794	252.6	6	244.1	2.5	327	59	244.1	1.25	0.2535168	0.03365	143.5	0.6097561
17NP439_g05b	0.369	0.028	0.04037	0.00046	0.38315	321	20	255.1	2.9	780	150	255.1	1.45	0.6729487	0.205296	119.9	0.422119
17NP439_g06	0.299	0.011	0.04159	0.00055	0.33707	265.3	8.8	262.6	3.4	298	75	262.6	1.7	0.1187919	0.0101772	80.2	0.6222775
17NP439_g06b	0.2794	0.0073	0.04079	0.00042	0.011391	249.9	5.8	257.7	2.6	179	61	257.7	1.3	-0.4396648	-0.0312125	90.03	0.4694836
17NP439_g07	0.4866	0.0099	0.06514	0.00059	0.16332	402.3	6.8	406.8	3.6	357	45	406.8	1.8	-0.1394958	-0.0111857	167.5	0.789266
17NP439_g07b	0.5268	0.0082	0.06802	0.00066	0.34606	430.6	5.4	424.2	4	464	32	424.2	2	0.0857759	0.014863	127.1	1.0615711
17NP439_g08	0.7	0.073	0.0678	0.0014	0.65314	543	45	423	8.6	1010	190	423	4.3	0.5811881	0.2209945	68.1	1.2738854
17NP439_g08b	0.528	0.014	0.06889	0.00094	0.21195	431.5	9.5	429.5	5.7	450	58	429.5	2.85	0.0455556	0.004635	103.1	0.6934813
17NP439_g09	0.2873	0.0072	0.03978	0.00039	0.035325	256.7	5.6	251.5	2.4	273	56	251.5	1.2	0.0787546	0.0202571	131.8	0.463392
17NP439_g09b	0.277	0.0048	0.03906	0.00032	0.25331	248.1	3.8	247	2	247	36	247	1	0	0.0044337	137.8	0.4593477
17NP439_g10	9.196	0.11	0.4441	0.0035	0.53224	2359.4	11	2369	15	2352	18	2352	9	-0.0072279	-0.0040688	158	0.5230126
17NP439_g11	0.4918	0.011	0.06477	0.00097	0.6204	405.8	7.4	404.5	5.9	393	39	404.5	2.95	-0.0292621	0.0032035	273	1.303781
17NP439_g11b	0.692	0.029	0.06926	0.00067	0.38512	532	17	431.7	4.1	988	78	431.7	2.05	0.5630567	0.1885338	260	0.6510417
17NP439_g12	0.2714	0.0088	0.04028	0.00063	0.36907	243.5	7	254.6	3.9	134	64	254.6	1.95	-0.9	-0.0455852	101.7	0.5521811
17NP439_g12b	0.291	0.011	0.0399	0.00046	0.11612	259.1	8.5	252.2	2.9	302	87	252.2	1.45	0.1649007	0.0266306	100.5	0.5688282
17NP439_g13	0.2749	0.0092	0.03935	0.00048	0.1039	246.3	7.3	248.8	3	222	73	248.8	1.5	-0.1207207	-0.0101502	124.5	0.598444
17NP439_g13b	0.2858	0.0047	0.04004	0.00032	0.28462	255.4	3.7	253.1	2	274	33	253.1	1	0.0762774	0.0090055	210.9	0.7189073
17NP439_g14	0.5323	0.0083	0.06875	0.00072	0.69544	434	5.5	428.6	4.3	448	27	428.6	2.15	0.0433036	0.0124424	937	0.499002
17NP439_g14b	0.5278	0.0043	0.06986	0.00052	0.54039	430.3	2.8	435.3	3.1	408	13	435.3	1.55	-0.0669118	-0.0116198	1241	0.3616637
17NP439_g15	0.5031	0.0098	0.06517	0.00065	0.47533	413.5	6.6	407	3.9	464	39	407	1.95	0.1228448	0.0157195	282.9	1.1523392
17NP439_g15b	0.53	0.013	0.0688	0.001	0.51397	431.6	8.8	428.9	6.3	432	47	428.9	3.15	0.0071759	0.0062558	174	0.9910803
17NP439_g16	0.2758	0.0062	0.03957	0.0004	0.24057	248.1	4.7	250.4	2.5	215	45	250.4	1.25	-0.1646512	-0.0092705	125.2	0.4557885
17NP439_g16b	0.2806	0.0059	0.03895	0.00035	0.050526	250.9	4.6	246.3	2.2	285	51	246.3	1.1	0.1357895	0.018334	128.22	0.5122951

Sample 17NP439 continued

	Conventional concordia				Ages								Discordance		~U[ppm]	Th/U
Sample #	207Pb	±2σ	206Pb	±2σ	error corr.	207Pb	±2σ	206Pb	±2σ	207Pb	±2σ	Best Age	±1σ	206/238	206/238		
_grain number	235U		238U		206/238 vs 207/235	235U		238U		206Pb				207/206	207/235		
17NP439_g17b	0.2837	0.0095	0.03929	0.00042	0.10813	254.4	7.7	248.4	2.6	296	75	248.4	1.3	0.1608108	0.0235849	170.4	0.4206984
17NP439_g18	0.356	0.023	0.04035	0.00046	0.39003	301	15	255	2.9	583	94	255	1.45	0.5626072	0.1528239	112.9	0.4450378
17NP439_g18b	0.2703	0.0062	0.0383	0.00031	0.11006	242.6	5	242.3	1.9	244	50	242.3	0.95	0.0069672	0.0012366	133.5	0.5720824
17NP439_g19	0.5482	0.011	0.06722	0.00063	0.41684	443.5	7.3	419.4	3.8	567	42	419.4	1.9	0.2603175	0.0543405	289.8	1.5267176
17NP439_g19b	0.55	0.016	0.06958	0.00096	0.038671	445	11	433.6	5.8	503	70	433.6	2.9	0.1379722	0.025618	135	0.805153
17NP439_g20	0.3146	0.0052	0.0433	0.00047	0.6681	277.6	4	273.3	2.9	326	32	273.3	1.45	0.1616564	0.0154899	641	0.9950249
17NP439_g20b	0.354	0.01	0.03965	0.00031	0.27858	306.8	7.8	250.6	1.9	748	58	250.6	0.95	0.6649733	0.1831812	380	0.621504
17NP439_g21	0.848	0.034	0.06756	0.00071	0.62902	620	18	421.4	4.3	1425	72	421.4	2.15	0.7042807	0.3203226	135.2	0.8404774
17NP439_g22	0.2753	0.01	0.03928	0.00055	0.026667	246.6	8.2	248.4	3.4	245	83	248.4	1.7	-0.0138776	-0.0072993	81.4	0.4071661
17NP439_g22b	0.2848	0.0065	0.03953	0.00039	0.14612	254.2	5.1	249.9	2.4	266	49	249.9	1.2	0.0605263	0.0169158	95.5	0.4314064
17NP439_g23	7.771	0.093	0.4021	0.0034	0.68244	2205	11	2178	16	2223.7	18	2223.7	9	0.0205513	0.0122449	473	0.2264493
17NP439_g23b	9.39	0.14	0.4578	0.0058	0.93166	2377	13	2428	26	2325.2	8.7	2325.2	4.35	-0.0442113	-0.0214556	345	0.4775549
17NP439_g24	0.2926	0.0082	0.04083	0.0005	0.2342	260.8	6.5	258	3.1	236	60	258	1.55	-0.0932203	0.0107362	74.9	0.4393673
17NP439_g25	0.2779	0.0071	0.03884	0.00042	0.011666	248.8	5.7	245.6	2.6	284	61	245.6	1.3	0.1352113	0.0128617	186.5	0.6761325
17NP439_g25b	0.2806	0.0075	0.03947	0.00039	0.16065	250.8	5.9	249.5	2.4	261	55	249.5	1.2	0.0440613	0.0051834	126.5	0.4651163
17NP439_g26	8.199	0.1	0.4176	0.0041	0.79382	2253.4	12	2249	19	2258.3	17	2258.3	8.5	0.0041181	0.0019526	542.2	0.6349206
17NP439_g27	0.641	0.078	0.0665	0.0012	0.6746	495	45	414.7	7	880	210	414.7	3.5	0.52875	0.1622222	194.1	2.3803856
17NP439_g27b	0.4873	0.0065	0.06391	0.00051	0.32521	402.8	4.4	399.4	3.1	414	28	399.4	1.55	0.0352657	0.0084409	218	2.0746888
17NP439_g28	0.2838	0.0064	0.0398	0.00039	0.11569	253.9	5	251.6	2.4	278	50	251.6	1.2	0.094964	0.0090587	132.4	0.4334634
17NP439_g29	0.4932	0.0085	0.06439	0.00057	0.26253	406.8	5.8	402.3	3.4	447	36	402.3	1.7	0.1	0.0110619	183.8	1.0869565
17NP439_g29b	0.2838	0.0075	0.03827	0.0004	0.12238	253.2	5.9	242.1	2.5	344	61	242.1	1.25	0.2962209	0.0438389	122.6	0.6337136
17NP439_g30	0.2834	0.0061	0.03978	0.00036	0.10788	253.5	4.8	251.5	2.2	261	47	251.5	1.1	0.0363985	0.0078895	147	0.4870921
17NP439_g30b	0.517	0.016	0.06825	0.00074	0.14204	423	11	425.6	4.5	389	71	425.6	2.25	-0.0940874	-0.0061466	73.2	1.0461345
17NP439_g31	0.4953	0.0099	0.06528	0.00063	0.1102	408.2	6.7	407.6	3.8	411	47	407.6	1.9	0.0082725	0.0014699	240	0.7326007

Sample 15NP245	Sample Type: igneous												Latitude:	39.31775	Longitude:	74.59724		
	Conventional concordia					Ages									Discordance		~U[ppm]	Th/U
Sample #	207Pb	±2σ	206Pb	±2σ	error corr.	207Pb	±2σ	206Pb	±2σ	207Pb	±2σ	Best Age	±1σ	206/238	206/238			
_grain number	235U		238U		206/238 vs 207/235	235U		238U		206Pb				207/206	207/235			
15NP245_g01	0.4411	0.0071	0.05564	0.00048	0.20094	0.20094	5	349	2.9	502	40	349	1.45	0.3047809	0.0587918	335.4	0.4512635	
15NP245_g02	0.455	0.011	0.05943	0.00063	0.23661	-0.23661	8	372.2	3.8	460	65	372.2	1.9	0.1908696	0.0218134	189.7	0.4275331	
15NP245_g03_c	0.831	0.049	0.0997	0.0049	0.984	0.984	27	610	29	571	32	610	14.5	-0.0683012	-0.0183639	257	0.265252	
15NP245_g04	0.4219	0.0054	0.05756	0.00047	0.61151	0.61151	3.9	360.7	2.8	346	24	360.7	1.4	-0.0424855	-0.0100812	490	0.3447087	
15NP245_g05	0.4223	0.0085	0.0568	0.00061	0.43936	0.43936	6.1	356.1	3.7	371	39	356.1	1.85	0.0401617	0.002521	137.2	0.3963535	
15NP245_g06	6.055	0.053	0.3622	0.0028	0.77078	0.77078	7.7	1993	13	1986	11	1986	5.5	-0.0035247	-0.0048402	95.8	0.9485866	
15NP245_g07	0.425	0.011	0.05837	0.00061	0.21462	0.21462	7.9	365.7	3.7	326	50	365.7	1.85	-0.1217791	-0.0180958	208.6	0.4301075	
15NP245_g08	0.469	0.024	0.0605	0.0011	0.49507	0.49507	17	378.4	6.5	460	110	378.4	3.25	0.1773913	0.0297436	103.3	0.3295979	
15NP245_g09	0.395	0.012	0.05329	0.00064	0.2676	0.2676	8.7	334.7	3.9	360	73	334.7	1.95	0.0702778	0.0082963	120.9	0.6169031	
15NP245_g10	0.4178	0.0056	0.05645	0.00043	0.39451	0.39451	4.1	354	2.6	352	29	354	1.3	-0.0056818	0.0014104	240.9	0.4086637	
15NP245_g11	0.4262	0.0078	0.05748	0.0006	0.3532	0.3532	5.5	360.2	3.7	386	39	360.2	1.85	0.0668394	0.0005549	151.8	0.4880429	
15NP245_g12	0.4296	0.0065	0.05808	0.00052	0.56719	0.56719	4.6	363.9	3.2	377	30	363.9	1.6	0.034748	-0.0038621	229	0.5002501	
15NP245_g13	1.104	0.041	0.1216	0.0024	0.39739	0.39739	20	739	14	826	68	739	7	0.1053269	0.0146667	25.51	0.9337068	
15NP245_g14	0.4069	0.0059	0.05512	0.00049	0.40465	0.40465	4.3	345.9	3	367	29	345.9	1.5	0.0574932	0.0014434	387.9	0.4130525	
15NP245_g15	0.4269	0.0078	0.05774	0.00051	0.39303	0.39303	5.2	361.8	3.1	358	32	361.8	1.55	-0.0106145	0.0013801	241	0.5733945	
15NP245_g16	0.443	0.013	0.05843	0.00065	0.16363	0.16363	9	366.1	4	418	64	366.1	2	0.1241627	0.0153308	174	0.4690432	
15NP245_g17	0.4025	0.0066	0.05479	0.00048	0.24239	0.24239	4.8	343.8	2.9	324	38	343.8	1.45	-0.0611111	-0.0017483	173	0.4378284	
15NP245_g18	0.4243	0.0088	0.0567	0.0005	0.32563	0.32563	6.4	355.5	3.1	384	50	355.5	1.55	0.0742188	0.0114016	195.5	0.3617945	
15NP245_g19	0.4272	0.0064	0.05703	0.00045	0.43815	0.43815	4.5	357.5	2.7	382	28	357.5	1.35	0.0641361	0.0091463	251.8	0.3685957	
15NP245_g20	0.421	0.013	0.05717	0.00066	0.096776	0.096776	9	358.3	4	332	64	358.3	2	-0.0792169	-0.0044856	43.47	0.3397893	
15NP245_g21	0.4246	0.009	0.05693	0.00059	0.43025	0.43025	6.3	356.9	3.6	377	38	356.9	1.8	0.0533156	0.0061264	225.5	0.5830904	
15NP245_g22	1.197	0.018	0.1291	0.0016	0.52137	0.52137	8.4	782.4	9	848	28	782.4	4.5	0.0773585	0.0205308	224.6	0.4086637	
15NP245_g23	0.4828	0.0075	0.06309	0.0007	0.582	0.582	5.1	394.4	4.3	434	27	394.4	2.15	0.0912442	0.0135068	728	0.1785714	
15NP245_g24	0.445	0.01	0.05986	0.00076	0.01714	0.01714	7.2	374.7	4.6	355	45	374.7	2.3	-0.055493	-0.004827	112.8	0.5889282	
15NP245_g25	0.4099	0.0059	0.05576	0.00041	0.52052	0.52052	4.2	349.8	2.5	340	28	349.8	1.25	-0.0288235	-0.0017182	305	0.5730659	
15NP245_g26	0.4141	0.0067	0.05584	0.00053	0.34284	0.34284	4.8	350.3	3.2	364	36	350.3	1.6	0.0376374	0.0042638	188.7	0.623558	
15NP245_g27	0.4176	0.0062	0.05694	0.00045	0.42833	0.42833	4.4	357	2.7	316	32	357	1.35	-0.1297468	-0.0076207	244	0.3386387	
15NP245_g28	0.408	0.02	0.05427	0.00086	0.20637	0.20637	14	340.6	5.3	370	100	340.6	2.65	0.0794595	0.0212644	24.88	0.3506311	
15NP245_g29	0.4339	0.0097	0.05789	0.00053	0.13588	0.13588	6.8	362.7	3.2	372	48	362.7	1.6	0.025	0.0063014	95	0.3015682	
15NP245_g30	0.425	0.012	0.05804	0.00069	0.42938	0.42938	8.6	363.7	4.2	349	61	363.7	2.1	-0.0421203	-0.0136566	214.6	0.4166667	
15NP245_g31	0.5271	0.0096	0.07102	0.00069	0.44888	0.44888	6.4	442.3	4.1	353	32	442.3	2.05	-0.2529745	-0.0293228	1070	0.8223684	

Sample 15NP245	Sample Type: igneous																
	Conventional concordia					Ages								Discordance		~U[ppm]	Th/U
Sample #	207Pb	±2σ	206Pb	±2σ	error corr.	207Pb	±2σ	206Pb	±2σ	207Pb	±2σ	Best Age	±1σ	206/238	206/238		
_grain number	235U		238U		206/238 vs 207/235	235U		238U		206Pb				207/206	207/235		
15NP245_g32	0.416	0.0097	0.056	0.00061	0.20123	0.20123	6.8	351.2	3.7	361	53	351.2	1.85	0.0271468	0.0065064	184.1	0.4798464
15NP245_g33	0.413	0.014	0.05591	0.00051	0.19622	0.19622	9.7	350.7	3.1	336	72	350.7	1.55	-0.04375	0.0025597	119.6	0.5580357
15NP245_g34	2.973	0.047	0.1932	0.0022	0.71594	0.71594	12	1139	12	1812	20	1812	10	0.3714128	0.1864286	154.3	0.4761905
15NP245_g35	0.44	0.016	0.0576	0.001	0.57053	0.57053	11	360.8	6.1	413	53	360.8	3.05	0.1263923	0.0301075	619	0.6997901
15NP245_g36	0.4344	0.0076	0.05897	0.00055	0.39571	0.39571	5.4	369.4	3.3	370	37	369.4	1.65	0.0016216	-0.0092896	347	0.5608525
15NP245_g37	0.4381	0.0068	0.05869	0.00055	0.46056	0.46056	4.8	367.6	3.4	407	30	367.6	1.7	0.0968059	0.0059492	255.5	0.4269855
15NP245_g38	0.4281	0.0062	0.05796	0.0005	0.51266	0.51266	4.4	363.2	3.1	347	30	363.2	1.55	-0.0466859	-0.0030378	395	0.6345983

Appendix A.8: LA-ICP-MS calcite U-Pb data.

Sample 17NP438	Sample Type: Limestone				Latitude:	39.30856	Longitude:	74.856774
	Tera-Wasserburg				Th/U	U/Pb	U238 [ppm]	U238 [ppm]
Sample # _grain number	238U 206Pb	±σ	207Pb 206Pb	±σ				2SE
17NP438_s01	1.60524	0.042825	0.756	0.0095	0.081683	0.557857	0.202	0.017
17NP438_s02	2.10055	0.042579	0.741	0.01	0.033938	0.640275	0.1488	0.0038
17NP438_s03	1.052646	0.021386	0.813	0.008	0.133333	0.306833	0.1455	0.0035
17NP438_s04	0.142825	0.0035	0.8328	0.005	0.086034	0.040939	0.0759	0.0033
17NP438_s05	0.189562	0.004431	0.847	0.006	0.032887	0.051573	0.0672	0.0021
17NP438_s06	1.619174	0.030922	0.776	0.009	0.02351	0.491916	0.1795	0.0044
17NP438_s07	0.266394	0.004565	0.859	0.0055	0.036902	0.0715	0.1149	0.0029
17NP438_s08	1.222339	0.027234	0.808	0.006	0.002837	0.359336	0.3137	0.0098
17NP438_s09	1.89948	0.05416	0.772	0.0095	0.114286	0.601989	0.224	0.013
17NP438_s10	0.613178	0.018746	0.838	0.006	0.273702	0.171086	0.1213	0.0034
17NP438_s11	1.80745	0.038531	0.769	0.0085	0.042713	0.562947	0.1887	0.0051
17NP438_s12	7.772037	0.187824	0.652	0.009	0.070667	2.762431	1.2	0.059
17NP438_s13	0.75274	0.019745	0.804	0.0075	0.020016	0.217522	0.1229	0.0034
17NP438_s14	0.500614	0.01142	0.843	0.007	0.025118	0.143148	0.1055	0.0045
17NP438_s15	1.343868	0.024205	0.776	0.0095	0.008622	0.414071	0.1183	0.0034
17NP438_s16	1.828714	0.03765	0.776	0.0105	-2.3E-06	0.542191	0.1465	0.0038
17NP438_s17	5.635314	0.100448	0.607	0.007	0.021894	2.180209	0.813	0.023
17NP438_s18	1.434838	0.027593	0.804	0.0095	0.004976	0.420056	0.1487	0.0041
17NP438_s19	2.711176	0.05911	0.751	0.0105	0.005685	0.834992	0.2181	0.0042
17NP438_s20	1.773089	0.035394	0.787	0.009	0.030385	0.52934	0.1741	0.0036
17NP438_s21	0.083796	0.002221	0.8559	0.0047	0.011282	0.023086	0.0585	0.0017
17NP438_s22	2.56221	0.049273	0.749	0.0105	0.004727	0.805045	0.1883	0.0032
17NP438_s23	1.040897	0.021492	0.812	0.01	0.069237	0.298732	0.1154	0.0035
17NP438_s24	1.075715	0.021092	0.816	0.008	0.028992	0.303657	0.1528	0.0034
17NP438_s25	0.87737	0.026412	0.803	0.008	0.072564	0.278269	0.1447	0.0098
17NP438_s26	0.210529	0.004515	0.861	0.006	0.016937	0.057251	0.0679	0.002
17NP438_s27	0.185786	0.004996	0.8427	0.005	0.04731	0.05077	0.0725	0.0023
17NP438_s28	-3.8E-05	3.9E-06	0.8619	0.0042	7.022222	0.000376	0.00135	0.00024
17NP438_s29	0.004687	0.000271	0.8603	0.0044	-5.2E-05	0.00165	0.0062	0.0006
17NP438_s30	0.00594	0.000359	0.8532	0.004	-6.8E-05	0.001947	0.00469	0.00059
17NP438_s31	0.003018	0.000156	0.8544	0.0039	-7.9E-05	0.000933	0.00397	0.00047
17NP438_s32	0.810291	0.023232	0.798	0.009	0.034867	0.239698	0.0826	0.0038
17NP438_s33	0.382231	0.014882	0.858	0.0095	0.182245	0.109429	0.0383	0.0014
17NP438_s34	0.008479	0.000501	0.8496	0.0045	0.051843	0.002931	0.00868	0.00066
17NP438_s35	1.466422	0.035738	0.797	0.0145	-4.2E-06	0.427005	0.074	0.0023
17NP438_s36	0.437861	0.016445	0.831	0.007	0.041404	0.131207	0.0983	0.0076
17NP438_s37	2.2637	0.046703	0.74	0.008	0.007462	0.728111	0.3002	0.0053
17NP438_s38	0.587308	0.014054	0.828	0.008	0.008189	0.165024	0.1038	0.0024
17NP438_s39	1.756392	0.034731	0.778	0.012	-3E-06	0.537203	0.1018	0.0023
17NP438_s40	1.730324	0.033708	0.8	0.011	-2.5E-06	0.511667	0.1206	0.0027
17NP438_s41	2.241934	0.048503	0.763	0.01	0.032667	0.703686	0.1451	0.0037
17NP438_s42	1.439266	0.027764	0.819	0.0125	0.029323	0.413043	0.0798	0.0021
17NP438_s43	0.885702	0.018925	0.817	0.01	0.034826	0.256968	0.1005	0.0026
17NP438_s44	0.007012	0.000369	0.8599	0.00485	1.446154	0.002142	0.0039	0.00046
17NP438_s45	0.156222	0.002878	0.8571	0.00475	0.022523	0.04326	0.1181	0.0029
17NP438_s46	0.554485	0.010549	0.838	0.006	0.012471	0.15819	0.1748	0.0036
17NP438_s47	0.21589	0.007496	0.846	0.006	0.132509	0.061555	0.1132	0.0042
17NP438_s48	0.419543	0.008682	0.827	0.0065	0.110927	0.120679	0.1208	0.003
17NP438_s49	0.806786	0.013958	0.829	0.0085	0.023577	0.228158	0.123	0.0027
17NP438_s50	0.31918	0.006008	0.852	0.006	0.01796	0.088179	0.1559	0.0041
17NP438_s51	2.38528	0.045753	0.755	0.011	0.015521	0.748072	0.1746	0.0044
17NP438_s52	0.635749	0.012351	0.85	0.008	0.009834	0.179955	0.0966	0.0023
17NP438_s53	2.297154	0.045264	0.742	0.0095	0.02818	0.737132	0.1604	0.0049
17NP438_s54	0.163622	0.00488	0.858	0.0065	-5.3E-06	0.047731	0.0526	0.0027
17NP438_s55	1.494622	0.032336	0.773	0.0115	0.071188	0.468245	0.1187	0.0042
17NP438_s56	2.507109	0.053916	0.763	0.014	-1.6E-06	0.781868	0.1699	0.0045
17NP438_s57	0.049164	0.001127	0.8491	0.0041	0.177234	0.013848	0.047	0.0019
17NP438_s58	2.500387	0.046924	0.767	0.012	-1.5E-06	0.775832	0.1772	0.0031
17NP438_s59	0.173354	0.010311	0.831	0.0115	0.501911	0.053767	0.0157	0.001
17NP438_s60	0.078373	0.003952	0.856	0.009	0.195972	0.023178	0.01291	0.00087
17NP438_s61	0.770144	0.025438	0.811	0.007	0.028758	0.237337	0.1996	0.0094
17NP438_s62	0.665224	0.013286	0.827	0.008	0.012298	0.183704	0.0992	0.0033

Sample 17NP472		Sample Type: Limestone			Latitude:	39.31515	Longitude:	74.872241
	Tera-Wasserburg				Th/U	U/Pb	U238 [ppm]	U238 [ppm]
Sample #	238U	±σ	207Pb	±σ				2SE
_grain number	206Pb		206Pb					
17NP472_s01	3.39143459	0.0801612	0.742	0.0055	0.10103017	0.982646	1.359	0.041
17NP472_s02	2.84342765	0.1560418	0.71	0.0095	0.45750185	0.830061	1.353	0.029
17NP472_s03	13.8374587	0.3387507	0.429	0.009	0.38354978	7.588699	1.155	0.027
17NP472_s04	1.01595288	0.0265609	0.8061	0.004	0.30314092	0.298985	1.178	0.021
17NP472_s05	8.62760814	0.2713586	0.555	0.0105	0.07000977	3.529885	0.6142	0.0085
17NP472_s06	4.52740016	0.1868102	0.693	0.007	0.20196078	1.511858	1.53	0.042
17NP472_s07	0.62425995	0.018803	0.8301	0.00415	0.53363229	0.174902	0.892	0.019
17NP472_s08	0.45606088	0.0080285	0.8389	0.00375	0.09233083	0.129126	0.665	0.014
17NP472_s09	15.9426424	0.3270285	0.278	0.0085	0.53703083	13.65675	0.5968	0.0083
17NP472_s10	0.42801487	0.0082499	0.8327	0.00385	0.23369763	0.122136	0.549	0.015
17NP472_s11	8.79853202	0.9545578	0.42	0.017	0.19676946	4.10241	0.681	0.018
17NP472_s12	17.2392699	0.3823867	0.251	0.0065	0.09111111	16.56442	0.81	0.051
17NP472_s13	15.3901718	0.3047559	0.312	0.008	0.10204082	12.09877	0.882	0.016
17NP472_s14	8.39463916	0.2531237	0.539	0.0115	0.04556962	3.472527	0.948	0.021
17NP472_s15	4.39926601	0.1763857	0.709	0.0065	0.42778335	1.514047	1.994	0.051
17NP472_s16	0.89162942	0.0170484	0.819	0.00425	0.07843373	0.252972	0.83	0.013
17NP472_s17	0.25878038	0.0039492	0.8402	0.0037	0.28782708	0.072108	0.879	0.021
17NP472_s18	5.55145493	0.181744	0.655	0.0085	0.08003663	2.149606	0.546	0.032
17NP472_s19	1.49942829	0.0518291	0.779	0.0055	0.12642998	0.455935	0.507	0.016
17NP472_s20	13.5954002	0.3369122	0.417	0.009	0.1942789	7.327511	0.839	0.028
17NP472_s21	0.90548003	0.0835151	0.92	0.065	0.87591241	0.399029	0.0411	0.0075
17NP472_s22	-0.0696003	0.0153225	1.09	0.125	1.26234568	0.302804	0.00324	0.00048
17NP472_s23	1.24352558	0.0572022	0.801	0.0075	0.3445122	0.383626	0.328	0.027
17NP472_s24	15.6221857	0.4971885	0.578	0.0135	0.13558179	6.315229	0.593	0.031
17NP472_s25	1.10372125	0.050941	0.771	0.01	0.62322695	0.359236	0.1128	0.0086
17NP472_s26	12.7934752	0.4036351	0.52	0.01	0.5202781	5.603896	0.863	0.044
17NP472_s27	16.7440637	0.3306727	0.319	0.01	0.09477534	12.41245	0.957	0.015
17NP472_s28	16.6246759	0.3259741	0.29	0.0085	0.14578189	12.85714	0.972	0.017
17NP472_s29	1.14999347	0.0311959	0.7966	0.005	0.37487352	0.322283	0.593	0.016
17NP472_s30	4.93462629	0.1566548	0.679	0.007	0.33360791	1.933121	0.607	0.048
17NP472_s31	1.07200481	0.038814	0.7993	0.0046	0.11740788	0.313546	0.787	0.019
17NP472_s32	0.24161777	0.0071985	0.8328	0.0035	0.31703704	0.068044	0.675	0.025
17NP472_s33	0.31950822	0.0060202	0.8339	0.0035	0.15264766	0.087914	0.982	0.03
17NP472_s34	0.49714518	0.0109976	0.8288	0.00385	0.20551471	0.141913	0.816	0.018
17NP472_s35	6.78780474	0.222308	0.637	0.0105	0.50942623	2.619431	0.488	0.013
17NP472_s36	7.63836526	0.181419	0.612	0.0075	0.37670068	2.932668	1.176	0.031
17NP472_s37	9.37330958	0.2119593	0.542	0.0085	0.4278297	4.046218	0.963	0.021
17NP472_s38	-0.092341	0.0173711	-0.04	0.415	2.06198347	0.378125	0.00242	0.00039
17NP472_s39	-0.0579282	0.010974	0.94	0.09	1.54545455	0.238144	0.00231	0.00036
17NP472_s40	10.782013	0.2617599	0.57	0.0095	0.41619798	4.666667	0.889	0.022
17NP472_s41	1.21596407	0.034085	0.8041	0.0043	0.40500569	0.35587	0.879	0.025
17NP472_s42	6.09571543	0.2390476	0.678	0.0075	0.34060721	2.155419	1.054	0.051
17NP472_s43	6.43203074	0.1330765	0.654	0.007	0.43942993	2.319559	0.842	0.028
17NP472_s44	10.8573241	0.2464702	0.489	0.0105	0.76574173	5.124886	0.5622	0.0075
17NP472_s45	0.48575227	0.0139148	0.8138	0.0041	0.37092846	0.134356	0.657	0.013

Appendix A.9: Whole-rock geochemistry of the investigated arc-magmatic rocks.

	Sample	17NP426	P09T32	P09T33	15NP247	16NP341	16NP342	RT13-108	RT13-109	RT13-111	RT13-115	RT13-146	RT13-149	15NP233-1	15NP233-2	15NP235	15NP236	31-08-13-01	15NP234	2011T49	01-09-13-01
	Outcrop Area	Oytag	Gez	Gez	Taergelake	Kalai Khumb	Kalai Khumb	Khingob Valley	Khingob Valley	Khingob Valley	Panj Valley	Kurguvad	Kurguvad	Qimgen - Akqiy	Qimgen - Akqiy	Qimgen - Akqiy	Qimgen - Akqiy	Altyn Darya	Qimgen - Akqiy	Quli river	Altyn Darya
	Latitude	38.946	38.816	38.837	39.318	38.661	38.657	38.752	38.748	38.786	38.525	38.456	38.427	39.305	39.305	39.301	39.305	39.236	39.305	39.288	39.260
	Longitude	75.359	75.457	75.478	74.597	70.902	70.894	71.232	71.233	71.212	70.819	71.114	71.041	74.863	74.863	74.857	74.858	72.255	74.863	74.889	72.259
	Petrology	Granitic gneiss	Granitoid	Granitoid	Granitoid	Granitoid	Granitoid	Granitoid	Granitoid	Granitoid	Granitoid	Granitic gneiss	Granitic gneiss	Basalt	Basalt	Basalt	Pillow basalt	Meta-basalt	Basalt	Basalt	Meta-basalt
Major elements in %	SiO2	75.60	75.10	74.90	69.70	76.20	42.90	73.58	77.61	62.93	69.90	73.60	68.95	37.67	37.74	47.45	38.54	54.16	49.56	51.23	50.43
	TiO2	0.24	0.24	0.25	0.45	0.19	0.07	0.22	0.06	0.53	0.29	0.21	0.29	0.84	0.84	1.57	0.93	0.69	0.86	2.49	1.34
	Al2O3	12.50	13.20	13.20	14.40	13.00	27.20	13.60	11.48	15.81	14.95	14.00	15.23	13.26	13.26	14.89	13.98	15.09	13.97	14.35	16.91
	FeO (0.89981*Fe2O3)	2.47	2.34	2.63	3.07	1.75	3.43	2.28	0.67	5.04	2.14	2.24	3.15	7.94	7.97	9.12	9.16	6.60	8.67	11.87	9.70
	Fe2O3	2.74	2.60	2.92	3.41	1.95	3.81	2.53	0.75	5.60	2.38	2.49	3.50	8.82	8.86	10.14	10.18	7.34	9.64	13.19	10.78
	MnO	0.06	0.07	0.04	0.05	0.01	0.06	0.05	0.03	0.10	0.05	0.03	0.06	0.11	0.11	0.21	0.14	0.13	0.16	0.15	0.15
	MgO	0.40	0.42	0.48	1.59	0.38	5.04	0.36	0.25	3.09	0.84	0.94	1.34	3.65	3.63	7.40	9.29	6.52	7.43	4.33	5.56
	CaO	2.45	1.97	2.59	0.86	2.15	15.14	1.96	1.79	4.32	1.42	2.53	4.00	17.45	17.34	7.18	9.52	7.13	8.54	5.63	6.40
	Na2O	4.71	4.96	4.64	3.79	4.15	0.91	3.60	5.49	3.64	4.01	3.79	3.53	2.84	2.84	2.97	1.78	5.40	4.00	4.80	4.92
	K2O	0.33	0.59	0.12	3.70	0.78	0.14	3.25	0.81	1.29	4.23	1.90	1.98	1.14	1.15	1.59	0.44	0.06	0.52	0.05	0.19
	P2O5	0.04	0.05	0.05	0.16	0.03	<0.01	0.05	0.01	0.09	0.07	0.05	0.06	0.12	0.12	0.14	0.10	0.08	0.10	0.35	0.12
Minor and trace elements in ppm	Ba	86.00	97.00	80.00	592.00	269.00	<10	485.00	196.00	354.00	665.00	797.00	788.00	52.00	45.00	241.00	22.00	32.00	73.00	54.00	42.00
	Rb	<10	14.00	<10	100.00	26.00	<10	103.00	30.00	42.00	131.00	58.00	61.00	19.00	19.00	54.00	12.00	<10	<10	19.00	<10
	Sr	80.00	56.00	98.00	89.00	95.00	245.00	89.00	75.00	123.00	92.00	351.00	446.00	256.00	259.00	121.00	112.00	52.00	292.00	118.00	267.00
	Zr	110.00	197.00	179.00	178.00	164.00	<10	140.00	70.00	121.00	120.00	85.00	92.00	40.00	40.00	104.00	40.00	45.00	46.00	330.00	92.00
	Nb	<10	2.02	3.66	12.35	7.09	3.62	9.89	5.42	6.86	6.92	7.03	4.52	<10	<10	<10	<10	<10	<10	<10	<10
	Ni	0.34	0.65	1.04	3.20	2.29	48.51	0.91	0.47	14.73	2.94	1.53	2.66	67.00	71.00	86.00	133.00	89.00	141.00	0.00	11.00
	Co	2.24	2.50	2.67	4.28	2.69	20.22	2.76	0.97	15.04	3.91	3.98	7.77	n.a.	n.a.	n.a.	n.a.	n.a.	n.a.	n.a.	n.a.
	Th	1.03	1.21	2.30	15.38	13.92	0.04	23.37	15.53	8.54	9.29	8.77	6.66	n.a.	n.a.	0.50	n.a.	n.a.	0.50	n.a.	0.20
	U	0.29	0.22	0.39	2.04	1.69	0.01	4.67	2.26	1.90	2.29	2.34	1.76	n.a.	n.a.	0.10	n.a.	n.a.	0.30	n.a.	0.10
	Pb	0.96	1.17	0.72	11.58	11.13	0.51	14.57	7.95	9.68	12.20	4.12	3.72	n.a.	n.a.	n.a.	n.a.	n.a.	n.a.	n.a.	n.a.
	V	14.49	10.19	13.53	26.37	9.52	26.58	14.44	5.02	109.90	26.63	42.70	77.53	n.a.	n.a.	n.a.	n.a.	n.a.	n.a.	n.a.	n.a.
	Zn	29.00	43.00	23.00	41.00	13.00	26.00	57.00	13.00	72.00	55.00	15.00	25.00	61.00	62.00	158.00	76.00	65.00	65.00	55.00	83.00
	Cr	0.40	1.11	2.01	5.76	2.43	153.83	2.23	0.86	61.57	7.47	2.79	4.75	178.00	180.00	196.00	345.00	365.00	431.00	<10	<10
	Sc	9.90	7.99	7.44	8.33	4.71	5.70	1.60	7.32	19.91	7.19	4.64	5.36	32.00	32.00	30.00	36.00	29.00	35.00	30.00	33.00
	Y	30.76	44.51	43.78	22.62	32.83	0.99	18.00	34.00	21.00	19.00	29.00	12.00	15.00	13.00	31.00	17.00	20.00	18.00	72.00	31.00
	La	8.39	6.56	10.39	32.37	33.06	0.73	14.98	23.34	21.09	27.04	54.50	20.10	3.20	3.10	4.20	3.10	3.06	3.80	21.79	4.84
	Ce	20.11	18.84	27.35	65.46	63.41	1.56	30.49	46.52	42.18	50.63	95.30	35.21	7.70	7.80	11.00	8.30	7.30	17.00	51.00	11.00
	Pr	2.51	2.78	3.51	7.56	6.38	<0.1	2.97	5.47	4.32	5.41	10.38	3.11	0.74	0.47	1.30	0.72	0.83	0.96	6.60	1.50
	Nd	13.03	15.44	18.43	29.79	24.57	0.75	13.87	22.54	19.57	22.35	39.35	12.55	5.60	5.30	7.70	6.30	6.00	6.20	32.00	9.20
	Sm	3.59	4.65	5.09	6.24	5.16	0.17	2.89	5.09	4.05	4.24	7.20	2.25	1.60	1.60	2.20	2.00	1.70	2.00	8.40	2.80
	Eu	0.71	1.06	0.91	0.60	0.57	0.22	0.29	0.63	0.70	0.59	0.59	0.37	0.65	0.65	0.91	0.83	0.80	0.73	2.30	1.30
	Gd	4.67	6.37	6.43	5.37	5.09	0.18	3.09	5.47	3.93	3.82	5.65	1.93	2.10	2.10	2.90	2.70	2.30	2.50	10.00	3.80
	Tb	0.84	1.17	1.18	0.85	0.85	<0.1	0.51	0.96	0.64	0.62	0.90	0.33	0.39	0.46	0.61	0.67	0.44	0.60	1.80	0.72
	Dy	5.44	7.77	7.61	4.77	5.58	0.19	2.99	6.03	3.94	3.73	5.49	1.99	2.40	2.40	3.20	3.00	2.60	2.80	11.00	4.30
	Ho	1.19	1.69	1.63	0.89	1.20	<0.1	0.65	1.28	0.79	0.74	1.11	0.42	0.53	0.52	0.69	0.63	0.53	0.60	2.40	0.89
	Er	3.67	5.30	5.07	2.45	3.64	0.13	2.07	3.85	2.36	2.12	3.43	1.32	1.60	1.60	2.10	1.90	1.70	1.80	7.00	2.90
	Tm	0.53	0.78	0.75	0.32	0.51	<0.1	0.32	0.58	0.31	0.29	0.49	0.20	0.22	0.22	0.28	0.22	0.27	0.21	1.10	0.43
	Yb	3.62	5.31	5.05	2.17	3.36	0.11	2.38	3.90	2.25	2.07	3.67	1.53	1.60	1.60	2.00	1.80	1.60	1.70	6.60	2.80
	Lu	0.55	0.80	0.76	0.31	0.51	<0.1	0.39	0.58	0.34	0.31	0.54	0.25	0.24	0.24	0.31	0.27	0.24	0.27	0.97	0.42
	REE	68.86	78.52	94.15	159.15	153.89	4.06		126.23	106.49	123.96	228.60	81.55	28.57	28.06	39.40	32.44	29.37	41.17	162.96	46.90
	La/Lu	1.64	0.87	1.46	11.17	7.01		4.13	4.30	6.66	9.21	10.81	8.53	1.43	1.38	1.45	1.23	1.36	1.51	2.41	1.23

Appendix A.10: Age compilation. Compiled and newly presented radiometric ages used for this study along with location name and coordinates of the samples.

Sample	Location	Age	Latitude	Longitude	Reference
		zircon U-Pb Data*			
15NP245	Taergelake valley	360.52±0.35	39.31775	74.59724	this study
RT13-109	Khingob valley	329.34±0.59	38.74758	71.23323	this study
RT13-108	Khingob valley	333.55±0.44	38.75177	71.23224	this study
RT13-111	Khingob valley	339.11±1.23	38.78572	71.21192	this study
RT13-115	Panj valley	334.29±0.52	38.52496	70.81857	this study
16NP342	Kalai Khumb	339.96±0.46	38.657017	70.89395	this study
16NP341	Kalai Khumb	337.43±0.38	38.660717	70.902117	this study
RT13-146	Kurguvad	322.14±0.66	38.45605	71.11402	this study
KL027 (Z06)	Oytag valley	331.07±14.47	39.011848	75.339947	Zhang et al., 2006
GZ-1 (J08)	Gez valley	338.03±2.09	38.818367	75.459894	Jiang et al., 2008
WYT-5 (J08)	Oytag valley	328.43±3.26	38.959667	75.377258	Jiang et al., 2008
10X01 (K15)	Oytag valley	322.76±1.57	38.984032	75.371532	Kang et al., 2015
D03-6 (J18)	Oytag valley	314.19±1.04	38.957673	75.362949	Ji et al., 2018
2RZ (L06)	East Mazar	338.52±8.31	36.475687	77.259808	Li et al., 2006
AD2a (S04)	Altyn Darya	5 ID-TIMS age	39.208433	72.239733	Schwab et al., 2004
AD6c (S04)	Altyn Darya	5 ID-TIMS age	39.30195	72.26975	Schwab et al., 2004
RT15-11	Khingob valley	576.19±1.34	38.69131	71.38139	this study
RT13-148	Panj valley	589.75±1.01	38.3997	71.06168	this study
17NP439	Qimgan	250.04±0.28	39.310325	74.856828	this study
		calcite U-Pb**			
17NP472	Qimgan	260.49 ± 2.20	39.315149	74.872241	this study
17NP438	Qimgan	347.02 ± 7.56	39.308558	74.856774	this study
		hornblende 40Ar/39Ar			
AD2e	Altyn Darya	357.1±2.5	39.227333	72.253	Schwab et al., 2004
AD6b	Altyn Darya	354.7±2.2	39.3048	72.267833	Schwab et al., 2004
		monazite U-Pb Data			
4717A2	Kurguvad	204.9±8.8	38.388317	71.1634	Schmidt et al., 2011

* Age of youngest coherant group of concordant grains (peakfit, Vermeesch, 2018) [Ma] ± 1s

** Calcite U-Pb ages (17NP472, 17NP438) are Tera-Wasserburg lower intercept ages.

Appendix A.11: Modal content of major minerals. Data (in percent), of thin sections from samples taken from plutonic rocks presented in this study, is used for Streckeisen-classification.

sample	Qz	Kfs	Pl	Bt	Ms	Chl	Am	Others	SUMME
RT13-146	50	0	10	20	10	0	0	10	100
17NP426	60	0	30	0	0	10	0	0	100
15NP247	42	0	40	0	0	18	0	0	100
P09T33	45	0	40	0	0	10	0	5	100
P09T32	45	0	40	5	0	9	0	1	100
RT13-108	35	0	45	10	0	0	10	0	100
RT13-111	25	0	50	0	0	24	0	1	100
16NP341	35	0	50	12	0	0	3	0	100
RT13-115	32	0	55	7	0	3	3	0	100
RT13-109	37	0	55	5	0	2	0	1	100
16NP342	20	0	70	0	0	0	0	10	100

B. Supplementary Material for Chapter 3

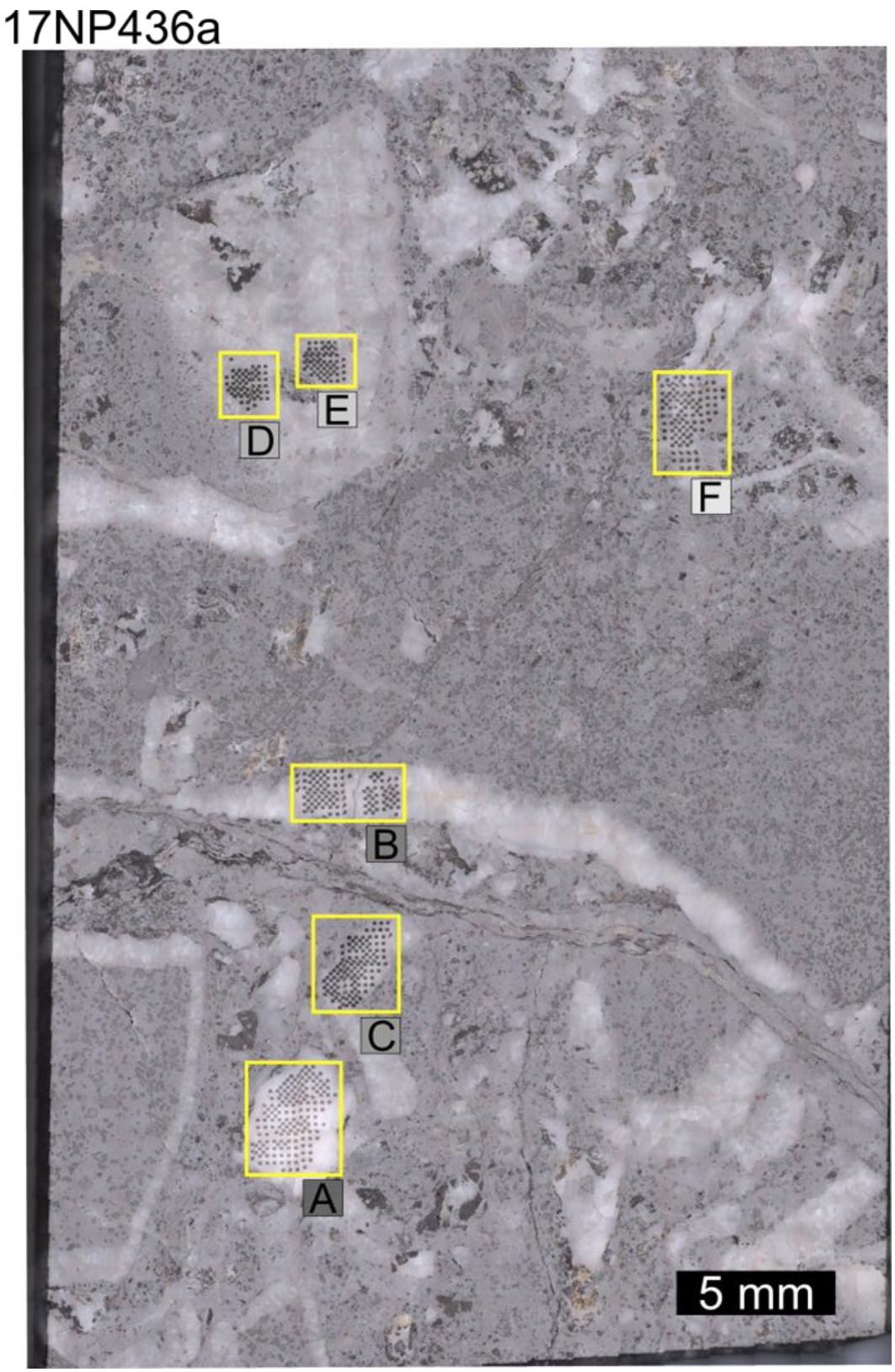

Appendix B.1: Reflected light image of sample 17NP436a with marked ablation areas. Letter, attached to the yellow boxes, appended to the sample name, labels the ablation areas. Colors of label boxes are consistent with colors of in-text figures.

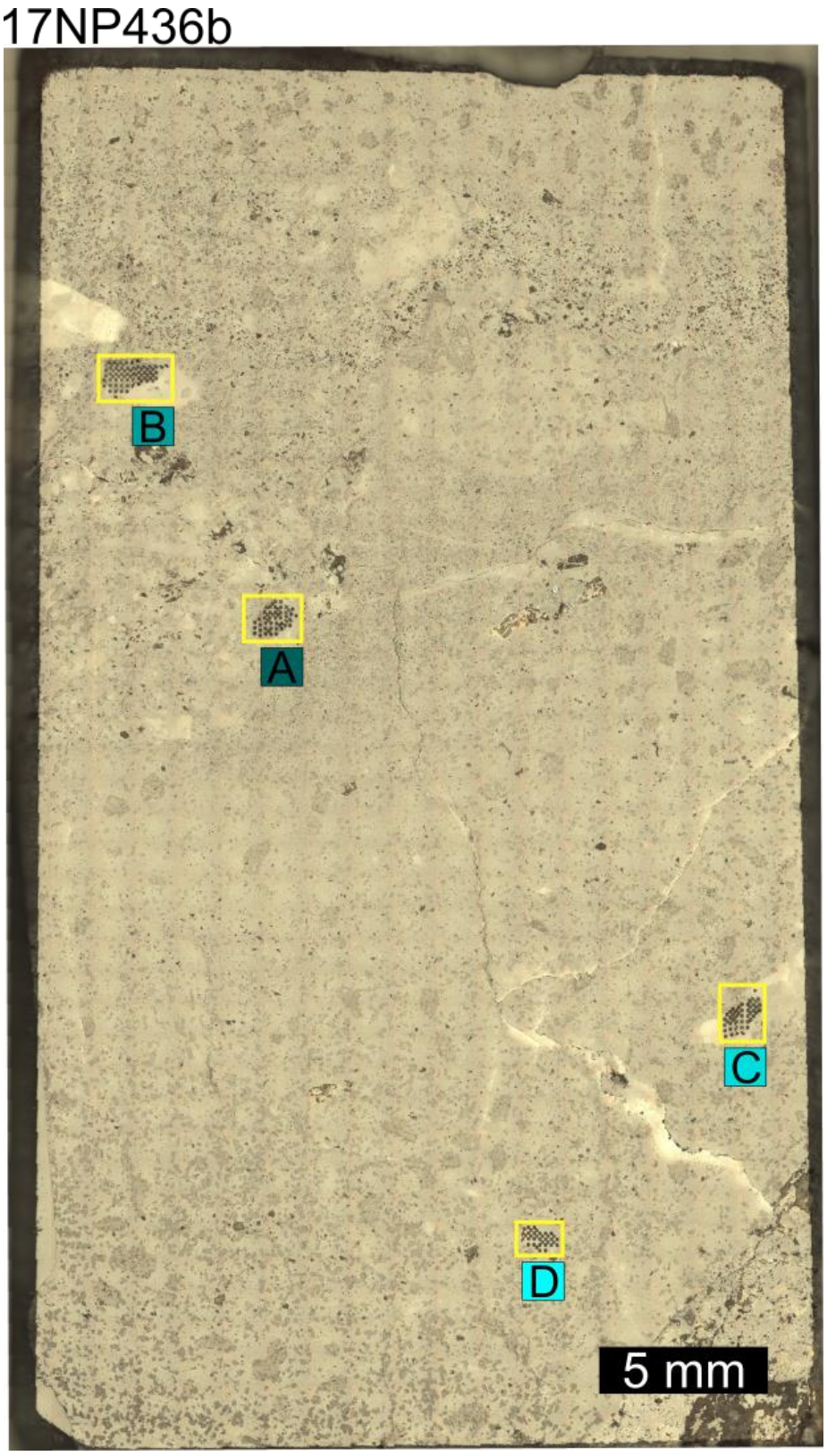

Appendix B.2: Reflected light image of sample 17NP436b with marked ablation areas. Letter, attached to the yellow boxes, appended to the sample name, labels the ablation areas. Colors of label boxes are consistent with colors of in-text figures.

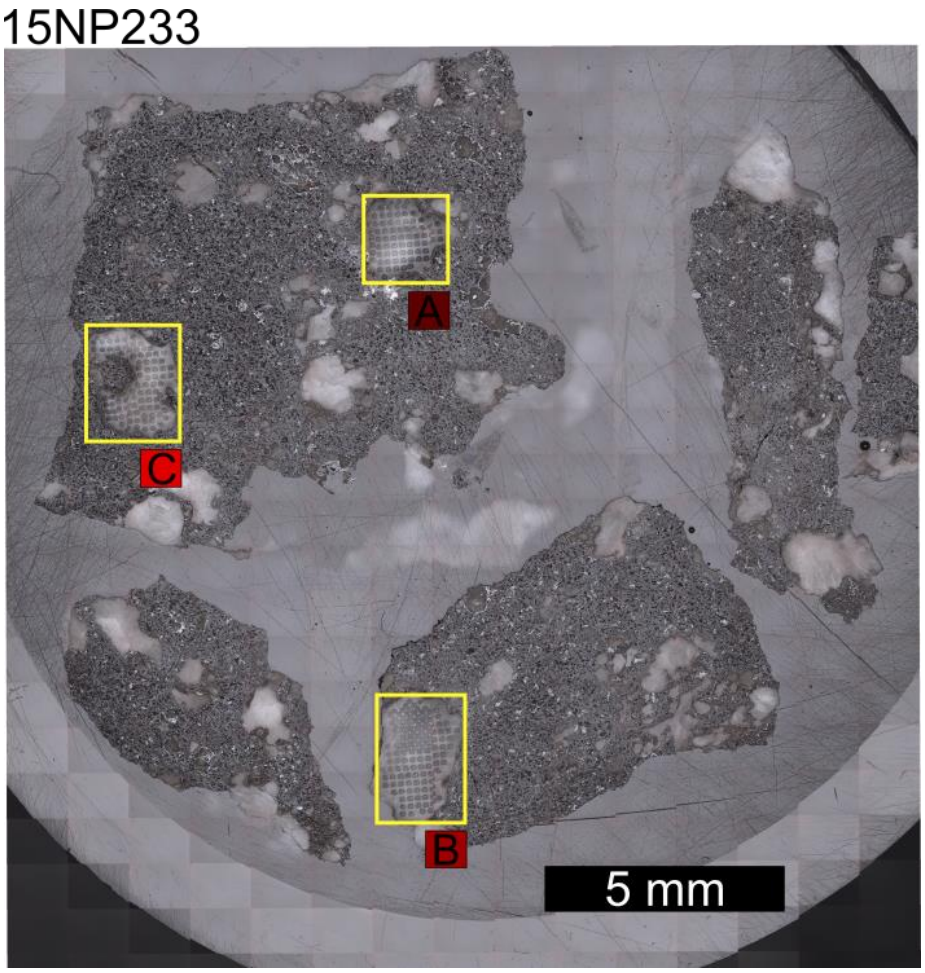

Appendix B.3: Reflected light image of sample 15NP233 with marked ablation areas. Letter, attached to the yellow boxes, appended to the sample name, labels the ablation areas. Colors of label boxes are consistent with colors of in-text figures.

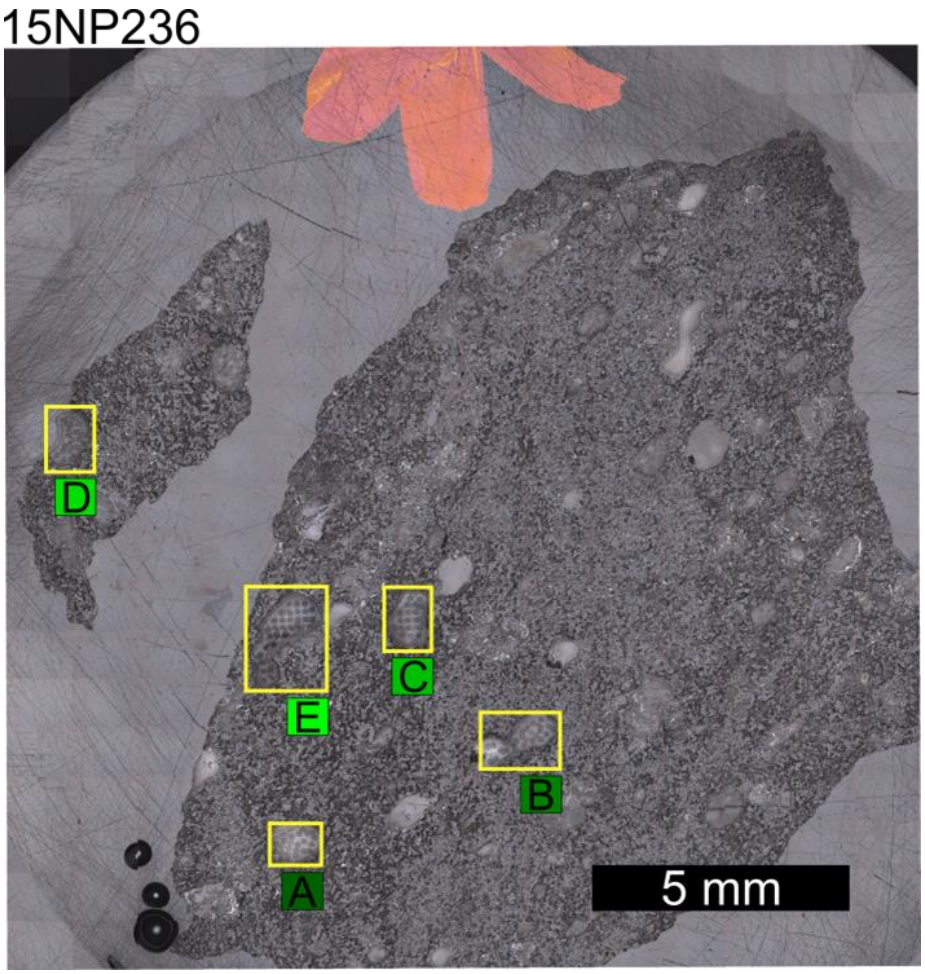

Appendix B.4: Reflected light image of sample 15NP236 with marked ablation areas. Letter, attached to the yellow boxes, appended to the sample name, labels the ablation areas. Colors of label boxes are consistent with colors of in-text figures.

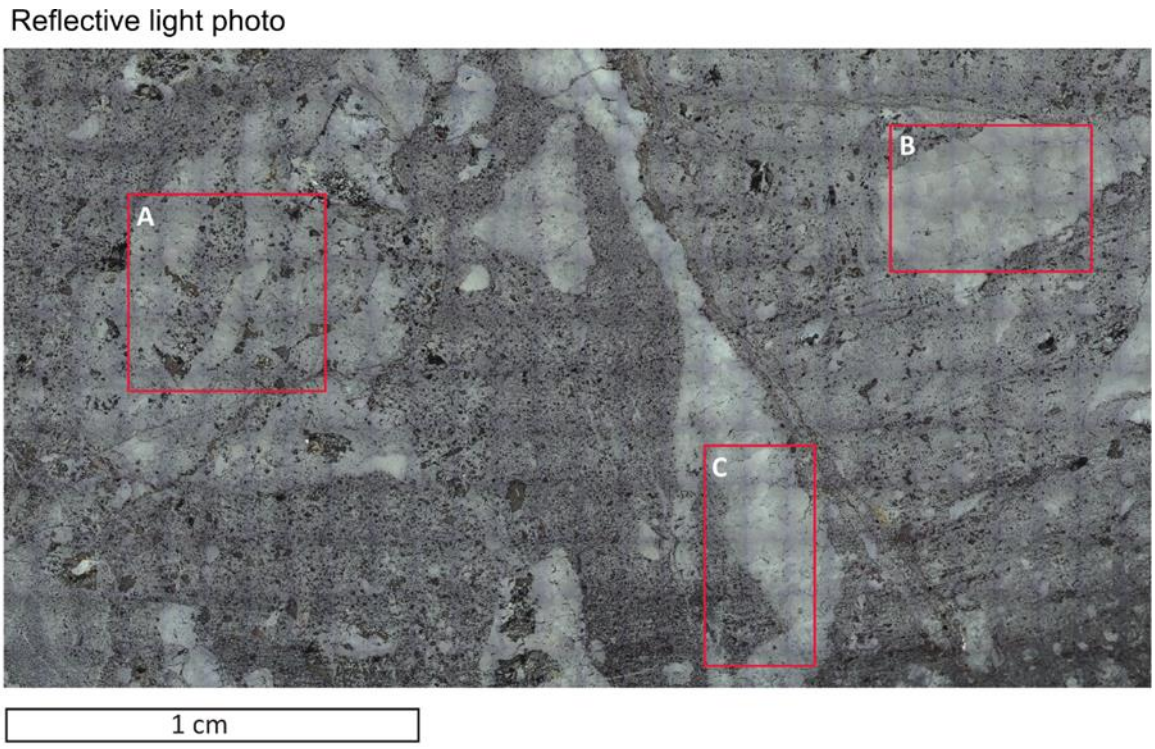

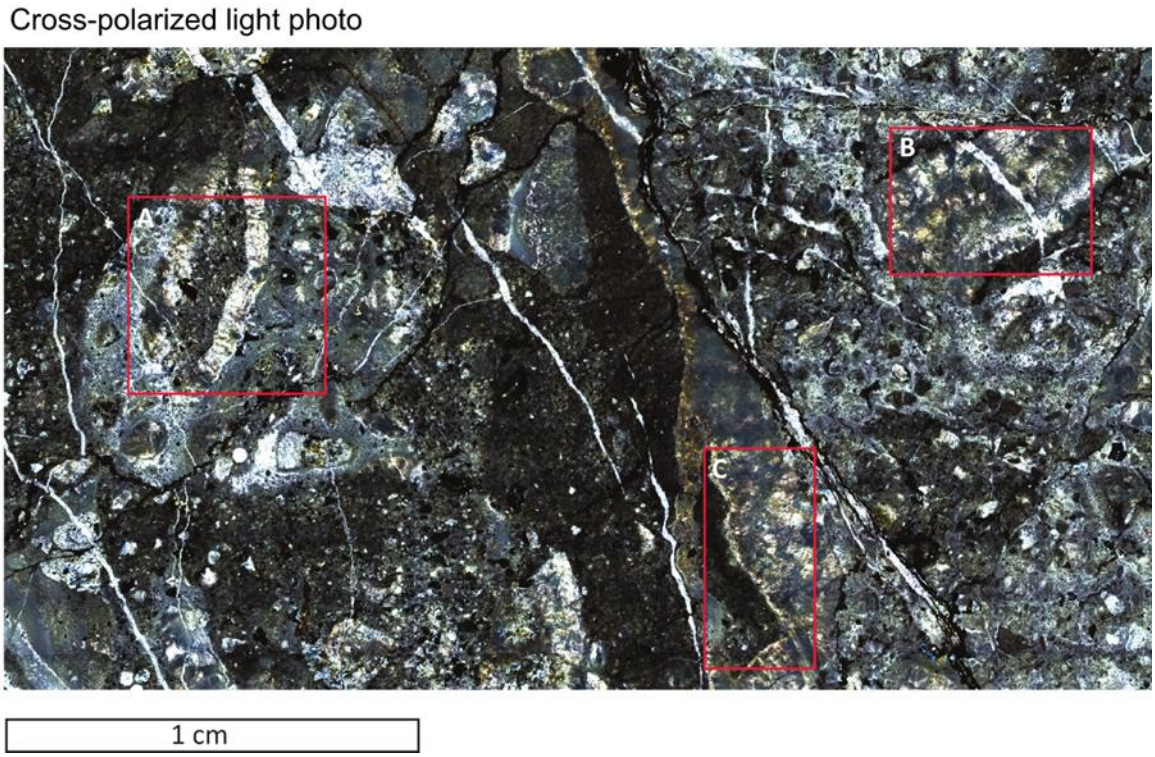

Appendix B.5: Reflected light image and cross-polarized light image of the investigation area on sample 17NP436a.

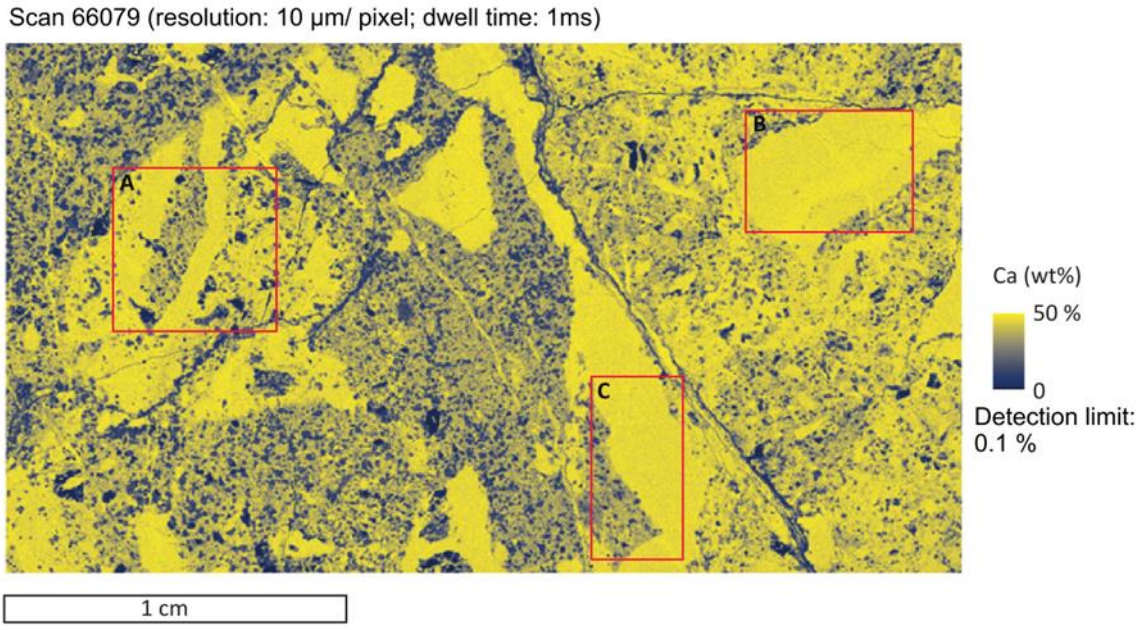

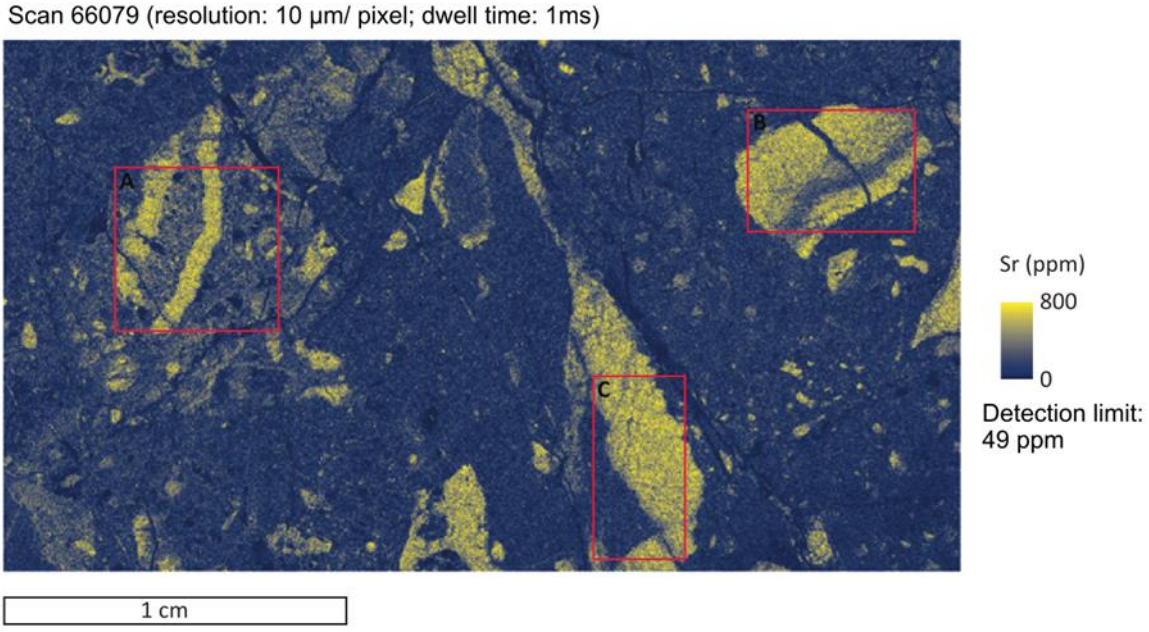

Appendix B.6: Coarse scan of the investigation areas on sample 17NP436a for Ca and Sr. Area A shows a rock fragment fringed by radial-fibrous calcite cement. The right fissure shows calcite growing from both walls toward the center, showing lower Sr values in the center of the vein. Area B shows an isolated fragment of radial-fibrous to equant cement with Sr and Ca zoning. High Sr/ low Ca values occur in the radial-fibrous calcite along the lower-right boundary with an abrupt change to low Sr/ high Ca values in the center that grade into high Sr/ low Ca values in a broad zone along the upper-left boundary. The low Sr/ high Ca values occur at the transition from radial-fibrous to equant calcite crystals. A younger calcite filled fissure crosscuts the calcite cement fragment. Crucial are the much lower Sr values. This fissure formed during tectonic straining of the rock, pressure solution and reprecipitation of calcite. Area C shows calcite crystals with highest Sr/ lowest Ca values in the center of the single crystals.

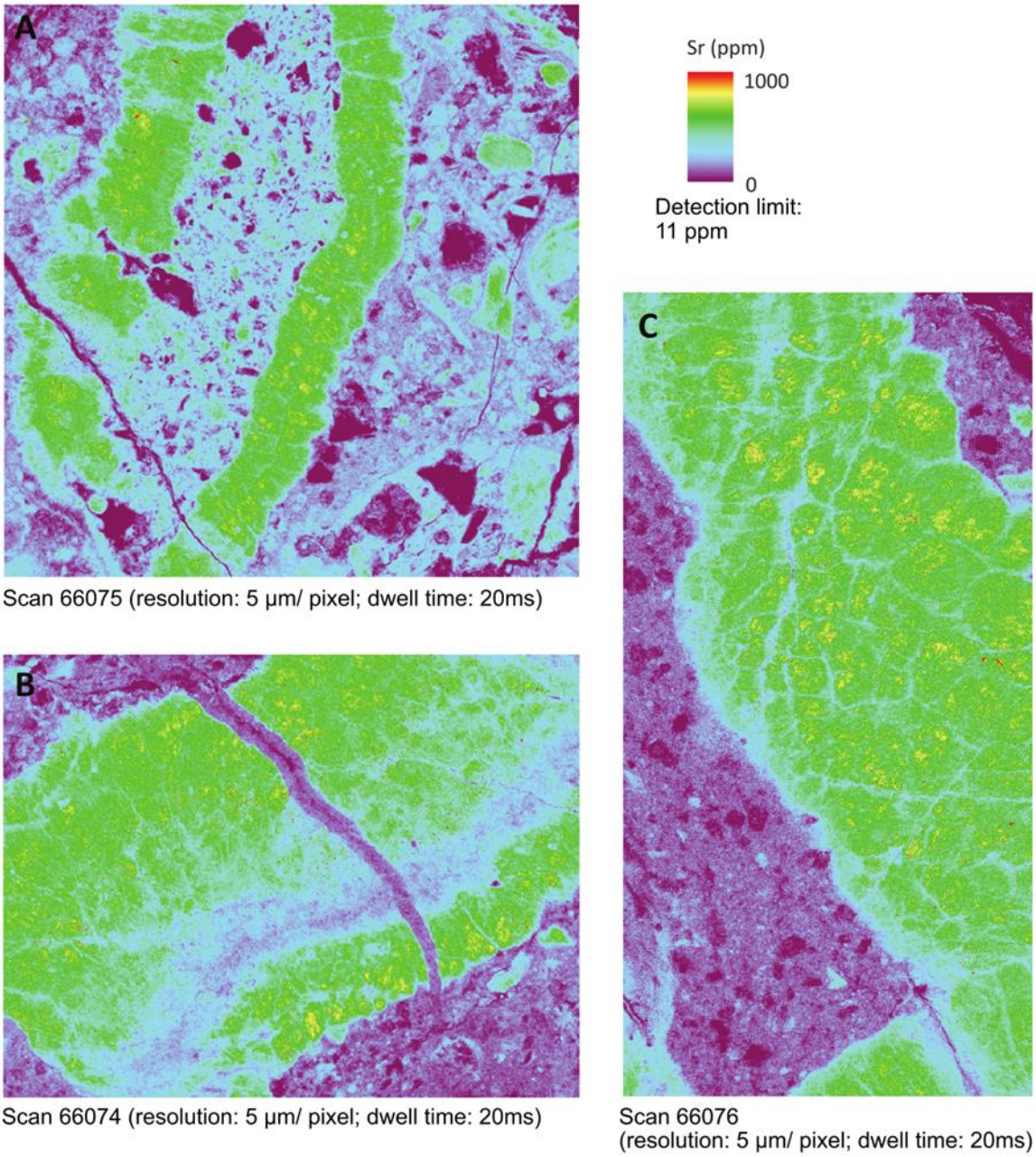

Appendix B.7: Fine scan of the investigation areas on sample 17NP436a for Sr.

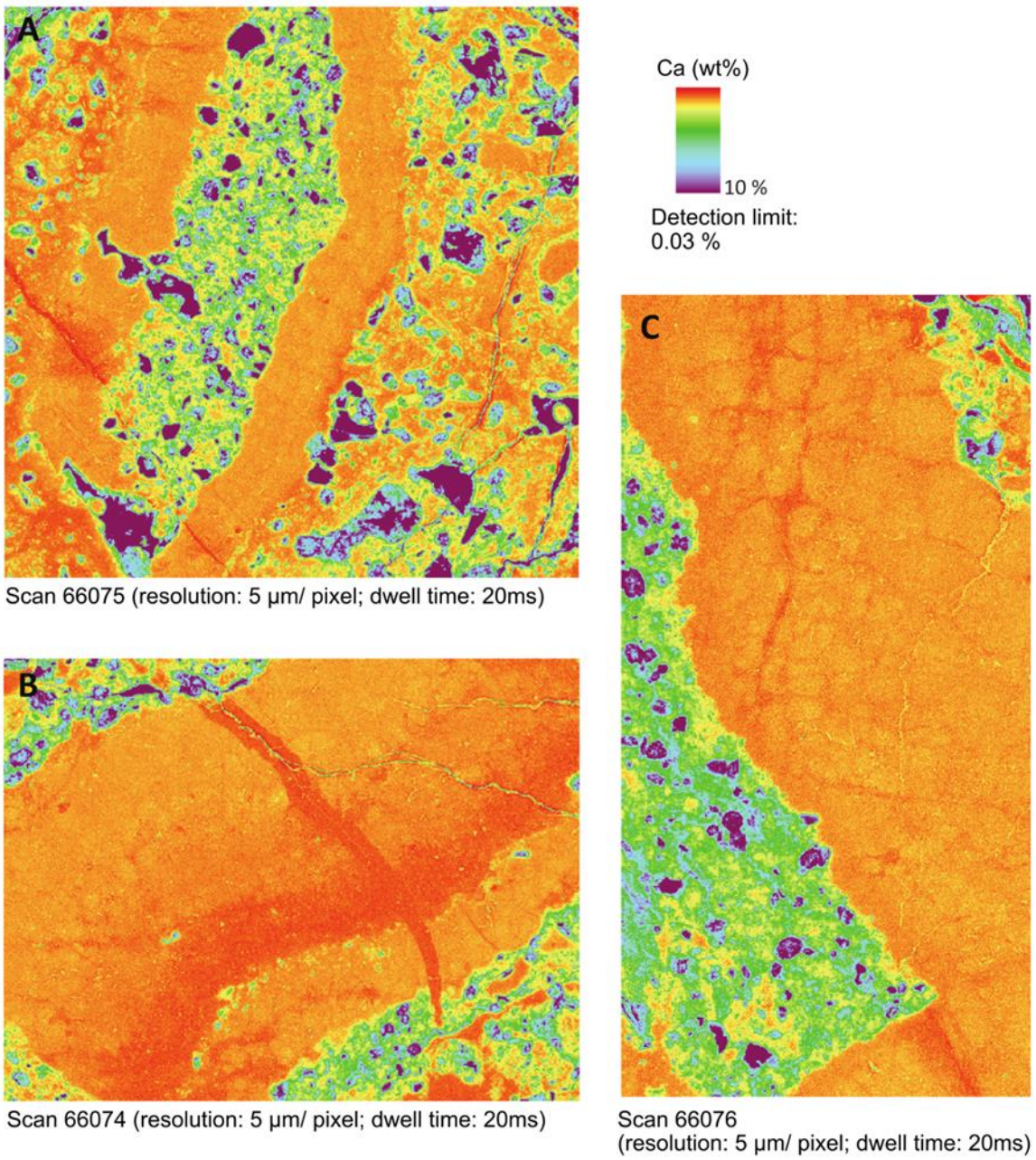

Appendix B.8: Fine scan of the investigation areas on sample 17NP436a for Ca.

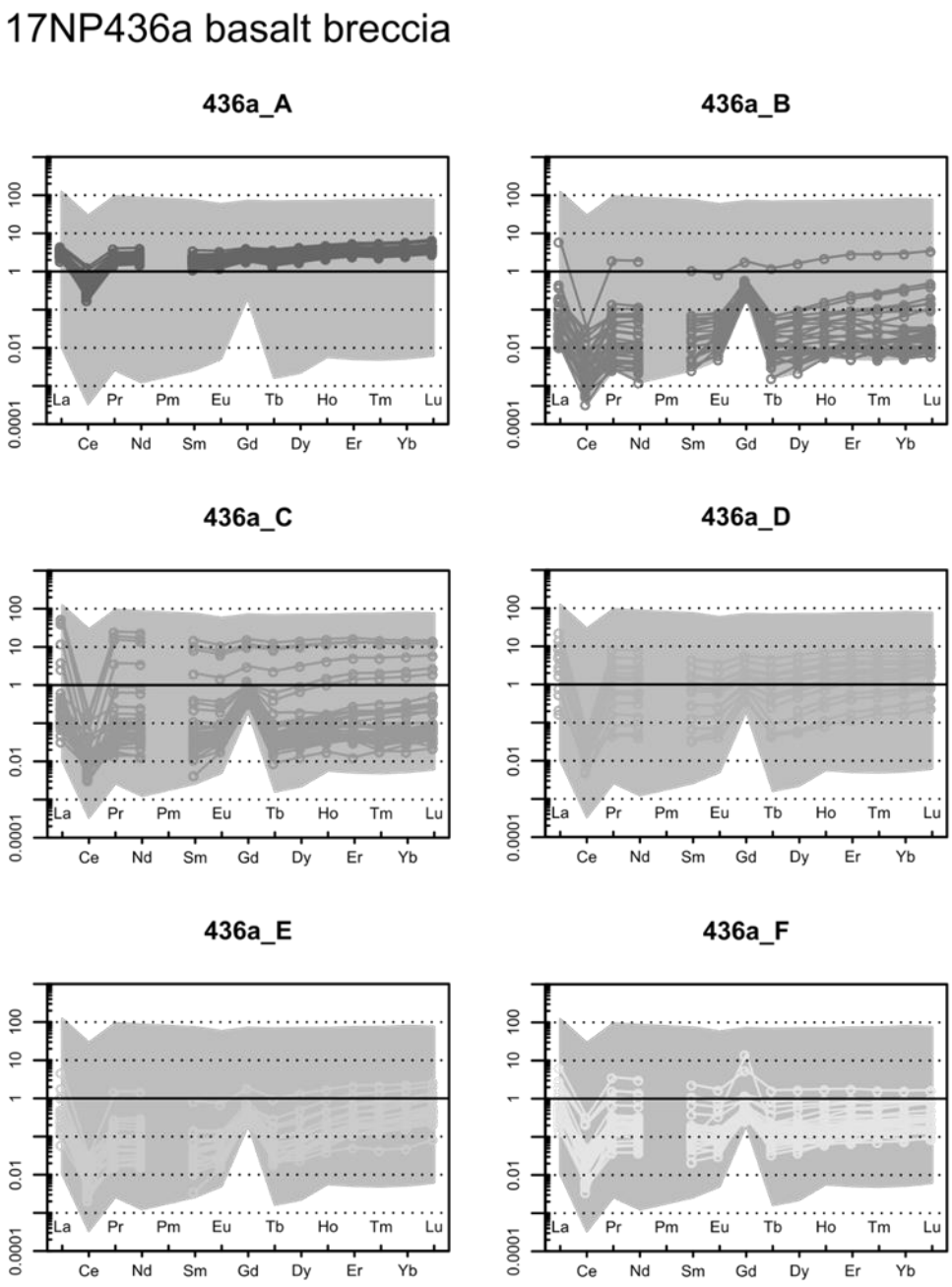

Appendix B.9: Rare earth element plots 17NP436a. Each plot represents one individual ablation area for sample 17NP436a. Grey shaded area in each diagram represents the range of chondrite normalized REE concentrations in all calcite ablation spots.

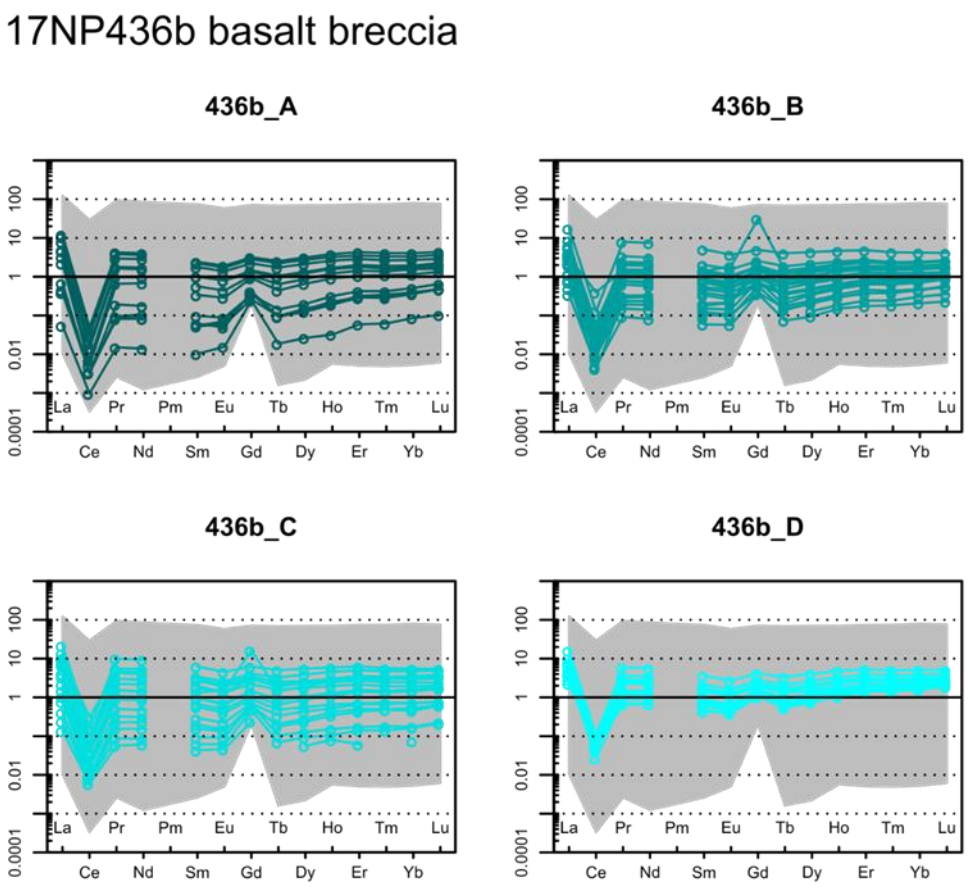

Appendix B.10: Rare earth element plots 17NP436b. Each plot represents one individual ablation area for sample 17NP436b. Grey shaded area in each diagram represents the range of chondrite normalized REE concentrations in all calcite ablation spots.

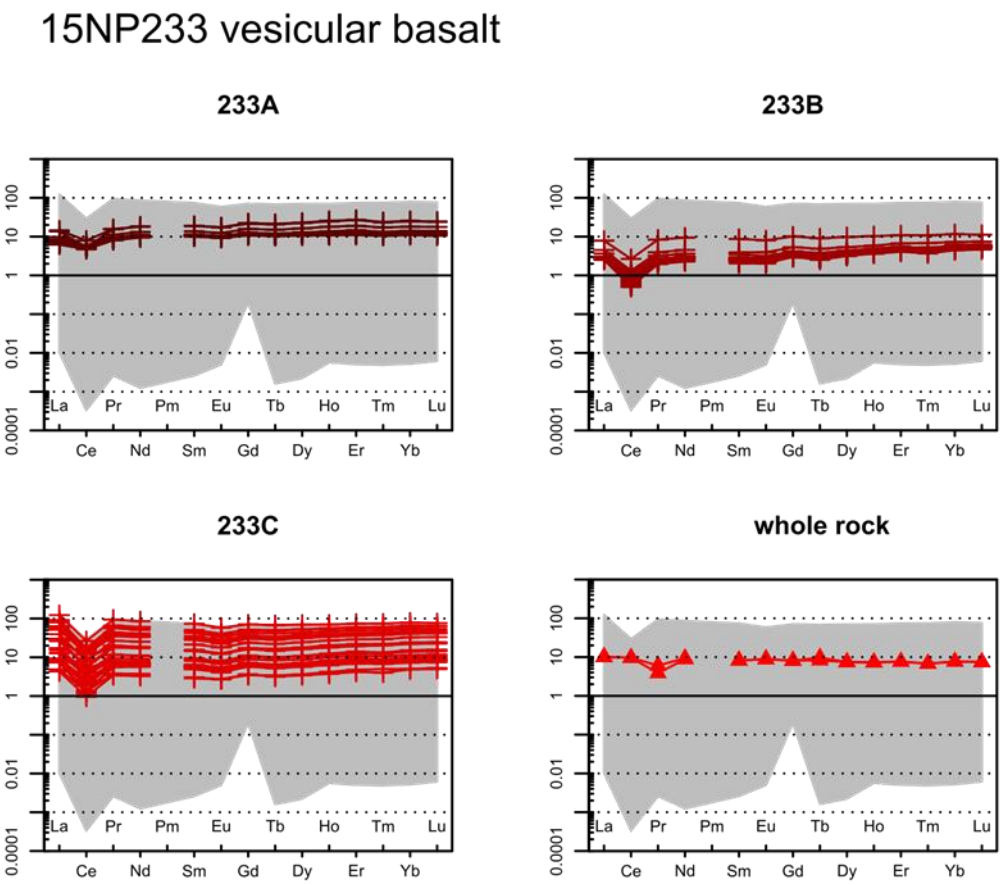

Appendix B.11: Rare earth element plots 15NP233. Each plot represents one individual ablation area for sample 15NP233. Whole rock data from Rembe et al. (2021). Grey shaded area in each diagram represents the range of chondrite normalized REE concentrations in all calcite ablation spots.

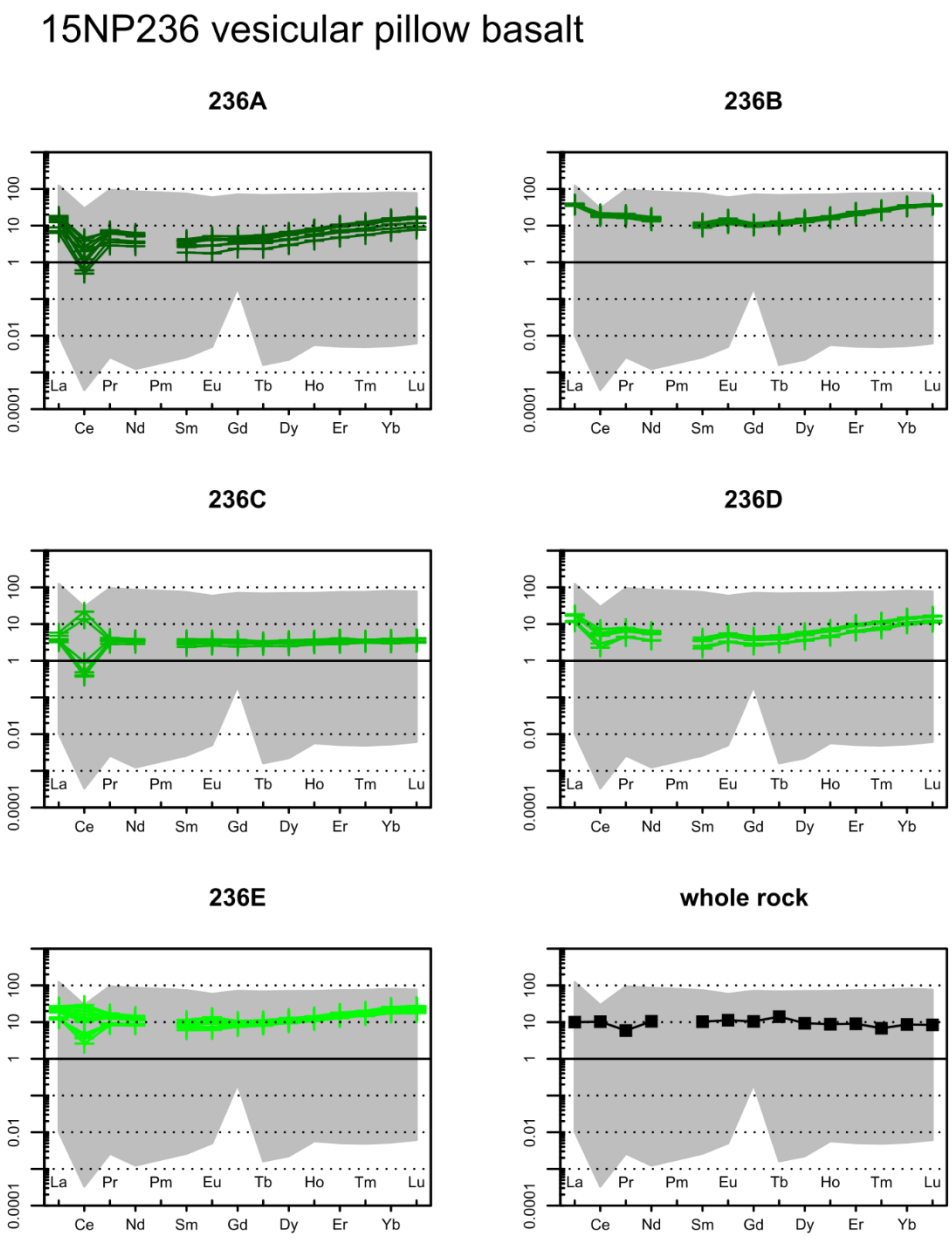

Appendix B.12: Rare earth element plots 15NP236. Each plot represents one individual ablation area for sample 15NP236. Whole rock data from Rembe et al. (2021). Grey shaded area in each diagram represents the range of chondrite normalized REE concentrations in all calcite ablation spots.

Appendix B.13: Whole rock geochemistry from Rembe et al., 2021

sample number		15NP233-1	15NP233-2	15NP236
locality		Qimgen - Akqiy	Qimgen - Akqiy	Qimgen - Akqiy
field description		altered, vesicular basalt	altered, vesicular basalt	altered, vesicular, pillow basalt
SiO2	(%)	37.67	37.74	38.54
TiO2	(%)	0.84	0.84	0.93
Al2O3	(%)	13.26	13.26	13.98
Fe2O3	(%)	8.82	8.86	10.18
MnO	(%)	0.11	0.11	0.14
MgO	(%)	3.65	3.63	9.29
CaO	(%)	17.45	17.34	9.52
Na2O	(%)	2.84	2.84	1.78
K2O	(%)	1.14	1.15	0.44
P2O5	(%)	0.12	0.12	0.10
LOI	(%)	13.91	13.91	14.88
Summe	(%)	99.81	99.80	99.78
Ba	(ppm)	52	45	22
Cr	(ppm)	178	180	345
Ga	(ppm)	13	10	14
Nb	(ppm)	<10	<10	<10
Ni	(ppm)	67	71	133
Rb	(ppm)	19	19	12
Sr	(ppm)	256	259	112
V	(ppm)	201	195	258
Y	(ppm)	15	13	17
Zn	(ppm)	61	62	76
Zr	(ppm)	40	40	40
Y	(ppm)	13	13	16
La	(ppm)	3.2	3.1	3.1
Ce	(ppm)	7.7	7.8	8.3
Pr	(ppm)	0.74	0.47	0.72
Nd	(ppm)	5.6	5.3	6.3
Sm	(ppm)	1.6	1.6	2.0
Eu	(ppm)	0.65	0.65	0.83
Gd	(ppm)	2.1	2.1	2.7
Tb	(ppm)	0.39	0.46	0.67
Dy	(ppm)	2.4	2.4	3.0
Ho	(ppm)	0.53	0.52	0.63
Er	(ppm)	1.6	1.6	1.9
Tm	(ppm)	0.22	0.22	0.22
Yb	(ppm)	1.6	1.6	1.8
Lu	(ppm)	0.24	0.24	0.27
Sc	(ppm)	32	32	36

Appendix B.14: LA-ISP-MS spot geochemical data. below LOI…below limit of identification

sample number	group	MnO (wt%)	Ba (ppm)	Sr (ppm)	Zr (ppm)	Y (ppm)	La (ppm)	Ce (ppm)	Pr (ppm)	Nd (ppm)	Sm (ppm)	Eu (ppm)	Gd (ppm)	Tb (ppm)	Dy (ppm)	Ho (ppm)	Er (ppm)	Tm (ppm)	Yb (ppm)	Lu (ppm)	Pb (ppm)	Th (ppm)	U (ppm)	U/Pb	Eu/Eu*	Gd/Gd*	Ce/Ce*	LREE(La to Sm)	HREE(Eu to Lu+Y)	ALLREE
NP236_Ag01	236A	0.093	0.71	314.47	1.26	21.11	5.20	3.13	0.91	3.80	0.84	0.38	1.33	0.26	2.18	0.60	2.23	0.41	3.31	0.56	0.14	0.00	0.33	2.27	1.06	0.31	0.35	13.88	32.37	46.25
NP236_Ag03	236A	0.028	1.07	385.76	0.86	20.44	3.98	0.98	0.75	3.28	0.73	0.30	1.16	0.23	1.84	0.55	1.97	0.35	2.92	0.51	0.13	0.00	0.32	2.44	0.96	0.32	0.14	9.72	30.27	39.99
NP236_Ag04	236A	0.087	1.13	311.39	0.35	12.07	1.96	0.40	0.35	1.65	0.36	0.13	0.61	0.11	0.95	0.28	0.99	0.18	1.41	0.25	0.08	0.00	0.21	2.55	0.85	0.36	0.12	4.72	16.99	21.71
NP236_Ag05	236A	0.313	14.54	315.15	0.24	14.82	2.19	1.64	0.43	2.02	0.57	0.21	0.89	0.17	1.37	0.38	1.38	0.24	1.73	0.30	0.07	0.00	0.19	2.88	0.88	0.34	0.41	6.85	21.49	28.34
NP236_Ag06	236A	0.098	138.83	953.86	0.66	16.72	2.77	0.49	0.51	2.21	0.51	0.21	0.85	0.16	1.34	0.41	1.55	0.27	2.23	0.38	0.10	0.00	0.23	2.30	0.96	0.33	0.10	6.49	24.12	30.61
NP236_Ag10	236A	0.050	1.17	343.03	0.79	19.45	4.42	1.67	0.79	3.32	0.76	0.32	1.14	0.23	1.92	0.55	2.07	0.36	3.00	0.52	0.13	0.00	0.24	1.90	1.00	0.30	0.22	10.96	29.55	40.51
NP236_Ag11	236A	0.010	0.45	449.24	0.56	17.49	5.71	3.68	0.83	3.06	0.63	0.32	0.99	0.20	1.79	0.51	2.00	0.35	2.94	0.51	0.21	0.01	0.40	1.95	1.18	0.28	0.41	13.91	27.11	41.02
NP236_Ag12	236A	0.047	0.75	382.22	0.77	18.44	4.76	2.20	0.83	3.44	0.75	0.32	1.11	0.23	1.83	0.54	2.05	0.36	2.83	0.50	0.15	0.00	0.27	1.76	1.01	0.30	0.27	11.98	28.21	40.19
NP236_Ag13	236A	0.025	1.27	361.14	0.87	20.55	3.84	0.77	0.75	3.17	0.73	0.30	1.12	0.22	1.91	0.54	2.13	0.36	2.97	0.52	0.13	0.00	0.31	2.42	0.98	0.31	0.11	9.26	30.62	39.88
NP236_Bg01	236B	0.025	1.08	366.40	1.05	41.18	12.33	16.97	2.44	9.91	2.21	1.07	2.94	0.58	4.65	1.25	4.97	0.87	7.11	1.18	0.19	0.12	0.22	1.17	1.24	0.27	0.74	43.86	65.79	109.65
NP236_Bg02	236B	0.130	1.84	298.97	1.10	40.04	10.89	16.31	2.34	9.57	2.28	1.07	2.96	0.57	4.55	1.20	4.77	0.82	6.83	1.13	0.12	0.26	0.16	1.37	1.23	0.27	0.78	41.39	63.94	105.33
NP236_Bg03	236B	0.032	0.89	317.87	1.19	42.52	12.36	17.46	2.54	10.34	2.37	1.15	3.01	0.62	4.98	1.30	4.98	0.91	7.50	1.23	0.17	0.13	0.22	1.36	1.24	0.26	0.75	45.07	68.22	113.29
NP236_Bg04	236B	0.066	1.59	324.26	1.10	40.52	11.52	15.63	2.29	9.10	2.02	0.93	2.65	0.53	4.37	1.17	4.48	0.81	6.75	1.14	0.14	0.16	0.21	1.52	1.18	0.27	0.73	40.56	63.35	103.91
NP236_Bg05	236B	0.035	1.87	371.68	1.19	40.59	11.23	15.01	2.14	8.62	1.93	0.88	2.63	0.50	4.23	1.14	4.31	0.80	6.72	1.11	0.18	0.07	0.23	1.28	1.17	0.29	0.74	38.93	62.91	101.84
NP236_Bg06	236B	0.017	0.91	376.32	1.49	43.95	12.19	15.87	2.26	9.28	1.97	0.93	2.76	0.56	4.56	1.22	4.61	0.86	7.35	1.23	0.18	0.09	0.25	1.37	1.16	0.28	0.73	41.57	68.02	109.59
NP236_Bg10	236B	0.090	0.88	360.02	1.29	39.47	10.78	13.88	1.96	7.87	1.71	0.81	2.43	0.48	4.00	1.08	4.08	0.79	6.50	1.12	0.15	0.03	0.23	1.55	1.17	0.28	0.73	36.20	60.75	96.95
NP236_Bg11	236B	0.048	6.09	313.24	1.46	40.80	11.23	14.70	2.12	8.39	1.83	0.87	2.57	0.51	4.25	1.14	4.26	0.81	6.79	1.18	0.13	0.04	0.26	1.96	1.18	0.28	0.72	38.27	63.17	101.44
NP236_Bg13	236B	0.039	1.71	377.79	1.31	42.12	11.76	15.45	2.20	9.04	2.03	0.89	2.68	0.53	4.46	1.18	4.39	0.83	7.02	1.17	0.17	0.14	0.23	1.36	1.12	0.28	0.73	40.48	65.26	105.74
NP236_Cg02	236C	0.062	4.17	301.84	0.01	5.98	0.99	0.32	0.35	1.72	0.46	0.19	0.63	0.12	0.80	0.20	0.60	0.10	0.62	0.10	0.02	0.01	0.07	3.34	1.06	0.30	0.13	3.84	9.33	13.17
NP236_Cg03	236C	2.072	0.72	218.81	0.01	6.87	1.48	10.91	0.44	2.09	0.62	0.23	0.75	0.14	0.96	0.22	0.66	0.10	0.68	0.10	0.02	0.01	0.04	1.97	1.02	0.30	0.25	15.54	10.73	26.27
NP236_Cg05	236C	3.010	0.62	206.91	0.01	7.54	1.80	17.47	0.51	2.30	0.68	0.24	0.79	0.15	1.05	0.25	0.77	0.11	0.73	0.11	0.02	0.01	0.03	1.91	0.98	0.30	4.39	22.76	11.74	34.50
NP236_Cg06	236C	0.132	0.73	187.82	0.02	9.24	1.07	0.74	0.46	2.30	0.75	0.28	0.96	0.16	1.17	0.27	0.84	0.12	0.82	0.13	0.02	0.00	0.05	3.22	1.06	0.32	0.25	5.32	14.00	19.32
NP236_Cg09	236C	0.037	0.44	330.88	0.01	8.44	1.20	0.39	0.42	2.17	0.60	0.25	0.84	0.15	1.12	0.26	0.84	0.12	0.82	0.13	0.03	0.01	0.10	3.39	1.09	0.31	0.13	4.78	12.98	17.76
NP236_Cg12	236C	0.027	0.83	313.40	0.01	7.08	1.14	0.30	0.42	1.98	0.54	0.22	0.80	0.14	0.95	0.23	0.75	0.12	0.77	0.13	0.03	0.00	0.10	3.72	1.05	0.33	0.11	4.38	11.19	15.57
NP236_Dg01	236D	0.005	0.50	328.63	0.91	20.38	5.29	4.07	0.83	3.29	0.68	0.37	0.95	0.20	1.64	0.48	1.94	0.36	2.99	0.52	0.10	0.01	0.22	2.15	1.31	0.26	0.47	14.16	29.81	43.97
NP236_Dg02	236D	0.010	0.56	335.88	1.01	21.19	5.72	5.87	0.95	3.88	0.83	0.41	1.17	0.23	1.94	0.53	2.12	0.38	3.13	0.54	0.12	0.01	0.25	2.03	1.23	0.28	0.61	17.25	31.62	48.87
NP236_Dg03	236D	0.009	0.45	334.38	0.96	20.21	5.33	4.66	0.87	3.46	0.72	0.37	1.05	0.21	1.73	0.47	1.99	0.35	2.90	0.51	0.10	0.01	0.24	2.35	1.24	0.27	0.52	15.04	29.79	44.83
NP236_Dg04	236D	0.009	1.40	323.06	0.92	20.30	5.25	4.43	0.83	3.27	0.68	0.35	0.96	0.19	1.64	0.47	1.91	0.36	2.98	0.54	0.10	0.01	0.22	2.32	1.27	0.27	0.51	14.46	29.69	44.15
NP236_Dg05	236D	0.009	0.79	375.60	1.31	15.44	3.78	2.38	0.54	2.16	0.42	0.24	0.67	0.14	1.19	0.32	1.38	0.26	2.28	0.40	0.14	0.00	0.23	1.67	1.29	0.27	0.40	9.28	22.32	31.60
NP236_Dg06	236D	0.005	2.67	333.94	0.95	20.65	5.21	3.87	0.77	3.19	0.69	0.34	0.95	0.18	1.63	0.46	1.89	0.34	2.94	0.52	0.09	0.01	0.20	2.20	1.26	0.27	0.47	13.73	29.90	43.63
NP236_Dg07	236D	0.046	1.22	303.76	1.19	14.70	3.47	1.84	0.55	2.15	0.49	0.24	0.75	0.14	1.14	0.34	1.29	0.23	2.04	0.35	0.12	0.00	0.26	2.12	1.20	0.29	0.32	8.50	21.23	29.73
NP236_Eg03	236E	0.169	1.01	301.01	0.86	25.00	6.13	10.74	1.53	6.68	1.60	0.67	2.05	0.40	3.02	0.77	2.71	0.49	3.93	0.64	0.10	0.02	0.22	2.18	1.10	0.28	0.84	26.68	39.69	66.37
NP236_Eg04	236E	0.085	3.56	341.12	0.22	27.37	4.06	2.09	1.01	4.87	1.17	0.45	1.92	0.38	3.07	0.82	2.91	0.48	3.80	0.63	0.08	0.00	0.18	2.21	0.88	0.33	0.25	13.20	41.82	55.02
NP236_Eg06	236E	0.211	1.91	262.10	0.13	26.44	3.68	3.21	1.05	5.00	1.38	0.52	2.07	0.42	3.22	0.83	2.85	0.48	3.65	0.57	0.07	0.01	0.12	1.67	0.89	0.32	0.39	14.32	41.06	55.38
NP236_Eg07	236E	0.095	1.45	368.79	1.07	29.30	7.54	16.20	1.75	7.27	1.72	0.82	2.29	0.46	3.55	0.92	3.34	0.58	4.84	0.77	0.15	0.04	0.27	1.83	1.21	0.27	1.07	34.48	46.88	81.36
NP236_Eg08	236E	0.079	0.99	360.01	1.23	29.99	7.00	10.25	1.70	7.26	1.75	0.76	2.40	0.47	3.63	0.93	3.44	0.59	4.82	0.79	0.14	0.02	0.30	2.19	1.10	0.29	0.72	27.96	47.82	75.78
NP236_Eg10	236E	0.164	9.37	326.44	0.38	28.12	4.18	2.94	1.13	5.36	1.36	0.52	2.07	0.40	3.26	0.86	3.12	0.51	3.89	0.64	0.09	0.01	0.20	2.10	0.92	0.33	0.33	14.97	43.40	58.37
NP236_Eg11	236E	0.256	1.18	263.68	0.13	25.73	3.70	3.90	1.09	5.19	1.46	0.54	2.16	0.42	3.31	0.84	2.97	0.48	3.64	0.57	0.05	0.01	0.11	2.26	0.90	0.32	0.47	15.34	40.65	55.99
NP236_Eg13	236E	0.088	6.03	418.98	0.88	30.00	6.37	9.24	1.62	7.00	1.70	0.76	2.43	0.48	3.65	0.94	3.43	0.57	4.68	0.75	0.16	0.03	0.28	1.81	1.10	0.29	0.69	25.93	47.69	73.62
NP236_Eg14	236E	0.224	2.02	288.35	1.38	27.88	5.64	8.17	1.61	7.27	1.87	0.71	2.43	0.46	3.55	0.91	3.20	0.52	4.24	0.66	0.26	0.06	0.18	0.67	1.00	0.31	0.65	24.56	44.56	69.12
NP236_Eg16	236E	0.09	1.95	316.61	1.24	31.15	8.30	23.57	2.10	8.82	2.23	1.00	2.77	0.53	4.14	1.03	3.76	0.66	5.40	0.88	0.14	0.05	0.23	1.04	1.20	0.27	1.36	45.02	51.31	96.33
NP236_Eg17	236E	0.048	1.06	353.73	1.16	30.81	8.31	19.91	2.02	8.28	2.05	0.96	2.60	0.50	4.11	0.99	3.70	0.64	5.26	0.86	0.14	0.05	0.29	2.10	1.24	0.27	1.17	50.42	50.42	90.99
NP236_Eg18	236E	0.136	1.36	353.38	0.91	29.20	6.69	13.11	1.68	7.26	1.76	0.78	2.46	0.48	3.77	0.94	3.40	0.59	4.74	0.76	0.12	0.04	0.27	2.18	1.11	0.29	0.94	30.50	47.12	77.62
NP233_Ag01	233A	0.004	0.34	442.27	0.10	25.66	2.06	4.76	1.07	6.13	2.08	0.74	2.96	0.50	3.69	0.84	2.49	0.37	2.44	0.37	0.04	0.02	0.19	4.79	0.95	0.35	0.77	16.10	40.06	56.16
NP233_Ag02	233A	0.005	0.44	446.24	0.09	26.64	2.12	4.81	1.10	6.26	2.17	0.74	3.05	0.53	3.74	0.84	2.53	0.37	2.57	0.37	0.05	0.02	0.19	3.86	0.90	0.35	0.76	16.46	41.40	57.86
NP233_Ag03	233A	0.003	0.37	435.11	0.09	27.15	2.12	4.55	1.08	6.28	2.13	0.73	3.13	0.55	3.77	0.87	2.53	0.37	2.48	0.39	0.04	0.02	0.19	4.48	0.88	0.36	0.72	16.16	41.96	58.12
NP233_Ag04	233A	0.018	0.37	381.29	0.09	28.64	2.27	4.50	1.07	6.18	2.06	0.71	2.95	0.53	3.67	0.85	2.53	0.37	2.51	0.37	0.04	0.02	0.16	4.33	0.89	0.35	0.70	16.08	43.11	59.19
NP233_Ag11	233A	0.016	0.39	391.95	0.09	24.99	1.93	3.82	0.98	5.69	1.95	0.68	2.78	0.49	3.41	0.78	2.31	0.34	2.30	0.34	0.04	0.01	0.18	4.69	0.91	0.35	0.67	14.37	38.40	52.77
NP233_Ag18	233A	0.004	0.41	432.59	0.08	26.72	2.08	4.39	1.04	6.12	2.07	0.70	2.99	0.51	3.58	0.84	2.57	0.36	2.40	0.36	0.03	0.02	0.18	6.72	0.89	0.36	0.72	15.70	41.04	56.74
NP233_Ag23	233A	0.003	0.34	428.74	0.08	30.23	2.31	4.61	1.15	6.66	2.22	0.76	3.26	0.56	4.10	0.96	2.86	0.41	2.73	0.40	0.04	0.01	0.18	4.84	0.89	0.36	0.68	16.95	46.29	63.24
NP233_Ag27	233A	0.008	0.36	424.01	0.10	30.66	2.26	4.20	1.08	6.37	2.16	0.75	3.23	0.56	4.01	0.94	2.86	0.40	2.82	0.42	0.04	0.01	0.18	4.34	0.89	0.36	0.64	16.07	46.63	62.70
NP233_Ag36	233A	0.03	0.34	412.54	0.10	30.41	2.22	4.09	1.04	6.03	1.98	0.72	3.13	0.52	3.80	0.89	2.82	0.38	2.64	0.40	0.04	0.01	0.17	4.59	0.93	0.37	0.65	15.36	45.71	61.07
NP233_Ag37	233A	0.016	0.35	374.30	0.09	43.45	3.02	4.63	1.36	7.93	2.67	0.91	4.09	0.71	5.24	1.29	3.98	0.56	3.76	0.57	0.04	0.02	0.15	4.17	0.86	0.37	0.55	19.61	64.57	84.18
NP233_Ag45	233A	0.055	0.44	325.93	0.10	32.80	2.61	4.54	1.14	6.46	2.10	0.74	3.23	0.56	4.04	0.98	3.07	0.43	2.96	0.45	0.04	0.02	0.14	3.97	0.89	0.36	0.63	16.85	49.27	66.12
NP233_Ag46	233A	0.011	0.30	314.03	0.06	57.77	4.48	6.39	1.92	10.80	3.67	1.28	5.57	0.98	7.24	1.77	5.63	0.76	5.19	0.79	0.02	0.02	0.10	5.41	0.88	0.36	0.52	27.26	86.99	114.25
NP233_Ag53	233A	0	0.19	328.75	0.06	58.60	4.22	4.26	1.88	11.03	3.67	1.28	5.78	1.01	7.38	1.83	5.68	0.77	5.31	0.77	0.02	0.02	0.12	5.04	0.87	0.37	0.36	25.06	88.42	113.48
NP233_Bg01	233B	0.024	0.34	394.31	0.11	12.42	0.81	0.84	0.29	1.60	0.49	0.17	0.81	0.14	1.08	0.29	0.95	0.14	1.10	0.17	0.05	0.00	0.20	4.17	0.85	0.37	0.41	4.03	17.28	21.31
NP233_Bg02	233B	0.032	0.37	373.68	0.10	12.02	0.81	0.90	0.29	1.65	0.51	0.18	0.84	0.15	1.12	0.29	0.97	0.14	1.02	0.16	0.04	0.00	0.18	4.67	0.85	0.37	0.44	4.16	16.88	21.04
NP233_Bg03	233B	0.159	0.50	255.63	0.08	11.06	0.88	0.87	0.30	1.61	0.46	0.16	0.80	0.13	1.05	0.26	0.86	0.12	0.93	0.15	0.03	0.00	0.11	3.67	0.86	0.39	0.41	4.12	15.53	19.65
NP233_Bg04	233B	0.075	0.25	120.57	0.09	13.23	0.83	0.69	0.30	1.72	0.54	0.21	0.91	0.16	1.20	0.32	1.02	0.15	1.15	0.19	0.02	0.00	0.06	2.95	0.93	0.37	0.33	4.08	18.53	22.61
NP233_Bg05	233B	0.011	0.28	346.62	0.10	14.21	0.89	0.81	0.32	1.80	0.54	0.21	0.97	0.15	1.22	0.32	1.09	0.16	1.23	0.19	0.04	Below LOI	0.20	4.98	0.97	0.40	0.36	4.36	19.76	24.12
NP233_Bg06	233B	0.009	0.36	394.94	0.10	12.95	0.84	0.73	0.30	1.65	0.49	0.19	0.91	0.16	1.19	0.30	1.04	0.15	1.10	0.18	0.04	0.00	0.19	4.69	0.89	0.38	0.35	4.01	18.18	22.19
NP233_Bg07	233B	0.011	0.33	362.19	0.08	12.47	0.81	0.75	0.30	1.65	0.50	0.17	0.87	0.14	1.15	0.29	0.96	0.15	1.07	0.17	0.04	0.00	0.19	4.26	0.84	0.40	0.37	4.01	17.44	21.45
NP233_Bg08	233B	0.003	0.30	420.55	0.10	13.14	0.85	0.78	0.30	1.69	0.54	0.18	0.88	0.15	1.13	0.31	1.01	0.16	1.10	0.18	0.04	0.00	0.22	5.95	0.83	0.38	0.37	4.16	18.25	22.41
NP233_Bg09	233B	0.031	0.38	216.35	0.08	13.46	0.84	0.77	0.31	1.68	0.57	0.18	0.90	0.15	1.18	0.32	1.02	0.15	1.11	0.19	0.02	0.00	0.10	4.29	0.81	0.40	0.37	4.17	18.66	22.83
NP233_Bg10	233B	0.079	0.39	337.53	0.11	12.11	0.82	0.53	0.28	1.55	0.47	0.16	0.84	0.13	1.05	0.28	0.92	0.14	1.01	0.17	0.03	Below LOI	0.17	5.11	0.85	0.40	0.27	3.65	16.82	20.47
NP233_Bg11	233B	0.028	0.43	370.81	0.10	12.67	0.81	0.41	0.28	1.59	0.45	0.18	0.85	0.14	1.12	0.30	0.98	0.15	1.07	0.17	0.04	0.00	0.18	4.88	0.94	0.38	0.21	3.54	17.64	21.18
NP233_Bg12	233B	0.02	0.44	364.61	0.12	13.34	0.83	0.54	0.28	1.65	0.50	0.18	0.89	0.14	1.16	0.30	1.03	0.16	1.11	0.18	0.03	0.00	0.18	5.54	0.89	0.40	0.27	3.80	18.51	22.31

sample number	group	MnO (wt%)	Ba (ppm)	Sr (ppm)	Zr (ppm)	Y (ppm)	La (ppm)	Ce (ppm)	Pr (ppm)	Nd (ppm)	Sm (ppm)	Eu (ppm)	Gd (ppm)	Tb (ppm)	Dy (ppm)	Ho (ppm)	Er (ppm)	Tm (ppm)	Yb (ppm)	Lu (ppm)	Pb (ppm)	Th (ppm)	U (ppm)	U/Pb	Eu/Eu*	Gd/Gd*	Ce/Ce*	LREE(La to Sm)	HREE(Eu to Lu+Y)	ALL REE
NP233_Bg13	233B	0.004	0.32	400.32	0.11	14.40	0.91	0.71	0.33	1.74	0.54	0.19	0.94	0.16	1.24	0.33	1.08	0.16	1.20	0.20	0.04	0.00	0.21	5.54	0.85	0.39	0.31	4.23	19.90	24.13
NP233_Bg16	233B	0.004	0.38	403.85	0.11	12.34	0.80	0.62	0.27	1.54	0.48	0.17	0.81	0.13	1.07	0.29	0.93	0.14	1.00	0.17	0.04	0.00	0.20	4.78	0.89	0.39	0.32	3.71	17.05	20.76
NP233_Bg17	233B	0.004	0.34	403.91	0.11	13.65	0.85	0.61	0.28	1.67	0.47	0.18	0.85	0.15	1.16	0.30	1.04	0.16	1.17	0.18	0.04	0.00	0.21	5.17	0.89	0.38	0.30	3.88	18.86	22.74
NP233_Bg18	233B	0.017	0.41	330.97	0.11	13.10	0.82	0.41	0.26	1.63	0.45	0.16	0.82	0.14	1.11	0.29	0.98	0.15	1.08	0.18	0.04	0.00	0.16	4.56	0.83	0.38	0.21	3.57	18.01	21.58
NP233_Bg19	233B	0.097	0.52	303.13	0.10	11.87	0.78	0.42	0.24	1.37	0.40	0.15	0.78	0.12	1.02	0.27	0.89	0.14	0.97	0.16	0.04	0.00	0.14	3.33	0.90	0.41	0.23	3.21	16.37	19.58
NP233_Bg20	233B	0.020	0.37	376.52	0.10	13.49	0.80	0.44	0.28	1.64	0.51	0.18	0.86	0.15	1.18	0.31	1.01	0.15	1.09	0.18	0.04	0.00	0.19	4.98	0.85	0.37	0.22	3.67	18.61	22.28
NP233_Bg25	233B	0.007	0.51	391.51	0.11	12.52	0.85	0.71	0.29	1.71	0.45	0.18	0.83	0.14	1.11	0.30	0.95	0.14	1.01	0.17	0.05	0.00	0.22	4.68	0.94	0.37	0.35	4.01	17.35	21.36
NP233_Bg26	233B	0.013	0.32	350.71	0.11	12.06	0.82	0.57	0.26	1.51	0.47	0.16	0.79	0.13	1.04	0.28	0.93	0.15	1.03	0.17	0.04	0.00	0.18	4.60	0.85	0.40	0.30	3.63	16.74	20.37
NP233_Bg27	233B	0.009	0.54	392.02	0.11	13.43	0.85	0.56	0.28	1.53	0.50	0.17	0.83	0.15	1.15	0.30	1.02	0.15	1.15	0.19	0.04	0.00	0.20	4.76	0.81	0.37	0.27	3.72	18.53	22.25
NP233_Bg28	233B	0.030	0.55	325.96	0.10	13.03	0.81	0.43	0.26	1.52	0.47	0.17	0.78	0.14	1.14	0.29	0.96	0.15	1.10	0.17	0.03	0.00	0.16	4.73	0.87	0.36	0.22	3.49	17.94	21.43
NP233_Bg29	233B	0.102	0.48	258.62	0.10	13.04	0.89	0.51	0.28	1.54	0.52	0.17	0.86	0.14	1.09	0.29	0.98	0.14	1.05	0.17	0.03	0.00	0.12	3.91	0.82	0.40	0.25	3.74	17.92	21.66
NP233_Bg35	233B	0.003	0.52	437.79	0.10	12.33	0.90	0.81	0.31	1.82	0.51	0.19	0.87	0.16	1.15	0.29	0.99	0.14	1.09	0.17	0.06	0.00	0.23	4.07	0.87	0.36	0.37	4.35	17.38	21.73
NP233_Bg36	233B	0.001	0.43	445.44	0.10	12.38	0.87	0.75	0.30	1.68	0.50	0.17	0.83	0.15	1.13	0.30	0.97	0.14	1.07	0.17	0.04	Below LOD	0.23	5.35	0.81	0.38	0.35	4.10	17.32	21.42
NP233_Bg37	233B	0.020	0.39	407.39	0.11	12.44	0.81	0.59	0.27	1.56	0.45	0.17	0.86	0.14	1.08	0.28	0.92	0.15	1.03	0.18	0.04	0.00	0.21	4.80	0.89	0.41	0.31	3.68	17.23	20.91
NP233_Bg38	233B	0.008	0.50	374.34	0.09	13.79	0.85	0.60	0.31	1.72	0.51	0.19	0.93	0.15	1.22	0.32	1.05	0.15	1.19	0.19	0.04	Below LOD	0.19	4.97	0.90	0.40	0.28	3.99	19.18	23.17
NP233_Bg39	233B	0.009	0.34	411.64	0.10	13.58	0.84	0.49	0.29	1.56	0.52	0.18	0.88	0.15	1.19	0.31	1.05	0.15	1.15	0.18	0.05	0.00	0.21	4.12	0.84	0.38	0.24	3.70	18.81	22.51
NP233_Bg44	233B	0.000	0.82	466.60	0.10	14.40	1.13	0.94	0.39	2.17	0.68	0.23	1.08	0.18	1.40	0.35	1.16	0.16	1.28	0.20	0.04	0.00	0.24	5.43	0.86	0.39	0.34	5.31	20.44	25.75
NP233_Bg45	233B	0.017	0.71	426.75	0.10	12.27	0.93	0.79	0.32	1.82	0.56	0.19	0.86	0.16	1.14	0.29	0.97	0.14	1.09	0.18	0.05	0.00	0.22	4.78	0.83	0.36	0.35	4.42	17.30	21.72
NP233_Bg46	233B	0.002	0.34	436.23	0.10	12.77	0.89	0.72	0.29	1.67	0.53	0.19	0.92	0.15	1.16	0.31	0.98	0.15	1.10	0.17	0.04	0.00	0.23	5.40	0.88	0.39	0.34	4.10	17.91	22.01
NP233_Bg47	233B	0.007	0.47	418.50	0.12	12.79	0.85	0.66	0.28	1.64	0.51	0.18	0.86	0.14	1.15	0.29	0.99	0.15	1.09	0.17	0.05	0.00	0.21	4.54	0.88	0.38	0.32	3.94	17.81	21.75
NP233_Bg48	233B	0.003	0.33	420.97	0.11	14.48	0.93	0.71	0.31	1.82	0.54	0.20	0.95	0.16	1.24	0.32	1.08	0.17	1.16	0.20	0.05	0.00	0.20	3.98	0.89	0.39	0.32	4.31	19.96	24.27
NP233_Bg95	233B	0.004	0.45	456.59	0.11	26.56	2.44	2.15	1.02	5.66	1.70	0.59	2.62	0.43	3.15	0.74	2.28	0.35	2.42	0.36	0.04	0.01	0.19	4.56	0.90	0.37	0.33	12.97	39.50	52.47
NP233_Bg96	233B	0.010	0.89	399.54	0.10	17.30	1.39	1.07	0.48	2.71	0.76	0.29	1.37	0.23	1.72	0.42	1.41	0.22	1.52	0.24	0.04	0.00	0.20	4.87	0.91	0.38	0.32	6.41	24.71	31.12
NP233_Bg97	233B	0.028	0.51	375.75	0.11	12.02	0.84	0.80	0.30	1.60	0.47	0.18	0.83	0.14	1.15	0.28	0.93	0.14	1.07	0.17	0.04	0.00	0.20	5.25	0.92	0.38	0.39	4.01	16.91	20.92
NP233_Bg98	233B	0.021	0.37	357.71	0.10	11.97	0.80	0.73	0.29	1.54	0.47	0.18	0.76	0.13	1.10	0.28	0.92	0.14	1.04	0.17	0.03	0.00	0.18	5.07	0.95	0.35	0.36	3.83	16.69	20.52
NP233_Bg99	233B	0.021	0.49	426.61	0.10	11.69	0.83	0.79	0.28	1.54	0.47	0.17	0.84	0.14	1.09	0.27	0.88	0.13	0.98	0.16	0.05	0.00	0.22	4.77	0.87	0.39	0.39	3.91	16.35	20.26
NP233_Cg01	233C	0.018	0.68	425.60	0.21	11.39	1.34	0.78	0.42	1.97	0.56	0.20	0.94	0.15	1.11	0.27	0.88	0.13	1.02	0.16	0.05	0.00	0.26	5.00	0.90	0.39	0.25	5.07	16.25	21.32
NP233_Cg02	233C	0.098	0.60	301.18	0.27	22.29	2.67	1.95	0.79	3.81	1.03	0.35	1.62	0.26	2.07	0.54	1.78	0.27	1.94	0.34	0.05	0.01	0.19	3.52	0.88	0.39	0.32	10.25	31.46	41.71
NP233_Cg03	233C	0.125	0.66	245.64	0.25	24.52	4.05	4.27	0.97	4.70	1.12	0.38	1.85	0.30	2.27	0.59	1.96	0.29	2.05	0.37	0.04	0.00	0.14	3.23	0.86	0.39	0.52	15.11	34.58	49.69
NP233_Cg07	233C	0.227	3.24	331.90	0.21	11.87	1.50	1.05	0.46	2.22	0.59	0.20	0.90	0.16	1.16	0.30	0.99	0.16	1.04	0.17	0.04	0.00	0.19	4.55	0.85	0.37	0.31	5.82	16.95	22.77
NP233_Cg08	233C	0.040	1.11	366.06	0.29	17.94	2.32	1.53	0.70	3.45	0.96	0.31	1.48	0.25	1.83	0.47	1.49	0.23	1.68	0.27	0.06	0.00	0.23	3.93	0.83	0.39	0.18	8.36	25.94	34.30
NP233_Cg09	233C	0.023	0.56	415.38	0.25	17.04	2.32	1.11	0.68	3.48	0.97	0.30	1.52	0.25	1.89	0.45	1.46	0.22	1.52	0.26	0.06	0.00	0.25	4.04	0.80	0.40	0.21	8.56	24.91	33.47
NP233_Cg10	233C	0.018	0.60	409.20	0.26	18.88	2.57	1.53	0.79	3.99	1.11	0.36	1.74	0.28	2.07	0.50	1.68	0.24	1.69	0.27	0.06	0.01	0.25	4.32	0.84	0.39	0.26	9.99	27.71	37.70
NP233_Cg11	233C	0.077	0.57	362.06	0.24	19.84	2.87	2.12	0.89	4.31	1.23	0.39	1.80	0.31	2.20	0.53	1.72	0.24	1.78	0.29	0.06	0.01	0.22	3.61	0.83	0.38	0.32	11.42	29.11	40.53
NP233_Cg12	233C	0.011	0.61	405.36	0.25	18.57	2.56	1.83	0.82	4.13	1.18	0.39	1.72	0.29	2.09	0.51	1.61	0.23	1.68	0.27	0.07	0.01	0.24	3.54	0.87	0.37	0.30	10.52	27.34	37.86
NP233_Cg22	233C	0.086	0.83	392.58	0.44	20.86	2.79	1.89	0.87	4.39	1.25	0.40	1.79	0.31	2.30	0.57	1.85	0.27	1.94	0.31	0.10	0.02	0.25	2.62	0.84	0.37	0.29	11.19	30.60	41.79
NP233_Cg34	233C	0.089	1.41	344.08	0.34	34.56	5.33	2.57	1.38	6.55	1.84	0.56	2.75	0.47	3.48	0.89	2.93	0.43	3.15	0.50	0.05	0.02	0.21	4.29	0.79	0.39	0.23	17.67	49.74	67.41
NP233_Cg35	233C	0.238	1.19	330.03	1.23	32.97	5.30	3.16	1.43	6.57	1.78	0.57	2.75	0.46	3.41	0.87	2.80	0.42	3.14	0.50	0.12	0.38	0.20	1.71	0.82	0.39	0.28	18.24	47.91	66.15
NP233_Cg36	233C	0.016	0.54	458.81	0.33	31.77	4.78	3.45	1.38	6.56	1.81	0.59	2.84	0.47	3.39	0.83	2.68	0.41	2.92	0.46	0.06	0.02	0.25	4.27	0.84	0.39	0.32	17.98	46.36	64.34
NP233_Cg40	233C	0.501	3.49	283.77	1.91	47.15	9.30	7.39	2.43	11.09	2.98	0.91	4.20	0.72	5.42	1.35	4.35	0.68	4.82	0.75	0.48	0.16	0.27	0.56	0.81	0.37	0.37	33.19	70.36	103.55
NP233_Cg41	233C	0.038	1.08	395.72	0.41	68.59	12.19	6.41	3.26	15.13	4.17	1.32	6.15	1.05	7.89	1.94	6.12	0.95	6.86	1.07	0.06	0.06	0.24	3.76	0.83	0.38	0.24	41.16	101.92	143.08
NP233_Cg43	233C	0.008	1.15	372.80	1.10	137.89	38.06	21.21	11.48	51.07	14.35	4.28	18.24	3.21	22.41	5.02	15.51	2.41	16.54	2.45	0.08	0.94	0.26	3.42	0.82	0.35	0.24	136.17	227.97	364.14
NP233_Cg44	233C	0.006	0.91	375.14	0.93	118.16	26.39	14.00	7.50	33.95	9.52	2.87	12.89	2.28	16.90	3.91	12.03	1.94	13.66	2.07	0.08	0.40	0.32	4.10	0.81	0.36	0.24	91.36	186.70	278.06
NP233_Cg45	233C	0.037	2.30	452.10	0.25	18.02	2.62	1.76	0.80	4.11	1.18	0.40	1.71	0.28	2.09	0.49	1.52	0.23	1.72	0.27	0.05	0.01	0.24	4.53	0.91	0.37	0.29	10.47	26.73	37.20
NP233_Cg46	233C	0.029	1.02	428.96	0.55	85.98	17.90	10.96	4.83	21.98	6.02	1.83	8.61	1.47	10.98	2.61	8.23	1.30	9.42	1.43	0.07	0.14	0.26	3.66	0.80	0.38	0.28	61.69	131.87	193.56
NP233_Cg47	233C	0.023	0.90	452.89	0.59	91.80	19.57	12.00	5.30	24.57	6.82	2.05	9.37	1.61	12.10	2.84	8.79	1.40	10.07	1.54	0.08	0.16	0.28	3.79	0.81	0.37	0.28	68.26	141.56	209.82
NP233_Cg49	233C	0.002	0.83	444.40	0.57	81.81	15.88	9.69	4.27	19.91	5.50	1.67	7.86	1.35	10.10	2.45	7.58	1.22	8.51	1.34	0.09	0.15	0.29	3.29	0.80	0.38	0.28	55.25	123.89	179.14
NP233_Cg50	233C	0.002	0.66	472.85	0.38	47.19	8.13	4.41	2.19	10.35	2.83	0.90	4.25	0.70	5.27	1.29	4.08	0.66	4.66	0.73	0.06	0.05	0.27	4.52	0.84	0.39	0.25	27.91	69.73	97.64
NP233_Cg51	233C	0.112	0.53	412.57	0.22	16.87	2.44	1.95	0.77	3.82	1.11	0.37	1.64	0.28	1.99	0.48	1.45	0.24	1.58	0.24	0.05	0.01	0.22	4.29	0.87	0.37	0.34	10.09	25.13	35.22
NP233_Cg52	233C	0.029	1.09	380.47	0.71	99.20	24.75	12.77	6.89	30.45	8.30	2.48	11.00	1.96	14.04	3.32	10.37	1.64	11.59	1.74	0.07	0.26	0.25	3.54	0.80	0.36	0.24	83.16	157.34	240.50
NP233_Cg53	233C	0.02	1.18	445.59	0.77	116.96	28.39	13.62	8.01	36.29	9.81	2.98	13.25	2.35	16.82	4.04	12.40	1.95	13.33	2.03	0.08	0.34	0.29	3.55	0.81	0.36	0.22	96.12	186.12	282.24
NP233_Cg55	233C	0.007	0.84	390.15	0.49	81.76	16.79	10.74	4.59	20.76	5.78	1.75	7.89	1.36	10.31	2.49	7.95	1.23	8.70	1.33	0.07	0.16	0.23	3.19	0.82	0.37	0.29	58.66	124.77	183.43
NP233_Cg56	233C	0.013	0.76	405.71	0.37	51.50	8.77	4.77	2.35	10.79	3.01	0.92	4.46	0.78	5.71	1.46	4.57	0.71	5.01	0.79	0.06	0.07	0.28	4.78	0.79	0.38	0.25	29.69	75.92	105.61
NP233_Cg57	233C	0.034	0.61	480.09	0.33	18.56	2.63	1.64	0.77	3.72	1.05	0.34	1.54	0.27	1.95	0.49	1.48	0.24	1.63	0.27	0.06	0.01	0.27	4.72	0.84	0.37	0.28	9.81	26.77	36.58
NP233_Cg58	233C	0.008	0.61	459.59	0.26	27.13	3.93	2.63	1.14	5.43	1.59	0.50	2.29	0.40	2.80	0.72	2.29	0.35	2.36	0.38	0.07	0.02	0.25	3.83	0.82	0.37	0.30	14.72	39.21	53.93
17NP436b_Ag05	436b_A	0.004	0.93	488.40	0.30	4.48	0.69	0.00	0.08	0.41	0.07	0.02	0.24	0.02	0.21	0.07	0.22	0.04	0.24	0.04	0.04	Below LOD	0.18	4.19	0.75	0.82	0.00	1.24	5.58	6.82
17NP436b_Ag10	436b_A	0.001	0.57	531.20	0.32	6.59	1.41	0.01	0.20	0.93	0.20	0.06	0.34	0.05	0.40	0.11	0.38	0.05	0.36	0.06	0.04	Below LOD	0.19	4.85	0.80	0.47	0.01	2.75	8.39	11.14
17NP436b_Ag11	436b_A	0.001	0.38	584.90	0.21	1.53	0.14	0.00	0.01	0.05	0.01	0.00	0.07	0.00	0.05	0.02	0.07	0.01	0.08	0.02	0.03	Below LOD	0.17	5.15	0.83	1.08	0.02	0.22	1.85	2.07
17NP436b_Ag12	436b_A	0.003	0.61	466.20	0.39	5.95	1.00	0.01	0.12	0.59	0.11	0.03	0.28	0.03	0.28	0.09	0.30	0.04	0.33	0.05	0.04	Below LOD	0.18	4.57	0.73	0.64	0.00	1.83	7.38	9.21
17NP436b_Ag13	436b_A	0.003	0.58	516.70	0.28	7.71	1.51	0.02	0.22	1.03	0.20	0.06	0.38	0.05	0.43	0.12	0.42	0.06	0.41	0.07	0.04	Below LOD	0.17	4.08	0.78	0.50	0.01	2.96	9.71	12.67
17NP436b_Ag15	436b_A	0.004	0.80	470.70	0.31	12.55	3.28	0.03	0.47	2.16	0.43	0.13	0.73	0.11	0.88	0.23	0.74	0.11	0.69	0.12	0.04	Below LOD	0.17	4.37	0.77	0.46	0.01	6.38	16.29	22.67
17NP436b_Ag16	436b_A	0.001	0.46	543.30	0.27	0.31	0.02	0.00	0.00	0.01	0.00	0.00	0.06	0.00	0.01	0.00	0.01	0.00	0.02	0.00	0.04	Below LOD	0.20	5.23	1.13	4.52	0.03	0.03	0.42	0.45
17NP436b_Ag17	436b_A	0.002	0.72	515.20	0.30	1.41	0.12	0.00	0.01	0.05	0.01	0.00	0.11	0.00	0.04	0.01	0.06	0.01	0.08	0.02	0.04	Below LOD	0.19	5.29	0.65	1.97	0.02	0.19	1.74	1.93
17NP436b_Ag32	436b_A	0.002	0.62	499.60	0.30	1.47	0.12	0.00	0.01	0.06	0.01	0.00	0.09	0.00	0.05	0.02	0.06	0.01	0.08	0.02	0.04	Below LOD	0.18	4.26	0.96	1.42	0.02	0.21	1.80	2.01
17NP436b_Ag33	436b_A	0	0.46	552.80	0.25	1.92	0.21	0.00	0.02	0.11	0.02	0.01	0.09	0.01	0.06	0.02	0.09	0.01	0.11	0.02	0.04	Below LOD	0.18	4.33	0.75	0.95	0.01	0.36	2.33	2.69
17NP436b_Ag34	436b_A	0.001	0.47	529.40	0.27	10.70	2.47	0.03	0.36	1.72	0.35	0.10	0.57	0.08	0.70	0.19	0.60	0.09	0.57	0.09	0.04	Below LOD	0.18	4.63	0.79	0.45	0.01	4.92	13.69	18.61
17NP436b_Ag35	436b_A	0.005	0.72	491.10	0.25	16.34	3.77	0.04	0.52	2.44	0.47	0.14	0.83	0.12	1.01	0.27	0.91	0.13	0.85	0.14	0.04	Below LOD	0.17	3.81	0.78	0.46	0.01	7.24	20.74	27.98
17NP436b_Bg02	436b_B	0.001	0.55	561.30	0.33	3.58	0.84	0.01	0.13	0.61	0.14	0.04	0.25	0.03	0.25	0.06	0.21	0.03	0.20	0.03	0.04	Below LOD	0.19	4.82	0.77	0.54	0.01	1.74	4.69	6.43

sample number	group	MnO (wt%)	Ba (ppm)	Sr (ppm)	Zr (ppm)	Y (ppm)	La (ppm)	Ce (ppm)	Pr (ppm)	Nd (ppm)	Sm (ppm)	Eu (ppm)	Gd (ppm)	Tb (ppm)	Dy (ppm)	Ho (ppm)	Er (ppm)	Tm (ppm)	Yb (ppm)	Lu (ppm)	Pb (ppm)	Th (ppm)	U (ppm)	U/Pb	Eu/Eu*	Gd/Gd*	Ce/Ce*	LREE(La to Sm)	HREE(Eu to Lu+Y)	ALL REE
17NP436b_Bg03	436b_B	0.001	0.45	522.20	0.50	1.77	0.27	0.01	0.03	0.14	0.02	0.01	0.10	0.01	0.07	0.02	0.08	0.01	0.10	0.02	0.05	Below LOD	0.21	4.71	0.78	0.97	0.02	0.47	2.18	2.65
17NP436b_Bg04	436b_B	0.028	1.53	310.60	0.22	4.30	1.00	0.32	0.19	0.91	0.21	0.08	0.48	0.05	0.33	0.08	0.22	0.03	0.17	0.03	0.02	0.00	0.08	3.43	1.04	0.59	0.18	2.63	5.76	8.39
17NP436b_Bg05	436b_B	0.002	0.92	513.50	0.41	5.90	1.70	0.03	0.27	1.24	0.26	0.07	0.48	0.06	0.44	0.11	0.36	0.05	0.33	0.06	0.04	Below LOD	0.20	4.59	0.78	0.55	0.01	3.50	7.85	11.35
17NP436b_Bg06	436b_B	0.003	0.84	510.50	0.46	1.70	0.22	0.01	0.02	0.11	0.02	0.01	0.15	0.01	0.07	0.02	0.08	0.01	0.10	0.02	0.05	Below LOD	0.19	4.15	0.80	1.55	0.02	0.39	2.15	2.54
17NP436b_Bg07	436b_B	0.005	0.52	565.90	0.35	14.74	5.43	0.10	0.98	4.46	0.99	0.27	1.28	0.19	1.40	0.33	1.02	0.14	0.87	0.13	0.04	0.00	0.16	3.82	0.82	0.40	0.01	11.96	20.37	32.33
17NP436b_Bg08	436b_B	0.004	1.53	527.00	0.35	4.49	0.91	0.01	0.11	0.57	0.11	0.03	0.40	0.03	0.26	0.07	0.25	0.04	0.25	0.04	0.05	Below LOD	0.18	3.94	0.82	0.90	0.01	1.71	5.85	7.56
17NP436b_Bg09	436b_B	0.001	0.61	529.30	0.41	0.72	0.11	0.00	0.01	0.05	0.01	0.00	0.09	0.00	0.03	0.01	0.04	0.01	0.04	0.01	0.05	Below LOD	0.20	4.35	0.86	1.78	0.03	0.18	0.96	1.14
17NP436b_Bg10	436b_B	0.002	0.55	507.60	0.46	1.15	0.15		0.02	0.08	0.02	Below LOD	0.09	Below LOD	0.04	0.01	0.05	0.01	0.06	0.01	0.04	Below LOD	0.18	4.32	Below LOD				0.27	1.44	1.71
17NP436b_Bg14	436b_B	0.006	1.12	474.10	0.36	9.04	1.78	0.01	0.24	1.15	0.22	0.07	0.50	0.06	0.51	0.14	0.50	0.07	0.48	0.08	0.05	Below LOD	0.16	3.38	0.78	0.59	0.01	3.41	11.44	14.85
17NP436b_Bg15	436b_B	0.001	0.66	541.00	0.35	6.11	1.68	0.03	0.29	1.34	0.29	0.08	0.45	0.06	0.46	0.12	0.38	0.06	0.35	0.06	0.04	Below LOD	0.17	4.43	0.79	0.46	0.01	3.63	8.12	11.75
17NP436b_Bg19	436b_B	0.003	0.74	561.20	0.25	3.94	0.70	0.01	0.10	0.45	0.09	0.03	0.23	0.02	0.22	0.06	0.22	0.03	0.21	0.04	0.05	Below LOD	0.18	4.02	0.80	0.64	0.01	1.34	5.01	6.35
17NP436b_Bg20	436b_B	0.004	1.61	512.90	0.36	4.26	1.15	0.02	0.18	0.83	0.18	0.05	0.43	0.04	0.29	0.08	0.25	0.04	0.24	0.04	0.05	Below LOD	0.17	3.29	0.84	0.69	0.01	2.35	5.71	8.06
17NP436b_Bg21	436b_B	0.007	2.14	474.20	0.27	3.13	0.37	0.01	0.04	0.20	0.04	0.02	0.35	0.01	0.12	0.04	0.15	0.02	0.17	0.03	0.04	Below LOD	0.14	2.58	0.95	1.78	0.03	0.66	4.04	4.70
17NP436b_Bg22	436b_B	0.015	1.14	328.50	0.21	6.10	1.20	0.03	0.16	0.77	0.15	0.04	0.40	0.04	0.34	0.10	0.34	0.05	0.34	0.06	0.04	Below LOD	0.10	2.50	0.77	0.68	0.02	2.31	7.81	10.12
17NP436b_Bg23	436b_B	0.019	0.54	260.40	0.20	4.71	1.10	0.04	0.15	0.71	0.14	0.04	0.27	0.03	0.28	0.08	0.27	0.04	0.26	0.04	0.02	Below LOD	0.08	3.79	0.77	0.56	0.02	2.14	6.02	8.16
17NP436b_Bg27	436b_B	0.002	1.17	531.10	0.24	6.00	1.11	0.02	0.17	0.81	0.17	0.05	0.38	0.04	0.35	0.10	0.32	0.05	0.32	0.05	0.04	Below LOD	0.15	3.78	0.76	0.61	0.01	2.27	7.66	9.93
17NP436b_Bg28	436b_B	0.005	1.21	448.10	0.20	1.97	0.24	0.00	0.03	0.14	0.03	0.01	0.21	0.01	0.08	0.03	0.10	0.01	0.10	0.02	0.04	Below LOD	0.15	4.26	0.87	1.57	0.01	0.44	2.53	2.97
17NP436b_Bg29	436b_B	0.002	0.81	466.10	0.32	9.09	2.66	0.03	0.42	1.87	0.39	0.11	0.66	0.09	0.70	0.18	0.57	0.08	0.51	0.08	0.04	Below LOD	0.16	4.15	0.81	0.47	0.01	5.37	12.07	17.44
17NP436b_Bg33	436b_B	0.007	56.00	489.20	0.20	9.39	1.98	0.05	0.29	1.38	0.27	0.14	8.10	0.07	0.55	0.16	0.51	0.08	0.50	0.09	0.04	Below LOD	0.14	3.42	1.30	5.99	0.02	3.97	19.58	23.55
17NP436b_Bg34	436b_B	0.013	4.30	348.50	0.37	2.79	0.35	0.01	0.03	0.18	0.03	0.02	0.61	0.01	0.11	0.03	0.13	0.02	0.15	0.03	0.03	Below LOD	0.13	4.28	1.11	3.52	0.03	0.61	3.90	4.51
17NP436b_Bg35	436b_B	0.002	0.69	491.00	0.23	7.25	1.29	0.01	0.18	0.87	0.17	0.05	0.35	0.05	0.42	0.12	0.41	0.06	0.40	0.07	0.03	Below LOD	0.15	4.92	0.79	0.52	0.00	2.52	9.17	11.69
17NP436b_Bg46	436b_B	0.022	0.44	194.40	0.14	3.25	0.69	0.04	0.09	0.41	0.08	0.02	0.19	0.02	0.16	0.05	0.18	0.03	0.20	0.03	0.02	Below LOD	0.06	4.04	0.78	0.66	0.04	1.31	4.12	5.43
17NP436b_Bg47	436b_B	0.020	0.42	231.50	0.15	2.98	0.61	0.03	0.08	0.35	0.07	0.02	0.16	0.02	0.15	0.05	0.16	0.02	0.18	0.03	0.04	Below LOD	0.08	4.27	0.75	0.67	0.04	1.13	3.77	4.90
17NP436b_Cg01	436b_C	0.003	1.12	457.90	0.48	0.73	0.13	0.01	0.02	0.09	0.02	0.01	0.17	0.00	0.04	0.01	0.04	0.01	0.04	0.01	0.04	Below LOD	0.19	4.42	0.93	2.13	0.03	0.26	1.05	1.31
17NP436b_Cg02	436b_C	0.003	0.95	479.00	0.42	8.94	2.87	0.05	0.52	2.37	0.52	0.14	0.75	0.10	0.75	0.18	0.57	0.08	0.51	0.08	0.05	0.00	0.19	3.80	0.79	0.46	0.01	6.34	12.10	18.44
17NP436b_Cg03	436b_C	0.008	1.72	466.30	0.26	13.71	2.50	0.05	0.36	1.73	0.34	0.10	0.78	0.09	0.78	0.22	0.75	0.11	0.74	0.12	0.05	Below LOD	0.13	2.79	0.75	0.59	0.01	4.99	17.39	22.38
17NP436b_Cg04	436b_C	0.000	0.50	501.90	0.43	2.11	0.32	0.01	0.04	0.18	0.04	0.01	0.12	0.01	0.09	0.03	0.11	0.02	0.11	0.02	0.04	Below LOD	0.21	4.76	0.72	0.86	0.01	0.59	2.62	3.21
17NP436b_Cg05	436b_C	0.000	0.42	516.00	0.43	0.28	0.04	0.00	0.01	0.04	0.01	0.00	0.06	Below LOD	0.02	0.01	0.01	Below LOD	0.02	Below LOD	0.04	Below LOD	0.21	4.72	Below LOD			0.07	0.39	0.49
17NP436b_Cg06	436b_C	0.005	0.99	484.80	0.46	7.34	2.22	0.04	0.38	1.68	0.38	0.10	0.57	0.07	0.57	0.14	0.45	0.06	0.41	0.06	0.05	Below LOD	0.18	3.69	0.77	0.48	0.01	4.70	9.78	14.48
17NP436b_Cg08	436b_C	0.003	0.96	476.60	0.51	1.86	0.24	0.01	0.03	0.14	0.03	0.01	0.17	0.01	0.08	0.02	0.09	0.02	0.09	0.02	0.05	Below LOD	0.21	3.87	0.78	1.32	0.02	0.44	2.36	2.80
17NP436b_Cg09	436b_C	0.001	0.82	489.30	0.53	0.61	0.07	0.01	0.01	0.05	0.01	0.00	0.12	0.00	0.03	0.01	0.03	0.00	0.03	0.01	0.04	Below LOD	0.21	4.78	0.94	2.25	0.05	0.15	0.85	1.00
17NP436b_Cg13	436b_C	0.022	1.56	336.30	0.78	10.88	3.22	0.25	0.58	2.66	0.57	0.16	0.90	0.12	0.94	0.22	0.69	0.10	0.61	0.10	0.06	0.00	0.13	2.38	0.80	0.47	0.04	7.27	14.62	21.89
17NP436b_Cg14	436b_C	0.003	1.02	474.60	0.45	5.85	1.27	0.02	0.19	0.85	0.18	0.05	0.38	0.04	0.34	0.09	0.32	0.05	0.33	0.06	0.04	Below LOD	0.19	4.36	0.73	0.62	0.01	2.51	7.50	10.01
17NP436b_Cg16	436b_C	0.003	0.90	467.30	0.29	18.34	4.24	0.08	0.68	3.24	0.66	0.19	1.06	0.16	1.26	0.33	1.06	0.15	0.99	0.16	0.04	Below LOD	0.14	3.51	0.78	0.44	0.01	8.89	23.69	32.58
17NP436b_Cg19	436b_C	0.004	0.97	485.20	0.36	5.70	1.21	0.03	0.19	0.86	0.18	0.05	0.37	0.04	0.34	0.09	0.31	0.05	0.30	0.05	0.04	0.00	0.18	3.96	0.78	0.57	0.02	2.47	7.31	9.78
17NP436b_Cg21	436b_C	0.001	0.71	490.50	0.47	5.25	1.02	0.01	0.14	0.61	0.13	0.04	0.29	0.03	0.28	0.08	0.29	0.04	0.31	0.05	0.04	Below LOD	0.21	5.30	0.73	0.61	0.01	1.91	6.66	8.57
17NP436b_Cg26	436b_C	0.002	0.81	479.70	0.38	19.94	6.73	0.13	1.22	5.57	1.21	0.33	1.62	0.24	1.79	0.43	1.32	0.18	1.15	0.17	0.05	0.00	0.16	3.42	0.81	0.41	0.01	14.86	27.17	42.03
17NP436b_Cg27	436b_C	28.00	0.35	357.20	0.21	12.04	2.03	0.05	0.27	1.29	0.26	0.11	4.20	0.07	0.63	0.19	0.64	0.10	0.68	0.11	0.04	Below LOD	0.11	3.00	1.13	3.43	0.02	3.89	18.77	22.66
17NP436b_Cg28	436b_C	0.003	0.80	488.40	0.42	2.79	0.67	0.02	0.11	0.51	0.11	0.03	0.23	0.02	0.18	0.05	0.15	0.02	0.15	0.02	0.04	Below LOD	0.19	4.64	0.76	0.65	0.02	1.41	3.65	5.06
17NP436b_Cg29	436b_C	0.001	0.76	490.30	0.43	2.64	0.47	0.01	0.06	0.28	0.06	0.02	0.18	0.02	0.14	0.04	0.14	0.02	0.15	0.02	0.04	Below LOD	0.23	4.63	0.71	0.81	0.02	0.88	3.37	4.25
17NP436b_Dg03	436b_D	0.006	1.24	428.00	0.25	8.77	1.24	0.06	0.15	0.73	0.16	0.05	0.41	0.04	0.38	0.12	0.43	0.07	0.47	0.09	0.04	Below LOD	0.15	3.93	0.78	0.64	0.03	2.34	10.83	13.17
17NP436b_Dg04	436b_D	0.002	0.71	427.90	0.23	14.51	3.16	0.06	0.44	2.08	0.41	0.12	0.72	0.10	0.87	0.23	0.81	0.12	0.77	0.13	0.03	Below LOD	0.15	4.72	0.77	0.47	0.01	6.14	18.38	24.52
17NP436b_Dg06	436b_D	0.008	1.02	391.70	0.29	6.29	0.73	0.04	0.08	0.42	0.09	0.03	0.26	0.03	0.26	0.08	0.30	0.05	0.35	0.06	0.04	Below LOD	0.14	3.59	0.82	0.67	0.04	1.36	7.71	9.07
17NP436b_Dg07	436b_D	0.002	0.82	455.90	0.24	12.15	2.54	0.04	0.35	1.64	0.33	0.10	0.59	0.08	0.66	0.19	0.66	0.10	0.65	0.11	0.04	Below LOD	0.16	4.38	0.76	0.49	0.01	4.90	15.28	20.18
17NP436b_Dg10	436b_D	0.005	1.00	299.50	0.17	8.79	1.45	0.04	0.18	0.88	0.17	0.05	0.42	0.04	0.41	0.12	0.45	0.07	0.48	0.08	0.03	Below LOD	0.10	3.47	0.74	0.64	0.02	2.72	10.92	13.64
17NP436b_Dg11	436b_D	0.002	0.60	356.30	0.19	19.39	4.98	0.08	0.74	3.38	0.70	0.20	1.08	0.16	1.32	0.35	1.12	0.16	1.06	0.17	0.03	Below LOD	0.12	4.76	0.78	0.44	0.01	9.88	25.01	34.89
17NP436b_Dg12	436b_D	0.004	0.43	405.30	0.18	10.00	2.08	0.08	0.28	1.31	0.27	0.08	0.47	0.07	0.61	0.16	0.58	0.09	0.58	0.10	0.03	0.00	0.12	3.96	0.78	0.45	0.03	4.01	12.73	16.74
17NP436b_Dg14	436b_D	0.003	0.54	371.60	0.21	7.59	1.14	0.06	0.14	0.69	0.14	0.04	0.32	0.04	0.36	0.11	0.39	0.06	0.42	0.08	0.03	Below LOD	0.14	4.89	0.80	0.54	0.03	2.17	9.40	11.57
17NP436b_Dg15	436b_D	0.003	0.48	294.00	0.17	10.49	2.29	0.04	0.31	1.48	0.28	0.08	0.50	0.07	0.62	0.17	0.56	0.09	0.57	0.09	0.02	Below LOD	0.09	3.56	0.76	0.47	0.01	4.41	13.25	17.66
17NP436b_Dg18	436b_D	0.005	2.00	430.30	0.25	6.79	0.90	0.05	0.11	0.53	0.11	0.04	0.42	0.03	0.29	0.09	0.33	0.05	0.37	0.07	0.04	Below LOD	0.15	3.44	0.89	0.87	0.04	1.70	8.48	10.18
17NP436b_Dg19	436b_D	0.003	0.63	373.80	0.19	7.85	1.11	0.02	0.12	0.60	0.11	0.03	0.30	0.03	0.33	0.10	0.39	0.06	0.43	0.08	0.03	Below LOD	0.12	4.00	0.74	0.64	0.01	1.97	9.61	11.58
17NP436b_Dg22	436b_D	0.007	0.71	378.80	0.25	7.63	1.72	0.08	0.29	1.35	0.30	0.08	0.49	0.06	0.50	0.13	0.43	0.06	0.40	0.07	0.03	0.00	0.11	3.68	0.77	0.50	0.03	3.74	9.85	13.59
17NP436b_Dg23	436b_D	0.001	1.02	466.50	0.28	5.94	0.70	0.05	0.08	0.41	0.09	0.03	0.28	0.03	0.24	0.08	0.29	0.05	0.34	0.06	0.04	Below LOD	0.16	4.35	0.79	0.74	0.05	1.32	7.33	8.65
17NP436a_Ag001	436a_A	0.002	0.31	240.80	0.03	13.81	1.29	0.45	0.35	1.92	0.50	0.20	0.89	0.15	1.22	0.32	1.08	0.17	1.13	0.20	0.03	Below LOD	0.11	4.40	0.96	0.37	0.16	4.51	19.15	23.66
17NP436a_Ag002	436a_A	0.002	0.38	274.50	0.02	10.04	0.90	0.32	0.26	1.42	0.37	0.15	0.68	0.11	0.86	0.23	0.78	0.12	0.82	0.14	0.03	0.00	0.12	3.67	0.95	0.38	0.16	3.27	13.93	17.20
17NP436a_Ag003	436a_A	0.005	0.61	290.40	0.02	7.40	0.87	0.18	0.19	0.93	0.23	0.09	0.48	0.07	0.60	0.16	0.55	0.08	0.57	0.10	0.03	Below LOD	0.07	2.56	0.94	0.43	0.11	2.40	10.12	12.52
17NP436a_Ag004	436a_A	0.009	0.99	329.50	0.02	8.46	0.84	0.20	0.21	1.10	0.29	0.11	0.62	0.08	0.66	0.18	0.61	0.09	0.63	0.11	0.04	0.00	0.10	2.77	0.96	0.47	0.11	2.63	11.56	14.19
17NP436a_Ag005	436a_A	0.015	0.50	169.60	0.03	8.62	0.97	0.22	0.22	1.11	0.29	0.12	0.59	0.09	0.74	0.20	0.69	0.10	0.71	0.12	0.02	Below LOD	0.05	3.14	0.96	0.42	0.12	2.81	11.98	14.79
17NP436a_Ag006	436a_A	0.004	0.34	265.50	0.02	7.65	0.71	0.14	0.19	1.00	0.27	0.10	0.52	0.07	0.61	0.17	0.56	0.08	0.57	0.11	0.03	Below LOD	0.11	4.17	0.96	0.44	0.09	2.31	10.44	12.75
17NP436a_Ag007	436a_A	0.001	0.23	254.70	0.02	10.90	0.92	0.41	0.30	1.62	0.45	0.17	0.76	0.12	1.00	0.26	0.87	0.14	0.93	0.15	0.03	0.00	0.14	3.94	0.96	0.38	0.19	3.71	15.30	19.01
17NP436a_Ag008	436a_A	0.009	0.84	259.90	0.03	9.01	1.08	0.21	0.24	1.23	0.32	0.12	0.64	0.09	0.75	0.20	0.67	0.10	0.70	0.13	0.03	Below LOD	0.09	2.71	0.90	0.45	0.10	3.09	12.41	15.50
17NP436a_Ag009	436a_A	0.008	0.62	287.10	0.02	9.67	1.09	0.32	0.27	1.38	0.34	0.14	0.68	0.10	0.84	0.23	0.78	0.12	0.81	0.15	0.03	0.00	0.10	3.32	0.96	0.42	0.14	3.40	13.51	16.91
17NP436a_Ag010	436a_A	0.007	0.53	267.40	0.02	8.87	1.12	0.31	0.25	1.26	0.31	0.12	0.59	0.09	0.77	0.21	0.72	0.12	0.76	0.14	0.02	Below LOD	0.08	3.58	0.92	0.41	0.14	3.25	12.39	15.64
17NP436a_Ag011	436a_A	0.009	0.52	278.10	0.02	7.40	0.84	0.15	0.18	0.92	0.22	0.09	0.49	0.07	0.57	0.16	0.55	0.08	0.56	0.10	0.02	Below LOD	0.06	3.28	1.00	0.44	0.09	2.31	10.07	12.38
17NP436a_Ag013	436a_A	0.012	0.42	205.60	0.02	6.83	0.59	0.18	0.18	0.95	0.25	0.10	0.49	0.07	0.59	0.16	0.53	0.08	0.53	0.09	0.03	Below LOD	0.09	3.32	0.97	0.42	0.13	2.15	9.46	11.61
17NP436a_Ag014	436a_A	0.004	0.32	258.80	0.02	10.63	0.92	0.41	0.29	1.57	0.43	0.17	0.76	0.12	0.96	0.25	0.84	0.13	0.89	0.15	0.03	0.00	0.13	4.16	0.96	0.39	0.19	3.62	14.90	18.52
17NP436a_Ag017	436a_A	0.013	0.54	291.30	0.02	9.21	1.03	0.37	0.27	1.42	0.37	0.14	0.69	0.10	0.84	0.22	0.76	0.12	0.80	0.14	0.03	0.00	0.10	3.99	0.94	0.41	0.17	3.46	13.02	16.48
17NP436a_Ag018	436a_A	0.019	0.65	248.40	0.03	8.49	0.99	0.45	0.27	1.35	0.36	0.14	0.65	0.10	0.82	0.21	0.74	0.11	0.76	0.13	0.02	Below LOD	0.07	3.31	0.94	0.40	0.21	3.42	12.14	15.56

sample number	group	MnO (wt%)	Ba (ppm)	Sr (ppm)	Zr (ppm)	Y (ppm)	La (ppm)	Ce (ppm)	Pr (ppm)	Nd (ppm)	Sm (ppm)	Eu (ppm)	Gd (ppm)	Tb (ppm)	Dy (ppm)	Ho (ppm)	Er (ppm)	Tm (ppm)	Yb (ppm)	Lu (ppm)	Pb (ppm)	Th (ppm)	U (ppm)	U/Pb	Eu/Eu*	Gd/Gd*	Ce/Ce*	LREE(La to Sm)	HREE(Eu to Lu+Y)	ALL REE
17NP436a_Ag019	436a_A	0.013	0.569	230.300	0.021	8.527	0.958	0.343	0.258	1.284	0.342	0.130	0.654	0.097	0.785	0.206	0.707	0.109	0.758	0.132	0.021	0.000	0.074	3.460	0.931	0.421	0.166	3.184	12.100	15.280
17NP436a_Ag020	436a_A	0.006	0.360	229.300	0.019	9.340	0.951	0.316	0.254	1.321	0.340	0.133	0.611	0.102	0.816	0.224	0.751	0.119	0.813	0.150	0.020	Below LOD	0.102	5.220	0.938	0.378	0.154	3.182	13.060	16.240
17NP436a_Ag022	436a_A	0.002	0.216	221.000	0.031	15.170	1.289	0.349	0.373	1.984	0.547	0.212	0.969	0.158	1.314	0.350	1.171	0.184	1.246	0.221	0.028	Below LOD	0.122	4.380	0.940	0.382	0.121	4.541	20.990	25.530
17NP436a_Ag023	436a_A	0.007	0.477	295.300	0.019	8.869	0.779	0.213	0.223	1.178	0.300	0.123	0.602	0.089	0.736	0.197	0.670	0.100	0.683	0.121	0.034	Below LOD	0.130	3.870	0.983	0.415	0.123	4.880	12.190	14.880
17NP436a_Ag026	436a_A	0.008	0.663	300.600	0.026	9.158	1.087	0.635	0.323	1.679	0.436	0.165	0.752	0.118	0.943	0.249	0.812	0.122	0.815	0.144	0.031	Below LOD	0.119	3.800	0.953	0.388	0.258	4.160	13.280	17.440
17NP436a_Ag027	436a_A	0.006	0.319	236.600	0.024	9.804	1.258	0.881	0.392	1.922	0.539	0.198	0.804	0.138	1.111	0.272	0.886	0.137	0.919	0.160	0.023	0.002	0.076	3.260	0.949	0.351	0.302	4.992	14.430	19.420
17NP436a_Ag028	436a_A	0.003	0.309	249.800	0.026	9.584	1.137	0.523	0.305	1.519	0.416	0.158	0.702	0.114	0.934	0.249	0.810	0.125	0.847	0.153	0.026	0.000	0.093	3.620	0.948	0.376	0.214	3.900	13.680	17.580
17NP436a_Ag029	436a_A	0.001	0.196	255.900	0.020	10.302	1.111	0.409	0.300	1.575	0.398	0.157	0.685	0.112	0.931	0.250	0.843	0.130	0.876	0.154	0.031	0.000	0.119	3.890	0.968	0.372	0.171	3.703	14.440	18.230
17NP436a_Ag056	436a_A	0.003	0.489	277.100	0.026	10.500	0.961	0.642	0.349	1.860	0.538	0.196	0.851	0.137	1.079	0.282	0.892	0.137	0.991	0.158	0.040	0.001	0.142	3.510	0.942	0.374	0.267	4.350	15.160	19.510
17NP436a_Ag057	436a_A	0.010	0.751	291.400	0.022	10.940	0.995	0.649	0.361	1.879	0.515	0.194	0.892	0.139	1.122	0.285	0.939	0.141	0.953	0.166	0.034	Below LOD	0.130	3.800	0.949	0.392	0.261	4.399	15.770	20.170
17NP436a_Ag058	436a_A	0.006	1.002	297.600	0.033	10.030	0.910	0.456	0.297	1.566	0.422	0.168	0.819	0.119	0.941	0.250	0.825	0.127	0.861	0.152	0.036	0.001	0.113	3.120	0.979	0.418	0.211	3.651	14.290	17.940
17NP436a_Ag059	436a_A	0.003	0.563	272.100	0.023	9.970	0.861	0.334	0.270	1.442	0.388	0.144	0.711	0.110	0.877	0.227	0.771	0.116	0.788	0.141	0.032	0.000	0.118	3.720	0.915	0.407	0.167	3.294	13.860	17.150
17NP436a_Ag060	436a_A	0.008	0.976	310.800	0.019	10.820	0.945	0.217	0.302	1.614	0.445	0.174	0.846	0.123	1.002	0.261	0.883	0.132	0.907	0.159	0.037	Below LOD	0.116	3.110	0.976	0.417	0.098	3.523	15.310	18.830
17NP436a_Ag061	436a_A	0.004	0.584	277.300	0.022	10.072	0.971	0.551	0.337	1.792	0.492	0.185	0.846	0.133	1.045	0.262	0.871	0.134	0.914	0.151	0.034	0.000	0.123	3.620	0.947	0.389	0.232	4.143	14.610	18.750
17NP436a_Ag065	436a_A	0.007	0.842	318.300	0.043	9.980	0.876	0.319	0.286	1.505	0.418	0.159	0.782	0.114	0.928	0.248	0.815	0.126	0.833	0.147	0.049	Below LOD	0.107	2.170	0.950	0.418	0.154	3.404	14.130	17.530
17NP436a_Ag066	436a_A	0.013	0.839	291.700	0.018	10.680	0.943	0.367	0.296	1.609	0.441	0.162	0.809	0.120	0.991	0.259	0.864	0.131	0.894	0.157	0.037	0.000	0.120	3.520	0.936	0.397	0.154	3.372	14.270	17.640
17NP436a_Ag067	436a_A	0.005	0.511	281.000	0.022	10.229	0.886	0.318	0.278	1.499	0.390	0.149	0.710	0.111	0.921	0.238	0.806	0.124	0.836	0.145	0.034	0.000	0.120	3.520	0.936	0.397	0.154	3.372	14.270	17.640
17NP436a_Ag068	436a_A	0.005	0.449	264.400	0.022	10.340	0.886	0.298	0.254	1.368	0.365	0.141	0.704	0.105	0.892	0.239	0.801	0.124	0.824	0.147	0.029	Below LOD	0.111	3.810	0.942	0.419	0.151	3.171	14.320	17.490
17NP436a_Ag069	436a_A	0.014	0.881	285.000	0.021	9.691	0.868	0.213	0.276	1.463	0.390	0.152	0.771	0.107	0.896	0.234	0.795	0.116	0.821	0.141	0.042	Below LOD	0.106	2.540	0.971	0.435	0.105	3.211	13.720	16.930
17NP436a_Ag070	436a_A	0.009	0.628	254.600	0.022	9.950	0.907	0.512	0.325	1.720	0.489	0.181	0.814	0.131	1.025	0.261	0.831	0.130	0.852	0.148	0.031	Below LOD	0.108	3.540	0.935	0.380	0.227	3.953	14.330	18.270
17NP436a_Ag100	436a_A	0.004	0.614	269.100	0.026	12.040	1.425	1.072	0.492	2.499	0.702	0.255	1.074	0.179	1.428	0.356	1.159	0.173	1.164	0.202	0.029	0.002	0.102	3.470	0.942	0.363	0.308	5.190	18.030	24.220
17NP436a_Ag101	436a_A	0.002	0.313	261.700	0.023	9.635	1.075	0.481	0.315	1.578	0.438	0.162	0.710	0.114	0.960	0.248	0.835	0.131	0.850	0.147	0.027	0.000	0.111	4.050	0.945	0.376	0.199	3.887	13.790	17.680
17NP436a_Ag103	436a_A	0.004	0.731	285.100	0.019	10.198	0.945	0.199	0.266	1.450	0.376	0.149	0.752	0.106	0.887	0.240	0.823	0.124	0.868	0.154	0.030	Below LOD	0.103	3.330	0.979	0.431	0.095	3.236	14.300	17.540
17NP436a_Ag104	436a_A	0.003	0.262	248.300	0.025	9.485	1.138	0.311	0.271	1.367	0.356	0.136	0.623	0.102	0.848	0.239	0.798	0.122	0.841	0.151	0.021	0.000	0.076	3.620	0.932	0.382	0.135	3.444	13.340	16.780
17NP436a_Ag108	436a_A	0.002	0.337	275.900	0.022	9.617	1.023	0.518	0.329	1.690	0.469	0.175	0.758	0.125	0.973	0.252	0.826	0.131	0.889	0.153	0.033	Below LOD	0.117	3.600	0.947	0.370	0.215	4.029	13.900	17.930
17NP436a_Ag109	436a_A	0.012	0.677	221.100	0.087	8.280	0.795	0.239	0.242	1.334	0.347	0.132	0.636	0.095	0.771	0.203	0.674	0.106	0.671	0.123	0.030	0.001	0.098	3.270	0.948	0.410	0.131	2.937	11.690	14.630
17NP436a_Bg17	436a_B	0.003	0.463	537.800	0.464	0.104	0.025	0.005	0.003	0.014	0.003	0.002	0.061	0.001	0.005	0.001	0.004	0.000	0.003	0.001	0.037	Below LOD	0.154	4.100	1.321	2.983	0.137	0.050	0.180	0.230
17NP436a_Bg18	436a_B	0.005	1.100	589.900	0.379	0.041	0.007	0.001	0.001	0.003	0.001	0.002	0.147	0.000	0.001	0.000	0.001	0.000	0.000	0.000	0.040	Below LOD	0.150	3.760	4.320	16.068	0.205	0.012	0.190	0.200
17NP436a_Bg19	436a_B	0.015	0.747	485.300	0.446	0.083	0.020	0.004	0.002	0.008	0.004	0.002	0.094	0.001	0.004	0.001	0.003	0.000	0.004	0.001	0.054	Below LOD	0.131	2.520	1.565	6.238	0.150	0.038	0.190	0.230
17NP436a_Bg20	436a_B	0.007	0.958	445.400	0.491	0.061	0.006	0.002	Below LOD	0.005	Below LOD	Below LOD	0.117	Below LOD	Below LOD	Below LOD	Below LOD	Below LOD	Below LOD	Below LOD	0.036	Below LOD	0.131	3.650	Below LOD			0.013	0.180	0.190
17NP436a_Bg21	436a_B	0.005	0.993	457.500	0.527	0.056	0.007	0.001	0.001	0.003	0.000	0.001	0.134	0.000	0.003	0.001	0.003	Below LOD	0.003	0.001	0.042	Below LOD	0.151	3.640	#DIV/0!	19.237	0.071	0.011	0.200	0.210
17NP436a_Bg24	436a_B	0.002	0.554	485.300	0.474	0.345	0.065	0.001	0.009	0.047	0.011	0.004	0.087	0.003	0.023	0.006	0.020	0.003	0.019	0.003	0.041	Below LOD	0.146	3.540	1.056	1.847	0.011	0.133	0.510	0.640
17NP436a_Bg25	436a_B	0.021	0.999	549.000	0.309	0.059	0.019	0.005	0.001	0.005	Below LOD	0.002	0.120	0.000	0.002	0.001	0.002	0.000	0.001	0.000	0.051	Below LOD	0.123	2.410	Below LOD	16.631	0.223	0.030	0.180	0.210
17NP436a_Bg26	436a_B	0.019	1.244	483.300	0.429	0.667	0.014	0.003	0.001	0.007	0.001	0.002	0.158	0.001	0.003	0.001	0.002	0.000	0.003	0.000	0.051	Below LOD	0.120	2.520	3.063	10.808	0.193	0.026	0.240	0.270
17NP436a_Bg27	436a_B	0.005	0.915	511.900	0.597	0.048	0.007		Below LOD	0.003	Below LOD	Below LOD	0.097	Below LOD	Below LOD	Below LOD	0.002	Below LOD	0.001	Below LOD	0.046	Below LOD	0.160	3.470	Below LOD			0.010	0.150	0.160
17NP436a_Bg28	436a_B	0.007	0.862	489.200	0.483	0.074	0.015	0.002	0.001	0.005	0.000	0.001	0.119	0.000	0.004	0.000	0.002	0.000	0.004	0.001	0.039	Below LOD	0.131	3.320	#DIV/0!	13.506	0.147	0.023	0.210	0.230
17NP436a_Bg36	436a_B	0.007	1.100	581.500	0.325	0.224	0.058	0.016	0.009	0.047	0.009	0.005	0.150	0.003	0.020	0.004	0.002	0.001	0.007	0.001	0.037	Below LOD	0.112	3.010	1.267	3.080	0.162	0.139	0.430	0.570
17NP436a_Bg37	436a_B	0.002	0.483	557.700	0.362	0.028	0.003	0.001	0.000	0.001	0.000	0.000	0.057	Below LOD	0.001	0.000	0.002	0.000	0.001	0.000	0.037	Below LOD	0.145	3.900	Below LOD		0.121	0.006	0.090	0.100
17NP436a_Bg38	436a_B	0.002	0.585	540.100	0.442	0.048	0.005	0.002	0.001	0.005	0.000	0.001	0.073	0.000	0.002	0.001	0.003	0.000	0.004	0.001	0.042	Below LOD	0.163	3.920	#DIV/0!	11.232	0.187	0.012	0.130	0.140
17NP436a_Bg39	436a_B	0.003	0.421	510.000	0.356	0.054	0.008		Below LOD	Below LOD	Below LOD	0.002	0.058	Below LOD	Below LOD	Below LOD	Below LOD	Below LOD	Below LOD	Below LOD	0.035	Below LOD	0.123	3.500	Below LOD			0.009	0.110	0.120
17NP436a_Bg44	436a_B	0.006	0.492	482.000	0.412	0.128	0.026	0.007	0.005	0.019	0.005	0.002	0.068	0.001	0.009	0.003	0.006	0.001	0.004	0.001	0.034	Below LOD	0.131	3.870	1.035	3.104	0.139	0.062	0.220	0.280
17NP436a_Bg45	436a_B	0.008	1.070	525.100	0.456	0.053	0.012	0.003	0.002	0.006	0.001	0.002	0.134	0.000	0.003	0.001	0.003	0.000	0.003	0.000	0.043	Below LOD	0.145	3.360	4.159	11.842	0.146	0.023	0.200	0.220
17NP436a_Bg46	436a_B	0.004	0.705	488.000	0.454	0.048	0.005	0.002	0.001	0.002	0.001	0.000	0.095	0.000	0.002	0.001	0.003	0.000	0.002	0.000	0.035	Below LOD	0.141	4.050	1.204	15.624	0.248	0.010	0.150	0.160
17NP436a_Bg47	436a_B	0.006	1.007	550.200	0.406	0.045	0.004	0.002	0.000	0.002	0.000	0.001	0.126	0.000	Below LOD	0.001	0.002	0.000	0.003	0.001	0.040	Below LOD	0.165	3.350	#DIV/0!	21.863	0.342	0.008	0.180	0.190
17NP436a_Bg48	436a_B	0.008	0.610	580.100	0.298	0.194	0.038	0.011	0.005	0.032	0.009	0.003	0.064	0.001	0.014	0.003	0.009	0.001	0.006	0.001	0.041	Below LOD	0.157	3.940	Below LOD			0.005	0.130	0.140
17NP436a_Bg52	436a_B	0.002	0.711	560.100	0.404	0.044	0.010	0.003	0.001	0.006	0.001	0.001	0.097	0.000	0.003	0.001	0.002	0.000	0.001	0.000	0.040	Below LOD	0.161	3.970	2.339	12.367	0.176	0.022	0.150	0.170
17NP436a_Bg53	436a_B	0.002	0.598	487.600	0.425	0.042	0.003	0.000	0.000	0.003	0.000	0.001	0.069	0.000	0.001	0.001	0.003	0.000	0.002	0.000	0.038	Below LOD	0.161	4.230	#DIV/0!	13.213	0.052	0.007	0.120	0.130
17NP436a_Bg55	436a_B	0.002	0.515	493.600	0.372	0.086	0.020	0.000	0.000	0.003	0.013	0.003	0.061	0.001	0.007	0.001	0.005	0.001	0.005	0.001	0.034	Below LOD	0.125	3.650	1.242	3.896	0.015	0.040	0.170	0.210
17NP436a_Bg56	436a_B	0.001	0.514	516.000	0.479	0.035	0.004		Below LOD	Below LOD	Below LOD	Below LOD	0.058	Below LOD	Below LOD	Below LOD	0.002	Below LOD	Below LOD	Below LOD	0.044	Below LOD	0.170	3.850	Below LOD			0.004	0.100	0.100
17NP436a_Bg57	436a_B	0.002	0.781	457.700	0.626	0.052	0.005	0.001	0.001	0.003	0.000	0.001	0.088	Below LOD	0.001	0.001	0.002	0.000	0.003	0.001	0.041	Below LOD	0.156	3.820	Below LOD		0.117	0.010	0.150	0.160
17NP436a_Bg60	436a_B	0.006	0.456	488.200	0.363	0.054	0.011	0.003	0.001	0.005	0.002	0.001	0.062	0.000	0.003	0.001	0.002	0.000	0.001	0.000	0.037	Below LOD	0.144	3.930	1.976	9.048	0.186	0.022	0.120	0.140
17NP436a_Bg61	436a_B	0.001	0.588	494.100	0.483	0.038	0.003	0.002	0.000	0.001	0.000	0.000	0.078	0.000	0.001	0.000	0.002	0.000	0.003	0.001	0.037	Below LOD	0.169	4.600	#DIV/0!	29.351	0.311	0.007	0.120	0.130
17NP436a_Bg64	436a_B	0.002	0.528	540.600	0.356	0.305	0.020	0.000	0.002	0.008	0.001	0.001	0.072	0.000	0.006	0.002	0.009	0.001	0.001	0.001	0.034	Below LOD	0.130	3.820	1.363	8.648	0.019	0.030	0.410	0.440
17NP436a_Bg68	436a_B	0.008	0.415	536.000	0.309	0.216	0.051	0.022	0.009	0.042	0.014	0.006	0.064	Below LOD	0.020	Below LOD	0.009	Below LOD	0.004	Below LOD	0.033	Below LOD	0.121	3.650	Below LOD		0.248	0.137	0.320	0.460
17NP436a_Bg69	436a_B	0.002	0.402	531.900	0.383	0.040	0.003	0.001	0.000	0.001	Below LOD	0.000	0.053	0.000	0.003	0.001	0.002	0.000	0.002	0.000	0.042	Below LOD	0.171	4.090	Below LOD	10.133	0.290	0.006	0.100	0.110
17NP436a_Bg72	436a_B	0.005	0.680	440.900	0.417	0.484	0.054	0.002	0.008	0.038	0.007	0.004	0.085	0.002	0.015	0.005	0.018	0.003	0.025	0.005	0.039	Below LOD	0.128	3.310	1.445	2.561	0.026	0.109	0.640	0.750
17NP436a_Bg75	436a_B	0.004	0.459	522.100	0.342	0.051	0.006	0.001	0.001	0.005	0.001	0.001	0.057	Below LOD	0.002	0.000	0.002	0.000	0.002	0.000	0.035	Below LOD	0.138	3.950	Below LOD		0.130	0.015	0.120	0.140
17NP436a_Bg76	436a_B	0.006	1.174	476.000	0.518	0.095	0.013	0.003	0.002	0.008	Below LOD	0.002	0.132	0.000	0.004	0.001	0.004	0.001	0.003	0.001	0.047	Below LOD	0.158	3.400	Below LOD	9.725	0.164	0.025	0.240	0.270
17NP436a_Bg77	436a_B	0.001	0.596	527.800	0.425	0.473	0.026		0.002	0.008	Below LOD	0.001	0.063	Below LOD	0.007	0.003	0.015	0.003	0.022	0.005	0.043	Below LOD	0.152	3.580	Below LOD			0.035	0.590	0.630
17NP436a_Bg78	436a_B	0.014	1.068	466.200	0.452	1.195	0.120	0.005	0.013	0.062	0.011	0.005	0.156	0.003	0.029	0.009	0.041	0.008	0.066	0.013	0.053	Below LOD	0.123	2.310	1.007	2.893	0.031	0.212	1.530	1.740
17NP436a_Bg80	436a_B	0.011	1.045	483.200	0.523	0.641	0.059	0.006	0.006	0.030	0.006	0.003	0.129	0.002	0.017	0.005	0.021	0.004	0.029	0.007	0.046	Below LOD	0.141	3.060	1.204	4.308	0.085	0.107	0.860	0.970
17NP436a_Bg81	436a_B	0.007	0.913	504.500	0.474	1.388	0.143	0.003	0.017	0.073	0.014	0.006	0.128	0.003	0.032	0.012	0.050	0.009	0.078	0.016	0.047	Below LOD	0.139	2.970	1.080	2.241	0.017	0.251	1.720	1.970
17NP436a_Bg82	436a_B	0.005	0.982	456.700	0.434	11.390	1.902	0.026	0.243	1.143	0.215	0.062	0.479	0.058	0.536	0.163	0.594	0.092	0.623	0.113	0.038	0.000	0.123	3.230	0.729	0.574	0.009	3.529	14.110	17.640
17NP436a_Cg01	436a_C	0.006	0.676	453.100	0.355	8.681	1.240	0.406	0.111	0.529	0.081	0.027	0.265	0.030	0.312	0.112	0.434	0.068	0.495	0.091	0.037	Below LOD	0.120	3.230	0.712	0.675	0.004	1.967	10.510	12.480
17NP436a_Cg02	436a_C	0.004	0.727	499.600	0.467	1.429	0.143	0.004	0.010	0.057	0.010	0.003	0.096	0.004	0.038	0.013	0.060	0.011	0.076	0.017	0.042	Below LOD	0.135	3.200	0.706	1.955	0.024	0.224	1.750	1.970
17NP436a_Cg03	436a_C	0.004	1.094	471.800	0.527	1.039	0.108	0.004	0.012	0.059	0.011	0.005	0.137	0.004	0.032	0.010	0.044	0.007	0.058	0.011	0.042	Below LOD	0.120	3.230	0.712	0.675	0.004	0.194	1.350	1.540
17NP436a_Cg04	436a_C	0.014	0.992	376.300	0.383	51.650	17.190	0.152	3.086	14.410	2.999	0.805	4.171	0.617	4.799	1.172	3.605	0.497	3.085	0.476	0.040	0.000	0.103	2.500	0.774	0.427	0.005	37.837	70.880	108.720

sample number	group	MnO (wt%)	Ba (ppm)	Sr (ppm)	Zr (ppm)	Y (ppm)	La (ppm)	Ce (ppm)	Pr (ppm)	Nd (ppm)	Sm (ppm)	Eu (ppm)	Gd (ppm)	Tb (ppm)	Dy (ppm)	Ho (ppm)	Er (ppm)	Tm (ppm)	Yb (ppm)	Lu (ppm)	Pb (ppm)	Th (ppm)	U (ppm)	U/Pb	Eu/Eu*	Gd/Gd*	Ce/Ce*	LREE(La to Sm)	HREE(Eu to Lu+Y)	ALL REE
17NP436a_Cg05	436a_C	0.009	0.973	494.700	0.437	20.770	3.840	0.015	0.460	2.170	0.397	0.112	0.809	0.111	1.040	0.310	1.107	0.169	1.182	0.197	0.047 Below LOD	0.133	2.820	0.698	0.523	0.003	6.882	25.810	32.690
17NP436a_Cg06	436a_C	0.011	1.107	359.900	0.379	1.104	0.121	0.005	0.012	0.054	0.010	0.004	0.151 Below LOD	0.035	0.012	0.043	0.007	0.054	0.010	0.040 Below LOD	0.112	2.800 Below LOD				0.034	0.203	1.420	1.620
17NP436a_Cg07	436a_C	0.001	1.027	525.100	0.500	0.609	0.049	0.003	0.004	0.017	0.002	0.002	0.114	0.001	0.016	0.005	0.023	0.004	0.032	0.007	0.037 Below LOD	0.146	3.910	1.563	4.960	0.052	0.076	0.810	0.890
17NP436a_Cg08	436a_C	0.005	1.513	503.500	0.552	0.238	0.027	0.003	0.003	0.018	0.003	0.003	0.193	0.001	0.009	0.003	0.011	0.001	0.015	0.003	0.046 Below LOD	0.140	3.060	1.989	9.199	0.081	0.055	0.480	0.540
17NP436a_Cg09	436a_C	0.006	0.999	428.200	0.489	6.447	0.828	0.006	0.078	0.375	0.067	0.020	0.254	0.020	0.227	0.076	0.300	0.049	0.349	0.064	0.041 Below LOD	0.129	3.180	0.716	0.929	0.005	1.353	7.810	9.160
17NP436a_Cg10	436a_C	0.017	0.601	333.200	0.290	0.998	0.199	0.005	0.022	0.103	0.017	0.006	0.108	0.005	0.042	0.013	0.045	0.007	0.047	0.009	0.025 Below LOD	0.072	2.850	0.802	1.480	0.018	0.345	1.280	1.630
17NP436a_Cg12	436a_C	0.012	0.776	344.700	0.293	0.382	0.086	0.007	0.011	0.048	0.011	0.005	0.116	0.003	0.023	0.006	0.019	0.002	0.016 Below LOD	0.029 Below LOD	0.088	3.060	1.121	2.433	0.059	0.163	0.570	0.730
17NP436a_Cg13	436a_C	0.010	0.665	357.200	0.260	0.343	0.076	0.007	0.009	0.041	0.007	0.004	0.107	0.003	0.020	0.006	0.019	0.002	0.012	0.003	0.029 Below LOD	0.099	3.390	1.185	2.452	0.061	0.139	0.520	0.660
17NP436a_Cg14	436a_C	0.005	0.937	368.900	0.396	0.142	0.022	0.007	0.003	0.019	0.002	0.002	0.109	0.001	0.009	0.002	0.009	0.002	0.008	0.002	0.038 Below LOD	0.140	3.660	1.947	5.434	0.195	0.053	0.290	0.340
17NP436a_Cg15	436a_C	0.012	1.833	434.600	0.457	0.980	0.100	0.005	0.009	0.045	0.009	0.004	0.234	0.003	0.029	0.009	0.033	0.007	0.049	0.010	0.048 Below LOD	0.110	2.300	0.994	5.229	0.041	0.168	1.360	1.530
17NP436a_Cg16	436a_C	0.006	1.129	426.900	0.471	0.212	0.037	0.003	0.004	0.018	0.004	0.003	0.139	0.001	0.010	0.003	0.010	0.002	0.011	0.002	0.034 Below LOD	0.125	3.670	1.901	6.300	0.054	0.065	0.390	0.460
17NP436a_Cg17	436a_C	0.016	1.817	376.500	0.374	0.179	0.034	0.007	0.006	0.026	0.005	0.005	0.234 Below LOD	0.014	0.004	0.011 Below LOD		0.002	0.010	0.002	0.040 Below LOD	0.101	2.510 Below LOD			0.128	0.078	0.460	0.540
17NP436a_Cg18	436a_C	0.011	1.190	419.900	0.334	0.224	0.036	0.014	0.006	0.028	0.006	0.004	0.151	0.002	0.016	0.004	0.013	0.002	0.010	0.002	0.035 Below LOD	0.124	3.540	1.545	3.875	0.231	0.090	0.430	0.520
17NP436a_Cg19	436a_C	0.008	0.937	410.100	0.288	0.188	0.039	0.007	0.005	0.023	0.006	0.003	0.124	0.002	0.012	0.003	0.009	0.001	0.009	0.001	0.027 Below LOD	0.100	3.680	1.001	3.949	0.130	0.079	0.350	0.430
17NP436a_Cg20	436a_C	0.011	0.723	372.100	0.296	0.153	0.035	0.010	0.005	0.021	0.005	0.003	0.096	0.001	0.010	0.003	0.007	0.001	0.008	0.001	0.025 Below LOD	0.097	3.440	1.652	3.910	0.183	0.075	0.280	0.360
17NP436a_Cg23	436a_C	0.008	2.299	449.100	0.345	0.146	0.028	0.008	0.003	0.021	0.004	Below LOD	0.251 Below LOD	0.010	0.010 Below LOD		0.007 Below LOD		0.007	0.001	0.041 Below LOD	0.119	2.320 Below LOD			0.191	0.064	0.420	0.480
17NP436a_Cg24	436a_C	0.014	1.470	444.000	0.247	0.210	0.050	0.013	0.008	0.033	0.007	0.006	0.204	0.002	0.015	0.003	0.007	0.001	0.006	0.001	0.036 Below LOD	0.119	3.360	1.987	3.992	0.159	0.110	0.460	0.570
17NP436a_Cg25	436a_C	0.020	2.170	313.200	0.341	0.338	0.084	0.037	0.014	0.061	0.013	0.008	0.287	0.005	0.023	0.005	0.018	0.003	0.014	0.003	0.042 Below LOD	0.098	2.300	1.276	3.498	0.258	0.210	0.700	0.910
17NP436a_Cg26	436a_C	0.008	1.310	481.600	0.388	0.170	0.032	0.015	0.006	0.027	0.004	0.004	0.175	0.002	0.013	0.003	0.010	0.001	0.013	0.001	0.033 Below LOD	0.146	4.450	1.636	4.648	0.265	0.084	0.390	0.470
17NP436a_Cg27	436a_C	0.012	1.351	333.800	0.413	0.179	0.030	0.006	0.004	0.022	0.006	0.002	0.174	0.001	0.011	0.003	0.011	0.001	0.009	0.001	0.029 Below LOD	0.105	3.690	1.002	7.104	0.131	0.069	0.390	0.460
17NP436a_Cg29	436a_C	0.018	1.063	283.800	0.383	0.397	0.077	0.024	0.016	0.079	0.022	0.007	0.167	0.004	0.038	0.008	0.022	0.003	0.039 Below LOD	0.028 Below LOD	0.107	3.800	0.963	2.212	0.164	0.218	0.660	0.880
17NP436a_Cg30	436a_C	0.025	1.684	341.300	0.308	0.580	0.153	0.092	0.033	0.156	0.045	0.015	0.272	0.009	0.063	0.013	0.041	0.007	0.041	0.006	0.024 Below LOD	0.077	3.240	0.980	1.681	0.311	0.480	1.050	1.530
17NP436a_Cg38	436a_C	0.002	0.811	508.400	0.356	43.510	12.900	0.052	1.892	8.610	1.671	0.466	2.610	0.402	3.300	0.863	2.779	0.401	2.596	0.398	0.041 Below LOD	0.136	3.350	0.744	0.435	0.003	25.125	57.290	82.420
17NP436a_Cg39	436a_C	0.005	0.963	441.600	0.379	43.290	14.590	0.119	2.328	10.400	2.078	0.559	3.056	0.459	3.640	0.922	2.871	0.415	2.573	0.410	0.048 0.000	0.124	2.600	0.749	0.435	0.005	29.515	58.190	87.710
17NP436a_Cg44	436a_C	0.012	1.230	392.500	0.310	0.338	0.060	0.007	0.010	0.046	0.010	0.004	0.163	0.003	0.022	0.007	0.017	0.003	0.021	0.003	0.031 Below LOD	0.119	3.860	1.038	3.425	0.068	0.133	0.580	0.710
17NP436a_Cg45	436a_C	0.011	1.222	381.000	0.542	0.286	0.051		0.007	0.029	0.006	Below LOD	0.157 Below LOD		0.025	0.004	0.014 Below LOD		0.015	0.002	0.029 Below LOD	0.128	4.430 Below LOD				0.092	0.490	0.580
17NP436a_Cg47	436a_C	0.008	1.450	539.700	0.358	1.044	0.077	0.006	0.006	0.028	0.005	0.003	0.181	0.002	0.008	0.002	0.008	0.037	0.006	0.050	0.047 Below LOD	0.146	3.080	1.536	5.231	0.062	0.122	1.370	1.490
17NP436a_Cg48	436a_C	0.003	0.713	468.200	0.479	0.911	0.066	0.003	0.006	0.029	0.004	0.002	0.088	0.002	0.018	0.002	0.007	0.034	0.006	0.046	0.009	0.031 Below LOD	0.128	4.180	0.970	3.362	0.033	0.108	1.120	1.230
17NP436a_Cg49	436a_C	0.009	1.034	429.600	0.382	0.122	0.015	0.006	0.003	0.014	0.004	0.002	0.140	0.001	0.008	0.002	0.009	0.001	0.009	0.001	0.034 Below LOD	0.129	3.760	1.447	6.741	0.228	0.042	0.300	0.340
17NP436a_Cg50	436a_C	0.017	2.489	335.000	0.402	0.347	0.075	0.011	0.009	0.044	0.009	0.005	0.344	0.003	0.025	0.006	0.017	0.003	0.016	0.003	0.032 Below LOD	0.095	2.950	1.400	6.698	0.106	0.147	0.770	0.920
17NP436a_Cg52	436a_C	0.015	1.157	522.000	0.465	0.176	0.042	0.009	0.005	0.026	0.007	0.003	0.151 Below LOD	0.012	0.004	0.004	0.009 Below LOD		0.010 Below LOD	0.049 Below LOD	0.131	2.660 Below LOD				0.144	0.090	0.360	0.450
17NP436a_Cg53	436a_C	0.010	0.687	549.400	0.352	0.218	0.050	0.012	0.007	0.034	0.009	0.003	0.084	0.002	0.017	0.004	0.011	0.002	0.011	0.001	0.039 Below LOD	0.134	3.440	0.980	2.186	0.147	0.112	0.350	0.460
17NP436a_Cg54	436a_C	0.003	0.597	466.400	0.413	0.097	0.010	0.005	0.002	0.008	0.002	0.001	0.084	0.001	0.007	0.002	0.008	0.001	0.008	0.001	0.031 Below LOD	0.136	4.420	1.455	5.945	0.273	0.028	0.210	0.240
17NP436a_Cg55	436a_C	0.008	1.489	414.200	0.475	0.158	0.025	0.006	0.004	0.019	0.004	0.003	0.186	0.001	0.013	0.003	0.008	0.001	0.008	0.001	0.034 Below LOD	0.125	3.700	1.661	7.201	0.154	0.058	0.380	0.440
17NP436a_Cg57	436a_C	0.010	1.292	430.500	0.522	0.151	0.039	0.014	0.005	0.024	0.004	0.004	0.167	0.002	0.013	0.003	0.008	0.001	0.007	0.001	0.036 Below LOD	0.135	3.800	1.912	4.664	0.226	0.086	0.360	0.450
17NP436a_Cg58	436a_C	0.006	2.000	549.700	0.380	0.137	0.037	0.016	0.006	0.025	0.006	0.004	0.254	0.001	0.010 Below LOD		0.008 Below LOD		0.008	0.001	0.038 Below LOD	0.136	3.530	1.744	8.175	0.268	0.089	0.420	0.510
17NP436a_Cg59	436a_C	0.004	0.705	518.400	0.442	0.063	0.010	0.005	0.002	0.009	0.001	0.001	0.085	0.000	0.004	0.001	0.003	0.001	0.004	0.001	0.037 Below LOD	0.153	4.170	2.947	7.953	0.310	0.027	0.160	0.190
17NP436a_Cg60	436a_C	0.010	1.258	433.400	0.511	0.228	0.053	0.028	0.011	0.047	0.014	0.006	0.175	0.003	0.026	0.005	0.013	0.002	0.014	0.003	0.034 Below LOD	0.133	3.860	1.229	3.244	0.282	0.153	0.470	0.620
17NP436a_Dg02	436a_D	0.003	0.653	554.500	0.275	13.810	2.674	0.016	0.332	1.561	0.299	0.091	0.570	0.081	0.717	0.208	0.738	0.108	0.727	0.126	0.043 Below LOD	0.192	4.500	0.764	0.480	0.004	4.882	17.180	22.060
17NP436a_Dg03	436a_D	0.007	0.700	529.300	0.261	8.487	0.935	0.008	0.081	0.383	0.059	0.020	0.231	0.025	0.272	0.093	0.377	0.064	0.450	0.085	0.042 Below LOD	0.186	4.400	0.689	0.752	0.007	1.466	10.100	11.570
17NP436a_Dg04	436a_D	0.011	0.939	456.000	0.283	1.268	0.069	0.014	0.006	0.026	Below LOD	Below LOD	0.115	0.002	0.021	0.008	0.039	0.008	0.062	0.013	0.048 Below LOD	0.151	3.160 Below LOD			0.174	0.114	1.540	1.650
17NP436a_Dg05	436a_D	0.020	0.708	392.400	0.269	0.771	0.054	0.020	0.006	0.032	0.007	0.003	0.098	0.002	0.019	0.006	0.025	0.005	0.037	0.008	0.037 Below LOD	0.130	3.530	1.081	2.748	0.263	0.117	0.970	1.090
17NP436a_Dg09	436a_D	0.012	0.688	455.300	0.229	10.180	1.889	0.017	0.237	1.163	0.219	0.068	0.438	0.060	0.513	0.150	0.521	0.082	0.522	0.093	0.041 Below LOD	0.146	3.580	0.771	0.495	0.006	3.525	12.630	16.160
17NP436a_Dg10	436a_D	0.010	1.460	438.100	0.259	2.460	0.173	0.004	0.010	0.053	0.007	0.004	0.201	0.004	0.047	0.020	0.090	0.016	0.125	0.027	0.038 Below LOD	0.177	4.630	1.026	3.396	0.023	0.247	2.990	3.240
17NP436a_Dg11	436a_D	0.007	0.880	493.100	0.287	6.140	0.535	0.009	0.040	0.192	0.026	0.011	0.182	0.012	0.153	0.054	0.247	0.041	0.313	0.060	0.049 Below LOD	0.183	3.710	1.108	0.014	0.802	3.480	7.210	8.010
17NP436a_Dg13	436a_D	0.001	0.515	624.800	0.222	2.940	0.251	0.005	0.021	0.090	0.014	0.005	0.108 Below LOD		0.070	0.028	0.124	0.021	0.153	0.031	0.041 Below LOD	0.197	4.450 Below LOD		0.015	0.380	0.702	0.005	2.784
17NP436a_Dg14	436a_D	0.005	0.757	527.000	0.205	10.543	1.613	0.011	0.159	0.787	0.132	0.046	0.360	0.046	0.441	0.136	0.494	0.079	0.532	0.099	0.041 Below LOD	0.161	3.950	0.765	0.568	0.005	2.702	12.780	15.480
17NP436a_Dg15	436a_D	0.010	1.100	468.600	0.240	9.680	1.598	0.011	0.150	0.929	0.163	0.056	0.431	0.048	0.445	0.136	0.470	0.073	0.488	0.066	0.047 Below LOD	0.159	3.410	0.826	0.601	0.005	2.691	11.910	14.800
17NP436a_Dg16	436a_D	0.009	0.760	469.900	0.244	21.450	4.640	0.028	0.623	2.900	0.563	0.162	1.034	0.139	1.263	0.351	1.190	0.177	1.134	0.187	0.045 Below LOD	0.173	3.860	0.757	0.497	0.004	8.754	27.090	35.840
17NP436a_Dg21	436a_D	0.006	0.710	507.800	0.237	16.980	3.276	0.021	0.370	1.749	0.313	0.096	0.638	0.091	0.830	0.248	0.872	0.133	0.889	0.145	0.051 Below LOD	0.158	3.070	0.745	0.493	0.005	5.729	20.920	26.650
17NP436a_Dg22	436a_D	0.009	0.697	404.100	0.201	14.090	2.870	0.018	0.352	1.640	0.329	0.095	0.611	0.087	0.775	0.219	0.742	0.112	0.723	0.124	0.043 Below LOD	0.127	2.980	0.734	0.484	0.004	5.209	17.580	22.790
17NP436a_Dg23	436a_D	0.005	0.910	464.600	0.250	13.530	2.644	0.016	0.337	1.605	0.315	0.092	0.615	0.082	0.716	0.211	0.710	0.109	0.695	0.121	0.044 Below LOD	0.159	3.600	0.746	0.511	0.004	4.917	16.880	21.800
17NP436a_Dg30	436a_D	0.001	0.604	517.500	0.257	14.030	2.658	0.014	0.348	1.689	0.337	0.095	0.620	0.085	0.724	0.215	0.717	0.111	0.731	0.126	0.039 Below LOD	0.183	4.750	0.738	0.498	0.004	5.046	17.450	22.500
17NP436a_Dg31	436a_D	0.005	1.500	473.300	0.250	6.880	0.768	0.013	0.068	0.322	0.056	0.020	0.292	0.021	0.224	0.076	0.298	0.052	0.365	0.066	0.052 Below LOD	0.159	3.080	0.781	1.029	0.013	1.227	8.290	9.520
17NP436a_Dg35	436a_D	0.000	0.480	542.500	0.216	29.140	7.200	0.047	0.998	4.640	0.904	0.264	1.496	0.228	1.902	0.523	1.687	0.243	1.524	0.248	0.040 Below LOD	0.160	4.050	0.762	0.440	0.004	13.789	37.250	51.040
17NP436a_Dg36	436a_D	0.002	1.680	510.600	0.270	8.546	1.543	0.008	0.189	0.875	0.169	0.051	0.509	0.044	0.410	0.123	0.440	0.065	0.458	0.079	0.036 Below LOD	0.182	5.130	0.777	0.771	0.004	2.784	10.720	13.500
17NP436a_Eg09	436a_E	0.018	1.087	389.500	0.220	1.585	0.118	0.024	0.013	0.060	0.014	0.008	0.152	0.005	0.039	0.014	0.056	0.010	0.090	0.017	0.038 Below LOD	0.122	3.200	1.239	1.798	0.143	0.228	1.980	2.210
17NP436a_Eg10	436a_E	0.005	0.666	464.100	0.288	2.710	0.161	0.007	0.010	0.053	0.007	0.004	0.099	0.005	0.045	0.021	0.095	0.015	0.138	0.029	0.040 Below LOD	0.164	4.060	0.962	1.618	0.041	0.237	3.160	3.400
17NP436a_Eg11	436a_E	0.015	0.727	344.700	0.259	1.299	0.062	0.007	0.003	0.017	0.003	0.002	0.093	0.001	0.016	0.007	0.034	0.007	0.061	0.014	0.032 Below LOD	0.118	3.670	1.284	4.858	0.129	0.092	1.530	1.620
17NP436a_Eg12	436a_E	0.023	0.854	318.200	0.205	1.354	0.092	0.014	0.009	0.036	0.008	0.005	0.123	0.003	0.030	0.010	0.047	0.008	0.069	0.016	0.031 Below LOD	0.099	3.220	1.291	2.389	0.117	0.158	1.660	1.820
17NP436a_Eg13	436a_E	0.023	0.889	330.300	0.203	1.784	0.136	0.016	0.012	0.062	0.014	0.006	0.140	0.004	0.041	0.014	0.062	0.011	0.094	0.020	0.034 Below LOD	0.102	3.010	1.026	2.015	0.093	0.240	2.180	2.420
17NP436a_Eg15	436a_E	0.021	0.820	333.100	0.194	0.901	0.086	0.013	0.009	0.046	0.010	0.005	0.114	0.003	0.027	0.008	0.036	0.005	0.044	0.008	0.030 0.000	0.102	3.380	1.126	2.083	0.106	0.164	1.150	1.310
17NP436a_Eg16	436a_E	0.012	0.708	440.300	0.215	0.271	0.019	0.004	0.002	0.014	0.005	0.002	0.093	0.001	0.008	0.003	0.011	0.001	0.010	0.003	0.038 Below LOD	0.133	3.510	1.174	4.635	0.144	0.043	0.400	0.440
17NP436a_Eg17	436a_E	0.003	0.782	474.700	0.368	3.334	0.116	0.002	0.004	0.020	0.003	0.002	0.111	0.001	0.030	0.017	0.087	0.018	0.160	0.036	0.046 Below LOD	0.171	3.750	1.062	5.006	0.022	0.144	3.800	3.940
17NP436a_Eg18	436a_E	0.004	0.746	487.800	0.284	1.537	0.057	0.002	0.002	0.011	0.001	0.001	0.084	0.001	0.016	0.008	0.040	0.008	0.071	0.017	0.040 Below LOD	0.150	3.760	1.665	5.143	0.049	0.073	1.780	1.850
17NP436a_Eg19	436a_E	0.004	0.673	482.200	0.272	1.092	0.044	Below LOD	0.012	0.002	Below LOD	0.002	0.080	Below LOD	0.015	0.006	0.035	0.006	0.060	0.013	0.046 Below LOD	0.164	3.600	Below LOD			0.059	1.310	1.370
17NP436a_Eg24	436a_E	0.010	0.634	263.700	0.266	1.248	0.077	0.011	0.006	0.028	0.004	0.002	0.094	0.002	0.016	0.007	0.038	0.007	0.055	0.015	0.027 Below LOD	0.091	3.370	1.300	3.475	0.127	0.126	1.480	1.610
17NP436a_Eg25	436a_E	0.003	0.647	479.100	0.322	1.131	0.041	0.003	0.002	0.010	0.002	0.001	0.075	0.001	0.012	0.006	0.032	0.006	0.054	0.011	0.047 Below LOD	0.175	3.700	1.327	4.728	0.083	0.059	1.330	1.390

sample number	group	MnO (wt%)	Ba (ppm)	Sr (ppm)	Zr (ppm)	Y (ppm)	La (ppm)	Ce (ppm)	Pr (ppm)	Nd (ppm)	Sm (ppm)	Eu (ppm)	Gd (ppm)	Tb (ppm)	Dy (ppm)	Ho (ppm)	Er (ppm)	Tm (ppm)	Yb (ppm)	Lu (ppm)	Pb (ppm)	Th (ppm)	U (ppm)	U/Pb	Eu/Eu*	Gd/Gd*	Ce/Ce*	LREE(La to Sm)	HREE(Eu to Lu+Y)	ALL REE
17NP436a_Eg26	436a_E	0.002	0.564	527.400	0.267	7.030	0.577	0.002	0.035	0.184	0.026	0.010	0.137	0.014	0.166	0.066	0.273	0.047	0.359	0.069	0.040	Below LOD	0.174	4.360	0.660	0.844	0.003		0.824	8.170	8.990
17NP436a_Eg27	436a_E	0.015	1.111	385.800	0.220	3.473	0.352	0.017	0.030	0.150	0.029	0.010	0.199	0.009	0.097	0.036	0.138	0.023	0.180	0.037	0.037	Below LOD	0.115	3.100	0.790	1.479	0.040		0.578	4.200	4.780
17NP436a_Eg28	436a_E	0.023	1.480	270.800	0.161	8.720	1.507	0.024	0.186	0.925	0.171	0.053	0.493	0.047	0.432	0.125	0.461	0.072	0.495	0.087	0.036	Below LOD	0.088	2.460	0.772	0.718	0.011		2.813	10.980	13.790
17NP436a_Eg31	436a_E	0.018	0.938	250.500	0.254	1.401	0.083	0.018	0.008	0.037	0.008	0.004	0.141	0.002	0.023	0.009	0.045	0.008	0.069	0.016	0.027	Below LOD	0.092	3.460	1.238	3.152	0.168		0.153	1.720	1.870
17NP436a_Eg32	436a_E	0.011	0.940	427.800	0.224	0.873	0.037	0.011	0.003	0.015	0.002	0.002	0.124	0.001	0.010	0.004	0.024	0.005	0.046	0.009	0.037	Below LOD	0.143	3.890	1.978	5.366	0.270		0.068	1.100	1.170
17NP436a_Eg33	436a_E	0.028	0.707	267.400	0.234	4.139	0.327	0.007	0.024	0.114	0.016	0.007	0.142	0.008	0.081	0.034	0.154	0.027	0.218	0.045	0.028	Below LOD	0.091	3.220	0.810	1.381	0.019		0.488	4.850	5.340
17NP436a_Eg34	436a_E	0.025	0.868	296.700	0.179	1.475	0.080	0.005	0.005	0.025	0.005	0.003	0.113	0.002	0.021	0.009	0.045	0.008	0.071	0.015	0.024	Below LOD	0.091	3.740	1.075	3.353	0.057		0.119	1.760	1.880
17NP436a_Eg37	436a_E	0.020	0.449	125.800	0.095	0.627	0.127	0.028	0.020	0.088	0.014	0.006	0.084	Below LOD	0.028	0.008	0.026	0.004	0.036	0.007	0.014	Below LOD	0.049	3.460	Below LOD		0.133		0.277	0.820	1.100
17NP436a_Eg38	436a_E	0.013	0.342	247.300	0.156	0.701	0.054	0.012	0.005	0.024	0.006	0.002	0.055	0.001	0.014	0.005	0.023	0.004	0.036	0.009	0.018	Below LOD	0.070	3.850	0.942	2.653	0.172		0.102	0.850	0.950
17NP436a_Fg01	436a_F	0.013	0.599	180.500	0.226	0.362	0.091	0.015	0.013	0.057	0.012	0.005	0.086	0.003	0.025	0.006	0.024	0.003	0.025	0.004	0.016	0.001	0.032	1.990	1.111	1.494	0.108		0.188	0.540	0.730
17NP436a_Fg05	436a_F	0.032	0.404	113.000	0.112	0.598	0.123	0.009	0.017	0.076	0.016	0.007	0.069	0.004	0.034	0.009	0.031	0.004	0.033	0.006	0.010	Below LOD	0.017	1.710	1.016	0.933	0.048		0.242	0.790	1.030
17NP436a_Fg12	436a_F	0.010	0.345	179.300	0.210	0.421	0.080	0.018	0.015	0.071	0.017	0.006	0.073	0.004	0.031	0.008	0.027	0.004	0.027	0.005	0.016	Below LOD	0.037	2.360	0.979	1.057	0.125		0.201	0.610	0.810
17NP436a_Fg13	436a_F	0.087	0.443	44.160	0.055	0.483	0.121	0.014	0.018	0.083	0.014	0.005	0.082	Below LOD	0.030	0.008	0.026	Below LOD	0.021	Below LOD	0.006	Below LOD		Below LOD			0.075		0.249	0.660	0.910
17NP436a_Fg14	436a_F	0.027	0.328	143.300	0.178	0.406	0.098	0.012	0.015	0.072	0.017	0.006	0.073	0.004	0.031	0.007	0.026	0.004	0.029	0.005	0.010	Below LOD	0.020	2.060	0.993	1.056	0.079		0.214	0.590	0.800
17NP436a_Fg15	436a_F	0.020	0.372	177.100	0.293	1.968	0.640	0.178	0.134	0.585	0.140	0.044	0.234	0.029	0.225	0.055	0.177	0.024	0.161	0.031	0.014	0.002	0.032	2.220	0.901	0.473	0.146		1.677	2.950	4.630
17NP436a_Fg21	436a_F	0.019	0.447	185.800	0.460	2.545	0.896	0.195	0.198	0.858	0.222	0.052	0.317	0.043	0.301	0.068	0.259	0.030	0.187	0.031	0.022	0.003	0.041	1.880	0.839	0.438	0.111		2.370	3.790	6.160
17NP436a_Fg23	436a_F	0.010	0.586	160.900	0.203	0.279	0.059	0.006	0.009	0.047	0.010	0.005	0.093	0.003	0.022	0.005	0.015	0.002	0.016	0.003	0.014	Below LOD	0.034	2.420	1.322	1.789	0.061		0.131	0.440	0.570
17NP436a_Fg24	436a_F	0.030	9.900	226.000	0.740	4.580	2.034	0.271	0.448	1.902	0.458	0.127	1.460	0.079	0.561	0.129	0.386	0.054	0.344	0.054	0.044	0.005	0.058	1.330	0.873	1.050	0.068		5.113	7.770	12.880
17NP436a_Fg25	436a_F	0.006	0.740	482.000	0.190	0.637	0.106	0.011	0.015	0.068	0.017	0.005	0.100	0.005	0.035	0.010	0.035	0.005	0.039	0.006	0.047	Below LOD	0.124	2.620	0.774	1.487	0.063		0.217	0.880	1.100
17NP436a_Fg32	436a_F	0.008	0.372	168.100	0.288	0.713	0.173	0.029	0.029	0.128	0.031	0.011	0.101	0.008	0.061	0.014	0.047	0.007	0.057	0.009	0.017	Below LOD	0.042	2.470	0.983	0.783	0.098		0.390	1.030	1.420
17NP436a_Fg34	436a_F	0.004	1.240	472.900	0.233	3.253	0.600	0.040	0.082	0.389	0.079	0.026	0.263	0.019	0.178	0.047	0.165	0.025	0.180	0.032	0.060	Below LOD	0.130	2.180	0.878	0.847	0.043		1.190	4.190	5.380
17NP436a_Fg47	436a_F	0.009	0.531	207.100	0.422	2.534	0.923	0.176	0.196	0.865	0.209	0.063	0.311	0.040	0.298	0.070	0.207	0.032	0.201	0.033	0.026	0.002	0.036	1.370	0.893	0.445	0.099		2.369	3.790	6.160
17NP436a_Fg48	436a_F	0.021	0.824	259.800	0.181	0.840	0.144	0.016	0.021	0.087	0.019	0.007	0.140	0.005	0.036	0.010	0.033	0.006	0.043	0.010	0.043	Below LOD	0.065	1.530	0.953	1.726	0.072		0.287	1.130	1.420
17NP436a_Fg49	436a_F	0.007	0.291	181.600	0.242	0.791	0.170	0.029	0.031	0.143	0.041	0.012	0.084	0.008	0.066	0.018	0.057	0.009	0.063	0.010	0.016	Below LOD	0.040	2.530	0.864	0.594	0.096		0.414	1.120	1.530
17NP436a_Fg54	436a_F	0.023	0.752	134.400	0.120	1.024	0.231	0.034	0.038	0.179	0.029	0.010	0.147	0.006	0.051	0.015	0.047	0.009	0.055	0.010	0.015	0.001	0.032	2.130	1.012	1.393	0.086		0.511	1.370	1.880
17NP436a_Fg55	436a_F	0.012	0.511	236.900	0.188	1.415	0.285	0.027	0.045	0.192	0.040	0.012	0.124	0.010	0.080	0.022	0.079	0.012	0.093	0.016	0.028	Below LOD	0.061	2.150	0.828	0.827	0.057		0.589	1.860	2.450
17NP436a_Fg56	436a_F	0.021	0.948	335.200	0.343	0.666	0.125	0.018	0.020	0.091	0.021	0.007	0.134	0.005	0.040	0.011	0.040	0.006	0.048	0.010	0.039	0.000	0.079	2.010	0.845	1.613	0.086		0.274	0.970	1.240
17NP436a_Fg60	436a_F	0.014	0.962	247.000	0.203	0.942	0.179	0.009	0.026	0.116	0.025	0.008	0.144	0.005	0.045	0.012	0.042	0.007	0.049	0.009	0.027	Below LOD	0.062	2.260	0.962	1.752	0.030		0.355	1.260	1.620
17NP436a_Fg61	436a_F	0.036	0.540	54.400	0.048	0.311	0.144	0.044	0.029	0.125	0.023	0.006	0.098	0.004	0.027	0.006	0.018	0.003	0.018	0.003	0.010	0.001	0.008	0.830	0.777	1.523	0.163		0.365	0.490	0.860
17NP436a_Fg62	436a_F	0.023	0.595	225.700	0.188	0.820	0.195	0.019	0.033	0.141	0.033	0.010	0.115	0.007	0.053	0.015	0.051	0.007	0.053	0.010	0.025	Below LOD	0.053	2.120	0.845	0.968	0.056		0.420	1.140	1.560
17NP436a_Fg63	436a_F	0.002	0.665	575.300	0.164	0.511	0.059	0.004	0.007	0.036	0.010	0.003	0.081	0.002	0.019	0.006	0.026	0.004	0.030	0.006	0.049	Below LOD	0.128	2.630	0.894	2.264	0.048		0.117	0.690	0.810
17NP436a_Fg64	436a_F	0.005	0.847	531.600	0.167	0.908	0.157	0.022	0.025	0.100	0.025	0.008	0.132	0.007	0.054	0.014	0.050	0.008	0.058	0.010	0.051	Below LOD	0.117	2.290	0.865	1.284	0.083		0.328	1.250	1.580
17NP436a_Fg65	436a_F	0.015	0.731	298.200	0.193	0.923	0.212	0.026	0.039	0.171	0.041	0.012	0.166	0.011	0.079	0.022	0.068	0.011	0.075	0.012	0.034	Below LOD	0.073	2.140	0.754	1.006	0.068		0.488	1.380	1.870
17NP436a_Fg70	436a_F	0.004	21.500	496.900	0.239	2.965	0.292	0.003	0.023	0.123	0.019	0.036	3.800	0.006	0.072	0.025	0.110	0.017	0.142	0.028	0.049	Below LOD	0.131	2.690	4.331	18.345	0.009		0.460	7.200	7.660
17NP436a_Fg71	436a_F	0.001	0.569	601.400	0.160	2.576	0.428	0.015	0.044	0.209	0.038	0.013	0.162	0.011	0.107	0.036	0.118	0.020	0.134	0.025	0.060	Below LOD	0.140	2.340	0.800	0.991	0.026		0.733	3.200	3.930
17NP436a_Fg72	436a_F	0.007	1.170	609.900	0.254	0.590	0.103	0.018	0.018	0.081	0.019	0.007	0.213	0.005	0.046	0.012	0.037	0.007	0.046	0.008	0.068	Below LOD	0.142	2.070	0.971	2.597	0.101		0.239	0.970	1.210
17NP436a_Fg73	436a_F	0.010	0.775	378.300	0.141	0.437	0.060	0.005	0.007	0.035	0.007	0.004	0.134	0.003	0.024	0.006	0.024	0.004	0.028	0.004	0.043	Below LOD	0.099	2.320	1.098	3.185	0.063		0.114	0.670	0.780
17NP436a_Fg74	436a_F	0.007	0.663	485.500	0.185	0.685	0.061		Below LOD	0.027	0.004	Below LOD	0.111	Below LOD	0.013	0.005	0.023	Below LOD	0.029	0.006	0.041	Below LOD	0.122	3.010	Below LOD					0.092	0.870	0.960
17NP436a_Fg75	436a_F	0.010	0.708	463.600	0.205	0.450	0.044	0.004	0.005	0.023	0.005	0.002	0.123	0.002	0.015	0.005	0.015	0.003	0.026	0.006	0.047	Below LOD	0.130	2.780	1.125	4.488	0.068		0.080	0.650	0.730
17NP436a_Fg76	436a_F	0.006	0.567	420.600	0.231	0.768	0.135	0.009	0.020	0.086	0.022	0.007	0.127	0.006	0.053	0.014	0.047	0.008	0.063	0.010	0.053	Below LOD	0.135	2.570	0.736	1.443	0.042		0.272	1.100	1.370

Appendix B.15: LA-ICP-MS calcite U-Pb spot data.

Spot ID	238U/206Pb	2s	207Pb/206Pb	2s
17NP436a_Ag001	14.195	1.027	0.244	0.018
17NP436a_Ag002	12.673	0.953	0.318	0.022
17NP436a_Ag003	13.022	1.009	0.278	0.021
17NP436a_Ag004	11.579	0.929	0.372	0.027
17NP436a_Ag005	15.819	1.101	0.192	0.015
17NP436a_Ag006	14.778	1.053	0.253	0.018
17NP436a_Ag007	15.519	1.032	0.175	0.013
17NP436a_Ag008	10.998	0.791	0.375	0.026
17NP436a_Ag009	12.258	0.893	0.331	0.022
17NP436a_Ag010	9.539	0.713	0.443	0.027
17NP436a_Ag011	12.800	0.998	0.332	0.027
17NP436a_Ag012	14.376	1.161	0.212	0.017
17NP436a_Ag013	15.903	1.153	0.188	0.015
17NP436a_Ag014	14.951	1.072	0.239	0.018
17NP436a_Ag015	14.587	1.051	0.249	0.019
17NP436a_Ag016	12.928	0.895	0.267	0.019
17NP436a_Ag017	14.400	1.049	0.213	0.017
17NP436a_Ag018	12.763	1.009	0.329	0.027
17NP436a_Ag019	13.909	1.048	0.289	0.022
17NP436a_Ag020	13.351	0.953	0.314	0.021
17NP436a_Ag021	13.655	0.986	0.288	0.023
17NP436a_Ag022	14.951	1.072	0.234	0.019
17NP436a_Ag023	15.412	1.230	0.227	0.023
17NP436a_Ag024	13.411	0.944	0.291	0.021
17NP436a_Ag025	12.673	0.897	0.357	0.023
17NP436a_Ag026	13.824	0.971	0.307	0.024
17NP436a_Ag027	13.760	1.101	0.301	0.029
17NP436a_Ag028	13.136	0.976	0.270	0.018
17NP436a_Ag029	13.022	0.963	0.313	0.024
17NP436a_Ag030	15.178	1.076	0.206	0.017
17NP436a_Ag031	16.337	1.201	0.174	0.018
17NP436a_Ag032	14.876	1.064	0.234	0.016
17NP436a_Ag033	13.532	1.125	0.267	0.026
17NP436a_Ag034	13.253	0.913	0.299	0.020
17NP436a_Ag035	12.745	0.864	0.294	0.017
17NP436a_Ag036	13.391	0.927	0.279	0.017
17NP436a_Ag037	11.823	0.846	0.341	0.022
17NP436a_Ag038	15.599	1.164	0.231	0.019
17NP436a_Ag039	14.446	1.018	0.225	0.018
17NP436a_Ag040	15.599	1.079	0.194	0.014
17NP436a_Ag041	15.178	1.137	0.226	0.018
17NP436a_Ag042	9.150	0.662	0.476	0.030
17NP436a_Ag043	15.709	1.154	0.164	0.017
17NP436a_Ag044	10.051	0.737	0.443	0.025
17NP436a_Ag045	14.262	1.000	0.257	0.019
17NP436a_Ag046	13.593	0.963	0.249	0.016
17NP436a_Ag047	13.214	0.924	0.346	0.021
17NP436a_Ag048	14.150	0.955	0.240	0.017

Spot ID	238U/206Pb	2s	207Pb/206Pb	2s
17NP436a_Ag049	16.487	1.103	0.173	0.014
17NP436a_Ag050	13.996	0.956	0.272	0.020
17NP436a_Ag051	12.727	0.902	0.316	0.023
17NP436a_Ag052	12.061	0.871	0.331	0.022
17NP436a_Ag053	12.292	0.820	0.342	0.019
17NP436a_Ag054	11.594	0.833	0.404	0.022
17NP436a_Ag055	12.763	0.963	0.318	0.020
17NP436a_Ag056	12.985	0.915	0.316	0.020
17NP436a_Ag057	11.359	0.786	0.328	0.019
17NP436a_Ag058	14.128	0.986	0.244	0.018
17NP436a_Ag059	14.730	0.994	0.243	0.018
17NP436a_Ag060	15.572	1.097	0.222	0.016
17NP436a_Ag061	14.563	0.995	0.239	0.017
17NP436a_Ag062	16.161	1.115	0.200	0.016
17NP436a_Ag063	15.931	1.134	0.174	0.015
17NP436a_Ag064	15.307	1.050	0.228	0.018
17NP436a_Ag065	13.451	0.996	0.285	0.022
17NP436a_Ag066	12.275	0.795	0.378	0.021
17NP436a_Ag067	11.490	0.778	0.369	0.021
17NP436a_Ag068	15.988	1.590	0.208	0.022
17NP436a_Ag069	13.214	0.881	0.286	0.018
17NP436a_Ag070	12.691	0.833	0.321	0.017
17NP436a_Ag071	15.847	1.084	0.198	0.015
17NP436a_Ag072	15.359	1.036	0.210	0.016
17NP436a_Ag073	16.985	1.174	0.140	0.013
17NP436a_Ag074	15.654	1.085	0.212	0.016
17NP436a_Ag075	14.195	1.010	0.285	0.021
17NP436a_Ag076	13.079	0.925	0.315	0.022
17NP436a_Ag077	14.240	1.015	0.244	0.020
17NP436a_Ag078	14.469	1.021	0.226	0.017
17NP436a_Ag079	15.026	1.080	0.238	0.017
17NP436a_Ag080	7.959	0.525	0.548	0.025
17NP436a_Ag081	14.975	1.055	0.195	0.015
17NP436a_Ag082	16.307	1.129	0.177	0.016
17NP436a_Ag083	13.888	0.994	0.265	0.018
17NP436a_Ag084	15.439	1.103	0.223	0.018
17NP436a_Ag085	15.229	1.081	0.221	0.020
17NP436a_Ag086	11.388	1.033	0.364	0.030
17NP436a_Ag087	10.735	0.804	0.410	0.030
17NP436a_Ag088	6.446	0.436	0.551	0.026
17NP436a_Ag089	10.164	0.846	0.489	0.041
17NP436a_Ag090	14.262	0.966	0.289	0.017
17NP436a_Ag091	15.519	1.133	0.231	0.018
17NP436a_Ag092	13.312	1.078	0.309	0.025
17NP436a_Ag093	16.161	1.205	0.210	0.017
17NP436a_Ag094	14.852	1.100	0.227	0.021
17NP436a_Ag095	14.563	1.165	0.258	0.025
17NP436a_Ag096	14.901	1.086	0.229	0.020

Spot ID	238U/206Pb	2s	207Pb/206Pb	2s
17NP436a_Ag097	11.4608	0.8536	0.3770	0.0250
17NP436a_Ag098	14.9506	1.0910	0.2380	0.0190
17NP436a_Ag099	15.7914	1.0987	0.2130	0.0180
17NP436a_Ag100	14.5865	1.1084	0.2690	0.0190
17NP436a_Ag101	16.6087	1.1368	0.1730	0.0160
17NP436a_Ag102	16.1606	1.1815	0.2280	0.0180
17NP436a_Ag103	15.5455	1.2015	0.2360	0.0210
17NP436a_Ag104	12.5668	0.8855	0.3160	0.0210
17NP436a_Ag105	13.3710	0.9709	0.2920	0.0210
17NP436a_Ag106	14.3535	1.0812	0.2380	0.0190
17NP436a_Ag107	15.4122	1.1213	0.1820	0.0160
17NP436a_Ag108	0.8183	0.0516	0.8450	0.0120
17NP436a_Ag109	13.4712	1.0143	0.2770	0.0220
17NP436a_Ag110	12.6021	0.9166	0.3420	0.0240
17NP436a_Ag111	12.1096	0.9702	0.3380	0.0270
17NP436a_Ag112	12.6021	0.9166	0.2980	0.0220
17NP436a_Ag113	15.8751	1.2416	0.2010	0.0210
17NP436a_Ag114	13.7600	0.9971	0.2730	0.0200
17NP436a_Ag115	13.8876	0.9457	0.2620	0.0200
17NP436a_Ag116	11.6692	1.0072	0.4420	0.0390
17NP436a_Ag117	10.7737	0.9071	0.3890	0.0330
17NP436a_Ag118	14.0835	1.0326	0.2790	0.0220
17NP436a_Ag119	11.3023	0.9433	0.3800	0.0330
17NP436a_Bg01	13.1749	0.9497	0.3110	0.0250
17NP436a_Bg02	12.4278	0.7975	0.3470	0.0190
17NP436a_Bg03	13.3710	0.8820	0.2960	0.0180
17NP436a_Bg04	12.8914	0.8385	0.2990	0.0180
17NP436a_Bg05	12.6553	0.8421	0.3250	0.0150
17NP436a_Bg06	13.5321	0.9725	0.2830	0.0200
17NP436a_Bg07	14.7059	0.9746	0.2530	0.0150
17NP436a_Bg08	4.5084	0.2821	0.6720	0.0200
17NP436a_Bg09	12.5318	0.8819	0.3590	0.0210
17NP436a_Bg10	12.3935	0.9074	0.3550	0.0150
17NP436a_Bg11	15.5995	1.0594	0.2020	0.0160
17NP436a_Bg12	13.2526	0.9133	0.2660	0.0200
17NP436a_Bg13	13.0411	0.8786	0.3000	0.0200
17NP436a_Bg14	12.6198	0.8388	0.3470	0.0180
17NP436a_Bg15	14.4226	1.0161	0.2340	0.0170
17NP436a_Bg16	15.0256	1.0226	0.2310	0.0170
17NP436a_Bg17	13.2526	0.8711	0.2970	0.0170
17NP436a_Bg18	14.0395	1.0105	0.2720	0.0190
17NP436a_Bg19	11.8696	0.8035	0.4100	0.0220
17NP436a_Bg20	11.9485	0.8111	0.3910	0.0210
17NP436a_Bg21	12.2083	0.8365	0.3720	0.0210
17NP436a_Bg22	15.4386	1.1035	0.2340	0.0150
17NP436a_Bg23	14.2624	0.9497	0.2440	0.0150
17NP436a_Bg24	13.4914	0.9222	0.2960	0.0190
17NP436a_Bg25	13.1556	0.9938	0.3430	0.0240

Spot ID	238U/206Pb	2s	207Pb/206Pb	2s
17NP436a_Bg26	12.1917	0.8472	0.3190	0.0170
17NP436a_Bg27	13.6971	0.9741	0.3480	0.0220
17NP436a_Bg28	11.4608	0.9267	0.4150	0.0250
17NP436a_Bg29	14.2398	0.9638	0.2390	0.0160
17NP436a_Bg30	15.3071	0.9771	0.2290	0.0150
17NP436a_Bg31	13.4109	0.9753	0.2810	0.0160
17NP436a_Bg32	15.4386	0.9885	0.2210	0.0140
17NP436a_Bg33	14.5158	0.9906	0.2570	0.0150
17NP436a_Bg34	14.5629	0.9952	0.2750	0.0170
17NP436a_Bg35	13.4109	0.9143	0.2960	0.0170
17NP436a_Bg36	14.2172	1.0655	0.3130	0.0210
17NP436a_Bg37	10.6335	0.7625	0.4230	0.0220
17NP436a_Bg38	12.8361	0.8724	0.3430	0.0200
17NP436a_Bg39	14.8272	1.0034	0.2480	0.0160
17NP436a_Bg40	12.2750	0.9077	0.2870	0.0200
17NP436a_Bg41	16.1606	1.0724	0.2120	0.0150
17NP436a_Bg42	14.6340	0.9514	0.2820	0.0170
17NP436a_Bg43	11.0520	0.7460	0.4010	0.0230
17NP436a_Bg44	12.9658	0.8988	0.3450	0.0220
17NP436a_Bg45	11.8853	0.8050	0.3670	0.0210
17NP436a_Bg46	15.9314	1.1564	0.1990	0.0140
17NP436a_Bg47	14.5865	0.9803	0.2130	0.0140
17NP436a_Bg48	14.8272	0.9859	0.2730	0.0160
17NP436a_Bg49	13.8235	0.9551	0.2910	0.0180
17NP436a_Bg50	13.1943	0.8526	0.2750	0.0150
17NP436a_Bg51	13.2722	0.9008	0.3040	0.0170
17NP436a_Bg52	13.6762	0.9252	0.2890	0.0180
17NP436a_Bg53	14.6340	0.9849	0.2310	0.0160
17NP436a_Bg54	15.3858	1.4879	0.2530	0.0250
17NP436a_Bg55	14.4691	1.0571	0.2810	0.0200
17NP436a_Bg56	15.7086	1.1111	0.2250	0.0180
17NP436a_Bg57	14.4226	1.0339	0.2780	0.0180
17NP436a_Bg58	13.2526	0.9133	0.3290	0.0180
17NP436a_Bg59	13.4914	0.8931	0.3280	0.0210
17NP436a_Bg60	14.3306	1.0066	0.2820	0.0190
17NP436a_Bg61	13.6555	0.9858	0.3040	0.0210
17NP436a_Bg62	13.3511	0.9231	0.3050	0.0190
17NP436a_Bg63	9.1500	0.6199	0.4570	0.0210
17NP436a_Bg64	13.1749	0.9649	0.3170	0.0220
17NP436a_Bg65	13.9523	0.9363	0.2680	0.0160
17NP436a_Bg66	12.9099	0.8530	0.3530	0.0180
17NP436a_Bg67	10.8257	0.7152	0.4000	0.0200
17NP436a_Bg68	14.3535	1.0089	0.3010	0.0200
17NP436a_Bg69	14.0176	0.9584	0.3240	0.0210
17NP436a_Bg70	12.1917	0.8853	0.3380	0.0190
17NP436a_Bg71	10.6461	0.6987	0.4310	0.0210
17NP436a_Bg72	9.0395	0.6294	0.4820	0.0230
17NP436a_Bg73	9.3792	0.6281	0.4810	0.0240

Spot ID	238U/206Pb	2s	207Pb/206Pb	2s
17NP436a_Bg74	8.6149	0.5932	0.5120	0.0250
17NP436a_Bg75	13.6347	0.9518	0.2900	0.0210
17NP436a_Bg76	14.2624	0.9497	0.2720	0.0160
17NP436a_Bg77	12.0933	0.8252	0.3660	0.0190
17NP436a_Bg78	11.9485	0.8228	0.3690	0.0190
17NP436a_Bg79	12.7814	0.8286	0.3440	0.0180
17NP436a_Bg80	13.4914	0.9526	0.3180	0.0190
17NP436a_Bg81	13.0222	0.8905	0.3670	0.0190
17NP436a_Bg82	9.7666	0.6281	0.4990	0.0260
17NP436a_Cg01	10.7608	0.6916	0.4460	0.0220
17NP436a_Cg02	12.5668	0.8592	0.3640	0.0200
17NP436a_Cg03	10.1529	0.6784	0.4550	0.0230
17NP436a_Cg04	12.0933	0.8372	0.4000	0.0210
17NP436a_Cg05	12.5493	0.8705	0.3960	0.0220
17NP436a_Cg06	11.1757	0.7479	0.4290	0.0220
17NP436a_Cg07	12.9471	0.8564	0.3590	0.0180
17NP436a_Cg08	10.2338	0.7117	0.4760	0.0230
17NP436a_Cg09	13.9091	1.0305	0.3150	0.0200
17NP436a_Cg10	12.4623	0.8747	0.3800	0.0190
17NP436a_Cg11	12.7090	0.8732	0.3560	0.0220
17NP436a_Cg12	12.0608	0.8968	0.3250	0.0180
17NP436a_Cg13	11.2176	0.7518	0.4020	0.0200
17NP436a_Cg14	14.3995	1.1442	0.3600	0.0230
17NP436a_Cg15	13.9958	1.0759	0.2920	0.0240
17NP436a_Cg16	11.3738	0.8671	0.4420	0.0290
17NP436a_Cg17	12.9099	0.8932	0.3550	0.0230
17NP436a_Cg18	11.9644	0.8732	0.4010	0.0250
17NP436a_Cg19	12.1423	0.9194	0.3610	0.0230
17NP436a_Cg20	12.1423	1.0027	0.3280	0.0220
17NP436a_Cg21	13.3511	1.0835	0.3610	0.0250
17NP436a_Cg22	13.0600	1.1122	0.3690	0.0210
17NP436a_Cg23	11.2881	0.8341	0.4250	0.0240
17NP436a_Cg24	12.9471	0.9849	0.3290	0.0240
17NP436a_Cg25	13.0790	1.0323	0.3610	0.0250
17NP436a_Cg26	10.6714	0.9383	0.4630	0.0310
17NP436a_Cg27	13.6762	0.9560	0.3280	0.0190
17NP436a_Cg28	12.1423	0.8671	0.4410	0.0220
17NP436a_Cg29	12.3424	1.0147	0.3710	0.0240
17NP436a_Cg30	10.8781	0.8205	0.4290	0.0260
17NP436a_Cg31	14.9755	1.0938	0.2420	0.0190
17NP436a_Cg32	14.8272	1.1572	0.2620	0.0160
17NP436a_Cg33	11.6390	0.9113	0.4490	0.0260
17NP436a_Cg34	15.0507	1.1847	0.3310	0.0250
17NP436a_Cg35	12.8729	0.8895	0.3900	0.0240
17NP436a_Cg36	13.5730	0.9611	0.3270	0.0210
17NP436a_Cg37	11.3738	0.8911	0.4220	0.0280
17NP436a_Cg38	9.2536	0.5965	0.4830	0.0210
17NP436a_Cg39	6.0062	0.4361	0.6290	0.0330

Spot ID	238U/206Pb	2s	207Pb/206Pb	2s
17NP436a_Cg40	12.8545	0.9156	0.3610	0.0230
17NP436a_Cg41	9.8307	0.6637	0.4770	0.0220
17NP436a_Cg42	11.1897	0.9527	0.3710	0.0250
17NP436a_Cg43	11.1619	0.8423	0.3960	0.0250
17NP436a_Cg44	14.9257	1.1902	0.2900	0.0190
17NP436a_Cg45	13.6762	0.9560	0.3190	0.0200
17NP436a_Cg46	12.5493	1.0423	0.3510	0.0270
17NP436a_Cg47	13.6762	0.9719	0.3250	0.0200
17NP436a_Cg48	13.0411	0.8786	0.3900	0.0230
17NP436a_Cg49	10.3756	0.8744	0.4660	0.0320
17NP436a_Cg50	14.6819	1.0248	0.2620	0.0190
17NP436a_Cg51	10.6587	0.7652	0.4480	0.0220
17NP436a_Cg52	12.9099	0.8795	0.3470	0.0170
17NP436a_Cg53	14.8763	1.0829	0.2770	0.0210
17NP436a_Cg54	14.3306	1.1163	0.3550	0.0240
17NP436a_Cg55	12.5318	0.8687	0.3560	0.0200
17NP436a_Cg56	11.9327	0.8824	0.3880	0.0250
17NP436a_Cg57	6.5064	0.4060	0.6060	0.0230
17NP436a_Cg58	12.1423	0.9604	0.3280	0.0230
17NP436a_Cg59	11.6692	0.7843	0.4060	0.0220
17NP436a_Cg60	12.0124	0.8057	0.3620	0.0170
17NP436a_Cg61	15.7361	1.2246	0.2280	0.0170
17NP436a_Cg62	14.9506	1.0524	0.2950	0.0180
17NP436a_Cg63	12.8178	0.8706	0.3300	0.0210
17NP436a_Cg64	10.4724	0.6747	0.4370	0.0210
17NP436a_Dg01	15.9597	1.0946	0.1810	0.0130
17NP436a_Dg02	16.5475	1.1087	0.1780	0.0130
17NP436a_Dg03	11.5196	0.8026	0.3990	0.0210
17NP436a_Dg04	11.8228	0.8219	0.4070	0.0190
17NP436a_Dg05	15.9314	1.0713	0.2190	0.0150
17NP436a_Dg06	17.2132	1.1727	0.2360	0.0140
17NP436a_Dg07	13.4712	1.0476	0.3030	0.0190
17NP436a_Dg08	14.4226	1.0520	0.2460	0.0160
17NP436a_Dg09	12.7996	0.8557	0.3700	0.0210
17NP436a_Dg10	15.8751	1.1503	0.1970	0.0160
17NP436a_Dg11	15.7914	1.1413	0.1930	0.0150
17NP436a_Dg12	15.0507	1.0628	0.2380	0.0180
17NP436a_Dg13	10.6209	0.6965	0.4010	0.0210
17NP436a_Dg14	10.4968	0.7386	0.4220	0.0240
17NP436a_Dg15	15.9881	1.0368	0.1980	0.0140
17NP436a_Dg16	10.3517	0.7897	0.4430	0.0260
17NP436a_Dg17	11.8696	0.9399	0.3740	0.0250
17NP436a_Dg18	16.1316	1.1556	0.2390	0.0160
17NP436a_Dg19	14.3995	1.0495	0.2890	0.0160
17NP436a_Dg20	13.0600	1.1122	0.3530	0.0250
17NP436a_Dg21	10.3876	0.6837	0.4510	0.0260
17NP436a_Dg22	10.9443	0.9072	0.3760	0.0220
17NP436a_Dg23	17.0499	1.1568	0.2470	0.0180

Spot ID	238U/206Pb	2s	207Pb/206Pb	2s
17NP436a_Dg24	16.4868	1.1703	0.2310	0.0160
17NP436a_Dg25	13.1943	0.9670	0.3020	0.0190
17NP436a_Dg26	13.0411	0.8924	0.3390	0.0220
17NP436a_Dg27	13.4309	1.0427	0.3760	0.0240
17NP436a_Dg28	15.0005	1.0202	0.2180	0.0150
17NP436a_Dg29	11.5492	0.7836	0.3560	0.0190
17NP436a_Dg30	16.3369	1.1547	0.2710	0.0170
17NP436a_Dg31	16.7636	1.1755	0.1950	0.0130
17NP436a_Dg32	13.1556	0.9037	0.3510	0.0220
17NP436a_Dg33	14.3078	1.1521	0.3130	0.0200
17NP436a_Dg34	12.1096	0.9290	0.3770	0.0230
17NP436a_Dg35	14.5865	0.9636	0.2780	0.0140
17NP436a_Dg36	14.9755	1.1339	0.3100	0.0210
17NP436a_Dg37	12.6021	1.0340	0.3810	0.0270
17NP436a_Dg38	15.0005	1.0576	0.2670	0.0200
17NP436a_Dg39	11.2316	0.8166	0.4130	0.0230
17NP436a_Dg40	15.7086	1.0700	0.2680	0.0170
17NP436a_Eg01	16.6703	1.0985	0.2040	0.0150
17NP436a_Eg02	12.9099	0.8661	0.3100	0.0190
17NP436a_Eg03	12.7451	0.9041	0.3230	0.0220
17NP436a_Eg04	12.9658	0.8451	0.3260	0.0180
17NP436a_Eg05	10.7095	0.6957	0.3440	0.0160
17NP436a_Eg06	12.6911	0.9698	0.3130	0.0210
17NP436a_Eg07	16.1606	1.0522	0.2300	0.0140
17NP436a_Eg08	12.8729	0.8759	0.3130	0.0210
17NP436a_Eg09	12.9845	0.9293	0.2950	0.0190
17NP436a_Eg10	12.0446	0.7861	0.3140	0.0160
17NP436a_Eg11	14.1056	1.1076	0.2700	0.0190
17NP436a_Eg12	14.1724	1.0074	0.2790	0.0170
17NP436a_Eg13	13.8235	0.9551	0.2830	0.0160
17NP436a_Eg14	10.7095	0.7510	0.4200	0.0210
17NP436a_Eg15	13.6555	0.9384	0.3030	0.0200
17NP436a_Eg16	16.3965	1.1382	0.2390	0.0190
17NP436a_Eg17	15.7914	1.1855	0.2590	0.0210
17NP436a_Eg18	16.1606	1.1364	0.2020	0.0160
17NP436a_Eg19	15.9032	1.0686	0.2030	0.0140
17NP436a_Eg20	14.2172	0.9781	0.2730	0.0180
17NP436a_Eg21	13.2526	0.9280	0.3190	0.0210
17NP436a_Eg22	12.6553	0.9084	0.3770	0.0230
17NP436a_Eg23	10.7480	0.7747	0.4640	0.0280
17NP436a_Eg24	11.8853	1.3528	0.4490	0.0910
17NP436a_Eg25	14.0395	1.2937	0.3330	0.0260
17NP436a_Eg26	14.5393	0.9272	0.2850	0.0160
17NP436a_Eg27	14.1056	0.9509	0.3030	0.0170
17NP436a_Eg28	13.5117	1.0525	0.3400	0.0230
17NP436a_Eg29	13.2919	0.9320	0.3540	0.0230
17NP436a_Eg30	11.8383	0.8235	0.3700	0.0210
17NP436a_Eg32	15.2293	1.1637	0.3000	0.0260

Spot ID	238U/206Pb	2s	207Pb/206Pb	2s
17NP436a_Eg33	13.7390	1.0628	0.3080	0.0220
17NP436a_Eg34	13.8448	1.1117	0.3690	0.0280
17NP436a_Eg35	11.9644	0.9118	0.3520	0.0240
17NP436a_Eg36	14.2850	1.0550	0.3130	0.0210
17NP436a_Eg38	14.4924	1.3006	0.3610	0.0320
17NP436a_Eg39	16.3667	1.6273	0.2740	0.0240
17NP436a_Eg40	13.4712	0.9979	0.3250	0.0220
17NP436a_Fg01	7.7260	0.6580	0.6290	0.0500
17NP436a_Fg02	8.5493	0.9017	0.5640	0.0680
17NP436a_Fg03	9.5997	0.8438	0.4500	0.0390
17NP436a_Fg04	10.0059	0.9875	0.4880	0.0480
17NP436a_Fg05	7.3051	0.8181	0.6420	0.0820
17NP436a_Fg06	7.5507	0.8682	0.6320	0.0890
17NP436a_Fg07	4.1407	0.5522	0.8500	0.1500
17NP436a_Fg08	10.3637	0.9048	0.4530	0.0450
17NP436a_Fg09	10.6084	0.8956	0.4220	0.0330
17NP436a_Fg10	5.4456	0.4110	0.6350	0.0370
17NP436a_Fg11	6.8070	0.5282	0.6080	0.0340
17NP436a_Fg12	10.2455	0.9517	0.4990	0.0470
17NP436a_Fg15	10.2106	0.9897	0.5140	0.0530
17NP436a_Fg16	5.9192	0.4485	0.6440	0.0360
17NP436a_Fg17	6.8800	0.4445	0.5700	0.0230
17NP436a_Fg18	6.5158	0.4859	0.6010	0.0370
17NP436a_Fg19	8.8963	0.6283	0.5040	0.0220
17NP436a_Fg20	2.0283	0.1208	0.7800	0.0130
17NP436a_Fg21	3.7439	0.2835	0.7170	0.0350
17NP436a_Fg22	10.3876	0.9967	0.4930	0.0490
17NP436a_Fg24	9.6202	1.0115	0.4810	0.0510
17NP436a_Fg25	7.6082	0.5500	0.5810	0.0310
17NP436a_Fg26	8.7833	0.6232	0.4910	0.0220
17NP436a_Fg27	8.9406	0.5999	0.5070	0.0220
17NP436a_Fg28	9.4483	0.5816	0.4840	0.0210
17NP436a_Fg29	10.1186	0.6440	0.4740	0.0230
17NP436a_Fg30	6.2311	0.5004	0.6360	0.0370
17NP436a_Fg31	10.9577	0.9564	0.4540	0.0500
17NP436a_Fg32	7.2287	0.6266	0.5980	0.0560
17NP436a_Fg33	7.8065	0.7061	0.5590	0.0470
17NP436a_Fg34	8.1908	0.5413	0.5610	0.0260
17NP436a_Fg35	9.2632	0.5974	0.4930	0.0210
17NP436a_Fg36	9.9066	0.6331	0.4970	0.0240
17NP436a_Fg37	9.5894	0.6265	0.4800	0.0210
17NP436a_Fg38	8.2738	0.8734	0.6560	0.0730
17NP436a_Fg39	9.5487	0.8734	0.4970	0.0580
17NP436a_Fg40	7.2113	0.5884	0.6090	0.0420
17NP436a_Fg41	6.3188	0.4745	0.6270	0.0360
17NP436a_Fg42	9.4284	0.6620	0.4750	0.0260
17NP436a_Fg43	8.9495	0.6476	0.4970	0.0280
17NP436a_Fg44	8.8875	0.5765	0.5130	0.0210

Spot ID	238U/206Pb	2s	207Pb/206Pb	2s
17NP436a_Fg45	9.0669	0.5863	0.5110	0.0230
17NP436a_Fg46	9.1129	0.8330	0.5890	0.0410
17NP436a_Fg47	5.9114	0.6016	0.6540	0.0610
17NP436a_Fg48	10.4480	0.7523	0.5170	0.0300
17NP436a_Fg49	7.9798	0.5579	0.5350	0.0280
17NP436a_Fg50	6.6068	0.4304	0.5680	0.0220
17NP436a_Fg51	8.1241	0.5105	0.5460	0.0230
17NP436a_Fg52	9.1968	0.5915	0.4860	0.0230
17NP436a_Fg53	7.9940	0.4952	0.6520	0.0240
17NP436a_Fg54	9.3988	0.7886	0.5520	0.0470
17NP436a_Fg56	9.3015	0.7421	0.4880	0.0280
17NP436a_Fg57	8.6397	0.6275	0.5250	0.0240
17NP436a_Fg58	9.3597	0.5993	0.4830	0.0250
17NP436a_Fg59	3.8399	0.2815	0.6980	0.0350
17NP436a_Fg60	8.0083	0.5346	0.5210	0.0240
17NP436a_Fg61	10.8126	0.9124	0.4610	0.0220
17NP436a_Fg62	5.9114	0.5646	0.7210	0.0690
17NP436a_Fg63	11.0930	0.7210	0.4010	0.0180
17NP436a_Fg64	9.6512	0.6180	0.4840	0.0220
17NP436a_Fg65	9.4682	0.6972	0.5110	0.0230
17NP436a_Fg66	11.6692	0.7953	0.3970	0.0220
17NP436a_Fg67	10.3756	0.6506	0.4190	0.0200
17NP436a_Fg68	9.6720	0.6129	0.4920	0.0220
17NP436a_Fg69	9.2346	0.6078	0.4970	0.0220
17NP436a_Fg70	11.5049	0.7687	0.4020	0.0190
17NP436a_Fg71	9.4185	0.6179	0.4830	0.0200
17NP436a_Fg72	8.5169	0.5335	0.4880	0.0190
17NP436a_Fg73	8.9406	0.6608	0.5640	0.0270
17NP436a_Fg74	11.2881	0.7899	0.4510	0.0250
17NP436a_Fg75	10.5709	0.7094	0.4510	0.0250
17NP436a_Fg76	10.0282	0.6747	0.4950	0.0220
17NP436b_Ag01	15.6538	1.0450	0.2010	0.0130
17NP436b_Ag02	16.7324	1.1723	0.1390	0.0100
17NP436b_Ag03	16.3667	1.0708	0.1460	0.0110
17NP436b_Ag04	15.5455	1.0348	0.2030	0.0120
17NP436b_Ag05	15.2811	1.0869	0.1850	0.0150
17NP436b_Ag06	17.0499	1.1336	0.1270	0.0091
17NP436b_Ag07	16.8896	1.1414	0.1288	0.0099
17NP436b_Ag08	17.0499	1.1568	0.1570	0.0110
17NP436b_Ag09	15.3071	1.0312	0.2190	0.0160
17NP436b_Ag10	17.1803	1.1938	0.1300	0.0110
17NP436b_Ag11	15.7637	1.0553	0.1700	0.0140
17NP436b_Ag12	16.4265	1.1190	0.1500	0.0130
17NP436b_Ag13	15.8751	1.0863	0.1660	0.0110
17NP436b_Ag14	15.0005	1.0576	0.2480	0.0160
17NP436b_Ag15	16.9534	1.1475	0.1400	0.0100
17NP436b_Ag16	17.1475	1.1428	0.1250	0.0110
17NP436b_Ag17	16.2483	1.1017	0.1460	0.0110

Spot ID	238U/206Pb	2s	207Pb/206Pb	2s
17NP436b_Ag18	15.6811	1.0673	0.1940	0.0140
17NP436b_Ag19	12.7632	0.8922	0.2980	0.0160
17NP436b_Ag20	15.2811	1.0287	0.2150	0.0140
17NP436b_Ag21	16.3667	1.0506	0.1430	0.0095
17NP436b_Ag22	17.2794	1.1093	0.1410	0.0110
17NP436b_Ag23	16.4868	1.1030	0.1440	0.0120
17NP436b_Ag24	15.6811	1.0097	0.1800	0.0120
17NP436b_Ag25	14.9755	0.9822	0.2240	0.0140
17NP436b_Ag26	15.4386	1.0438	0.1870	0.0140
17NP436b_Ag27	14.0176	1.0081	0.3190	0.0170
17NP436b_Ag28	15.2811	1.0103	0.2140	0.0160
17NP436b_Ag29	16.3369	1.0889	0.1830	0.0120
17NP436b_Ag30	15.5186	1.0712	0.2130	0.0140
17NP436b_Ag31	15.7086	1.0903	0.1890	0.0150
17NP436b_Ag32	16.4265	1.0762	0.1530	0.0110
17NP436b_Ag33	16.8896	1.1187	0.1580	0.0100
17NP436b_Ag34	15.0005	0.9845	0.2230	0.0130
17NP436b_Ag35	14.9010	0.9928	0.2280	0.0140
17NP436b_Ag36	16.1027	1.0876	0.1710	0.0120
17NP436b_Ag37	16.5171	1.1059	0.1630	0.0120
17NP436b_Ag38	15.7914	1.1413	0.1910	0.0150
17NP436b_Bg01	13.9307	0.8755	0.2610	0.0150
17NP436b_Bg02	16.3965	1.1161	0.1730	0.0130
17NP436b_Bg03	17.1475	1.1428	0.1450	0.0110
17NP436b_Bg04	13.2137	0.9094	0.2700	0.0170
17NP436b_Bg05	17.0499	1.0893	0.1360	0.0110
17NP436b_Bg06	16.1897	1.0352	0.1740	0.0140
17NP436b_Bg07	13.6555	0.8939	0.2900	0.0170
17NP436b_Bg08	16.5780	1.0900	0.1740	0.0120
17NP436b_Bg09	11.9964	0.7817	0.3270	0.0170
17NP436b_Bg10	16.9215	1.1444	0.1490	0.0110
17NP436b_Bg11	3.6675	0.2514	0.7210	0.0150
17NP436b_Bg12	15.0256	0.9868	0.2170	0.0120
17NP436b_Bg13	16.6394	1.0541	0.1770	0.0130
17NP436b_Bg14	17.1475	1.1199	0.1325	0.0097
17NP436b_Bg15	11.4462	0.7737	0.3400	0.0160
17NP436b_Bg16	7.0639	0.4725	0.5810	0.0220
17NP436b_Bg17	14.2850	0.9519	0.2770	0.0170
17NP436b_Bg18	16.3072	1.0861	0.1830	0.0120
17NP436b_Bg19	15.9032	1.0293	0.1630	0.0110
17NP436b_Bg20	11.8072	0.8561	0.3540	0.0180
17NP436b_Bg21	14.7784	1.3217	0.2820	0.0200
17NP436b_Bg22	13.7180	0.9763	0.2810	0.0190
17NP436b_Bg23	12.6553	0.9084	0.3180	0.0180
17NP436b_Bg24	18.1521	1.3820	0.2430	0.0170
17NP436b_Bg25	15.7361	1.1792	0.1940	0.0160
17NP436b_Bg26	11.4901	0.9305	0.3750	0.0230
17NP436b_Bg27	13.9958	0.9250	0.2700	0.0150

Spot ID	238U/206Pb	2s	207Pb/206Pb	2s
17NP436b_Bg28	13.9091	1.0305	0.3460	0.0190
17NP436b_Bg29	18.5264	1.4264	0.1690	0.0130
17NP436b_Bg30	16.0739	1.1059	0.2000	0.0150
17NP436b_Bg31	16.2777	1.0628	0.1790	0.0120
17NP436b_Bg32	17.6876	1.2195	0.1810	0.0130
17NP436b_Bg33	16.1027	1.2455	0.2220	0.0150
17NP436b_Bg34	15.2811	1.0869	0.2500	0.0150
17NP436b_Bg35	12.9471	0.8696	0.3150	0.0180
17NP436b_Bg36	15.9032	1.0890	0.1660	0.0130
17NP436b_Bg37	15.7361	1.3192	0.2420	0.0180
17NP436b_Bg38	14.5393	1.5528	0.3040	0.0310
17NP436b_Bg39	9.0486	0.6953	0.4610	0.0300
17NP436b_Bg40	11.0656	0.8998	0.4030	0.0210
17NP436b_Bg41	11.4901	0.9820	0.4040	0.0270
17NP436b_Bg42	15.0256	1.3589	0.2540	0.0220
17NP436b_Bg43	12.9099	1.0271	0.2970	0.0190
17NP436b_Bg44	13.9091	1.3949	0.3230	0.0280
17NP436b_Bg45	11.1067	0.8700	0.4100	0.0190
17NP436b_Bg46	18.2628	1.9000	0.2430	0.0280
17NP436b_Bg47	17.8990	1.5999	0.1890	0.0180
17NP436b_Cg01	15.5995	1.5752	0.1740	0.0300
17NP436b_Cg02	12.1587	0.8562	0.3580	0.0230
17NP436b_Cg03	13.0981	0.9414	0.3540	0.0220
17NP436b_Cg04	16.8896	1.1414	0.1580	0.0120
17NP436b_Cg05	17.6528	1.1906	0.0965	0.0078
17NP436b_Cg06	14.6819	0.9557	0.2460	0.0150
17NP436b_Cg07	11.4171	0.7709	0.3610	0.0200
17NP436b_Cg08	17.2132	1.1727	0.1270	0.0100
17NP436b_Cg09	15.7086	1.0308	0.2070	0.0150
17NP436b_Cg10	12.9845	0.8732	0.3270	0.0170
17NP436b_Cg11	13.2919	0.9172	0.2990	0.0180
17NP436b_Cg12	12.9471	0.8066	0.3470	0.0190
17NP436b_Cg13	15.2293	0.9704	0.2460	0.0150
17NP436b_Cg14	16.9534	1.1475	0.1560	0.0120
17NP436b_Cg15	16.3072	1.0861	0.1930	0.0140
17NP436b_Cg16	15.7086	0.9939	0.1670	0.0120
17NP436b_Cg17	17.4472	1.1710	0.1211	0.0097
17NP436b_Cg18	15.6811	1.0283	0.1980	0.0120
17NP436b_Cg19	16.9534	1.1024	0.1207	0.0075
17NP436b_Cg20	16.8896	1.0968	0.1710	0.0120
17NP436b_Cg21	17.6876	1.1692	0.1053	0.0083
17NP436b_Cg22	16.3667	1.1132	0.1500	0.0100
17NP436b_Cg23	16.8896	1.1187	0.1650	0.0110
17NP436b_Cg24	15.7637	1.0169	0.2000	0.0130
17NP436b_Cg25	18.5647	1.1981	0.1110	0.0100
17NP436b_Cg26	17.4134	1.0987	0.1330	0.0083
17NP436b_Cg27	11.9168	0.7967	0.3480	0.0170
17NP436b_Cg28	17.8990	1.1401	0.1247	0.0096

Spot ID	238U/206Pb	2s	207Pb/206Pb	2s
17NP436b_Cg29	17.0176	1.1537	0.1510	0.0110
17NP436b_Dg01	14.4458	0.9670	0.2530	0.0160
17NP436b_Dg02	13.8876	1.0281	0.3060	0.0200
17NP436b_Dg03	12.4450	0.9269	0.3460	0.0240
17NP436b_Dg04	13.2919	0.9320	0.3150	0.0180
17NP436b_Dg05	11.1067	0.7414	0.3840	0.0180
17NP436b_Dg06	16.1027	1.2942	0.1970	0.0140
17NP436b_Dg07	16.9534	1.2968	0.1740	0.0140
17NP436b_Dg08	15.7914	1.1197	0.2240	0.0180
17NP436b_Dg09	14.7784	0.9480	0.2340	0.0140
17NP436b_Dg10	15.1779	1.1789	0.2610	0.0180
17NP436b_Dg11	15.7637	1.4992	0.2230	0.0220
17NP436b_Dg12	16.3369	1.2010	0.2160	0.0140
17NP436b_Dg13	14.2850	0.9682	0.2120	0.0140
17NP436b_Dg14	16.2483	1.3383	0.1670	0.0160
17NP436b_Dg15	14.2172	1.1025	0.2260	0.0160
17NP436b_Dg16	15.8751	1.3631	0.2140	0.0180
17NP436b_Dg17	15.9032	1.1315	0.1970	0.0150
17NP436b_Dg18	15.2811	1.0869	0.2370	0.0160
17NP436b_Dg19	16.9854	1.2232	0.1790	0.0130
17NP436b_Dg20	15.7914	1.1855	0.2460	0.0150
17NP436b_Dg21	11.1619	0.7466	0.3990	0.0190
17NP436b_Dg22	16.8580	1.1158	0.1740	0.0130
17NP436b_Dg23	15.7914	1.0384	0.2470	0.0160
NP233_Ag01	19.6242	1.7915	0.0740	0.0390
NP233_Ag02	19.3374	1.9311	0.2380	0.0550
NP233_Ag03	15.4377	1.4336	0.2760	0.0390
NP233_Ag04	17.9508	1.9582	0.1460	0.0550
NP233_Ag05	17.0582	1.5583	0.0830	0.0420
NP233_Ag06	16.3940	1.4837	0.2660	0.0430
NP233_Ag07	15.5153	1.2646	0.2800	0.0380
NP233_Ag08	15.0367	1.3496	0.2280	0.0380
NP233_Ag09	14.3829	1.3933	0.3300	0.0440
NP233_Ag10	18.0206	1.5851	0.1660	0.0240
NP233_Ag11	17.2167	1.5260	0.1260	0.0220
NP233_Ag12	17.6431	1.5305	0.1310	0.0210
NP233_Ag13	14.6098	1.2863	0.2340	0.0240
NP233_Ag14	16.9645	1.4890	0.0810	0.0230
NP233_Ag15	13.0276	1.1941	0.2580	0.0380
NP233_Ag16	12.7760	1.0486	0.2390	0.0310
NP233_Ag17	5.2569	0.3777	0.6210	0.0280
NP233_Ag18	17.2167	1.4156	0.1500	0.0290
NP233_Ag19	17.3457	1.4883	0.1560	0.0300
NP233_Ag20	17.6767	1.6551	0.1810	0.0310
NP233_Ag21	17.1848	1.6354	0.1560	0.0350
NP233_Ag22	17.9161	1.8208	0.1420	0.0370
NP233_Ag23	18.5623	1.6652	0.1160	0.0330
NP233_Ag24	15.2848	1.4782	0.2210	0.0460

Spot ID	238U/206Pb	2s	207Pb/206Pb	2s
NP233_Ag25	17.8470	1.6513	0.1920	0.0340
NP233_Ag26	16.2787	1.7290	0.1550	0.0470
NP233_Ag27	17.2167	1.6698	0.1610	0.0520
NP233_Ag28	16.0253	1.5784	0.0750	0.0460
NP233_Ag29	17.1530	1.8669	0.1320	0.0450
NP233_Ag30	16.7801	1.5429	0.0470	0.0380
NP233_Ag31	15.9700	1.4690	0.1210	0.0360
NP233_Ag32	16.4231	1.5933	0.1400	0.0380
NP233_Ag33	15.4634	1.4609	0.1440	0.0360
NP233_Ag34	15.1103	1.4719	0.3290	0.0460
NP233_Ag35	16.7801	1.6816	0.1940	0.0600
NP233_Ag36	16.7195	1.5336	0.1360	0.0280
NP233_Ag37	17.5761	1.6092	0.1930	0.0320
NP233_Ag38	17.8815	1.4468	0.0760	0.0240
NP233_Ag39	16.1651	1.4995	0.1070	0.0270
NP233_Ag40	18.1620	1.8315	0.1330	0.0340
NP233_Ag41	18.4147	1.7415	0.0790	0.0270
NP233_Ag42	18.3418	1.6005	0.0950	0.0300
NP233_Ag43	15.7796	1.6367	0.2750	0.0500
NP233_Ag44	18.6370	2.0938	0.1200	0.0330
NP233_Ag45	16.9335	1.4575	0.1470	0.0280
NP233_Ag46	17.4437	1.5021	0.0980	0.0220
NP233_Ag47	18.8264	1.8436	0.1370	0.0310
NP233_Ag48	17.6431	1.5896	0.1200	0.0290
NP233_Ag49	17.3782	1.5499	0.0920	0.0210
NP233_Ag50	18.4147	1.8422	0.0980	0.0300
NP233_Ag51	17.1213	1.7121	0.1120	0.0350
NP233_Ag52	17.9161	1.7887	0.1610	0.0330
NP233_Ag53	17.1848	1.6644	0.0850	0.0390
NP233_Ag54	16.8105	1.5205	0.0830	0.0260
NP233_Ag55	16.7195	1.5880	0.1050	0.0270
NP233_Ag56	17.7105	1.7532	0.0880	0.0400
NP233_Ag58	16.0253	1.8405	0.1460	0.0750
NP233_Ag59	16.5700	1.5908	0.1820	0.0400
NP233_Ag60	18.1620	1.7333	0.1160	0.0360
NP233_Ag61	18.2335	1.8108	0.1650	0.0350
NP233_Bg01	17.0897	1.7950	0.2540	0.0580
NP233_Bg02	15.6728	1.7430	0.1890	0.0530
NP233_Bg03	13.6818	1.3531	0.3220	0.0450
NP233_Bg04	15.3609	1.6574	0.3120	0.0570
NP233_Bg05	15.9976	1.5232	0.1980	0.0280
NP233_Bg06	16.4815	1.6031	0.1880	0.0370
NP233_Bg07	16.2787	1.5693	0.1800	0.0340
NP233_Bg08	16.9956	1.6331	0.1520	0.0330
NP233_Bg09	14.9397	1.4434	0.2630	0.0390
NP233_Bg10	17.7105	1.7532	0.1400	0.0300
NP233_Bg11	16.7497	1.6205	0.2000	0.0310
NP233_Bg12	17.8470	1.9381	0.1790	0.0470

Spot ID	238U/206Pb	2s	207Pb/206Pb	2s
NP233_Bg13	17.4109	1.7628	0.2030	0.0390
NP233_Bg14	17.9856	1.8332	0.1460	0.0390
NP233_Bg15	15.0857	1.6284	0.2010	0.0510
NP233_Bg16	13.9287	1.2624	0.2510	0.0350
NP233_Bg17	16.5109	1.5543	0.1880	0.0270
NP233_Bg18	16.3940	1.5620	0.1940	0.0320
NP233_Bg19	15.1350	1.4309	0.2520	0.0420
NP233_Bg20	15.2095	1.4657	0.1970	0.0420
NP233_Bg21	15.1846	1.3280	0.2330	0.0280
NP233_Bg22	17.6767	1.6551	0.1270	0.0240
NP233_Bg23	17.6767	1.7475	0.1330	0.0320
NP233_Bg24	9.4037	0.8010	0.2640	0.0350
NP233_Bg25	16.1934	1.3072	0.1020	0.0210
NP233_Bg26	15.9425	1.2083	0.1320	0.0250
NP233_Bg27	17.9161	1.6621	0.0960	0.0230
NP233_Bg28	17.9508	1.7307	0.1770	0.0280
NP233_Bg29	15.8606	1.4521	0.1320	0.0220
NP233_Bg30	15.5153	1.4225	0.1520	0.0270
NP233_Bg31	17.6095	1.6143	0.1410	0.0260
NP233_Bg32	14.1198	1.3499	0.2640	0.0320
NP233_Bg33	13.6617	1.2580	0.1360	0.0220
NP233_Bg34	14.8677	1.3243	0.1970	0.0280
NP233_Bg35	18.5252	1.6597	0.1080	0.0180
NP233_Bg36	18.2335	1.4627	0.0840	0.0150
NP233_Bg37	17.3133	1.4559	0.1480	0.0210
NP233_Bg38	17.7785	1.5500	0.0980	0.0170
NP233_Bg39	17.1530	1.4888	0.1220	0.0190
NP233_Bg40	17.9508	1.5749	0.1360	0.0290
NP233_Bg41	17.3133	1.5402	0.1300	0.0220
NP233_Bg42	16.8105	1.4402	0.1430	0.0210
NP233_Bg43	16.1651	1.5249	0.2040	0.0220
NP233_Bg44	17.7105	1.4248	0.1180	0.0170
NP233_Bg45	17.5428	1.4311	0.1100	0.0170
NP233_Bg46	17.3782	1.5499	0.1480	0.0200
NP233_Bg47	17.2488	1.4198	0.0850	0.0170
NP233_Bg48	18.1977	1.5488	0.1410	0.0230
NP233_Bg49	18.5252	1.7594	0.0980	0.0250
NP233_Bg50	17.3782	1.6968	0.1600	0.0340
NP233_Bg51	17.4109	1.5260	0.1150	0.0240
NP233_Bg52	16.9335	1.5117	0.1750	0.0280
NP233_Bg53	16.9026	1.3743	0.1290	0.0180
NP233_Bg54	16.9026	1.5345	0.1000	0.0190
NP233_Bg55	18.3782	1.6057	0.0950	0.0190
NP233_Bg56	17.1213	1.4569	0.0930	0.0170
NP233_Bg57	17.5761	1.6693	0.1180	0.0200
NP233_Bg58	18.0206	1.6160	0.1110	0.0240
NP233_Bg59	18.7882	1.7677	0.0910	0.0240
NP233_Bg60	15.9425	1.5142	0.2370	0.0330

Spot ID	238U/206Pb	2s	207Pb/206Pb	2s
NP233_Bg61	15.4634	1.4145	0.2410	0.0280
NP233_Bg62	17.4766	1.6532	0.1360	0.0200
NP233_Bg63	17.3133	1.4012	0.1060	0.0170
NP233_Bg64	17.3782	1.5499	0.1250	0.0200
NP233_Bg65	16.8718	1.4224	0.0780	0.0120
NP233_Bg66	17.2167	1.5260	0.1210	0.0190
NP233_Bg67	19.1376	1.7883	0.1270	0.0270
NP233_Bg68	17.5428	1.5452	0.1210	0.0180
NP233_Bg69	15.9700	1.4201	0.1820	0.0240
NP233_Bg70	17.2488	1.5591	0.1320	0.0180
NP233_Bg71	17.1530	1.4888	0.1050	0.0200
NP233_Bg72	16.8411	1.4711	0.1190	0.0170
NP233_Bg73	19.2170	1.7651	0.1080	0.0200
NP233_Bg74	18.4147	1.5792	0.0970	0.0160
NP233_Bg75	18.4514	1.5527	0.1030	0.0160
NP233_Bg76	18.1620	1.5134	0.1030	0.0180
NP233_Bg77	16.8105	1.5751	0.1570	0.0210
NP233_Bg78	16.7801	1.4889	0.1230	0.0210
NP233_Bg79	17.0268	1.5815	0.1480	0.0210
NP233_Bg80	18.2335	1.6481	0.1340	0.0230
NP233_Bg81	16.9645	1.3824	0.0970	0.0170
NP233_Bg82	17.5428	1.5162	0.0990	0.0160
NP233_Bg83	16.6295	1.4407	0.1160	0.0180
NP233_Bg84	16.7195	1.5067	0.1300	0.0210
NP233_Bg85	17.6095	1.6143	0.1420	0.0220
NP233_Bg86	16.9026	1.4532	0.0940	0.0170
NP233_Bg87	17.5761	1.5209	0.1410	0.0200
NP233_Bg88	17.1213	1.5680	0.1510	0.0210
NP233_Bg89	16.4815	1.3944	0.1850	0.0260
NP233_Bg90	17.3782	1.5499	0.1370	0.0210
NP233_Bg91	17.3782	1.4648	0.1220	0.0190
NP233_Bg92	17.0897	1.5351	0.1380	0.0190
NP233_Bg93	18.1264	1.5696	0.0970	0.0180
NP233_Bg94	18.2335	1.6481	0.1060	0.0180
NP233_Bg95	17.4766	1.6532	0.1010	0.0210
NP233_Bg96	19.4593	1.8029	0.1400	0.0240
NP233_Bg97	17.3782	1.6670	0.1180	0.0230
NP233_Bg98	17.1213	1.5119	0.0940	0.0170
NP233_Bg99	17.2167	1.6116	0.1270	0.0230
NP233_Cg01	15.2596	1.2525	0.1880	0.0240
NP233_Cg02	11.7248	0.9894	0.2070	0.0250
NP233_Cg03	10.9229	0.9710	0.1710	0.0210
NP233_Cg04	12.0764	0.9980	0.1620	0.0190
NP233_Cg05	14.0983	1.1578	0.2000	0.0240
NP233_Cg06	15.9425	1.2303	0.1710	0.0170
NP233_Cg07	12.3832	1.0253	0.1630	0.0200
NP233_Cg08	15.1103	1.2746	0.1870	0.0250
NP233_Cg09	13.1013	1.0302	0.1730	0.0190

Spot ID	238U/206Pb	2s	207Pb/206Pb	2s
NP233_Cg10	11.3512	0.9625	0.2510	0.0230
NP233_Cg11	14.7494	1.2256	0.1630	0.0170
NP233_Cg12	11.3373	0.9487	0.1690	0.0200
NP233_Cg13	16.6894	1.3219	0.1990	0.0240
NP233_Cg14	16.3940	1.3332	0.1370	0.0150
NP233_Cg15	17.0268	1.3906	0.1450	0.0210
NP233_Cg16	16.9956	1.4394	0.1690	0.0190
NP233_Cg17	14.4955	1.2499	0.1560	0.0200
NP233_Cg18	17.2167	1.3888	0.1400	0.0160
NP233_Cg19	17.8815	1.4758	0.1420	0.0170
NP233_Cg20	16.8718	1.3962	0.1630	0.0210
NP233_Cg21	17.9856	1.4897	0.1380	0.0170
NP233_Cg22	17.1848	1.3847	0.1640	0.0190
NP233_Cg23	16.9956	1.3095	0.1320	0.0160
NP233_Cg24	16.4522	1.4410	0.1340	0.0190
NP233_Cg25	17.0897	1.4255	0.1180	0.0160
NP233_Cg26	15.9151	1.3407	0.1340	0.0200
NP233_Cg27	14.9638	1.2341	0.1530	0.0180
NP233_Cg28	15.2848	1.2347	0.1550	0.0200
NP233_Cg29	15.9700	1.4938	0.1930	0.0240
NP233_Cg30	17.4437	1.5021	0.1860	0.0220
NP233_Cg31	17.6767	1.4487	0.1370	0.0180
NP233_Cg32	17.3457	1.4883	0.1730	0.0230
NP233_Cg33	16.1369	1.3235	0.1400	0.0190
NP233_Cg34	15.4893	1.2830	0.2150	0.0200
NP233_Cg35	15.7796	1.2108	0.2180	0.0200
NP233_Cg36	16.8105	1.3121	0.1650	0.0160
NP233_Cg37	16.6594	1.3181	0.1700	0.0220
NP233_Cg38	16.8411	1.3921	0.1300	0.0170
NP233_Cg39	16.6295	1.3390	0.1490	0.0180
NP233_Cg40	14.5868	1.0734	0.2590	0.0180
NP233_Cg41	15.1846	1.2012	0.2660	0.0250
NP233_Cg42	15.4634	1.1531	0.2020	0.0210
NP233_Cg43	16.5109	1.2757	0.1900	0.0190
NP233_Cg44	16.9645	1.4890	0.1870	0.0210
NP233_Cg45	16.2502	1.3145	0.1600	0.0180
NP233_Cg46	12.0138	0.8884	0.3160	0.0220
NP233_Cg47	14.2502	1.0877	0.2850	0.0200
NP233_Cg48	13.6415	1.0490	0.2560	0.0240
NP233_Cg49	17.2167	1.3362	0.1880	0.0190
NP233_Cg50	15.0367	1.2232	0.1810	0.0210
NP233_Cg51	16.8105	1.3371	0.1780	0.0190
NP233_Cg52	12.5680	0.9654	0.4130	0.0290
NP233_Cg53	12.9910	0.9729	0.3680	0.0240
NP233_Cg54	14.1198	1.0896	0.2810	0.0210
NP233_Cg55	15.0857	1.1889	0.2200	0.0220
NP233_Cg56	15.3101	1.1962	0.1850	0.0190
NP233_Cg57	16.1651	1.4243	0.1950	0.0260

Spot ID	238U/206Pb	2s	207Pb/206Pb	2s
NP233_Cg58	15.6993	1.2665	0.1660	0.0200
NP236_Ag01	6.7169	0.5604	0.6040	0.0260
NP236_Ag02	7.5306	0.4799	0.5290	0.0200
NP236_Ag03	9.1078	0.5608	0.4680	0.0150
NP236_Ag04	8.8131	0.5630	0.4640	0.0210
NP236_Ag05	9.2074	0.5858	0.4340	0.0230
NP236_Ag06	8.5924	0.7057	0.4770	0.0220
NP236_Ag07	9.9813	0.7403	0.4380	0.0190
NP236_Ag08	9.0016	0.5575	0.4630	0.0190
NP236_Ag09	8.9580	0.5646	0.5010	0.0200
NP236_Ag10	7.3049	0.4369	0.5220	0.0180
NP236_Ag11	6.9749	0.5647	0.5740	0.0160
NP236_Ag12	6.5322	0.4799	0.5910	0.0230
NP236_Ag13	7.2083	0.5145	0.5310	0.0200
NP236_Ag14	8.7881	0.5556	0.4850	0.0190
NP236_Bg01	4.6593	0.2861	0.6750	0.0230
NP236_Bg02	4.3507	0.2945	0.6770	0.0240
NP236_Bg03	4.4532	0.3420	0.6760	0.0190
NP236_Bg04	3.7807	0.2909	0.7150	0.0240
NP236_Bg05	5.0893	0.3579	0.6550	0.0190
NP236_Bg06	6.1139	0.3846	0.6130	0.0210
NP236_Bg07	5.2929	0.3222	0.6600	0.0200
NP236_Bg08	4.8018	0.3307	0.6790	0.0270
NP236_Bg09	5.4358	0.3453	0.6640	0.0200
NP236_Bg10	5.9376	0.3587	0.6190	0.0200
NP236_Bg11	5.0588	0.3822	0.6560	0.0220
NP236_Bg12	5.3852	0.4634	0.6270	0.0290
NP236_Bg13	4.5139	0.3012	0.6600	0.0230
NP236_Bg14	5.4776	0.3639	0.6490	0.0230
NP236_Bg15	5.2479	0.3331	0.6210	0.0210
NP236_Cg01	12.9728	1.1059	0.2560	0.0320
NP236_Cg02	8.5448	0.7606	0.5050	0.0490
NP236_Cg03	7.2364	0.7674	0.6400	0.0910
NP236_Cg04	14.6560	1.4392	0.2770	0.0390
NP236_Cg05	9.0367	0.8917	0.5610	0.0700
NP236_Cg06	13.0643	1.0257	0.3160	0.0340
NP236_Cg07	11.6952	0.8644	0.3300	0.0280
NP236_Cg08	10.6467	0.8884	0.3500	0.0340
NP236_Cg09	13.8662	1.1802	0.2410	0.0320
NP236_Cg10	2.3873	0.2011	0.8000	0.0270
NP236_Cg11	7.0385	0.5294	0.5380	0.0380
NP236_Cg12	11.7546	1.0586	0.3760	0.0360
NP236_Cg13	9.6687	0.8296	0.4530	0.0440
NP236_Dg01	7.2819	0.4812	0.5630	0.0260
NP236_Dg02	8.5134	0.5474	0.5320	0.0220
NP236_Dg03	6.8057	0.4517	0.5900	0.0290
NP236_Dg04	7.7968	0.4947	0.5360	0.0250
NP236_Dg05	6.5184	0.4193	0.5700	0.0220
NP236_Dg06	6.7364	0.4387	0.5520	0.0250
NP236_Dg07	6.6590	0.4165	0.5650	0.0270
NP236_Dg08	6.3097	0.3932	0.5850	0.0250
NP236_Dg09	6.0699	0.4213	0.5950	0.0250
NP236_Dg10	4.9269	0.4700	0.6000	0.0240
NP236_Eg01	7.4759	0.6213	0.5380	0.0260
NP236_Eg02	7.8497	0.8236	0.6250	0.0500
NP236_Eg03	8.3824	0.5774	0.4860	0.0190
NP236_Eg04	8.6324	0.6328	0.4590	0.0280
NP236_Eg05	6.5926	0.4450	0.4980	0.0280
NP236_Eg06	6.9854	0.5573	0.5080	0.0310
NP236_Eg07	8.8048	0.5845	0.4620	0.0260
NP236_Eg08	8.4900	0.5609	0.4810	0.0230
NP236_Eg09	9.0988	0.6185	0.4880	0.0250
NP236_Eg10	8.0474	0.6357	0.5030	0.0320
NP236_Eg11	8.1825	0.6349	0.4800	0.0360
NP236_Eg12	7.8831	0.5152	0.5420	0.0210
NP236_Eg13	8.5056	0.5570	0.5140	0.0230
NP236_Eg14	8.4667	0.5640	0.4860	0.0240
NP236_Eg15	7.9644	0.5715	0.4990	0.0310
NP236_Eg16	7.1526	0.6308	0.5760	0.0280
NP236_Eg17	7.4220	0.4822	0.5020	0.0230
NP236_Eg18	6.2249	0.4433	0.5490	0.0220

C. Supplementary Material for Chapter 4

Appendix C.1: LA-ICP-MS zircon U-Pb data tables. Discordia distance after Vermeesch (2020) was used as discordance criterion -1<d_c<5.

Sample 20101020-3 Sample Type: igneous Latitude: 38.9188 Longitude: 75.4938

	Conventional concordia					Ages										Discordance		Conc. Dist., dc	Th/U
Sample # _grain number	207Pb/235U	±2σ	206Pb/238U	±2σ	error corr. 206/238 vs 207/235	207Pb/235U	±2σ	206Pb/238U	±2σ	207Pb/206Pb	±2σ	Best Age	±1σ [abs]	±1σ [%]	206/238 207/206	206/238 207/235		
20101020-3_g188	0.271789	0.0266353	0.0385784	0.002469	0.65	256.1	21.2	258.2	16.2	236.4	159	258.2	8.1	3.14%	-0.09	-0.01	-1	0.12
20101020-3_g189	0.288266	0.0276735	0.0418686	0.0026796	0.67	257.2	21.8	264.41	16.58	192	165.8	264.41	8.29	3.14%	-0.38	-0.03	-3.2	0.15
20101020-3_g190	0.30041	0.03665	0.0431234	0.0028461	0.54	266.7	28.6	272.16	17.58	219	238	272.16	8.79	3.23%	-0.24	-0.02	-2.2	0.13
20101020-3_g191	0.328754	0.0295879	0.0374006	0.0023936	0.71	288.6	22.6	236.7	14.88	733.4	134.2	236.7	7.44	3.14%	0.68	0.18	23	0.14
20101020-3_g192	0.326353	0.0306772	0.0384403	0.0023833	0.66	286.8	23.4	243.16	14.8	659.4	151.4	243.16	7.4	3.04%	0.63	0.15	19	0.2
20101020-3_g193	0.286817	0.0269608	0.0408667	0.0026155	0.68	244.1	21.2	244.02	15.32	245.2	171.6	244.02	7.66	3.14%	0	0	-0.01	0.19
20101020-3_g194	0.307676	0.033229	0.0420444	0.0027749	0.61	272.4	25.8	265.49	17.16	332	194	265.49	8.58	3.23%	0.2	0.03	3	0.18
20101020-3_g195	0.314072	0.0276383	0.0419008	0.0026817	0.73	277.3	21.4	264.6	16.6	386.1	135	264.6	8.3	3.14%	0.31	0.05	5.3	0.15
20101020-3_g196	0.322275	0.0393176	0.0445926	0.0029431	0.54	283.7	30.2	281.24	18.16	304	234	281.24	9.08	3.23%	0.07	0.01	0.96	0.17
20101020-3_g197	0.489423	0.0489423	0.0456449	0.0030126	0.66	404.5	33.4	287.73	18.58	1140.9	149.4	287.73	9.29	3.23%	0.75	0.29	42	0.17
20101020-3_g198	0.414317	0.0397744	0.0355272	0.0023448	0.69	352	28.6	225.05	14.6	1305.9	135	225.05	7.3	3.24%	0.83	0.36	54	0.16
20101020-3_g199	0.27583	0.0270313	0.0389168	0.0024907	0.65	267.3	24.4	269.16	17.4	251.2	185.8	269.16	8.7	3.23%	-0.07	-0.01	-0.67	0.2
20101020-3_g200	0.353203	0.0339075	0.0471152	0.0030154	0.67	307.1	25.4	296.79	18.56	386.4	160	296.79	9.28	3.13%	0.23	0.03	4	0.16
20101020-3_g201	0.402308	0.0450585	0.0438766	0.0029836	0.61	343.3	32.6	276.82	18.42	822.2	185.2	276.82	9.21	3.33%	0.66	0.19	25	0.18
20101020-3_g202	0.337768	0.0317502	0.0451737	0.0028911	0.68	295.5	24	284.82	17.84	380.6	155	284.82	8.92	3.13%	0.25	0.04	4.1	0.14
20101020-3_g203	0.301168	0.0313215	0.0426366	0.002814	0.63	268.4	28.4	266.91	17.26	282	230	266.91	8.63	3.23%	0.05	0.01	0.57	0.15
20101020-3_g204	0.302591	0.0363109	0.0422743	0.0027901	0.55	247.3	21.6	246.12	15.46	259	171.2	246.12	7.73	3.14%	0.05	0	0.59	0.18
20101020-3_g205	0.398341	0.0414275	0.0452893	0.0029891	0.63	340.4	30	285.54	18.44	734.7	171	285.54	9.22	3.23%	0.61	0.16	21	0.15
20101020-3_g206	0.277859	0.0261187	0.0382498	0.0025245	0.7	249	20.8	241.98	15.68	315.3	152.6	241.98	7.84	3.24%	0.23	0.03	3.3	0.12
20101020-3_g207	0.295304	0.0313022	0.0415759	0.002744	0.62	262.7	24.6	262.59	16.98	263.9	191	262.59	8.49	3.23%	0	0	-0.01	0.17

Sample 15NP213	Sample Type: igneous					Latitude:	38.924	Longitude:	75.4978									
	Conventional concordia					Ages									Discordance		Conc. Dist., Th/U	
Sample # _grain number	207Pb 235U	±2σ	206Pb 238U	±2σ	error corr. 206/238 vs 207/235	207Pb 235U	±2σ	206Pb 238U	±2σ	207Pb 206Pb	±2σ	Best Age	±1σ [abs]	±1σ [%]	206/238 207/206	206/238 207/235		
15NP213_g01	0.2896	0.0037	0.03756	0.00026	0.30192	258.1	2.9	237.7	1.6	449	27	237.7	0.8	0.0034	0.47	0.08	9.3	0.46
15NP213_g02_c	0.2591	0.0045	0.03706	0.00032	0.29188	234.1	3.7	234.6	2	231	37	234.6	1	0.0043	-0.02	0	-0.31	0.61
15NP213_g03	0.274	0.01	0.0377	0.001	0.38615	245	8.1	238.6	6.5	218	59	238.6	3.25	0.0136	-0.09	0.03	3.4	0.48
15NP213_g04	0.2783	0.0059	0.03887	0.00047	0.47957	249	4.7	245.8	2.9	284	42	245.8	1.45	0.0059	0.13	0.01	1.6	0.55
15NP213_g05_c	0.2696	0.0059	0.03815	0.0004	0.40976	242.6	4.6	241.3	2.5	281	45	241.3	1.25	0.0052	0.14	0.01	0.47	0.55
15NP213_g06	0.2778	0.0084	0.03836	0.00078	0.78698	248.4	6.6	242.6	4.9	280	45	242.6	2.45	0.0101	0.13	0.02	2.9	0.64
15NP213_g07	0.2971	0.0062	0.03701	0.00037	0.25641	263.8	4.9	234.3	2.3	522	43	234.3	1.15	0.0049	0.55	0.11	13	0.74
15NP213_g08	0.2707	0.0072	0.03686	0.00044	0.63795	243.1	5.8	233.3	2.7	270	47	233.3	1.35	0.0058	0.14	0.04	4.8	0.47
15NP213_g10	0.346	0.021	0.0435	0.002	0.17904	301	16	274	12	550	130	274	6	0.0219	0.5	0.09	11	0.43
15NP213_g11	0.2938	0.0044	0.04095	0.00028	0.52727	261.4	3.4	258.7	1.7	272	28	258.7	0.85	0.0033	0.05	0.01	1.2	0.61
15NP213_g12	0.265	0.0043	0.03702	0.00031	0.068712	238.8	3.5	234.3	1.9	275	36	234.3	0.95	0.0041	0.15	0.02	2.1	0.58
15NP213_g13	0.256	0.0055	0.03642	0.00032	0.26211	231.1	4.4	230.6	2	235	49	230.6	1	0.0043	0.02	0	0.4	0.46
15NP213_g14	0.255	0.0044	0.03687	0.00029	0.42883	230.4	3.6	233.4	1.8	222	36	233.4	0.9	0.0039	-0.05	-0.01	-1.3	0.43
15NP213_g15	0.2599	0.0045	0.03722	0.0003	0.45302	234.4	3.6	235.6	1.8	224	33	235.6	0.9	0.0038	-0.05	-0.01	-0.47	0.55
15NP213_g16	0.343	0.014	0.04748	0.00077	0.19344	299	11	299	4.7	343	90	299	2.35	0.0079	0.13	0	0.16	0.69
15NP213_g17	0.2626	0.0072	0.03756	0.00038	0.2067	236.3	5.8	237.7	2.4	209	55	237.7	1.2	0.005	-0.14	-0.01	-0.44	0.43
15NP213_g18	0.2691	0.0053	0.03772	0.00029	0.5349	241.7	4.2	238.6	1.8	271	41	238.6	0.9	0.0038	0.12	0.01	1.5	0.37
15NP213_g19	0.2738	0.0051	0.0383	0.00031	0.42268	245.8	4.1	242.3	1.9	268	39	242.3	0.95	0.0039	0.1	0.01	1.6	0.68
15NP213_g20	0.2818	0.0084	0.03955	0.0005	0.16253	251.7	6.6	250.1	3.1	316	67	250.1	1.55	0.0062	0.21	0.01	0.91	0.47
15NP213_g21	0.2764	0.0051	0.03867	0.00029	0.37147	248	4	244.6	1.8	269	37	244.6	0.9	0.0037	0.09	0.01	1.5	0.49
15NP213_g23	0.3129	0.0093	0.03617	0.00037	0.20269	275.9	7.2	229.1	2.3	664	65	229.1	1.15	0.005	0.65	0.17	21	0.47
15NP213_g24	0.2509	0.0093	0.03739	0.00041	0.19201	226.5	7.6	236.6	2.5	102	74	236.6	1.25	0.0053	-1.32	-0.04	-4.5	0.62
15NP213_g25	0.3073	0.0049	0.04045	0.00035	0.73912	271.9	3.8	255.6	2.1	408	34	255.6	1.05	0.0041	0.37	0.06	7.4	0.44
15NP213_g26	0.2643	0.0055	0.03713	0.0003	0.096401	237.8	4.4	235	1.9	261	45	235	0.95	0.004	0.1	0.01	1.5	0.51
15NP213_g27	0.3803	0.0097	0.03984	0.00039	0.48344	327.6	7	251.8	2.4	921	44	251.8	1.2	0.0048	0.73	0.23	30	0.59
15NP213_g28	0.2926	0.0045	0.03795	0.00028	0.50794	260.4	3.5	240.1	1.8	444	32	240.1	0.9	0.0037	0.46	0.08	9.3	0.52
15NP213_g29	0.2747	0.0061	0.03961	0.00032	0.18906	246.1	4.9	250.4	2	197	46	250.4	1	0.004	-0.27	-0.02	-1.8	0.55
15NP213_g30	0.2793	0.0073	0.03759	0.00044	0.34546	249.7	5.7	237.8	2.7	340	53	237.8	1.35	0.0057	0.3	0.05	5.6	0.65
15NP213_g31	0.2651	0.0071	0.03833	0.00031	0.27273	238.2	5.7	242.5	1.9	203	50	242.5	0.95	0.0039	-0.19	-0.02	-1.7	0.43
15NP213_g32	0.2847	0.0051	0.03986	0.00039	0.58171	254.2	4.1	252	2.4	267	29	252	1.2	0.0048	0.06	0.01	1.1	0.52
15NP213_g33	0.2572	0.0056	0.03631	0.00034	0.16923	233	4.5	229.9	2.1	236	49	229.9	1.05	0.0046	0.03	0.01	1.2	0.4

Sample 15NP213 continued

	Conventional concordia					Ages									Discordance		Conc. Dist., Th/U	
Sample #	207Pb	±2σ	206Pb	±2σ	error corr.	207Pb	±2σ	206Pb	±2σ	207Pb	±2σ	Best Age	±1σ [abs]	±1σ [%]	206/238	206/238		
_grain number	235U		238U		207/235	235U		238U		206Pb					207/206	207/235		
15NP213_g34	0.269	0.0067	0.03761	0.00037	0.11329	241.5	5.3	238	2.3	264	47	238	1.15	0.0048	0.1	0.01	1.8	0.41
15NP213_g35	0.2633	0.0051	0.03672	0.00042	0.51649	237.1	4.1	232.5	2.6	271	40	232.5	1.3	0.0056	0.14	0.02	2.3	0.38
15NP213_g36	0.2639	0.0046	0.03707	0.0003	0.20717	237.6	3.7	234.6	1.8	254	33	234.6	0.9	0.0038	0.08	0.01	1.5	0.5
15NP213_g37	0.2655	0.0044	0.03609	0.00028	0.69408	238.9	3.6	228.6	1.8	338	31	228.6	0.9	0.0039	0.32	0.04	5.2	0.5
15NP213_g38	0.2705	0.0049	0.03793	0.00027	0.30841	243.3	4	240	1.7	267	40	240	0.85	0.0035	0.1	0.01	1.4	0.48
15NP213_g39	0.319	0.012	0.03736	0.00036	0.33508	281	9.2	236.4	2.2	604	93	236.4	1.1	0.0047	0.61	0.16	20	0.45
15NP213_g40	0.3508	0.0057	0.03825	0.00034	0.31854	305.1	4.3	242	2.1	772	38	242	1.05	0.0043	0.69	0.21	26	0.62
15NP213_g41	0.2651	0.007	0.03689	0.00035	0.052968	238.5	5.7	233.5	2.2	329	59	233.5	1.1	0.0047	0.29	0.02	2.5	0.42
15NP213_g42	0.3377	0.0072	0.03725	0.00025	0.31913	295.5	5.4	235.8	1.5	784	44	235.8	0.75	0.0032	0.7	0.2	26	0.39
15NP213_g43	0.2556	0.0054	0.03615	0.00027	0.39191	230.8	4.4	228.9	1.7	238	41	228.9	0.85	0.0037	0.04	0.01	1.1	0.47
15NP213_g44	0.2682	0.005	0.0374	0.0004	0.18875	241	4	236.7	2.5	249	33	236.7	1.25	0.0053	0.05	0.02	2.1	0.43
15NP213_g45	0.2783	0.0056	0.03952	0.00033	0.57142	249	4.4	249.8	2	238	41	249.8	1	0.004	-0.05	0	-0.25	0.42
15NP213_g46	0.3343	0.0083	0.03703	0.00029	0.287	292.9	6.2	234.4	1.8	765	47	234.4	0.9	0.0038	0.69	0.2	25	0.44

Sample 15NP220	Sample Type: igneous					Latitude:	39.3215	Longitude:	74.9084									
	Conventional concordia					Ages									Discordance		Conc. Dist., Th/U	
Sample # _grain number	207Pb 235U	±2σ	206Pb 238U	±2σ	error corr. 206/238 vs 207/235	207Pb 235U	±2σ	206Pb 238U	±2σ	207Pb 206Pb	±2σ	Best Age	±1σ [abs]	±1σ [%]	206/238 207/206	206/238 207/235		
15NP220_g01	0.2821	0.0056	0.03971	0.00035	0.28242	252	4.4	251	2.2	245	42	251	1.1	0.0044	-0.02	0	0.57	0.4
15NP220_g02	0.504	0.034	0.04206	0.00034	0.36422	407	23	265.6	2.1	1190	140	265.6	1.05	0.004	0.78	0.35	52	0.32
15NP220_g03	0.414	0.023	0.04179	0.00055	0.061756	351	16	263.9	3.4	910	110	263.9	1.7	0.0064	0.71	0.25	33	0.39
15NP220_g04	0.2693	0.0073	0.03817	0.00037	0.13468	241.8	5.9	241.5	2.3	222	59	241.5	1.15	0.0048	-0.09	0	0.3	0.47
15NP220_g05	0.356	0.014	0.03706	0.00068	0.25442	311	12	234.5	4.2	893	87	234.5	2.1	0.009	0.74	0.25	31	0.51
15NP220_g06	0.2779	0.0061	0.03934	0.00036	0.23239	248.6	4.9	248.7	2.2	233	48	248.7	1.1	0.0044	-0.07	0	0.11	0.47
15NP220_g07	0.2727	0.0066	0.0393	0.00044	0.21525	244.4	5.3	248.5	2.7	198	51	248.5	1.35	0.0054	-0.26	-0.02	-1.7	0.41
15NP220_g08	0.2792	0.0069	0.03948	0.0004	0.15001	249.7	5.5	249.6	2.5	243	52	249.6	1.25	0.005	-0.03	0	0.19	0.42
15NP220_g09	0.2698	0.0051	0.03838	0.0003	0.32005	242.3	4.1	242.8	1.9	227	39	242.8	0.95	0.0039	-0.07	0	-0.12	0.37
15NP220_g10	0.2714	0.0054	0.03811	0.00033	0.41466	243.5	4.3	241.1	2.1	253	39	241.1	1.05	0.0044	0.05	0.01	1.3	0.43
15NP220_g11	0.2715	0.0076	0.03824	0.00048	0.2733	244.2	6.2	241.9	3	249	59	241.9	1.5	0.0062	0.03	0.01	0.91	0.44
15NP220_g12	0.39	0.0078	0.03886	0.0003	0.54904	333.9	5.7	245.7	1.9	999	37	245.7	0.95	0.0039	0.75	0.26	36	0.4
15NP220_g13	0.2847	0.0066	0.03987	0.00038	0.29894	253.9	5.2	252	2.4	262	49	252	1.2	0.0048	0.04	0.01	1	0.48
15NP220_g14	0.2785	0.007	0.03916	0.00047	0.011522	249.1	5.6	247.6	2.9	251	60	247.6	1.45	0.0059	0.01	0.01	0.83	0.54
15NP220_g15	0.2713	0.0062	0.03874	0.00038	0.32108	243.4	4.9	245	2.4	222	46	245	1.2	0.0049	-0.1	-0.01	-0.59	0.44
15NP220_g16	0.2827	0.0066	0.03915	0.00036	0.14835	252.4	5.2	247.5	2.2	288	50	247.5	1.1	0.0044	0.14	0.02	2.3	0.68
15NP220_g17	0.295	0.013	0.04051	0.00064	0.080196	262	10	256	3.9	318	99	256	1.95	0.0076	0.19	0.02	2.8	0.35
15NP220_g18	0.2935	0.0092	0.04081	0.00042	0.3367	260.9	7.2	257.8	2.6	289	68	257.8	1.3	0.005	0.11	0.01	1.5	0.58
15NP220_g19	0.292	0.016	0.0414	0.00073	0.1747	259	13	261.5	4.5	250	110	261.5	2.25	0.0086	-0.05	-0.01	-0.59	0.78
15NP220_g20	0.2749	0.0079	0.03953	0.0004	0.24552	246	6.3	249.9	2.5	212	60	249.9	1.25	0.005	-0.18	-0.02	-1.5	0.41
15NP220_g21	0.565	0.014	0.04201	0.00038	0.14491	453.6	9.1	265.3	2.4	1572	46	265.3	1.2	0.0045	0.83	0.42	64	0.42
15NP220_g22	0.2698	0.007	0.03882	0.00043	0.29849	242.1	5.6	245.5	2.7	223	51	245.5	1.35	0.0055	-0.1	-0.01	-1.4	0.44
15NP220_g23	0.2733	0.0054	0.03884	0.00039	0.34296	245	4.3	245.6	2.4	246	42	245.6	1.2	0.0049	0	0	-0.14	0.42
15NP220_g24	0.2848	0.0058	0.03987	0.00042	0.44523	254.1	4.5	252	2.6	276	42	252	1.3	0.0052	0.09	0.01	1.1	0.61
15NP220_g25	0.4889	0.007	0.05393	0.00045	0.42895	404.1	4.8	338.6	2.7	813	24	338.6	1.35	0.004	0.58	0.16	21	0.1
15NP220_g26	0.2795	0.0077	0.03917	0.00047	0.53521	249.7	6.1	247.7	2.9	274	53	247.7	1.45	0.0059	0.1	0.01	1.2	0.43
15NP220_g27	0.27	0.01	0.03908	0.00043	0.082807	241.9	8.3	247.1	2.7	196	79	247.1	1.35	0.0055	-0.26	-0.02	-2	0.27
15NP220_g28	0.274	0.0043	0.03924	0.00033	0.35385	245.7	3.4	248.1	2	210	33	248.1	1	0.004	-0.18	-0.01	-1	0.32
15NP220_g29	0.2691	0.0055	0.03819	0.00037	0.30391	241.6	4.4	241.6	2.3	225	43	241.6	1.15	0.0048	-0.07	0	0.17	0.51
15NP220_g30	0.2797	0.0092	0.03948	0.00046	0.13799	250	7.3	249.6	2.8	237	70	249.6	1.4	0.0056	-0.05	0	0.36	0.49
15NP220_g31	0.2793	0.0094	0.03856	0.00055	0.21051	249.8	7.4	243.9	3.4	272	76	243.9	1.7	0.007	0.1	0.02	2.8	0.64

Sample 15NP220 continued

	Conventional concordia					Ages									Discordance		Conc. Dist., Th/U	
Sample # _grain number	207Pb 235U	±2σ	206Pb 238U	±2σ	error corr. 206/238 vs 207/235	207Pb 235U	±2σ	206Pb 238U	±2σ	207Pb 206Pb	±2σ	Best Age	±1σ [abs]	±1σ [%]	206/238 207/206	206/238 207/235		
15NP220_g33	0.2973	0.0061	0.03982	0.00036	0.24455	264	4.8	251.7	2.2	343	44	251.7	1.1	0.0044	0.27	0.05	5.5	0.45
15NP220JR_g01	0.2595	0.0052	0.03637	0.00041	0.20959	234.1	4.2	230.3	2.5	257	45	230.3	1.25	0.0054	0.1	0.02	1.9	0.53
15NP220JR_g02	0.2641	0.0051	0.03754	0.00029	0.0020528	237.6	4.1	237.6	1.8	234	40	237.6	0.9	0.0038	-0.02	0	0.19	0.44
15NP220JR_g03_c	0.245	0.0055	0.03463	0.00041	0.32577	222.3	4.5	219.4	2.6	249	50	219.4	1.3	0.0059	0.12	0.01	1.5	0.54
15NP220JR_g04_c	0.2775	0.0075	0.03907	0.00055	0.17727	248.2	5.9	247.1	3.4	231	52	247.1	1.7	0.0069	-0.07	0	0.73	0.41
15NP220JR_g05	0.291	0.01	0.0404	0.001	0.38886	258.6	8.2	255.4	6.3	318	75	255.4	3.15	0.0123	0.2	0.01	1.8	0.42
15NP220JR_g06	0.2583	0.0044	0.03702	0.0003	0.10798	233.1	3.6	234.4	1.9	209	40	234.4	0.95	0.0041	-0.12	-0.01	-0.5	0.46
15NP220JR_g07	0.2788	0.0039	0.03943	0.0003	0.3627	249.9	3.1	249.3	1.9	242	27	249.3	0.95	0.0038	-0.03	0	0.18	0.35
15NP220JR_g08	0.2535	0.0069	0.03615	0.00044	0.11622	229.2	5.6	228.9	2.8	228	61	228.9	1.4	0.0061	0	0	0.24	0.55
15NP220JR_g09	0.2717	0.0039	0.03887	0.00028	0.30261	243.8	3.1	245.8	1.8	239	31	245.8	0.9	0.0037	-0.03	-0.01	-0.81	0.46
15NP220JR_g10	0.2641	0.0057	0.0374	0.00033	0.25698	237.7	4.6	236.7	2.1	228	48	236.7	1.05	0.0044	-0.04	0	0.6	0.46
15NP220JR_g11	0.288	0.0058	0.0405	0.00046	0.050714	256.8	4.6	255.9	2.8	261	48	255.9	1.4	0.0055	0.02	0	0.47	0.89
15NP220JR_g12	0.2968	0.0089	0.04144	0.00054	0.46707	263.6	7	261.7	3.3	271	55	261.7	1.65	0.0063	0.03	0.01	0.93	0.5
15NP220JR_g13	0.2676	0.0042	0.03826	0.00028	0.28579	241.2	3.3	242	1.8	220	32	242	0.9	0.0037	-0.1	0	-0.59	0.45
15NP220JR_g14	0.2789	0.0059	0.03856	0.00042	0.46248	249.6	4.7	243.9	2.6	292	45	243.9	1.3	0.0053	0.16	0.02	2.7	0.67
15NP220JR_g15	0.2809	0.0081	0.03944	0.00056	0.18362	251.6	6.4	249.3	3.5	260	60	249.3	1.75	0.007	0.04	0.01	0.9	0.38
15NP220JR_g16	0.272	0.0058	0.03855	0.00045	0.33844	244.1	4.6	243.8	2.8	231	50	243.8	1.4	0.0057	-0.06	0	0.21	0.36
15NP220JR_g17	0.2855	0.0064	0.04005	0.00034	0.34925	254.7	5	253.1	2.1	256	50	253.1	1.05	0.0041	0.01	0.01	0.83	0.45
15NP220JR_g18	0.2807	0.0048	0.03985	0.00037	0.46455	250.9	3.8	251.9	2.3	242	34	251.9	1.15	0.0046	-0.04	0	-0.31	0.4
15NP220JR_g19	0.2706	0.0035	0.03849	0.0003	0.45263	243.5	2.8	243.5	1.9	236	26	243.5	0.95	0.0039	-0.03	0	-0.13	0.37
15NP220JR_g20	0.2787	0.004	0.03986	0.00027	0.35231	249.7	3.2	251.9	1.7	226	31	251.9	0.85	0.0034	-0.11	-0.01	-1	0.46
15NP220JR_g21	0.267	0.0042	0.03808	0.0003	0.31476	240.1	3.3	240.9	1.9	229	35	240.9	0.95	0.0039	-0.05	0	-0.29	0.46
15NP220JR_g22	0.2742	0.007	0.0384	0.00041	0.3813	245.8	5.6	242.9	2.5	277	54	242.9	1.25	0.0051	0.12	0.01	1.4	0.46
15NP220JR_g23	0.2724	0.0044	0.03816	0.00041	0.33951	244.7	3.5	241.4	2.6	257	36	241.4	1.3	0.0054	0.06	0.01	1.5	0.4
15NP220JR_g24	0.2743	0.0036	0.03862	0.00027	0.44359	245.9	2.9	244.3	1.7	253	28	244.3	0.85	0.0035	0.03	0.01	0.85	0.73
15NP220JR_g25	0.272	0.011	0.03875	0.00046	0.32896	244.3	8.5	245.1	2.8	246	78	245.1	1.4	0.0057	0	0	-0.36	0.4
15NP220JR_g26	0.2682	0.0071	0.03715	0.00032	0.26239	241	5.6	235.2	2	292	56	235.2	1	0.0043	0.19	0.02	2.9	0.65
15NP220JR_g27	0.2741	0.0076	0.03744	0.0004	0.43464	245.6	6.1	236.9	2.5	310	57	236.9	1.25	0.0053	0.24	0.04	4.2	0.57
15NP220JR_g28	0.28	0.01	0.03741	0.00054	0.43627	250.1	8	236.7	3.4	366	71	236.7	1.7	0.0072	0.35	0.05	6.4	0.39
15NP220JR_g29	0.2649	0.005	0.03777	0.00045	0.31925	238.5	4	239	2.8	213	44	239	1.4	0.0059	-0.12	0	-0.18	0.38

Sample 15NP213 continued

	Conventional concordia					Ages									Discordance		Conc. Dist., Th/U	
Sample #	207Pb	±2σ	206Pb	±2σ	error corr.	207Pb	±2σ	206Pb	±2σ	207Pb	±2σ	Best Age	±1σ [abs]	±1σ [%]	206/238	206/238		
_grain number	235U		238U		206/238 vs 207/235	235U		238U		206Pb					207/206	207/235		
15NP220JR_g30	0.3501	0.0046	0.04911	0.00041	0.46654	304.7	3.5	309	2.5	284	27	309	1.25	0.004	-0.09	-0.01	-1.6	0.45
15NP220JR_g31	0.2812	0.0043	0.03871	0.00028	0.31035	251.7	3.3	244.8	1.8	309	33	244.8	0.9	0.0037	0.21	0.03	3.1	0.45
15NP220JR_g32	0.316	0.012	0.03839	0.0006	0.80876	279	8.9	242.9	3.7	616	64	242.9	1.85	0.0076	0.61	0.13	17	0.41
15NP220JR_g33	0.2657	0.0095	0.038	0.00042	0.36837	240	7.4	240.4	2.6	223	72	240.4	1.3	0.0054	-0.08	0	-0.55	0.53
15NP220JR_g34	0.306	0.034	0.0395	0.0039	0.94109	269	26	250	24	504	77	250	12	0.048	0.5	0.07	10	0.54
15NP220JR_g35	0.2633	0.004	0.03723	0.00029	0.20529	238	3	235.6	1.8	232	32	235.6	0.9	0.0038	-0.02	0.01	0.8	0.46
15NP220JR_g36	0.2701	0.005	0.03824	0.00028	0.18921	242.8	3.9	241.9	1.8	225	39	241.9	0.9	0.0037	-0.08	0	0.4	0.41
15NP220JR_g37	0.283	0.0064	0.03954	0.00049	0.36425	252.7	5.1	250	3.1	259	43	250	1.55	0.0062	0.03	0.01	1.4	0.36
15NP220JR_g38	0.2651	0.0048	0.03738	0.00028	0.40943	238.8	3.8	236.6	1.8	245	37	236.6	0.9	0.0038	0.03	0.01	1	0.51
15NP220JR_g39	0.307	0.01	0.04035	0.00052	0.53244	271.2	7.9	255	3.2	397	57	255	1.6	0.0063	0.36	0.06	7.3	0.44
15NP220JR_g40	0.294	0.044	0.0408	0.0015	0.51624	261	35	257.7	9.4	280	300	257.7	4.7	0.0182	0.08	0.01	1.7	0.45
15NP220JR_g41	0.2773	0.0051	0.03932	0.00053	0.78277	248.4	4.1	248.6	3.3	231	32	248.6	1.65	0.0066	-0.08	0	-0.05	0.41
15NP220JR_g42	0.2718	0.0044	0.03838	0.00034	0.44958	243.9	3.5	242.8	2.1	250	34	242.8	1.05	0.0043	0.03	0	0.62	0.44
15NP220JR_g43	0.282	0.01	0.04001	0.00051	0.34449	252.3	8.3	252.9	3.2	273	74	252.9	1.6	0.0063	0.07	0	-0.29	0.45
15NP220JR_g44	0.2711	0.0054	0.03882	0.0004	0.30268	244.5	4.2	245.5	2.5	225	39	245.5	1.25	0.0051	-0.09	0	-0.89	0.6
15NP220JR_g45	0.281	0.011	0.0398	0.00079	0.64855	251.2	8.7	251.6	4.9	271	84	251.6	2.45	0.0097	0.07	0	-0.07	0.49
15NP220JR_g46	0.2773	0.0053	0.03916	0.00031	0.29735	248.8	4.2	247.6	1.9	245	40	247.6	0.95	0.0038	-0.01	0	0.4	0.59
15NP220JR_g47	0.2715	0.0053	0.03858	0.00038	0.53585	243.8	4.2	244	2.4	237	40	244	1.2	0.0049	-0.03	0	-0.06	0.38
15NP220JR_g48	0.2598	0.0064	0.03739	0.00048	0.31673	234.3	5.2	236.6	3	206	52	236.6	1.5	0.0063	-0.15	-0.01	-1	0.52
15NP220JR_g49	0.2881	0.0053	0.04072	0.0004	0.4358	257	4.2	257.3	2.5	248	45	257.3	1.25	0.0049	-0.04	0	-0.1	0.52
15NP220JR_g50	0.2674	0.0077	0.03802	0.00054	0.5611	240.4	6.2	240.5	3.4	270	55	240.5	1.7	0.0071	0.11	0	0.03	0.45
15NP220JR_g51	0.2661	0.005	0.03832	0.00027	0.28264	239.2	4	242.4	1.6	208	39	242.4	0.8	0.0033	-0.17	-0.01	-1.3	0.61
15NP220JR_g52	0.2723	0.0045	0.03845	0.00028	0.31156	244.2	3.6	243.2	1.7	235	35	243.2	0.85	0.0035	-0.03	0	0.6	0.57
15NP220JR_g53	0.2734	0.0051	0.03851	0.0003	0.22959	245.2	4.1	243.6	1.9	257	40	243.6	0.95	0.0039	0.05	0.01	0.83	0.44
15NP220JR_g54	0.2776	0.0057	0.03883	0.00033	0.15109	248.4	4.5	245.7	2.1	264	40	245.7	1.05	0.0043	0.07	0.01	1.4	0.44
15NP220JR_g55	0.2754	0.0041	0.03913	0.00029	0.36398	246.8	3.2	247.5	1.8	241	33	247.5	0.9	0.0036	-0.03	0	-0.2	0.46
15NP220JR_g56	0.285	0.012	0.04099	0.00054	0.34636	254	9.7	259	3.4	190	89	259	1.7	0.0066	-0.36	-0.02	-1.9	0.43

Sample 17NP445	Sample Type: igneous					Latitude:	39.4053	Longitude:	74.4569									
	Conventional concordia					Ages									Discordance		Conc. Dist., Th/U	
Sample #	207Pb	±2σ	206Pb	±2σ	error corr.	207Pb	±2σ	206Pb	±2σ	207Pb	±2σ	Best Age	±1σ [abs]	±1σ [%]	206/238	206/238		
_grain number	235U		238U		206/238 vs 207/235	235U		238U		206Pb					207/206	207/235		
17NP445_g01	0.2964	0.0069	0.0408	0.00052	0.32834	263.3	5.4	257.8	3.3	310	49	257.8	1.65	0.0064	0.17	0.02	2.5	0.57
17NP445_g01b	0.2995	0.0052	0.04101	0.00041	0.48307	265.8	4.1	259.1	2.5	314	35	259.1	1.25	0.0048	0.17	0.03	3	0.42
17NP445_g02	0.3035	0.0059	0.04182	0.00041	0.1193	269	4.6	264.1	2.6	308	50	264.1	1.3	0.0049	0.14	0.02	2.1	0.4
17NP445_g02b	0.2923	0.0034	0.04125	0.00032	0.28704	260.6	2.7	260.6	2	266	26	260.6	1	0.0038	0.02	0	-0.09	0.38
17NP445_g03	8.357	0.12	0.4297	0.0048	0.90989	2270.5	13	2306	22	2241.3	17	2241.3	8.5	0.0038	-0.03	-0.02	-3	0.51
17NP445_g03b	7.789	0.093	0.4094	0.0044	0.92743	2209	11	2214	20	2202.1	7.7	2202.1	3.85	0.0017	-0.01	0	-0.48	0.49
17NP445_g04	0.2764	0.0044	0.0386	0.00038	0.307	247.7	3.5	244.1	2.4	277	33	244.1	1.2	0.0049	0.12	0.01	1.7	0.46
17NP445_g04b	0.2904	0.0062	0.0409	0.00055	0.71415	258.8	4.9	258.4	3.4	261	32	258.4	1.7	0.0066	0.01	0	0.2	0.55
17NP445_g05	0.2957	0.0072	0.04194	0.00057	0.46508	262.9	5.7	264.8	3.5	266	52	264.8	1.75	0.0066	0	-0.01	-0.77	0.45
17NP445_g05b	0.3242	0.0067	0.04529	0.00069	0.5982	284.8	5.2	285.5	4.2	280	36	285.5	2.1	0.0074	-0.02	0	-0.17	0.49
17NP445_g06	6.468	0.12	0.3736	0.0042	0.59932	2043	16	2046	19	2050	26	2050	13	0.0063	0	0	-0.4	0.35
17NP445_g06b	8.81	0.1	0.4349	0.004	0.86321	2317.3	10	2329	18	2301	11	2301	5.5	0.0024	-0.01	-0.01	-0.74	0.24
17NP445_g07	0.2955	0.0056	0.04191	0.00041	0.26045	262.7	4.4	264.7	2.6	240	41	264.7	1.3	0.0049	-0.1	-0.01	-0.76	0.45
17NP445_g07b	0.3031	0.0053	0.04184	0.00035	0.31756	269.1	4	264.2	2.2	309	33	264.2	1.1	0.0042	0.14	0.02	1.9	0.26
17NP445_g08	8.707	0.11	0.431	0.0036	0.6727	2307.4	11	2310	16	2308	18	2308	9	0.0039	0	0	-0.18	0.86
17NP445_g08b	9.178	0.068	0.4425	0.0032	0.68718	2356.6	6.8	2361.4	14	2349.3	7.7	2349.3	3.85	0.0016	-0.01	0	-0.42	0.76
17NP445_g09	11.67	0.33	0.1322	0.0035	0.56907	2576	26	800	20	4603	37	800	10	0.0125	0.83	0.69	250	3.06
17NP445_g10	0.2965	0.01	0.04128	0.00054	0.045073	263.1	8.1	260.8	3.3	271	79	260.8	1.65	0.0063	0.04	0.01	1.2	0.52
17NP445_g10b	0.293	0.012	0.04161	0.00046	0.001	260.2	9.4	262.8	2.8	230	91	262.8	1.4	0.0053	-0.14	-0.01	-0.81	0.33
17NP445_g11	8.514	0.12	0.4336	0.0036	0.65807	2286.7	12	2321.8	16	2263	19	2263	9.5	0.0042	-0.03	-0.02	-2.6	0.56
17NP445_g11b	6.28	0.25	0.3589	0.0087	0.98324	2018	35	1974	41	2051	29	2051	14.5	0.0071	0.04	0.02	8.1	0.21
17NP445_g12	4.097	0.059	0.261	0.0032	0.8521	1654.2	12	1496	17	1862	19	1862	9.5	0.0051	0.2	0.1	17	0.33
17NP445_g12b	4.25	0.13	0.2554	0.006	0.98191	1677	26	1470	31	1956	17	1956	8.5	0.0043	0.25	0.12	41	0.43

Sample P09T19	Sample Type: igneous					Latitude:	39.3688	Longitude:	74.0494									
	Conventional concordia					Ages									Discordance		Conc. Dist., Th/U	
Sample #	207Pb	±2σ	206Pb	±2σ	error corr.	207Pb	±2σ	206Pb	±2σ	207Pb	±2σ	Best Age	±1σ [abs]	±1σ [%]	206/238	206/238		
_grain number	235U		238U		206/238 vs 207/235	235U		238U		206Pb					207/206	207/235		
P09T19_g01	0.294	0.012	0.04151	0.00049	0.29717	262.7	9.7	262.2	3.1	247	84	262.2	1.55	0.59%	-0.06	0	-0.21	0.45
P09T19_g02	0.296	0.015	0.04084	0.00062	0.0050255	262	11	258	3.8	270	110	258	1.9	0.74%	0.04	0.02	2.3	0.35
P09T19_g03	0.297	0.013	0.04102	0.0007	0.33869	263	10	259.1	4.4	287	89	259.1	2.2	0.85%	0.1	0.01	2.1	0.29
P09T19_g04	0.2984	0.0079	0.04185	0.00053	0.21723	264.7	6.2	264.3	3.3	255	58	264.3	1.65	0.62%	-0.04	0	0.37	0.59
P09T19_g05	0.2905	0.0085	0.04049	0.0004	0.16532	258.2	6.7	255.8	2.5	262	61	255.8	1.25	0.49%	0.02	0.01	1.3	0.34
P09T19_g06	0.2832	0.0076	0.03968	0.00045	0.0008376	252.8	6.1	250.8	2.8	250	63	250.8	1.4	0.56%	0	0.01	1	0.51
P09T19_g07	0.3026	0.0096	0.04216	0.00071	0.11974	267.8	7.5	266.2	4.4	279	71	266.2	2.2	0.83%	0.05	0.01	0.94	0.35
P09T19_g08	0.302	0.011	0.04279	0.00063	0.078321	267.4	8.4	270.1	3.9	248	78	270.1	1.95	0.72%	-0.09	-0.01	-0.9	0.36
P09T19_g09	0.303	0.01	0.04257	0.00055	0.091585	267.6	7.9	268.7	3.4	275	76	268.7	1.7	0.63%	0.02	0	0	0.36
P09T19_g10	0.2981	0.0079	0.04123	0.00037	0.1784	264.3	6.1	260.4	2.3	284	56	260.4	1.15	0.44%	0.08	0.01	1.9	0.38
P09T19_g11	0.2705	0.0095	0.03771	0.00056	0.2428	242.2	7.6	238.6	3.5	267	73	238.6	1.75	0.73%	0.11	0.01	2.1	0.36
P09T19_g12	0.2973	0.0066	0.04186	0.00049	0.35481	263.8	5.2	264.3	3	257	47	264.3	1.5	0.57%	-0.03	0	-0.03	0.42
P09T19_g13	0.297	0.013	0.04015	0.00056	0.010544	263	10	253.8	3.5	332	99	253.8	1.75	0.69%	0.24	0.03	4.5	0.4
P09T19_g14	0.291	0.0086	0.04172	0.00054	0.28505	258.7	6.8	263.5	3.3	226	60	263.5	1.65	0.63%	-0.17	-0.02	-1.8	0.39
P09T19_g15	0.306	0.01	0.04226	0.00057	0.19813	270.1	8	266.8	3.5	310	73	266.8	1.75	0.66%	0.14	0.01	1.8	0.4
P09T19_g16	0.489	0.052	0.04552	0.00076	0.42951	395	34	286.9	4.7	960	190	286.9	2.35	0.82%	0.7	0.27	41	0.38
P09T19_g17	0.2975	0.0099	0.04191	0.00061	0.1411	264.1	7.7	264.6	3.8	231	81	264.6	1.9	0.72%	-0.15	0	-0.09	0.52
P09T19_g18	0.29	0.013	0.04077	0.00057	0.21885	257	10	257.6	3.5	237	87	257.6	1.75	0.68%	-0.09	0	0.42	0.39
P09T19_g19	0.305	0.0091	0.0422	0.00051	0.32418	269.4	7.1	266.4	3.1	286	60	266.4	1.55	0.58%	0.07	0.01	1.6	0.44
P09T19_g20	0.2951	0.0078	0.04152	0.00039	0.21121	261.9	6.1	262.2	2.4	246	55	262.2	1.2	0.46%	-0.07	0	0.14	0.46
P09T19_g21	0.357	0.012	0.04363	0.00044	0.24382	308.7	8.8	275.2	2.7	532	69	275.2	1.35	0.49%	0.48	0.11	14	0.36
P09T19_g22	0.288	0.01	0.04198	0.00049	0.31528	256.6	7.9	265.1	3	166	67	265.1	1.5	0.57%	-0.6	-0.03	-3.5	0.48
P09T19_g23	0.302	0.0098	0.04237	0.0006	0.29503	267.2	7.6	267.5	3.7	253	66	267.5	1.85	0.69%	-0.06	0	0.19	0.5
P09T19_g24	0.306	0.017	0.04213	0.00096	0.35044	270	14	266	5.9	300	120	266	2.95	1.11%	0.11	0.01	2.1	0.41
P09T19_g25	0.296	0.01	0.04145	0.00041	0.084911	264	7.5	261.8	2.6	277	69	261.8	1.3	0.50%	0.05	0.01	0.63	0.49
P09T19_g26	0.2851	0.007	0.04094	0.00041	0.25015	255.2	5.7	258.7	2.6	210	54	258.7	1.3	0.50%	-0.23	-0.01	-1.7	0.49
P09T19_g27	0.2923	0.0097	0.04082	0.00062	0.078934	260	7.6	257.9	3.8	263	81	257.9	1.9	0.74%	0.02	0.01	1.1	0.6
P09T19_g28	0.262	0.0084	0.03743	0.00056	0.30179	235.7	6.8	236.9	3.5	213	62	236.9	1.75	0.74%	-0.11	-0.01	-0.29	0.36
P09T19_g29	0.2944	0.0094	0.04096	0.00073	0.087003	261.4	7.3	258.8	4.5	274	72	258.8	2.25	0.87%	0.06	0.01	1.4	0.42
P09T19_g30	0.305	0.011	0.04268	0.00051	0.040876	269.9	8.3	269.4	3.2	269	77	269.4	1.6	0.59%	0	0	0.37	0.42
P09T19_g31	0.3036	0.0097	0.04273	0.0006	0.29191	268.6	7.6	269.7	3.7	251	66	269.7	1.85	0.69%	-0.07	0	-0.22	0.38

Appendix C.2: Whole rock geochemistry data for Permo-Triassic volcanic rocks investigated for this chapter.

Sample	15NP204	15NP206	15NP208	15NP209	15NP211	15NP212	15NP219	15NP225	15NP226	15NP227	15NP228	15NP230	15NP231	15NP264	15NP270	17NP435	17NP446	17NP448	2011T52	99WT31	99WT36
Group	Triassic	Triassic	Triassic	Triassic	Triassic	Triassic	Triassic	Triassic	Triassic	Triassic	Triassic	Triassic	Triassic	Triassic	Triassic	Triassic	Permian	Permian	Triassic	Triassic	Triassic
Location	Qimgan/Gez	Qimgan/Gez	Qimgan/Gez	Qimgan/Gez	Qimgan/Gez	Qimgan/Gez	Qimgan/Gez	Qimgan/Gez	Qimgan/Gez	Qimgan/Gez	Qimgan/Gez	Qimgan/Gez	Qimgan/Gez	Qimgan/Gez	Qimgan/Gez	Qimgen - Akqiy	Biyertuokuoyi	Biyertuokuoyi	Qimgan/Gez	Qimgan/Gez	Qimgan/Gez
Latitude (N)	38.97001	38.9696	38.93393	38.93287	38.92758	38.92799	39.31897	39.32964	39.32882	39.3287	39.32125	39.32508	39.32508	38.93077	38.93031	39.322977	39.4053	39.40642	39.31871342	39.322222	39.313333
Longitude (E	75.46497	75.4664	75.48344	75.4864	75.49801	75.49825	74.92573	74.91448	74.91501	74.91522	74.89802	74.89732	74.89732	75.49877	75.50143	74.905659	74.4569	74.448821	74.92465617	74.917778	74.905833
SiO2 [wt%]	58.88	54.15	56.67	50.40	44.91	25.56	54.45	52.85	52.33	50.88	66.90	72.08	74.64	53.14	53.14	66.80	70.30	39.10	48.37	51.99	59.38
TiO2 [wt%]	1.22	1.14	0.46	0.73	0.46	0.33	0.74	0.83	0.77	0.89	0.35	0.20	0.18	0.88	0.97	0.25	0.35	0.49	0.76	0.89	0.63
Al2O3 [wt%]	14.88	17.65	16.54	16.05	10.03	6.74	18.02	21.09	20.06	21.19	17.11	13.88	13.26	16.43	15.51	14.20	15.00	12.10	18.76	18.62	14.50
Fe2O3 [wt%]	7.91	8.72	11.24	9.27	19.20	16.44	8.44	9.29	7.91	8.59	2.21	2.55	1.72	8.92	7.75	3.16	1.86	6.32	9.32	7.59	5.42
MnO [wt%]	0.18	0.25	0.24	0.27	0.22	0.90	0.15	0.15	0.28	0.16	0.08	0.05	0.04	0.15	0.10	0.07	0.02	0.36	0.15	0.13	0.12
MgO [wt%]	2.41	3.72	1.32	1.65	0.64	0.47	4.27	1.72	4.00	3.29	1.84	0.53	0.37	6.77	3.34	0.43	0.53	4.21	5.42	2.32	2.54
CaO [wt%]	3.71	2.99	4.01	8.87	9.70	22.84	5.37	8.69	6.17	7.20	2.46	1.15	1.11	8.19	5.46	4.89	1.02	15.80	9.36	10.65	6.50
Na2O [wt%]	4.91	7.04	3.94	3.22	<0.01	<0.01	4.77	3.26	4.35	4.64	5.96	2.86	2.97	2.69	2.68	<0.01	6.01	2.78	2.28	5.01	3.66
K2O [wt%]	2.82	0.19	0.58	0.45	0.08	0.02	1.09	0.48	0.33	0.32	1.26	4.96	4.35	0.95	2.24	0.33	1.62	1.04	0.33	0.66	1.91
P2O5 [wt%]	0.37	0.29	0.25	0.24	1.89	0.87	0.17	0.23	0.22	0.23	0.11	0.05	0.04	0.21	0.30	0.04	0.10	0.34	0.10	0.10	0.10
LOI [wt%]	2.36	3.44	4.45	8.53	12.37	25.52	2.32	1.23	3.38	2.41	1.37	1.44	1.05	1.26	7.94	9.67	2.96	17.10	4.98	1.81	4.91
Total [wt%]	99.66	99.58	99.70	99.68	99.50	99.68	99.80	99.81	99.80	99.79	99.65	99.75	99.74	99.59	99.44	99.90	99.70	99.70	99.85	99.80	99.67
Ti [ppm]	7313.71	6834.12	2757.63	4376.24	2727.65	1960.31	4436.18	4975.72	4616.03	5335.41	2098.20	1198.97	1079.07	5275.46	5815.00	1498.71	2098.20	2937.47	4556.08	5335.41	3776.75
V [ppm]	<10	<10	16.72	73.75	41.00	20.00	181.42	157.00	153.00	177.86	36.00	<10	9.03	188.76	124.94	21.00	35.00	96.00	236.00	213.00	91.33
Cr [ppm]	34.00	78.00	12.00	13.00	15.00	10.00	50.00	<10	11.00	10.00	13.00	<10	<10	215.00	21.00	<10	15.00	40.00	33.00	11.00	64.00
Ga [ppm]	14.00	15.00	24.00	18.00	10.00	<10	19.00	22.00	19.00	21.00	21.00	18.00	15.00	18.00	13.00	20.00	13.00	20.00	17.00	25.00	23.00
Rb [ppm]	82.00	12.00	27.00	22.00	70.00	99.00	16.00	<10	<10	<10	21.00	191.00	157.00	22.00	22.00	23.00	44.00	57.00	<10	11.00	75.00
Sr [ppm]	148.00	162.00	369.00	303.00	61.76	42.36	536.00	633.00	509.00	577.00	669.00	127.00	162.00	432.00	2745.00	70.00	319.00	264.00	448.00	494.00	294.00
Y [ppm]	25.79	29.18	18.20	22.99	107.00	61.00	14.00	16.00	14.00	19.00	2.30	24.00	22.00	14.84	18.00	53.00	10.00	25.00	15.00	18.00	30.00
Zr [ppm]	203.00	136.00	140.00	94.00	107.00	61.00	72.00	79.00	81.00	75.00	74.00	151.00	138.00	93.00	157.00	286.00	101.00	81.00	44.00	68.00	225.00
Nb [ppm]	11.00	<10	<10	<10	77.00	112.00	<10	<10	<10	<10	<10	12.00	10.00	<10	<10	15.00	<10	<10	<10	<10	11.00
Ba [ppm]	535.00	56.00	272.00	186.00	77.00	112.00	414.00	237.00	228.00	182.00	1548.00	976.00	978.00	289.00	1014.00	32.00	91.00	116.00	148.00	207.00	599.00
Ni [ppm]	16.00	29.00	<10	<10	6.02	17.00	15.00	<10	10.00	<10	<10	<10	<10	81.00	16.00	11.00	12.00	20.00	12.00	<10	33.00
Th [ppm]			8.09	5.41	3.58		0.40			0.52			20.63	3.33	4.01						11.94
U [ppm]			4.37	5.06	2.64		0.20			0.21			5.77	0.91	0.88						2.84
Hf [ppm]			3.59	2.57	8.72		1.81			1.86			2.89	2.29	2.34						5.04
Pb [ppm]			15.95	10.63	1.49		4.48			6.35			21.56	6.27	3.84						19.33
Cs [ppm]			1.61	1.83	64.40		1.20			0.18			3.73	0.34	0.30						4.27
Sc [ppm]	16.36	27.74	4.78	12.58	10.14	8.05	21.00	18.00	17.00	21.00	4.50	3.80	2.90	27.21	20.00	10.26	3.10	13.70	28.19	25.93	15.68
La [ppm]	28.07	18.10	18.43	13.67	48.20	35.52	7.20	8.20	7.30	8.90	14.00	40.00	32.00	13.60	15.00	45.43	13.55	15.32	4.56	7.56	26.67
Ce [ppm]	60.33	46.42	39.29	31.26	111.47	73.69	17.00	19.00	17.00	20.00	20.00	71.00	57.00	28.69	32.00	91.91	25.40	30.61	10.24	15.27	52.97
Pr [ppm]	6.51	5.43	4.28	3.44	15.13	8.67	2.00	2.20	2.00	2.50	1.80	7.20	6.10	3.03	3.30	8.97	2.39	1.95	1.23	1.66	5.73
Nd [ppm]	29.16	24.85	19.27	18.05	73.80	44.65	11.00	13.00	12.00	14.00	7.50	24.00	22.00	14.72	16.00	39.15	11.16	13.17	7.09	9.55	24.17
Sm [ppm]	6.12	5.31	3.89	4.09	18.34	10.41	2.50	3.00	2.60	3.00	1.40	4.60	4.20	3.19	3.70	8.20	2.22	2.78	1.76	2.29	5.07
Eu [ppm]	1.36	1.36	1.06	1.14	4.80	2.95	0.86	0.99	0.93	1.10	0.45	0.45	0.39	0.97	1.10	1.19	0.51	0.61	0.74	0.89	0.85
Gd [ppm]	5.71	5.33	3.42	3.99	22.28	12.34	2.70	3.00	2.70	3.30	0.93	3.90	3.50	3.19	3.50	7.75	1.87	2.84	2.12	2.65	4.94
Tb [ppm]	1.03	0.97	0.57	0.67	2.99	1.66	0.41	0.73	0.44	0.60	0.21	0.71	0.64	0.50	0.53	1.29	0.29	0.48	0.39	0.50	0.90
Dy [ppm]	5.12	4.90	3.15	3.71	12.80	7.87	2.60	3.00	2.50	3.30	0.58	4.20	3.70	2.81	3.20	7.69	1.32	2.81	2.24	2.72	4.89
Ho [ppm]	0.98	1.02	0.65	0.78	2.01	1.32	0.52	0.64	0.49	0.70	0.10	0.87	0.78	0.54	0.63	1.62	0.19	0.63	0.46	0.54	1.02
Er [ppm]	2.75	2.87	1.96	2.34	4.12	3.02	1.60	1.90	1.40	2.10	0.22	2.60	2.40	1.59	1.80	4.72	0.66	1.92	1.41	1.66	2.91
Tm [ppm]	0.30	0.32	0.25	0.30	0.40	0.33	0.21	0.22	0.18	0.27	0.01	0.34	0.33	0.20	0.24	0.64	0.07	0.26	0.22	NA	NA
Yb [ppm]	2.50	2.52	2.03	2.26	2.59	2.05	1.50	1.80	1.30	2.00	0.17	2.90	2.80	1.48	1.70	4.67	0.60	1.94	1.41	1.64	2.94
Lu [ppm]	0.38	0.38	0.32	0.35	0.38	0.31	0.23	0.29	0.18	0.30	0.03	0.45	0.44	0.22	0.26	0.68	< 0.1	0.29	0.22	NA	NA
Eu/Eu*	0.70	0.78	0.89	0.86	0.73	0.80	1.01	1.01	1.07	1.07	1.21	0.32	0.31	0.93	0.93	0.46	0.77	0.66	1.17	1.10	0.52
MgNumber	0.40	0.48	0.21	0.28	0.07	0.06	0.53	0.29	0.53	0.46	0.65	0.31	0.32	0.63	0.49	0.23	0.39	0.59	0.56	0.40	0.51

D. Supplementary Material for Chapter 5

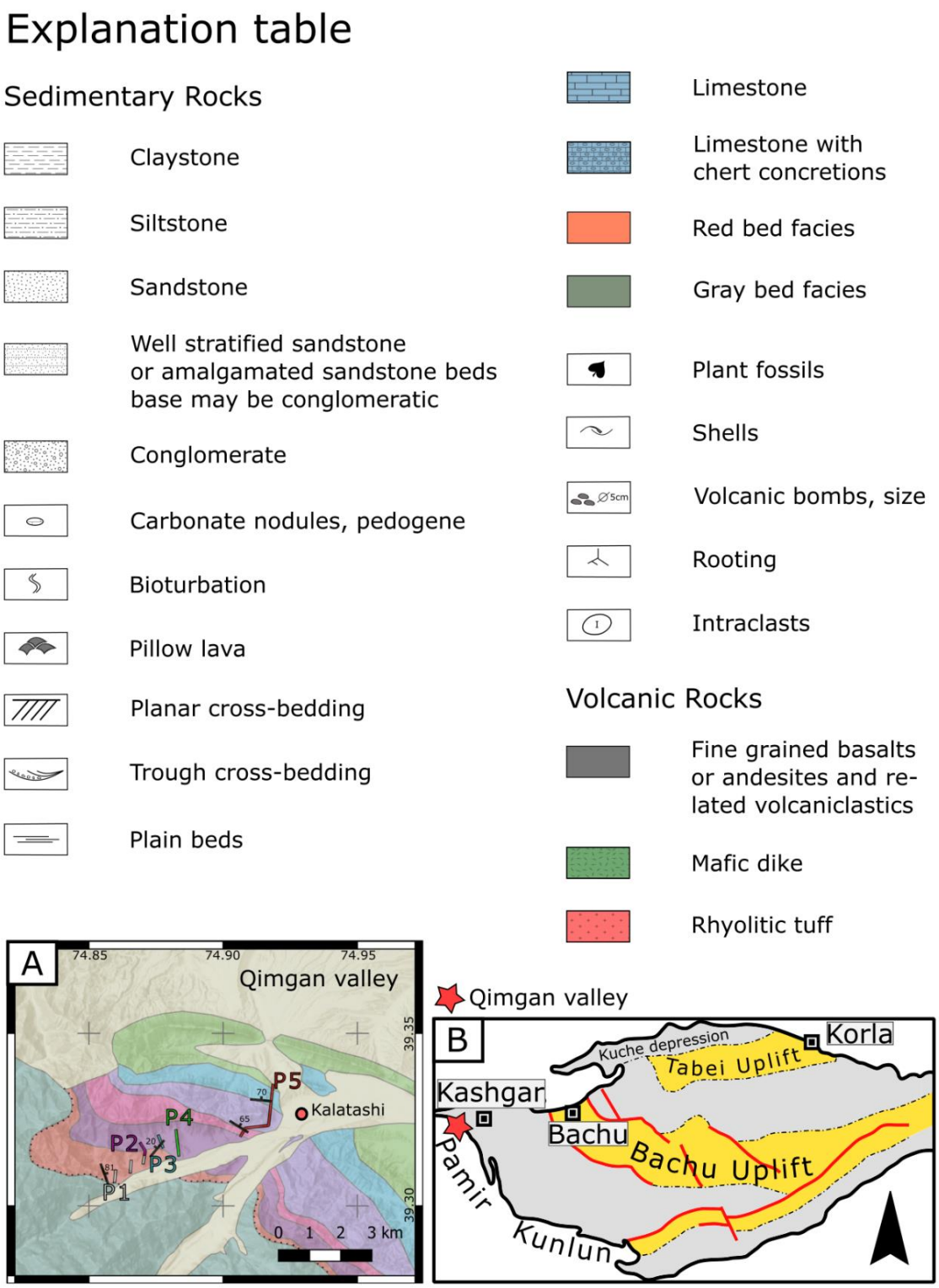

Appendix D.1: Explanation for Appendix D.3 to Appendix D.6. Inset A shows the position of the profiles in the Qimgan valley, inset B shows the present extend of the Tarim basin (grey) with uplift zones (yellow) and major faults (red lines).

Appendix D.2: Facies types defined for the Qimgan section.

Facies code	Lithofacies	Interpretation
Gms	massiv, matrix supported gravel	debris flow deposits
Gm	massive or crudely bedded gravel, often errosive at base	longitudinal bars, lag deposits, sheetflood to channel deposits
Gt	gravel stratified, trough crossbeds, often errosive at base	minor channel fills
St	sand, medium to very coarse, may be conglomeratic, trough crossbeds	dunes, sheetflood to channel deposites
Sp	sand, medium to very coarse, may be conglomeratic, planar crossbeds	lingoid bars or traverse bars, sheetflood to channel deposits
Sl	sand, fine, well sorted, low angle (<10°) cross beds	scour fills or crevasse splays
Sh	sand, fine to medium, horizontal lamination	planar bed flow
Fr	massive silt and mudstone, bleached, light coloured root traces	soil formation on overbank deposits
Fl	fine sand, silt, mud, laminated	overbank or waning flood deposits
Fsc	massive silt and mudstone	overbank deposits or lacustrine/marine
Pn	nodular limestone	pedogenic limestone, soil fomation
Pt	redeposited limestone	lacustrine or marine
P1	massive limestone, fresh dark gray/light gray on weathered surface, ostracode mass layers	lacustrine or marine
P1c	banked limestone, fresh dark gray/light gray on weathered surface, silicified, interlayered with dark gray chert	lacustrine or marine

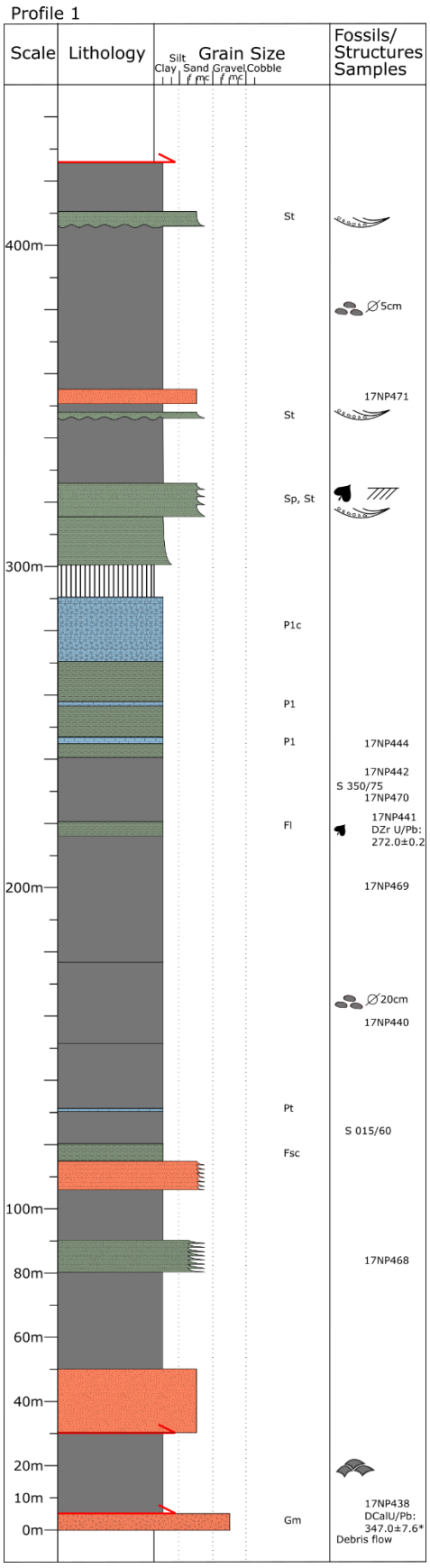

Appendix D.3: Profile 1.

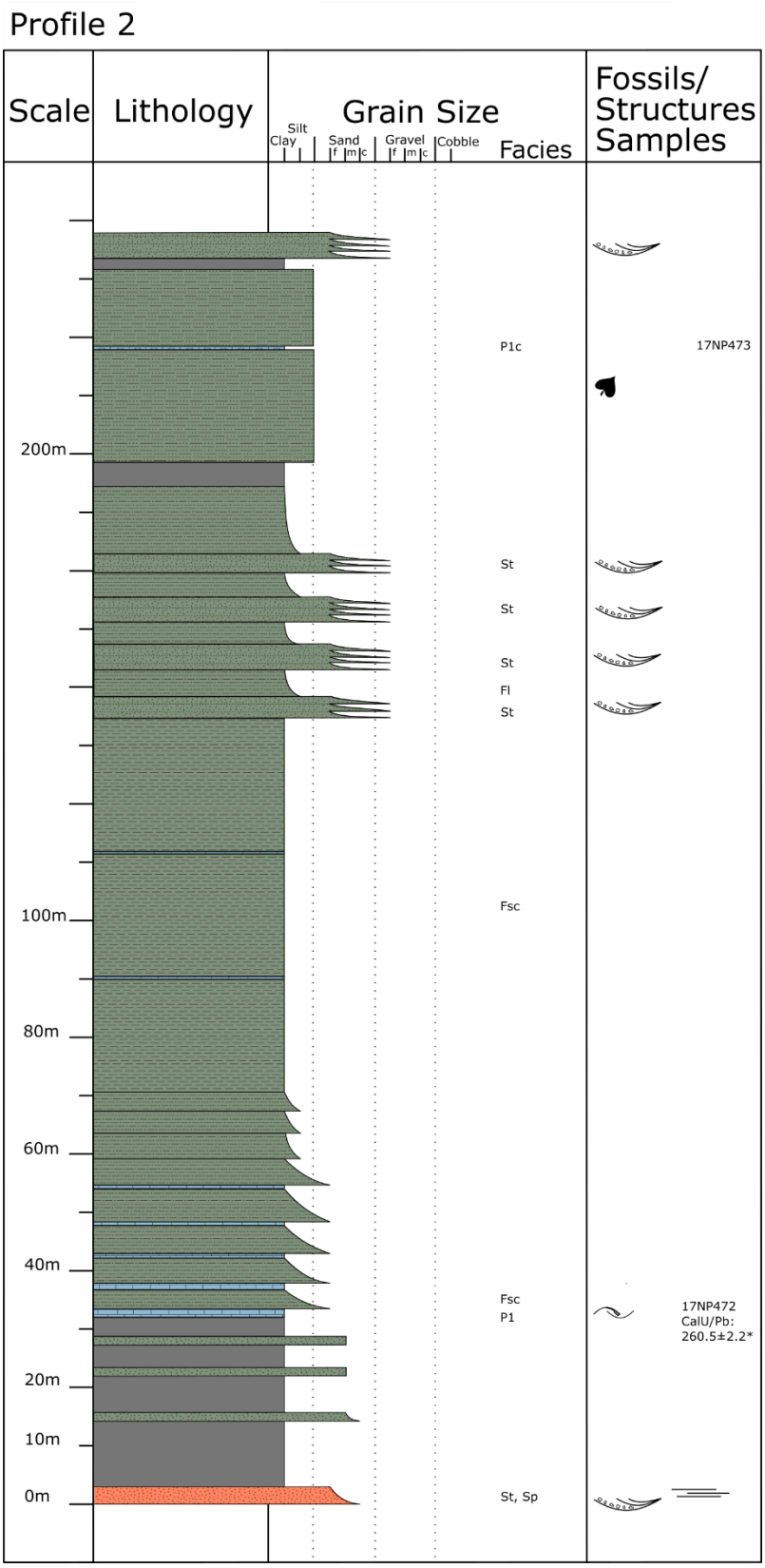

Appendix D.4: Profile 2. It follows stratigraphically above profile 1.

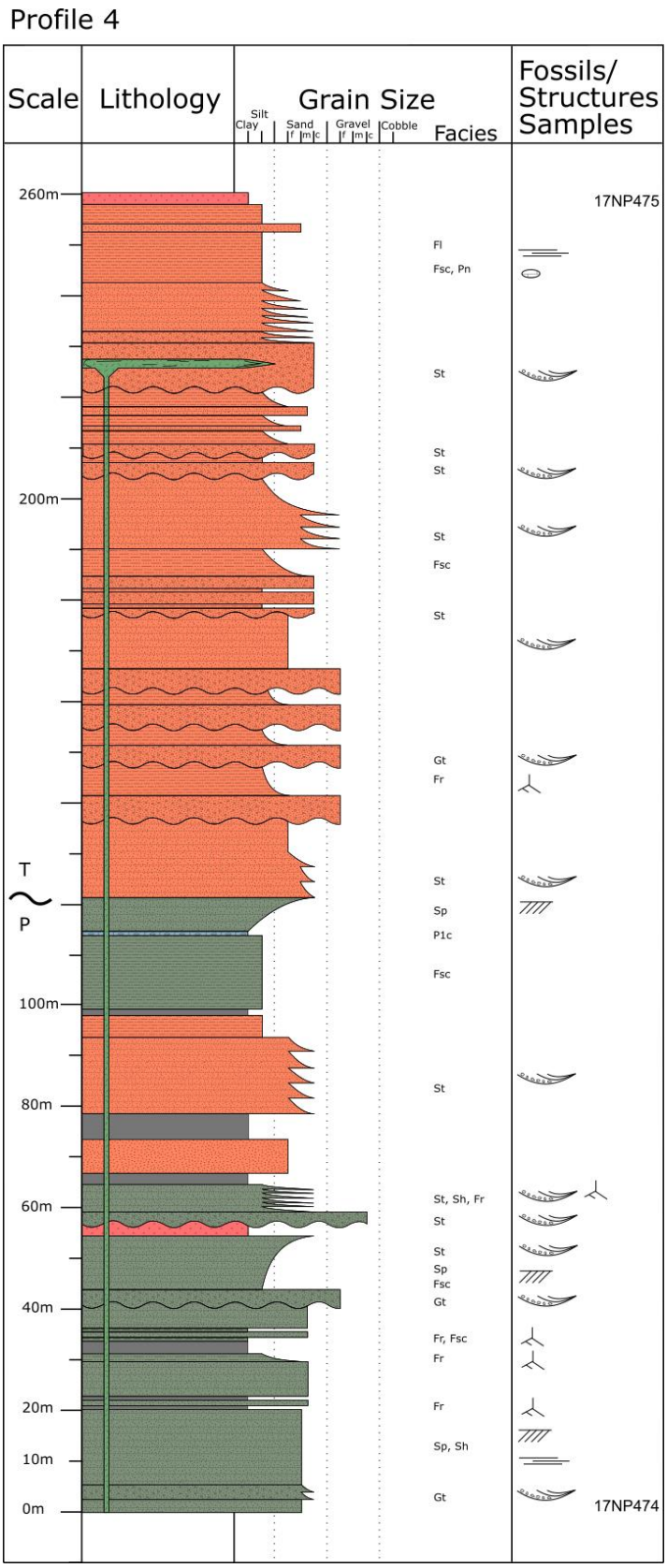

Appendix D.5: Profile 4. It follows stratigraphically above profile 2. P~T marks the Permo-Triassic boundary.

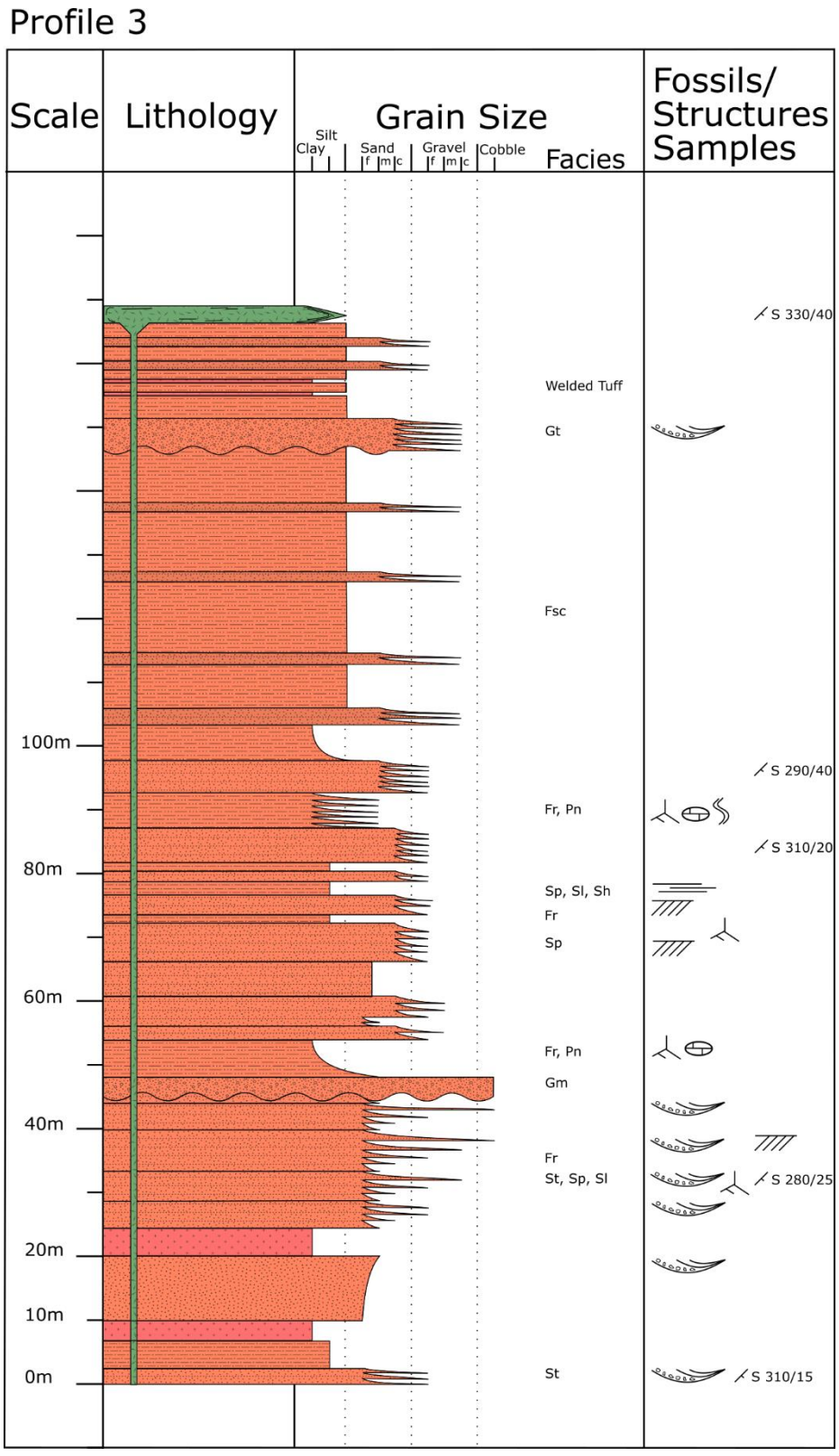

Appendix D.6: Profile 3. It follows stratigraphically above profile 4.

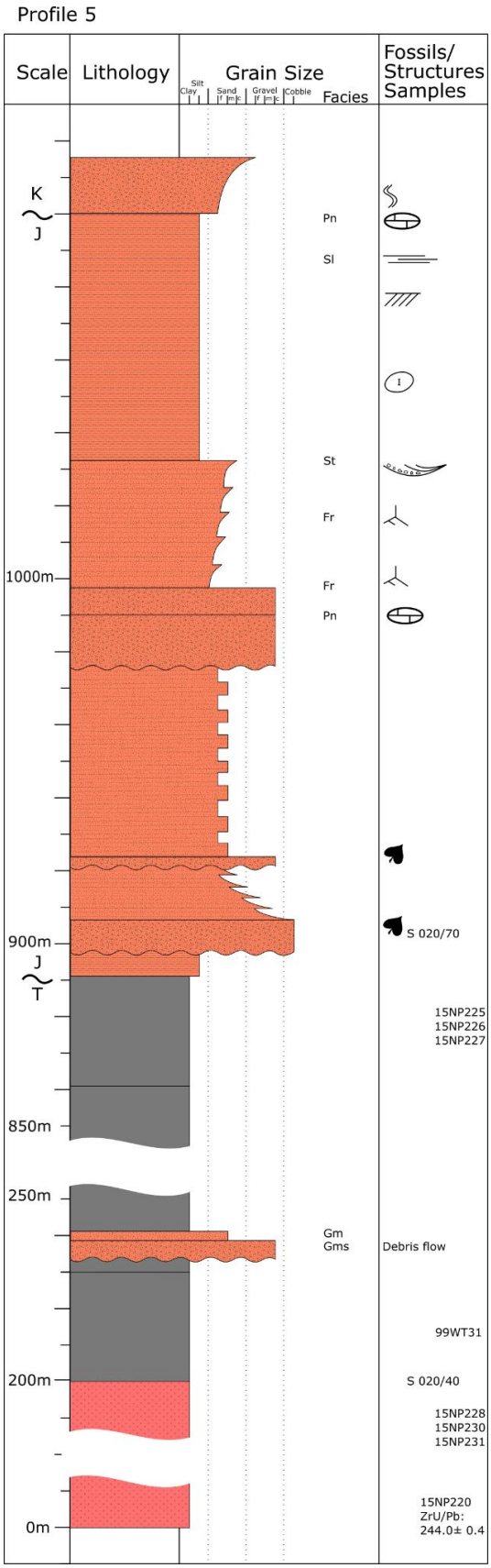

Appendix D.7: Profile 5. It follows stratigraphically above profile 3. T~J marks the Trias-Jura boundary. J~K marks the Jura-Cretaceous boundary.

Appendix D.8: LA-ICP-MS zircon U-Pb data analyzed in this chapter.

Sample 17NP447	Sample Type: detrital					Latitude:	39.40642	Longitude:	74.448821								
	Conventional concordia					Ages								Discordance		Conc.Dist., dc	Th/U
Sample #	207Pb	±2σ	206Pb	±2σ	error corr.	207Pb	±2σ	206Pb	±2σ	207Pb	±2σ	Best Age	±1σ	206/238	206/238		
_grain number	235U		238U		206/238 vs 207/235	235U		238U		206Pb				207/206	207/235		
17NP447_g015	0.3199	0.0039	0.04539	0.00035	0.67044	281.8	3	286.1	2.1	248	18	286.1	1.05	-0.15	-0.02	-1.70	1.38
17NP447_g071	0.3804	0.0045	0.05272	0.00041	0.39238	327.3	3.3	331.2	2.5	301	20	331.2	1.25	-0.10	-0.01	-1.40	0.45
17NP447_g049	0.2688	0.0043	0.03767	0.00029	0.51486	241.6	3.4	238.4	1.8	255	28	238.4	0.9	0.07	0.01	1.60	1.02
17NP447_g030	0.2725	0.0056	0.03852	0.00039	0.48919	244.6	4.5	243.7	2.4	221	42	243.7	1.2	-0.10	0.00	0.48	0.94
17NP447_g054	0.2756	0.0043	0.03855	0.00028	0.20562	247.1	3.4	243.8	1.8	266	31	243.8	0.9	0.08	0.01	1.50	0.70
17NP447_g040	0.279	0.0042	0.03871	0.00036	0.51977	249.8	3.3	244.8	2.2	263	28	244.8	1.1	0.07	0.02	2.30	0.98
17NP447_g022	0.2809	0.0063	0.03876	0.0003	0.17658	251	5	245.2	1.9	285	47	245.2	0.95	0.14	0.02	2.80	0.84
17NP447_g043	0.2749	0.005	0.03881	0.00033	0.3388	246.8	4	245.4	2.1	247	37	245.4	1.05	0.01	0.01	0.52	0.70
17NP447_g037	0.2777	0.0048	0.03885	0.00029	0.11597	249	3.7	245.7	1.8	262	36	245.7	0.9	0.06	0.01	1.40	0.83
17NP447_g003	0.276	0.0098	0.03888	0.00045	0.03372	247.2	7.8	245.9	2.8	253	79	245.9	1.4	0.03	0.01	0.72	1.04
17NP447_g002	0.2756	0.0057	0.03897	0.00032	0.001	247.8	4.5	246.4	2	273	46	246.4	1	0.10	0.01	0.33	0.63
17NP447_g060	0.2779	0.0088	0.03902	0.0004	0.17348	248.7	7	246.8	2.5	280	66	246.8	1.25	0.12	0.01	1.00	0.38
17NP447_g051	0.2755	0.0042	0.03905	0.00032	0.076095	246.9	3.3	246.9	2	236	33	246.9	1	-0.05	0.00	0.06	0.49
17NP447_g055	0.2803	0.0076	0.03906	0.00036	0.001	250.6	6.1	247	2.2	282	60	247	1.1	0.12	0.01	1.80	0.74
17NP447_g061	0.2817	0.0057	0.03906	0.00035	0.16062	251.7	4.5	247	2.2	293	44	247	1.1	0.16	0.02	2.20	0.49
17NP447_g053	0.2777	0.006	0.03916	0.00037	0.40495	248.7	4.8	247.7	2.3	244	41	247.7	1.15	-0.02	0.00	0.55	1.01
17NP447_g021	0.2768	0.007	0.03921	0.00037	0.2825	247.9	5.6	248	2.3	244	50	248	1.15	-0.02	0.00	0.08	0.48
17NP447_g010	0.2811	0.006	0.03939	0.00034	0.1717	251.3	4.7	249	2.1	273	43	249	1.05	0.09	0.01	1.10	0.76
17NP447_g070	0.2805	0.0051	0.03942	0.00034	0.18631	250.9	4	249.2	2.1	275	38	249.2	1.05	0.09	0.01	0.82	0.74
17NP447_g008	0.2766	0.0051	0.03942	0.00033	0.22685	247.8	4	249.3	2	239	38	249.3	1	-0.04	-0.01	-0.58	0.59
17NP447_g075	0.2837	0.0068	0.03943	0.00035	0.12065	253.3	5.3	249.3	2.1	276	53	249.3	1.05	0.10	0.02	1.90	0.46
17NP447_g058	0.2859	0.01	0.03943	0.00034	0.05484	251.9	4.4	249.3	2.1	261	42	249.3	1.05	0.04	0.01	2.70	0.81
17NP447_g076	0.2792	0.0048	0.03952	0.00033	0.21764	250.6	3.8	249.8	2	250	37	249.8	1	0.00	0.00	0.07	0.87
17NP447_g024	0.2826	0.0053	0.0396	0.00031	0.16654	252.6	4.2	250.3	1.9	265	40	250.3	0.95	0.06	0.01	1.10	0.55
17NP447_g045	0.2794	0.0051	0.03963	0.00036	0.37932	250.1	4	250.5	2.2	243	38	250.5	1.1	-0.03	0.00	-0.16	0.65
17NP447_g039	0.2825	0.004	0.03963	0.0003	0.36997	252.5	3.1	250.5	1.9	262	27	250.5	0.95	0.04	0.01	0.94	0.89
17NP447_g041	0.2824	0.0045	0.03971	0.00035	0.46037	252.8	3.6	251.1	2.1	257	30	251.1	1.05	0.02	0.01	0.68	0.97
17NP447_g057	0.2836	0.0044	0.03976	0.00037	0.56199	253.4	3.4	251.3	2.3	261	29	251.3	1.15	0.04	0.01	0.96	0.81
17NP447_g016	0.2861	0.0063	0.0398	0.00038	0.096348	255.3	5	251.6	2.3	288	48	251.6	1.15	0.13	0.01	1.70	0.76
17NP447_g031	0.2864	0.0042	0.03982	0.00032	0.33248	255.6	3.3	251.7	2	290	28	251.7	1	0.13	0.02	1.80	1.00
17NP447_g046	0.2869	0.0045	0.03982	0.00036	0.37148	256	3.5	251.7	2.2	262	30	251.7	1.1	0.04	0.02	1.90	1.06

Sample 17NP447 continued

	Conventional concordia				Ages								Discordance		Conc.Dist., dc	Th/U
Sample # _grain number	207Pb 235U	±2σ	206Pb 238U	±2σ	error corr. 206/238 vs 207/235	207Pb 235U	±2σ	206Pb 238U	±2σ	207Pb 206Pb	±2σ	Best Age	±1σ	206/238 207/206	206/238 207/235	
17NP447_g050	0.2832	0.0044	0.03984	0.0003	0.36833	253.7	3.6	251.8	1.9	251	31	251.8	0.95	0.00	0.01	0.60	0.93
17NP447_g001	0.2823	0.0095	0.03985	0.00047	0.001	252.1	7.5	251.9	2.9	273	77	251.9	1.45	0.08	0.00	0.26	0.76
17NP447_g038	0.2831	0.0052	0.03984	0.00039	0.29699	253.1	4.1	251.9	2.4	260	35	251.9	1.2	0.03	0.00	0.57	0.64
17NP447_g036	0.2875	0.0076	0.03987	0.00038	0.079057	256.4	6	252	2.3	280	62	252	1.15	0.10	0.02	2.00	0.46
17NP447_g025	0.2886	0.0086	0.03991	0.00043	0.13588	257.2	6.8	252.3	2.7	274	63	252.3	1.35	0.08	0.02	2.30	0.52
17NP447_g019	0.2868	0.0091	0.04023	0.0005	0.28761	255.4	7.2	254.3	3.1	254	65	254.3	1.55	0.00	0.00	0.78	0.73
17NP447_g072	0.2971	0.0095	0.04035	0.00047	0.52339	263.6	7.4	255	2.9	343	61	255	1.45	0.26	0.03	4.00	0.53
17NP447_g026	0.2925	0.0049	0.04053	0.00035	0.42038	260.4	3.8	256.1	2.2	306	32	256.1	1.1	0.16	0.02	1.90	0.81
17NP447_g006	0.289	0.0048	0.04068	0.00036	0.38325	257.6	3.8	257.1	2.2	254	30	257.1	1.1	-0.01	0.00	0.32	0.96
17NP447_g044	0.2877	0.0093	0.04088	0.00045	0.21224	257.5	7.5	258.3	2.8	234	71	258.3	1.4	-0.10	0.00	-0.67	0.74
17NP447_g011	0.2885	0.0046	0.04097	0.00042	0.61556	257.2	3.6	258.8	2.6	241	27	258.8	1.3	-0.07	-0.01	-0.64	1.19
17NP447_g012	0.2956	0.0052	0.04111	0.00043	0.66491	262.8	4.1	259.7	2.6	275	27	259.7	1.3	0.06	0.01	1.40	1.07
17NP447_g069	0.2957	0.0047	0.04138	0.00054	0.68169	263.2	3.7	261.4	3.4	259	24	261.4	1.7	-0.01	0.01	0.73	0.61
17NP447_g014	0.3022	0.0053	0.04163	0.00046	0.61327	267.9	4.1	262.9	2.9	305	29	262.9	1.45	0.14	0.02	2.20	0.97
17NP447_g079	0.2968	0.0048	0.04229	0.00037	0.4303	263.8	3.8	267	2.3	243	30	267	1.15	-0.10	-0.01	-1.30	0.44
17NP447_g074	0.3108	0.0054	0.04304	0.00034	0.33941	274.6	4.2	271.6	2.1	304	34	271.6	1.05	0.11	0.01	1.30	0.38
17NP447_g067	0.316	0.0067	0.04313	0.00043	0.335	279.2	5.2	272.2	2.7	330	41	272.2	1.35	0.18	0.03	2.70	0.68
17NP447_g063	0.3103	0.0037	0.04345	0.00033	0.43463	274.4	2.9	274.2	2.1	268	22	274.2	1.05	-0.02	0.00	0.10	1.30
17NP447_g042	0.3173	0.0049	0.04379	0.00038	0.43152	279.7	3.8	276.3	2.3	293	27	276.3	1.15	0.06	0.01	1.40	0.89
17NP447_g005	0.3146	0.0037	0.04434	0.00033	0.51853	277.7	2.9	279.7	2.1	274	19	279.7	1.05	-0.02	-0.01	-0.79	1.09
17NP447_g062	0.3205	0.0042	0.04482	0.00035	0.053554	282.2	3.2	282.6	2.2	270	18	282.6	1.1	-0.05	0.00	-0.14	1.80
17NP447_g059	0.3214	0.0037	0.04515	0.00033	0.47158	282.9	2.8	284.7	2	266	20	284.7	1	-0.07	-0.01	-0.68	1.07
17NP447_g048	0.331	0.0064	0.04535	0.00039	0.18975	290.1	4.9	285.9	2.4	314	41	285.9	1.2	0.09	0.01	1.70	0.47
17NP447_g029	0.327	0.0059	0.0455	0.00042	0.27624	287.1	4.5	286.8	2.6	272	39	286.8	1.3	-0.05	0.00	0.17	0.70
17NP447_g034	0.3285	0.0058	0.04551	0.00038	0.061313	288.2	4.4	286.9	2.3	285	38	286.9	1.15	-0.01	0.00	0.60	0.72
17NP447_g028	0.3322	0.008	0.04584	0.00038	0.24042	291.8	6.2	289	2.3	295	51	289	1.15	0.02	0.01	0.91	0.58
17NP447_g035	0.3425	0.0062	0.04668	0.00041	0.035728	298.8	4.7	294.1	2.5	313	37	294.1	1.25	0.06	0.02	1.90	0.78
17NP447_g018	0.3373	0.0062	0.04713	0.00058	0.68972	295	4.7	296.9	3.6	269	29	296.9	1.8	-0.10	-0.01	-0.68	0.52
17NP447_g065	0.3423	0.0068	0.04733	0.00051	0.36816	298.9	5.2	298.1	3.1	323	39	298.1	1.55	0.08	0.00	0.31	0.38
17NP447_g017	0.3496	0.0056	0.04758	0.00046	0.35596	304.3	4.2	299.6	2.8	316	32	299.6	1.4	0.05	0.02	1.80	0.44
17NP447_g004	0.3436	0.0046	0.04761	0.00036	0.44512	299.8	3.5	299.8	2.2	297	26	299.8	1.1	-0.01	0.00	0.03	0.36

Sample 17NP447 continued

	Conventional concordia					Ages								Discordance		Conc.Dist., dc	Th/U
Sample # _grain number	207Pb 235U	±2σ	206Pb 238U	±2σ	error corr. 206/238 vs 207/235	207Pb 235U	±2σ	206Pb 238U	±2σ	207Pb 206Pb	±2σ	Best Age	±1σ	206/238 207/206	206/238 207/235		
17NP447_g056	0.3464	0.0063	0.0476	0.00045	0.29207	301.9	4.8	299.8	2.8	312	35	299.8	1.4	0.04	0.01	0.85	0.48
17NP447_g013	0.3517	0.0064	0.0481	0.00037	0.21991	306.3	4.8	303	2.3	316	38	303	1.15	0.04	0.01	1.20	0.96
17NP447_g023	0.36	0.006	0.0494	0.0005	0.63703	312	4.5	310.8	3.1	302	27	310.8	1.55	-0.03	0.00	0.51	0.47
17NP447_g032	0.3612	0.0057	0.04992	0.00047	0.64281	313.3	4.2	314	2.9	296	23	314	1.45	-0.06	0.00	-0.34	0.46
17NP447_g009	0.3624	0.0053	0.05033	0.00053	0.64336	313.9	3.9	316.5	3.2	293	24	316.5	1.6	-0.08	-0.01	-0.93	0.49
17NP447_g047	0.4133	0.0057	0.05617	0.00053	0.67828	351.1	4.1	352.3	3.2	326	21	352.3	1.6	-0.08	0.00	-0.35	0.66
17NP447_g033	0.4395	0.0059	0.05828	0.00049	0.55525	369.7	4.1	365.2	3	394	22	365.2	1.5	0.07	0.01	1.50	1.06
17NP447_g064	0.838	0.013	0.10047	0.00082	0.17436	618.2	7	617.1	4.8	616	31	617.1	2.4	0.00	0.00	0.18	0.53
17NP447_g077	0.8924	0.012	0.106	0.0012	0.81399	647.3	6.7	649.6	7.1	646	17	649.6	3.55	-0.01	0.00	-0.38	0.25
17NP447_g073	1.938	0.029	0.184	0.0015	0.37313	1093.8	9.9	1088.7	8.1	1109	24	1109	12	0.02	0.00	0.76	0.53
17NP447_g027	10.05	0.14	0.4605	0.0047	0.24156	2438	13	2442	21	2441	24	2441	12	0.00	0.00	-0.17	1.22
17NP447_g068	11.07	0.14	0.4791	0.0046	0.71012	2528.6	12	2523	20	2531	15	2531	7.5	0.00	0.00	0.38	1.16
17NP447_g052	0.291	0.0086	0.03924	0.00044	0.42813	259.2	6.8	248.1	2.7	319	65	248.1	1.35	0.22	0.04	5.00	0.42
17NP447_g080	0.3195	0.0067	0.04238	0.00043	0.028049	281.3	5.2	267.6	2.7	395	50	267.6	1.35	0.32	0.05	5.80	0.66
17NP447_g007	0.3074	0.0097	0.03966	0.00033	0.21872	271.8	7.5	250.7	2.1	467	68	250.7	1.05	0.46	0.08	9.30	1.03
17NP447_g078	0.3198	0.0065	0.04096	0.0004	0.19153	281.5	5	258.8	2.5	462	44	258.8	1.25	0.44	0.08	9.60	1.11
17NP447_g066	1.19	0.017	0.116	0.0024	0.76568	795.5	7.8	707	14	1065	28	707	7	0.34	0.11	19.00	0.39

Sample 17NP441	Sample Type: detrital					Latitude:	39.309971	Longitude:	74.865998								
	Conventional concordia					Ages								Discordance		Conc.Dist., dc	Th/U
Sample #	207Pb	±2σ	206Pb	±2σ	error corr.	207Pb	±2σ	206Pb	±2σ	207Pb	±2σ	Best Age	±1σ	206/238	206/238		
_grain number	235U		238U		206/238 vs 207/235	235U		238U		206Pb				207/206	207/235		
17NP441_g055	8.725	0.094	0.4525	0.0037	0.80336	2308.9	9.8	2408	16	2230.9	14	2230.9	7	-0.08	-0.04	-7.20	0.35
17NP441_g053	8.422	0.11	0.4402	0.0042	0.78105	2278.6	11	2351	19	2208	17	2208	8.5	-0.06	-0.03	-5.50	0.21
17NP441_g032	0.293	0.013	0.04252	0.00062	0.075242	261	10	268.4	3.8	220	100	268.4	1.9	-0.22	-0.03	-3.20	0.56
17NP441_g065	9.059	0.1	0.4471	0.0035	0.76488	2343.5	10	2382	16	2311.9	15	2311.9	7.5	-0.03	-0.02	-2.80	0.43
17NP441_g016	9.186	0.092	0.4498	0.0032	0.78315	2356.8	9.1	2394	14	2326.8	14	2326.8	7	-0.03	-0.02	-2.70	0.53
17NP441_g037	0.2982	0.0074	0.04292	0.0005	0.057447	264.8	5.8	270.9	3.1	209	63	270.9	1.55	-0.30	-0.02	-2.50	0.56
17NP441_g038	0.3012	0.0066	0.04325	0.00035	0.13548	267	5.2	272.9	2.2	217	46	272.9	1.1	-0.26	-0.02	-2.30	0.51
17NP441_g033	0.317	0.0074	0.04513	0.0004	0.36854	280.3	5.5	284.5	2.5	252	50	284.5	1.25	-0.13	-0.01	-2.00	0.75
17NP441_g029	0.3024	0.0055	0.04323	0.00029	0.26792	268	4.3	272.8	1.8	219	40	272.8	0.9	-0.25	-0.02	-1.90	0.47
17NP441_g020	0.2968	0.0048	0.04246	0.00032	0.19048	264.9	3.9	268.1	2	235	37	268.1	1	-0.14	-0.01	-1.80	0.43
17NP441_g061	0.3105	0.0069	0.04424	0.00036	0.11445	274.9	5.4	279	2.2	235	51	279	1.1	-0.19	-0.01	-1.80	0.46
17NP441_g004	0.2897	0.0064	0.0415	0.00031	0.16096	258.7	5.1	262.1	1.9	222	49	262.1	0.95	-0.18	-0.01	-1.60	0.70
17NP441_g031	0.3039	0.0071	0.04328	0.00033	0.11653	269.1	5.5	273.1	2.1	237	54	273.1	1.05	-0.15	-0.01	-1.50	0.53
17NP441_g084	0.3067	0.0076	0.04364	0.00036	0.16594	271.2	5.9	275.3	2.2	239	55	275.3	1.1	-0.15	-0.02	-1.50	0.73
17NP441_g079	0.2862	0.0096	0.03989	0.00058	0.32921	255.4	7.5	252.2	3.6	294	68	252.2	1.8	0.14	0.01	1.50	0.61
17NP441_g051	0.2864	0.0043	0.04027	0.00032	0.1726	255.6	3.4	254.5	2	265	37	254.5	1	0.04	0.00	0.54	0.74
17NP441_g025	0.3058	0.0087	0.04142	0.00035	0.16878	270.5	6.8	261.6	2.2	318	61	261.6	1.1	0.18	0.03	4.00	0.67
17NP441_g057	0.3019	0.0048	0.0419	0.00029	0.19366	267.8	3.7	264.7	1.8	301	36	264.7	0.9	0.12	0.01	1.40	0.43
17NP441_g080	0.3067	0.0059	0.04201	0.00041	0.07822	271.5	4.6	265.2	2.5	334	47	265.2	1.25	0.21	0.02	2.70	0.81
17NP441_g064	0.3008	0.005	0.04217	0.00029	0.17481	266.8	3.9	266.3	1.8	266	38	266.3	0.9	0.00	0.00	0.32	0.73
17NP441_g070	0.2974	0.0067	0.04224	0.00036	0.19946	264.6	5.3	266.7	2.2	237	49	266.7	1.1	-0.13	-0.01	-0.99	0.61
17NP441_g059	0.3027	0.0046	0.04226	0.00035	0.19738	269.1	3.4	266.8	2.1	283	36	266.8	1.05	0.06	0.01	0.71	0.44
17NP441_g098	0.3084	0.0069	0.04229	0.00035	0.026895	272.6	5.4	267	2.1	320	54	267	1.05	0.17	0.02	2.50	0.46
17NP441_g067	0.2982	0.0042	0.04231	0.00027	0.25118	265.2	3.2	267.1	1.7	243	32	267.1	0.85	-0.10	-0.01	-0.91	0.54
17NP441_g100	0.3042	0.0076	0.04231	0.00038	0.1514	269.9	6	267.1	2.3	294	56	267.1	1.15	0.09	0.01	1.10	0.60
17NP441_g021	0.3021	0.0048	0.04239	0.00028	0.001	267.9	3.7	267.6	1.7	266	38	267.6	0.85	-0.01	0.00	0.17	0.54
17NP441_g102	0.3038	0.0059	0.04239	0.00037	0.21789	269.1	4.6	267.6	2.3	278	45	267.6	1.15	0.04	0.01	0.73	0.60
17NP441_g043_B2	0.304	0.0069	0.04239	0.00034	0.1958	269.8	5.3	267.6	2.1	281	50	267.6	1.05	0.05	0.01	0.80	0.62
17NP441_g066	0.3053	0.0053	0.04239	0.00033	0.16377	270.8	4.2	267.6	2.1	287	39	267.6	1.05	0.07	0.01	1.20	0.59
17NP441_g028	0.304	0.0054	0.04243	0.00029	0.30084	269.3	4.2	267.9	1.8	284	40	267.9	0.9	0.06	0.01	0.69	0.46
17NP441_g022	0.3067	0.0054	0.04249	0.00031	0.11219	271.5	4.2	268.2	1.9	280	43	268.2	0.95	0.04	0.01	1.40	0.63

Sample 17NP441 continued

	Conventional concordia					Ages								Discordance		Conc.Dist., dc	Th/U
Sample #	207Pb	±2σ	206Pb	±2σ	error corr.	207Pb	±2σ	206Pb	±2σ	207Pb	±2σ	Best Age	±1σ	206/238	206/238		
_grain number	235U		238U		206/238 vs 207/235	235U		238U		206Pb				207/206	207/235		
17NP441_g086	0.301	0.0045	0.0425	0.00027	0.16928	267.4	3.4	268.3	1.7	263	34	268.3	0.85	-0.02	0.00	-0.48	0.60
17NP441_g034	0.3039	0.0046	0.0425	0.00027	0.33184	269.6	3.6	268.3	1.7	289	32	268.3	0.85	0.07	0.00	0.48	0.41
17NP441_g075	0.3102	0.007	0.04253	0.00038	0.047608	274.7	5.3	268.5	2.4	307	52	268.5	1.2	0.13	0.02	2.40	0.56
17NP441_g049	0.2987	0.0075	0.04255	0.0004	0.18825	265	5.8	268.6	2.5	237	55	268.6	1.25	-0.13	-0.01	-1.40	0.35
17NP441_g076	0.3047	0.006	0.04255	0.00036	0.36328	269.9	4.6	268.6	2.2	286	47	268.6	1.1	0.06	0.00	0.61	0.61
17NP441_g052	0.3082	0.0055	0.04255	0.00031	0.24938	272.6	4.3	268.6	1.9	297	40	268.6	0.95	0.10	0.01	1.70	0.48
17NP441_g040	0.2996	0.007	0.04256	0.00037	0.073858	265.8	5.4	268.7	2.3	250	53	268.7	1.15	-0.07	-0.01	-1.10	0.78
17NP441_g014	0.3024	0.0047	0.04256	0.00027	0.054739	268.5	3.6	268.7	1.7	268	36	268.7	0.85	0.00	0.00	-0.17	0.90
17NP441_g048	0.309	0.0059	0.04258	0.00032	0.21239	273.6	4.6	268.8	2	312	44	268.8	1	0.14	0.02	1.90	0.70
17NP441_g006	0.3034	0.0053	0.04261	0.00031	0.17705	269.2	4.2	269	1.9	273	41	269	0.95	0.01	0.00	0.03	0.68
17NP441_g058	0.307	0.0056	0.04262	0.00033	0.16682	271.6	4.4	269	2	269	42	269	1	0.00	0.01	1.20	0.52
17NP441_g026	0.3073	0.007	0.04263	0.00039	0.18888	271.7	5.5	269.1	2.4	300	51	269.1	1.2	0.10	0.01	1.20	0.45
17NP441_g005	0.2993	0.0057	0.04264	0.00035	0.49346	265.7	4.5	269.2	2.1	231	40	269.2	1.05	-0.17	-0.01	-1.40	0.81
17NP441_g078	0.3049	0.0052	0.04264	0.0003	0.29106	270.1	4	269.2	1.8	262	38	269.2	0.9	-0.03	0.00	0.44	0.43
17NP441_g087	0.306	0.0074	0.04267	0.00041	0.15771	270.8	5.7	269.3	2.6	292	57	269.3	1.3	0.08	0.01	0.72	0.39
17NP441_g054	0.3042	0.0055	0.04268	0.00033	0.001	270	4.4	269.4	2	272	45	269.4	1	0.01	0.00	0.11	0.59
17NP441_g073	0.305	0.017	0.04269	0.0007	0.037591	270	13	269.5	4.3	280	130	269.5	2.15	0.04	0.00	0.34	0.32
17NP441_g085	0.3064	0.0063	0.0427	0.00029	0.15107	271.1	4.9	269.5	1.8	263	46	269.5	0.9	-0.02	0.01	0.77	0.68
17NP441_g097	0.306	0.0056	0.04271	0.00033	0.16696	271.5	4.4	269.6	2	275	43	269.6	1	0.02	0.01	0.61	0.49
17NP441_g044	0.3069	0.0052	0.04273	0.00033	0.308	271.6	4	269.7	2	285	36	269.7	1	0.05	0.01	0.85	0.43
17NP441_g095	0.3063	0.0056	0.04275	0.00038	0.11291	271.6	4.3	269.8	2.3	279	43	269.8	1.15	0.03	0.01	0.61	0.61
17NP441_g035	0.3059	0.0051	0.04276	0.00029	0.33988	270.9	4	269.9	1.8	279	35	269.9	0.9	0.03	0.00	0.45	0.84
17NP441_g094	0.305	0.0057	0.04277	0.00033	0.28738	270	4.4	270	2	246	42	270	1	-0.10	0.00	0.13	0.49
17NP441_g042_B1	0.3066	0.0068	0.04278	0.00039	0.16235	271.8	5.4	270	2.4	286	51	270	1.2	0.06	0.01	0.63	0.46
17NP441_g003	0.3025	0.0049	0.04278	0.00032	0.31678	268.3	3.8	270.1	2	246	37	270.1	1	-0.10	-0.01	-0.71	0.38
17NP441_g074	0.313	0.0062	0.0428	0.00037	0.1836	276.3	4.8	270.1	2.3	314	46	270.1	1.15	0.14	0.02	2.60	0.41
17NP441_g081	0.3037	0.0049	0.04285	0.00028	0.046875	269.1	3.8	270.6	1.8	258	38	270.6	0.9	-0.05	-0.01	-0.50	0.71
17NP441_g046	0.3072	0.0095	0.04288	0.00043	0.22354	272.6	7.2	270.7	2.7	279	63	270.7	1.35	0.03	0.01	0.56	0.62
17NP441_g088	0.3095	0.0049	0.04294	0.00031	0.31914	274.1	3.8	271	1.9	298	33	271	0.95	0.09	0.01	1.10	1.01
17NP441_g083	0.3055	0.0051	0.04298	0.00029	0.21379	270.5	3.9	271.3	1.8	251	37	271.3	0.9	-0.08	0.00	-0.25	0.66
17NP441_g047	0.3036	0.006	0.04304	0.00033	0.15794	269.5	4.8	271.7	2	258	47	271.7	1	-0.05	-0.01	-1.00	0.52

Sample 17NP441 continued

	Conventional concordia					Ages								Discordance		Conc.Dist., dc	Th/U
Sample # _grain number	207Pb 235U	±2σ	206Pb 238U	±2σ	error corr. 206/238 vs 207/235	207Pb 235U	±2σ	206Pb 238U	±2σ	207Pb 206Pb	±2σ	Best Age	±1σ	206/238 207/206	206/238 207/235		
17NP441_g072	0.3119	0.006	0.04307	0.00032	0.2652	275.9	4.6	271.8	2	303	39	271.8	1	0.10	0.01	1.60	0.80
17NP441_g039	0.3091	0.0045	0.04309	0.00027	0.12453	273.3	3.5	272	1.7	282	33	272	0.85	0.04	0.00	0.63	0.93
17NP441_g090	0.3066	0.0052	0.04337	0.00033	0.15412	272.2	4.1	273.7	2	239	38	273.7	1	-0.15	-0.01	-0.89	0.60
17NP441_g024_A2	0.313	0.012	0.0434	0.00052	0.067768	276.5	8.9	273.9	3.2	316	85	273.9	1.6	0.13	0.01	1.10	0.55
17NP441_g068	0.3142	0.0071	0.0434	0.00038	0.30824	277.2	5.5	273.9	2.3	301	49	273.9	1.15	0.09	0.01	1.50	0.51
17NP441_g015	0.3101	0.006	0.04344	0.00045	0.4934	275.4	4.7	274.1	2.8	284	43	274.1	1.4	0.03	0.00	0.06	0.61
17NP441_g060	0.327	0.014	0.0435	0.00056	0.16518	287	10	274.5	3.5	400	92	274.5	1.75	0.31	0.04	5.20	0.46
17NP441_g027	0.3084	0.0045	0.04352	0.00031	0.2419	273.2	3.5	274.6	1.9	263	32	274.6	0.95	-0.04	-0.01	-0.69	0.53
17NP441_g018	0.3098	0.0059	0.04357	0.00036	0.044947	273.9	4.6	274.9	2.2	286	44	274.9	1.1	0.04	0.00	-0.37	0.43
17NP441_g082	0.3164	0.0052	0.04361	0.00038	0.30421	279.1	4	275.1	2.3	325	35	275.1	1.15	0.15	0.01	1.60	0.60
17NP441_g091	0.3085	0.0044	0.04363	0.00033	0.36686	272.9	3.4	275.3	2.1	256	33	275.3	1.05	-0.08	-0.01	-0.94	0.75
17NP441_g010	0.3208	0.0081	0.04371	0.00058	0.67581	283.6	6.5	275.8	3.6	322	40	275.8	1.8	0.14	0.03	2.80	0.46
17NP441_g092	0.3175	0.0061	0.04376	0.00035	0.11599	279.7	4.7	276.1	2.2	295	44	276.1	1.1	0.06	0.01	1.60	0.51
17NP441_g023_A1	0.3136	0.0068	0.0438	0.00038	0.11068	277.2	5.1	276.3	2.3	269	49	276.3	1.15	-0.03	0.00	0.26	0.59
17NP441_g071	0.3146	0.0068	0.04402	0.00048	0.17227	277.6	5.3	277.7	2.9	287	51	277.7	1.45	0.03	0.00	0.02	0.45
17NP441_g063	0.3182	0.007	0.04412	0.00037	0.22496	280.2	5.4	278.3	2.3	298	49	278.3	1.15	0.07	0.01	0.89	0.49
17NP441_g012	0.3126	0.0066	0.04423	0.00038	0.27053	276.4	5.1	279	2.4	254	46	279	1.2	-0.10	-0.01	-1.10	0.48
17NP441_g077	0.3178	0.0071	0.0445	0.00045	0.18592	280	5.5	280.6	2.8	271	52	280.6	1.4	-0.04	0.00	-0.19	0.61
17NP441_g009	0.3208	0.0043	0.04467	0.00042	0.58702	282.4	3.3	281.7	2.6	295	28	281.7	1.3	0.05	0.00	0.32	0.73
17NP441_g008	0.3195	0.0067	0.04476	0.00051	0.45421	281.4	5.1	282.3	3.2	271	42	282.3	1.6	-0.04	0.00	-0.30	0.62
17NP441_g001	0.3268	0.0053	0.04521	0.00043	0.5896	287	4.1	285	2.7	277	34	285	1.35	-0.03	0.01	0.83	0.85
17NP441_g056	0.3247	0.0047	0.04524	0.00029	0.28792	285.4	3.6	285.2	1.8	277	33	285.2	0.9	-0.03	0.00	0.11	0.62
17NP441_g036	0.3301	0.0076	0.04528	0.0005	0.58727	289.5	5.8	285.4	3.1	324	46	285.4	1.55	0.12	0.01	1.70	0.47
17NP441_g045	0.3219	0.004	0.04538	0.00035	0.51137	283.3	3.1	286.1	2.2	262	26	286.1	1.1	-0.09	-0.01	-1.10	0.42
17NP441_g007	0.3282	0.0064	0.0457	0.00041	0.44547	287.9	4.9	288	2.5	300	40	288	1.25	0.04	0.00	0.05	0.62
17NP441_g069	0.3448	0.006	0.04752	0.00039	0.30177	300.7	4.5	299.3	2.4	315	39	299.3	1.2	0.05	0.00	0.58	0.56
17NP441_g030	0.3454	0.0055	0.04799	0.00047	0.19059	301.1	4.2	302.4	2.8	296	36	302.4	1.4	-0.02	0.00	-0.35	0.51
17NP441_g050	0.3589	0.0087	0.05005	0.00073	0.66053	311.3	6.5	314.8	4.5	309	46	314.8	2.25	-0.02	-0.01	-1.30	0.38
17NP441_g062	6.712	0.084	0.3699	0.003	0.60857	2073.9	11	2029	14	2121	21	2121	10.5	0.04	0.02	3.70	0.31
17NP441_g101	7.349	0.088	0.3955	0.0033	0.85543	2154.2	11	2148	15	2170	16	2170	8	0.01	0.00	0.53	0.56
17NP441_g019	0.3188	0.0096	0.042	0.0005	0.12489	280.7	7.4	265.2	3.1	396	73	265.2	1.55	0.33	0.06	6.50	0.49

Sample 17NP441 continued

	Conventional concordia					Ages								Discordance		Conc.Dist., dc	Th/U
Sample #	207Pb	±2σ	206Pb	±2σ	error corr.	207Pb	±2σ	206Pb	±2σ	207Pb	±2σ	Best Age	±1σ	206/238	206/238		
_grain number	235U		238U		206/238 vs 207/235	235U		238U		206Pb				207/206	207/235		
17NP441_g089	0.3179	0.0079	0.04184	0.00039	0.35414	280.1	6.1	264.2	2.4	409	53	264.2	1.2	0.35	0.06	6.70	0.59
17NP441_g011	0.3533	0.0052	0.04537	0.00034	0.2657	307	3.9	286.1	2.1	453	33	286.1	1.05	0.37	0.07	8.20	0.54
17NP441_g002	0.394	0.027	0.04619	0.00062	0.54923	335	19	291.1	3.8	630	130	291.1	1.9	0.54	0.13	17.00	0.49
17NP441_g093	6.079	0.067	0.3237	0.003	0.87377	1987.2	9.8	1807	15	2181	14	2181	7	0.17	0.09	17.00	0.41
17NP441_g096	0.2839	0.0047	0.03472	0.00065	0.89349	254	3.8	220	4	564	23	220	2	0.61	0.13	19.00	0.03
17NP441_g013	1.352	0.02	0.1273	0.0012	0.86284	867.9	8.7	772.3	7.1	1117	20	772.3	3.55	0.31	0.11	20.00	0.25
17NP441_g017	0.411	0.033	0.04375	0.00077	0.40502	347	23	276	4.8	830	160	276	2.4	0.67	0.20	28.00	0.36
17NP441_g099	2.666	0.09	0.1936	0.004	0.98217	1318	25	1140	22	1607	27	1607	13.5	0.29	0.14	56.00	0.37

Sample 17NP454	Sample Type: detrital					Latitude:	39.184725	Longitude:	75.069937								
	Conventional concordia					Ages								Discordance		Conc.Dist., dc	Th/U
Sample #	207Pb	±2σ	206Pb	±2σ	error corr.	207Pb	±2σ	206Pb	±2σ	207Pb	±2σ	Best Age	±1σ	206/238	206/238		
_grain number	235U		238U		206/238 vs 207/235	235U		238U		206Pb				207/206	207/235		
17NP454_g071	0.3746	0.005	0.05226	0.00036	0.46657	322.9	3.7	328.4	2.2	286	28	328.4	1.1	-0.15	-0.02	-1.90	0.34
17NP454_g035	0.3693	0.0053	0.05158	0.00034	0.58704	319.1	3.9	324.2	2.1	287	27	324.2	1.05	-0.13	-0.02	-1.90	0.55
17NP454_g103	0.3744	0.0049	0.05223	0.0004	0.44133	322.8	3.6	328.2	2.4	311	24	328.2	1.2	-0.06	-0.02	-1.90	0.40
17NP454_g015	0.3729	0.0041	0.05201	0.00028	0.56118	322	3.1	326.8	1.7	281	23	326.8	0.85	-0.16	-0.01	-1.80	0.96
17NP454_g047	0.3474	0.0069	0.04881	0.00038	0.199	302.5	5.2	307.2	2.4	260	43	307.2	1.2	-0.18	-0.02	-1.70	0.48
17NP454_g102	0.3788	0.0045	0.0527	0.00038	0.39492	326.1	3.3	331.1	2.3	301	21	331.1	1.15	-0.10	-0.02	-1.70	0.34
17NP454_g055	0.3768	0.0069	0.05238	0.00047	0.47919	324.5	5.1	329.1	2.9	290	36	329.1	1.45	-0.13	-0.01	-1.60	0.50
17NP454_g089	0.3381	0.0069	0.0476	0.00042	0.40756	295.9	5.1	299.8	2.6	268	38	299.8	1.3	-0.12	-0.01	-1.60	0.60
17NP454_g068	0.3942	0.0048	0.05449	0.00037	0.53121	337.3	3.5	342	2.2	310	25	342	1.1	-0.10	-0.01	-1.60	0.40
17NP454_g070	0.3807	0.0043	0.05282	0.00032	0.42952	327.5	3.2	331.8	2	298	25	331.8	1	-0.11	-0.01	-1.50	0.37
17NP454_g099	0.3697	0.0058	0.05149	0.00057	0.55981	319.3	4.3	323.6	3.5	298	28	323.6	1.75	-0.09	-0.01	-1.50	0.36
17NP454_g009	0.3207	0.0053	0.04493	0.00036	0.1525	282.3	4.1	283.3	2.2	266	38	283.3	1.1	-0.07	0.00	-0.35	0.51
17NP454_g024	0.3289	0.0052	0.04555	0.00028	0.46999	289.1	3.9	287.2	1.7	307	34	287.2	0.85	0.06	0.01	0.63	0.45
17NP454_g051	0.3335	0.0048	0.04594	0.00026	0.32528	292.1	3.7	289.5	1.6	315	32	289.5	0.8	0.08	0.01	1.10	0.51
17NP454_g007	0.3321	0.0061	0.04599	0.00028	0.24542	290.9	4.6	289.9	1.7	312	40	289.9	0.85	0.07	0.00	0.52	0.46
17NP454_g094	0.3281	0.0059	0.04605	0.00039	0.39301	288	4.5	290.2	2.4	272	35	290.2	1.2	-0.07	-0.01	-0.83	0.64
17NP454_g080	0.3404	0.007	0.04612	0.00044	0.26947	297.2	5.3	290.6	2.7	348	39	290.6	1.35	0.16	0.02	2.70	0.44
17NP454_g054	0.3309	0.0052	0.04623	0.00033	0.41114	290.9	4	291.3	2.1	287	35	291.3	1.05	-0.01	0.00	-0.43	0.68
17NP454_g062	0.3404	0.0057	0.04655	0.00025	0.1946	297.3	4.3	293.3	1.5	325	38	293.3	0.75	0.10	0.01	1.60	0.50
17NP454_g075	0.3418	0.0055	0.0467	0.00038	0.43024	298.4	4.2	294.2	2.3	332	31	294.2	1.15	0.11	0.01	1.70	0.63
17NP454_g011	0.3344	0.0053	0.04689	0.00026	0.1929	292.8	4.1	295.4	1.6	266	35	295.4	0.8	-0.11	-0.01	-0.96	0.34
17NP454_g031	0.3427	0.0062	0.04689	0.00033	0.28255	299.1	4.7	295.4	2.1	332	38	295.4	1.05	0.11	0.01	1.50	0.35
17NP454_g101	0.3363	0.0062	0.04699	0.00036	0.129	294.1	4.7	296	2.2	290	39	296	1.1	-0.02	-0.01	-0.64	0.46
17NP454_g022	0.3377	0.0071	0.04705	0.00039	0.32652	295.2	5.4	296.4	2.4	274	44	296.4	1.2	-0.08	0.00	-0.37	0.53
17NP454_g028	0.3409	0.0059	0.04706	0.00039	0.46484	297.8	4.5	296.4	2.4	292	36	296.4	1.2	-0.02	0.00	0.54	0.43
17NP454_g098	0.337	0.0064	0.04706	0.00039	0.083182	295.3	4.7	296.5	2.4	282	42	296.5	1.2	-0.05	0.00	-0.60	0.63
17NP454_g029	0.3392	0.0052	0.04708	0.00026	0.27976	296.4	3.9	296.6	1.6	284	35	296.6	0.8	-0.04	0.00	0.00	0.44
17NP454_g044	0.338	0.005	0.0472	0.00032	0.36841	295.5	3.8	297.3	2	290	32	297.3	1	-0.03	-0.01	-0.64	0.45
17NP454_g027	0.3412	0.0054	0.04726	0.00027	0.50653	298.3	4.2	297.6	1.7	313	33	297.6	0.85	0.05	0.00	0.16	0.53
17NP454_g066	0.3423	0.0046	0.04727	0.00027	0.235	298.8	3.5	297.7	1.7	304	32	297.7	0.85	0.02	0.00	0.45	0.48
17NP454_g038	0.3407	0.0069	0.04729	0.0003	0.36255	297.5	5.3	297.9	1.8	290	45	297.9	0.9	-0.03	0.00	-0.06	0.40

Sample 17NP454 continued

	Conventional concordia					Ages								Discordance		Conc.Dist., dc	Th/U
Sample # _grain number	207Pb 235U	±2σ	206Pb 238U	±2σ	error corr. 206/238 vs 207/235	207Pb 235U	±2σ	206Pb 238U	±2σ	207Pb 206Pb	±2σ	Best Age	±1σ	206/238 207/206	206/238 207/235		
17NP454_g065	0.3467	0.0055	0.04736	0.00031	0.32927	302.1	4.2	298.3	1.9	329	36	298.3	0.95	0.09	0.01	1.50	0.68
17NP454_g097	0.345	0.007	0.0475	0.00044	0.32026	300.8	5.3	299.5	2.6	323	35	299.5	1.3	0.07	0.00	0.69	0.34
17NP454_g013	0.3429	0.005	0.04758	0.00032	0.36862	299.7	3.7	299.6	2	299	30	299.6	1	0.00	0.00	-0.11	0.42
17NP454_g087	0.3416	0.0066	0.04759	0.00039	0.23319	298.6	5.1	299.7	2.4	298	39	299.7	1.2	-0.01	0.00	-0.51	0.46
17NP454_g046	0.3507	0.0051	0.04758	0.00038	0.47676	305.1	3.9	299.7	2.4	342	28	299.7	1.2	0.12	0.02	2.10	0.49
17NP454_g010	0.343	0.0058	0.04759	0.00032	0.56014	299.9	4.2	300	1.9	302	35	300	0.95	0.01	0.00	-0.10	0.68
17NP454_g059	0.3508	0.0048	0.0477	0.00028	0.18058	305.2	3.6	300.4	1.7	339	30	300.4	0.85	0.11	0.02	1.90	0.33
17NP454_g025	0.3465	0.005	0.04774	0.00025	0.43808	302	3.8	300.6	1.5	309	29	300.6	0.75	0.03	0.00	0.56	0.48
17NP454_g067	0.3459	0.007	0.04777	0.00044	0.3148	301.5	5.3	300.8	2.7	279	44	300.8	1.35	-0.08	0.00	0.31	0.44
17NP454_g012	0.3432	0.0077	0.04782	0.00034	0.37194	299.2	5.8	301.1	2.1	295	47	301.1	1.05	-0.02	-0.01	-0.59	0.48
17NP454_g033	0.3449	0.0059	0.04797	0.00032	0.35228	300.7	4.5	302	2	313	35	302	1	0.04	0.00	-0.45	0.54
17NP454_g006	0.3428	0.0052	0.04799	0.00028	0.40482	299.2	3.9	302.2	1.7	285	33	302.2	0.85	-0.06	-0.01	-1.10	0.31
17NP454_g018	0.3491	0.0048	0.04813	0.00035	0.58112	304	3.6	303	2.1	319	29	303	1.05	0.05	0.00	0.39	0.38
17NP454_g091	0.3562	0.0074	0.04822	0.00048	0.29594	309.2	5.5	303.6	3	361	43	303.6	1.5	0.16	0.02	2.20	0.30
17NP454_g073	0.3542	0.0061	0.04823	0.00037	0.25967	307.7	4.6	303.7	2.3	316	40	303.7	1.15	0.04	0.01	1.60	0.51
17NP454_g060	0.3552	0.0084	0.04833	0.00038	0.26383	308.4	6.3	304.2	2.3	334	48	304.2	1.15	0.09	0.01	1.60	0.41
17NP454_g041	0.3525	0.0056	0.04854	0.00028	0.19868	306.4	4.2	305.5	1.7	314	36	305.5	0.85	0.03	0.00	0.39	0.46
17NP454_g020	0.3558	0.0071	0.04862	0.00032	0.13649	309.5	5.2	306	1.9	314	45	306	0.95	0.03	0.01	1.10	0.50
17NP454_g034	0.3473	0.0055	0.04866	0.00027	0.31257	302.6	4.2	306.3	1.7	278	35	306.3	0.85	-0.10	-0.01	-1.40	0.85
17NP454_g086	0.3657	0.0078	0.04867	0.00047	0.22723	316.1	5.8	306.3	2.9	393	46	306.3	1.45	0.22	0.03	3.70	0.44
17NP454_g074	0.3619	0.0075	0.04883	0.00037	0.26299	313.5	5.6	307.3	2.3	352	43	307.3	1.15	0.13	0.02	2.30	0.53
17NP454_g008	0.3627	0.0086	0.04896	0.00032	0.14969	313.8	6.4	308.1	2	355	51	308.1	1	0.13	0.02	2.30	0.55
17NP454_g079	0.3508	0.0061	0.04906	0.00052	0.47147	305.1	4.6	308.7	3.2	277	33	308.7	1.6	-0.11	-0.01	-1.30	0.37
17NP454_g077	0.3582	0.0062	0.04907	0.00049	0.36747	310.8	4.6	308.8	3	308	32	308.8	1.5	0.00	0.01	0.77	0.49
17NP454_g085	0.3645	0.0085	0.04907	0.0005	0.38202	315.3	6.3	308.8	3	385	49	308.8	1.5	0.20	0.02	2.50	0.37
17NP454_g023	0.355	0.0051	0.04915	0.00034	0.10367	308.4	3.8	309.3	2.1	299	35	309.3	1.05	-0.03	0.00	-0.31	0.46
17NP454_g017	0.3555	0.0052	0.04916	0.00027	0.10912	308.7	3.9	309.4	1.6	304	31	309.4	0.8	-0.02	0.00	-0.19	0.37
17NP454_g043	0.3568	0.0053	0.04917	0.00044	0.53918	309.7	4	309.4	2.7	308	29	309.4	1.35	0.00	0.00	0.15	0.46
17NP454_g083	0.3549	0.0057	0.04925	0.00047	0.5267	308.2	4.3	309.9	2.9	291	28	309.9	1.45	-0.06	-0.01	-0.56	0.38
17NP454_g016	0.353	0.0055	0.0492	0.00028	0.4123	307.1	4.1	310	1.8	297	33	310	0.9	-0.04	-0.01	-0.99	0.46
17NP454_g005	0.3736	0.0073	0.04941	0.00041	0.001	322.2	5.4	310.9	2.5	420	45	310.9	1.25	0.26	0.04	4.20	0.46

Sample 17NP454 continued

	Conventional concordia					Ages								Discordance		Conc.Dist., dc	Th/U
Sample # _grain number	207Pb 235U	±2σ	206Pb 238U	±2σ	error corr. 206/238 vs 207/235	207Pb 235U	±2σ	206Pb 238U	±2σ	207Pb 206Pb	±2σ	Best Age	±1σ	206/238 207/206	206/238 207/235		
17NP454_g061	0.3552	0.0062	0.04951	0.00059	0.51296	308.5	4.6	311.5	3.6	276	35	311.5	1.8	-0.13	-0.01	-1.10	0.34
17NP454_g057	0.3618	0.0056	0.04951	0.00038	0.32454	313.5	4.1	311.5	2.3	326	35	311.5	1.15	0.04	0.01	0.75	0.52
17NP454_g030	0.3625	0.007	0.04954	0.00043	0.53897	314.6	5.3	311.7	2.6	315	40	311.7	1.3	0.01	0.01	0.89	0.33
17NP454_g001	0.3569	0.0069	0.04965	0.00053	0.60837	310.4	5.3	312.4	3.3	296	37	312.4	1.65	-0.06	-0.01	-0.92	0.33
17NP454_g076	0.3639	0.0057	0.04967	0.00045	0.67997	315	4.3	312.5	2.7	307	28	312.5	1.35	-0.02	0.01	0.98	0.43
17NP454_g050	0.3586	0.0084	0.04981	0.00035	0.001	311.5	6.4	313.3	2.1	292	54	313.3	1.05	-0.07	-0.01	-0.81	0.63
17NP454_g052	0.3604	0.0052	0.04985	0.00037	0.62536	312.4	3.9	313.6	2.3	292	29	313.6	1.15	-0.07	0.00	-0.41	0.57
17NP454_g064	0.366	0.0051	0.04988	0.00027	0.25812	316.6	3.8	313.8	1.7	329	34	313.8	0.85	0.05	0.01	1.10	0.54
17NP454_g072	0.3667	0.0046	0.05015	0.00036	0.56743	317.2	3.4	315.5	2.2	322	26	315.5	1.1	0.02	0.01	0.64	0.59
17NP454_g081	0.3704	0.0069	0.05018	0.00051	0.4475	319.8	5.1	315.6	3.1	342	36	315.6	1.55	0.08	0.01	1.60	0.36
17NP454_g039	0.3631	0.0069	0.05038	0.00068	0.68073	314.3	5.2	316.8	4.2	297	34	316.8	2.1	-0.07	-0.01	-0.85	0.36
17NP454_g002	0.3707	0.008	0.05055	0.00039	0.42233	320	5.9	317.9	2.4	336	46	317.9	1.2	0.05	0.01	0.83	0.44
17NP454_g082	0.366	0.0052	0.05058	0.0005	0.54681	316.9	3.8	318.1	3.1	306	25	318.1	1.55	-0.04	0.00	-0.51	0.28
17NP454_g049	0.3719	0.0048	0.05065	0.00037	0.52494	320.9	3.6	318.5	2.2	330	27	318.5	1.1	0.03	0.01	0.92	0.61
17NP454_g056	0.3698	0.0054	0.05067	0.00044	0.60771	319.4	4	318.6	2.7	312	31	318.6	1.35	-0.02	0.00	0.32	0.54
17NP454_g003	0.3727	0.0067	0.05071	0.00048	0.42454	321.6	4.9	318.9	2.9	348	38	318.9	1.45	0.08	0.01	1.00	0.64
17NP454_g026	0.3685	0.0048	0.0508	0.00028	0.46221	318.5	3.5	319.4	1.7	307	26	319.4	0.85	-0.04	0.00	-0.32	0.57
17NP454_g090	0.3657	0.0054	0.05086	0.0004	0.35063	317	4	319.8	2.5	305	28	319.8	1.25	-0.05	-0.01	-1.20	0.72
17NP454_g063	0.3756	0.0056	0.05117	0.00031	0.42832	324	4.1	321.7	1.9	326	31	321.7	0.95	0.01	0.01	0.76	0.42
17NP454_g053	0.3737	0.0043	0.05121	0.00026	0.482	322.6	3.2	321.9	1.6	314	24	321.9	0.8	-0.03	0.00	0.16	0.44
17NP454_g032	0.3711	0.005	0.05133	0.00043	0.61454	320.4	3.7	323.1	2.7	302	25	323.1	1.35	-0.07	-0.01	-0.80	0.48
17NP454_g088	0.3708	0.0051	0.05142	0.00043	0.66285	320.1	3.7	323.2	2.6	310	21	323.2	1.3	-0.04	-0.01	-1.10	0.61
17NP454_g040	0.3767	0.0075	0.05143	0.00055	0.13206	324.5	5.5	323.3	3.4	323	49	323.3	1.7	0.00	0.00	0.47	0.37
17NP454_g019	0.3764	0.0048	0.0516	0.00028	0.58666	324.3	3.5	324.3	1.7	331	25	324.3	0.85	0.02	0.00	0.02	0.32
17NP454_g014	0.3753	0.0047	0.05176	0.00032	0.41471	323.8	3.5	325.3	1.9	323	26	325.3	0.95	-0.01	0.00	-0.62	0.56
17NP454_g021	0.3786	0.005	0.05198	0.00038	0.53888	326.3	3.7	326.7	2.3	328	27	326.7	1.15	0.00	0.00	-0.23	0.50
17NP454_g095	0.3795	0.0047	0.05254	0.00043	0.56192	326.6	3.5	330.1	2.6	317	21	330.1	1.3	-0.04	-0.01	-1.20	0.69
17NP454_g096	0.3844	0.0057	0.05272	0.00046	0.53517	330.6	4.1	331.2	2.8	344	23	331.2	1.4	0.04	0.00	-0.33	0.41
17NP454_g078	0.3894	0.0061	0.0528	0.00063	0.42915	333.8	4.4	331.7	3.8	347	34	331.7	1.9	0.04	0.01	0.80	0.39
17NP454_g045	0.3863	0.0054	0.05291	0.00044	0.5346	331.9	3.9	332.3	2.7	323	28	332.3	1.35	-0.03	0.00	-0.24	0.62
17NP454_g069	0.3856	0.0054	0.05313	0.0004	0.4736	331	4	333.7	2.5	303	28	333.7	1.25	-0.10	-0.01	-0.89	0.37

Sample 17NP454 continued

	Conventional concordia					Ages								Discordance		Conc.Dist., dc	Th/U
Sample #	207Pb	±2σ	206Pb	±2σ	error corr.	207Pb	±2σ	206Pb	±2σ	207Pb	±2σ	Best Age	±1σ	206/238	206/238		
_grain number	235U		238U		206/238 vs 207/235	235U		238U		206Pb				207/206	207/235		
17NP454_g004	0.3848	0.0045	0.05315	0.00029	0.61934	330.5	3.3	333.9	1.8	313	23	333.9	0.9	-0.07	-0.01	-1.20	0.37
17NP454_g037	0.3848	0.0052	0.05319	0.00042	0.58772	330.8	3.9	334	2.5	312	29	334	1.25	-0.07	-0.01	-1.20	0.36
17NP454_g036	0.3902	0.0048	0.0532	0.00033	0.47458	334.5	3.5	334.1	2	347	26	334.1	1	0.04	0.00	0.13	0.45
17NP454_g042	0.3898	0.0049	0.05349	0.00036	0.46938	334.1	3.6	335.9	2.2	319	26	335.9	1.1	-0.05	-0.01	-0.59	0.36
17NP454_g058	0.3955	0.0058	0.05401	0.00053	0.69948	338.2	4.2	339.1	3.2	316	27	339.1	1.6	-0.07	0.00	-0.25	0.54
17NP454_g100	0.5508	0.0088	0.07139	0.00058	0.15902	445.2	5.8	444.5	3.5	471	35	444.5	1.75	0.06	0.00	0.27	0.39
17NP454_g093	0.3777	0.01	0.04895	0.00051	0.30181	324.9	7.6	308.1	3.1	470	59	308.1	1.55	0.34	0.05	6.30	0.42
17NP454_g092	0.378	0.012	0.04766	0.00052	0.52388	325	9	300.1	3.2	511	64	300.1	1.6	0.41	0.08	9.60	0.62
17NP454_g048	5.197	0.071	0.3053	0.0024	0.7727	1851.5	12	1718	12	1998	19	1998	9.5	0.14	0.07	14.00	0.05
17NP454_g084	0.404	0.012	0.04827	0.00064	0.39879	344.4	8.5	303.9	3.9	613	56	303.9	1.95	0.50	0.12	15.00	0.81

Sample 17NP478	Sample Type: detrital					Latitude:	39.223968	Longitude:	75.025066								
	Conventional concordia					Ages								Discordance		Conc.Dist., dc	Th/U
Sample #	207Pb	±2σ	206Pb	±2σ	error corr.	207Pb	±2σ	206Pb	±2σ	207Pb	±2σ	Best Age	±1σ	206/238	206/238		
_grain number	235U		238U		206/238 vs 207/235	235U		238U		206Pb				207/206	207/235		
17NP478_g001	0.3621	0.0045	0.05014	0.00042	0.53319	313.7	3.3	315.4	2.6	300	21	315.4	1.3	-0.05	-0.01	-3.75	0.70
17NP478_g002	0.3892	0.0048	0.05365	0.00042	0.41445	333.7	3.5	336.9	2.6	305	21	336.9	1.3	-0.10	-0.01	-2.72	0.29
17NP478_g006	0.3574	0.005	0.04794	0.00041	0.4293	310.2	3.8	301.8	2.5	371	26	301.8	1.25	0.19	0.03	-2.52	0.93
17NP478_g009	0.3411	0.0056	0.04737	0.00035	0.23597	297.9	4.3	298.4	2.2	278	33	298.4	1.1	-0.07	0.00	-2.31	0.71
17NP478_g084	0.3543	0.0051	0.04891	0.00044	0.5343	307.8	3.8	307.8	2.7	306	25	307.8	1.35	-0.01	0.00	-2.21	0.87
17NP478_g003	0.3427	0.0056	0.0478	0.00045	0.47774	299.1	4.2	301	2.8	280	31	301	1.4	-0.08	-0.01	-2.13	0.67
17NP478_g007	0.381	0.011	0.04874	0.00056	0.74816	327.6	7.8	306.8	3.4	476	42	306.8	1.7	0.36	0.06	-1.97	0.95
17NP478_g091	0.355	0.0057	0.04896	0.00046	0.49325	308.3	4.3	308.1	2.8	330	29	308.1	1.4	0.07	0.00	-1.81	0.40
17NP478_g016	0.3379	0.0059	0.0459	0.00042	0.21441	295.4	4.5	289.3	2.6	327	37	289.3	1.3	0.12	0.02	-1.79	0.43
17NP478_g048	0.3133	0.0062	0.04403	0.00035	0.1016	276.6	4.8	277.7	2.1	250	41	277.7	1.05	-0.11	0.00	-0.13	0.38
17NP478_g027	0.317	0.011	0.04454	0.00052	0.067988	279.8	8.7	280.9	3.2	267	75	280.9	1.6	-0.05	0.00	-0.11	0.27
17NP478_g109	0.3237	0.0051	0.04467	0.00033	0.34273	284.6	3.9	281.7	2.1	328	28	281.7	1.05	0.14	0.01	5.52	0.46
17NP478_g108	0.3371	0.0065	0.04518	0.00065	0.48174	294.9	4.9	284.9	4	348	38	284.9	2	0.18	0.03	3.16	0.45
17NP478_g029	0.3273	0.0056	0.04524	0.00041	0.29246	287.3	4.3	285.2	2.5	288	33	285.2	1.25	0.01	0.01	-0.41	0.41
17NP478_g039	0.3257	0.0055	0.04532	0.00036	0.46656	286.1	4.2	285.7	2.2	287	33	285.7	1.1	0.00	0.00	-0.17	0.55
17NP478_g040	0.313	0.012	0.04533	0.00054	0.056123	275.2	9.1	285.8	3.4	195	77	285.8	1.7	-0.47	-0.04	-0.81	0.70
17NP478_g099	0.3246	0.0081	0.04534	0.00084	0.74353	285.2	6.2	285.8	5.2	289	38	285.8	2.6	0.01	0.00	1.78	0.52
17NP478_g023	0.3261	0.009	0.04553	0.00048	0.034734	286.8	7	287	3	272	62	287	1.5	-0.06	0.00	2.09	0.34
17NP478_g057	0.335	0.0066	0.0456	0.00038	0.45396	293.2	5	287.4	2.3	338	36	287.4	1.15	0.15	0.02	0.05	0.34
17NP478_g064	0.3342	0.0064	0.0456	0.00046	0.3286	292.7	4.9	287.4	2.8	319	37	287.4	1.4	0.10	0.02	0.72	0.50
17NP478_g019	0.3323	0.0058	0.04587	0.00037	0.32169	291.2	4.4	289.1	2.3	298	34	289.1	1.15	0.03	0.01	0.90	0.36
17NP478_g070	0.3288	0.0048	0.04598	0.00034	0.32035	288.8	3.7	289.8	2.1	292	28	289.8	1.05	0.01	0.00	0.27	0.56
17NP478_g043	0.3424	0.0094	0.04611	0.00045	0.12066	298.9	7.1	290.6	2.8	379	72	290.6	1.4	0.23	0.03	0.36	0.51
17NP478_g052	0.3459	0.0075	0.04614	0.00042	0.15103	302.5	5.7	290.7	2.6	376	44	290.7	1.3	0.23	0.04	-0.25	0.77
17NP478_g041	0.359	0.03	0.04635	0.00098	0.63955	311	22	292	6	440	160	292	3	0.34	0.06	-0.42	0.58
17NP478_g020	0.3331	0.0059	0.04637	0.00047	0.27118	291.8	4.5	292.2	2.9	275	37	292.2	1.45	-0.06	0.00	0.22	0.52
17NP478_g085	0.3349	0.0048	0.04672	0.00043	0.55434	293.2	3.6	294.3	2.6	303	25	294.3	1.3	0.03	0.00	0.34	0.65
17NP478_g078	0.3349	0.0054	0.04672	0.00043	0.45598	293.2	4.1	294.4	2.6	280	29	294.4	1.3	-0.05	0.00	-0.04	0.51
17NP478_g102	0.377	0.015	0.04701	0.0004	0.36452	323	10	296.1	2.5	509	71	296.1	1.25	0.42	0.08	1.22	0.93
17NP478_g005	0.3407	0.0071	0.04701	0.00038	0.039657	297.4	5.4	296.2	2.4	279	45	296.2	1.2	-0.06	0.00	-1.25	0.71

Sample 17NP478 continued

	Conventional concordia				Ages								Discordance		Conc.Dist., dc	Th/U
Sample # _grain number	207Pb 235U	±2σ	206Pb 238U	±2σ	error corr. 206/238 vs 207/235	207Pb 235U	±2σ	206Pb 238U	±2σ	207Pb 206Pb	±2σ	Best Age	±1σ	206/238 207/206	206/238 207/235		
17NP478_g013	0.3461	0.0082	0.04724	0.00053	0.13515	301.7	6.2	297.5	3.3	331	52	297.5	1.65	0.10	0.01	-0.42	0.37
17NP478_g062	0.3476	0.0056	0.04752	0.00059	0.66924	302.8	4.2	299.3	3.6	329	25	299.3	1.8	0.09	0.01	-1.13	0.90
17NP478_g100	0.3401	0.0073	0.04755	0.00045	0.23116	297.1	5.5	299.4	2.8	275	48	299.4	1.4	-0.09	-0.01	2.46	0.47
17NP478_g045	0.3466	0.0054	0.04758	0.00038	0.08981	302.7	4.2	299.7	2.3	315	34	299.7	1.15	0.05	0.01	0.59	0.67
17NP478_g060	0.3491	0.0057	0.04761	0.00036	0.15117	304.3	4.2	299.8	2.2	355	33	299.8	1.1	0.16	0.01	0.72	0.58
17NP478_g018	0.3504	0.0057	0.04769	0.00037	0.37863	304.8	4.3	300.3	2.3	337	32	300.3	1.15	0.11	0.01	-0.54	0.63
17NP478_g044	0.37	0.012	0.04771	0.00054	0.53526	319.1	9	300.4	3.3	462	57	300.4	1.65	0.35	0.06	-1.49	0.48
17NP478_g072	0.3503	0.0068	0.04775	0.00051	0.38944	304.6	5.1	300.7	3.1	360	36	300.7	1.55	0.16	0.01	-1.15	0.66
17NP478_g053	0.3439	0.0049	0.04778	0.00043	0.5952	300	3.7	300.9	2.6	282	24	300.9	1.3	-0.07	0.00	0.43	1.02
17NP478_g042	0.3542	0.0054	0.04784	0.0004	0.39727	307.7	4.1	301.3	2.4	354	27	301.3	1.2	0.15	0.02	-0.72	0.80
17NP478_g071	0.345	0.0084	0.0479	0.00047	0.30853	300.7	6.3	301.6	2.9	305	52	301.6	1.45	0.01	0.00	0.33	0.46
17NP478_g065	0.3433	0.0051	0.04793	0.00037	0.19554	299.5	3.8	301.8	2.3	291	30	301.8	1.15	-0.04	-0.01	0.80	0.66
17NP478_g024	0.3456	0.0058	0.04794	0.00038	0.13005	301.6	4.3	301.8	2.3	284	35	301.8	1.15	-0.06	0.00	0.87	0.57
17NP478_g080	0.3449	0.0061	0.04796	0.00046	0.60412	300.7	4.6	302	2.8	297	30	302	1.4	-0.02	0.00	-0.93	0.34
17NP478_g063	0.3442	0.0053	0.048	0.00038	0.33086	300.2	4	302.2	2.3	281	29	302.2	1.15	-0.08	-0.01	0.01	0.49
17NP478_g077	0.342	0.0056	0.04806	0.00039	0.22958	298.5	4.2	302.6	2.4	285	34	302.6	1.2	-0.06	-0.01	0.34	0.65
17NP478_g050	0.3383	0.0092	0.04812	0.00043	0.23656	296	7	302.9	2.6	239	55	302.9	1.3	-0.27	-0.02	-0.06	0.63
17NP478_g094	0.3504	0.0049	0.0482	0.00036	0.27941	304.9	3.7	303.4	2.2	333	26	303.4	1.1	0.09	0.00	0.56	0.44
17NP478_g046	0.483	0.015	0.04822	0.00041	0.41604	398.8	9.8	303.5	2.5	983	53	303.5	1.25	0.69	0.24	0.02	0.74
17NP478_g098	0.3498	0.0067	0.04837	0.00038	0.037712	304.3	5	304.5	2.3	288	42	304.5	1.15	-0.06	0.00	0.82	0.51
17NP478_g106	0.3499	0.006	0.04841	0.00037	0.32733	304.4	4.5	304.8	2.3	300	35	304.8	1.15	-0.02	0.00	1.61	0.61
17NP478_g112	0.3505	0.0087	0.04852	0.00043	0.087504	305.2	6.6	305.4	2.7	305	54	305.4	1.35	0.00	0.00	3.26	0.63
17NP478_g047	0.3474	0.0053	0.04854	0.00048	0.6141	303	4.1	305.5	2.9	276	25	305.5	1.45	-0.11	-0.01	-0.04	0.41
17NP478_g054	0.3508	0.0054	0.04861	0.00049	0.52038	305.2	4.1	306	3	306	27	306	1.5	0.00	0.00	-0.53	0.56
17NP478_g105	0.3765	0.0064	0.04865	0.00049	0.14155	324.4	4.7	306.2	3	476	32	306.2	1.5	0.36	0.06	1.60	0.54
17NP478_g086	0.3524	0.0057	0.04869	0.00037	0.36379	306.7	4.3	306.7	2.3	314	31	306.7	1.15	0.02	0.00	1.59	0.88
17NP478_g107	0.3508	0.006	0.04873	0.00041	0.21476	305.6	4.4	306.7	2.5	292	35	306.7	1.25	-0.05	0.00	4.03	0.95
17NP478_g104	0.3548	0.0052	0.04883	0.00036	0.29748	308.2	3.9	307.3	2.2	322	27	307.3	1.1	0.05	0.00	2.34	0.39
17NP478_g032	0.3573	0.0059	0.04898	0.00046	0.46793	310.1	4.4	308.2	2.8	309	30	308.2	1.4	0.00	0.01	-0.13	0.77
17NP478_g101	0.461	0.033	0.049	0.00058	0.73299	387	23	308.3	3.5	890	130	308.3	1.75	0.65	0.20	2.14	0.83

Sample 17NP478 continued

	Conventional concordia					Ages								Discordance		Conc.Dist., dc	Th/U
Sample #	207Pb	±2σ	206Pb	±2σ	error corr.	207Pb	±2σ	206Pb	±2σ	207Pb	±2σ	Best Age	±1σ	206/238	206/238		
_grain number	235U		238U		206/238 vs 207/235	235U		238U		206Pb				207/206	207/235		
17NP478_g095	0.3519	0.0051	0.04899	0.00037	0.36388	306	3.8	308.3	2.3	302	25	308.3	1.15	-0.02	-0.01	5.57	0.46
17NP478_g037	0.443	0.011	0.04907	0.00047	0.58889	373.3	7.9	308.8	2.9	791	43	308.8	1.45	0.61	0.17	-0.68	0.25
17NP478_g103	0.3515	0.0054	0.04908	0.00052	0.67035	305.7	4	308.9	3.2	294	22	308.9	1.6	-0.05	-0.01	2.50	0.43
17NP478_g015	0.3559	0.0048	0.04912	0.00042	0.55721	309.3	3.6	309.1	2.6	306	23	309.1	1.3	-0.01	0.00	-1.05	0.52
17NP478_g030	0.3591	0.0051	0.0492	0.00048	0.54325	312	3.7	309.6	2.9	321	24	309.6	1.45	0.04	0.01	0.60	0.38
17NP478_g083	0.3598	0.0053	0.04925	0.00035	0.25725	312.3	3.9	309.9	2.2	334	28	309.9	1.1	0.07	0.01	-1.33	0.80
17NP478_g049	0.3591	0.005	0.04928	0.00034	0.1962	311.4	3.8	310.1	2.1	329	26	310.1	1.05	0.06	0.00	-1.12	0.51
17NP478_g022	0.3575	0.0073	0.04931	0.00044	0.18594	310.5	5.5	310.3	2.7	297	43	310.3	1.35	-0.04	0.00	-0.17	0.59
17NP478_g082	0.352	0.0067	0.04936	0.0005	0.66105	306.6	5	310.6	3.1	277	30	310.6	1.55	-0.12	-0.01	-0.42	0.66
17NP478_g036	0.3609	0.0091	0.04937	0.00046	0.036117	312.3	6.8	310.7	2.8	317	56	310.7	1.4	0.02	0.01	-0.29	0.59
17NP478_g008	0.3567	0.0053	0.04941	0.00036	0.28857	309.6	4	310.9	2.2	319	29	310.9	1.1	0.03	0.00	-1.65	0.44
17NP478_g025	0.3598	0.0053	0.04948	0.00037	0.24813	312.3	3.9	311.3	2.3	316	26	311.3	1.15	0.01	0.00	-0.45	0.44
17NP478_g059	0.3568	0.0053	0.04972	0.00047	0.21248	309.7	3.9	312.8	2.9	282	33	312.8	1.45	-0.11	-0.01	0.13	0.46
17NP478_g061	0.3619	0.0064	0.04971	0.00043	0.39059	313.4	4.8	313	2.6	302	33	313	1.3	-0.04	0.00	-0.81	0.43
17NP478_g076	0.358	0.0068	0.04989	0.0004	0.19476	311.4	5.2	313.8	2.4	302	41	313.8	1.2	-0.04	-0.01	-0.37	0.56
17NP478_g074	0.445	0.021	0.05002	0.00052	0.10057	373	15	314.6	3.2	756	94	314.6	1.6	0.58	0.16	0.03	0.35
17NP478_g026	0.365	0.0065	0.05022	0.00045	0.31637	315.7	4.8	315.8	2.7	313	34	315.8	1.35	-0.01	0.00	-1.34	0.39
17NP478_g090	0.3647	0.0055	0.05034	0.00064	0.64247	315.6	4.1	316.6	3.9	341	24	316.6	1.95	0.07	0.00	-1.19	0.65
17NP478_g017	0.3647	0.0081	0.05036	0.00045	0.32337	316	5.9	316.7	2.8	302	46	316.7	1.4	-0.05	0.00	-1.08	0.40
17NP478_g111	0.3743	0.0063	0.05039	0.00044	0.42006	322.6	4.7	316.9	2.7	368	34	316.9	1.35	0.14	0.02	4.19	0.63
17NP478_g096	0.3696	0.0062	0.05042	0.00045	0.43226	319.2	4.6	317.1	2.7	358	31	317.1	1.35	0.11	0.01	2.03	0.38
17NP478_g011	0.3683	0.0074	0.05048	0.00069	0.58704	319	5.3	317.5	4.2	307	33	317.5	2.1	-0.03	0.00	-0.81	0.31
17NP478_g056	0.3669	0.0056	0.05048	0.00048	0.61103	317.2	4.1	317.5	2.9	310	24	317.5	1.45	-0.02	0.00	0.37	0.79
17NP478_g058	0.3731	0.0094	0.05071	0.00057	0.12692	321.6	7	318.8	3.5	326	54	318.8	1.75	0.02	0.01	-0.51	0.71
17NP478_g051	0.364	0.0048	0.05105	0.00051	0.47409	315.2	3.6	320.9	3.1	273	23	320.9	1.55	-0.18	-0.02	-0.50	0.64
17NP478_g028	0.372	0.011	0.05102	0.00091	0.43959	320.6	7.9	321.6	5.4	281	57	321.6	2.7	-0.14	0.00	-0.41	0.49
17NP478_g004	0.375	0.007	0.05117	0.00055	0.46709	323.3	5.1	321.7	3.4	339	30	321.7	1.7	0.05	0.00	0.13	0.39
17NP478_g075	0.3723	0.0071	0.0513	0.00077	0.63908	321.2	5.3	322.5	4.8	327	31	322.5	2.4	0.01	0.00	-0.34	0.66
17NP478_g081	0.3833	0.0055	0.05153	0.00039	0.44554	329.7	3.9	323.9	2.4	403	25	323.9	1.2	0.20	0.02	0.59	0.64
17NP478_g093	0.3692	0.0067	0.05155	0.0004	0.12001	319.2	5	324	2.5	293	39	324	1.25	-0.11	-0.02	-0.15	0.49

Sample 17NP478 continued

	Conventional concordia					Ages								Discordance		Conc.Dist., dc	Th/U
Sample #	207Pb	±2σ	206Pb	±2σ	error corr.	207Pb	±2σ	206Pb	±2σ	207Pb	±2σ	Best Age	±1σ	206/238	206/238		
_grain number	235U		238U		206/238 vs 207/235	235U		238U		206Pb				207/206	207/235		
17NP478_g088	0.3729	0.0049	0.05219	0.00048	0.49737	322	3.6	328	2.9	298	22	328	1.45	-0.10	-0.02	-0.69	0.73
17NP478_g055	0.471	0.025	0.05231	0.00065	0.8124	389	15	328.7	4	701	63	328.7	2	0.53	0.16	0.02	0.81
17NP478_g035	0.3797	0.0052	0.05238	0.00047	0.54356	327	3.8	329.1	2.9	295	23	329.1	1.45	-0.12	-0.01	0.96	0.79
17NP478_g079	0.3739	0.0055	0.05245	0.00056	0.49346	322.4	4	329.5	3.5	290	28	329.5	1.75	-0.14	-0.02	1.11	0.56
17NP478_g010	0.3951	0.0069	0.0531	0.00059	0.68056	337.9	5	333.5	3.6	363	28	333.5	1.8	0.08	0.01	-1.59	0.36
17NP478_g014	0.461	0.014	0.05324	0.00048	0.65056	383.7	9.5	334.4	3	679	56	334.4	1.5	0.51	0.13	-1.11	0.17
17NP478_g066	0.3828	0.0059	0.05329	0.00049	0.67068	328.9	4.3	334.7	3	295	24	334.7	1.5	-0.13	-0.02	0.53	0.48
17NP478_g067	0.3929	0.0066	0.05346	0.00042	0.29834	336.7	4.8	335.7	2.6	355	32	335.7	1.3	0.05	0.00	0.02	0.33
17NP478_g068	0.385	0.0049	0.05372	0.00043	0.42157	330.6	3.6	337.3	2.6	301	22	337.3	1.3	-0.12	-0.02	0.83	1.15
17NP478_g033	0.3881	0.005	0.05378	0.00046	0.45042	332.9	3.7	337.7	2.8	303	23	337.7	1.4	-0.11	-0.01	1.39	0.90
17NP478_g012	0.3944	0.0054	0.05409	0.00046	0.53611	337.9	3.9	339.6	2.8	314	22	339.6	1.4	-0.08	-0.01	-1.64	0.27
17NP478_g073	0.3915	0.0058	0.0542	0.00044	0.40759	335.8	4.2	340.5	2.6	322	26	340.5	1.3	-0.06	-0.01	-0.59	0.42
17NP478_g021	0.47	0.014	0.05468	0.00067	0.3434	390.4	9.8	343.2	4.1	659	62	343.2	2.05	0.48	0.12	-0.17	0.33
17NP478_g069	0.4469	0.0095	0.05473	0.00058	0.34079	375	6.6	343.5	3.5	573	39	343.5	1.75	0.40	0.08	-0.43	1.54
17NP478_g092	0.4004	0.0067	0.05535	0.00063	0.68639	341.8	4.9	347.3	3.8	317	25	347.3	1.9	-0.10	-0.02	0.31	0.61
17NP478_g038	0.4151	0.0066	0.05606	0.00046	0.52252	352.5	4.8	351.6	2.8	351	30	351.6	1.4	0.00	0.00	-0.25	0.31
17NP478_g097	1.212	0.071	0.05684	0.00086	0.73861	801	33	356.3	5.3	2378	85	356.3	2.65	0.85	0.56	1.78	0.50
17NP478_g089	0.4894	0.011	0.06484	0.00056	0.11564	403.9	7.3	405	3.4	404	45	405	1.7	0.00	0.00	-1.65	0.98
17NP478_g110	1.372	0.085	0.0672	0.0015	0.96363	872	35	419	9.1	2305	70	419	4.55	0.82	0.52	1.97	0.84
17NP478_g031	0.689	0.013	0.08219	0.00092	0.35894	532	7.8	509.2	5.5	633	39	509.2	2.75	0.20	0.04	1.62	0.12
17NP478_g087	1.502	0.017	0.15475	0.0011	0.48846	932.1	6.8	927.5	6	953	15	927.5	3	0.03	0.00	0.26	0.22
17NP478_g034	11.068	0.12	0.4621	0.0038	0.79527	2529	11	2449	17	2600.4	10	2600.4	5	0.06	0.03	-0.85	0.83
17NP478_g116	0.3508	0.0058	0.04853	0.00044	0.2468	305.2	4.4	305.5	2.7	307	36	305.5	1.35	0.00	0.00	6.70	0.57
17NP478_g114	0.371	0.013	0.04755	0.0006	0.226	320	10	299.5	3.7	489	74	299.5	1.85	0.39	0.06	7.28	0.71
17NP478_g113	0.3853	0.0059	0.05252	0.00049	0.53846	330.7	4.4	329.9	3	346	26	329.9	1.5	0.05	0.00	7.61	0.29
17NP478_g118	0.3289	0.0063	0.04636	0.00035	0.25049	289.5	4.9	292.1	2.2	274	39	292.1	1.1	-0.07	-0.01	7.80	0.87
17NP478_g117	0.402	0.013	0.0491	0.00037	0.26095	341.8	9.1	309	2.3	548	63	309	1.15	0.44	0.10	8.11	0.36
17NP478_g115	0.4166	0.01	0.05112	0.00044	0.26533	353	7.1	321.4	2.7	571	49	321.4	1.35	0.44	0.09	8.14	0.43
17NP478_g119	0.4582	0.0071	0.06028	0.00063	0.34441	382.9	4.9	377.3	3.8	426	30	377.3	1.9	0.11	0.01	10.40	0.24
17NP478_g120	0.3713	0.0066	0.0516	0.00062	0.62085	320.5	4.9	324.3	3.8	314	28	324.3	1.9	-0.03	-0.01	10.80	0.45

Sample 17NP478 continued

	Conventional concordia					Ages								Discordance		Conc.Dist., dc	Th/U
Sample # _grain number	207Pb 235U	±2σ	206Pb 238U	±2σ	error corr. 206/238 vs 207/235	207Pb 235U	±2σ	206Pb 238U	±2σ	207Pb 206Pb	±2σ	Best Age	±1σ	206/238 207/206	206/238 207/235		
17NP478_g122	0.3481	0.0046	0.04802	0.00037	0.35392	303.5	3.5	302.3	2.3	307	24	302.3	1.15	0.02	0.00	11.20	0.45
17NP478_g121	0.3427	0.006	0.04819	0.00038	0.287	299	4.5	303.4	2.3	271	36	303.4	1.15	-0.12	-0.01	12.20	0.74
17NP478_g123	0.3534	0.0062	0.04864	0.00045	0.70946	307.1	4.6	306.1	2.7	308	26	306.1	1.35	0.01	0.00	15.50	1.08
17NP478_g124	0.3596	0.0052	0.05013	0.00039	0.28181	311.8	3.9	315.3	2.4	276	24	315.3	1.2	-0.14	-0.01	17.20	0.49
17NP478_g126	0.3471	0.0056	0.04853	0.0004	0.1675	302.4	4.2	305.5	2.5	288	34	305.5	1.25	-0.06	-0.01	20.20	0.61
17NP478_g125	0.3764	0.0065	0.04802	0.00038	0.27256	324.7	4.8	302.4	2.4	476	33	302.4	1.2	0.36	0.07	21.80	0.65
17NP478_g127	0.3643	0.0056	0.04925	0.00054	0.61544	315.3	4.2	309.9	3.3	346	26	309.9	1.65	0.10	0.02	22.50	0.91
17NP478_g128	0.3939	0.0057	0.05427	0.00045	0.45746	337.5	4.1	340.7	2.8	323	24	340.7	1.4	-0.05	-0.01	26.70	0.72
17NP478_g129	0.3674	0.0055	0.05094	0.00056	0.63981	317.7	4.1	320.3	3.4	305	27	320.3	1.7	-0.05	-0.01	32.90	0.52
17NP478_g130	0.35	0.005	0.04862	0.00037	0.11989	304.6	3.8	306	2.3	301	31	306	1.15	-0.02	0.00	107.00	1.01
17NP478_g131	0.3524	0.0052	0.04892	0.00036	0.11959	306.7	4	307.9	2.2	304	30	307.9	1.1	-0.01	0.00	109.00	0.89

Sample 15NP207	Sample Type: detrital					Latitude:	38.92799	Longitude:	75.49825								
	Conventional concordia					Ages								Discordance		Conc.Dist., dc	Th/U
Sample #	207Pb	±2σ	206Pb	±2σ	error corr.	207Pb	±2σ	206Pb	±2σ	207Pb	±2σ	Best Age	±1σ	206/238	206/238		
_grain number	235U		238U		206/238 vs 207/235	235U		238U		206Pb				207/206	207/235		
15NP207_g012	0.33	0.042	0.048	0.0016	0.040938	275	30	302	10	20	200	302	5	-14.10	-0.10	-4.90	0.00
15NP207_g018	0.557	0.063	0.0753	0.0047	0.071687	425	40	466	27	230	200	466	13.5	-1.03	-0.10	-4.90	0.00
15NP207_g087	0.261	0.011	0.03843	0.00046	0.084966	234.1	9.2	243.1	2.9	134	89	243.1	1.45	-0.81	-0.04	-3.60	0.75
15NP207_g128	0.3089	0.0078	0.04473	0.00043	0.24148	272.8	6	282	2.6	185	52	282	1.3	-0.52	-0.03	-3.60	0.48
15NP207_g139	10.841	0.098	0.4857	0.0047	0.91691	2508.5	8.4	2551	21	2461.1	6.2	2461.1	3.1	-0.04	-0.02	-3.20	0.50
15NP207_g009	0.595	0.038	0.078	0.0025	0.27664	465	24	484	15	350	130	484	7.5	-0.38	-0.04	-2.60	0.00
15NP207_g127	0.273	0.01	0.03958	0.00047	0.1338	243.8	8.1	250.2	2.9	188	76	250.2	1.45	-0.33	-0.03	-2.30	1.05
15NP207_g124	0.2921	0.0074	0.04205	0.00049	0.37008	260	5.8	265.5	3	230	55	265.5	1.5	-0.15	-0.02	-2.30	0.47
15NP207_g029	0.513	0.066	0.0687	0.003	0.012109	393	41	428	18	210	210	428	9	-1.04	-0.09	-2.20	0.00
15NP207_g114	0.258	0.011	0.03752	0.00053	0.093229	232	8.8	237.4	3.3	176	85	237.4	1.65	-0.35	-0.02	-2.10	0.70
15NP207_g096	0.2726	0.0092	0.03941	0.00051	0.35552	244	7.3	249.2	3.1	180	65	249.2	1.55	-0.38	-0.02	-2.00	0.60
15NP207_g020	6.58	0.12	0.381	0.0047	0.42846	2055	16	2080	22	2025	32	2025	16	-0.03	-0.01	-2.00	0.84
15NP207_g092	0.238	0.012	0.03481	0.00048	0.017665	215.7	9.7	220.5	3	170	100	220.5	1.5	-0.30	-0.02	-1.90	0.77
15NP207_g034	1.065	0.037	0.1227	0.0019	0.080722	731	18	746	11	684	73	746	5.5	-0.09	-0.02	-1.80	1.06
15NP207_g136	0.2624	0.0056	0.03797	0.00033	0.29544	236.3	4.5	240.2	2.1	174	45	240.2	1.05	-0.38	-0.02	-1.70	0.77
15NP207_g131	0.3277	0.0085	0.04627	0.0007	0.41431	287.5	6.4	291.6	4.3	245	54	291.6	2.15	-0.19	-0.01	-1.50	0.56
15NP207_g071	0.24	0.0058	0.03436	0.00033	0.22795	218.1	4.7	217.8	2.1	223	51	217.8	1.05	0.02	0.00	0.33	0.71
15NP207_g106	0.2409	0.0044	0.03471	0.00031	0.21761	219	3.6	220	1.9	198	39	220	0.95	-0.11	0.00	-0.41	1.09
15NP207_g046	0.2427	0.0069	0.03491	0.00033	0.24948	220.2	5.6	221.2	2	193	57	221.2	1	-0.15	0.00	-0.29	0.54
15NP207_g141	0.2469	0.0046	0.03563	0.00032	0.39847	223.9	3.8	225.7	2	181	38	225.7	1	-0.25	-0.01	-0.81	0.81
15NP207_g050	0.2538	0.0049	0.03595	0.00029	0.35614	229.4	4	227.7	1.8	232	39	227.7	0.9	0.02	0.01	0.96	0.45
15NP207_g089	0.257	0.0055	0.03608	0.00034	0.22701	232	4.4	228.5	2.1	228	40	228.5	1.05	0.00	0.02	1.80	0.56
15NP207_g069	0.2564	0.0094	0.03649	0.00048	0.19463	230.8	7.7	231	3	231	76	231	1.5	0.00	0.00	0.35	0.74
15NP207_g077	0.2568	0.0071	0.03701	0.00041	0.15126	231.6	5.7	234.2	2.6	191	58	234.2	1.3	-0.23	-0.01	-1.00	0.61
15NP207_g049	0.2591	0.0064	0.03701	0.00034	0.23794	233.5	5.1	234.2	2.1	218	53	234.2	1.05	-0.07	0.00	-0.16	0.69
15NP207_g033	0.2585	0.0061	0.03702	0.00034	0.26149	233.1	4.9	234.3	2.1	205	48	234.3	1.05	-0.14	-0.01	-0.42	0.98
15NP207_g111	0.27	0.019	0.03701	0.00073	0.048122	241	15	234.3	4.6	270	140	234.3	2.3	0.13	0.03	3.90	0.66
15NP207_g030	0.272	0.032	0.0371	0.0013	0.071137	235	25	234.7	8.3	180	210	234.7	4.15	-0.30	0.00	4.40	0.00
15NP207_g026	0.2596	0.0069	0.0371	0.00046	0.46982	233.9	5.5	234.8	2.8	216	49	234.8	1.4	-0.09	0.00	-0.23	0.60
15NP207_g120	0.2659	0.0046	0.03711	0.00034	0.32678	239.2	3.7	234.9	2.1	272	37	234.9	1.05	0.14	0.02	2.10	0.43
15NP207_g081	0.2728	0.0044	0.03718	0.00032	0.15591	244.8	3.5	235.3	2	319	38	235.3	1	0.26	0.04	4.50	0.41

Sample 15NP207 continued

	Conventional concordia					Ages								Discordance		Conc.Dist., dc	Th/U
Sample # _grain number	207Pb 235U	±2σ	206Pb 238U	±2σ	error corr. 206/238 vs 207/235	207Pb 235U	±2σ	206Pb 238U	±2σ	207Pb 206Pb	±2σ	Best Age	±1σ	206/238 207/206	206/238 207/235		
15NP207_g048	0.274	0.022	0.03729	0.00083	0.12845	241	17	236	5.2	280	150	236	2.6	0.16	0.02	4.60	0.97
15NP207_g117	0.2661	0.0068	0.03738	0.00039	0.3099	239.1	5.4	236.6	2.4	249	52	236.6	1.2	0.05	0.01	1.40	0.54
15NP207_g037	0.2653	0.0057	0.03766	0.00036	0.39261	238.6	4.5	238.3	2.3	228	44	238.3	1.15	-0.05	0.00	0.29	0.72
15NP207_g144	0.272	0.011	0.03784	0.00054	0.087387	244	8.9	239.4	3.3	276	92	239.4	1.65	0.13	0.02	2.20	0.66
15NP207_g051	0.271	0.011	0.03803	0.00054	0.054476	242.1	8.5	240.6	3.3	246	86	240.6	1.65	0.02	0.01	1.30	0.63
15NP207_g035	0.2718	0.0084	0.03808	0.00037	0.26952	243.5	6.7	240.9	2.3	253	65	240.9	1.15	0.05	0.01	1.50	1.15
15NP207_g025	0.278	0.025	0.03821	0.0009	0.18191	243	19	241.7	5.6	220	170	241.7	2.8	-0.10	0.01	3.40	1.02
15NP207_g031	0.2739	0.0084	0.03826	0.00044	0.073873	245.1	6.6	242	2.7	259	65	242	1.35	0.07	0.01	1.70	0.91
15NP207_g038	0.2735	0.0074	0.03833	0.00042	0.18699	245	5.9	242.4	2.6	258	58	242.4	1.3	0.06	0.01	1.40	0.66
15NP207_g056	0.2679	0.0069	0.03848	0.00044	0.12998	240.5	5.6	243.4	2.7	208	58	243.4	1.35	-0.17	-0.01	-1.10	0.60
15NP207_g105	0.2711	0.0059	0.03847	0.00039	0.41168	243.3	4.7	243.4	2.4	229	43	243.4	1.2	-0.06	0.00	0.11	0.83
15NP207_g098	0.2693	0.0074	0.0385	0.00053	0.26358	242.4	5.8	243.5	3.3	203	58	243.5	1.65	-0.20	0.00	-0.64	0.85
15NP207_g135	0.2738	0.0078	0.03852	0.00034	0.13803	245.1	6.2	243.6	2.1	236	61	243.6	1.05	-0.03	0.01	0.95	0.70
15NP207_g083	0.2752	0.006	0.03853	0.00042	0.49328	246.5	4.7	243.7	2.6	248	40	243.7	1.3	0.02	0.01	1.40	0.97
15NP207_g063	0.277	0.011	0.03864	0.00048	0.10095	247.2	8.7	244.4	3	283	84	244.4	1.5	0.14	0.01	1.80	0.76
15NP207_g084	0.285	0.011	0.03866	0.00046	0.14944	253.1	8.9	244.5	2.9	296	82	244.5	1.45	0.17	0.03	4.50	0.68
15NP207_g088	0.2763	0.0081	0.03873	0.00044	0.04744	247.5	6.4	244.9	2.7	250	64	244.9	1.35	0.02	0.01	1.30	0.45
15NP207_g132	0.2764	0.0065	0.03872	0.00039	0.22309	247.4	5.2	244.9	2.4	257	51	244.9	1.2	0.05	0.01	1.30	0.38
15NP207_g061	0.2725	0.0061	0.03873	0.00042	0.35568	244.4	4.8	245	2.6	234	45	245	1.3	-0.05	0.00	-0.12	0.79
15NP207_g133	0.283	0.01	0.03881	0.00048	0.17704	251.9	8.2	245.4	3	274	75	245.4	1.5	0.10	0.03	3.40	0.55
15NP207_g052	0.274	0.012	0.03889	0.00053	0.056739	244.3	9.2	245.9	3.3	225	89	245.9	1.65	-0.09	-0.01	-0.03	0.57
15NP207_g145	0.2792	0.0063	0.03894	0.00046	0.31873	249.6	5	246.3	2.9	253	43	246.3	1.45	0.03	0.01	1.70	0.57
15NP207_g021	0.275	0.011	0.03899	0.00046	0.14933	245.2	8.7	246.5	2.9	247	85	246.5	1.45	0.00	-0.01	0.05	1.10
15NP207_g108	0.2802	0.0094	0.03899	0.00056	0.30867	250.4	7.5	246.6	3.5	256	70	246.6	1.75	0.04	0.02	1.90	0.49
15NP207_g039	0.2847	0.0073	0.03929	0.00038	0.080868	254	5.8	248.5	2.3	302	59	248.5	1.15	0.18	0.02	2.70	0.40
15NP207_g085	0.285	0.017	0.03932	0.00088	0.034067	253	13	248.6	5.5	300	120	248.6	2.75	0.17	0.02	2.70	0.73
15NP207_g121	0.2848	0.0058	0.03963	0.00038	0.34551	254.1	4.6	250.5	2.3	276	43	250.5	1.15	0.09	0.01	1.70	0.82
15NP207_g080	0.2862	0.0073	0.03971	0.00037	0.12302	255	5.8	251	2.3	270	54	251	1.15	0.07	0.02	2.00	0.58
15NP207_g100	0.285	0.014	0.03973	0.00062	0.2037	253	11	251.1	3.8	236	97	251.1	1.9	-0.06	0.01	1.50	0.76
15NP207_g151	0.2816	0.0052	0.04015	0.00038	0.32795	252.3	4.2	253.8	2.4	214	41	253.8	1.2	-0.19	-0.01	-0.82	0.85
15NP207_g097	0.287	0.011	0.04019	0.00054	0.071724	254.6	9.1	254	3.4	240	84	254	1.7	-0.06	0.00	0.96	0.37

Sample 15NP207 continued

	Conventional concordia					Ages								Discordance		Conc.Dist., dc	Th/U
Sample #	207Pb	±2σ	206Pb	±2σ	error corr.	207Pb	±2σ	206Pb	±2σ	207Pb	±2σ	Best Age	±1σ	206/238	206/238		
_grain number	235U		238U		206/238 vs 207/235	235U		238U		206Pb				207/206	207/235		
15NP207_g142	0.2911	0.0066	0.0402	0.00037	0.27948	259	5.2	254.4	2.4	272	47	254.4	1.2	0.06	0.02	2.30	0.51
15NP207_g055	0.2895	0.0094	0.04027	0.00055	0.14392	257.3	7.4	254.5	3.4	271	65	254.5	1.7	0.06	0.01	1.60	0.27
15NP207_g023	0.2826	0.0041	0.04039	0.00031	0.23944	252.6	3.2	255.2	1.9	216	33	255.2	0.95	-0.18	-0.01	-1.10	0.43
15NP207_g065	0.2861	0.0051	0.04043	0.00038	0.40225	255.3	4	255.5	2.3	255	35	255.5	1.15	0.00	0.00	-0.01	0.78
15NP207_g068	0.2868	0.0097	0.04067	0.00042	0.091711	255.1	7.7	257	2.6	241	71	257	1.3	-0.07	-0.01	-0.42	1.25
15NP207_g101	0.2888	0.0088	0.04076	0.00054	0.083437	256.9	7	257.5	3.4	229	69	257.5	1.7	-0.12	0.00	0.03	0.58
15NP207_g143	0.2894	0.0084	0.04114	0.00046	0.17279	258.3	6.8	259.9	2.8	198	64	259.9	1.4	-0.31	-0.01	-0.79	0.68
15NP207_g134	0.2947	0.0054	0.04131	0.00043	0.37294	262.6	4.4	260.9	2.7	266	43	260.9	1.35	0.02	0.01	0.56	0.46
15NP207_g118	0.299	0.012	0.0416	0.00061	0.14761	264	9	262.7	3.8	268	82	262.7	1.9	0.02	0.00	1.20	0.72
15NP207_g110	0.3094	0.0081	0.04287	0.00041	0.12207	273.1	6.3	270.6	2.5	276	54	270.6	1.25	0.02	0.01	1.30	0.49
15NP207_g059	0.3116	0.0075	0.04288	0.00042	0.17087	274.9	5.8	270.6	2.6	297	51	270.6	1.3	0.09	0.02	2.00	0.47
15NP207_g149	0.3074	0.0098	0.04292	0.00052	0.24784	271.3	7.7	270.9	3.2	258	67	270.9	1.6	-0.05	0.00	0.52	0.67
15NP207_g082	0.3132	0.0046	0.04354	0.00047	0.73787	276.4	3.5	274.7	2.9	271	25	274.7	1.45	-0.01	0.01	0.79	0.46
15NP207_g094	0.3128	0.0056	0.04422	0.0004	0.38742	276	4.3	278.9	2.5	226	37	278.9	1.25	-0.23	-0.01	-1.10	0.63
15NP207_g126	0.338	0.024	0.0453	0.0011	0.22398	293	18	285.2	6.9	340	150	285.2	3.45	0.16	0.03	4.00	0.62
15NP207_g076	0.331	0.011	0.04612	0.00064	0.1034	290.4	9	290.6	4	276	73	290.6	2	-0.05	0.00	-0.13	1.15
15NP207_g112	0.347	0.026	0.04774	0.00095	0.08613	297	19	300.5	5.8	220	140	300.5	2.9	-0.37	-0.01	0.70	0.91
15NP207_g047	0.437	0.047	0.057	0.0018	0.070145	351	33	357	11	270	200	357	5.5	-0.32	-0.02	3.50	1.40
15NP207_g107	0.492	0.035	0.0637	0.0014	0.11275	400	24	398.1	8.4	360	140	398.1	4.2	-0.11	0.00	2.40	0.68
15NP207_g040	0.476	0.018	0.06374	0.00083	0.21978	393	12	398.3	5	339	76	398.3	2.5	-0.17	-0.01	-0.91	0.90
15NP207_g086	0.4977	0.0077	0.06541	0.00061	0.43201	409.7	5.2	408.4	3.7	391	32	408.4	1.85	-0.04	0.00	0.50	0.37
15NP207_g070	0.516	0.055	0.066	0.0026	0.17624	410	36	412	15	400	220	412	7.5	-0.03	0.00	3.00	0.06
15NP207_g022	0.522	0.054	0.066	0.0022	0.27864	419	37	412	13	400	190	412	6.5	-0.03	0.02	4.20	0.51
15NP207_g024	0.503	0.013	0.06608	0.00066	0.21934	413.5	8.2	412.5	4	401	54	412.5	2	-0.03	0.00	0.36	0.54
15NP207_g044	0.5057	0.0051	0.06679	0.00058	0.55891	415.4	3.4	416.7	3.5	405	19	416.7	1.75	-0.03	0.00	-0.37	0.49
15NP207_g116	0.526	0.04	0.0669	0.0015	0.21252	419	26	417.1	9	370	150	417.1	4.5	-0.13	0.00	3.40	0.49
15NP207_g093	0.517	0.014	0.06703	0.00075	0.24868	421.6	9.5	418.2	4.5	403	59	418.2	2.25	-0.04	0.01	1.40	0.62
15NP207_g129	0.513	0.017	0.06781	0.00077	0.16853	420	12	422.9	4.7	376	71	422.9	2.35	-0.12	-0.01	-0.71	0.63
15NP207_g122	0.529	0.044	0.0679	0.0017	0.01713	418	29	423	10	350	150	423	5	-0.21	-0.01	2.20	0.56
15NP207_g001	0.542	0.028	0.0682	0.0015	0.18451	435	19	425	9.1	450	110	425	4.55	0.06	0.02	4.00	0.00
15NP207_g011	0.543	0.036	0.0684	0.0018	0.052258	432	23	426	11	410	130	426	5.5	-0.04	0.01	3.90	0.00

Sample 15NP207 continued

	Conventional concordia					Ages								Discordance		Conc.Dist., dc	Th/U
Sample # _grain number	207Pb 235U	±2σ	206Pb 238U	±2σ	error corr. 206/238 vs 207/235	207Pb 235U	±2σ	206Pb 238U	±2σ	207Pb 206Pb	±2σ	Best Age	±1σ	206/238 207/206	206/238 207/235		
15NP207_g102	0.531	0.027	0.0684	0.0014	0.14354	428	18	426.3	8.4	375	98	426.3	4.2	-0.14	0.00	1.70	0.00
15NP207_g140	0.531	0.025	0.06875	0.00087	0.18879	428	17	428.6	5.3	425	84	428.6	2.65	-0.01	0.00	1.10	0.58
15NP207_g036	0.5269	0.0089	0.06912	0.00062	0.38176	429.2	5.9	430.8	3.8	410	36	430.8	1.9	-0.05	0.00	-0.31	0.02
15NP207_g017	0.541	0.021	0.0697	0.0018	0.011113	442	15	434	11	450	85	434	5.5	0.04	0.02	1.30	0.00
15NP207_g123	0.529	0.012	0.06991	0.00071	0.069814	430.6	8.2	435.6	4.3	393	55	435.6	2.15	-0.11	-0.01	-1.20	0.37
15NP207_g153	0.548	0.017	0.07052	0.00082	0.1616	443	11	439.3	4.9	429	64	439.3	2.45	-0.02	0.01	1.20	0.78
15NP207_g014	0.569	0.047	0.0709	0.0022	0.20677	444	30	441	13	450	160	441	6.5	0.02	0.01	4.30	0.00
15NP207_g099	0.561	0.018	0.0712	0.0012	0.079571	452	12	443.6	7.4	508	83	443.6	3.7	0.13	0.02	2.40	0.56
15NP207_g154	0.543	0.015	0.07133	0.00078	0.14177	438.8	9.5	444.1	4.7	380	58	444.1	2.35	-0.17	-0.01	-1.00	0.67
15NP207_g147	0.55	0.014	0.07133	0.00077	0.23411	443.7	9.2	444.1	4.6	403	55	444.1	2.3	-0.10	0.00	0.23	0.55
15NP207_g119	0.571	0.025	0.07142	0.00096	0.18598	454	16	444.6	5.8	487	97	444.6	2.9	0.09	0.02	3.80	0.84
15NP207_g113	0.552	0.012	0.07151	0.00065	0.17316	446.1	7.9	445.2	3.9	423	51	445.2	1.95	-0.05	0.00	0.29	0.37
15NP207_g146	0.5476	0.009	0.07177	0.00068	0.10706	442.9	5.9	446.8	4.1	394	34	446.8	2.05	-0.13	-0.01	-0.93	0.60
15NP207_g013	0.573	0.023	0.0721	0.0011	0.15314	456	15	448.9	6.5	462	86	448.9	3.25	0.03	0.02	3.00	0.69
15NP207_g125	0.562	0.02	0.07236	0.00085	0.28183	450	13	450.3	5.1	417	74	450.3	2.55	-0.08	0.00	0.67	0.71
15NP207_g137	0.579	0.015	0.07283	0.00061	0.17826	465.4	9.5	453.2	3.6	491	55	453.2	1.8	0.08	0.03	2.90	0.48
15NP207_g138	0.566	0.011	0.07297	0.00074	0.40376	454.9	6.9	454	4.5	427	39	454	2.25	-0.06	0.00	0.38	0.59
15NP207_g103	0.584	0.032	0.0733	0.0014	0.41578	465	21	456.2	8.5	500	110	456.2	4.25	0.09	0.02	3.00	0.64
15NP207_g032	0.5849	0.0076	0.07517	0.00069	0.46465	467.9	4.8	467.2	4.1	460	27	467.2	2.05	-0.02	0.00	0.10	0.26
15NP207_g115	0.581	0.0094	0.07536	0.00066	0.35653	464.6	6.1	468.3	3.9	432	35	468.3	1.95	-0.08	-0.01	-0.85	0.66
15NP207_g075	0.632	0.012	0.07988	0.00084	0.41205	496.3	7.4	495.4	5	498	40	495.4	2.5	0.01	0.00	0.48	0.23
15NP207_g027	1.5	0.016	0.1567	0.0012	0.46179	929.5	6.6	938.2	6.7	906	21	938.2	3.35	-0.04	-0.01	-1.20	0.92
15NP207_g058	1.583	0.023	0.1602	0.0016	0.61871	962.3	9	958	8.6	966	25	958	4.3	0.01	0.00	0.84	0.36
15NP207_g064	1.646	0.036	0.1654	0.0017	0.059362	985	14	986.5	9.3	977	41	986.5	4.65	-0.01	0.00	0.19	1.10
15NP207_g060	4.08	0.15	0.2886	0.0092	0.51997	1643	30	1630	46	1672	59	1672	29.5	0.03	0.01	1.50	0.61
15NP207_g148	4.944	0.09	0.3259	0.0042	0.65828	1808	16	1818	20	1781	26	1781	13	-0.02	-0.01	-0.77	0.65
15NP207_g130	4.718	0.097	0.3126	0.0048	0.59788	1767	17	1752	24	1793	32	1793	16	0.02	0.01	1.60	0.53
15NP207_g079	4.745	0.067	0.3068	0.0028	0.75517	1773	12	1725	14	1825	21	1825	10.5	0.05	0.03	4.70	0.78
15NP207_g054	5.67	0.091	0.3462	0.0037	0.43818	1924	14	1916	17	1931	28	1931	14	0.01	0.00	0.91	1.21
15NP207_g072	5.598	0.052	0.3442	0.0028	0.62325	1914.7	8.1	1906	14	1934	14	1934	7	0.01	0.00	0.77	0.83
15NP207_g095	6.035	0.064	0.3586	0.003	0.70106	1979.6	9.3	1975	14	1968	14	1968	7	0.00	0.00	0.45	1.53

Sample 15NP207 continued

	Conventional concordia					Ages								Discordance		Conc.Dist., dc	Th/U
Sample #	207Pb	±2σ	206Pb	±2σ	error corr.	207Pb	±2σ	206Pb	±2σ	207Pb	±2σ	Best Age	±1σ	206/238	206/238		
_grain number	235U		238U		206/238 vs 207/235	235U		238U		206Pb				207/206	207/235		
15NP207_g078	6.158	0.058	0.3654	0.0036	0.73094	1997.5	8.2	2007	17	1982.1	8.9	1982.1	4.45	-0.01	0.00	-0.78	1.68
15NP207_g073	0.291	0.014	0.03906	0.00063	0.0045677	258	11	247	3.9	320	110	247	1.95	0.23	0.04	5.50	0.54
15NP207_g067	0.293	0.013	0.03928	0.00057	0.10765	259	10	248.4	3.6	340	91	248.4	1.8	0.27	0.04	5.50	0.70
15NP207_g053	0.289	0.013	0.03879	0.00055	0.21397	256	10	245.3	3.4	323	89	245.3	1.7	0.24	0.04	5.60	0.78
15NP207_g152	0.271	0.017	0.03642	0.00062	0.23084	241	14	230.5	3.8	300	120	230.5	1.9	0.23	0.04	6.10	0.37
15NP207_g043	3.88	0.12	0.2705	0.0045	0.56345	1607	25	1543	23	1690	47	1690	23.5	0.09	0.04	7.20	1.61
15NP207_g091	0.288	0.011	0.03713	0.00064	0.15059	255.5	8.7	235	4	405	84	235	2	0.42	0.08	10.00	0.62
15NP207_g010	0.444	0.07	0.0542	0.0029	0.10262	343	47	340	18	260	270	340	9	-0.31	0.01	11.00	0.00
15NP207_g062	5.55	0.14	0.3204	0.0034	0.27142	1902	22	1791	17	2027	40	2027	20	0.12	0.06	12.00	0.69
15NP207_g057	5.82	0.17	0.3274	0.0046	0.66669	1953	26	1825	22	2095	43	2095	21.5	0.13	0.07	13.00	1.12
15NP207_g109	0.2933	0.0087	0.0367	0.00039	0.28204	260.6	6.6	232.3	2.4	497	59	232.3	1.2	0.53	0.11	13.00	0.95
15NP207_g090	2.997	0.032	0.2189	0.002	0.58306	1406.1	8.3	1276	10	1587	16	1587	8	0.20	0.09	15.00	0.70
15NP207_g066	3.88	0.1	0.2558	0.0039	0.5438	1607	21	1468	20	1799	38	1799	19	0.18	0.09	16.00	0.59
15NP207_g074	0.295	0.011	0.03595	0.00043	0.17384	261.9	8.7	227.7	2.7	551	80	227.7	1.35	0.59	0.13	16.00	0.43
15NP207_g008	0.8	0.17	0.083	0.014	0.13658	510	85	506	75	430	350	506	37.5	-0.18	0.01	19.00	0.00
15NP207_g104	0.346	0.015	0.04043	0.00045	0.41681	302	11	255.5	2.8	608	84	255.5	1.4	0.58	0.15	19.00	0.71
15NP207_g155	0.304	0.014	0.03588	0.00049	0.028681	269	11	227.2	3.1	590	100	227.2	1.55	0.61	0.16	19.00	1.27
15NP207_g045	0.666	0.022	0.06889	0.00082	0.1326	517	13	430.9	3.9	890	69	430.9	1.95	0.52	0.17	23.00	0.65
15NP207_g041	0.339	0.026	0.03833	0.00079	0.1027	290	20	242.4	4.9	590	160	242.4	2.45	0.59	0.16	23.00	0.66
15NP207_g005	0.758	0.071	0.0747	0.0026	0.12829	549	40	464	16	850	200	464	8	0.45	0.15	26.00	0.00
15NP207_g042	0.351	0.024	0.03846	0.00078	0.076766	301	18	243.2	4.9	690	150	243.2	2.45	0.65	0.19	26.00	0.67
15NP207_g006	0.8	0.16	0.0749	0.0045	0.23664	498	78	464	27	520	330	464	13.5	0.11	0.07	32.00	0.00
15NP207_g028	0.533	0.024	0.04032	0.00055	0.20477	434	15	254.8	3.4	1530	76	254.8	1.7	0.83	0.41	63.00	0.94
15NP207_g004	1.16	0.14	0.076	0.0033	0.1366	740	74	471	20	1360	280	471	10	0.65	0.36	67.00	0.00
15NP207_g003	7.14	0.42	0.205	0.0081	0.75147	2116	51	1200	43	3201	57	3201	28.5	0.63	0.43	140.00	0.26
15NP207_g150	3.27	0.21	0.0703	0.0019	0.71635	1436	54	438	11	3551	87	438	5.5	0.88	0.69	190.00	1.24
15NP207_g015	35.3	3.9	0.388	0.042	0.67808	3560	110	2040	180	4790	180	4790	90	0.57	0.43	230.00	0.00

Sample 15NP217	Sample Type: detrital					Latitude:	38.81429	Longitude:	75.44386								
	Conventional concordia					Ages								Discordance		Conc.Dist., dc	Th/U
Sample #	207Pb	±2σ	206Pb	±2σ	error corr.	207Pb	±2σ	206Pb	±2σ	207Pb	±2σ	Best Age	±1σ	206/238	206/238		
_grain number	235U		238U		206/238 vs 207/235	235U		238U		206Pb				207/206	207/235		
15NP217_g104	5.7	0.073	0.3663	0.0034	0.81633	1930.8	11	2013	16	1842.5	19	1842.5	9.5	-0.09	-0.04	-7.00	0.29
15NP217_g140	0.5459	0.0072	0.07315	0.00059	0.46663	442.2	4.7	455.1	3.6	379	25	455.1	1.8	-0.20	-0.03	-3.50	0.11
15NP217_g115	0.554	0.019	0.07363	0.00092	0.001	447	12	458	5.5	402	78	458	2.75	-0.14	-0.02	-2.80	0.96
15NP217_g139	4.719	0.059	0.3218	0.0028	0.72646	1770.8	10	1799.5	13	1740	19	1740	9.5	-0.03	-0.02	-2.50	0.73
15NP217_g127	0.2791	0.005	0.0402	0.00048	0.62206	249.9	4	254.1	3	216	36	254.1	1.5	-0.18	-0.02	-1.80	0.53
15NP217_g091	0.356	0.012	0.04993	0.00065	0.078262	308.9	9	314.1	4	269	80	314.1	2	-0.17	-0.02	-1.80	1.13
15NP217_g128	0.2526	0.0048	0.03669	0.00033	0.41267	228.5	3.9	232.3	2	182	38	232.3	1	-0.28	-0.02	-1.70	0.59
15NP217_g001	0.2291	0.0085	0.03354	0.00045	0.001	209	7	212.6	2.8	183	86	212.6	1.4	-0.16	-0.02	-1.70	0.79
15NP217_g037	0.2308	0.0058	0.03333	0.00032	0.0016868	210.7	4.8	211.4	2	198	56	211.4	1	-0.07	0.00	-0.26	0.41
15NP217_g060	0.2358	0.006	0.03406	0.00033	0.15743	214.7	4.9	215.9	2	208	54	215.9	1	-0.04	-0.01	-0.48	0.99
15NP217_g076	0.2494	0.0062	0.03405	0.0003	0.6028	225.8	5	215.9	1.9	319	48	215.9	0.95	0.32	0.04	5.20	1.07
15NP217_g119	0.2433	0.0054	0.03428	0.00033	0.24392	221.4	4.5	217.2	2	274	49	217.2	1	0.21	0.02	1.90	0.87
15NP217_g027	0.2383	0.0048	0.03441	0.00037	0.29459	216.9	4	218.1	2.3	204	45	218.1	1.15	-0.07	-0.01	-0.54	0.62
15NP217_g044	0.2423	0.0041	0.03444	0.00035	0.65378	220.2	3.4	218.3	2.2	228	32	218.3	1.1	0.04	0.01	1.00	0.77
15NP217_g030	0.2388	0.0041	0.03451	0.00033	0.50477	217.4	3.4	218.7	2.1	207	35	218.7	1.05	-0.06	-0.01	-0.65	0.40
15NP217_g103	0.252	0.0079	0.03473	0.00041	0.028509	227.7	6.4	220	2.6	288	69	220	1.3	0.24	0.03	4.00	1.00
15NP217_g113	0.24	0.0085	0.03487	0.00047	0.11077	219.6	6.7	220.9	2.9	210	78	220.9	1.45	-0.05	-0.01	-1.30	0.69
15NP217_g067	0.256	0.022	0.03516	0.00075	0.57875	231	18	222.8	4.7	290	160	222.8	2.35	0.23	0.04	4.30	0.65
15NP217_g008	0.2468	0.0065	0.03568	0.00038	0.094402	224.2	5.4	226	2.3	201	56	226	1.15	-0.12	-0.01	-1.00	1.03
15NP217_g043	0.249	0.008	0.03573	0.00042	0.001	225.9	6.6	226.5	2.6	211	72	226.5	1.3	-0.07	0.00	-0.27	1.20
15NP217_g033	0.2575	0.007	0.03583	0.00036	0.11532	233.1	5.8	227	2.3	265	62	227	1.15	0.14	0.03	2.80	0.78
15NP217_g019	0.2529	0.0053	0.03626	0.00032	0.32429	228.7	4.3	229.6	2	221	44	229.6	1	-0.04	0.00	-0.33	0.83
15NP217_g065	0.2557	0.0044	0.03651	0.00033	0.63996	231.1	3.5	231.2	2.1	215	38	231.2	1.05	-0.08	0.00	0.02	0.75
15NP217_g040	0.2579	0.0061	0.03656	0.00036	0.24344	232.7	4.9	231.5	2.2	230	49	231.5	1.1	-0.01	0.01	0.72	0.96
15NP217_g036	0.2581	0.0046	0.03661	0.00046	0.51464	233	3.7	231.8	2.9	245	37	231.8	1.45	0.05	0.01	0.65	0.90
15NP217_g031	0.2557	0.0071	0.03669	0.00035	0.023419	231.3	5.8	232.3	2.2	231	62	232.3	1.1	-0.01	0.00	-0.52	0.68
15NP217_g092	0.2602	0.0049	0.03669	0.00033	0.2188	234.7	3.9	232.3	2.1	244	40	232.3	1.05	0.05	0.01	1.20	0.58
15NP217_g090	0.2649	0.0067	0.03671	0.00032	0.23539	239.3	5.4	232.4	2	297	54	232.4	1	0.22	0.03	2.90	1.23
15NP217_g121	0.2558	0.008	0.03678	0.00036	0.0058069	231.5	6.4	232.8	2.3	227	68	232.8	1.15	-0.03	-0.01	-0.75	0.80
15NP217_g093	0.2624	0.005	0.03703	0.00032	0.23328	236.8	4	234.4	2	229	41	234.4	1	-0.02	0.01	1.00	1.22
15NP217_g102	0.2625	0.0042	0.03717	0.00033	0.24729	236.9	3.4	235.3	2	242	35	235.3	1	0.03	0.01	0.67	1.30

Sample 15NP217 continued

	Conventional concordia					Ages								Discordance		Conc.Dist., dc	Th/U
Sample #	207Pb	±2σ	206Pb	±2σ	error corr.	207Pb	±2σ	206Pb	±2σ	207Pb	±2σ	Best Age	±1σ	206/238	206/238		
_grain number	235U		238U		206/238 vs 207/235	235U		238U		206Pb				207/206	207/235		
15NP217_g045	0.2577	0.0081	0.03717	0.00044	0.068461	233.1	6.4	235.5	2.8	214	61	235.5	1.4	-0.10	-0.01	-1.20	0.94
15NP217_g063	0.2714	0.0074	0.03722	0.00033	0.30579	244.2	5.8	235.6	2	321	53	235.6	1	0.27	0.04	3.90	0.63
15NP217_g069	0.2722	0.0071	0.03735	0.00034	0.29029	244.2	5.6	236.4	2.1	315	55	236.4	1.05	0.25	0.03	3.80	0.55
15NP217_g010	0.2648	0.005	0.03737	0.00046	0.67796	238.4	4	236.5	2.9	253	36	236.5	1.45	0.07	0.01	0.95	0.40
15NP217_g100	0.2647	0.0053	0.03739	0.00031	0.29769	238.2	4.3	236.6	1.9	227	40	236.6	0.95	-0.04	0.01	0.85	1.00
15NP217_g034	0.2671	0.0056	0.03749	0.00034	0.23109	240.2	4.5	237.2	2.1	256	46	237.2	1.05	0.07	0.01	1.50	0.73
15NP217_g039	0.2639	0.0068	0.03754	0.00037	0.028111	238	5.5	237.6	2.3	231	58	237.6	1.15	-0.03	0.00	0.11	1.22
15NP217_g082	0.2651	0.0046	0.03757	0.00034	0.23948	238.7	3.7	237.8	2.1	238	38	237.8	1.05	0.00	0.00	0.48	0.77
15NP217_g053	0.2674	0.0093	0.03773	0.00046	0.21977	240	7.5	238.7	2.9	237	70	238.7	1.45	-0.01	0.01	0.87	0.86
15NP217_g083	0.2707	0.0073	0.03773	0.0004	0.001	243	5.8	238.7	2.5	272	58	238.7	1.25	0.12	0.02	2.10	1.05
15NP217_g084	0.2643	0.0073	0.03791	0.00042	0.001	237.7	5.8	239.8	2.6	212	62	239.8	1.3	-0.13	-0.01	-0.81	0.87
15NP217_g106	0.2712	0.0048	0.03819	0.00035	0.42473	243.5	3.8	241.6	2.2	257	37	241.6	1.1	0.06	0.01	0.94	0.88
15NP217_g111	0.2813	0.006	0.03818	0.00034	0.001	251.5	4.7	241.6	2.1	348	49	241.6	1.05	0.31	0.04	4.60	0.90
15NP217_g134	0.2742	0.0043	0.03828	0.00034	0.30743	246.3	3.5	242.1	2.1	283	36	242.1	1.05	0.14	0.02	1.80	0.80
15NP217_g080	0.2661	0.0084	0.03836	0.00046	0.088171	241.5	6.8	242.6	2.8	209	74	242.6	1.4	-0.16	0.00	-1.40	0.76
15NP217_g075	0.2748	0.0089	0.03842	0.00047	0.18108	247	6.9	243	2.9	257	70	243	1.45	0.05	0.02	1.60	0.71
15NP217_g005	0.2762	0.008	0.03847	0.00057	0.50457	247.5	6.4	243.3	3.5	275	50	243.3	1.75	0.12	0.02	2.00	0.49
15NP217_g089	0.2721	0.0044	0.03885	0.00035	0.29495	244.6	3.4	245.7	2.2	237	36	245.7	1.1	-0.04	0.00	-0.61	0.73
15NP217_g056	0.2761	0.0057	0.03889	0.00041	0.50429	247.7	4.5	245.9	2.5	260	41	245.9	1.25	0.05	0.01	0.73	1.01
15NP217_g129	0.2722	0.005	0.03896	0.00032	0.060204	244.6	4	246.4	2	225	40	246.4	1	-0.10	-0.01	-0.88	0.73
15NP217_g105	0.284	0.0085	0.03922	0.00043	0.37962	253.7	6.7	248	2.7	270	63	248	1.35	0.08	0.02	2.60	0.96
15NP217_g042	0.2819	0.0058	0.03934	0.00035	0.23937	252	4.6	248.7	2.2	279	45	248.7	1.1	0.11	0.01	1.50	0.95
15NP217_g116	0.2922	0.006	0.0394	0.00036	0.17634	260.6	4.8	249.1	2.2	391	45	249.1	1.1	0.36	0.04	4.90	0.96
15NP217_g126	0.2791	0.005	0.03947	0.00036	0.21581	249.8	4	249.5	2.3	263	40	249.5	1.15	0.05	0.00	0.18	0.86
15NP217_g101	0.2804	0.0037	0.03964	0.00038	0.53911	250.9	3	250.6	2.3	255	28	250.6	1.15	0.02	0.00	0.17	0.74
15NP217_g004	0.2798	0.0086	0.03974	0.00039	0.16006	249.9	6.8	251.2	2.4	244	64	251.2	1.2	-0.03	-0.01	-0.32	0.50
15NP217_g057	0.2842	0.0071	0.03988	0.00063	0.57417	253.8	5.6	252.1	3.9	266	47	252.1	1.95	0.05	0.01	0.84	0.87
15NP217_g132	0.2797	0.0055	0.03997	0.00041	0.48297	250.9	4.5	252.7	2.6	254	42	252.7	1.3	0.01	-0.01	-0.99	0.77
15NP217_g020	0.286	0.011	0.03999	0.00056	0.085028	255.1	8.3	252.8	3.4	279	84	252.8	1.7	0.09	0.01	1.20	1.11
15NP217_g133	0.2841	0.0059	0.04005	0.00036	0.29611	253.7	4.6	253.1	2.2	256	44	253.1	1.1	0.01	0.00	0.34	0.83
15NP217_g073	0.2879	0.0044	0.04005	0.00041	0.51102	256.8	3.4	253.1	2.5	287	30	253.1	1.25	0.12	0.01	1.70	0.64

Sample 15NP217 continued

	Conventional concordia					Ages								Discordance		Conc.Dist., dc	Th/U
Sample # _grain number	207Pb 235U	±2σ	206Pb 238U	±2σ	error corr. 206/238 vs 207/235	207Pb 235U	±2σ	206Pb 238U	±2σ	207Pb 206Pb	±2σ	Best Age	±1σ	206/238 207/206	206/238 207/235		
15NP217_g021	0.2911	0.0055	0.04091	0.00035	0.001	259.3	4.3	258.5	2.1	266	43	258.5	1.05	0.03	0.00	0.42	0.80
15NP217_g079	0.2995	0.01	0.04194	0.00058	0.34672	265.7	7.8	264.9	3.6	256	69	264.9	1.8	-0.03	0.00	0.50	0.78
15NP217_g025	0.2977	0.0042	0.04202	0.00035	0.49175	264.6	3.3	265.4	2.2	255	29	265.4	1.1	-0.04	0.00	-0.32	0.51
15NP217_g124	0.2962	0.0056	0.04206	0.00045	0.62919	263.3	4.4	265.6	2.8	260	36	265.6	1.4	-0.02	-0.01	-0.93	0.48
15NP217_g061	0.3125	0.0082	0.04372	0.00047	0.30133	276.8	6.1	275.8	2.9	295	51	275.8	1.45	0.07	0.00	0.11	1.26
15NP217_g059	0.3158	0.0052	0.04382	0.00038	0.24073	278.6	4	276.5	2.4	294	36	276.5	1.2	0.06	0.01	0.90	0.53
15NP217_g041	0.3293	0.0064	0.04506	0.00043	0.13711	288.8	4.9	284.1	2.6	315	43	284.1	1.3	0.10	0.02	2.00	0.70
15NP217_g137	0.3284	0.0087	0.04551	0.00056	0.049846	289	6.8	286.9	3.4	284	62	286.9	1.7	-0.01	0.01	0.57	0.83
15NP217_g122	0.3528	0.008	0.04861	0.00043	0.2218	307.1	5.9	306	2.6	311	50	306	1.3	0.02	0.00	0.32	0.70
15NP217_g002	0.3613	0.0078	0.05008	0.00047	0.27287	313.5	5.9	315	2.9	288	49	315	1.45	-0.09	0.00	-0.67	0.68
15NP217_g055	0.426	0.018	0.05622	0.00075	0.001	358	13	353	4.5	362	87	353	2.25	0.02	0.01	2.50	0.52
15NP217_g046	0.4971	0.0095	0.06261	0.00054	0.30748	409.9	6.3	391.5	3.3	513	39	391.5	1.65	0.24	0.04	5.50	1.21
15NP217_g136	0.4682	0.0084	0.06287	0.00065	0.4366	389.7	5.9	393	3.9	383	38	393	1.95	-0.03	-0.01	-0.94	0.67
15NP217_g094	0.4781	0.0077	0.063	0.00054	0.19298	396.5	5.3	393.8	3.3	405	36	393.8	1.65	0.03	0.01	0.88	1.40
15NP217_g049	0.4839	0.0089	0.06369	0.00055	0.1845	400.4	6.1	398	3.3	410	39	398	1.65	0.03	0.01	0.81	0.57
15NP217_g077	0.493	0.026	0.0643	0.0011	0.18083	407	18	402.1	6.7	390	110	402.1	3.35	-0.03	0.01	1.60	0.72
15NP217_g098	0.4863	0.01	0.06469	0.00062	0.22112	402.1	6.8	404.1	3.8	389	44	404.1	1.9	-0.04	0.00	-0.50	0.37
15NP217_g062	0.499	0.02	0.06513	0.00089	0.11598	413	14	406.7	5.4	417	85	406.7	2.7	0.02	0.02	1.30	0.97
15NP217_g054	0.4958	0.0084	0.06528	0.00059	0.34994	408.6	5.7	407.6	3.6	407	36	407.6	1.8	0.00	0.00	0.35	0.61
15NP217_g130	0.494	0.018	0.06571	0.00082	0.10076	407	12	410.2	5	346	80	410.2	2.5	-0.19	-0.01	-0.77	0.91
15NP217_g047	0.512	0.013	0.06616	0.00065	0.089152	419.9	8.5	413.3	4	453	56	413.3	2	0.09	0.02	2.00	1.21
15NP217_g071	0.507	0.016	0.06632	0.0008	0.13108	415	11	413.9	4.8	406	72	413.9	2.4	-0.02	0.00	0.72	0.82
15NP217_g131	0.5022	0.0075	0.06647	0.00051	0.3688	413	5.1	414.8	3.1	395	30	414.8	1.55	-0.05	0.00	-0.48	0.59
15NP217_g012_A2	0.5018	0.0082	0.06669	0.00054	0.1808	412.6	5.5	416.2	3.3	395	34	416.2	1.65	-0.05	-0.01	-0.94	0.37
15NP217_g011_A1	0.514	0.028	0.0668	0.0012	0.37196	420	19	416.8	7	410	110	416.8	3.5	-0.02	0.01	1.20	0.47
15NP217_g009	0.5055	0.01	0.06724	0.00062	0.10525	415.7	6.7	419.5	3.7	406	45	419.5	1.85	-0.03	-0.01	-1.20	0.44
15NP217_g026	0.5183	0.0091	0.06759	0.00059	0.22939	423.7	6.1	421.6	3.6	437	36	421.6	1.8	0.04	0.00	0.68	0.52
15NP217_g038	0.5271	0.0086	0.06866	0.00058	0.37122	429.7	5.7	428	3.5	428	34	428	1.75	0.00	0.00	0.51	0.67
15NP217_g086	0.518	0.014	0.06866	0.00074	0.081348	423	9.3	428.1	4.4	387	59	428.1	2.2	-0.11	-0.01	-1.20	0.77
15NP217_g074	0.5309	0.0076	0.06905	0.00056	0.38005	432.2	5	430.4	3.4	429	29	430.4	1.7	0.00	0.00	0.55	1.15
15NP217_g072	0.5385	0.008	0.06923	0.00061	0.31285	437.3	5.3	431.5	3.7	464	32	431.5	1.85	0.07	0.01	1.60	1.15

Sample 15NP217 continued

	Conventional concordia					Ages								Discordance		Conc.Dist., dc	Th/U
Sample #	207Pb	±2σ	206Pb	±2σ	error corr.	207Pb	±2σ	206Pb	±2σ	207Pb	±2σ	Best Age	±1σ	206/238	206/238		
_grain number	235U		238U		206/238 vs 207/235	235U		238U		206Pb				207/206	207/235		
15NP217_g029	0.536	0.014	0.06984	0.00067	0.23103	435	9.3	435.2	4	430	57	435.2	2	-0.01	0.00	0.17	0.69
15NP217_g118	0.5342	0.011	0.07005	0.00065	0.13671	434.8	7.4	436.4	3.9	433	47	436.4	1.95	-0.01	0.00	-0.52	0.97
15NP217_g110	0.5427	0.0089	0.07046	0.00056	0.35475	439.9	5.8	438.9	3.3	432	33	438.9	1.65	-0.02	0.00	0.35	1.16
15NP217_g108	0.5438	0.0082	0.07067	0.00066	0.59864	441.2	5.3	440.2	4	442	28	440.2	2	0.00	0.00	0.20	0.17
15NP217_g078	0.547	0.01	0.07077	0.0007	0.083705	442.6	6.7	440.8	4.2	432	42	440.8	2.1	-0.02	0.00	0.61	0.97
15NP217_g096	0.548	0.012	0.0709	0.00062	0.12962	443.2	7.9	441.6	3.7	448	47	441.6	1.85	0.01	0.00	0.58	0.48
15NP217_g024_C2	0.5482	0.0085	0.07092	0.00058	0.29124	443.5	5.6	441.7	3.5	441	32	441.7	1.75	0.00	0.00	0.58	0.54
15NP217_g023_C1	0.5584	0.0088	0.07184	0.00061	0.47944	450.7	5.8	447.2	3.7	466	31	447.2	1.85	0.04	0.01	0.88	0.34
15NP217_g035	0.572	0.011	0.07362	0.00064	0.11867	458.8	7	457.9	3.9	457	40	457.9	1.95	0.00	0.00	0.37	1.14
15NP217_g070	0.5952	0.0092	0.07562	0.00059	0.31067	474.3	5.8	469.9	3.5	485	31	469.9	1.75	0.03	0.01	1.10	1.31
15NP217_g081	0.5893	0.0088	0.07614	0.0007	0.62835	470.2	5.6	473	4.2	452	27	473	2.1	-0.05	-0.01	-0.68	0.25
15NP217_g016	0.6299	0.011	0.08004	0.00074	0.35998	496.4	6.7	496.3	4.4	515	35	496.3	2.2	0.04	0.00	-0.08	0.64
15NP217_g097	0.651	0.013	0.08242	0.00071	0.18452	508.2	7.8	510.5	4.2	494	41	510.5	2.1	-0.03	0.00	-0.36	0.15
15NP217_g112	0.6913	0.011	0.08652	0.00076	0.33646	533.2	6.9	534.9	4.5	549	32	534.9	2.25	0.03	0.00	-0.31	0.61
15NP217_g114	0.913	0.014	0.10884	0.00093	0.32315	658.2	7.6	666	5.4	629	31	666	2.7	-0.06	-0.01	-1.50	0.41
15NP217_g109	0.989	0.016	0.11254	0.001	0.22892	697.8	8.2	687.5	5.8	733	34	687.5	2.9	0.06	0.01	2.00	0.73
15NP217_g014_B2	1.074	0.016	0.1214	0.0014	0.68462	740.5	7.6	738.8	7.8	746	25	738.8	3.9	0.01	0.00	0.38	0.33
15NP217_g013_B1	1.159	0.017	0.1301	0.0015	0.772	780.8	7.8	789.1	8.6	758	23	789.1	4.3	-0.04	-0.01	-1.20	0.40
15NP217_g087	1.228	0.017	0.1343	0.0011	0.3938	812.9	7.7	812.3	6.1	799	25	812.3	3.05	-0.02	0.00	0.18	1.62
15NP217_g066	1.392	0.031	0.1431	0.0018	0.68843	885	13	862.1	10	938	41	862.1	5	0.08	0.03	3.90	3.56
15NP217_g085	1.496	0.032	0.1539	0.0027	0.84513	928	13	922	15	930	26	922	7.5	0.01	0.01	0.96	0.32
15NP217_g028	1.502	0.023	0.1546	0.0013	0.46391	931.4	9.5	926.7	7.5	922	28	926.7	3.75	-0.01	0.01	0.69	0.45
15NP217_g050	1.521	0.019	0.15568	0.0012	0.33451	938.6	7.6	932.7	6.7	938	24	932.7	3.35	0.01	0.01	0.93	1.15
15NP217_g003	3.154	0.045	0.2507	0.0024	0.50335	1445.9	11	1442	12	1458	24	1458	12	0.01	0.00	0.42	0.16
15NP217_g138	3.812	0.049	0.2689	0.0023	0.36686	1596.2	10	1535.2	12	1679	22	1679	11	0.09	0.04	6.20	0.87
15NP217_g048	4.4	0.076	0.3059	0.0032	0.28889	1711	14	1720	16	1686	31	1686	15.5	-0.02	-0.01	-0.79	0.87
15NP217_g022	4.35	0.1	0.3033	0.0033	0.32328	1703	19	1708	16	1706	40	1706	20	0.00	0.00	-0.49	0.62
15NP217_g117	4.475	0.057	0.3104	0.0025	0.6422	1725.8	10	1742.8	12	1712	20	1712	10	-0.02	-0.01	-1.50	1.49
15NP217_g018	4.529	0.06	0.3047	0.0028	0.56988	1736.3	11	1714	14	1758	20	1758	10	0.03	0.01	2.00	0.93
15NP217_g125	4.676	0.056	0.3166	0.0025	0.63441	1763.1	9.9	1772.8	12	1761	19	1761	9.5	-0.01	-0.01	-0.93	0.69
15NP217_g095	4.52	0.057	0.301	0.0024	0.56238	1734.1	11	1695.9	12	1773	20	1773	10	0.04	0.02	3.70	0.52

Sample 15NP217 continued

	Conventional concordia					Ages								Discordance		Conc.Dist., dc	Th/U
Sample # _grain number	207Pb 235U	±2σ	206Pb 238U	±2σ	error corr. 206/238 vs 207/235	207Pb 235U	±2σ	206Pb 238U	±2σ	207Pb 206Pb	±2σ	Best Age	±1σ	206/238 207/206	206/238 207/235		
15NP217_g032	4.718	0.067	0.3068	0.0026	0.54145	1770.5	12	1725	13	1815	22	1815	11	0.05	0.03	4.40	0.86
15NP217_g064	4.786	0.057	0.3112	0.0024	0.55828	1782.7	9.9	1746.5	12	1821.4	19	1821.4	9.5	0.04	0.02	3.40	1.15
15NP217_g015	5.094	0.062	0.3289	0.0026	0.52674	1835.3	11	1832.9	12	1835	19	1835	9.5	0.00	0.00	0.19	0.65
15NP217_g141	5.574	0.065	0.348	0.0027	0.47422	1912.3	10	1925.2	13	1895	19	1895	9.5	-0.02	-0.01	-1.10	0.50
15NP217_g058	6.083	0.1	0.3621	0.0037	0.53648	1990	15	1992	18	1987	26	1987	13	0.00	0.00	-0.37	0.01
15NP217_g017	6.219	0.079	0.363	0.003	0.60459	2008.2	11	1996.1	14	2026	19	2026	9.5	0.01	0.01	0.90	0.45
15NP217_g052	10.077	0.14	0.4571	0.0038	0.58035	2441.4	13	2427	17	2443	19	2443	9.5	0.01	0.01	1.10	0.94
15NP217_g120	9.605	0.14	0.4336	0.0041	0.8063	2398.4	13	2322	18	2466.7	17	2466.7	8.5	0.06	0.03	5.40	1.27
15NP217_g088	10.61	0.13	0.471	0.0038	0.7119	2490.4	11	2488	17	2481.4	17	2481.4	8.5	0.00	0.00	0.11	0.66
15NP217_g007	11.011	0.13	0.4821	0.0041	0.77879	2524.1	11	2536	18	2505	16	2505	8	-0.01	0.00	-0.84	0.38
15NP217_g099	21.51	0.49	0.6378	0.0099	0.94198	3158	22	3181	38	3135	19	3135	9.5	-0.01	-0.01	-1.40	1.78
15NP217_g107	21.61	0.25	0.6284	0.0051	0.50698	3166.7	11	3143	20	3180.9	16	3180.9	8	0.01	0.01	1.30	0.61
15NP217_g006	9.66	0.17	0.4295	0.0062	0.93119	2401	16	2302	28	2488.8	17	2488.8	8.5	0.08	0.04	8.90	0.37
15NP217_g051	7.376	0.1	0.3727	0.0034	0.783	2157.2	12	2042	16	2269	19	2269	9.5	0.10	0.05	9.10	0.74
15NP217_g068	2.605	0.054	0.1935	0.0026	0.68884	1302	15	1140	14	1570	30	1570	15	0.27	0.12	21.00	1.12
15NP217_g135	5.688	0.082	0.2958	0.0034	0.91017	1930.3	12	1670	17	2225.2	17	2225.2	8.5	0.25	0.13	29.00	0.87

Sample 15NP237	Sample Type: detrital					Latitude:	39.20403	Longitude:	75.0696								
	Conventional concordia					Ages								Discordance		Conc.Dist., dc	Th/U
Sample #	207Pb	±2σ	206Pb	±2σ	error corr.	207Pb	±2σ	206Pb	±2σ	207Pb	±2σ	Best Age	±1σ	206/238	206/238		
_grain number	235U		238U		206/238 vs 207/235	235U		238U		206Pb				207/206	207/235		
15NP237_g071	0.3204	0.0064	0.04403	0.00029	0.16676	281.8	4.9	278	1.7	314	42	278	0.85	0.11	0.01	1.80	0.57
15NP237_g170	0.3177	0.0059	0.0441	0.0004	0.28733	279.8	4.5	278.2	2.5	293	39	278.2	1.25	0.05	0.01	0.79	0.33
15NP237_g125	0.3204	0.0057	0.04421	0.00026	0.095177	281.9	4.4	278.9	1.6	297	38	278.9	0.8	0.06	0.01	1.40	0.42
15NP237_g102	0.3327	0.0082	0.04423	0.00061	0.42338	291.4	6.2	279	3.8	349	54	279	1.9	0.20	0.04	5.00	0.46
15NP237_g091	0.3167	0.0069	0.04428	0.0004	0.12711	278.9	5.3	279.3	2.5	274	50	279.3	1.25	-0.02	0.00	0.02	0.38
15NP237_g043	0.3198	0.0074	0.04431	0.00035	0.18585	281.2	5.7	279.5	2.2	288	48	279.5	1.1	0.03	0.01	0.91	0.60
15NP237_g110	0.3243	0.008	0.04431	0.0004	0.27813	284.5	6.2	279.5	2.4	341	51	279.5	1.2	0.18	0.02	2.30	0.58
15NP237_g112	0.3218	0.0071	0.04433	0.00049	0.11243	284.5	5.5	279.6	3	305	50	279.6	1.5	0.08	0.02	1.50	0.62
15NP237_g026	0.3247	0.0062	0.04433	0.00041	0.3745	285.3	4.7	279.6	2.5	267	41	279.6	1.25	-0.05	0.02	2.40	0.65
15NP237_g023	0.3188	0.0098	0.0444	0.00045	0.053892	281.6	7.6	280.1	2.8	268	69	280.1	1.4	-0.05	0.01	0.38	0.55
15NP237_g019	0.3205	0.0052	0.04441	0.00042	0.42368	282.9	3.8	280.1	2.6	272	34	280.1	1.3	-0.03	0.01	0.88	0.42
15NP237_g154	0.317	0.011	0.04442	0.00047	0.098468	278.1	8.4	280.2	2.9	274	73	280.2	1.45	-0.02	-0.01	-0.24	0.40
15NP237_g005	0.3151	0.0076	0.04448	0.00045	0.42975	277.8	5.8	280.5	2.8	280	47	280.5	1.4	0.00	-0.01	-0.99	0.47
15NP237_g158	0.324	0.015	0.04449	0.00067	0.27792	286	11	280.6	4.1	367	95	280.6	2.05	0.24	0.02	1.80	0.53
15NP237_g003	0.3173	0.0083	0.0445	0.00056	0.21791	281.2	6.1	280.7	3.4	320	58	280.7	1.7	0.12	0.00	-0.34	0.30
15NP237_g025	0.3281	0.0071	0.04454	0.00044	0.25668	287.9	5.4	280.9	2.7	282	50	280.9	1.35	0.00	0.02	2.90	0.45
15NP237_g065	0.3166	0.0085	0.04455	0.00039	0.079749	279.2	6.5	281	2.4	274	61	281	1.2	-0.03	-0.01	-0.69	0.59
15NP237_g136	0.3265	0.0058	0.04456	0.00037	0.25526	286.6	4.4	281	2.3	332	37	281	1.15	0.15	0.02	2.30	0.33
15NP237_g056	0.3187	0.0051	0.0446	0.0003	0.19065	280.6	3.9	281.3	1.8	262	39	281.3	0.9	-0.07	0.00	-0.15	0.56
15NP237_g035	0.3273	0.0072	0.04478	0.00039	0.34917	287.6	5.5	282.4	2.4	311	47	282.4	1.2	0.09	0.02	2.00	0.68
15NP237_g119	0.3178	0.0085	0.0448	0.00044	0.40074	279.5	6.6	282.5	2.7	264	56	282.5	1.35	-0.07	-0.01	-0.94	0.64
15NP237_g097	0.3244	0.0064	0.04488	0.00034	0.28175	286.2	4.8	283	2.1	305	39	283	1.05	0.07	0.01	0.91	0.50
15NP237_g103	0.3227	0.0045	0.0449	0.00033	0.39638	283.8	3.5	283.1	2.1	305	28	283.1	1.05	0.07	0.00	0.34	0.40
15NP237_g122	0.3196	0.0059	0.04494	0.00045	0.29644	281.3	4.5	283.3	2.8	260	41	283.3	1.4	-0.09	-0.01	-0.72	0.36
15NP237_g171	0.3209	0.0052	0.04494	0.00043	0.19173	282.3	4	283.4	2.6	254	39	283.4	1.3	-0.12	0.00	-0.32	0.37
15NP237_g107	0.3286	0.0054	0.04495	0.00032	0.27001	288.2	4.2	283.4	1.9	320	36	283.4	0.95	0.11	0.02	2.00	0.49
15NP237_g079	0.3325	0.0045	0.04495	0.00036	0.44768	291.6	3.3	283.4	2.2	343	28	283.4	1.1	0.17	0.03	3.20	0.43
15NP237_g018	0.3329	0.0079	0.04497	0.00052	0.10597	291.3	6	283.5	3.2	326	54	283.5	1.6	0.13	0.03	3.30	0.60
15NP237_g123_c	0.3217	0.0052	0.04498	0.00041	0.34044	283.4	3.9	283.6	2.5	294	34	283.6	1.25	0.04	0.00	-0.17	0.50
15NP237_g117	0.3234	0.0062	0.04502	0.00033	0.33626	284.3	4.7	283.9	2	335	38	283.9	1	0.15	0.00	0.26	0.36

Sample 15NP237 continued

	Conventional concordia					Ages								Discordance		Conc.Dist., dc	Th/U
Sample # _grain number	207Pb 235U	±2σ	206Pb 238U	±2σ	error corr. 206/238 vs 207/235	207Pb 235U	±2σ	206Pb 238U	±2σ	207Pb 206Pb	±2σ	Best Age	±1σ	206/238 207/206	206/238 207/235		
15NP237_g077	0.3243	0.0039	0.04503	0.00029	0.61094	285.1	3	283.9	1.8	305	24	283.9	0.9	0.07	0.00	0.51	0.51
15NP237_g180	0.3254	0.0081	0.04503	0.00037	0.29637	284.7	6	283.9	2.3	290	48	283.9	1.15	0.02	0.00	0.85	0.50
15NP237_g126	0.3204	0.0079	0.04505	0.00034	0.19594	282.2	6.1	284	2.1	279	53	284	1.05	-0.02	-0.01	-0.75	0.50
15NP237_g044	0.3233	0.0063	0.04504	0.00036	0.27633	284.1	4.8	284	2.2	277	42	284	1.1	-0.03	0.00	0.18	0.45
15NP237_g086	0.3236	0.006	0.04505	0.00045	0.19822	284.3	4.6	284	2.8	300	41	284	1.4	0.05	0.00	0.24	0.40
15NP237_g159	0.3206	0.007	0.04508	0.00034	0.12087	284.2	5.2	284.2	2.1	267	48	284.2	1.05	-0.06	0.00	-0.76	0.36
15NP237_g022	0.3286	0.0055	0.04507	0.00035	0.29615	288.2	4.2	284.2	2.2	285	38	284.2	1.1	0.00	0.01	1.70	0.43
15NP237_g164	0.3201	0.0042	0.04512	0.00036	0.62115	281.8	3.2	284.4	2.2	259	27	284.4	1.1	-0.10	-0.01	-1.00	0.53
15NP237_g013	0.3347	0.0071	0.0451	0.0004	0.10446	293.2	5.5	284.4	2.5	332	52	284.4	1.25	0.14	0.03	3.50	0.48
15NP237_g114	0.3251	0.0065	0.04513	0.00041	0.0594	285.4	5	284.5	2.5	276	41	284.5	1.25	-0.03	0.00	0.51	0.54
15NP237_g084	0.326	0.0049	0.04514	0.00035	0.28768	286.3	3.8	284.6	2.1	279	31	284.6	1.05	-0.02	0.01	0.76	0.36
15NP237_g006	0.3243	0.0079	0.04518	0.00037	0.15809	284.6	6.1	284.8	2.3	245	51	284.8	1.15	-0.16	0.00	0.14	0.60
15NP237_g055	0.326	0.015	0.0452	0.00073	0.12496	286	11	285	4.5	360	100	285	2.25	0.21	0.00	0.61	0.53
15NP237_g087	0.3301	0.0061	0.04521	0.00045	0.37479	290.3	4.6	285	2.8	345	35	285	1.4	0.17	0.02	1.80	0.39
15NP237_g120	0.3326	0.0093	0.04518	0.00048	0.24274	291.5	7.1	285.1	2.9	314	57	285.1	1.45	0.09	0.02	2.60	0.56
15NP237_g038	0.33	0.01	0.04526	0.00056	0.22944	288.9	7.7	285.3	3.4	269	65	285.3	1.7	-0.06	0.01	1.70	0.68
15NP237_g108	0.3237	0.0042	0.04536	0.00035	0.6458	284.6	3.2	285.7	2.1	269	25	285.7	1.05	-0.06	0.00	-0.49	0.52
15NP237_g135	0.3283	0.0068	0.04532	0.00032	0.070424	287.8	5.2	285.7	2	295	45	285.7	1	0.03	0.01	1.00	0.45
15NP237_g134	0.3259	0.0081	0.04533	0.00042	0.066349	285.9	6.2	285.8	2.6	283	55	285.8	1.3	-0.01	0.00	0.26	0.48
15NP237_g085	0.3443	0.0081	0.04535	0.00039	0.4268	299.9	6	285.9	2.4	387	41	285.9	1.2	0.26	0.05	5.70	0.38
15NP237_g173	0.3285	0.0067	0.04537	0.00042	0.51696	288.5	5.1	286	2.6	303	35	286	1.3	0.06	0.01	0.96	0.49
15NP237_g014	0.326	0.011	0.0454	0.00064	0.71077	286.2	8.2	286.2	3.9	325	57	286.2	1.95	0.12	0.00	0.12	0.58
15NP237_g148	0.3256	0.0043	0.04543	0.00031	0.34828	286.4	3.4	286.4	1.9	298	28	286.4	0.95	0.04	0.00	-0.08	0.50
15NP237_g057	0.3275	0.0044	0.04544	0.00033	0.5156	288.2	3.2	286.4	2	296	28	286.4	1	0.03	0.01	0.47	0.54
15NP237_g029	0.3274	0.0051	0.04547	0.00049	0.82049	287.4	3.9	286.7	3	305	27	286.7	1.5	0.06	0.00	0.38	0.35
15NP237_g124	0.3346	0.0062	0.04552	0.00045	0.52241	292.8	4.7	287	2.8	322	32	287	1.4	0.11	0.02	2.40	0.47
15NP237_g032	0.3264	0.0084	0.04554	0.00057	0.54866	286.7	6.4	287.1	3.5	331	44	287.1	1.75	0.13	0.00	-0.11	0.37
15NP237_g096	0.3293	0.005	0.04556	0.00033	0.58405	288.3	3.7	287.2	2.1	307	28	287.2	1.05	0.06	0.00	0.73	0.53
15NP237_g160	0.3356	0.0044	0.04564	0.0004	0.8287	293.7	3.3	287.7	2.5	323	24	287.7	1.25	0.11	0.02	2.50	0.26
15NP237_g150	0.3262	0.0049	0.04565	0.00031	0.33893	286.5	3.7	287.8	1.9	285	28	287.8	0.95	-0.01	0.00	-0.44	0.64

Sample 15NP237 continued

	Conventional concordia					Ages								Discordance		Conc.Dist., dc	Th/U
Sample #	207Pb	±2σ	206Pb	±2σ	error corr.	207Pb	±2σ	206Pb	±2σ	207Pb	±2σ	Best Age	±1σ	206/238	206/238		
_grain number	235U		238U		206/238 vs 207/235	235U		238U		206Pb				207/206	207/235		
15NP237_g062	0.3238	0.0061	0.04567	0.00042	0.24207	285.3	4.8	287.9	2.6	326	43	287.9	1.3	0.12	-0.01	-1.20	0.35
15NP237_g067	0.3315	0.0062	0.04569	0.00065	0.43334	290.6	4.7	288	4	260	48	288	2	-0.11	0.01	1.10	0.37
15NP237_g174	0.3278	0.004	0.04571	0.00034	0.11487	287.7	3	288.1	2.1	278	28	288.1	1.05	-0.04	0.00	-0.10	0.43
15NP237_g165	0.3272	0.006	0.04572	0.00034	0.25642	287.5	4.7	288.2	2.1	259	38	288.2	1.05	-0.11	0.00	-0.30	0.51
15NP237_g066	0.3321	0.0069	0.04572	0.00042	0.22229	291.7	5.2	288.2	2.6	298	45	288.2	1.3	0.03	0.01	1.20	0.43
15NP237_g128	0.3298	0.0049	0.04583	0.00033	0.17797	289.9	3.8	288.8	2	292	33	288.8	1	0.01	0.00	0.21	0.36
15NP237_g157	0.3259	0.0046	0.04585	0.00044	0.47667	286.3	3.6	289	2.7	274	28	289	1.35	-0.05	-0.01	-1.00	0.38
15NP237_g095	0.3261	0.0046	0.04588	0.0003	0.22547	286.7	3.5	289.1	1.8	267	30	289.1	0.9	-0.08	-0.01	-1.00	0.42
15NP237_g161	0.335	0.011	0.04588	0.00064	0.49083	293	8	289.2	4	308	84	289.2	2	0.06	0.01	1.70	0.43
15NP237_g181	0.3289	0.0067	0.04589	0.00036	0.23647	288.8	5.1	289.3	2.2	279	43	289.3	1.1	-0.04	0.00	-0.20	0.50
15NP237_g155_c	0.3459	0.0046	0.04593	0.00048	0.76437	301.5	3.5	289.4	3	395	25	289.4	1.5	0.27	0.04	4.70	0.36
15NP237_g061	0.3404	0.0055	0.04594	0.00036	0.71031	297.7	4.1	289.5	2.2	352	29	289.5	1.1	0.18	0.03	3.20	0.58
15NP237_g167	0.3299	0.0045	0.04595	0.00033	0.41604	289.6	3.4	289.6	2	288	26	289.6	1	-0.01	0.00	-0.05	0.51
15NP237_g175	0.3326	0.0055	0.04596	0.00035	0.35772	291.7	4.1	289.7	2.2	294	35	289.7	1.1	0.01	0.01	0.74	0.57
15NP237_g042	0.331	0.0067	0.04608	0.00034	0.36388	289.9	5.1	290.4	2.1	250	39	290.4	1.05	-0.16	0.00	-0.03	0.51
15NP237_g053	0.3332	0.0061	0.0461	0.00049	0.39268	293.2	4.8	290.5	3	275	38	290.5	1.5	-0.06	0.01	0.58	0.38
15NP237_g060	0.337	0.011	0.04613	0.00051	0.25506	294.2	8.6	290.7	3.2	375	72	290.7	1.6	0.22	0.01	1.60	0.41
15NP237_g031	0.34	0.0077	0.04613	0.00037	0.023806	296.6	5.8	290.7	2.3	343	53	290.7	1.15	0.15	0.02	2.50	0.42
15NP237_g027	0.3409	0.0055	0.04617	0.00031	0.39551	297.6	4.2	291	1.9	321	32	291	0.95	0.09	0.02	2.70	0.53
15NP237_g048	0.331	0.0054	0.0462	0.00035	0.29642	290.1	4.1	291.1	2.2	271	34	291.1	1.1	-0.07	0.00	-0.32	0.47
15NP237_g009	0.3401	0.0081	0.04626	0.00048	0.14201	297	6.2	291.5	2.9	276	50	291.5	1.45	-0.06	0.02	2.20	0.40
15NP237_g184	0.3348	0.0069	0.04627	0.00037	0.36362	292.8	5.2	291.6	2.3	288	40	291.6	1.15	-0.01	0.00	0.64	0.65
15NP237_g185	0.3307	0.0042	0.0463	0.00025	0.40248	290.2	3.2	291.7	1.5	278	26	291.7	0.75	-0.05	-0.01	-0.66	0.50
15NP237_g149	0.331	0.0059	0.04623	0.00044	0.48759	290	4.6	291.7	2.8	271	37	291.7	1.4	-0.08	-0.01	-0.39	0.33
15NP237_g051	0.3337	0.0057	0.04633	0.0003	0.18345	292.1	4.3	292	1.9	295	38	292	0.95	0.01	0.00	0.17	0.56
15NP237_g082	0.3437	0.0045	0.04634	0.00025	0.33187	300.1	3.4	292	1.5	363	27	292	0.75	0.20	0.03	3.10	0.43
15NP237_g137	0.3484	0.0083	0.04634	0.0004	0.1515	303.5	6.2	292	2.4	389	50	292	1.2	0.25	0.04	4.40	0.74
15NP237_g041	0.3337	0.0058	0.04635	0.00033	0.080505	292.1	4.4	292.1	2.1	296	39	292.1	1.05	0.01	0.00	0.12	0.49
15NP237_g039	0.3439	0.0087	0.04639	0.00042	0.34363	300.1	6.5	292.3	2.6	340	52	292.3	1.3	0.14	0.03	3.00	0.51
15NP237_g129	0.3318	0.0046	0.04641	0.00036	0.48038	291.1	3.5	292.4	2.2	279	28	292.4	1.1	-0.05	0.00	-0.59	0.38

Sample 15NP237 continued

	Conventional concordia					Ages								Discordance		Conc.Dist., dc	Th/U
Sample # _grain number	207Pb 235U	±2σ	206Pb 238U	±2σ	error corr. 206/238 vs 207/235	207Pb 235U	±2σ	206Pb 238U	±2σ	207Pb 206Pb	±2σ	Best Age	±1σ	206/238 207/206	206/238 207/235		
15NP237_g144	0.3369	0.0045	0.04644	0.00042	0.28372	295	3.5	292.6	2.6	315	33	292.6	1.3	0.07	0.01	0.86	1.04
15NP237_g111	0.3359	0.0041	0.04648	0.00035	0.69317	293.9	3.1	292.9	2.1	292	23	292.9	1.05	0.00	0.00	0.47	0.42
15NP237_g081	0.3345	0.0052	0.04654	0.00041	0.5148	293.1	3.9	293.2	2.5	280	31	293.2	1.25	-0.05	0.00	-0.10	0.56
15NP237_g033	0.3373	0.006	0.04656	0.00041	0.60862	294.8	4.5	293.4	2.5	293	29	293.4	1.25	0.00	0.00	0.69	0.45
15NP237_g050	0.3396	0.0073	0.0466	0.0004	0.2636	296.4	5.5	293.6	2.5	306	38	293.6	1.25	0.04	0.01	1.30	0.35
15NP237_g021	0.3342	0.0093	0.04663	0.00045	0.11625	292.1	7.1	293.8	2.7	252	59	293.8	1.35	-0.17	-0.01	-0.40	0.63
15NP237_g153	0.3449	0.0053	0.04664	0.00034	0.16806	300.6	4	293.9	2.1	342	37	293.9	1.05	0.14	0.02	2.70	0.44
15NP237_g063	0.344	0.016	0.04667	0.00093	0.30384	300	12	294	5.7	320	100	294	2.85	0.08	0.02	2.40	0.37
15NP237_g092	0.3353	0.0045	0.04668	0.00035	0.32682	294.1	3.5	294.1	2.1	304	29	294.1	1.05	0.03	0.00	-0.20	0.42
15NP237_g100	0.3402	0.0045	0.04669	0.00031	0.18824	297.5	3.5	294.2	1.9	310	32	294.2	0.95	0.05	0.01	1.20	0.46
15NP237_g058	0.3449	0.0061	0.04672	0.00034	0.23215	300.5	4.6	294.3	2.1	346	32	294.3	1.05	0.15	0.02	2.50	0.46
15NP237_g045	0.3414	0.0065	0.04674	0.00036	0.29769	297.8	4.9	294.5	2.2	314	43	294.5	1.1	0.06	0.01	1.50	0.59
15NP237_g037	0.332	0.013	0.04676	0.00047	0.25772	291.5	9.8	294.6	2.9	298	76	294.6	1.45	0.01	-0.01	-1.40	0.49
15NP237_g166	0.3324	0.0054	0.04677	0.00044	0.32356	291.1	4.1	294.7	2.7	267	33	294.7	1.35	-0.10	-0.01	-1.30	0.27
15NP237_g054	0.3382	0.0059	0.04681	0.00035	0.44722	295.5	4.5	294.9	2.2	292	34	294.9	1.1	-0.01	0.00	0.35	0.57
15NP237_g143	0.3348	0.0049	0.04685	0.00034	0.24797	293	3.8	295.1	2.1	276	30	295.1	1.05	-0.07	-0.01	-0.75	0.61
15NP237_g064	0.35	0.013	0.04685	0.00065	0.50789	306	10	295.2	4	337	69	295.2	2	0.12	0.04	3.70	0.46
15NP237_g049	0.3389	0.0065	0.0469	0.0004	0.43688	296	4.9	295.5	2.4	290	38	295.5	1.2	-0.02	0.00	0.34	0.42
15NP237_g169	0.3445	0.006	0.04698	0.00031	0.26049	300.2	4.5	295.9	1.9	337	37	295.9	0.95	0.12	0.01	1.80	0.56
15NP237_g182	0.3379	0.0067	0.04699	0.00036	0.25538	295.1	5.1	296	2.2	289	42	296	1.1	-0.02	0.00	-0.17	0.54
15NP237_g109	0.3383	0.0072	0.04702	0.00037	0.28006	296.6	5.3	296.4	2.3	288	39	296.4	1.15	-0.03	0.00	-0.12	0.42
15NP237_g069	0.349	0.015	0.04705	0.00099	0.35466	304	11	296.4	6.1	300	110	296.4	3.05	0.01	0.03	2.90	0.31
15NP237_g106	0.344	0.018	0.04711	0.0008	0.1612	299	13	296.7	4.9	420	110	296.7	2.45	0.29	0.01	1.30	0.44
15NP237_g168	0.3448	0.0066	0.04736	0.00048	0.38362	300.5	5	298.3	2.9	275	41	298.3	1.45	-0.08	0.01	0.96	0.47
15NP237_g101	0.3438	0.009	0.0474	0.00057	0.19402	299.7	6.8	298.5	3.5	368	56	298.5	1.75	0.19	0.00	0.58	0.37
15NP237_g179	0.3485	0.0097	0.04745	0.00047	0.18304	304.1	7.1	298.8	2.9	351	59	298.8	1.45	0.15	0.02	1.80	0.63
15NP237_g130	0.3409	0.0051	0.04748	0.00039	0.56686	298.4	4	299	2.4	306	26	299	1.2	0.02	0.00	-0.45	0.41
15NP237_g183	0.347	0.0053	0.04744	0.00034	0.43507	302.6	4	299	2.1	318	28	299	1.05	0.06	0.01	1.40	0.48
15NP237_g046	0.345	0.006	0.04749	0.00035	0.15687	300.6	4.5	299.1	2.2	284	37	299.1	1.1	-0.05	0.00	0.71	0.64
15NP237_g176	0.3563	0.0082	0.04749	0.00041	0.37185	308.8	6.1	299.1	2.5	365	34	299.1	1.25	0.18	0.03	3.90	0.66

Sample 15NP237 continued

	Conventional concordia				Ages								Discordance		Conc.Dist., dc	Th/U
Sample #	207Pb	±2σ	206Pb	±2σ	error corr.	207Pb	±2σ	206Pb	±2σ	207Pb	±2σ	Best Age	±1σ	206/238	206/238		
_grain number	235U		238U		206/238 vs 207/235	235U		238U		206Pb				207/206	207/235		
15NP237_g141	0.346	0.0082	0.04751	0.00054	0.23521	301.5	6.1	299.2	3.3	285	52	299.2	1.65	-0.05	0.01	0.95	0.34
15NP237_g070	0.3458	0.0051	0.04767	0.00032	0.35811	301.3	3.9	300.2	2	303	33	300.2	1	0.01	0.00	0.52	0.35
15NP237_g083	0.3421	0.0055	0.04775	0.00029	0.24006	298.5	4.1	300.7	1.8	285	33	300.7	0.9	-0.06	-0.01	-0.74	0.38
15NP237_g131	0.345	0.007	0.04782	0.00037	0.44177	300.5	5.3	301.1	2.3	283	40	301.1	1.15	-0.06	0.00	-0.07	0.33
15NP237_g151	0.3523	0.0054	0.04795	0.00034	0.26622	306.6	4	301.9	2.1	328	36	301.9	1.05	0.08	0.02	1.70	0.32
15NP237_g073	0.369	0.0048	0.04791	0.00032	0.42996	318.7	3.6	301.9	1.9	452	26	301.9	0.95	0.33	0.05	6.40	0.42
15NP237_g007	0.3527	0.0091	0.04797	0.00043	0.0026584	306.4	6.8	302.1	2.6	269	55	302.1	1.3	-0.12	0.01	1.80	0.48
15NP237_g099	0.3421	0.0061	0.04805	0.00036	0.091863	298.4	4.6	302.6	2.2	275	37	302.6	1.1	-0.10	-0.01	-1.40	0.53
15NP237_g059	0.359	0.012	0.0483	0.00085	0.53784	314.2	7.2	304.1	5.2	335	70	304.1	2.6	0.09	0.03	2.80	0.51
15NP237_g162	0.3553	0.0063	0.04852	0.00038	0.57713	308.8	4.8	305.4	2.3	346	33	305.4	1.15	0.12	0.01	1.20	0.42
15NP237_g127	0.361	0.0067	0.04865	0.00038	0.089449	313.2	5.1	306.2	2.3	359	44	306.2	1.15	0.15	0.02	2.50	0.50
15NP237_g072	0.3611	0.0089	0.04864	0.00044	0.37201	312.3	6.6	306.2	2.7	359	49	306.2	1.35	0.15	0.02	2.60	0.56
15NP237_g052	0.3634	0.0046	0.04901	0.00037	0.13817	314.6	3.4	308.4	2.3	349	30	308.4	1.15	0.12	0.02	2.30	0.46
15NP237_g076	0.361	0.011	0.0494	0.00044	0.010967	311.6	8.3	310.8	2.7	316	64	310.8	1.35	0.02	0.00	0.78	0.64
15NP237_g020	0.365	0.017	0.04955	0.00077	0.34488	315	12	311.7	4.8	342	98	311.7	2.4	0.09	0.01	1.50	0.47
15NP237_g074	0.3606	0.0055	0.04965	0.00042	0.28076	313.7	4.1	312.3	2.6	326	34	312.3	1.3	0.04	0.00	0.11	0.29
15NP237_g178	0.373	0.012	0.05066	0.00077	0.088252	320.4	8.8	318.5	4.7	322	69	318.5	2.35	0.01	0.01	1.20	0.42
15NP237_g156	0.392	0.013	0.0533	0.0013	0.80292	334.7	9.1	334.6	7.8	301	36	334.6	3.9	-0.11	0.00	0.38	0.41
15NP237_g068	0.3626	0.0053	0.04696	0.00035	0.51198	314.3	3.9	295.8	2.1	454	27	295.8	1.05	0.35	0.06	6.90	0.54
15NP237_g030	0.3313	0.007	0.04288	0.00064	0.49586	291.2	5.5	270.7	4	402	48	270.7	2	0.33	0.07	8.10	0.47
15NP237_g116	0.382	0.01	0.0481	0.00053	0.017459	328.1	7.7	302.8	3.2	496	65	302.8	1.6	0.39	0.08	9.40	0.48
15NP237_g015	0.365	0.016	0.04529	0.00048	0.33007	314	12	285.5	3	469	87	285.5	1.5	0.39	0.09	12.00	0.38
15NP237_g078	0.3581	0.0083	0.04442	0.00045	0.32695	310.2	6.2	280.2	2.8	551	49	280.2	1.4	0.49	0.10	12.00	0.43
15NP237_g138	0.3902	0.0091	0.04672	0.00037	0.60115	333.9	6.6	294.3	2.3	561	31	294.3	1.15	0.48	0.12	15.00	0.78
15NP237_g146	0.3764	0.0061	0.04538	0.0003	0.47154	324.1	4.5	286.1	1.8	621	28	286.1	0.9	0.54	0.12	15.00	0.40
15NP237_g142	0.4185	0.0047	0.04624	0.00038	0.49661	354.8	3.4	291.4	2.3	793	20	291.4	1.15	0.63	0.18	23.00	0.82
15NP237_g105	0.445	0.019	0.04862	0.00042	0.20691	371	13	306	2.6	763	92	306	1.3	0.60	0.18	24.00	0.48
15NP237_g098	0.454	0.017	0.04723	0.00034	0.37789	379	12	297.5	2.1	899	68	297.5	1.05	0.67	0.22	29.00	0.46
15NP237_g115	0.5	0.024	0.04883	0.00041	0.29587	411	16	307.6	2.6	1020	100	307.6	1.3	0.70	0.25	35.00	0.64
15NP237_g140	0.3146	0.0052	0.04488	0.00035	0.43999	277.9	4.1	283	2.1	241	32	283	1.05	-0.17	-0.02	-2.10	0.39

Sample 15NP237 continued

	Conventional concordia					Ages								Discordance		Conc.Dist., dc	Th/U
Sample # _grain number	207Pb 235U	±2σ	206Pb 238U	±2σ	error corr. 206/238 vs 207/235	207Pb 235U	±2σ	206Pb 238U	±2σ	207Pb 206Pb	±2σ	Best Age	±1σ	206/238 207/206	206/238 207/235		
15NP237_g104	0.3407	0.0051	0.04808	0.00036	0.44263	297.5	3.8	302.7	2.2	230	28	302.7	1.1	-0.32	-0.02	-1.90	0.47
15NP237_g047	0.3192	0.0058	0.04535	0.00029	0.32673	281.9	4.3	285.9	1.8	233	39	285.9	0.9	-0.23	-0.01	-1.90	0.50
15NP237_g172	0.3375	0.0062	0.04766	0.0004	0.063428	294.9	4.7	300.1	2.5	248	42	300.1	1.25	-0.21	-0.02	-1.90	0.52
15NP237_g028	0.336	0.011	0.04742	0.00054	0.18153	292.8	8.6	298.6	3.3	226	64	298.6	1.65	-0.32	-0.02	-1.70	0.52
15NP237_g113	0.3203	0.0055	0.04534	0.00037	0.56065	281.8	4.3	285.8	2.3	256	33	285.8	1.15	-0.12	-0.01	-1.50	0.48
15NP237_g133	0.3389	0.0051	0.04768	0.00033	0.4777	296.9	3.9	300.3	2	279	28	300.3	1	-0.08	-0.01	-1.50	0.55
15NP237_g177	0.2542	0.006	0.03667	0.00032	0.019513	230.1	4.9	232.1	2	217	54	232.1	1	-0.07	-0.01	-1.00	0.47
15NP237_g132	0.3074	0.0088	0.04206	0.00055	0.35701	271.9	6.9	265.6	3.4	302	66	265.6	1.7	0.12	0.02	2.80	0.44
15NP237_g040	0.3051	0.0062	0.0426	0.0004	0.29369	270.1	4.8	268.9	2.5	290	42	268.9	1.25	0.07	0.00	0.61	0.67
15NP237_g016	0.3199	0.0088	0.04276	0.00073	0.16697	281.4	6.7	269.9	4.5	310	57	269.9	2.25	0.13	0.04	4.90	0.52
15NP237_g152	0.3091	0.0054	0.0428	0.00038	0.18368	273.3	4.2	270.2	2.3	344	45	270.2	1.15	0.21	0.01	1.40	0.42
15NP237_g008	0.3174	0.007	0.04294	0.00031	0.26374	279.5	5.4	271	1.9	318	42	271	0.95	0.15	0.03	3.70	0.53
15NP237_g088	0.313	0.0079	0.043	0.00046	0.19346	275.9	6.1	271.4	2.8	304	54	271.4	1.4	0.11	0.02	2.10	0.42
15NP237_g012	0.317	0.016	0.04306	0.00084	0.14908	279	12	271.8	5.2	380	110	271.8	2.6	0.28	0.03	3.20	0.45
15NP237_g024	0.3075	0.0078	0.04308	0.0004	0.031876	271.7	6.1	271.9	2.5	251	58	271.9	1.25	-0.08	0.00	0.14	0.71
15NP237_g163	0.3116	0.0068	0.04321	0.00038	0.38631	275.5	5.3	272.7	2.4	284	44	272.7	1.2	0.04	0.01	1.10	0.36
15NP237_g080	0.3151	0.0051	0.04326	0.00041	0.41541	278.3	3.9	273	2.5	311	34	273	1.25	0.12	0.02	2.10	0.44
15NP237_g036	0.3124	0.0074	0.0433	0.00048	0.57064	275.8	5.7	273.2	2.9	369	44	273.2	1.45	0.26	0.01	1.20	0.62
15NP237_g001	0.3078	0.0071	0.04336	0.00043	0.32337	272.3	5.5	273.6	2.7	288	50	273.6	1.35	0.05	0.00	-0.48	0.52
15NP237_g011	0.3114	0.0056	0.04337	0.00036	0.26465	275	4.3	273.7	2.2	287	41	273.7	1.1	0.05	0.00	0.65	0.49
15NP237_g093	0.3184	0.0086	0.04343	0.00048	0.26868	280	6.6	274	3	336	61	274	1.5	0.18	0.02	2.70	0.61
15NP237_g004	0.3129	0.0072	0.04348	0.00042	0.27792	276	5.6	274.4	2.6	249	49	274.4	1.3	-0.10	0.01	0.85	0.41
15NP237_g118	0.3131	0.0084	0.04371	0.00037	0.20846	275.9	6.5	275.8	2.3	283	55	275.8	1.15	0.03	0.00	0.33	0.80
15NP237_g121	0.3137	0.0063	0.04371	0.0003	0.20784	277.1	4.9	275.8	1.8	290	43	275.8	0.9	0.05	0.00	0.52	0.45
15NP237_g017	0.3139	0.0077	0.04379	0.0004	0.18251	276.6	5.9	276.3	2.5	290	52	276.3	1.25	0.05	0.00	0.38	0.57
15NP237_g089	0.3103	0.0062	0.04381	0.00041	0.1683	275	4.8	276.4	2.5	269	45	276.4	1.25	-0.03	-0.01	-0.82	0.40
15NP237_g090	0.3142	0.0084	0.04387	0.00041	0.15566	276.8	6.5	276.8	2.5	278	58	276.8	1.25	0.00	0.00	0.27	0.58
15NP237_g034	0.3244	0.0073	0.04389	0.00036	0.23989	285.1	5.6	276.9	2.3	398	44	276.9	1.15	0.30	0.03	3.40	0.39
15NP237_g010	0.3136	0.0089	0.04401	0.00042	0.16238	276.2	6.9	277.6	2.6	251	63	277.6	1.3	-0.11	-0.01	-0.28	0.60
15NP237_g075	0.313	0.013	0.04402	0.00055	0.38241	276	10	277.7	3.4	245	88	277.7	1.7	-0.13	-0.01	-0.50	0.62
15NP237_g094	0.3171	0.0097	0.04403	0.00038	0.22361	278.8	7.4	277.8	2.4	277	60	277.8	1.2	0.00	0.00	0.78	0.51
15NP237_g002	0.3291	0.005	0.04405	0.00039	0.37352	289.1	3.7	277.9	2.4	341	34	277.9	1.2	0.19	0.04	4.40	0.57

Sample 99WT44	Sample Type: detrital					Latitude:	39.242222	Longitude:	75.055278								
	Conventional concordia					Ages								Discordance		Conc.Dist., dc	Th/U
Sample #	207Pb	±2σ	206Pb	±2σ	error corr.	207Pb	±2σ	206Pb	±2σ	207Pb	±2σ	Best Age	±1σ	206/238	206/238		
_grain number	235U		238U		206/238 vs 207/235	235U		238U		206Pb				207/206	207/235		
99WT44_g10	0.379	0.015	0.05372	0.00084	0.35017	326	11	337.3	5.2	292	91	337.3	2.6	-0.16	-0.03	-3.90	0.52
99WT44_g28	0.3585	0.0088	0.0504	0.00057	0.15798	311.5	6.5	316.9	3.5	280	56	316.9	1.75	-0.13	-0.02	-2.20	0.44
99WT44_g47	0.326	0.011	0.0463	0.00085	0.25014	286	8.6	291.7	5.2	254	90	291.7	2.6	-0.15	-0.02	-2.10	0.37
99WT44_g73	0.3452	0.0085	0.04868	0.00044	0.2039	300.8	6.4	306.4	2.7	254	63	306.4	1.35	-0.21	-0.02	-2.00	1.03
99WT44_g79	0.349	0.012	0.04914	0.00065	0.39836	303.6	9.2	309.2	4	257	69	309.2	2	-0.20	-0.02	-2.00	0.63
99WT44_g14	0.3559	0.0048	0.04982	0.00037	0.34159	308.9	3.6	313.4	2.2	280	30	313.4	1.1	-0.12	-0.01	-1.60	1.03
99WT44_g70	0.3562	0.0074	0.04982	0.0004	0.21947	309.4	5.4	313.4	2.4	259	42	313.4	1.2	-0.21	-0.01	-1.50	0.37
99WT44_g20	0.3688	0.0088	0.05136	0.00059	0.4633	318.4	6.5	322.9	3.6	299	50	322.9	1.8	-0.08	-0.01	-1.50	0.84
99WT44_g76	0.393	0.026	0.0543	0.0014	0.1963	339	18	340.6	8.5	370	120	340.6	4.25	0.08	0.00	-1.50	0.41
99WT44_g50	0.3023	0.007	0.04141	0.0005	0.15737	268	5.5	261.6	3.1	331	55	261.6	1.55	0.21	0.02	2.80	0.78
99WT44_g53	0.3127	0.0084	0.04251	0.00042	0.12035	276.4	6.4	268.4	2.6	297	62	268.4	1.3	0.10	0.03	3.30	0.43
99WT44_g72	0.3111	0.0051	0.04308	0.00035	0.19592	274.8	3.9	271.9	2.2	296	36	271.9	1.1	0.08	0.01	1.30	0.50
99WT44_g69	0.3114	0.0037	0.04324	0.00042	0.72318	275.4	2.8	272.9	2.6	290	21	272.9	1.3	0.06	0.01	1.00	1.02
99WT44_g63	0.3128	0.005	0.044	0.00037	0.24654	276.5	3.8	277.5	2.3	247	35	277.5	1.15	-0.12	0.00	-0.50	0.51
99WT44_g38	0.3245	0.0094	0.04403	0.00049	0.18097	285	7.2	277.8	3	324	67	277.8	1.5	0.14	0.03	3.10	0.39
99WT44_g61	0.3171	0.0046	0.04409	0.00058	0.79531	279.5	3.5	278.1	3.6	278	24	278.1	1.8	0.00	0.01	0.66	0.93
99WT44_g26	0.3138	0.0092	0.04423	0.00048	0.14261	276.5	7.1	279	3	238	64	279	1.5	-0.17	-0.01	-0.77	0.74
99WT44_g11	0.3291	0.0053	0.04471	0.0004	0.48893	288.7	4.1	281.9	2.5	352	33	281.9	1.25	0.20	0.02	2.80	0.49
99WT44_g30	0.338	0.01	0.04481	0.00069	0.28545	295.2	7.7	282.5	4.2	386	57	282.5	2.1	0.27	0.04	5.20	0.78
99WT44_g60	0.3304	0.0079	0.0449	0.00065	0.68572	289.6	6.1	283.1	4	330	41	283.1	2	0.14	0.02	2.70	0.57
99WT44_g67	0.3248	0.0041	0.04501	0.00035	0.6523	285.4	3.1	283.8	2.1	279	23	283.8	1.05	-0.02	0.01	0.71	0.39
99WT44_g57	0.3266	0.0079	0.04548	0.00054	0.58431	287.2	5.9	286.7	3.3	274	44	286.7	1.65	-0.05	0.00	0.10	0.58
99WT44_g23	0.3351	0.0059	0.04561	0.00039	0.32549	293.2	4.5	287.5	2.4	319	37	287.5	1.2	0.10	0.02	2.30	1.39
99WT44_g06	0.3283	0.0068	0.04576	0.0004	0.02944	288	5.2	288.4	2.5	304	49	288.4	1.25	0.05	0.00	-0.07	0.70
99WT44_g84	0.3343	0.0048	0.0459	0.00039	0.50398	293.3	3.7	289.3	2.4	339	33	289.3	1.2	0.15	0.01	1.40	0.94
99WT44_g85	0.3302	0.0057	0.04631	0.00036	0.27387	289.4	4.4	291.8	2.2	272	38	291.8	1.1	-0.07	-0.01	-0.83	0.50
99WT44_g03	0.3297	0.0049	0.04634	0.00035	0.30343	288.6	3.7	292	2.2	275	30	292	1.1	-0.06	-0.01	-1.10	0.55
99WT44_g68	0.3359	0.009	0.0465	0.00065	0.36117	293.6	6.8	293	4	319	54	293	2	0.08	0.00	0.41	0.50
99WT44_g52	0.3452	0.0087	0.047	0.0006	0.15942	300.9	6.6	296.1	3.7	346	59	296.1	1.85	0.14	0.02	1.90	0.50
99WT44_g37	0.3442	0.008	0.04703	0.00044	0.32084	301.1	5.8	296.2	2.7	289	53	296.2	1.35	-0.02	0.02	1.60	0.74

Sample 99WT44 continued

	Conventional concordia					Ages								Discordance		Conc.Dist., dc	Th/U
Sample # _grain number	207Pb 235U	±2σ	206Pb 238U	±2σ	error corr. 206/238 vs 207/235	207Pb 235U	±2σ	206Pb 238U	±2σ	207Pb 206Pb	±2σ	Best Age	±1σ	206/238 207/206	206/238 207/235		
99WT44_g54	0.3418	0.0063	0.04736	0.00048	0.50486	299	4.7	298.3	3	279	38	298.3	1.5	-0.07	0.00	0.09	0.63
99WT44_g42	0.3465	0.0084	0.04748	0.00038	0.13376	301.3	6.3	299	2.4	294	53	299	1.2	-0.02	0.01	1.20	0.59
99WT44_g49	0.343	0.013	0.04749	0.00084	0.39512	299	10	299.1	5.2	320	78	299.1	2.6	0.07	0.00	0.13	0.55
99WT44_g25	0.3469	0.0071	0.04766	0.00046	0.2469	301.8	5.3	300.1	2.8	314	42	300.1	1.4	0.04	0.01	0.86	0.87
99WT44_g15	0.3457	0.0085	0.04768	0.00049	0.26262	302	6.5	300.3	3	298	58	300.3	1.5	-0.01	0.01	0.46	0.82
99WT44_g80	0.3417	0.0085	0.04787	0.00048	0.22624	298.8	6.3	301.4	2.9	271	52	301.4	1.45	-0.11	-0.01	-1.10	0.55
99WT44_g39	0.3534	0.0089	0.04788	0.00054	0.24526	307	6.6	301.5	3.3	346	58	301.5	1.65	0.13	0.02	2.20	0.83
99WT44_g77	0.355	0.021	0.04808	0.00089	0.0088697	308	16	302.7	5.4	350	140	302.7	2.7	0.14	0.02	2.20	0.86
99WT44_g59	0.3558	0.0098	0.0482	0.00064	0.31088	309.9	7.5	303.5	3.9	311	59	303.5	1.95	0.02	0.02	2.10	0.73
99WT44_g31	0.3531	0.0061	0.04823	0.00044	0.27428	306.6	4.6	303.6	2.7	297	35	303.6	1.35	-0.02	0.01	1.30	0.62
99WT44_g87	0.3534	0.0056	0.04832	0.00038	0.17966	306.5	4.1	304.2	2.3	343	36	304.2	1.15	0.11	0.01	1.20	0.58
99WT44_g19	0.346	0.014	0.04845	0.00088	0.35745	301	11	305	5.4	343	67	305	2.7	0.11	-0.01	-1.20	0.54
99WT44_g24	0.3595	0.0071	0.0486	0.00037	0.27842	311.5	5.3	305.9	2.2	339	41	305.9	1.1	0.10	0.02	2.20	1.05
99WT44_g71	0.3577	0.0094	0.04878	0.00052	0.13283	309.5	7	307	3.2	297	51	307	1.6	-0.03	0.01	1.30	0.66
99WT44_g01	0.3519	0.006	0.04902	0.00039	0.27996	306.5	4.3	308.5	2.4	281	39	308.5	1.2	-0.10	-0.01	-0.88	0.61
99WT44_g51	0.3584	0.0044	0.04902	0.00037	0.53309	310.9	3.3	308.5	2.3	306	23	308.5	1.15	-0.01	0.01	0.93	1.47
99WT44_g88	0.3529	0.0091	0.04904	0.00062	0.21823	306.5	6.8	308.6	3.8	288	61	308.6	1.9	-0.07	-0.01	-0.64	0.84
99WT44_g13	0.3588	0.0074	0.04923	0.00036	0.21942	310.7	5.5	309.8	2.2	313	43	309.8	1.1	0.01	0.00	0.57	0.60
99WT44_g04	0.3549	0.0083	0.04925	0.00066	0.049913	308	6.2	309.9	4.1	291	48	309.9	2.05	-0.06	-0.01	-0.57	0.69
99WT44_g16	0.362	0.017	0.04931	0.00072	0.12891	313	13	310.3	4.4	340	100	310.3	2.2	0.09	0.01	1.30	0.79
99WT44_g56	0.365	0.011	0.04938	0.00063	0.15516	316.5	8	310.7	3.9	322	65	310.7	1.95	0.04	0.02	1.90	0.66
99WT44_g81	0.357	0.013	0.04943	0.00054	0.25913	308.7	9.7	311.3	3.4	276	70	311.3	1.7	-0.13	-0.01	-0.39	0.52
99WT44_g58	0.3648	0.0069	0.04958	0.00051	0.30902	315.5	5.2	311.9	3.1	317	44	311.9	1.55	0.02	0.01	1.40	0.56
99WT44_g65	0.3629	0.0051	0.04974	0.00042	0.51411	314.1	3.8	312.9	2.6	291	27	312.9	1.3	-0.08	0.00	0.53	1.13
99WT44_g18	0.3724	0.0074	0.0501	0.00049	0.069481	320.9	5.4	315.1	3	368	36	315.1	1.5	0.14	0.02	2.30	0.54
99WT44_g32	0.3715	0.0066	0.05005	0.0005	0.55041	320.5	4.9	315.2	3	320	33	315.2	1.5	0.02	0.02	2.20	0.31
99WT44_g05	0.3615	0.0061	0.05017	0.00042	0.46631	312.9	4.5	315.6	2.6	303	35	315.6	1.3	-0.04	-0.01	-0.82	0.81
99WT44_g36	0.3683	0.0052	0.05023	0.00041	0.41669	318.4	3.8	315.9	2.5	319	29	315.9	1.25	0.01	0.01	0.89	0.57
99WT44_g07	0.3645	0.0059	0.05028	0.00045	0.31328	315.6	4.3	316.5	2.7	327	36	316.5	1.35	0.03	0.00	-0.25	0.50
99WT44_g41	0.3716	0.0082	0.05051	0.00059	0.55069	320.4	6.1	317.7	3.6	331	44	317.7	1.8	0.04	0.01	1.20	0.89

Sample 99WT44 continued

	Conventional concordia					Ages								Discordance		Conc.Dist., dc	Th/U
Sample #	207Pb	±2σ	206Pb	±2σ	error corr.	207Pb	±2σ	206Pb	±2σ	207Pb	±2σ	Best Age	±1σ	206/238	206/238		
_grain number	235U		238U		206/238 vs 207/235	235U		238U		206Pb				207/206	207/235		
99WT44_g83	0.3715	0.0049	0.05056	0.00038	0.46161	320.5	3.6	317.9	2.3	337	29	317.9	1.15	0.06	0.01	1.00	0.28
99WT44_g35	0.376	0.011	0.05056	0.00076	0.47622	324.4	8.4	317.9	4.7	316	59	317.9	2.35	-0.01	0.02	2.20	0.85
99WT44_g27	0.3701	0.0059	0.05057	0.00039	0.20268	319.4	4.4	318	2.4	321	31	318	1.2	0.01	0.00	0.62	0.82
99WT44_g44	0.368	0.01	0.05071	0.00066	0.18016	318.7	7.4	318.8	4	321	57	318.8	2	0.01	0.00	-0.26	0.56
99WT44_g08	0.3654	0.0075	0.05072	0.00043	0.22771	315.6	5.6	319.1	2.7	299	42	319.1	1.35	-0.07	-0.01	-0.98	0.84
99WT44_g46	0.3709	0.0097	0.05078	0.00058	0.09516	320	7.2	319.3	3.5	323	70	319.3	1.75	0.01	0.00	0.37	0.58
99WT44_g40	0.383	0.012	0.05098	0.00053	0.50685	327.7	9.1	320.5	3.3	358	64	320.5	1.65	0.10	0.02	3.20	0.62
99WT44_g45	0.3741	0.0081	0.05104	0.00073	0.56562	322.4	6	320.8	4.5	344	45	320.8	2.25	0.07	0.00	0.64	0.60
99WT44_g66	0.382	0.012	0.0512	0.00083	0.4238	327.8	8.6	321.8	5.1	341	62	321.8	2.55	0.06	0.02	2.40	0.51
99WT44_g74	0.3782	0.0067	0.05139	0.00052	0.26877	325.3	5	323	3.2	341	30	323	1.6	0.05	0.01	0.95	1.07
99WT44_g09	0.379	0.014	0.05138	0.00079	0.61636	328	11	323	4.8	390	79	323	2.4	0.17	0.02	1.20	0.59
99WT44_g33	0.3833	0.0091	0.05144	0.00044	0.12457	327.8	6.5	323.4	2.7	336	50	323.4	1.35	0.04	0.01	2.20	0.62
99WT44_g12	0.374	0.0079	0.05172	0.00058	0.38181	323.6	5.6	325.1	3.6	315	44	325.1	1.8	-0.03	0.00	-0.88	0.83
99WT44_g22	0.377	0.013	0.05216	0.00064	0.054645	324.5	9.5	327.7	3.9	294	79	327.7	1.95	-0.11	-0.01	-1.00	0.51
99WT44_g02	0.3784	0.0035	0.05226	0.00034	0.51368	325.8	2.6	328.4	2.1	303	21	328.4	1.05	-0.08	-0.01	-0.90	0.45
99WT44_g29	0.395	0.016	0.0527	0.001	0.41801	341	12	330.9	6.2	379	88	330.9	3.1	0.13	0.03	2.40	0.47
99WT44_g64	0.464	0.017	0.06007	0.00079	0.57412	391	12	376	4.8	410	65	376	2.4	0.08	0.04	3.50	1.50
99WT44_g21	0.5336	0.0056	0.06901	0.0005	0.38439	434	3.7	430.2	3	443	24	430.2	1.5	0.03	0.01	1.10	0.69
99WT44_g75	0.838	0.01	0.1	0.00068	0.52091	617.7	5.8	614.4	4	638	24	614.4	2	0.04	0.01	0.76	0.71
99WT44_g78	0.8673	0.008	0.10303	0.00071	0.62066	633.8	4.4	632.1	4.2	646	16	632.1	2.1	0.02	0.00	0.40	0.74
99WT44_g55	0.931	0.03	0.1099	0.0018	0.43203	667	16	672	11	685	67	672	5.5	0.02	-0.01	-0.79	1.33
99WT44_g86	1.641	0.058	0.161	0.003	0.41092	984	22	962	16	1091	61	962	8	0.12	0.02	3.60	0.97
99WT44_g34	1.609	0.048	0.1611	0.002	0.32923	972	19	963	11	990	57	963	5.5	0.03	0.01	1.70	1.29
99WT44_g48	13.07	0.21	0.5197	0.0086	0.87061	2684	15	2697	36	2685	20	2685	10	0.00	0.00	-0.89	0.69
99WT44_g43	0.3669	0.0098	0.04801	0.0005	0.28046	316.8	7.3	302.3	3.1	377	54	302.3	1.55	0.20	0.05	5.60	0.48
99WT44_g17	0.369	0.01	0.04521	0.00047	0.37085	318.6	7.7	285.1	2.9	568	61	285.1	1.45	0.50	0.11	13.00	0.67
99WT44_g82	0.427	0.021	0.0471	0.00039	0.57952	357	14	296.7	2.4	704	84	296.7	1.2	0.58	0.17	23.00	0.71

Appendix D.9: K-Ar data used for Chapter 5.

Geowissenschaftliches Zentrum der Universität Göttingen, Goldschmidtstr. 3, 37077 GÖTTINGEN

K/Ar - Age Determinations Johannes Rembe, Universität Potsdam

Ar - Isotopic Abundance		**Spike-Isotopic Comp.**		**Decay Constants [1/a]:**		**Potassium**	
40 Ar :	99.6000%	40 Ar :	0.0099980%	l e :	5.810E-11	40K :	0.011670%
38 Ar :	0.0630%	38 Ar :	99.9890000%	l b :	4.962E-10	K2O/K :	0.8302
36 Ar :	0.3370%	36 Ar :	0.0009998%			**Atomic Weight [g/mol]:**	
Standard Temperature Pressure (STP)				l tot:	5.543E-10	tot Ar :	39.9477
0° C; 760 mm Hg				**Molar Volume**		40Ar :	39.9624
Normal Atmosphere (DIN 1343)				[ml] :	22413.8	tot K :	39.1027
273,15K; 1013,25 mbar							

Sample	**Spike [No.]**	**K2O [Wt. %]**	**40 Ar * [nl/g] STP**	**40 Ar * [%]**	**Age [Ma]**	**2s-Error [Ma]**	**2s-Error [%]**
17NP483 2-6 µm	6110	2.08	14.64	86.55	**205.9**	3.6	1.7
17NP483 <2 µm	5966	3.96	28.98	92.61	**214.0**	4.8	2.2
17NP483 <0.2 µm	5965	4.13	28.97	91.19	**205.3**	6.1	3.0
17NP484 2-6 µm	6117	2.78	19.93	93.45	**209.4**	2.3	1.1
17NP484 <2 µm	5972	4.63	35.22	95.72	**205.9**	2.9	1.4
17NP484 <0.2 µm	5971	5.28	37.23	93.72	**206.4**	2.3	1.1
17NP485 2-6 µm	6118	3.23	22.55	80.85	**204.6**	3.1	1.5
17NP485 <2 µm	5929	4.22	29.61	92.43	**205.6**	4.6	2.3
17NP485 <0.2 µm	5928	4.83	33.95	94.58	**205.9**	4.7	2.3
17NP486 2-6 µm	6183	0.98	6.54	78.72	**196.9**	4.3	2.2
17NP486 <2 µm	5927	3.83	26.81	96.77	**204.9**	3.3	1.6
17NP486 <0.2 µm	5926	3.24	22.04	90.69	**199.4**	4.3	2.1
17NP487 2-6 µm		0.68	4.95	69.53	**213.5**	5.2	2.4
17NP487 <2 µm	5925	1.48	9.61	82.07	**190.7**	2.5	1.3
17NP487 <0.2 µm	5924	1.89	14.43	78.44	**222.8**	5.0	2.2